On Aspects of Large-Eddy Simulation Validation for Near-Surface Atmospheric Flows

Dissertation

zur Erlangung des Doktorgrades der Naturwissenschaften
im Fachbereich Geowissenschaften
der Universität Hamburg

vorgelegt von

Denise Hertwig

aus
Hamburg

Hamburg

2013

Als Dissertation angenommen vom Fachbereich Geowissenschaften der Universität Hamburg

auf Grund der Gutachten von Prof. Dr. Michael Schatzmann,
Prof. Dr. Bernd Leitl
und Prof. Dr. Ian P. Castro.

Hamburg, den 29. Januar 2013

Prof. Dr. Jürgen Oßenbrügge
(Leiter des Fachbereichs Geowissenschaften)

Abstract

The availability of *suitable* and *reliable* reference data together with the application of *model-specific* comparison methods are the essential ingredients to establish confidence in the capabilities of a numerical model and to truly assess its strengths and limitations. This thesis is motivated by the striking lack of proportion between the increasing use of large-eddy simulation (LES) as a standard modeling technique in micro-meteorological research as opposed to the level of scrutiny that is commonly applied to the quality of the generated numerical predictions.

With this study, I suggest and apply a novel validation strategy for LES consisting of a *multi-level hierarchy* of comparative analysis methods. Unlike standard LES validation procedures that are based on the comparison of low-order statistical moments, the new approach advocated here specifically aims at the *time-dependent nature* of the problem. The sequence in which statistical quantities are compared mirrors the increase of information provided by the analysis methods. The target area is turbulent flow in the near-surface atmospheric boundary layer. The test scenario for the validation approach is urban flow in the city of Hamburg, Germany. Qualified reference data are generated in the boundary-layer wind tunnel facility at the University of Hamburg through high-resolution flow measurements in a scale-reduced model. Fine-meshed numerical simulations are conducted at the U.S. Naval Research Laboratory in Washington, D.C., with implicit LES.

On the basis of an initial *exploratory data analysis* of mean flow and turbulence statistics, a high level of agreement between simulation and experiment is apparent. Inspecting frequency distributions of the underlying instantaneous data, however, proves to be necessary for a more rigorous assessment of the overall prediction quality. From histograms, local accuracy limitations caused by under-resolution as well as particular strengths of the model to capture complex urban flow features are readily determined. Further crucial information about the physical validity of the LES need to be obtained from *eddy statistics*. Comparisons of temporal autocorrelations, integral time scales, and auto-spectral energy densities show that the simulation reliably reproduces statistical characteristics of the energy and flux-carrying roughness sublayer structures. At higher elevations, however, inflow generation artifacts are reflected in dubiously short fluctuation time scales and energy peaks that are dislocated toward high frequencies. With the comparison of scale-dependent flow statistics, to which the preceding diagnostics have been blind, the emphasis eventually shifts to *structure identification*. The quadrant analysis of the vertical turbulent momentum flux discloses strong similarities between ejection-sweep patterns and the occurrence of rare, but extreme, flux events in roof-level vicinity and above the canopy layer. Further scale-wise comparisons of wavelet-coefficient frequency distributions and associated high-order statistics reveal consistent location-dependent intermittency patterns induced by eddies in the energy-production range.

Compared with usual methods that rely on single figures of merit, the detailed, multi-level validation strategy presented in this thesis allows to draw more wide-ranging and tenable conclusions about the quality of the simulation and to specify the model's fitness for purpose in greater detail. The proposed validation concept has the potential to be used as a starting point for community-wide activities aiming at the formulation and harmonization of best-practice standards for the quality assurance of micro-meteorological eddy-resolving simulations.

Keywords: large-eddy simulation, atmospheric boundary-layer flow, model validation, urban turbulence, boundary-layer wind tunnel, time-series analysis, structure identification

Kurzfassung

Die Verfügbarkeit *geeigneter* und *verlässlicher* Referenzdaten sowie der Einsatz *modell-spezifischer* Vergleichsmethoden sind essenzielle Bestandteile einer eingehenden Qualitätsprüfung numerischer Modelle. Die Motivation der vorliegenden Arbeit beruht auf der erkennbaren Diskrepanz zwischen der zunehmenden Anwendung der sogenannten Grobstruktursimulation (engl.: *large-eddy simulation*, LES) auf mikro-meteorologische Fragestellungen und dem oftmals geringen Nachdruck, mit dem die Qualität der dabei erzielten Prognosen kritisch hinterfragt wird.

In dieser Studie entwerfe und erprobe ich einen neuen Ansatz zur differenzierten LES-Validierung, bestehend aus einer *mehrstufigen Abfolge* vergleichender Analysemethoden. Im Gegensatz zu in der Praxis gängigen Verfahren, die auf den Vergleich rein mittelwert-basierter Größen abzielen, ist das hier vorgestellte Validierungskonzept insbesondere auf den *zeitabhängigen Charakter* der LES abgestimmt. Die Reihenfolge, in der die jeweiligen Vergleichsanalysen durchlaufen werden, spiegelt dabei deren anwachsenden informativen Gehalt wider. Turbulente Strömungsfelder der bodennahen atmosphärischen Grenzschicht sind das Zielgebiet der Studie. Der Testfall zur Erprobung des neuen Validierungsansatzes ist urbane Turbulenz in der Hansestadt Hamburg. Hierfür werden qualifizierte Referenzdaten aus hochauflösenden Strömungsmessungen in einem maßstäblich verkleinerten Stadtmodell im Grenzschichtwindkanal-Labor der Universität Hamburg gewonnen. Hochaufgelöste numerische Strömungssimulationen, basierend auf impliziter LES, werden am U.S. Naval Research Laboratory in Washington, D.C., durchgeführt.

Der einleitende *klassische Vergleich* mittlerer Strömungs- und Turbulenzgrößen deutet auf ein hohes Maß an Übereinstimmung zwischen Simulation und Experiment hin. Als notwendig für eine eindeutigere Einschätzung der Simulationsqualität erweist sich allerdings die Untersuchung von Häufigkeitsverteilungen der zugrundeliegenden Instantanwerte. Sowohl Einschränkungen der Modellgüte durch das gewählte Gitter als auch besondere Stärken der LES bei der Reproduktion komplexer urbaner Strömungsmuster lassen sich hier erkennen. Zusätzlich werden wesentliche Informationen über den physikalischen Gehalt der Simulation aus *Wirbelstatistiken* erschlossen. Durch den Vergleich zeitlicher Autokorrelationen, integraler Zeitskalen und turbulenter Energiedichtespektren zeigt sich, dass elementare statistische Charakteristiken der großskaligen, energiereichen Wirbel innerhalb der urbanen Rauhigkeitsschicht verlässlich wiedergegeben werden. In größeren Höhen führen Artefakte der Einstrombedingungen allerdings zu unrealistisch kurzen Fluktuationszeiten und hochfrequenten Energiedichtemaxima. Schließlich verlagert sich die Validierung auf den Bereich der *Strukturerkennung*, die durch skalenabhängige Analysen Einblicke in die raumzeitliche Struktur der Strömung erlaubt. Quadrantanalysen des vertikalen turbulenten Impulsflusses zeigen in diesem Zusammenhang weitgehende Übereinstimmungen dominanter *ejection-sweep* Muster sowie des Auftretens seltener, aber intensiver Impulsfluss-Episoden oberhalb der Hindernisschicht. Zudem belegen Häufigkeitsverteilungen experimenteller und numerischer Wavelet-Koeffizienten die qualitative Kongruenz ortsabhängiger Intermittenzmuster der dominanten Wirbelstrukturen.

Im Vergleich zu etablierten Methoden, die auf eindimensionalen Bewertungsmaßstäben basieren, ermöglicht das hier entworfene Validierungskonzept weitreichendere Aussagen zur Simulationsgüte und erlaubt somit, belastbarere Rückschlüsse über die Eignung des Modells für seinen Einsatzzweck zu ziehen. Der Validierungsansatz kann somit auch als Ausgangspunkt interdisziplinärer Aktivitäten zur Etablierung und Harmonisierung umfassender Qualitätssicherungsstandards für wirbelauflösende mikro-meteorologische Modelle dienen.

Schlagwörter: Grobstruktursimulation (LES), atmosphärische Grenzschichtströmung, Modellvalidierung, urbane Turbulenz, Grenzschichtwindkanal, Zeitserienanalyse, Strukturerkennung

Acknowledgments

"When you come to the end of your rope,
tie a knot and hang on."

Franklin D. Roosevelt
(— *32nd President of the United States, 1882–1945.*)

Without the love, support and understanding of my extraordinary family and friends, this thesis would have never been written. I thank you for believing in me, for your constant encouragement, for tolerating my absence during the tough times, and for giving this story a happy ending. — This is for you.

In the course of my dissertation, I had the privilege to meet and collaborate with great scientists in innovative research projects. This I owe to my advisers, Michael Schatzmann and Bernd Leitl. Their invaluable advice and the freedom they allowed me for my PhD studies helped me to develop my own research profile. I believe that they were among the first to really grasp the dimensions and consequences of the LES validation issue in micrometeorology and environmental wind engineering and to point this out to the scientific community – and I am very grateful that they trusted me to deal with this topic.

The beauty and challenges of LES were really laid open to me by Evgeni Fedorovich of the University of Oklahoma, who was a great inspiration for many aspects of this thesis and whom I would like to thank for giving me new research perspectives.

I thank the entire wind-tunnel group at the University of Hamburg for the great years, for an inspiring working environment, and for many unforgettable moments. I thank all colleagues and students who were involved in the *"Hamburg Pilot Project"* for their time and energy that made it a success. A special thanks goes to Christine Peeck for her invaluable support during the wind-tunnel flow measurements and the analysis of the field data. Stephan Werk is thanked for the thorough processing of the Hamburg geometry and topography data (it was a pain in the neck!) and the technical support during the wind-tunnel campaigns.

A big thanks is directed to Gopal Patnaik, Jay Boris, Mi-Young Obenschain and other collaborators of the Naval Research Laboratory in Washington, D.C., for the great teamwork in the *Pilot Project*, for providing the LES data for this study, for numerous critical and constructive discussions about aspects of this work, and for always being very open-minded when it comes to experiments and the improvement of numerical models.

I express my sincere appreciation to Susanne Fischer, Holger Poser, Peer Rechenbach and other partners in the *Pilot Project* at the Department of the Interior and Sports of the Free and Hanseatic City of Hamburg for very actively proving that collaborating with administrative bodies cannot only be very effective but also be fun. A special thanks goes to Susanne Fischer for providing much needed moral support during the final stages of the thesis-writing.

A further thanks is directed to Ingo Lange at the University of Hamburg for giving access to the meteorological tower data in Billwerder, for answering my numerous questions about the data records, for providing photographs of the field site and for his constructive review of the field data analysis part of the thesis.

The wavelet analysis approach in the validation study would not have got into its final shape without the helpful discussions with Romain Nguyen van yen of the Free University of Berlin. Romain had the talent to guide me to unravel the mathematical 'mysteries' of the technique and to achieve a better understanding of its strengths and limitations with a view to the analysis of turbulent flows.

I am grateful for the many discussions with Jörg Franke of the University of Siegen about approaches in computational fluid dynamics, numerical schemes and efforts in model validation ranging from engineering to micro-meteorological applications. I also wish to thank Heinke Schlünzen at the University of Hamburg for her insightful comments on this work from the perspective of numerical modeling in boundary-layer meteorology.

Giorgos Efthimiou, Nektarios Koutsourakis, and John Bartzis at the University of West Macedonia in Greece are acknowledged for generously sharing their knowledge about numerical urban flow and dispersion modeling with Reynolds-averaged Navier-Stokes and large-eddy simulation approaches with me and for being great collaborators in the IKYDA MODEX project.

I also would like to express my appreciation to the librarians at the Center for Marine and Atmospheric Sciences (ZMAW) for helping me many times with 'hard-to-get' articles, with the retrieval of gray-literature reports, and for the support in the bibliographic search about LES publications.

Last but not least, I thank the members of my thesis committee for taking the time and effort to review this work of three years.

The study presented with this thesis was conducted in the framework of the '*Hamburg Pilot Project*' funded by the German Federal Office of Civil Protection and Disaster Assistance and by the Free and Hanseatic City of Hamburg.[1] Parts of the wind-tunnel model construction were financially supported by the KlimaCampus at Hamburg University.

The dissertation project was conceptually supported through a (non-material) scholarship from the German National Academic Foundation (Studienstiftung des deutschen Volkes).

[1]Projekt: 'Entwicklung eines Werkzeugs zur Optimierung der Einsatzsteuerung bei Gefahrstofffreisetzungen in Stadtgebieten'; *BBK III.1-413-10-364*.

Contents

Nomenclature

Acronyms & Abbreviations

ABL	Atmospheric Boundary Layer
AGL	Above Ground Level
ASL	Atmospheric Surface Layer
ASME	American Society of Mechanical Engineers
BL	Comparison Location Identifier
CBL	Convective Boundary Layer
CFD	Computational Fluid Dynamics
COSMO	Comprehensive Outdoor Scale Model Experiments
COST	Cooperation in the Field of Scientific and Technical Research
CT	Contaminant Transport
CWT	Continuous Wavelet Transform
DAPPLE	Dispersion Field Study in London
DES	Detached-Eddy Simulation
DFT	Discrete Fourier Transform
DM	Comparison Location Identifier
DNS	Direct Numerical Simulation
DWT	Discrete Wavelet Transform
ESDU	Engineering Sciences Data Unit
EWTL	Environmental Wind Tunnel Laboratory at Hamburg University
FAST3D-CT	Urban Aerodynamics LES code developed by NRL
FCT	Flux-Corrected Transport
FFT	Fast Fourier Transform
FS	Full Scale
GK3	Gauss-Krüger (Zone 3)
HATS	Horizontal Array Turbulence Studies
ILES	Implicit Large-Eddy Simulation
IQR	Interquartile Range
ISL	Inertial Sublayer
JPDF	Joint Probability Density Function
JU2003	Joint Urban 2003 Atmospheric Dispersion Study, Oklahoma City
K41	Kolmogorov (1941) Theory
LES	Large-Eddy Simulation
LDA	Laser Doppler Anemometry/Anemometer
NRL	U.S. Naval Research Laboratory

MILES	Monotone Integrated Large-Eddy Simulation
M-O	(Monin-)Obukhov Similarity Theory
MUST	Mock Urban Setting Test Field Study
NCAR	National Center for Atmospheric Research
PBL	Planetary Boundary Layer
PIV	Particle Image Velocimetry
POD	Proper Orthogonal Decomposition
RANS	Reynolds-Averaged Navier Stokes (Equations)
RM	Comparison Location Identifier
RMS	Root-Mean-Square
RSL	Roughness Sublayer
SE	Standard Error
S & H	Sample-and-Hold Resampling
SBL	Stable Boundary Layer
SFS	Subfilter Scale
SGS	Subgrid Scale
TKE	Turbulence Kinetic Energy
UCL	Urban Canopy Layer
UTM32	Universal Transverse Mercator (Zone 32)
VALIUM	Dispersion Field Study in Hannover
VDI	Verein Deutscher Ingenieure (Association of German Engineers)
VLES	Very Large-Eddy Simulation
WMO	World Meteorological Organization
WT	Wind Tunnel (Scale)

Roman symbols

a_{ij}	Anisotropic Reynolds stress tensor
b_{ij}	Normalized anisotropic Reynolds stress tensor
C	Kolmogorov constant
C_e	Universal constant
C_{ii}	Temporal autocovariance function
$C_{k,u,\mu}$	Model constants
C_s	Smagorinsky constant
$\mathcal{C}_{ij}$	Cross stress
C_ψ	Admissibility constant (wavelet analysis)
$C_{1C,2C,3C}$	Barycentric coordinates of b_{ij}
Co_{ij}	Co-spectrum
Coh_{ij}	Spectral coherence
c	Phase speed
d_0	Displacement height

Ex	Flux exuberance, $Ex = (S_1 + S_3)/(S_2 + S_4)$
E_{ii}	Auto-spectral energy density
E_{ij}	Cross-spectral energy density
E^{ψ}	Global wavelet energy density spectrum
$\mathcal{E}$	Expectation operator
Fr	Froude number (densimetric)
f	Frequency
f_c	Coriolis parameter
$f_{iq,i\Theta}$	Subfilter-scale mass and heat fluxes
f_{Ny}	Nyquist frequency
f_r	Sampling-frequency to data-rate ratio
f_s	Sampling frequency
f_{ψ}	Characteristic wavelet frequency
G	LES filter function
g	Gravitational acceleration
H	Local building height
$\mathcal{H}$	Heaviside step function
H_c	Hole size (quadrant analysis)
$\mathrm{H_m}$	Mean building height
H_r	Height of roughness element
$\mathcal{H}_0$	Null hypothesis
h_e	Effective numerical grid size
h_i	Numerical grid size in ith direction
I_i	Trigger function (quadrant analysis)
K	von Kármán constant
k	Turbulence kinetic energy
k_s	SFS kinetic energy
L	Monin-Obukhov length
$\mathcal{L}$	Characteristic flow length scale
$\mathcal{L}_{ij}$	Leonard stress
L_{ref}	Reference length scale
ℓ	Eddy length scale
ℓ_{DI}	Eddy scale limit of the dissipation range
ℓ_{EI}	Eddy scale limit of the production range
ℓ_{ii_x}	Autocorrelation length scale in x-direction
ℓ_m	Mixing length
ℓ_s	Smagorinsky length scale
ℓ_t	Characteristic eddy length scale
ℓ_0	Integral length scale
N_{ψ}	Wavelet function normalization factor
$\dot{N}$	Mean LDA data rate
n	Translation (location) parameter (wavelet analysis)

$\mathcal{P}$	Production rate of turbulence kinetic energy
$\mathcal{P}_r$	Production rate of SFS kinetic energy
Pr_t	Turbulent Prandtl number
p	Modified pressure
p_d	Dynamic pressure
Q^i	ith quartile of a sample distribution ($i = 1, 2, 3$)
Q_i	Reynolds stress quadrant ($i = 1, \ldots, 4$)
Q_{ij}	Quadrature spectrum
q	Water vapor concentration
R_{ii}	Temporal autocorrelation coefficient
R_{ij}	Reynolds stress correlation coefficient
$\mathcal{R}_{ij}$	SFS Reynolds stress
Re	Flow Reynolds number, $Re \equiv \mathcal{U}\mathcal{L}/\nu$
Re_{crit}	Critical Reynolds number, $Re_{\text{crit}} \equiv U_{\text{ref}_{\text{crit}}} L_{\text{ref}}/\nu$
Re_{H}	Reynolds number based on mean building height, $Re_{\text{H}} = U_{\text{H}}\text{H}_{\text{m}}/\nu$
Re_{ref}	Reference Reynolds number, $Re_{\text{ref}} \equiv U_{\text{ref}} L_{\text{ref}}/\nu$
Re_λ	Taylor-scale Reynolds number, $Re_\lambda \equiv \sigma_u \lambda/\nu$
Re_0	Turbulence Reynolds number, $Re \equiv \sigma_u \ell_0/\nu$
Ri_f	Flux Richardson number
Ri_g	Gradient Richardson number
Ro	Rossby number
$\mathcal{S}$	Characteristic strain rate
S_i	Relative contribution of the ith Reynolds stress quadrant
S_{ii}	Two-sided auto-spectral energy density
S_{ij}	Strain-rate tensor of the mean flow
Sc_t	Turbulent Schmidt number
s	Scale (dilation) parameter (wavelet analysis)
s_{ij}	Strain-rate tensor
T	Duration; averaging time scale
T_a	Temperature of air
T_i	Stress-fraction occurrence rate (quadrant analysis)
T_t	Particle transit time
T^ψ	Local wavelet energy density spectrum
t	Time
t_l	Time lag
U	Streamwise (longitudinal) velocity component (U_1)
$\mathcal{U}$	Characteristic flow velocity scale
$\mathbf{U}$	Velocity vector, $U_i = (U_1, U_2, U_3) = (U, V, W)$
U_a	Advection velocity
U_d	Horizontal wind direction
U_h	Horizontal wind speed
U_{H}	Mean streamwise velocity at H_{m}

U_g	Zonal component of the geostrophic wind
U_r	Resampled velocity
U_{ref}	Mean streamwise reference velocity
U_∞	Free-stream velocity
u_ℓ	Eddy velocity scale
u_t	Characteristic velocity scale
u_η	Kolmogorov velocity scale
V	Spanwise (lateral) velocity component (U_2)
V_g	Meridional component of the geostrophic wind
$\mathbf{v}_f^H$	High-order numerical flux
$\mathbf{v}_f^L$	Low-order numerical flux
W	Street-canyon width
W	Vertical velocity component (U_3)
$\mathrm{W_m}$	Mean street-canyon width
$W_n(s)$	Wavelet coefficients (scale and location dependent)
x	Streamwise (longitudinal) coordinate (x_1)
$\mathbf{x}$	Spatial position vector, $x_i = (x_1, x_2, x_3) = (x, y, z)$
y	Spanwise (lateral) coordinate (x_2)
z	Vertical coordinate (x_3)
z_r	Blending height
z_{ref}	Reference height
z_0	Roughness length

Greek symbols

α	Power-law exponent of the ABL velocity profile
β	Polar angle
β_2	Kurtosis
Γ	Flux limiter
$\Gamma_{m,h}$	Turbulent diffusivities of mass and heat
γ	LDA laser beam crossing angle
γ_1	Skewness
Δ	LES filter width
δ	Boundary-layer depth
δ_{ASL}	Surface-layer depth
δ_{ij}	Kronecker delta
δ_{RSL}	Roughness-layer depth
$\delta S_{4,2}$	Relative stress difference, $\delta S_{4,2} = S_4 - S_2$
δt	Time step; inter-arrival time
δt_r	Resampling time step
δx_i	Space resolution

$\lvert\delta z\rvert$	Absolute difference between comparison heights
δ_∞	Boundary-layer top
$\epsilon_{\mathrm{input}}$	Input parameter uncertainty
ϵ_{meas}	Measurement uncertainty
$\epsilon_{\mathrm{model}}$	Model uncertainty
ϵ_{num}	Numerical uncertainty
ϵ_{val}	Validation uncertainty
ε	Dissipation rate of turbulence kinetic energy
ε_{ijk}	Levi-Civita permutation tensor
ε_s	SFS dissipation rate
ζ	Monin-Obukhov stability parameter
η	Kolmogorov length scale
Θ	Potential temperature
Θ_0	Reference value of potential temperature
κ	Wavenumber
Λ_i	Peak wavelength/frequency
λ	Taylor micro-scale length scale
λ_i	Eigenvalue (anisotropy analysis)
μ	Dynamic (molecular) viscosity
ν	Kinematic (molecular) viscosity
ν_t	Turbulent viscosity (eddy viscosity)
ξ	One invariant of the anisotropy tensor b_{ij}
ρ	Density
σ_i	Root-mean-square velocity
σ_i^2	Velocity variances
σ_{ij}	Viscous stress tensor
σ_s	Inherent uncertainty (stochastic variability)
τ_{ii}	Autocorrelation time scale
τ_{ij}	Reynolds stress tensor
τ_{ij}^a	Anisotropic subfilter-scale stress tensor
τ_{ij}^h	Numerical stress tensor
τ_{ij}^s	Subfilter-scale stress tensor
τ_η	Kolmogorov time scale
τ_0	Integral time scale
υ	One invariant of the anisotropy tensor b_{ij}
Φ	Wind-tunnel model blockage coefficient
ϕ	Meteorological wind direction angle
ϕ_c	Universal function of dimensionless mass gradient
ϕ_h	Universal function of dimensionless temperature gradient
ϕ_m	Universal function of dimensionless wind shear
ψ	Wavelet function (mother wavelet)

ψ_{m}	Morlet wavelet
$\psi_{s,n}$	Two-parametric wavelet function (daughter wavelet)
ψ_2	Mexican-hat wavelet (Marr wavelet)
Ω_j	Angular velocity of the Earth
ω	Angular frequency, $\omega = 2\pi f$
ω_0	Central frequency of ψ_{m} (*here*: $\omega_0 = 6$)

Operators, Superscripts & Subscripts

$\langle A \rangle_n = \langle A \rangle$	Ensemble average
$\langle A \rangle_t = \overline{A}$	Time average
$\langle A \rangle_t^c = \overline{(A)}^c$	Conditional time average
$\langle A \rangle_{x_i} = \widetilde{A}$	Space average
$\mathcal{E}(A)$	Expectation value (first moment)
$\mathrm{Im}(A)$	Imaginary part
$\mathrm{Re}(A)$	Real part
a'	Fluctuation about ensemble or time average
$a^{\star}$	Dimensionless (referenced) quantity
a^*	Complex conjugate
$\hat{a}$	Fourier transform
a_{exp}	Experimental quantity
a_{fs}	Quantity in full scale
a_{les}	LES quantity
a_{ref}	Reference quantity
a_{wt}	Quantity in wind-tunnel scale

1 Introduction

"Every great and deep difficulty bears in itself its own solution.
It forces us to change our thinking in order to find it."

Niels Bohr
(— *Danish physicist, 1885–1962.*)

Research on atmospheric turbulence rests on the triad of *theory*, *experiment*, and *computation*, whose interactions are subject to historical and scientific development.

In planetary boundary-layer research, *computational fluid dynamics* (CFD) approaches not only have proven to be a crucial complement to observations and theoretical concepts, but have augmented the fundamental understanding of complex atmospheric processes in a way that was hardly conceivable before. As pointed out by Zabusky (1981, 1984), computers have the power to shine "(...) the light of inspiration into areas which had been thought devoid of possible new concepts or new fundamental truths" and to "(...) discover unforeseen linkages among ideas." This appraisal closely mirrors the developments in turbulence research after the disenchantment following the search for a unified theory. In the 1970s, increasing computer capacity for the first time facilitated the use of eddy-resolving methods to *simulate* turbulence, resulting in a tremendous gain of information about its structure.

Meanwhile, methods like *large-eddy simulation* (LES) are technically applicable to high Reynolds number flows of the atmospheric boundary layer (ABL) with computational costs that have become acceptable to a broad research community. Providing the potential to realistically describe the spatio-temporal evolution of turbulent processes, LES emerged as a fashionable research tool in micro-meteorology and wind engineering and is currently advancing to applications for regulatory purposes, too. Whether or not the simulation outcome agrees with the physical reality, however, depends on different components of the modeling chain, which require critical review. This involves the verification of mathematical parameterizations, conceptual and numerical implementations, and – eventually – the *validation* of simulation results as a conglomeration of all possible uncertainties. This task demands comprehensive exchange and communication within the research triad, offering room for synergy effects from which all three communities can equally benefit.

1.1 Motivation & background

About 30 years ago, Wyngaard et al. (1984) anticipated that large-eddy simulation would be applied as a *"numerical laboratory"* alongside the trend toward an increasing use of computation, away from experimental testing. While in the 1980s eddy-resolving methods were the prerogative of few universities and research institutions developing and operating "home-made" research codes, today, commercial and open-source alternatives are available to a large community. Progress in supercomputing, computer clusters, and parallelization techniques further fostered the accessibility of LES. Most of the prevalent commercial CFD packages now provide their users with the option to switch into an LES mode and perform time-dependent calculations with a wide range of subfilter-scale (SFS) schemes. However, emerging notions like "CFD for the masses" or "click-and-point CFD" (Coirier, 2005) indicate that this development also provokes reservations by the community.

The growing interest in LES and its application can, for example, be disclosed by the corresponding scientific output. Figure 1.1 depicts the increase of research publications per year that are concerned with LES, its theory, applications, and advancements.[1] Subject areas with a clear connection to fluid mechanics, physics or mathematics (e.g. geosciences, engineering disciplines, computational physics, computer sciences, applied mathematics) have been grouped into *All Relevant Categories*. In addition, the fraction of publications that have a direct connection to *Atmospheric Sciences* is shown. Publication years of some of the pioneering works on LES are indicated as well.[2] While it is not claimed that the presented time record is precise with regard to absolute numbers, it mirrors the general trend. The number of publications per year rose almost exponentially during the last two decades, with more than 900 articles being published in 2010 alone. The number of LES publications related to studies of the atmosphere grew as well, although the fraction of publications within all relevant categories decreased over the years, despite the fact that the technique originated in the field of meteorology. The majority of today's scientific articles about LES stems from studies concerned with engineering problems.

Given these developments and the fact that comprehensive experiments in the field or laboratory can be quite costly when it is aimed at a high level of description (e.g. through measurements of multi-point time-dependent information about the quantities of interest), Jiménez (2003) discusses whether turbulence simulations will eventually replace experimental observations. As far as the *direct numerical simulation* (DNS) of atmospheric boundary-layer flow at realistically high Reynolds numbers is concerned, the answer is – and will most probably remain for the foreseeable future – *no*. Voller and Porté-Agel (2002) provided an estimate of the rate of increase of computational grid sizes over time, measured by the node number, and discovered a coherence with *Moore's law*, which describes the growth of computing power by a doubling every 1½ to 2 years (Moore, 1965).

[1] The *Web of Science* online repository was used for this search. It has been restricted to peer-reviewed journal articles, letters, books, and reviews as well as to articles published in conference proceedings.

[2] E.g. suggestion of the SFS closure approach by Smagorinsky (1963) and Lilly (1967); landmark study of turbulent channel flow by Deardorff (1970a); advancement of the technique by Schumann (1975); spectral LES of atmospheric boundary-layer flow by Moeng (1984). It should be noted that the term "large-eddy simulation" was presumably established around the mid-1970s. Therefore, prior articles about the technique without explicit reference to LES are not found by the search algorithm.

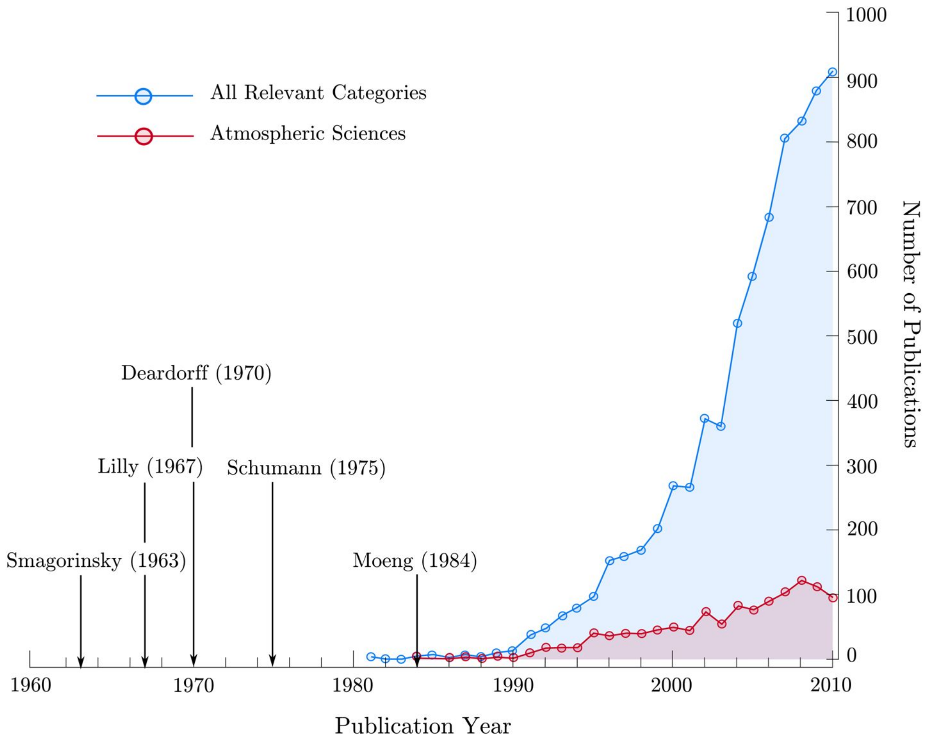

Figure 1.1: Time series showing the increase of scientific publications on LES.

Despite large bounds of uncertainty, the trend derived from the analysis is revealing: A full three-dimensional DNS of a turbulent atmospheric boundary-layer with a domain length of 10 km and a mesh size of 1 mm is expected not to become realizable before 2070.

— *And what about LES?* In addition to being far less cost-intensive than the DNS of all turbulent scales, the large-eddy approach is of great attraction for applied and fundamental research on flow situations that are believed to be primarily controlled by the energy-containing eddies. Examples are studies on turbulent exchange processes, dispersion of airborne contaminants, as well as flows over complex terrain, heterogeneous ground, and in built-up environments. Those are problems that are not easily approached with classic *in-situ* experimental techniques, which still are the standard in boundary-layer research and micro-meteorology. Under the understandable impression of witnessing "reality" in LES visualizations, the modeling character of the technique often takes a back seat and the predictions are being increasingly recognized as the "ground truth" (Wyngaard and Peltier, 1996). As for DNS, however, the numerical approximation scheme as well as the initial and boundary conditions inevitably introduce uncertainties to the calculation, which, together with uncertainties generated by the SFS parameterizations, add to the total error of the simulation. This bias can only be identified in comparison to a suitable *reference*. The time-dependent nature of the problem complicates the assessment of the prediction quality, making the validation of LES results a great challenge.

1.1.1 LES validation

The validation of a numerical model primarily depends on two essential prerequisites: the *availability* of suitable reference data sets and the *applicability* of comparison strategies that allow for *model-specific* performance assessments.

Starting with the first aspect, the suitability of a reference experiment is primarily connected to the level of description provided by the numerical model. In this context, Bradshaw (1972) – being aware of the rapid advancements in computer technology – pictured the *"fact gap"* that had already emerged between the capability to simulate turbulent flows in unprecedented detail and the potential to determine the accuracy of such predictions based on qualified experiments stating, "(...) too many computers chasing too few facts." In their review of the role of experiments in an era of turbulence simulation, Wyngaard and Peltier (1996) conclude that this gap "(...) seems wider than ever in micrometeorology." In the case of large-eddy simulation or other eddy-resolving techniques, the experimental design should allow for the characterization of flow structures, since the depth in which the validation can be performed is given by the level of insight that is derivable from the reference data. In an ideal case, the quantities of interest are measured with a spatio-temporal resolution that is comparable to that of the numerical output. Alongside the computational quantum leap of the last decades, the experimental side experienced its own revolutions with respect to measurement techniques both in the field and the laboratory. Today, state-of-the-art *in-situ* instrumentation usually offers high temporal resolution, while new multi-point measurement techniques and remote sensing approaches have started to become applicable for detailed and reliable studies of the space structure of the atmospheric boundary layer. Bradshaw's fact gap, thus, is shrinking.

However, even if suitable reference data for the specific problem of interest are available or can be produced, there is still the need to formulate comparison strategies and accuracy limits by which the model performance can be adequately assessed. Since the non-linear nature of turbulence prohibits the direct comparison of *instantaneous* fields or time series from experimental observations and numerical simulations, the validation has to rely on statistical approaches. If conducted at all, comparisons between LES and experiments typically restrict to low-order statistical moments like averages and variances. Thus, the depth of the comparison is strictly speaking only sufficient for the quality appraisal of simulations that are based on ensemble-averaged conservation equations. It is clear that in case of turbulence-resolving models like LES this approach only scratches the surface and in particular does not allow for an appraisal as to what degree the code captures the transient structure of the turbulent flow. Here, established methods from the field of signal analysis and flow pattern recognition have the potential to provide further insight into turbulence characteristics in the reference experiment and the simulation. This can open new ways to define quality criteria by which to assess the model output.

While the need for the validation step is generally recognized in both the experimental and numerical communities, so far no real validation standard for LES has been established. The increasing use of eddy-resolving methods for planning and regulatory purposes, however, enhances the urgency of this task. Due to the real-life impact the simulation can have, a quantitative evaluation of the likely bounds of uncertainty is crucial if the model is going to be applied to problems yet unsolved.

1.2 Scope & contribution of this work

This thesis approaches the LES validation challenge by proposing a novel, multi-step comparison concept that allows to study the simulation quality in detail and to derive wide-ranging and credible conclusions about the fitness of the model for its intended use. The target area is flow in the near-surface atmospheric boundary layer.

The following general questions are raised and elaborately discussed:

1. How can the spatio-temporal predictions of LES be validated?
2. What information is necessary and/or sufficient for the performance quality appraisal?
3. What level of detail is needed, and how is this range connected to the purpose of the simulation and/or the expectation toward the model performance?

Instead of relying on single figures of merit, the validation concept introduced here represents a holistic approach that comprises the comparative analysis of a multitude of relevant flow quantities. By putting the main focus on eddy statistics and the characterization of turbulence structures in simulation and experiment, the procedure specifically aims at the heart of LES: the time-dependent representation of energy-containing eddies.

The suitability of the proposed validation hierarchy is verified on the basis of a particularly complex representative of atmospheric flow: turbulence in an urban environment. For this field of application, LES offers great potential for an improved understanding, characterization, and realistic prediction of flow and dispersion processes. The results, in turn, can have strong implications for real-life applications like emergency response activities in connection with the release of hazardous contaminants (– as in the case of the present study), wind comfort assessments or urban design and planning decisions focusing on street ventilation or other micro-climatic issues. However, for flow near the surface and within complex geometries LES tends to be used beyond its ideal operating point with respect to the relevance of parameterizations and the influence of imposed inflow and boundary conditions. Thus, in studies of the urban roughness layer and the atmospheric surface layer, there is much room for LES improvements as a result of comprehensive and problem-specific comparisons with qualified experiments.

The high-density urban center of the city of Hamburg, Germany, represents the test environment for this study. Turbulent flow is simulated by the U.S. Naval Research Laboratory with a fine-meshed, eddy-resolving aerodynamics code based on an implicit LES approach. With respect to resolution, domain size, and computing times, the code is a representative of advanced state-of-the-art techniques. The reference database is generated from well-documented measurements in an urban scale-model, mounted in the specialized boundary-layer wind-tunnel facility of the University of Hamburg.

The validation is carried out as a *blind test*: No experimental results were communicated to the numerical side in the run-up to the simulations, apart from necessary information about inflow and boundary conditions of the laboratory experiment.

Figure 1.2 shows flow visualizations through the dispersion of passive tracers in the wind tunnel and in the numerical simulation. The scenario illustrates the high spatial variability and general heterogeneity of the urban flow field. The time-dependency of these spatial structures further complicates the comparison of both realizations.

(a) (b)

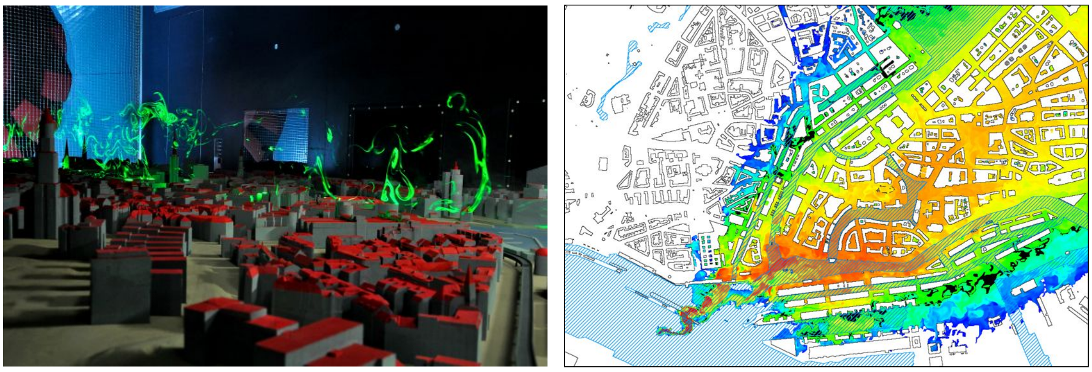

Figure 1.2: (a) Visualization of turbulent flow structures above the wind-tunnel model of Hamburg city using trace particles and a vertical laser-light sheet. Flow is from right to left. (b) Snapshot of a plume dispersion simulation with LES in downtown Hamburg, visualized in a horizontal plane at street level. Flow is from bottom left to top right.

1.2.1 Thesis outline

Following this preface, the thesis starts by setting the scene for the validation study with an introduction to the theory and application of large-eddy simulation in connection with surface layer and urban roughness layer flow fields. This is followed by a discussion on the *status quo* of validation approaches for eddy-resolving numerical methods as opposed to the true demands concerning this simulation type, which then are approached through the introduction of an in-depth LES validation hierarchy. Subsequently provided is a description of the experimental and numerical data sets that are to be compared and a discussion of data properties and their implications for the comparison. The centerpiece of the thesis concentrates on the validation example of urban roughness layer flow, with main conclusions, general recommendations, and implications for future validation efforts being summarized in the final part of the document.

The detailed outline of the respective chapters is as follows:

Chapter 2 — Starting with an introduction to the notion and basic concepts of turbulence, the chapter reviews connections between statistical turbulence theory and prevalent modeling strategies: the steady-state Reynolds-averaged Navier Stokes approach (RANS), large-eddy simulation, and direct numerical simulation. Essential properties of atmospheric boundary-layer flows over homogeneous terrain and in built-up environments are discussed from a micro-meteorological point of view, together with a brief retrospective of example LES studies in these areas.

Chapter 3 — Having set out the inherent difference between large eddy and ensemble-average simulations, this chapter discusses implications for the *validation* of LES results and parameterizations. Following the introduction of terminologies and quality-assurance activities in micro-meteorology, a hierarchy of qualified, model-specific validation methods for a detailed LES validation is proposed. Furthermore, demands on reference data are discussed by focusing on benefits, drawbacks, and prospects of laboratory and field-site experiments. The section concludes with an overview of *a priori* and *a posteriori* LES validation approaches and a brief review of related studies.

Chapter 4 — Introducing the Hamburg city validation test case, this chapter focuses on the discussion of particular experimental and numerical data properties that are relevant for the comparison. The generation of reference data from flow measurements in a boundary-layer wind tunnel as well as the implicit LES approach, which was used to carry out the numerical simulation, are presented together with a critical discussion of the respective levels of physical and geometrical detail, experimental accuracy, data post-processing strategies, and bounds of uncertainty of inferred statistics.

Chapter 5 — This chapter presents results of the detailed comparison of experimental and LES time series of turbulent flow in the roughness sublayer of the inner city of Hamburg. The analysis focuses on the application and problem-oriented expansion of well-known time-series analysis methods and strategies from the field of flow-structure characterization. Starting from the comparison of first and second order statistics, the analysis concentrates on the investigation of sample characteristics revealed by the shape and spread of frequency distributions of instantaneous flow quantities. Temporal autocorrelation information, integral time scales, energy density spectra as well as conditional averaging and joint-probability analyses are employed to disclose structural information. Finally, the comparison of scale-dependent signal characteristics is pursued by means of joint time-frequency analyses of single-point time series with the continuous wavelet transform. The chapter further comprehends critical examinations of the applied approaches, evaluations of their level of insight concerning the LES performance quality, as well as a discussion of benefits and caveats associated with the respective techniques.

Chapter 6 — The concluding section gives a summary of results from the Hamburg validation test case and discusses implications concerning the general suitability of the suggested multi-step validation concept for the conclusive evaluation of eddy-resolving numerical simulations. The outlook indicates possible further extensions of the validation hierarchy given the availability of space-resolving experimental reference data. The thesis closes with a discussion of necessary future steps for the harmonization of LES quality assurance procedures as a joint effort by experimental and numerical communities.

The Appendices A–G provide supplementary information that is referred to in the respective chapters.

2 Theory and Applications

"We believe (...) that, even after 100 years,
turbulence studies are still in their infancy.
We are naturalists, observing butterflies in the wild."

Lumley and Yaglom (2001)
(— *A century of turbulence.*)

2.1 Turbulent flows

2.1.1 Phenomenological perception

The transition from a laminar to a turbulent flow occurs if a dimensionless parameter, denoted as *Reynolds number*, exceeds a critical level. The Reynolds number is defined as $Re = \mathcal{U}\mathcal{L}/\nu$, with $\mathcal{U}$ and $\mathcal{L}$ being characteristic velocity and length scales of the flow, and ν is the kinematic viscosity. Re, thus, can be understood as a weighting between inertial and viscous forces acting on the fluid. Turbulence itself, however, should be regarded as a feature of the flow and not as a property of the flowing matter. As a consequence, leading characteristics of turbulent flows are not determined by molecular properties of the fluid.

Since turbulence is a phenomenon that comes in many different flavors and occurs in nearly all natural and technical flow categories, it is almost impossible to give an exact definition. Nevertheless, there are some features about turbulence that can be regarded as universal. Some of these were reviewed in the text by Tennekes and Lumley (1972) and are reproduced below:

> **Irregularity** — Turbulent flows are irregular and essentially unpredictable. The random nature of turbulence is mirrored in the non-linearity of the governing equations of motion, which are analytically intractable. The seminal work of Lorenz (1963) first revealed the high sensitivity of numerical solutions of deterministic equations to even marginal changes in boundary and initial conditions and provided the foundations of what is now called *chaos theory*.

Three-dimensionality — A turbulent flow field is rotational and three-dimensional with regard to velocity and vorticity and exhibits high variability in space and time.

Diffusivity — Turbulent motions have the ability to effectively mix and redistribute momentum and scalar quantities. Turbulent diffusivity, as a property of a turbulent flow, is much larger than molecular diffusivity, which is an essential characteristic of the fluid itself.

Dissipativeness — In turbulent flows, kinetic energy is constantly transformed into internal energy (i.e. heat) due to the deformation work of viscous shear stresses. Without continuous supply of energy, turbulence ceases and the flow will ultimately relaminarize.

The relevance of these properties can be most easily appreciated by means of observations. Indeed, the roots of our understanding of turbulent flows mostly stem from early experimental work. Apart from measurements of fluid quantities, it was the visualization of turbulent flows that gave new impetus to theoretical and numerical work. Results from first extensive visualization studies revolutionized many branches of turbulence research – most evidently in the field of coherent structure detection. Figure 2.1 shows shadowgraphs analyzed in the pioneering work of Brown and Roshko (1974) of one of the most prominent canonical turbulent flow scenarios: the plane mixing layer.

(a)

(b)

Figure 2.1: Flow visualizations of the plane mixing layer between helium and nitrogen for different flow Reynolds numbers. (a) Flow at low Reynolds number, exhibiting nearly parallel streamlines. (b) Flow at high Reynolds number, showing characteristics of fully turbulent flows. From Brown and Roshko (1974); reproduced with permission from *Cambridge University Press.*

The Reynolds numbers of the mixing layer flow depicted in Figure 2.1a is four times smaller than for the flow scenario shown in Figure 2.1b. Especially in its initial upstream state, the low-*Re* mixing layer appears to be almost laminar, showing parallel streamlines. However, as eddy sizes grow secondary instabilities act on the vortices and the flow clearly becomes turbulent. In the case of the high-*Re* mixing layer, the flow patterns are irregular in every growing stage of the dominant eddies. Clearly identifiable is the large fraction of small-scale structures superimposed on the large vortices. This broadening of the range of turbulent flow scales subject to the Reynolds number is an important characteristic and will be discussed in detail in Section 2.1.4.

2.1.2 Governing equations of fluid motion

The subsequent paragraphs give a brief introduction to the fundamental equations that describe fluid motion. Core assumptions, hypotheses, and some results of seminal works in the field of turbulence theory are discussed in addition. The section mainly follows the textbooks by Tennekes and Lumley (1972), Pope (2000), and Wyngaard (2010).

Hypotheses & frameworks

Fluid motion is usually studied from the viewpoint of continuum mechanics. The so-called *continuum hypothesis* postulates that the fluid can be treated as a continuous medium. Instead of studying the motion of individual atoms or molecules, it is dealt with so-called *fluid elements* or *fluid parcels*. From a practical perspective, this notion is convenient since the governing equations do not have to be solved for every single constituent on a molecular level. The physical justification stems from the differences in characteristic length and time scales, which are significantly larger/longer compared with those of molecular motions in the majority of turbulent flows.

It is also common practice to specify the governing equations of motion for so-called *Newtonian fluids*. In this case, the fluid's molecular viscosity coefficient, μ, only depends on pressure and temperature and is not altered by the influence of external forces acting on the fluid. This feature becomes important for the specification of *surface forces* in the *momentum equation*, introduced later in this section.

Another important predefinition concerns the choice between a *Eulerian* or *Lagrangian description* of fluid motion. In this work, it is exclusively dealt with the Eulerian framework. The fluid velocity $\mathbf{U}$ is expressed as a function of position $\mathbf{x}$ and time t in a fixed reference system. The Lagrangian approach, on the other hand, is based on tracking the motion of fluid elements along their trajectories in space and time.

Navier-Stokes equations

The following and most of the later equations are presented in *Cartesian tensor notation*. Hence, the velocity vector $\mathbf{U}(\mathbf{x}, t)$ is expressed as $U_i = (U, V, W)$ at the spatial positions $\mathbf{x}$ given by $x_i = (x, y, z)$ and at time t. The indices refer to the streamwise (longitudinal), spanwise (lateral), and vertical direction, respectively. Furthermore, the *Einstein summation convention* is used, i.e. it is summed over repeated indices in an expression.

The mass conservation equation or *continuity equation* is given by

$$\frac{\partial \rho}{\partial t} + \frac{\partial \rho U_i}{\partial x_i} = 0 \; , \tag{2.1}$$

where ρ is the density of the fluid. If the density is constant in space and time, the continuity equation reduces to

$$\frac{\partial U_i}{\partial x_i} = 0 \; , \tag{2.2}$$

which implies that the flow is divergence free. Fluids for which Eq. (2.2) holds are called *incompressible*. The concept of incompressibility is applicable for most liquid fluids and for air flow at moderate advection velocities.

The *momentum equation* for a fluid can be derived from Newton's second law. Considering the prerequisites discussed above, the fluid motion is described by

$$\frac{\partial U_i}{\partial t} + U_j \frac{\partial U_i}{\partial x_j} = -\frac{1}{\rho}\frac{\partial p}{\partial x_i} + \frac{1}{\rho}\frac{\partial \sigma_{ij}}{\partial x_j} \; , \tag{2.3}$$

where p is the *modified pressure*, in which effects of gravity are included, and ρ is the density of the fluid. The last term on the right-hand-side of Eq. (2.3) describes effects of surface forces acting on the fluid on a molecular level. For a Newtonian fluid, the *viscous stress tensor*, σ_{ij}, depends linearly on the *strain-rate tensor*, s_{ij}, and is independent of the rate of rotation such that $\sigma_{ij} = 2\mu s_{ij}$. With the strain-rate tensor defined as

$$s_{ij} = \frac{1}{2}\left(\frac{\partial U_i}{\partial x_j} + \frac{\partial U_j}{\partial x_i}\right) \tag{2.4}$$

and assuming an incompressible fluid, Eq. (2.3) becomes

$$\frac{\partial U_i}{\partial t} + U_j \frac{\partial U_i}{\partial x_j} = -\frac{1}{\rho}\frac{\partial p}{\partial x_i} + \nu \frac{\partial^2 U_i}{\partial x_j \partial x_j} \; , \tag{2.5}$$

with $\nu \equiv \mu/\rho$ being the *kinematic viscosity* of the fluid. Equation (2.5) is the so-called *Navier-Stokes equation* in one of its purest forms for non-buoyant, non-rotating flow. Depending on the particular problem that is studied, the appearance of the Navier-Stokes equations can be significantly altered. Concepts like *homogeneity*, *stationarity* or *isotropy* of turbulence can be adopted to further simplify the equation and to allow for an analytical treatment of the problem in very idealized situations. In order to make *numerical* predictions of high Reynolds number flows feasible, the governing equations usually are further modified by introducing averaging techniques and applying statistical concepts to represent turbulent motion.

The enumeration of governing equations is completed by the *thermal energy equation*, which follows from the first law of thermodynamics and describes the conservation of heat, and by the *mass conservation equation for scalar flow constituents* that are transported with the fluid (e.g. atmospheric water vapor or pollutants).

2.1.3 Statistical treatment of turbulence

The mathematical intractability of the Navier-Stokes equations and the random nature of turbulence resulted in the use of statistical approaches to investigate turbulent flows. The seminal contributions by Osbourne Reynolds provided the groundwork for the modification of the fundamental conservation equations by averaging the physical quantities involved. Following the outline by Wyngaard (2010), the next paragraphs give a brief overview of the concept of *Reynolds averaging* and discuss its implications for our understanding of turbulence and as a first step toward the numerical modeling of turbulent flows.

Reynolds averaging

The concept of *Reynolds decomposition* denotes the separation of a turbulent quantity – for example the instantaneous velocity U_i – into a mean value, $\langle U_i \rangle$, and a fluctuating part, u'_i, according to

$$U_i = \langle U_i \rangle + u'_i \ . \tag{2.6}$$

Apart from velocity fields, scalar turbulent quantities like pressure, temperature or density (in case of compressible fluids) can also be separated in the above manner. From the definition of the Reynolds decomposition it is clear that the type of averaging plays an important role. The "native" averaging concept associated with the original investigations of Reynolds (1895) is that of an *ensemble averaging.*[1] The mean velocity of U_i in terms of an *ensemble average* is defined as

$$\langle U_i \rangle_n = \lim_{N \to \infty} \frac{1}{N} \sum_{n=1}^{N} U_i^{(n)}(x_i, t) \ , \tag{2.7}$$

where the summation index $n = 1, \ldots, N$ refers to the individual realization of the turbulent flow, i.e. to the respective member of a representative ensemble of N repetitions of the flow scenario, which were conducted under the same mean boundary conditions. Thus, the ensemble average in its most general representation depends on space and time. From a mathematical perspective, ensemble averaging has ideal properties. As a linear operation it commutes with differentiation and integration (*commutative* property) and it is *distributive*. Two further rules are of great importance: Averaging an already averaged quantity has no effect, and the average of a fluctuating variable vanishes.

The concept of ensemble averaging is widely used in many fields associated with the statistical description of turbulence in a more or less theoretical sense in order to provide a basis for the assumptions used to simplify the governing equations. In the case of most "real-world" applications, however, ensemble averaging is seldom used due to practical limitations connected to this approach.[2] Thus, other averaging techniques are usually invoked to substitute the ensemble mean.

[1] Originally, Reynolds actually used a volume average in his seminal work, but the averaging properties he derived are generally only valid for ensemble averages.

[2] Experimental data, for example, are often available in terms of single-point time series of the quantity of interest. Even if the experiment is repeated, a statistically representative approximation to the ideal limit of $N \to \infty$ is rather unfeasible.

If the flow is *statistically stationary*, i.e. if statistics calculated from the turbulent flow are independent of time, t, and remain invariant under temporal shifts, a *time average* can be used

$$\langle U_i \rangle_t = \frac{1}{T} \int\limits_{t_0}^{t_0+T} U_i(x_i, t)\, dt \; . \tag{2.8}$$

The definition of the time-mean velocity field given by Eq. (2.8) is most often used in practice. However, it is also possible to derive the mean value from a *space average*

$$\langle U_i \rangle_{x_i} = \frac{1}{L} \int\limits_{x_{0i}}^{x_{0i}+L} U_i(x_i, t)\, dx_i \; . \tag{2.9}$$

In the above expression, averaging is performed in one dimension (i.e. along a line of length L). It can be shown that there is an ergodicity of time and space means for a single realization of the flow (Wyngaard, 2010). That is, in the limit of $T \to \infty$ the time mean approaches the ensemble mean if the concept of stationarity is applicable. The same is true for spatial averages derived from Eq. (2.9) for an increasing averaging distance $L \to \infty$.

Reynolds-averaged equations

Applying the concepts of Reynolds decomposition, ensemble averaging and the associated averaging rules to the governing flow equations described in Section 2.1.2 yields the so-called *Reynolds-averaged Navier Stokes* (RANS) equations. For a fluid of constant density, the ensemble averaged continuity equation consists of the following statements

$$\frac{\partial \langle U_i \rangle}{\partial x_i} = 0 \quad \text{and} \quad \frac{\partial u_i'}{\partial x_i} = 0 \; . \tag{2.10}$$

Thus, both the mean and the fluctuating velocity field have zero divergence in the case of an incompressible fluid.

The non-linearity of the advection term in the momentum equation results in a less straightforward representation. Considering the rules of averaging (for details see Pope, 2000), the Reynolds average (here and thereafter denoted by the $\langle \ldots \rangle$ operator) of the substantial derivative (left-hand side of Eq. 2.5) yields

$$\left\langle \frac{dU_i}{dt} \right\rangle = \frac{\partial \langle U_i \rangle}{\partial t} + \frac{\partial \langle U_i U_j \rangle}{\partial x_j} = \frac{\partial \langle U_i \rangle}{\partial t} + \frac{\partial}{\partial x_j} \left(\langle U_i \rangle \langle U_j \rangle + \langle u_i' u_j' \rangle \right) \; , \tag{2.11}$$

introducing the new variable $\langle u_i' u_j' \rangle$ to the momentum equation since the average of the product of fluctuating variables does not vanish. The so-called *Reynolds equation* for the mean flow field of an incompressible fluid, thus, is given by

$$\frac{\partial \langle U_i \rangle}{\partial t} + \langle U_j \rangle \frac{\partial \langle U_i \rangle}{\partial x_j} = -\frac{1}{\rho} \frac{\partial \langle p \rangle}{\partial x_i} + \nu \frac{\partial^2 \langle U_i \rangle}{\partial x_j \partial x_j} + \frac{1}{\rho} \frac{\partial \tau_{ij}}{\partial x_j} \; , \tag{2.12}$$

with the so-called *Reynolds stress tensor*, $\tau_{ij} \equiv -\rho\langle u_i' u_j' \rangle$, as an additional contribution to the time-space behavior of the flow, which only involves velocity fluctuations.

Similarly, Reynolds averaging applied to the heat balance equation and the mass conservation for scalars creates new variables in terms of the so-called *turbulent heat flux* and the *turbulent mass flux*.

Reynolds stress tensor

The Reynolds stress tensor τ_{ij} is a symmetric matrix: $\langle u_i' u_j' \rangle = \langle u_j' u_i' \rangle$. Often, only the quantity $\langle u_i' u_j' \rangle = -\tau_{ij}/\rho$ is investigated, whose correct physical interpretation is that of a *kinematic momentum flux*, as opposed to the *dynamic momentum stress* represented by $-\rho\langle u_i' u_j' \rangle$ as the native expression of the Reynolds tensor.[3] Analogous to the definition of the viscous stress, the Reynolds stress reflects the (mean) transfer of momentum by velocity fluctuations. In a fully turbulent flow at high Reynolds number, the turbulent stresses have a much larger influence on the time-dependency of the mean flow than the viscous dissipation (second and third term on the right-hand-side of Eq. 2.12).

The diagonal components of $\langle u_i' u_j' \rangle$ (i.e. in the case of $i = j$) are called *normal fluxes* (or stresses) and measure the *variances* of turbulent velocities, i.e. $\langle u_1' u_1' \rangle = \langle u_1'^2 \rangle = \sigma_1^2$, $\langle u_2' u_2' \rangle = \langle u_2'^2 \rangle = \sigma_2^2$, and $\langle u_3' u_3' \rangle = \langle u_3'^2 \rangle = \sigma_3^2$. The deviatoric parts of the Reynolds tensor (where $i \neq j$) are *shear fluxes* and measure turbulent *covariances*. Thus, both normal and shear fluxes are measures of second order turbulence moments.

The off-diagonal parts of the Reynolds flux tensor only are non-zero if there is a correlation between the multiplied quantities. Thus, instead of investigating the momentum fluxes, sometimes the degree of correlation between the turbulent variables is studied. This given by the *correlation coefficient tensor*

$$R_{ij} = \frac{\langle u_i' u_j' \rangle}{\sqrt{\langle u_i'^2 \rangle}\sqrt{\langle u_j'^2 \rangle}} = \frac{\langle u_i' u_j' \rangle}{\sigma_i \sigma_j} \ , \tag{2.13}$$

where $R_{ij} \in [-1, 1]$ due to the normalization, and the Einstein summation convention is *not* applied here. In turbulent flows usually exists a strong degree of correlation between the velocity fluctuations. Thus, the influence on the mean flow expressed by τ_{ij} is always significant. Depending on the specifics of the flow, some components of the Reynolds stress tensor can be more important than others, as will be discussed later in connection with atmospheric boundary-layer flows (Section 2.3.1).

Another important quantity can be directly derived from the Reynolds flux tensor: the *turbulence kinetic energy* $k(\mathbf{x}, t)$ (TKE) defined as half of its trace according to

$$k \equiv \frac{1}{2}\langle u_i' u_i' \rangle = \frac{1}{2}\left(\sigma_1^2 + \sigma_2^2 + \sigma_3^2\right) \ . \tag{2.14}$$

The above equation describes the mean kinetic energy of the fluctuating velocity field per unit mass.

[3]In literature, however, stress and flux terminologies are often used interchangeably, which is not correct from a physical point of view, but nevertheless became conventional.

Turbulence closure

Reynolds averaging introduced six new independent variables to the momentum equation (Eq. 2.12) due to the presence of the Reynolds stress tensor. Now, there are more unknowns than equations and the algebraic system is *unclosed*. There exist several ways to close the system of equations by means of parameterizing the unknown variables associated with turbulent processes. In this context, the *order of turbulence closure* is determined by the highest order of turbulence moments that remain in the problem.

The way in which turbulence is statistically treated, is the most prominent distinguishing feature of numerical models operating on the RANS equations (so-called *RANS models*). The earliest approach toward a parameterization of turbulent processes is based on the *turbulent-viscosity hypothesis*. It originated from the assumption of an analogy between viscous and turbulent stresses which was introduced by Boussinesq (1877). Mathematically, this analogy is reflected in a dependence of the Reynolds stresses on the rate of strain in the mean flow – similar to the relation for viscous stresses in Newtonian fluids. Accordingly, the deviatoric part of the Reynolds stress tensor is given by

$$-\rho\langle u_i'u_j'\rangle + \frac{2}{3}\rho k\delta_{ij} = \rho\nu_t\left(\frac{\partial\langle U_i\rangle}{\partial x_j} + \frac{\partial\langle U_j\rangle}{\partial x_i}\right) = 2\rho\nu_t S_{ij}\ , \tag{2.15}$$

in which S_{ij} is the strain-rate tensor of the mean flow, and $\nu_t(\mathbf{x},t)$ is the *turbulent viscosity* (or *eddy viscosity*). Similarly, the *gradient-diffusion hypothesis* states that turbulent heat and mass fluxes are aligned with mean scalar gradients and introduces *turbulent diffusivities* of heat and mass, $\Gamma_h(\mathbf{x},t)$ and $\Gamma_m(\mathbf{x},t)$. The *turbulent Prandtl number*, $Pr_t = \nu_t/\Gamma_h$, and the *turbulent Schmidt number*, $Sc_t = \nu_t/\Gamma_m$, measure the relative importance of turbulent heat or mass diffusion in comparison to the turbulent momentum transport.

In order to close the system of RANS equations, the turbulent viscosity has to be determined. Having the dimension of ($\mathrm{m^2/s}$), the eddy viscosity can be related to the product of a velocity and a length scale, i.e. $\nu_t = u_t\ell_t$, and closure is achieved by parameterizing these two scales. The simplest approach to this problem is given by the algebraic *mixing-length model*, which relates ℓ_t to a mixing length ℓ_m, whose notion was independently suggested by Ludwig Prandtl and G. I. Taylor, and u_t is associated with mean flow gradients. The empirical specification of ℓ_m strongly depends on the flow scenario and often involves further heuristic assumptions about involved physics. The mixing-length model represents a first-order turbulence closure (Pope, 2000).

Building on that, *one-equation models* use the mixing-length definition, but determine the velocity scale from the relation $u_t \sim k^{1/2}$ by solving a separate transport equation for the TKE. With the so-called *two-equation models*, however, no flow-dependent mixing-length assumptions are required. A prominent example is the k–ε model, where ε is the energy *dissipation rate* per unit mass. Here, the eddy viscosity, $\nu_t(k^2/\varepsilon)$, is obtained by solving transport equations of k and ε. These approaches represent intermediate steps between first and second-order modeling and are usually denoted as $1\frac{1}{2}$-order closure.

Second-order turbulent closure requires to directly solve the model transport equations for the Reynolds stresses, $\langle u_i'u_j'\rangle$. These equations, however, include third-order turbulence terms such as the pressure-strain-rate tensor or the stress flux, which – again – often require very sophisticated parameterizations.

Compared with this approach, eddy-viscosity models are much simpler and have a wide range of applications. Yet, the involved assumptions have shortcomings and lack generality. The *local alignment* of turbulent stresses with mean flow gradients as well as their *linear relation* through the eddy viscosity have been disproved in many flow categories (Pope, 2000). In this regard, Taylor (1970) commented,

> "(...) the idea that a fluid mass would go a certain distance unchanged and then deliver up its transferable property, and become identical with the mean condition at that point, is not a realistic picture of a physical process."

However, following the argumentation by Pope (2000), for simple shear flows, in which turbulence features evolve slowly, these assumptions are more reasonable. In such situations, the production, $\mathcal{P}$, and dissipation rate, ε, of turbulence kinetic energy are of comparable magnitude. The two processes are linked by a transfer of energy across all turbulent scales of motion – a conceptual model that dominates the perception of turbulence and will be introduced in the next paragraphs.

2.1.4 Turbulent scales and K41 theory

The view of turbulent flows as being composed of vortices of different sizes, ℓ, and certain velocity scales, u_ℓ, superimposed on a mean velocity field provides the basis for most of the scientific work devoted to the theoretical description of turbulence, numerical modeling procedures, and practical data analysis concepts. In this regard, two perceptions stand out as exceptionally inspiring: the cascading energy transfer between turbulent eddies and the hypotheses of local isotropy and universal scaling behavior.

The energy cascade

The largest eddies in the flow have a characteristic size ℓ_0 comparable to the length scale $\mathcal{L}$ that is specific to the geometry of the flow (following the notation in Pope, 2000). These eddies are responsible for the production of turbulence kinetic energy through the extraction of energy from the mean flow. Since their characteristic Reynolds number, $Re_0 = u_0\ell_0/\nu$, is large, viscous effects are negligible. Most of the TKE resides at these scales. The energy, however, is passed on to somewhat smaller vortices, which are created through dynamical instabilities and nonlinear interactions between the large eddies of the energy-containing range. The break-up process continues among the smaller eddies and will go on as long as the eddy Reynolds number is sufficiently high. As eddy sizes decrease, the vortices become isotropic and more stable until ultimately the energy is dissipated due to the dominance of viscous effects. The transfer of TKE to successively smaller scales of motion is referred to as *energy cascade* and was first described by Richardson (1922) and fortified in seminal works by Taylor (1935, 1938). The conceptual model implies that under equilibrium conditions the dissipation rate is given by the rate $\mathcal{P}$, at which energy is produced: ε varies as u_0^3/ℓ_0. If the TKE supply is cut off, turbulence eventually decays, and the flow relaminarizes. The range of eddies in which energy is neither created nor dissipated, but only transferred between groups of vortices, is called *inertial subrange*. It is bordered by eddy-scale limits of the production and dissipation range, ℓ_{EI} and ℓ_{DI}.

Kolmogorov's hypotheses

As stated by Lumley and Yaglom (2001), there are only very few great hypotheses in turbulence research. The ones that can certainly be regarded as most far-reaching were formulated more than 70 years ago by Andrei Nikolaevich Kolmogorov, who provided the first unified picture of turbulent dynamics across eddy ranges with three brief statements (K41 theory; Kolmogorov, 1941, 1991).[4] Following Pope (2000), the first hypothesis reads:

> **Local isotropy hypothesis** — Motions of small-scale eddies with $\ell \ll \ell_0$ are locally isotropic given a sufficiently high Reynolds number.

A turbulent flow is called *isotropic* if statistics derived at a certain point in space show no directional dependency: The velocity field is invariant under coordinate translations, rotations or reflections. *Local isotropy* refers only to the isotropy of the small eddy scales. While the energy-containing eddies of size ℓ_0 are strongly *anisotropic* and essentially limited by the geometry of the respective scenario, the smaller eddies created through the break-up chain are expected to have lost the memory of these boundary conditions. Statistics derived from the small-scale motions are *universal* in every high-*Re* flow. In the so-called *universal equilibrium range*, the second hypothesis holds:

> **First similarity hypothesis** — At sufficiently high Reynolds number, the statistics of the motions of small-scale eddies with size $\ell < \ell_{EI}$ are universally defined by the viscosity of the fluid, ν, and the energy dissipation rate, ε.

From these two quantities, scaling terms for the smallest eddies can be formulated as

$$\eta \equiv \left(\frac{\nu^3}{\varepsilon}\right)^{1/4} , \qquad u_\eta \equiv (\nu\varepsilon)^{1/4} , \qquad \tau_\eta \equiv \left(\frac{\nu}{\varepsilon}\right)^{1/4} , \tag{2.16}$$

which are referred to as the *Kolmogorov length*, *velocity*, and *time scales*, respectively. The scales characterize the dissipative eddies with $Re_\eta \equiv u_\eta \eta/\nu = 1$. For motions in the equilibrium range, all turbulent flows are statistically *similar* and statistically *identical* if statistics are referenced to the Kolmogorov scales. The ratios of the smallest and the largest eddy scales depend on the Reynolds number according to

$$\frac{\eta}{\ell_0} \sim Re^{-3/4} , \qquad \frac{u_\eta}{u_0} \sim Re^{-1/4} , \qquad \frac{\tau_\eta}{\tau_0} \sim Re^{-1/2} . \tag{2.17}$$

Thus, the higher the Reynolds number of the flow scenario, the smaller the length scale of the smallest eddies, η, and the larger the range of eddy sizes. Figure 2.1 illustrates this behavior. The third hypothesis describes scaling dependencies in the inertial subrange:

> **Second similarity hypothesis** — Assuming a sufficiently high Reynolds number, the statistics of eddy motions in the scale range of $\ell_0 \gg \ell \gg \eta$ (or more precisely: $\ell_{EI} > \ell > \ell_{DI}$) are universal and solely determined by the rate of dissipation, ε.

[4]Kolmogorov's original 1941 article was written in Russian. An English translation was later provided by the *Royal Society of London* (see Kolmogorov, 1991). Simultaneously and independently of Kolmogorov's studies, Onsager (1945), von Weizsäcker (1948), and Heisenberg (1948) developed similar ideas concerning spectral properties of turbulence and scaling laws.

Because the eddy Reynolds number in the inertial subrange is still large, Kolmogorov postulated that the energy transfer is solely defined by inertial forces. The viscous stresses only act on small-scale eddies in the dissipation range. Within the inertial subrange, eddy velocity and time scales decrease with decreasing eddy sizes. Through dimensional inference, Kolmogorov (1941) derived that the theoretical shape of the energy distribution among the inertial subrange eddies is given by

$$E(\kappa) = C\varepsilon^{2/3}\kappa^{-5/3} \;, \tag{2.18}$$

where the wavenumber κ is defined as $\kappa = 2\pi/\ell$, with the length scale in the range of $\ell_{EI} > \ell > \ell_{DI}$, and C is the universal *Kolmogorov constant*, often assigned a value of $C = 1.5$ as suggested by experimental observations (see the survey by Sreenivsan, 1995).

Figure 2.2a shows the turbulence spectrum of high Reynolds number flow in wavenumber space with indications of the eddy ranges. A different perspective on this picture was presented by Frisch et al. (1978) and Frisch (1995) in relation to the eddy cascade and is reproduced in Figure 2.2b. The distribution of eddy sizes within the three distinct energy ranges is schematically represented by successive eddy generations of length scales $\ell_n = r^n \ell_0$, where $n = 0, 1, 2, \ldots$ for a fixed $r \in (0, 1)$. With decreasing size, the number of eddies per unit volume increases such that the smaller eddies are as space-filling as the larger ones. In the sense of the K41 theory this behavior reflects the assumptions of *self-similarity* and *scale-invariance*. The diagram further illustrates that the energy transfer is assumed to take place between eddies of comparable size, i.e. between neighboring eddy generations. This is referred to as *localness of interactions* in the inertial range.

One of the first experimental substantiations of the K41 theory was presented by Grant et al. (1962), who observed several decades of inertial subrange behavior in a high Reynolds number tidal channel flow. Later works by Kaimal et al. (1972), Mestayer (1982) or Saddoughi and Veeravalli (1994) further documented the existence of universal inertial subrange behavior and provided evidence of local isotropy in different flows.

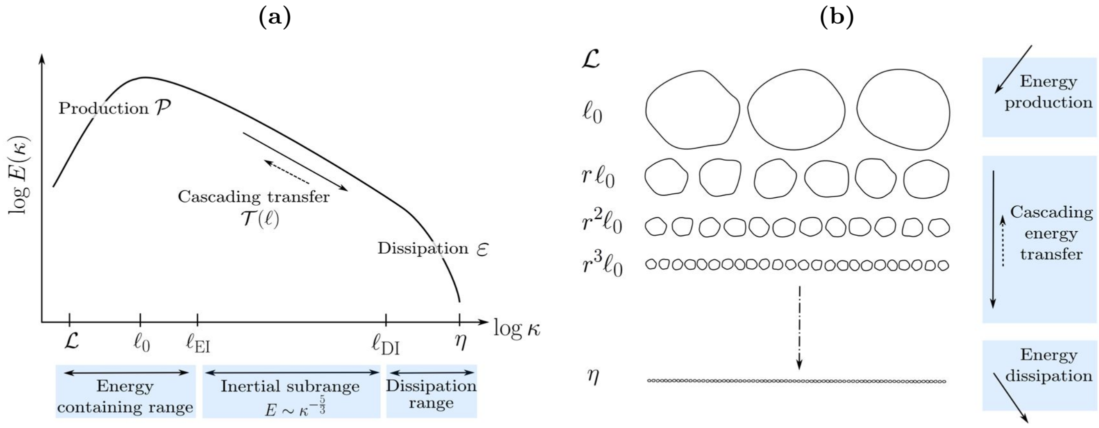

Figure 2.2: (a) Energy density spectrum at very high Reynolds number showing a –5/3 slope in the inertial subrange. Length scale notation is adopted from Pope (2000). (b) Phenomenological picture of the eddy cascade in view of the K41 theory (with $r = 1/2$), after Frisch et al. (1978) and Frisch (1995).

New insights & refinements

The conceptual frameworks established through the Richardson cascade and Kolmogorov's hypotheses provide a broad theoretical basis for many fields of applications. As will be discussed in Section 2.2, the primary legitimation to have confidence in the potential of large-eddy simulations is based on the assumptions of universality and local isotropy of small-scale turbulence and their major implication – universal scaling potential. Great effort was spent on theoretical, numerical, and experimental research studies in order to verify, extend or disprove K41 for different types of turbulent flows.

An important limitation of the original hypotheses originates from the fact that they are only applicable in the case of "sufficiently high" Reynolds numbers. It was shown that higher-order statistics of dissipation range quantities (e.g. skewness or kurtosis of velocity derivatives) exhibit a strong dependence on the Reynolds number in contrast to predictions following the universal equilibrium assumption (e.g. Wyngaard and Tennekes, 1970; Champagne, 1978). Associated similarity constants, thus, are flow-dependent and *not* universal. Anselmet et al. (1984) could show that *anomalous scaling* behavior, in which scaling exponents cannot be retrieved from dimensional analyses, exists for high-order velocity structure functions in the inertial subrange. Both observations are ascribed to the spatial randomness and intermittency of the small eddies, that is expressed in strong fluctuations of the *instantaneous* magnitude of the dissipation rate. This phenomenon has been theoretically considered earlier and was approached with the so-called *refined similarity hypotheses* (Kolmogorov, 1962; Obukhov, 1962). Here, the ensemble mean dissipation rate of the original theory is replaced by a *locally averaged* dissipation rate, which is assumed to be a log-normal random variable in order to include intermittency effects. A thorough survey about the phenomenology and scaling behavior of small-scale turbulence in the view of the refined K41 theory and other intermittency models is presented by Sreenivasan and Antonia (1997).

Further studies gave new insights into the details of the energy cascade. On average, the transfer of turbulence kinetic energy is always directed from the larger to the smaller eddies. Instantaneously, however, theoretical models and time-dependent numerical simulations have shown that this process can be reversed (e.g. studies by Domaradzki and Rogallo, 1990). The instantaneous and local transfer of energy from small to large eddies is now known as *backscatter* or *inverse cascade* (schematically represented by the dotted arrows in Fig. 2.2). Zhou (1993) and others investigated the phenomenon of scale interactions in isotropic turbulence, which is assumed to be local according to the K41 theory. It could be shown, however, that *nonlocal* interactions between eddies of significantly different size are also occurring (so-called *triad interactions*).

Other refinements of K41 and its later reformulations in 1962 (proposed e.g. by Kraichnan, 1974) as well as advanced theoretical models like the direct interaction approximation (DIA; e.g. Kraichnan, 1959) or the eddy-damped quasi-normal *Markovian* theory for homogeneous isotropic turbulence (EDQNM; e.g. Orszag, 1970) are frequently incorporated today to study fundamental features of inertial range and dissipative turbulence. However, as Moffatt (2002) pointed out, many of the post-K41 approaches "(...) were of such mathematical complexity that it was really difficult to retain that essential link between mathematical description and physical understanding, which is so essential for real progress."

2.2 Fundamentals of large-eddy simulation

Approaches in *computational fluid dynamics* can be grouped into two categories:

- *turbulence modeling* and
- *turbulence simulation.*

The first addresses techniques that use full *parameterizations* of turbulence in order to predict turbulent flow behavior, the latter refers to numerical simulations of turbulent flows using the original equations (cf. Wyngaard, 1992; Breuer, 2002). According to this binary classification, numerical codes based on the Reynolds-averaged Navier-Stokes equations are representatives of the first type. As Lumley (1983) states, even advanced two-equation models should only be regarded as a *"calibrated surrogate of turbulence."* The way in which the spectrum of turbulent eddies is represented in RANS solutions is neither eddy-scale dependent nor limited by the flow Reynolds number. Due to comparatively low computational costs, RANS models are in wide use in micro-meteorology and computational wind engineering for research and practical applications.

The *direct numerical simulation* (DNS) stands for the second branch, in which the Navier-Stokes equations are numerically solved with flow-dependent boundary and initial conditions. The spatio-temporal evolution of all scales of motion is directly resolved, exclusive of any turbulence parameterization. The computational costs of DNS exceed those of RANS approaches by far and are strongly Reynolds-number dependent.

The approach taken in what is known as *large-eddy simulation* can be regarded as the gray area added to the above black-and-white picture: Subject to the eddy scale, turbulence is both resolved and modeled in LES. Generally speaking, LES denotes a three-dimensional, time-dependent numerical simulation technique based on volume-averaged conservation equations, which works on computational meshes fine enough to resolve turbulent eddies and uses turbulence parameterizations for the unresolved scales.

Figure 2.3 shows a schematic energy density spectrum of high Reynolds number flow with indications of the important eddy scale ranges and associated dynamic processes (cf. Section 2.1.4). The representation of the eddy spectrum through the three CFD approaches – DNS, LES, and RANS – is indicated.

The following sections give a brief introduction to the fundamental concepts of LES. Developments in LES modeling techniques, results of atmospheric LES studies, as well as trends and challenges of the approach will be discussed. It is started from a classification of eddy-resolving methods with respect to computational constraints given by the flow Reynolds number and the flow type.

2.2.1 A Reynolds number point of view

The applicability of eddy-resolving methods like DNS or LES depends on the nature of the turbulent flow and the range of eddy scales involved in the problem. In DNS, the computational domain has to be large enough to accurately resolve the large-scale, energy-containing eddies (i.e. $\mathcal{O}(\mathcal{L})$), while the numerical grid is bound to be fine enough to resolve the smallest eddies in the flow (i.e. $\mathcal{O}(\eta)$).

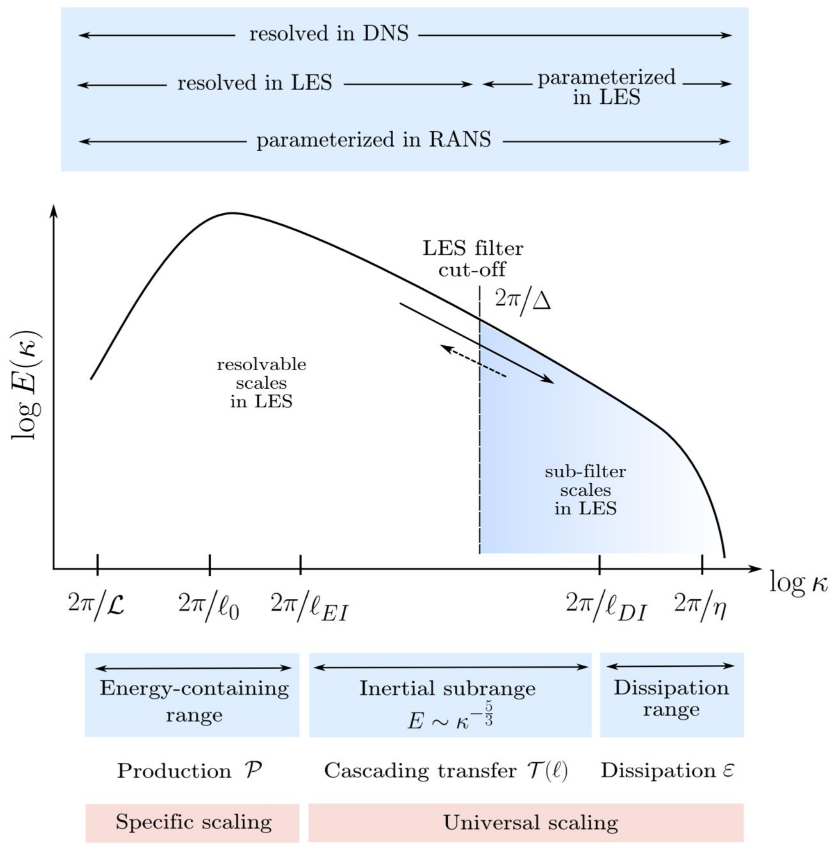

Figure 2.3: Turbulence spectrum in wavenumber space, where $\kappa = 2\pi/\ell$. Important scale ranges, associated dynamical processes and scaling assumptions are indicated together with the three common CFD approaches (notation after Pope, 2000).

As the computational cost of a numerical simulation, e.g. measured based on the number of required floating-point operations, is resolution-dependent, it is instantly clear that DNS is a heavyweight among its neighbors (Pope, 2000). Based on Kolmogorov's scaling assumptions, the ratio ℓ_0/η scales with $Re^{3/4}$. This means that the total number of computational grid points roughly scales as $N_x \times N_y \times N_z \sim Re^{9/4}$ for a full three-dimensional DNS. The time advancement of the solution has to be proportional to the grid spacing. For an accurate solution it is necessary that the time step is short enough so that fluid particles will only cover a small distance within the grid cells. Pope (2000) indicates a *Courant number* of $1/20$ for a careful DNS computation. Taking this into account, the actual computational cost of DNS scales roughly as

$$(N_x \times N_y \times N_z) \times N_t \sim Re^3 . \tag{2.19}$$

The review by Reynolds (1990) presents a more detailed assessment of the resolution requirements for different flow types together with discussions on the computational methods and boundary constraints for DNS, which have to be highly accurate.

Orszag and Patterson (1972) carried out the first DNS of a three-dimensional turbulent flow at a Taylor-scale Reynolds number of $Re_\lambda = 35$ using 32^3 grid points.[5] Today, DNS is feasible for studying low Reynolds number canonical flows in simple geometries. One of the largest DNS of a homogeneous turbulent flow so far was performed with a grid resolution of 4096^3 points at a Reynolds number of $Re_\lambda = 1,200$, which is in the order of typical laboratory flows (Kaneda and Ishihara, 2006). Coleman et al. (1990) presented an early application of DNS to the atmospheric boundary layer at a Reynolds number that did not allow for inertial subrange behavior. Direct simulations of turbulent flow in idealized *urban* environments (e.g. cube arrays) barely exist. First studies were restricted to very low Reynolds numbers and limited eddy-scale ranges (e.g. Coceal et al., 2007; Branford et al., 2011). For realistic Reynolds numbers of atmospheric boundary-layer flows in the range of $Re \sim 10^7$ to 10^9, DNS will probably always remain impracticable.

The great potential of DNS lies withing fundamental studies of turbulence physics since the method certainly provides the most complete picture of turbulent flows (cf. review of DNS as a tool in turbulence research by Moin and Mahesh, 1998). The predictive potential of DNS is limited to special cases of engineering and atmospheric applications. Among those, an interesting research area is biological flow at moderate Reynolds numbers – for example cardiovascular circulations or animal locomotion in air or water (e.g. Mittal, 2005; Sherwin and Blackburn, 2005; Tullio et al., 2009).

Figure 2.4 shows a classification of eddy-resolving approaches based on the Reynolds number of different flow types and current computational capacities, following Piomelli (2010). Together with the restricted scope for direct turbulence simulations, the practicability of LES is indicated to depend strongly on the flow scenario. For free shear flows (e.g. mixing layers or jets) LES can be applied over a wide range of Reynolds numbers.

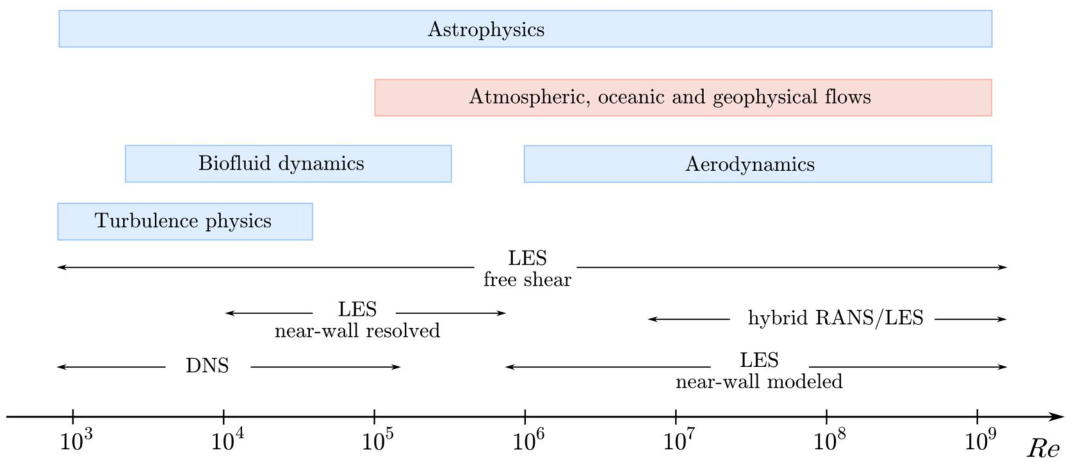

Figure 2.4: Eddy-resolving CFD methods in the context of their ranges of applications as a function of the flow Reynolds number. Adapted from Piomelli (2010).

[5] The Reynolds number based on the Taylor micro-scale (Taylor, 1935) is defined as $Re_\lambda \equiv \sigma_u \lambda/\nu$, with λ being an intermediate eddy size between ℓ_0 and η. Roughly, $Re_\lambda \sim \sqrt{2Re}$ holds (Pope, 2000).

For flows that are influenced by boundaries, as encountered in aerodynamic or environmental studies, the Reynolds number determines whether the near-wall region can be resolved in LES or has to be modeled. For flows at low to moderate Reynolds numbers, the limitation of the eddy-scale range permits to resolve small-scale near-wall motions without severe increase of computational costs. In typical LES studies of the atmospheric boundary layer at high Reynolds numbers, the vertical grid resolution ranges from few meters up to some decameters, and near-wall flow modeling is always involved. The appropriate parameterization of near-surface turbulence in LES is known to be crucial for the overall quality of the simulation and, thus, is an area of intensive research (cf. Section 2.2.3).

So-called *hybrid* modeling approaches like *detached-eddy simulation* (DES) attempt to tackle the near-wall grid resolution problem by combining LES and RANS methodologies (e.g. review by Spalart, 2009). Whereas research using the new hybrid models is very active (and successful) in engineering disciplines, the approach is still uncommon in the micro-meteorological research community.

2.2.2 LES in a nutshell

Having its roots in the development of early numerical weather prediction models (with seminal works by Smagorinsky, 1963; Lilly, 1967), first comprehensive applications of LES in the context of turbulence research and important theoretical advancements were made in the 1970s for engineering flows (e.g. first LES studies of turbulent channel flow by Deardorff, 1970a; Schumann, 1975). Today, LES emerged as a frequently applied method in micro-meteorology to study problems in which time-space evolution is of special interest: e.g. diurnal transformations of the ABL structure, flow and dispersion processes in complex environments, severe storm dynamics or cloud physics. For certain research topics, which are not easily explored by experimental means, LES offers the potential of a fundamental understanding of the involved dynamics. A prominent example is the convective atmospheric boundary layer investigated by Deardorff (1974a,b); see Section 2.3.2. In a survey about future prospects of LES for atmospheric boundary-layer research from the mid-1980s, Wyngaard et al. (1984) anticipate the use of LES as a "*numerical laboratory*" for testing and developing scaling laws and turbulence closure parameterizations. And indeed, many studies devoted to these issues were made in the last decades.

Why is LES so successful? — The answer lies in the fact that the technique has the potential to provide a realistic picture of turbulent flows with feasible computational expenses. The great economical advantage over DNS stems from the fact that only the large-scale motions, which contain the bulk of turbulence kinetic energy and are affected by the flow geometry, are directly resolved. The small-scale turbulence, which to some extent can be regarded as universal, is parameterized. Ideally, the LES cut-off, Δ, lies somewhere within the inertial subrange of turbulence, i.e. $\ell_0 \gg \Delta \gg \eta$ (see Fig. 2.3).

Pope (2000) gives a revealing illustration of the benefits arising from the limitation of directly resolved turbulence in LES. Virtually the entire computational efforts in DNS are expended on the small-scale motions belonging to the dissipation range, with $\ell < \ell_{DI}$. For a comparatively low Reynolds number flow at $Re_\lambda = 70$, Pope (2000) showed that less than 0.02 % of the modes in wavenumber space belong to the energy-containing and inertial-range eddies. For higher Re flows, this fraction becomes even smaller.

Filtered equations

Formally, the LES decomposition of the velocity field $U_i(x_i,t)$ into *filtered* and *residual* components is achieved by the convolution with a spatial *filter function* G, which depends on the cut-off width Δ. This concept was first introduced and discussed by Leonard (1974). In conformity with the classic notion of Reynolds decomposition, this yields

$$U_i(x_i,t) = \widetilde{U_i}\,(x_i,t) + u_i(x_i,t) = \int_{-\infty}^{\infty} U_i(x'_j,t)\,G(x_i - x'_j)\,dx'_j + u_i(x_i,t)\ , \tag{2.20}$$

in which the tilde denotes a spatially filtered variable, and the prime is only formally introduced for the integration. The residual velocity field, $u_i(x_i,t)$, represents the so-called *subfilter-scale* (SFS) motions. In general, filtering is independent of the employed numerical method, e.g. in terms of the spatial discretization of the governing equations. In practice and especially for meteorological LES applications, filtering and numerics are strongly connected and often merged into one step.[6] This also explains the common use of the term sub*grid*-scale (S*G*S) motions for the residual velocity field.

Although spatial filtering is to some extent very similar to the concept of ensemble averaging, it has to be emphasized that both $\widetilde{U_i}$ and u_i are *random fields* and filtering is *a priori* not a Reynolds operator. This, for example, leads to the fact that in general

$$\widetilde{u_i} \neq 0 \quad \text{and} \quad \widetilde{\widetilde{U_i}} \neq \widetilde{U_i}\,. \tag{2.21}$$

If the filter is spatially uniform (*homogeneous*), filtering and differentiation commute. The filtered continuity equation of an incompressible fluid (Eq. 2.2), thus, is given by

$$\frac{\partial \widetilde{U_i}}{\partial x_i} = 0 \quad \text{and} \quad \frac{\partial u_i}{\partial x_i} = 0\ . \tag{2.22}$$

Applying the spatial filtering to the Navier-Stokes equation (Eq. 2.5) results in

$$\frac{\partial \widetilde{U_i}}{\partial t} + \widetilde{U_j}\frac{\partial \widetilde{U_i}}{\partial x_j} = -\frac{1}{\rho}\frac{\partial \widetilde{p}}{\partial x_i} + \nu \frac{\partial^2 \widetilde{U_i}}{\partial x_j \partial x_j} - \frac{\partial \tau^s_{ij}}{\partial x_j}\ , \tag{2.23}$$

with τ^s_{ij} being the *subfilter-scale flux* (more commonly *SFS stress*) defined as

$$\tau^s_{ij} = \widetilde{U_i U_j} - \widetilde{U_i}\,\widetilde{U_j}\ . \tag{2.24}$$

This expression is similar to that of the kinematic Reynolds flux $\tau_{ij} = \langle u'_i u'_j \rangle = \langle U_i U_j \rangle - \langle U_i \rangle \langle U_j \rangle$ (Section 2.1.2). The different natures of the involved averaging approaches, however, lead to some very important general distinctions between both quantities.

Filtering the conservation equations of thermal energy and scalar concentrations leads to the *SFS heat* and *scalar fluxes*, $f_{i\Theta} = \widetilde{U_i \Theta} - \widetilde{U_i}\,\widetilde{\Theta}$ and $f_{iq} = \widetilde{U_i q} - \widetilde{U_i}\,\widetilde{q}$, where Θ is the potential temperature and q, for example, water vapor concentration.

[6] Filtering can comply with a volume average over the grid cell dimensions as in the historic approach by Deardorff (1970a), defined as $\widetilde{U_i}\,(x_i,t) = (\delta x\,\delta y\,\delta z)^{-1} \int_{x-\frac{1}{2}\delta x}^{x+\frac{1}{2}\delta x} \int_{y-\frac{1}{2}\delta y}^{y+\frac{1}{2}\delta y} \int_{z-\frac{1}{2}\delta z}^{z+\frac{1}{2}\delta z} U_i(x'_i,t)\,dx'_i$, where δx, δy, and δz are the grid increments of the finite difference equations.

Germano (1986) proposed a decomposition of the SFS stress (flux) tensor into three *Galilean-invariant* terms: $\tau^s_{ij} = \mathcal{L}_{ij} + \mathcal{C}_{ij} + \mathcal{R}_{ij}$, which are the so-called *Leonard stress*, the *cross stress* and the *SFS Reynolds stress*, respectively. They are defined as

$$\mathcal{L}_{ij} = \widetilde{\widetilde{U}_i \widetilde{U}_j} - \widetilde{\widetilde{U}}_i \widetilde{\widetilde{U}}_j \,, \tag{2.25}$$

$$\mathcal{C}_{ij} = \widetilde{\widetilde{U}_i u_j} + \widetilde{\widetilde{U}_j u_i} - \widetilde{\widetilde{U}}_i \widetilde{u_j} - \widetilde{\widetilde{U}}_j \widetilde{u_i} \,, \text{ and} \tag{2.26}$$

$$\mathcal{R}_{ij} = \widetilde{u_i u_j} - \widetilde{u_i}\,\widetilde{u_j} \,, \tag{2.27}$$

If filtering was a Reynolds operator, $\mathcal{L}_{ij}$ and $\mathcal{C}_{ij}$ would vanish and $\mathcal{R}_{ij} = \widetilde{u_i u_j}$. The resolved and SFS fields can be subject to further averaging operations. For averaging times sufficiently longer than the filter time-scale $\Delta/\overline{U}$ the relation $\overline{\widetilde{U}_i} \simeq \widetilde{\overline{\widetilde{U}_i}}$ can be assumed valid, so that $u_i = u'_i$ (Sullivan et al., 2003). The overbar denotes the time average over the signal length T (cf. Eq. 2.8) and u'_i, thus, is the fluctuation about the time mean. It can be shown that the instantaneous LES velocity can be essentially decomposed into

$$U_i = \overline{U_i} + u_i = \overline{\widetilde{U_i}} + \widetilde{U_i}' + u_i \,. \tag{2.28}$$

Figure 2.5 gives a qualitative impression about how filtering modifies the characteristics of a turbulent signal in physical and spectral space. A wind-tunnel time series of the streamwise velocity component, $U(t)$, was filtered by applying Eq. (2.20) using a *Gaussian filter* function (following Leonard's, 1974, definition) and three different filter widths, Δ_i. The transformation of time-dependent into space-dependent data, $U(x)$, was done through the relation $x = t\,\overline{U}$, assuming the applicability of *Taylor's frozen turbulence hypothesis* (cf. Taylor, 1938) – a concept that will be further discussed in Section 2.3.1.

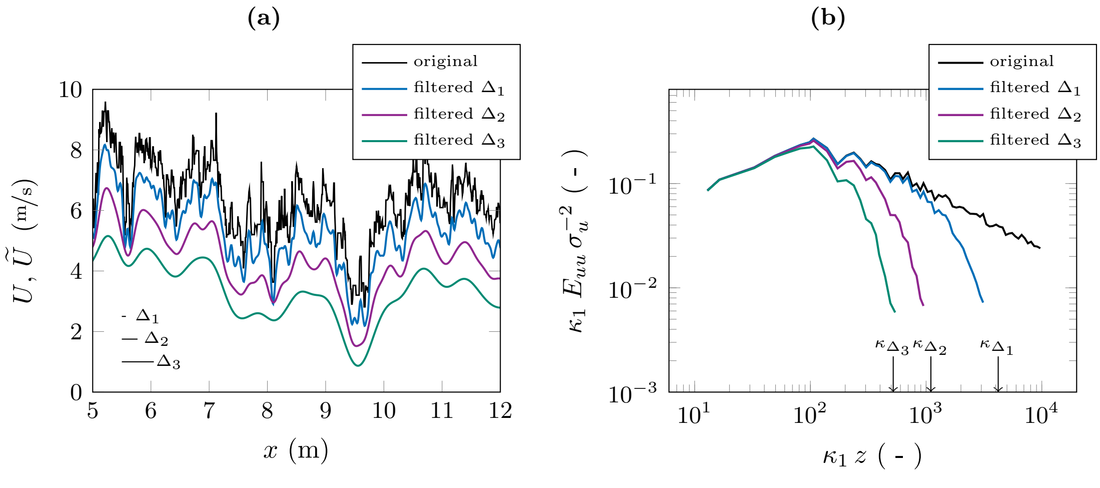

Figure 2.5: (a) Cut-out sample of the original (U) and filtered ($\widetilde{U}$) streamwise wind-tunnel velocities, obtained with the Gaussian filter function for three filter widths, Δ_i, $i = 1, 2, 3$. Note that the data were shifted along the ordinate for a clearer display. (b) Corresponding one-dimensional energy-density spectra in wavenumber space. Filter widths and cut-off wavenumbers are additionally displayed.

The enhanced damping of small-scale fluctuations with increasing filter width is clearly evident in physical space (Fig. 2.5a), and is reflected in a reduction of the corresponding energy spectra at the high-wavenumber end, with $\kappa_{\Delta_i} = 2\pi/\Delta_i$ being the wavenumber of the highest directly resolved mode (Fig. 2.5b). The one-dimensional energies of the resolved LES fields, $1/2\,\overline{u^2}$, correspond to 90% (Δ_1), 78% (Δ_2), and 64% (Δ_3) of the original energy given by $1/2\,\overline{u'^2}$. Thus, following the usual convention that a simulation qualifies as a "true LES" if more than 80% of the energy of the flow is resolved (e.g. Pope, 2000), at least the last filter width would be too broad. Simulations using numerical grids and filters too coarse to resolve the bulk of the TKE are referred to as *very large-eddy simulations* (VLES). In this case, the higher savings with respect to computational costs come at the price of a stronger dependence on the accuracy of the SFS parameterization.

Besides the Gaussian function, other commonly used filters are the top-hat function (box filter) and the sharp spectral filter (cf. Pope, 2000, p. 563). Because Gaussian and box filters are not well-localized (*sharp*) in spectral space, an attenuation of energies at scales $\ell > \Delta$ is generally observed. This is also evident in Figure 2.5b. The resolved scales that are directly affected by the filtering are sometimes referred to as *resolved SFS* (Chow et al., 2005). The sharp spectral filter, on the other hand, directly eliminates spectral modes with $\kappa > \kappa_\Delta$ while leaving the smaller wavenumbers unaffected.

The limiting behaviors of LES are straightforwardly deduced from the approximate bounds of the filter width. In the limit of $\Delta \to 0$ (in effect $\Delta \to \eta$) a DNS of the flow is approached and as $\Delta \to \infty$ (in effect $\Delta \to \mathcal{L}$) the filtering operation approaches the ensemble average with the limiting RANS state.

Subfilter-scale models

The parameterization of SFS stresses is a crucial step of the LES procedure. Similar to the developments of turbulence closure formulations for RANS equations, efforts to model the influence of the residual motions in LES – primarily in terms of an energy removal from the resolved fields – resulted in a variety of different approaches.

In the subsequent paragraphs, some of the most influential and prevalent SFS models are briefly reviewed. It is followed Lesieur and Métais (1996), Piomelli (1999), Meneveau and Katz (2000), as well as to the textbooks by Pope (2000), Sagaut (2005), and Fröhlich (2006), in which detailed discussions can be found.

The theoretical foundation of the majority of subfilter-scale models is given by the classic K41 assumption of local isotropy of small-scale eddies (see Section 2.1.4). The conceptual framework most commonly employed in order to relate the residual stress to the resolved flow quantities, is borrowed from the classic turbulence closure of the ensemble-averaged equations: Boussinesq's *turbulent-viscosity hypothesis* (see Section 2.1.3). The *anisotropic* SFS-stress tensor $\tau^a_{ij} \equiv \tau^s_{ij} - \frac{2}{3}k_s\delta_{ij}$, with $k_s \equiv \frac{1}{2}\tau^s_{ii}$ being the *SFS kinetic energy*, is related to the filtered strain-rate tensor

$$\widetilde{S_{ij}} \equiv \frac{1}{2}\left(\frac{\partial \widetilde{U_i}}{\partial x_j} + \frac{\partial \widetilde{U_j}}{\partial x_i}\right) \tag{2.29}$$

through the expression $\tau^a_{ij} = -2\,\nu_r\,\widetilde{S_{ij}}$. This formulation is analogous to Eq. (2.15).

The above model was first proposed by Smagorinsky (1963). In a next step, the eddy viscosity of the residual motions, $\nu_r(\mathbf{x},t)$, is parameterized through an algebraic mixing-length model as the product of a length and velocity scale (cf. Pope, 2000), yielding

$$\nu_r = \ell_s^2\,\widetilde{\mathcal{S}} = (C_s\,\Delta)^2\,\widetilde{\mathcal{S}}\ , \tag{2.30}$$

where $\ell_s \equiv C_s\,\Delta$ is the characteristic length scale, which relates to the filter width via the so-called *Smagorinsky coefficient*, C_s, and $\widetilde{\mathcal{S}} \equiv (2\widetilde{S_{ij}}\widetilde{S_{ij}})^{1/2}$ represents the characteristic velocity difference at that scale. In the Smagorinsky model, the rate in which energy is transferred from the resolved to the residual motions is given by $\mathcal{P}_r \equiv -\tau_{ij}^a\,\widetilde{S_{ij}} = \nu_r\,\widetilde{\mathcal{S}}^2$. For all types of eddy-viscosity models with $\nu_r > 0$, $\mathcal{P}_r$ is always positive, and inverse cascade effects (i.e. energy backscatter to the resolved scales) are not incorporated.

Lilly (1967) derived an expression for C_s for the case that Δ lies well within the inertial subrange. Assuming that for isotropic turbulence the mean rates of energy production and dissipation balance, i.e.

$$\varepsilon = \langle \mathcal{P}_r \rangle = (C_s\Delta)^2 \langle \widetilde{\mathcal{S}}^3 \rangle \simeq (C_s\Delta)^2 \langle \widetilde{\mathcal{S}}^2 \rangle^{3/2}\ , \tag{2.31}$$

and expressing $\langle \widetilde{\mathcal{S}}^2 \rangle$ through the Kolmogorov spectrum (Eq. 2.18), Lilly arrives at the classic result $C_s = \frac{1}{\pi}(\frac{2}{3C})^{3/4} \simeq 0.17$ using $C = 1.5$ as the Kolmogorov constant.

For the standard Smagorinsky model, C_s is a flow-dependent, scale-invariant coefficient derived under the assumption of isotropic homogeneous turbulence at the filter scale. This can lead to inaccuracies of SFS dissipation rates in cases where Δ approaches the inertial range limits (e.g. near solid boundaries) and in flow situations dominated by strong shear, buoyancy effects or rotation. In particular, the model is found to be *over-dissipative* in many flows. In order to overcome these issues, Germano et al. (1991) proposed the so-called *dynamic model*, which allows for a *local, scale-invariant* derivation of C_s without flow-dependent off-line tuning. Assuming that the dynamically most active SFS scales are those near the filter-cutoff, the dynamic model relates the Smagorinsky coefficient to the smallest resolved scales between the original filter, Δ, and a slightly larger test filter, $\breve{\Delta}$, such that C_s can be fully determined from the resolved fields in the course of the simulation. In order to decrease the rather high noise-level of the obtained values of C_s, which can cause numerical instabilities, averaging techniques are usually employed in the dynamic model. For LES of inhomogeneous flows in complex geometries, Meneveau et al. (1996) proposed a Lagrangian time averaging along the paths of fluid particles.

While the performance of the dynamic model is in many cases superior to the standard Smagorinsky model, a strong point of critique concerns the scale-invariance of the approach. Porté-Agel et al. (2000) developed a scale-dependent variation of the dynamic model in which C_s depends on Δ to a power that is derived from the introduction of a second test filter $\hat{\Delta}$. Later Bou-Zeid et al. (2005) extended this approach into a Lagrangian framework to stabilize the performance in geometrically complex flows.

Earlier efforts to improve the Smagorinsky model led to the so-called *mixed models*, of which the *scale-similarity model* (Bardina et al., 1980) is the most prominent example. This model takes advantage of the decomposition of the SFS stress tensor (Eqs. 2.25–2.27). Because the Leonard stress is solely composed of resolved flow quantities, the Smagorinsky model is only used to parameterize the cross and Reynolds SFS stresses.

Parallel to the developments of the algebraic Smagorinsky model and its refinements, research concentrated on approaches that are based on the solution of transport equations for the residual quantities. Deardorff (1974a,b) renounced relying on the eddy-viscosity hypothesis and presented an SFS closure by solving a modeled version of the conservation equation for τ_{ij}^{a}, which is computationally very demanding. The instantaneous dissipation rate is related to the SFS kinetic energy and to the filter scale via

$$\varepsilon_s = \frac{C_k}{\Delta}\, k_s^{3/2} \,, \tag{2.32}$$

where C_k is a constant in the order of 0.7 (see Pope, 2000).

A widely-used approach associated with reduced computational efforts is based on an eddy-viscosity model given by $\nu_r = C_u\, k_s^{1/2}\Delta$, where C_u is a constant and the SFS kinetic energy, $k_s(\mathbf{x}, t)$, is obtained from the solution of its transport equation, in which the diffusion and dissipation terms are modeled (cf. Schumann, 1975; Deardorff, 1980). This *kinetic energy model* is extensively used in meteorological LES codes because it incorporates flow memory effects and has proved to be successful in the simulation of atmospheric boundary-layer flows with different thermal stratifications.

A further strategy links the drainage of energy from the resolved scales to the *numerical dissipation* resulting from spatial-truncation errors (cf. Boris, 1990; Grinstein et al., 2007). No explicit SFS model is used, but both filtering and the parameterization of SFS contributions are obtained from the employed numerical method. This approach is referred to as *implicit large-eddy simulation* (ILES) and turned out to be very useful for computing complex flow types. Further details of the ILES approach are discussed in Section 4.3.1 in the context of introducing the urban aerodynamics code FAST3D-CT, of which simulation results are validated against wind-tunnel data in Chapter 5.

2.2.3 Trends, challenges & limitations

Since its early applications, physical and numerical specifications in LES have been subject to continuous advancements. These were attended and often stimulated by the rapid increase of computational power since the 1970s. As Liepmann (1979) stated, turbulence research "(...) continues to produce technological advances, but the path of progress is anything but straight" – the same is true for the evolution of LES. A major issue that needs to be addressed by numerical and experimental communities concerns the definition of appropriate validation strategies for LES predictions. This topic will be discussed separately in Chapter 3. Other challenges in performing an LES are for example related to the definition of realistic inflow and boundary constraints, to the SFS-model performance, and to issues regarding numerical setups and implementations (see Fig. 2.6a for an illustrative overview). Related discussions can, for example, be found in Reynolds (1990), Piomelli (1999) or Pope (2004), and some aspects are reviewed below.

SFS modeling As discussed in the previous paragraphs, an appropriate working point for LES is given if the bulk of energy resides in the filtered (resolved) length scales. For wall-bounded flows, like those in the high Reynolds-number atmospheric boundary layer, this requirement is generally met in regions that are sufficiently far away from the surface.

In vicinity of the surface, however, the length scale of the energy and flux-carrying eddies decreases until finally the viscous-sublayer length scale of near-wall eddies is reached, which is tiny compared with that of the dominant eddies well above. As $\Delta \to \ell_0$, the well-conditioned LES approaches the state of a VLES, which strongly depends on the accuracy of the SFS model. In general, however, the latter is neither conceptually developed nor calibrated for this scope. Wyngaard (2004) coined the term *"terra incognita"* for situations in which the SFS motions contribute excessively to the flux and energy budget of the flow (Fig. 2.6b) and further introduced an analogy to ensemble-averaged turbulence parameterizations in meso-scale meteorological modeling at decreasing grid sizes.

Another limitation of traditional eddy-viscosity models is related to the fact that they usually are purely dissipative. The local and instantaneous backscatter of kinetic energy or scalar variance from the residual to the resolved scales, however, can be significant (e.g. shown by Piomelli et al., 1991; Porté-Agel et al., 2000a). Several studies are devoted to the extension of standard dissipative SFS parameterizations to include inverse cascade effects (c.p. Mason and Thomas, 1992; Schumann, 1995; Domaradzki and Saiki, 1997). At least in atmospheric LES, however, none of these extensions is routinely applied. This is probably due to the fact that SFS models of high complexity tend to be computationally very demanding, so that the pros of an allegedly higher simulation accuracy have to be weighed up against rising costs.

Boundary conditions Any numerical model operating on a limited computational domain depends on the prescription of boundary conditions. Atmospheric LES studies often impose periodic lateral boundary conditions, whereas at the top usually free-slip (symmetry) or no-gradient conditions are applied, and the outlet is often specified by open boundary conditions (e.g. outflow or radiation-type). Quoting Pope (2000), the "major outstanding issue in LES," however, is related to the formulation of the boundary condition at the bottom of the domain. Given the range of scales present in atmospheric flows, resolving the near-wall flow field in LES, in effect, would be equivalent to performing a full DNS. Therefore, the first grid point of the simulation usually lies well above the viscous sublayer and wall-boundary conditions must comprehend all near-surface turbulent interactions and exchanges. Typically, the instantaneous value of the filtered *wall shear stress*, $\tau_{i3,w}$, is related to the filtered horizontal velocity at the first grid point by making use of flow similarity (cf. surveys by Piomelli, 2008; Chamorro and Porté-Agel, 2010). These assumptions are based on the log-law function (e.g. Grötzbach, 1981) or on alternative power-law formulations (cf. Werner and Wengle, 1993), which are usually only deemed applicable for ensemble-averaged states of spatially homogeneous, stationary flows. The conceptual validity in the more general sense of a time-dependent LES is questionable. As in the case of SFS models, such limitations are well-known and several studies originated to test and refine the methods. Of particular interest is the synchronized refinement of both SFS and wall models (see Anderson and Meneveau, 2011, for a recent approach).

Inflow conditions Defining realistic turbulent inflow conditions for LES is yet another demanding challenge that stimulated research activities in engineering and meteorology. Depending on the flow type, the simulation can be strongly affected by specifications made at the inlet. Klein et al. (2003) describes the situation as a *"vicious circle"* since the characteristics of turbulence must be known in order to simulate turbulence.

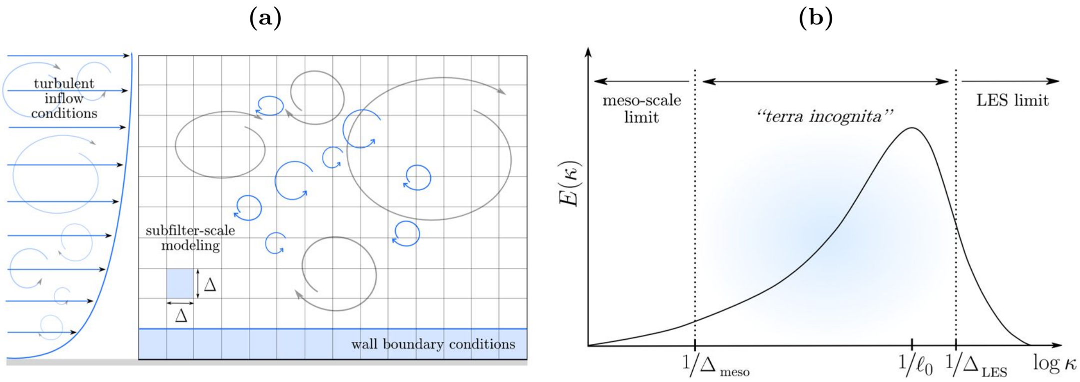

Figure 2.6: (a) Some challenges of wall-bounded LES. (b) Notion of the *"terra incognita"* in LES and meso-scale modeling, adapted from Wyngaard (2004).

It is pointed to Lund et al. (1998) for a thorough review of common inflow generation techniques for LES and an evaluation of their accuracy versus efficiency ratios. For atmospheric boundary-layer flows, which usually are wall-bounded as well as spatially developing, the required level of accuracy is rather high. A widely-used inflow generation approach is the *fluctuation method*, in which artificial turbulence is superimposed on a mean field. The fluctuations can be generated from random noise. More targeted approaches, however, require the artificial turbulence to satisfy certain statistics, e.g. in terms of Reynolds stresses, integral length scales or spectral properties (e.g. Kempf et al., 2005; Xie and Castro, 2008). A *development section* is usually implemented upstream of the region of interest, in which the artificial turbulence can further evolve to reach a mature state. The length of this section is adjusted dependent on the physical depth contained in the inlet turbulence and can strongly affect the overall computational costs. The same is true if the inflow is extracted from a self-contained *auxiliary simulation* at each time step of the main simulation, which represents another common approach.

The efficient generation of accurate inflow conditions for LES still offers great potential for advancements. Recent studies showed that experimental data analyzed by structure identification methods might provide the duality of being both economical and realistic (e.g. Bonnet et al., 2003; Perret et al., 2006; Maruyama et al., 2012).

Computational grids LES fields generally depend both on the numerical method and the computational grid. Numerical errors have to be anticipated for commonly chosen grids with $\Delta/h = 1$ or $1/2$ (Pope, 2004), where h is the node distance. However, only few studies discuss the grid-dependence of LES in detail (cf. Chow and Moin, 2003; Sullivan and Patton, 2011, as some exceptions). The generation of the computational mesh is another demanding and time-consuming task, especially if complex geometries like urban environments or structured terrain have to be represented. Approaches like *immersed boundary methods* (e.g. Mittal and Iaccarino, 2005) show great promise to overcome some of these drawbacks. Another very active area of research is devoted to the testing of *local grid refinements*, e.g. in regions that exhibit strong gradients (e.g. Sullivan et al., 1996; Moeng et al., 2007), and the development of *solution-adaptive* gridding techniques for LES (e.g. Behrens, 2006; Löbig et al., 2009; Hertel and Fröhlich, 2011).

2.3 Atmospheric boundary-layer flows

The *atmospheric boundary layer* (ABL) is the lowest part of the troposphere. Being in direct contact with Earth's surface, the physics of ABL processes strongly differ from those of the so-called *free atmosphere* aloft, where the *geostrophic wind* is affected by horizontal gradients of synoptic pressure. The ABL extent can therefore be defined as the height up to that flow dynamics are considerably influenced by the planetary surface and deviate from geostrophic balance. The vertical structure of the boundary layer is variable in space and time. Typical depths are in the order of some 10^1 m to few 10^3 m (Stull, 1988). Among other factors, the ABL depth is influenced by radiative heating or cooling of the ground, wind magnitude, and surface structure and is subject to diurnal, seasonal, and geographic variations. The ABL is also commonly referred to as *planetary boundary layer* (PBL) – a term that stresses the planetary character of near-surface flows, e.g. with relation to the influence of Earth's rotation on flow dynamics.

With typical flow Reynolds numbers of $Re \sim 10^8$, boundary-layer motions are always turbulent. Dynamics and thermodynamics of the ABL are characterized by intricate processes that complicate data analysis and interpretation, numerical modeling, and theoretical descriptions (e.g. turbulent mixing, buoyancy effects, radiative transfer or phase-changes). Furthermore, the flow is considerably influenced by characteristics of the underlying surface and its roughness texture (e.g. smooth water or grassland surfaces in contrast to rough plant or urban canopies), its elevation (e.g. hilly or mountainous terrain), its inclination (e.g. triggering of katabatic or anabatic flows), or its albedo.

The following paragraphs give a brief overview of important ABL properties with a focus on the characteristics of near-surface atmospheric turbulence. A survey of LES studies of atmospheric boundary-layer flows completes the section. It is followed the textbooks by Stull (1988), Garratt (1994), Arya (2001), and Wyngaard (2010).

2.3.1 ABL characteristics

The main forcing of ABL air flow is the geostrophic wind in the free atmosphere. Turbulence is produced by wind shear due to frictional effects at the surface. The thermal structure of fluid layers and associated buoyancy effects are another major source for turbulence and have a significant influence on the mechanically produced eddies.

A commonly employed division of the ABL forming over rough ground is reproduced in Figure 2.7a following Arya (2001), where the indicated heights are typical for neutral stability conditions and strong winds. The lowest ~10% of the ABL represent the so-called *atmospheric surface layer* (ASL), which includes the *roughness sublayer* and the *viscous sublayer* (not depicted). The latter denotes a very thin layer ($\mathcal{O}(10^{-2}\,\mathrm{m})$) in direct contact with the ground, which represents the only ABL region where viscous stresses are prevailing and the flow is laminar. To engineers the ASL is better known as *Prandtl layer*.

Within the *inertial sublayer*, as the outer part of the ABL, the dynamical influence of the surface decreases with height and the flow eventually readjusts to the conditions of the free atmosphere. Meteorologists usually refer to this region as *Ekman layer*, in honor of the Swedish oceanographer who first described its flow dynamics as a result of the balance of pressure gradient force, surface drag, and Coriolis force (*Ekman spiral*).

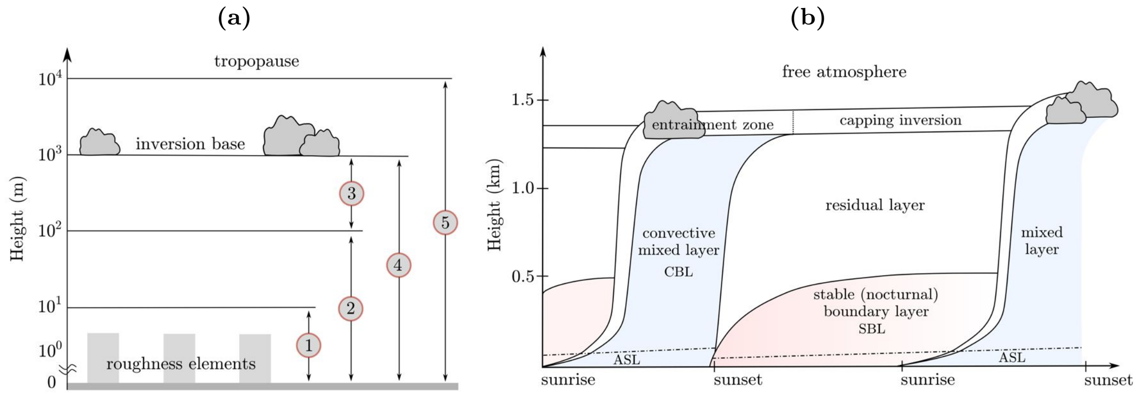

Figure 2.7: Static height structure and diurnal evolution of the ABL. (a) Layer classification for neutral stability and strong winds according to Arya (2001), including the ① roughness sublayer, ② atmospheric surface layer, ③ inertial sublayer, ④ ABL, and ⑤ troposphere. (b) Daily cycle of the ABL structure over land during fair weather conditions as indicated by Stull (1988, 2000).

Stull (1988) schematically describes the typical time evolution of the mid-latitude ABL during fair weather as the dynamical response to the diurnal cycle of surface heating and cooling (Fig. 2.7b). During daytime, solar heating results in enhanced turbulent mixing in the so-called *convective* boundary-layer (CBL), which is often accompanied by cloud formation at the boundary-layer top. As a consequence of nocturnal radiative cooling, this *mixed layer* is replaced by a *stable* boundary-layer (SBL) of much smaller vertical extent, in which turbulence is suppressed. The remains of the daytime CBL well above the stable near-ground layer are called *residual layer*. Arya (2001) specified typical boundary-layer depths in the range of ∼0.2–5 km for the CBL and ∼20–500 m for the SBL.

Governing equations

For an incompressible fluid with the continuity condition given by Eq. (2.2), a common formulation of the *momentum balance equation* for the ABL (Wyngaard, 2010) yields

$$\frac{\partial U_i}{\partial t} + U_j \frac{\partial U_i}{\partial x_j} = -\frac{1}{\rho}\frac{\partial P}{\partial x_i} + \frac{g}{\Theta_0}\Theta' \delta_{3i} - 2\epsilon_{ijk}\Omega_j U_k + \nu \frac{\partial^2 U_i}{\partial x_j \partial x_j} \,. \tag{2.33}$$

Two additional forcing terms have entered the earlier expression given in Eq. (2.5): *gravitation/buoyancy* and the *Coriolis effect*. The latter enters through the third term on the right-hand-side, where Ω_j is the angular velocity of the rotating Earth and ϵ_{ijk} is the *Levi-Civita permutation tensor*. The Coriolis term is often simplified to its dominant contribution, $\epsilon_{ij3}\, f_c\, U_j$, where the *Coriolis parameter* is defined as $f_c \equiv 2\,|\mathbf{\Omega}|\sin\varphi$, and φ is the geographic latitude. The sign of φ determines the direction of flow deflection.

The gravitational acceleration only acts in the vertical, i.e. $\mathbf{g} = (0, 0, -g)$. Using a frequently employed assumption, buoyancy effects only enter the system through the balance equation of the vertical velocity component and are combined with the gravitational acceleration through the term $g\,\Theta'/\Theta_0$. Here, Θ' are boundary-layer perturbations of the synoptic-scale reference value of *potential temperature* Θ_0. It is assumed that these perturbations are of much smaller magnitude than the reference value. The term represents the vertical buoyancy acceleration of air parcels in the presence of density (or temperature) perturbations. This formulation is known as *Boussinesq approximation* and often used in boundary-layer and meso-scale meteorology. Especially in boundary-layer modeling, a further common practice is to introduce the notion of *geostrophic balance* between the pressure gradient force and Coriolis acceleration to Eq. (2.33) and to replace the horizontal pressure gradients with

$$-\frac{1}{\rho}\frac{\partial P}{\partial x} = -\frac{1}{\rho_0}\frac{\partial P'}{\partial x} - f_c V_g \quad \text{and} \quad -\frac{1}{\rho}\frac{\partial P}{\partial y} = -\frac{1}{\rho_0}\frac{\partial P'}{\partial y} + f_c U_g \,, \tag{2.34}$$

where U_g and V_g are the horizontal components of the geostrophic wind, P' represents pressure perturbations, and ρ_0 is the reference value of density.

Typical ABL scales

A pronounced time-space variability is common to all turbulent flows. Atmospheric turbulence, however, represents a special case due to the high Reynolds number and correspondingly large ranges of eddy length, velocity, and time scales. Typical processes in the ABL have durations in the order of 1 s to 1 day. Long-term temporal changes of boundary-layer structure and depth are caused by the generation and propagation of synoptic systems. Typical velocity scales are 1 m/s in the lower ABL and 10 m/s at its top.

The characteristic vertical length scale is usually defined by the ABL depth, δ, and is in the order of 1 km. Typical horizontal length scales commonly extend over 10 km. Over longer periods, interactions between the atmosphere and Earth's surface can affect the entire troposphere (i.e. $z \sim 10$ km). Following Wyngaard (2010), typical turbulent eddy sizes in the daytime ABL are spanning six decades, ranging from scales in the order of 1000 m to 1 mm. For ABL flows over homogeneous terrain, energy-containing eddies have typical sizes in the order of $\ell_0 \sim 100$ m. Corresponding inertial subrange eddies have length scales of 30 m to 3 cm, and dissipative eddy sizes range from 1 cm to less than 1 mm.

The dynamical and physical separation of macro-scale and meso-scale phenomena from micro-scale turbulence is common practice in boundary-layer meteorology. This approach was mainly motivated and is still legitimated by the early study of Van der Hoven (1957) about the large-range energy density spectrum of ABL wind speed. His analysis of contributions to the total wind speed variance from various frequency components pointed out distinct peaks associated with synoptic-scale pressure disturbances with periods of $\sim$ 4 days, diurnal variations ($\sim$ 12 hours), and turbulence with typical peak time scales of few minutes (see the reproduction of Van der Hoven's spectrum in Fig. 2.8). Between these regions, a local minimum of spectral energy centered at about 1 hour is evident, which is now commonly referred to as the *"spectral gap."* While further studies could substantiate at least the *tendency* toward a gap (e.g. Oort and Taylor, 1969; Hess and Clarke, 1973), the generality of its existence and its flow characteristics are still a topic of ongoing research. As discussed by Smedman-Högström and Högström (1975), the gap region includes a variety of motions ranging from roll vortices and gravity waves to local circulation phenomena like land-sea breezes or deep convection.

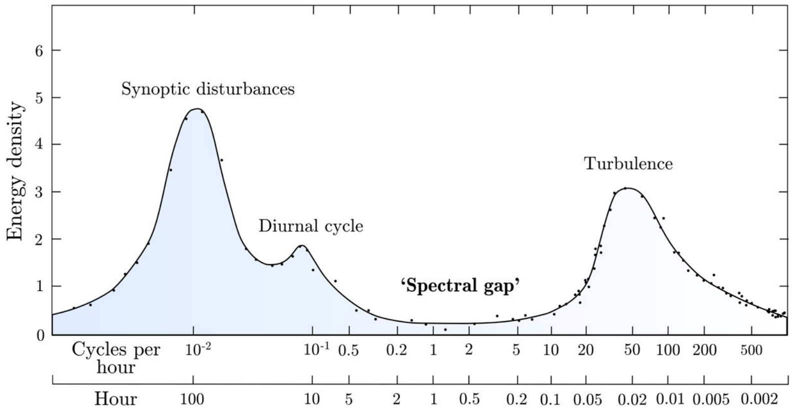

Figure 2.8: Energy density spectrum of horizontal wind speed in the atmospheric boundary layer from observations at $z \simeq 100\,\mathrm{m}$ obtained by Van der Hoven (1957).

The spectral gap or the assumption of its existence, to be more precise, is a far-reaching prerequisite for the analysis of field observations. The replacement of the ensemble average by a temporal mean, for example, can only be justified if the averaging time falls into the spectral gap. As Finnigan (2004) argues, only then "(...) turbulent motions will be varying on much shorter time scales than the means and on time scales that characterize changes in the means, [and] the turbulence moments may approximate statistical stationarity." Typical meso-scale models use grid spacings that lie in the gap region to disconnect the deterministic forecast of large-scale motions from turbulence, which only enters in parameterized form.

Inherent uncertainty

Another characteristic of atmospheric turbulence is reflected in the unavoidable difference between its most likely state in an ensemble-mean sense and its average behavior over a finite timespan in a single realization. Lumley and Panofsky (1964) and Wyngaard (1992) discuss this *inherent uncertainty* in terms of a stochastic variability defined as $\sigma_s^2 = \langle(\overline{U} - \langle U\rangle)^2\rangle$, where U can be a velocity component or any other turbulent variable, brackets imply an ensemble average as in Eq. (2.7) and the overbar denotes a time average (Eq. 2.8). If the flow is stationary over the averaging period T, σ_s^2 can be expressed as

$$\sigma_s^2 = 2\,\sigma_u^2\,\frac{\tau_0}{T}\ , \tag{2.35}$$

where σ_u^2 is the ensemble variance of U and $\tau_0 \ll T$ is the integral time-scale of the process. The relevance of the stochastic variability arises from the fact that the ratio $\sigma_s/\langle U\rangle$ can be of order unity for averaging times during which stationarity of the mean flow can be assumed (approximately 1 hour with reference to the preceding paragraph). During field measurements, it is usually not possible to measure sufficiently long under roughly the same boundary conditions to significantly reduce the stochastic variability of turbulence statistics derived from these observations. This fact is "increasingly recognized as an important aspect of boundary-layer meteorology" (Wyngaard et al., 1984) and will be addressed again in Chapter 3 in the context of validation data requirements.

Taylor's frozen turbulence hypothesis

Typical measurements in the ABL, being it in the field or the laboratory, are carried out with time-recording sensors positioned at only a few static locations. The *spatial* variability of the turbulent flow, thus, can usually not be directly determined from experiments since this would require simultaneous measurements at a multitude of positions.[7]

A workaround was proposed by Taylor (1938) as a byproduct of his classic paper on the spectrum of turbulence. The assumption is now known as *frozen turbulence hypothesis* and relates the time record of a turbulent variable, e.g. U, at a fixed spatial location to its space record detected upstream of the sensor. From the relation $t = x/\overline{U}_a$, where $\overline{U}_a$ is understood as a mean *advection velocity* over the recording time and the distance x being measured at time $t = 0$ upstream of the location where U has been recorded, Taylor's (1938) hypothesis proposes $U = f(t) = f(x/\overline{U}_a)$. The reliability of this approximation is highest if the turbulence level of the flow (e.g. measured in terms of the root-mean-square velocity, σ_u) is low compared with the mean velocity, if turbulence statistics are stationary, and if the flow field is spatially homogeneous. Then the structure of turbulent eddies with length scale ℓ can be assumed unvaried (*"frozen"*) during the timespan required for their uniform advection past the sensor, i.e. $\ell/\sigma_u \gg \ell/\overline{U}_a$ (Wyngaard, 2010).

The approach is frequently used for the analysis of turbulence data, e.g. to relate autocorrelations or derivatives in time and space or to convert frequencies into wavenumbers for spectral analyses (i.e. $\kappa_1 = 2\pi f/\overline{U}_a$). The validity of the hypothesis in ABL flows has been critically discussed in several studies and refinements for its application to flows of high turbulence intensity were proposed (see e.g. Lumley, 1965; Powell and Elderkin, 1974; Wyngaard and Clifford, 1977). However, in situations in which the mean velocity is small compared with the turbulent velocity scale, as it is the case for typical flow scenarios within urban canopies, it should generally be refrained from using Taylor's hypothesis.

Atmospheric surface layer

Important characteristics and scaling concepts of the *atmospheric surface layer* as the lowest part of the ABL are discussed in the next paragraphs. Because the ASL is readily amenable through ground-based observations – especially over homogeneous surfaces – its characteristics are rather well explored. Furthermore, the deflecting influence of the Coriolis force is usually negligible (Tennekes and Lumley, 1972), which makes the ASL a typical working area for boundary-layer wind-tunnel studies of atmospheric turbulence.

In contrast to the depth of the entire boundary layer, the vertical extent of the surface layer is not as well-defined and readily determinable. For stationary, horizontally homogeneous flows, experimental data indicate that turbulent fluxes of momentum and scalars as well as the turbulence kinetic energy are approximately constant with height throughout the ASL. The alternative notion of a *constant-flux layer* indicates that this constancy of fluxes is often used as a definition for the surface layer and its depth. Another distinct characteristic of the ASL is its height-dependent velocity structure, which can be described

[7] With recent advances in laboratory measurement techniques (e.g. *particle image velocimetry*) and remote-sensing instrumentation in the field, this issue starts to be eased. However, innovative space-resolving techniques still are far from being standard for most research applications.

by the so-called *logarithmic law* that is valid in the very idealized situation of stationary, neutrally stratified flow over flat and homogeneous terrain within the constant-flux layer.

The *log-law* can be purely derived from dimensional argumentation (cf. Arya, 2001). Another approach is based on *Boussinesq's analogy* (Eq. 2.15; Section 2.1.3), which relates the vertical turbulent momentum flux to the vertical mean flow gradient according to $\langle u'w' \rangle = -\nu_t \, \partial\langle U \rangle / \partial z$, where $\langle U \rangle$ is the ensemble-mean streamwise velocity, and it is assumed that the gradient $\partial\langle W \rangle/\partial x$ is negligibly small. Following the classic argumentation, the eddy viscosity, ν_t, can be represented as the product of characteristic length and velocity scales of the flow. In the spirit of Prandtl's *mixing length hypothesis*, the representative length scale l_m of the near-wall turbulent momentum exchange is proportional to the distance from the surface, z. The proportionality factor is the so-called *von Kármán constant* K – a dimensionless universal parameter – resulting in the relation $l_m = K\,z$. The experimentally determined values of K vary between 0.32 and 0.65 (Högström, 1996) with a usually anticipated value of $K = 0.39 \pm 0.01$ (Frenzen and Vogel, 1995).

The characteristic velocity scale of the near-wall flow is referred to as *friction velocity* and defined by $u_* \equiv \sqrt{\tau_{13,w}/\rho} = \sqrt{-\langle u'w' \rangle_w}$, where the index w refers the stress at the *wall* (i.e. at $z = 0$). Since the actual wall shear stress is difficult to determine experimentally, the constant-flux concept is often used to obtain u_* through the height-averaged value of $\langle u'w' \rangle$ over the ASL depth. With the eddy viscosity expressed as $\nu_t = u_* l_m = u_* K z$ and the definition for u_*, the vertical derivative of the mean streamwise velocity is given by

$$\frac{\partial\langle U \rangle}{\partial z} = \frac{u_*}{K\,z} \; . \tag{2.36}$$

Integrating the above formulation yields $\langle U \rangle(z) = u_*/K \ln z + C \equiv u_*/K \ln\left(z/z_0\right)$, in which z_0 is the so-called aerodynamic *roughness length* introduced as an integration constant. At $z = z_0$, the mean velocity $\langle U \rangle$ is zero. Figure 2.9a shows an example of a logarithmic velocity profile with z_0-identification obtained from boundary-layer wind-tunnel measurements of ASL flow over a moderately rough surface. The corresponding values of the von Kármán constant (see Fig. 2.9b) were derived by solving Eq. (2.36) at each height.

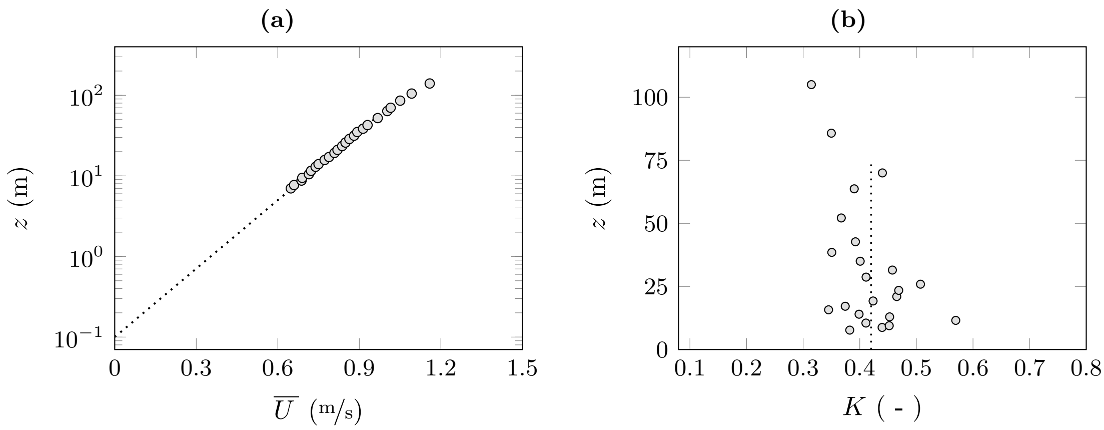

Figure 2.9: (a) Vertical profile of the mean streamwise velocity, $\overline{U}$, for flow over a moderately rough surface with a roughness length of 0.1 m. (b) Respective values of the von Kármán constant, K, with an ASL mean value of ~ 0.42 (dotted line).

The roughness length is usually determined by extrapolating the velocity profile on a semi-logarithmic graph to its intersection with the ordinate at an abscissa value of $\langle U \rangle = 0$, as illustrated in Figure 2.9a. The value of z_0 is connected to the height of roughness elements at the ground. For smooth to moderately rough surfaces, Plate (1971) derived the approximate relation $z_0/\langle \mathrm{H_r} \rangle \sim 0.15$, with $\langle \mathrm{H_r} \rangle$ being the average height of the roughness elements. An overview of empirically estimated z_0-values for different surfaces, ranging from few millimeters over calm seas or snow cover up to few meters for densely built-up urban environments with high-rise buildings, is presented by Stull (1988).

Based on similarity arguments and experimental evidence, further ASL relations for important turbulent parameters can be defined for neutral stratification. Counihan (1975) found that the *standard deviations* of velocity fluctuations have relations $\sigma_2/\sigma_1 \simeq 0.75$ and $\sigma_3/\sigma_1 \simeq 0.5$, and the *turbulent fluctuation levels* are given by $\sigma_1/u_* \simeq 2.5$, $\sigma_2/u_* \simeq 1.875$, and $\sigma_3/u_* \simeq 1.25$ in the neutral ASL over homogeneous rural terrain. In the near-wall region, the *turbulence kinetic energy* is related to the friction velocity through $k = C_e\, u_*$, where C_e is a universal dimensionless constant, which typically takes values between 5 and 6. Following from dimensional analysis and assuming an equilibrium between TKE production and destruction, the ASL *dissipation rate* is given by $\varepsilon = u_*^3/(K\, z) = C_k^{-3/2} k^{3/2}/(K\, z)$. Further statistical properties of ASL flow are discussed by Counihan (1975).

An important extension of the above considerations to *stratified* flow is the *Monin-Obukhov similarity theory* (cf. Obukhov, 1946, 1971).[8] It is postulated that for locally homogeneous, quasi-steady flows, turbulence and mean field characteristics only depend on the height above ground, z, the kinematic momentum flux, $\langle u'w' \rangle_w$, the kinematic potential temperature flux, $\langle w'\theta' \rangle_w$, and on buoyancy expressed as g/Θ_0. These four quantities are combined in the *stability parameter* $\zeta \equiv z/L$, which takes the form of a dimensionless height. The quantity L is the so-called *Monin-Obukhov length*, defined as

$$L = \frac{u_*^3\, \langle \Theta \rangle}{K\, g\, \langle w'\theta' \rangle_w} \ . \tag{2.37}$$

In the case of neutral stability, $L \to \infty$ since the temperature flux vanishes and $\zeta = 0$. The Monin-Obukhov length takes positive values if the ASL is stably stratified and is negative in convective conditions. The parameter ζ, thus, is a measure of the dominance of buoyancy or wind shear effects in the stratified ASL. The refined similarity relation for the vertical gradient of the mean wind in *diabatic* conditions as a function of z/L yields

$$\frac{K\, z}{u_*}\, \frac{\partial \langle U \rangle}{\partial z} \equiv \phi_m(\zeta) \ , \tag{2.38}$$

where $\phi_m(\zeta)$ is a *universal function* of dimensionless wind shear. The constraint for neutral stability requires that $\phi_m(0) = 1$ in order to result in Eq. (2.36). Similarly, Monin-Obukhov similarity yields representations for the surface-layer gradients of mean potential temperature (via ϕ_h) and mean scalar concentrations (e.g. in terms of atmospheric water vapor through ϕ_c). For the convective and stable case, empirical expressions for ϕ_m and ϕ_h were formulated based on extensive analyses of early ASL field data (frequently employed analytic functions were proposed by Dyer and Hicks, 1970; Businger et al., 1971).

[8] Obukhov's 1971 article is the English translation of his Russian 1946 original paper.

Figure 2.10a shows dimensionless wind shear and potential temperature gradients as a function of the stability parameter, ζ, according to the empirical relations derived by Dyer and Hicks (1970). These are given by $\phi_m^2 = \phi_h = (1 - 16\,\zeta)^{-1/2}$ for $\zeta \leq 0$ (unstable) and $\phi_m = \phi_h = 1 + 5\,\zeta$ for $\zeta \geq 0$ (stable).

An alternative measure of atmospheric stability, which is frequently employed, is the so-called turbulence *Richardson number*, which weighs buoyancy against inertia forces per unit mass. Two common expressions of this dimensionless parameter exist: the *gradient Richardson number*, Ri_g, and the *flux Richardson number*, Ri_f, defined as

$$Ri_g = \frac{\frac{g}{\Theta_0}\frac{\partial\langle\Theta\rangle}{\partial z}}{\left(\frac{\partial\langle U\rangle}{\partial z}\right)^2} \qquad \text{and} \qquad Ri_f = \frac{\frac{g}{\Theta_0}\langle w'\theta'\rangle_w}{\langle u'w'\rangle_w \frac{\partial\langle U\rangle}{\partial z}}\,, \tag{2.39}$$

where the latter is specified in terms of TKE production rates resulting from buoyancy and shear, respectively (Wyngaard, 2010). The gradient Richardson number can be related to the universal M-O functions through $Ri_g = f(\zeta) = \zeta\,\phi_h/\phi_m^2$. Invoking the eddy-viscosity hypothesis to relate turbulent fluxes to mean flow gradients, it can be shown that $\phi_h/\phi_m = \Gamma_h/\nu_t$ and the Richardson numbers are related through $Ri_f = \Gamma_h/\nu_t\,Ri_g$. Using Dyer's expressions for the ϕ-functions, the quantitative dependence of Ri_g on ζ can be computed as $Ri_g = \zeta \leq 0$ (unstable) and $Ri_g = \zeta/(1+5\,\zeta) \geq 0$ (stable). Figure 2.10b shows this dependency. Based on the analytical relationship, Ri_g converges to a *critical value* of 0.2 for infinitely large positive values of ζ. Testing the validity of the empirical expressions in extremely stable or unstable conditions, is a topic of strong scientific interest.

The influence of stratification on turbulent eddy structures can for example be evaluated based on modifications of their energy spectra. Kaimal et al. (1972) observed systematic shifts of the spectral peaks as a function of ζ in field data, with a tendency toward lower peak frequencies for stable conditions and higher ones in the unstable case, where a leveling toward constancy has been found as a state of free convection was reached.

For further insights into similarity relations and discussions of flux and TKE budgets in the diabatic ABL, it is pointed to the reviews by Sorbjan (1986) and Wyngaard (1992).

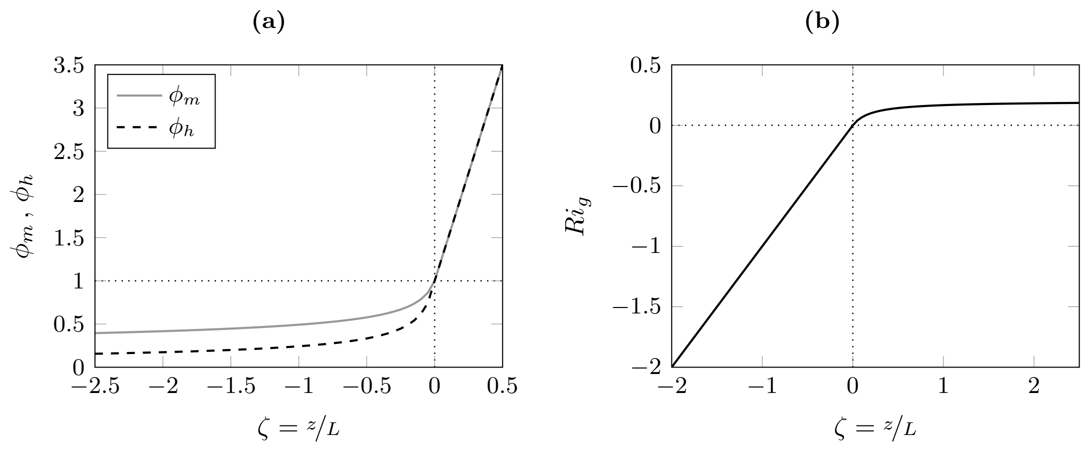

Figure 2.10: (a) ϕ-functions and (b) gradient Richardson number for different values of the parameter ζ, following the parameterization by Dyer and Hicks (1970).

2.3.2 Examples of LES studies of the ABL

Since the first comprehensive studies with LES in the 1970s, the technique has been intensively applied in research on atmospheric dynamics under the influence of thermal stratification, topographical forcing or surface roughness characteristics.

The focus of these studies ranges from fundamental problems (e.g. the investigation of similarity relations or SFS dynamics and parameterizations) to applied research in the field of micro-meteorology. Sullivan et al. (2003) summarize: "Most LES of the PBL adopt the following working flow model: high Reynolds number (implying that the molecular viscosity is small and not included in the set of governing equations), incompressible, Bousinessq equations with Monin-Obukhov similarity theory as a lower boundary condition (...)."

Starting with Deardorff (1970b), studies of the *neutrally stratified* ABL as an idealized dynamical state provided insight into spatial characteristics of turbulent flow structures and allowed to test classic similarity hypotheses. Via two-point spatial correlations, Mason and Thomson (1987) could identify similarities with technical shear flows concerning the elongated structure of boundary-layer eddies. Today, the neutral stability state is still the prevalent starting point for numerical studies in complex geometries.

In the case of the *unstable* atmospheric boundary layer, early LES led to the formulation of fundamental scaling laws. Based on comprehensive simulations of the CBL, Deardorff (1970c) derived convective scales for length, velocity, and temperature, which for the first time allowed a dynamical treatment of the problem in the framework of statistical similarity. In later experimental and numerical studies, the now classic *Deardorff scaling* could be successfully applied. The time-space structure of the growing and fully developed CBL has been further investigated with LES. for example, by Mason (1989), Schmidt and Schumann (1989), Letzel and Raasch (2003), and in direct comparison to wind-tunnel data by Fedorovich et al. (2001a,b). LES also substantially contributed to the understanding of *entrainment* processes, in which stably stratified air is mixed into the growing CBL. Early investigations by Deardorff (1974b) revealed the influence of entrainment on turbulence characteristics even deep within the mixed layer. Through flow visualization and quadrant-analysis techniques, Sullivan et al. (1998) could derive structural information about buoyant plumes and draw conclusions about driving physical mechanisms.

While a well-grounded theoretical framework had been established for the CBL, this task turned out to be more complicated for the *stable* case, in which turbulent intermittency as well as inertial and gravitational oscillations enhance the unsteadiness of the boundary-layer structure. The first LES of the SBL was conducted by Mason and Derbyshire (1990), who determined a strong dependence of the mean fields on the fully-dissipative Smagorinsky-type SFS model under moderate spatial resolution. Switching to a parameterization scheme that included stochastic backscatter, Brown et al. (1994) obtained more realistic results with reference to what has been known about the SBL structure from observations. Further studies illustrated the complexity of the SBL through the interplay of turbulence and wave motions (e.g. Andrén, 1995) and discussed the evolution of SBL parameters toward a quasi-steady state (e.g. Kosović and Curry, 2000).

In view of rapid advancements in LES, efforts have been made to combine the knowledge of different research groups world-wide in terms of code comparison studies. Comprehensive surveys were presented by Andrén et al. (1994) for the neutral ABL, by Nieuwstadt et al. (1993) for the CBL, by Moeng et al. (1996) for the strato-cumulus topped boundary layer, and more recently by Beare et al. (2006) for the SBL. Bringing together the *status quo*, these studies allowed to assess the simulation performance with respect to variations of SFS parameterizations, initial and boundary conditions, and numerical methods, resulting in a better understanding of necessary improvements.

Further insightful discussions on the parametric and structural uncertainties of the LES approach were presented by Chlond and Wolkau (2000) for the test case of a nocturnal, strato-cumulus topped, marine ABL. In a systematic approach, the authors were able to determine uncertainty ranges of the numerical results based on the simulation duration and on changes in mean flow parameters prescribed as initial and boundary conditions.

The earlier LES studies almost exclusively focused on atmospheric flows that were characterized by a horizontally homogeneous surface at the bottom boundary — a constraint, which allows for the "safe" use of periodic boundary conditions in horizontal directions. Realistic surfaces, however, are rarely perfectly homogeneous. Extreme cases of complex surface forms are forests and urban canopies. The prevalent implementation of vegetated surfaces in LES is to use a homogeneous drag layer, in which the local *leaf area density* is linearly related to the drag force (e.g. Shaw and Schumann, 1992; Huang et al., 2009). Recently, Schlegel et al. (2012) presented an LES study with a very detailed, vertically and horizontally heterogeneous representation of a real forest derived from high-resolution laser scans. In comparison to a homogeneous plant area distribution, the authors showed that complex flow pattern could only be captured in the detailed model. A review of LES studies in urban environments is presented in Section 2.4.2.

The influence of hilly or mountainous topography on ABL flow is another promising area for LES. The effect of idealized, hilly terrain on CBL dynamics was for example investigated by Walko et al. (1992) and Gopalakrishnan et al. (2000). Chow and Street (2009) conducted an LES study of neutral flow around the Askervein hill in order to test the performance of different SFS models in the presence of terrain and discuss the potential of explicit filtering to improve future LES.

The dispersion of scalar quantities within the ABL has been another focus of recent LES studies. Taking advantage of the fact that LES time series have the potential to provide insight into transient events, Xie et al. (2004) apply concepts of extreme value theory to their simulation results of plume dispersion over a rough surface. Other studies concentrated on dispersion characteristics in the CBL (e.g. Gopalakrishnan and Avissar, 2000), in complex terrain (e.g. Michioka and Chow, 2008), or subject to chemistry models that allow for the representation of reactive plumes (Meeder and Nieuwstadt, 2000).

The dependence of LES on the numerical grid and advancements of *nesting* strategies for LES are of growing interest as well. Allowing for the refinement of the computational grid in certain flow regions, the two-way nesting of a fine-grid LES into a coarse grid has been proposed by Sullivan et al. (1996) and was applied within the Weather Research and Forecasting model by Moeng et al. (2007). Chow et al. (2006) used a one-way nesting of LES into a meso-scale simulation in order to specify the lateral boundary conditions for flow inside a steep alpine valley, for which periodicity would have led to erroneous results. The major practical challenge of such activities is given by the merging of two intrinsically different model categories at the nest boundaries: a turbulence-resolving large-eddy model and a meso-scale model, which fully parameterizes turbulence.

2.4 Urban boundary-layer flows

Urban environments represent the roughest surfaces on Earth. The aerodynamic, thermodynamic, and radiative effects of cities not only locally affect turbulence and ABL flow characteristics, but can also have strong impact on surrounding rural regions and on synoptic-scale atmospheric patterns. Urban areas are locations where people are exposed to a wide range of environmental hazards and climatic stresses (e.g. Hopke, 2009). The worldwide progression of urbanization resulted in an increasing awareness of the importance of research in the fields of urban micro-meteorology, urban climate, and air quality by governmental and regulatory bodies (Austin et al., 2002). The additional fact that cities and their residents are major actors in climate-change scenarios and future projections further urge decision makers to improve concepts of urban planning and sustainability (see Grimmond et al., 2010, for a recent appeal from the scientific community).

Cities are major perturbations for ABL flow and can be regarded as *"roughness islands"* and *"heat islands"* (Arya, 2001). The surface structure of urban areas typically is heterogeneous and characterized by pronounced roughness changes (e.g. high-rise city cores surrounded by low-rise residential areas). Thermodynamic and radiative processes in urban areas are affected by anthropogenic heat and moisture productions, heat-storage capacities of concrete and other building materials, and the fact that soils are mostly sealed, causing a reduction of evapo-transpiration potential. The most prominent climatic manifestation of these effects is the urban heat island, reflected in distinct air temperature differences between urban and rural areas (see Oke, 1987, for details). The diversity of dynamical components and their complex interactions make urban environmental studies key research areas of many scientific disciplines like micro-meteorology, wind and civil engineering, physical geography, atmospheric chemistry or architecture.

Figure 2.11 schematically indicates the evolution of an *urban boundary layer* (UBL) in response to a roughness transition as an internal layer of the ABL. The depth of the UBL grows with increasing distance (fetch) from the transition region. Typically, a very long fetch is needed until the ABL flow has adjusted to the new roughness and the UBL is in equilibrium with the underlying structure. Only then, the UBL can generate further internal layers, in which physical properties can be studied by statistical means.

The next paragraphs present an overview of some physical aspects of urban environments and their numerical investigation. It is followed the reviews by Grimmond and Oke (1999), Roth (2000), and Britter and Hanna (2003) and the texts by Oke (1987) and Arya (2001).

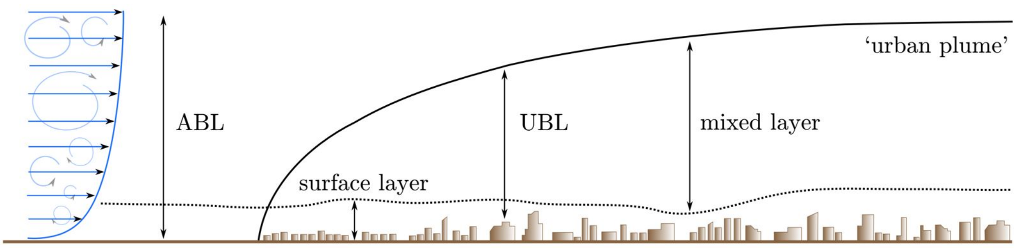

Figure 2.11: Meso-scale view of the urban boundary layer after Oke (1976, 1988).

2.4.1 UBL characteristics

The vertical structure of the UBL is usually broken down into further sublayers according to their driving physics and distinct scaling behavior (see Fig. 2.12 and Oke, 1988). The *urban canopy layer* (UCL) extends from the ground up to roof level. Here, the local dynamical and thermal structure of the flow is directly influenced by the surrounding roughness elements, e.g. in terms of separation and wake regions, recirculation zones, and heat emissions. The UCL is the lower part of the so-called *roughness sublayer* (RSL). In the upper part of the RSL, the influence of individual buildings is attenuated and the flow tends to respond to the united effects of groups of obstacles. Here, the flow is still strongly heterogeneous and three-dimensional due to local advection and dispersive stresses.

The depth of the RSL may locally vary in response to the respective morphology of the underlying surface. As discussed by Roth (2000), a criterion for the existence of an RSL is the deviation of observed height-profile functions from relationships derived for flow over homogeneous terrain (Section 2.3.1). A heuristic but practical approach is to relate the vertical dimension of the roughness sublayer to the average building height, $\mathrm{H_m}$. Raupach et al. (1991) derived values of $\delta_{\mathrm{RSL}} \sim 2-5\,\mathrm{H_m}$ from a review of wind-tunnel measurements and field observations, which is mostly substantiated by other studies.

The top of the roughness layer is known as *blending height*, z_r. At this elevation, the flow is in a state of spatial homogeneity. Citing Grimmond and Oke (1999), the blending height, thus, "(...) represents the minimum elevation above a city at which observations are representative of the integrated surface rather than of its individual elements." The subsequent layer is denoted as *inertial sublayer* (ISL). Standard similarity concepts for the atmospheric surface layer may be applied here, assuming that the dominant gradients only occur in vertical direction. It is, however, acknowledged that a "sufficiently" long fetch is required for the development of a representative ISL and that this condition might not be met for areas that exhibit frequent roughness transitions (e.g. laboratory studies by Cheng and Castro, 2002a,b). In cities with very tall and dense building structures or in conditions of extremely unstable stratification, the ISL is likely to be very thin or even non-existent.

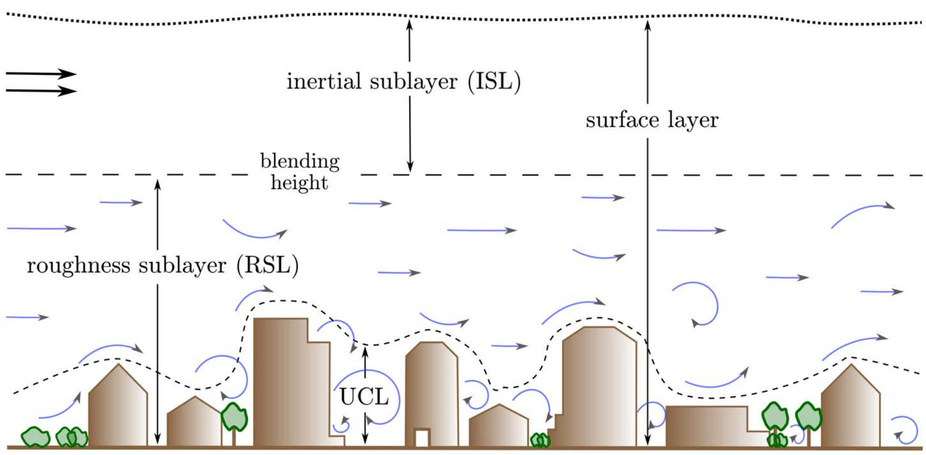

Figure 2.12: Micro-scale view of the urban boundary layer after Oke (1988).

Aerodynamic influence of buildings

The main roughness elements in cities are buildings and urban greenery, especially in the form of trees. From an aerodynamic point of view, buildings can be considered sharp-edged *bluff bodies*. The influence of isolated obstacles and building clusters on turbulent flow has been rather well investigated, primarily owing to fundamental studies in the field of environmental fluid mechanics, which have been accompanied by experiments in boundary-layer wind-tunnels at reduced scale (see Section 3.2 for further discussions on laboratory studies of urban flow). The aerodynamic role of trees in cities, on the other hand, is still poorly understood and devoid of broadly substantiated parameterization concepts and quantitative measures of aerodynamic impact. This is mainly due to the fact that trees are porous and bendable, which makes their physical and numerical modeling tricky and statistical generalizations from field measurements almost unfeasible.

Well above the urban canopy, the dense roughness structure of the city acts as a *displaced surface*. Hence, standard similarity approaches for ASL flow over homogeneous ground have to be modified for the application to the urban ISL. The analytic form of the vertical mean wind profile *above* the urban canopy, for example, is given by

$$\langle U\rangle(z) = \frac{u_*}{K}\left[\ln\left(\frac{z-d_0}{z_0}\right) + \phi_m(\zeta)\right] , \tag{2.40}$$

where d_0 is the so-called *displacement height*. According to the above refinement, the mean velocity is zero at a height of $z = z_0 + d_0$. In an extensive review study, Grimmond and Oke (1999) report typical values of the roughness length z_0 in the range of 0.3 m to > 2 m for low-rise/low-density to high-rise/high-density urban surface forms, deduced from micro-meteorological measurements and similarity assumptions. Corresponding values of the displacement height d_0 may vary from 2 m to more than 12 m. Another approach toward the derivation of aerodynamic roughness properties is based on algorithms that use *morphometric* measures for the urban structure (λ-*parameters*; see Grimmond and Oke, 1999, for details). In particular, measures of the buildings' *frontal area* and the *building density* are employed for this purpose. Another frequently inferred measure of building structure is the *aspect ratio* of building height to street-canyon width, H/W.

Inside the UCL, the presence of buildings evokes complex flow patterns associated with phenomena like separation, wakes and corner vortices – often perceived as discomforting by pedestrians. For flow approaching normal to the building surface, the leeward domain is dominated by the turbulent wake, which can form freely due to the sheltering effect of the upstream obstacle. The particular structure of the wake region depends on the arrangement of the roughness cluster. Assuming a homogeneous structure of roof heights, Hussain and Lee (1980) suggest that three general types of urban flow regimes can be distinguished: *Isolated flow* in terms of wakes from individual obstacles as a consequence of low building density; *wake interference* for shorter distances between buildings causing an intensification of wake structures; and *skimming flow* resulting from dense obstacle packing inducing a street-canyon flow behavior that seems to be decoupled from the wind field above rooftop. For certain aspect ratios and approach flow wind speeds, pronounced standing vortices may develop in leeward cavities in the skimming regime. Inside these *recirculation zones*, pollutants are effectively trapped and the flow field is characterized by high gustiness (Arya, 2001). As discussed by Oke (1987), the alignment of street canyons parallel to the approach flow can trigger an acceleration of wind speeds inside the canopy, known as *channeling effect*. An acceleration of velocities may also be observed just above rooftop. In the case of oblique angles between the approach flow wind direction and the building front, helical vortices can develop within leeward street canyons due to the interaction of recirculation and channeling effects.

Urban effects on different spatial scales

Britter and Hanna (2003) introduced four distinct horizontal scales on which climatic effects of urban environments are perceptible and typically studied: the *regional scale*, the *city scale*, the *neighborhood scale*, and the *street (canyon) scale*. Table 2.1 gives an overview of corresponding spatial extents and characteristic physical features that can be anticipated in these domains.

On the regional and city scale, urban areas basically represent a (thermo-)dynamical perturbation of the ambient conditions. The resulting effects can be advected into downstream rural areas as plumes of heat and pollution. The influence of individual roughness elements is blurred and only enters in integrated form. Effects on these scales have to be parameterized in numerical weather prediction models and meso-scale meteorological codes. In the latter case, the typical grid spacing is in the range of 2 to 10 km for general research and operational models, which allows detailed classifications of land-use features of downtown, residential or industrial settlements – typically in terms of characteristic roughness lengths, albedo specifications, and bulk parameterizations of sensible and latent heat fluxes as well as moisture at the surface (Britter and Hanna, 2003).

On the neighborhood and street scale, however, roughness elements have to be considered individually in order to reproduce obstacle-induced phenomena that dominate flow in these regimes. Numerical approaches for predictions on these urban micro scales need to be able to cope with this level of physical complexity.

Table 2.1: Urban boundary-layer effects on different horizontal scales following the classification by Britter and Hanna (2003).

Type	**Extent (km)**	**Features**
regional scale	$\sim$ 100 to 200	urban heat island & urban pollutant plume; perturbing influence on synoptic patterns; impacts on surface-energy balance
city scale	$\sim$ 10 to 20	increased surface drag; infusion of heat & moisture; horizontal displacements of regional flow
neighborhood scale	$\sim$ 1 to 2	isolation, wake interference & skimming flow; similarity approaches above the RSL
street scale	$\sim$ 0.1 to 0.2	building wakes; recirculation zones; corner vortices; flow separation & channeling

Obstacle-resolving micro-scale meteorological models and RANS-based CFD solutions are primarily used for the investigation of neighborhood and street-scale physics – with a strong focus on urban wind fields and contaminant dispersion processes. Most of the eddy-resolving CFD approaches like LES that are used in the context of environmental fluid mechanics focus on the investigation of very local phenomena in individual street canyons or around isolated roughness elements. Increasing computer power, however, rapidly augmented the use of LES for predictions of turbulent flow and concentration fields in much larger spatial domains. Further discussions of the current status of urban LES including a brief literature review are later presented in Section 2.4.2.

Urban atmospheric stratification

The influence of ambient atmospheric stratification and local thermal forcing due to differential heating of urban surfaces on flow and dispersion processes is another area of strong scientific interest because of its consequences for numerical modeling. It is often assumed that inside the roughness sublayer mechanical TKE production dominates over buoyancy contributions. As Britter and Hanna (2003) state, the aerodynamic effects described earlier "(...) all conspire to force the stability over urban areas toward neutral (adiabatic) conditions." The physical reasoning behind this assumptions is connected to the definition of the Monin-Obukhov length (Eq. 2.37). Since L scales with u_*^3, which can take large values over rough surfaces, and urban heat fluxes are assumed not to be excessively enhanced, $\zeta = z/L$ is expected to be close to zero. Britter and Hanna (2003) further argument that the heat storage capacities of building materials cause the vertical heat fluxes to mostly vanish at night, so that "(...) nearly neutral stability is assured." Roth (2000) argues similarly: The rough surface and the release of heat from buildings and other anthropogenic sources often result in neutral to slightly unstable conditions – making field site measurements of the stable UBL very rare. This "dogma" of a near-neutral state of urban flow provides the usual working point for boundary-layer wind-tunnel studies as well as numerical and statistical calculations of pollutant dispersion in cities.

Other studies demonstrated, however, that atmospheric stability does have an influence even on small-scale localized flow patterns below rooftop. Based on experimental data from a thermally stratified boundary-layer wind tunnel, Uehara et al. (2000) found that the recirculating flow inside a street canyon responded to the specified stratification with enhanced (unstable situation) or suppressed (stable case) intensities. Using a 2D RANS-based numerical model, Kim and Baik (2001) determined that the structure and strength of a thermally reinforced canyon vortex may also depend on the aspect ratio of the scenario. The derivation of fundamental findings from field observations, on the other hand, is difficult as the more recent analysis of field data from street-canyon towers by Ramamurthy et al. (2007) showed. However, for a limited range of stability classes that could be investigated, the authors could deduce that the momentum-related turbulence statistics are hardly affected by the ambient atmospheric stratification, while temperature-related statistics tend to exhibit much stronger sensitivity. Thus, while for moderate to high winds the surmise of shear production dominance might be justified, during weak wind conditions buoyancy is not negligible. In general, however, it can be argued that the conditions for neutral flow are more easily met in the UBL than over natural surfaces.

Some aspects of urban turbulence

Urbanized areas exert an increased aerodynamic drag and generate strong wind shear above roof level. The amplified momentum loss is compensated by enhanced turbulent fluxes above the canopy, resulting in stronger turbulence levels and TKE production rates compared with flows over homogeneous surfaces. In addition, aerodynamic effects inside the UCL produce strong turbulent mixing. Knowledge about turbulence characteristics in cities mostly stems from a multitude of laboratory studies in idealized or realistic urban scale models and from few field measurement campaigns that qualified for the retrieval of mean flow and turbulence statistics (see the review by Roth, 2000, for a comprehensive compilation of urban field studies covering the years 1918–1998).

A common approach to characterize urban turbulence is to compare urban RSL statistics with their homogeneous ASL counterparts. The comprehensive analysis of street-canyon field data measured in a city center by Rotach (1993a,b, 1995) revealed a clear alteration of turbulent flow characteristics in the urban roughness sublayer, away from standard similarity predictions. For example, a strong height-dependence of the Reynolds-stress component $-\langle u'w' \rangle$ was observed.[9] While the average Reynolds stress essentially yields zero at the mean level of the displacement height, d_0, a later increase with height is observed until a maximum is reached at an elevation of $z \sim 2\,\mathrm{H_m}$. It is argued that this peak marks the onset of the transition to the ISL regime. Following the maximum, other experimental studies indicated a linear decrease of the shear stress with height (e.g. Cheng and Castro, 2002a). The existence of a shear-stress peak is substantiated by further field investigations, although different peak heights are being reported, e.g.: $\sim 1.5\,\mathrm{H_m}$ by Oikawa and Meng (1995), $\sim 2.1\,\mathrm{H_m}$ by Feigenwinter et al. (1999) or $\sim 1\,\mathrm{H_m}$ by Louka et al. (2000). The span of $1 - 1.5\,\mathrm{H_m}$ was also obtained through densely-spaced boundary-layer wind-tunnel measurements inside a realistic urban canopy model by Kastner-Klein and Rotach (2004), who indicated a dependence of the maximum Reynolds-stress magnitude and its height on the immediate geometric surroundings of the analysis point. The authors further employed parameterization concepts to the vertical shear-stress profiles and discussed possible quantitative connections between peak height and building packing density. Figure 2.13a qualitatively shows the height structure of temporal averages of shear stress and streamwise velocity over an idealized two-dimensional street canyon.

Through the *quadrant analysis* of the instantaneous vertical momentum flux (see Raupach, 1981, for detailed definitions), Rotach (1993a) investigated the relative contributions of an upward transport of momentum deficit (*ejection*; $u' < 0$, $w' > 0$) and the downward transport of momentum excess (*sweep*; $u' > 0$, $w' < 0$). It was found that the momentum exchange in the vicinity of the roof level was largely dominated by sweeps, while the upward transport of fluid mass played a minor role. This prevalence, however, vanished at higher elevations. The strongest intermittency of the turbulent momentum flux was observed just below rooftop. The dominance of sweeps within the UCL has been confirmed in field observations by Oikawa and Meng (1995) and Christen et al. (2007), who reported an ejection prevalence only at heights well above the canopy.

[9] Rotach (1993a) uses the expression $(\langle u'w' \rangle^2 + \langle v'w' \rangle^2)^{1/2}$ to obtain the turbulent transport of horizontal momentum in the vertical direction and for the definition of the friction velocity u_*. Under the conditions that the x-axis is aligned with the mean wind direction, however, $\langle v'w' \rangle$ vanishes.

The shear stress profile plays a crucial role for the description of turbulence statistics when it comes to the derivation of scaling expressions for RSL integral quantities, which may be used as predictive parameterizations. Whereas over homogeneous surfaces the constancy of turbulent fluxes allows for a straightforward deduction of the surface friction velocity that is needed in the Monin-Obukhov similarity framework, no clear definition of a representative value of u_* exists for the UBL. The usually applied workaround is to use local shear-stress values instead. This concept of *local scaling* was introduced by Högström et al. (1982) in the context of an early urban field site study. As Rotach (1993a) states, this approach permits that flow statistics like the dimensionless velocity gradient "(...) can be described with the same semi-empirical function as in the inertial sublayer, provided that all variables are considered as local values." However, different specifications of local reference values are employed in literature without any general consensus being established yet.

The unique roughness structure of urban surfaces also leaves its footprint in the energy density spectrum of turbulence. The inertial-subrange behavior in terms of well-established $-5/3$-slopes is comparable to spectral shapes of flow over a uniform roughness. However, based on a more stringent test for local isotropy, Rotach (1995) found that urban flow is not truly isotropic in the inertial subrange at heights well within the RSL. While similar conclusions were drawn by Feddersen (2005), Högström et al. (1982) and Feigenwinter et al. (1999) saw clear evidence of fully-developed inertial subrange physics in their urban spectra – indicating the need for further research in this area. Furthermore, the sizes of integral length scale eddies associated with the spectral peak frequencies show deviations from anticipated empirical references for flow over homogeneous surfaces (e.g. spectral functions proposed by Kaimal et al., 1972). In his study overview, Roth (2000) reported that inside the UCL and in the vicinity of the canopy top a shift toward higher frequencies is evident in the spectra of the horizontal velocity components, while the peak of the vertical velocity spectrum is offset toward lower frequencies at all heights. The increase of the vertical eddy-length scale suggests that the vertical transport is dominated by wake turbulence that scales with the building dimensions. This is qualitatively in agreement with results by Rotach (1995), who reported maximum frequency shifts of the horizontal spectra in the mid-RSL in the order of a decade and by Feigenwinter et al. (1999), who additionally described dependencies on atmospheric stability.

It is also increasingly recognized that the study of *transient* (i.e. time-dependent) flow phenomena is at least as important as the averaged view on turbulence in order to characterize UBL processes. While research on *coherent flow structures* in the ABL initially had a strong focus on flow over plant canopies (e.g. Raupach and Thom, 1981; Finnigan, 2000), the scientific interest is continuously shifting toward investigating connections between organized eddy motions and turbulent transport in the urban RSL. For this purpose, field-site tower measurements permit to retrieve local, time-dependent flow features, which can be assessed through quadrant analysis. Early on, Oikawa and Meng (1995) described characteristic sweep and ejection patterns associated with sudden fluid bursts and connected distinctive ramp structures in temperature signals with the passage of large-scale coherent eddies. Based on conditional averages of ejection-sweep cycles within and above a street canyon, Feigenwinter and Vogt (2005) showed that fluctuation levels were highest just above the canopy and decreased with increasing distance from the buildings. The analyses by Christen et al. (2007) focused on the role of coherent structures for turbulent exchange at the interface between canopy and roughness sublayer. The authors associated ejection-sweep events with the advection and penetration of coherent structures from the roughness layer into the street canyon.

Progress in time-dependent, three-dimensional numerical modeling played an important role in coherent structure research since this approach, for the first time, permitted a spatially resolved view on urban turbulence. Based on DNS data, Coceal et al. (2007) took a first step toward the development of a conceptual model to describe unsteady RSL dynamics for the idealized case of a cube-array roughness at low flow Reynolds numbers. They associated low momentum streaks found above roof level with the passage of so-called *hairpin vortices* – an eddy class composed of counter-rotating vortex structures, which has been extensively studied in flat-wall boundary-layer flows (see e.g. Robinson, 1991; Adrian, 2007, for reviews on coherent eddy shapes). Figure 2.13b depicts a visualization of these urban coherent structures proposed by Coceal et al. (2007). Ejection zones are associated with flow locations between hairpin legs and sweep events with areas outside the vortex. A second flow regime evolves in the shear layer on top of the canopy. In this region, large-scale eddies are generated by the rolling-up of shear zones and intermittent vortex shedding from rooftops. These structures travel downstream, impinge on other buildings, and may excite recirculation patterns in street canyons. Within the UCL, the authors found inclined vortex structures with characteristic vorticity patterns. Due to the strong interaction of eddy motions in the UCL, a predominance of particular length scales, however, could not be determined. The building-induced eddies are considered to be of great importance for urban flow dynamics, particularly with view to their influence on momentum, heat, and pollutant transport.

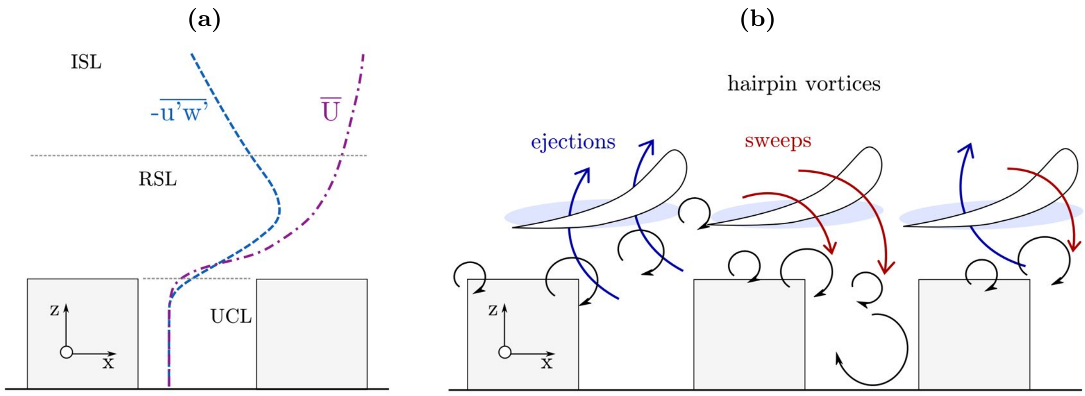

Figure 2.13: (a) Qualitative height evolution of $-\overline{u'w'}$ and $\overline{U}$ anticipated in the center of an idealized 2D street canyon. (b) Conceptual picture of turbulent motion in the urban RSL within and above a cube array, developed by Coceal et al. (2007). Hairpin vortices trigger low-speed streaks (shaded blue), ejections (blue arrows), and sweeps (red arrows). Smaller shear-layer eddies shed off of roofs to impinge on downstream buildings and might cause street-canyon recirculation. The mean approach flow is from left to right in both graphs.

2.4.2 Examples of urban LES studies

The application of LES to flow and dispersion predictions in urban environments started quite recently compared with early studies using the technique for ABL simulations. This is mainly due to practical challenges encountered in CFD simulations of complex urban structures like the physical and geometrical representation of obstacles, grid resolution requirements, and adjustments of the prevalent subfilter-scale models. However, particularly in the field of urban wind engineering and micro-meteorology, eddy-resolving approaches offer tremendous potential for practical and scientific applications, as, for example discussed in the review by Tamura (2008). Since the first comprehensive studies at the end of the 1990s, LES has been applied to a broad range of geometries such as

- *isolated buildings (e.g. wall-mounted cubes or other bluff bodies),*
- *isolated street canyons or intersections (e.g. as idealized 2D problems),*
- *idealized building arrangements (e.g. homogeneous or staggered cube arrays), and*
- *realistic environments on street to city scales.*

Most of today's urban LES literature focuses on strongly idealized urban environments, which allow to study fundamental flow features in isolation and systematically explore the parameter space of the simulation. However, especially within the last couple of years the number of urban LES publications has significantly increased and the analyzed flow problems became more complex, for example, by addressing heat transfer and including realistic geometries. The practical interest of such studies for micro-climatic applications is obvious, but time-dependent simulations also have strongly contributed to the comprehension of fundamental mechanisms of urban flow phenomena.

While RANS models still are the standard for engineering and micro-meteorological flow and dispersion calculations in the UBL, comparative studies revealed the benefits of LES, even on the mean-flow level. One of the earliest comparative RANS-LES studies that illustrated advantages of eddy-resolving simulations over steady-state methods was presented by Rodi (1997) for flow around different bluff bodies. Later, Xie and Castro (2006) compared LES and RANS predictions of flow over a cube array to wind-tunnel measurements and to the DNS data of Coceal et al. (2007). While the authors found the steady RANS results to be comparable to LES well above the urban canopy, the accuracy of the steady-state calculations significantly decreased below rooftop. The better performance of LES in the UCL was attributed to the ability to capture the inherent unsteadiness of urban flow. Similar conclusions were drawn by Salim et al. (2011) in the case of pollutant dispersion in a street canyon and by Tominaga and Stathopoulos (2011, 2012), who compared RANS and LES dispersion results inside an isolated street and within a cube array. In both configurations, the LES results were in better agreement with the reference experiments and provided a more realistic picture of the plume characteristics. These findings are also in agreement with the recent dispersion study in a realistic urban site (street scale) by Gousseau et al. (2011), in which the authors determined qualitative and practical benefits from LES predictions close to the pollutant source.

In the case of "pure" LES studies, the street-canyon scenario is a popular test case because it can be treated as an idealized two-dimensional problem (assuming infinitely long building rows through periodic lateral boundaries, which creates, however, a flow situation that will neither exist in nature nor in the laboratory). In recent years, sensitivity studies concerning the characteristics of street-canyon vortices or the efficiency of pollutant removal from cavities focused on the influence of the building morphology and thermal stratification. By varying the H/W ratio of their street canyon, Liu et al. (2004) determined typical pollutant retention and removal characteristics. Cheng and Liu (2011) studied skimming flow and dispersion characteristics under neutral, stable, and unstable ambient conditions imposed by ground-level heating/cooling and determined clear structural responses. Further studies in this context concentrated on combined effects of ground heating and varying aspect ratios (Li et al., 2012) and on the influence of differential heating of upwind and downwind building walls (Park et al., 2012). In an effort to move closer to reality, Gu et al. (2011) designed uneven building layouts to study dispersion processes in non-uniform street canyons. As expected, heterogeneous building forms enhanced the complexity of turbulent flow fields and the authors could show that certain obstacle arrangements can promote the removal of pollutants at pedestrian level.

Kanda et al. (2004) and Kanda (2006a) were among the first to systematically study *coherent flow structures* over urban canopies with LES and documented essential differences between flows over urban-like roughness and the conceptual understanding of flow over vegetation canopies. Their geometric test case consisted of cubic building arrays with adjustable building densities and configurations. For a square building arrangement (*D-type* roughness), Kanda et al. (2004) computed longitudinally elongated low speed streaks and corresponding streamwise eddies above the urban canopy, which were similar to well-studied structures in wall turbulence. In the case of staggered building geometries (*K-type* roughness), Kanda (2006a) determined characteristics of typical mixing layers.

A discussion on physical mechanisms of pollutant removal from the UCL was recently presented by Michioka et al. (2011) on the basis of time-dependent LES flow and concentration fields in successive street canyons. The study could relate emission events to the ejection of low-momentum fluid in the presence of small-scale coherent structures appearing just above the canyons. Recently, Inagaki et al. (2012) extended existent urban coherent flow-structure analyses to a classification of instantaneous flow patterns well below rooftop (i.e. flushing and cavity eddies). The authors identified coherent flow patterns inside the cube-array canopy that have length scales larger than the obstacle dimensions. These structures appeared to be closely related to organized motions at higher elevations.

LES studies in genuine urban complexities still are rather infrequent, and horizontal domains do usually not extend further than to the neighborhood scale (i.e. ~ 1 to $2\,\text{km}$). Examples of early successful applications of LES to flow and dispersion in realistic geometries were presented by Pullen et al. (2005) and Patnaik et al. (2007) for different U.S. cities. The authors could demonstrate that LES outperforms prevalent analytic plume models and discuss advantages of the implicit LES approach for large-scale urban simulations (cf. Section 4.3.1). Other examples of LES calculations in complex environments are the visualization study of scalar dispersion in downtown Tokyo by Letzel et al. (2008), simulations of flow and dispersion in a quarter of London by Xie and Castro (2009), or the recent LES of wind and concentration fields in downtown Macao by Liu et al. (2011).

Against this background, the LES of flow in the city of Hamburg that is subject of the following validation study, stands at the front line of what is currently feasible.

3 Simulation Validation

"State-of-the-art experiments and computations are certainly a prerequisite for progress in turbulence. However, it is a long way from measuring and seeing everything to understanding."

Frisch (1995)

(— *Turbulence: The Legacy of A.N. Kolmogorov.*)

3.1 Statement of the problem

The key to a successful application of a CFD model is the quantitative appraisal of its potential and limitations. The following paragraphs address conceptual and practical approaches of simulation validation with a focus on prognostic micro-scale meteorological codes used to study environmental flow. Challenges concerning the validation of time-dependent simulations are discussed together with demands on reference data for LES. In-depth further discussions of evaluation concepts and applications can be found in the reviews by Oberkampf and Trucano (2002) and Oberkampf and Roy (2010).

Established validation methodologies mostly originated from engineering disciplines and were formulated as a guidance for the effective application of CFD to problems of technical interest. This evolution is comprehensible since engineering simulations are mostly carried out to solve real-life problems, and inaccuracies of model predictions can have far-reaching consequences. Early on, the *European Research Community on Flow, Turbulence and Combustion* (ERCOFTAC), for example, compiled a comprehensive best practice guideline for *industrial* CFD applications (cf. ERCOFTAC, 2000; Hutton and Casey, 2001).

In the case of fundamental research conducted in traditional boundary-layer meteorology, on the other hand, erroneous simulation results tended to have little to no impact. The urgency of a rigorous model testing and the need for a legitimation of the simulation results were perhaps strongest communicated in the field of environmental fluid mechanics, which has a natural bridge to boundary-layer meteorology. By now, steady-state micro-scale meteorological models are routinely applied for regulatory purposes, and the meteorological research community on their part responded with activities to compile validation guidelines and best-practice protocols.

In order to assess the merits of a numerical model, Pope (2000) proposes five criteria:

- **level of description** — *What kind of information can be retrieved from the model?*
- **completeness** — *What flow-dependent specifications are made in the model?*
- **cost and ease of use** — *What resources are needed to develop and operate the model?*
- **range of applicability** — *What scope of application is covered by the model?*
- **accuracy** — *What uncertainties must be anticipated in the results of the model?*

In case of DNS, LES, and RANS models, the first three criteria have been, for the most part, discussed in the previous chapter. The *range of applicability* of the model is determined by the physical reality that is emulated by mathematical and computational means. It is inexpedient and generally unfeasible to develop a single model that is applicable to all kinds of problems, covering all levels of complexity. The obvious reason is that this would require all physical processes involved in the problem to be known and to be amenable to a mathematical description. Moving closer to reality, Bradshaw (1972) defines the *"optimum model"* as a predictive tool that is neither perfect nor all-embracing, but the best model that can be used within the foreseeable future until further studies have improved the understanding of the particular problem. As Pope (2000) points out, the general applicability of a model to a certain problem does not, at the same time, imply its *fitness for purpose*. This quality has to be investigated in terms of the fifth criterion.

Appraising and quantifying the *accuracy* of numerical predictions is the effort commonly embraced in the term *model evaluation*. Generally speaking, it is aimed to demonstrate that the conglomeration of conceptual, mathematical, and numerical constructs that constitute the model are suitable to describe the physical reality of interest. In this regard, the term "accuracy" embraces a combination of qualities like correctness, reliability, suitability, robustness, credibility, and safety. Validation, thus, is also a prerequisite for goal-oriented model improvements. The substantiation of the predictive skill of a model for its intended use is a multi-step process, and it is helpful to first introduce common terminologies. Based on definitions proposed by Schlünzen (1997), Oberkampf and Trucano (2002), ASME (2006), and Grinstein (2010), the following list is compiled:

> **Verification** — the process of determining whether the computational model is an accurate representation of the conceptual model and its mathematical solution.
>
> – *Does the model correctly solve the underlying equations?*
>
> **Validation** — the process of determining whether the computational model is an accurate representation of the physical reality of the problem.
>
> – *Does the model use the appropriate equations for the problem of interest?*
>
> **Evaluation** — the process of determining the validity of a computational model and its results with regard to its range of application.
>
> – *Does the model accurately perform within its domain of applicability?*

While code verification is mainly a mathematics problem, model validation is primarily concerned with physics (Roache, 1998). The distinction between validation and evaluation, on the other hand, is more subtle, and the terms are often used interchangeably. The above definition, however, implies that one of the premises of a successful evaluation is that the model has already been verified and validated. Schlünzen (1997) defines further criteria to appraise the standard of a model like *code quality* (the computer code should be documented and easy to use), *result control* (on-line and off-line monitoring of results should verify internal consistency and plausibility), and *comprehensibility* (verification and validation efforts should be traceable). The main challenge of the validation process is related to the rather philosophical problem of determining how results from mathematical constructs of nature can be compared with physical observations (Oberkampf and Trucano, 2002). This involves considering questions like: *What comparison strategies are meaningful? How can the level of agreement between model and observations be quantified? What level of accuracy is desired and what is realistic? When is a comparison fair?*

Responding to these questions requires to be aware of possible sources of uncertainties, which add up to the overall discrepancy between measured and simulated quantities. Along these lines, Pope (2000) defines the validation uncertainty, ϵ_{val}, as a composition of

$$\epsilon_{\text{val}} = \epsilon_{\text{model}} + \epsilon_{\text{num}} + \epsilon_{\text{input}} + \epsilon_{\text{meas}} \,, \tag{3.1}$$

where the formal structure of the equation has to be regarded as suggestive rather than mathematically correct. The uncertainty of the computational model, ϵ_{model}, arises from inadequacies of the underlying set of equations for the purpose of the simulation as well as from parameterization deficiencies. The numerical uncertainty, ϵ_{num}, follows from imprecisions of the computerized version of these equations and comprises discretization, iterative, coding and computer round-off errors. Uncertainties of the input parameters of the simulation, ϵ_{input}, for example, relate to the prescribed initial and boundary conditions, model geometries, the flow Reynolds number or material properties. Finally, the measurement uncertainty, ϵ_{meas}, comprises technical inaccuracies of the sensing instruments as well as random and bias errors that determine the overall representativeness of the experiments (cf. discussion in the next section). The investigation and quantification of these error sources are the primary aims of model verification and validation processes.

For the most part, Eq. (3.1) contains systematic (*epistemic*) uncertainties. In principal, these could be avoided if it was not for insufficient information about the physical problem (or the unawareness thereof) as well as mathematical, computational, and technical limitations. The other major source for discrepancies are statistical (*aleatoric*) uncertainties, which are unavoidable. The inherent uncertainty, σ_s, of a turbulent process is such an example and is indirectly embodied in different aspects of the problem (cf. Section 2.3.1).

Figure 3.1 shows a general verification and validation sequence proposed by the *American Society of Mechanical Engineers* (ASME, 2006) to quantify "(...) confidence in model predictions through the logical combination of hierarchical model building, focused laboratory and field experimentation, and uncertainty quantification." The diagram emphasizes the iterative nature of the process, i.e. the recommended sequence can be repeated if the required level of agreement has not yet been reached, and the need for a revision of the conceptual, mathematical or computational model or of the experiment has been determined.

3.1.1 Comparing apples with apples

The common starting point for numerical and experimental activities is the *conceptual model* as an abstraction of the "reality of interest" (see Fig. 3.1). In order to ensure that a comparison between both data sets is meaningful, driving dynamical processes, important physical constraints, and boundary conditions have to match. Only then the encountered differences can be assumed to truly originate from inherent deficiencies of either model.

Ideally, validation experiments should be jointly designed by experimenters and modelers. A close collaboration should be continued during the entire validation process in order to assure that both sides are constantly aware of assumptions in simulations and experiments (Oberkampf and Trucano, 2002; ASME, 2006). In general, *preliminary calculations* are recommended in order to optimize the experimental design or to identify meaningful measurement locations and quantities. It is, however, important to maintain essential *independence* during the generation of both data sets. Independence ensures that the comparison can be conducted in terms of a *blind test* so that a conscious or subconscious bias of experimental or numerical results is precluded from the outset.

In order to reliably assess the performance quality of a numerical model, reference data, on their part, have to comply with certain demands. These mainly include a high level of reliability, their general representativeness for the physical problem of interest, as well as a comprehensive documentation. Ensuring high standards is essential for an equitable comparison and the overall usefulness of the data set. In connection with the validation of micro-scale dispersion models, Leitl (2000) proposed three criteria by which the suitability of experiments for the validation process can be assessed:

Completeness — Boundary conditions classifying the state of the turbulent flow and the basic conditions of the reference experiment are measured and documented.

Applicability — Inflow and boundary conditions for the numerical model can be purely derived from the experimental reference data set.

Representativeness — The reliability and repeatability of the reference experiment are demonstrated. Bounds of uncertainty (statistical scatter) of the reference statistics are quantified and can be used to assess the experimental reproducibility.

Although being formulated for steady-state RANS models, these quality criteria can be adapted to eddy-resolving models without reservation. Completeness ensures that the numerical model and the experiment can be harmonized for the validation process. Another prerequisite is the applicability of the measured data for the identification of characteristic inflow and boundary conditions and respective uncertainties. Provided professional calibration and operation, state-of-the-art measurement techniques in the field and the laboratory are usually able to produce highly accurate results. Hence, the major source of uncertainty is related to the representativeness of the measurement process. This statistical data range can be obtained from repetitive measurements, which ensures that the derived scatter includes all sources of bias and random errors. In general, all steps involved in the data processing have to be traceable. The role of laboratory and field data for the validation of LES will be addressed in more detail in Section 3.2.

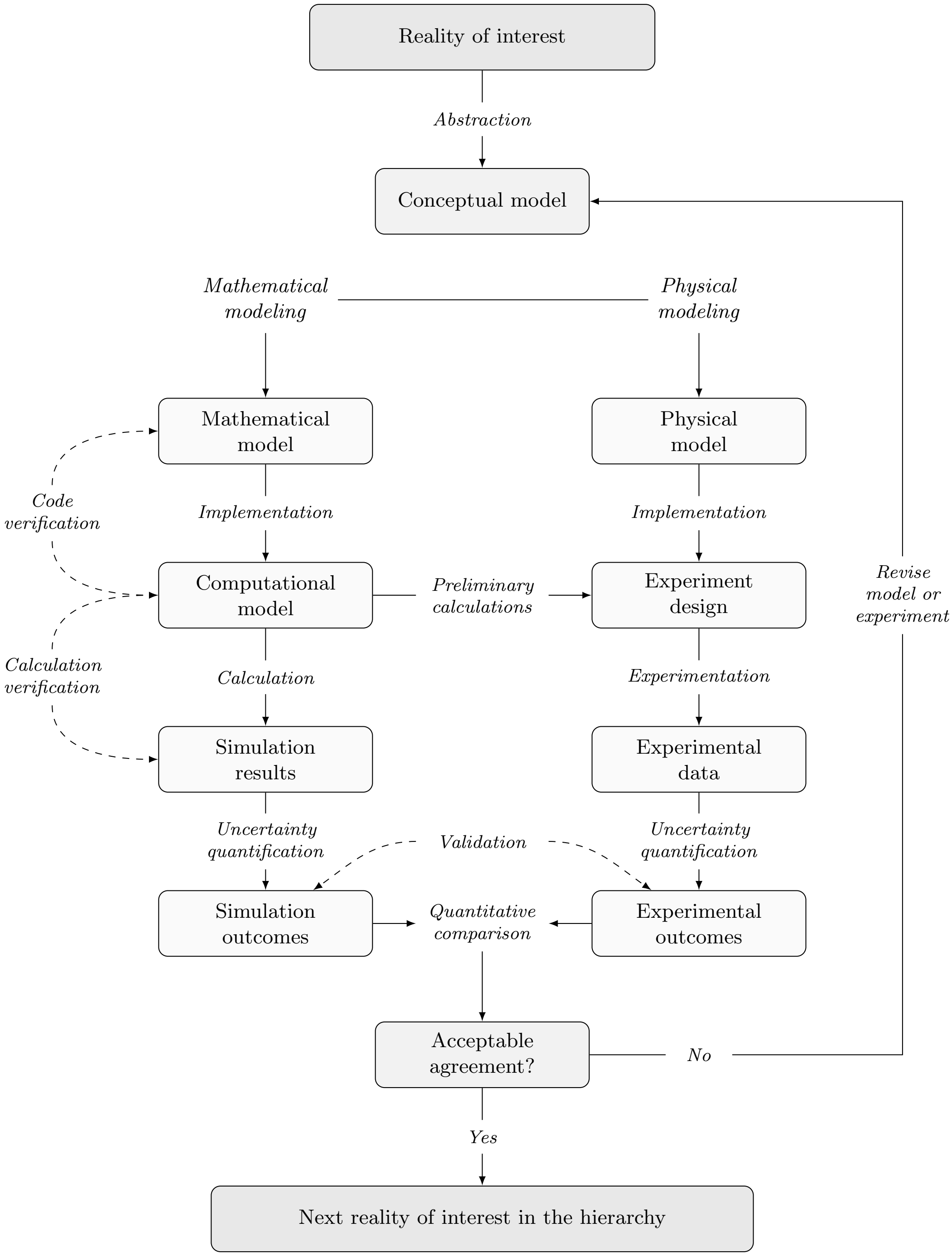

Figure 3.1: Verification and validation activities specified by the ASME (2006). Modeling, simulation and experimental activities are connected by solid lines. Validation and quality assessment steps are indicated by dashed arrows.

3.1.2 Validation activities in micro-meteorology

With the beginning of the 2000s, prognostic micro-scale meteorological models of the RANS type were increasingly used for environmental assessments and micro-climatological studies – especially for problems in urban environments. As stated by Schatzmann and Britter (2011), the increasing availability and practicability of micro-scale models have also been accompanied by " (...) a growing awareness that the majority of these models have never been the subject of rigorous evaluation. Consequently there is a lack of confidence in the modelled results." The urgency for the definition of community-wide accepted validation procedures and the compilation of a new generation of quality-assured reference data sets has been addressed earlier by Schatzmann and Leitl (2002) in connection with obstacle-resolving dispersion models. Pointing out the huge diversity of available numerical codes, the authors recommend that validation procedures are adjusted to specific groups of models depending on their operational scale (e.g. meso-scale or micro-scale), their type (e.g. prognostic, diagnostic or stochastic), their field of application, and their intended use.

In 2005, the micro-meteorological community reacted with a European initiative involving research institutions and scientists from 22 countries (COST action 732),[1] which aimed at the quality assurance and improvement of micro-scale meteorological models predicting flow and pollutant dispersion in urban and industrial areas on street to neighborhood scales (Britter and Schatzmann, 2007a,b; Schatzmann et al., 2010). As stated in the review by Schatzmann and Britter (2011), it was expected that a widely accepted standard for quality assurance will contribute to "(...) significantly improve 'the culture' within which such models are developed and applied." The main objectives of COST732 included to

- develop a coherent, structured, and accepted quality-assurance procedure,
- prove the practicability of this validation procedure for different models and applications,
- compile a set of appropriate and sufficiently detailed experimental reference data,
- build consensus about best practices for the operation of micro-scale models, and
- stimulate the preparation of quality-assurance protocols to document fitness for purpose.

In order to allow for quantitative statements about the model performance, COST732 recommends the use of well-known statistical measures based on first and second order moments as so-called *validation metrics*, for which quality acceptance thresholds can be defined (see also Oberkampf and Barone, 2006). In addition, Franke et al. (2007) compiled a best-practice guideline for the implementation and uncertainty quantification of steady-state CFD-RANS models applied to urban problems (e.g. addressing the choice of the domain size, initial and boundary conditions, and solution verification schemes).

Other noteworthy efforts to streamline validation practices in environmental meteorology were, for example, made by *The Association of German Engineers* (VDI), which published a guideline for the evaluation of flow around buildings (VDI, 2005), largely based on investigations by Panskus (2000). The guideline proposes a multi-step procedure to validate steady-state CFD results based on a set of wind-tunnel test cases, at the end of which a certificate for the validated model can be completed to document the efforts.

[1] European Cooperation in the Field of Scientific and Technical Research. The oldest and largest intergovernmental network for research cooperation in Europe.

Particular issues of LES validation

The importance of building confidence in model predictions through rigorous validation is generally acknowledged by LES communities in meteorology and engineering. However, to the author's knowledge, nothing comparable to the quality-assurance activities for RANS models has been attempted for LES so far, and numerical modelers and experimentalists are far from defining, let alone agreeing on, best-practice validation standards. Oberkampf and Trucano (2002) assess the situation of model validation from a historical perspective by stating that it is "(...) fair to say that the field of CFD has, in general, proceeded along a path that is largely independent of validation." The authors describe that particularly in the early stages of the computer revolution, numerical and experimental approaches in engineering had the tendency to be competitive and antagonistic rather than complementary and synergistic. In micro-meteorology, by contrast, the cooperation used to be rather vital in the case of RANS simulations. For meteorological LES, however, the traditional coupling to experiments has been remarkably lacking from the start (Wyngaard and Peltier, 1996).

Reasons for the imbalance between the increasing use of eddy-resolving techniques and the scrutiny their predictions are subject to mostly stem from the high *level of description* provided by the models. As will be discussed in the following sections, the huge gain of information from unsteady simulations makes high demands on the quality and quantity of reference data and calls for extended validation concepts. Wyngaard and Peltier (1996) identified another cause for the communication barrier in boundary-layer meteorology: the unique framework of LES. They speculate that "(...) the absence of this historically strong tie [between experiments and modeling, D.H.] in the case of LES reflects the difficulty of experimentally addressing issues posed in the less familiar resolvable scale, subgrid-scale framework." LES provides numerically-resolved filtered quantities that, to some extent, depend on the parameterized SFS effects. Experimental raw data, on their part, can be regarded as filtered quantities as well, since measurement techniques usually involve averaging over the probe dimension. Local flow measurements in the laboratory using *laser Doppler anemometry*, for example, depend on the dimension of the measurement volume (acting as a spatial filter) and the particle transit time through this volume (see Section 4.2.3 for details). Similarly, temporally resolved velocities from *in-situ* field observations with *sonic anemometers* depend on the instrument's path lengths and the probing time. While for some technical problems it might be advisable to make filter widths and probe sizes compatible (cf. Kempf, 2008), typical single-point atmospheric measurement techniques provide high spatial resolution such that $\Delta_{\mathrm{exp}} \ll \Delta_{\mathrm{les}}$. With reference to earlier discussions in Section 2.2.2, it can be assumed that for $\Delta \ll \ell_0$ and signal durations much longer then the filter time-scale, low-order statistical moments obtained through temporal averaging are mostly unaffected by the presence of a filter, since integral quantities are primarily influenced by the low-frequency variability of the turbulent field.[2] Thus, experimental and LES statistics are usually directly compared for the validation of the resolvable scales. In order to investigate subfilter-scale quantities, however, reference data need to be filtered. This approach provides the basis for the so-called *a priori* validation of SFS parameterizations and is further discussed in Section 3.3.1.

[2] Attention must be paid, however, when approaching the *terra incognita*, i.e. a VLES regime with $\Delta \simeq \ell_0$, less than $\sim 80\%$ of the TKE being resolved, and strong contributions from the SFS model.

Validation studies for LES results are often conducted on the basis of reference experiments that were designed for steady-state models and provide flow statistics instead of time-series information. The data situation, however, has started to change with innovative field trials that have recently been carried out to aid *a priori* testing of SFS models, as well as comprehensive boundary-layer wind-tunnel campaigns focusing on the generation of reference data that are suitable for comparisons with LES (see Section 3.2). Today, extensive ABL research projects usually include numerical and experimental activities and, thus, provide a good starting point for model assessment. Benchmark validation test scenarios as defined in engineering (e.g. canonical cylinder wake flows, mixing layers, etc.), on the other hand, are not yet established in meteorological LES, but some common geometrical choices exist for urban simulations (i.e. isolated cubes or cube arrays).

A validation hierarchy for LES

Just as the quality of experimental data sets has to be adjusted to the level of description provided by eddy-resolving techniques, established validation strategies need to be adapted for a thorough evaluation. More often than not, LES validation (if conducted at all) follows the same standards as the validation of RANS codes, although the informative description of the latter is restricted to the mean flow level. This practice does not at all do justice to the great amount of information that can be extracted from an LES. One of the few publications that discusses this apparent dissonance not only as a scientific side issue was presented by Kempf (2008) with relation to turbulent combustion. From this engineering point of view, the use of a cost-intensive LES instead of cheaper RANS techniques can only be justified if the resulting first and second-order statistics are clearly more accurate. While this may also *imply* a realistic representation of the time-space structure of turbulent eddies by LES, it can certainly not be regarded as unambiguous proof.

This thesis is concerned with the question: *How can the fidelity of resolvable-scale LES predictions be tested?* — Since time-dependent experimental and numerical flows are both realizations of a stochastic process, a statistical treatment is inevitable. However, the level of insight that can be gained naturally depends on the selected statistical measures. Beyond comparing low-order moments, numerical and (suitable) experimental data should be analyzed by means of more advanced techniques that preserve essential information about the structure of turbulence. In this study, a novel *hierarchy of validation methods* for time-dependent turbulent flow in the near-surface ABL predicted by LES is put forward and tested in a comprehensive validation study, which is presented in Chapter 5.

Figure 3.2 illustrates the proposed multi-step concept for an in-depth LES validation based on experimental data. The starting points are instantaneous LES velocities, $U_i^{\mathrm{les}}(\mathbf{x}, t)$, which depend on the filter width Δ_i, the mesh size h_i, and the time resolution δt, as well as experimentally resolved instantaneous velocities, $U_i^{\mathrm{exp}}(\mathbf{x}, t)$, with space and time resolutions, δx_i and δt, provided by the respective measurement technique.

The comparison sequence starts with an initial *exploratory data analysis* that gives a global performance overview by comparing low-order statistics. The results, in turn, are substantiated by analyzing frequency distributions of the underlying instantaneous velocities and derived quantities, which allows for conclusions about sample characteristics.

Since LES predicts dynamics of the energy-carrying eddies, a comparison of statistical features of dominant *turbulent scales* is included in the second step. Based on multi-point and/or multi-time correlations, integral length and time scales as well as spatial or temporal structure functions can be derived and compared. Valuable insights into the structure of turbulence can also be gained from the analysis of energy-density spectra.

In the last step of the validation concept, advanced methods from the field of *flow pattern recognition* are applied in order to further evaluate the representation of eddy structures. Depending on the available data, established approaches based on conditional resampling techniques, joint time-frequency analyses using wavelet transforms or flow-reconstruction methods by means of empirical orthogonal functions could be employed here.

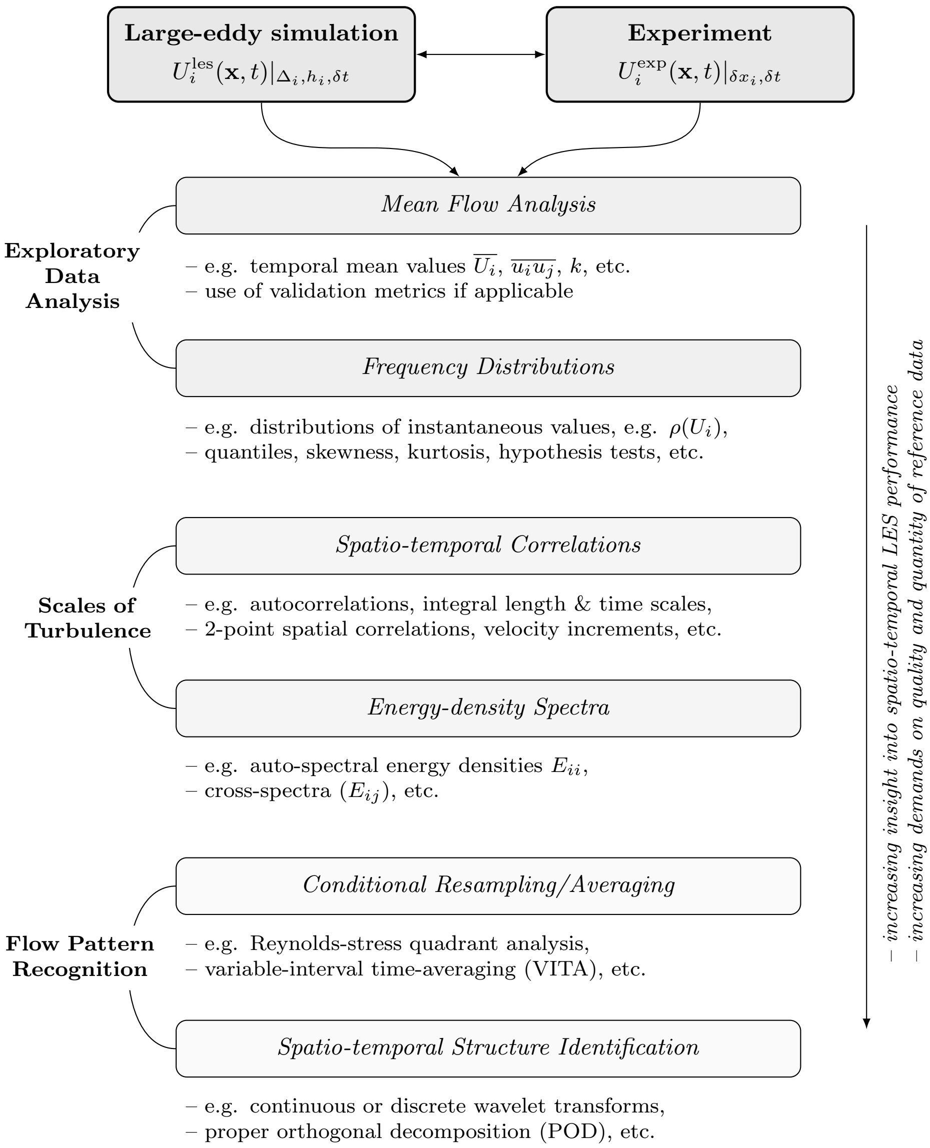

Figure 3.2: A hierarchy of analysis methods for LES validation of turbulent ABL flow.

3.2 Validation data for LES

The following paragraphs discuss demands on reference data for the validation of LES results and LES parameterizations. It is focused on presenting advantages and limitations of the two principal data sources: laboratory and field experiments. The fundamental principles of physical modeling in boundary-layer wind tunnels is covered in greater detail in order to provide a conceptual and theoretical framework for later discussions of experimental methods in Chapter 4.

3.2.1 Requirements on validation data

As Rogallo and Moin (1984) comment, "(...) the primary difficulty with experimental turbulence data is the lack of it". And although this statement was made almost three decades ago, it still holds in spite of strong advancements in measuring techniques over the years. From the multitude of experimental measurement campaigns in engineering or micrometeorological disciplines, only few were specifically designed for the use as benchmark tests for numerical models, let alone for time-dependent predictions. Out of those that have been, only a small fraction had been planned in close collaboration with numerical modelers. In this regard, the chain of verification and validation activities depicted in Figure 3.1 represents a rather idealized scenario. There have been, however, activities to address the issue of LES validation in a broader context, like the *"Turbulence Measurements for LES"* workshop, from which a final report has been published by Adrian et al. (2000). Although the authors direct their attention to engineering problems, their appeal toward the numerical and experimental communities to "educate each other regarding what is required in LES" and to start a discussion on the "role of experiments in LES development" can be directly adapted to the field of boundary-layer meteorology.

It is convenient to make a distinction between *necessary*, *ideal*, and *realistic* qualities that LES validation data should possess. A necessary requirement on experimental data for LES should be that they allow to evaluate the turbulence (fluctuation) characteristics predicted by the model. This aspect represents the inherent difference between data requirements for the validation of time-resolved codes and steady RANS models. Validation experiments need to be comprehensively documented with regard to all relevant technical, physical, and geometrical conditions. Ideally, the validation data should have a sufficient time resolution and provide a high-dimensional spatial coverage (i.e. *4D* fields), which facilitates the characterization of turbulence structures resolved with LES by means of single and multi-point statistics. With regard to the current status of instruments that are used to study atmospheric boundary-layer turbulence, measurements of *simultaneously* high space and time resolution are not feasible. Presently, temporally well-resolved single-point time series together with spatially resolved multi-point (usually 2D) data fields of low time resolution represent the realistic state-of-the-art of experimental technology.

Advanced laboratory measuring techniques permit to retrieve highly accurate signals, for which the statistical data scatter primarily originates from the stochastic variability of turbulence and not from technical constraints. The same is mostly true for field-site instrumentation – ranging from classic *in-situ* observations to spatially-resolved remote-sensing techniques. However, in the same way as advanced computational models require a high level of knowledge and awareness from their users, advanced measuring apparatus also make high demands on the experimentalists in order to assure an adequate level of quality and reliability of the recorded data. Post-processing, quality control, analysis (analytical and visual), as well as the archiving of huge amounts of generated data pose further challenges to both the experimental and numerical sides.

Data sources

As aforementioned, this section concentrates on the role of *experiments* for the validation of LES. It is, however, acknowledged that time-dependent predictions from DNS are used for this purpose as well and are even deemed more reliable than experimental data for certain academic flows. Currently, validation against DNS is primarily focused on canonical turbulence scenarios like mixing layers, channel flow or flat-plate boundary layers. However, with reference to earlier discussions, DNS is still unfeasible for ABL flows at realistic Reynolds numbers and in domains containing large-scale complex geometries. Furthermore, DNS and LES both should be considered numerical experiments. In a recent comparison study of different DNS results for the same generic turbulent boundary-layer flow, Schlatter and Örlü (2010) could document the strong sensitivity of the numerical solutions to inflow and boundary conditions as well as to the selected domain dimensions. They conclude that DNS should be "(...) subject to the same scrutiny as experimental data" in order to provide *well-documented*, *reliable*, and *reproducible* results.

With regard to the fact that DNS, in general, is still in a developing stage for most real-world applications, it is agreed with the assessment by Kempf (2008) that validation based on experiments currently represents the most *integrated* and *independent* approach.

3.2.2 Laboratory experiments

Studies of atmospheric flow and dispersion scenarios in specialized boundary-layer wind tunnels made strong contributions to the fundamental understanding of physical processes in the ABL, and – together with laboratory experiments in water channels or convection tanks – complement field observations since the second half of the last century.

The popularity of laboratory measurements stems from cost-related advantages and from the ability to freely choose the conceptual design of the experiment. Through the reduction of the degrees of freedom of the physical reality of interest, it is possible to investigate certain physical processes in isolation over a broad range of dynamical and geometrical conditions (Wyngaard et al., 1984). Having control over the inflow and boundary characteristics of the experiment allows to repeat measurements under the same constraints for quality control and for the derivation of reliable bounds of data scatter. Provided that the flow is stationary (– as it is the usual practice), the inherent uncertainty of statistics derived from laboratory data can be significantly reduced by adjusting measurement durations (i.e. averaging times) to the demands of the respective problem.

For certain ABL phenomena, wind-tunnel measurements currently provide the only realizable way for a detailed investigation and the generation of comprehensive data sets. Prominent examples are *space-covering* measurements of micro-scale flow, pollutant transport or building aerodynamics in urban environments (see the early review by Cermak, 1976), as well as flow over complex terrain (e.g. Cermak, 1984).

Traditionally, boundary-layer wind-tunnel facilities have an established role in environmental and civil engineering. Thus, laboratory studies often are of interest for applications outside of academia, which fostered the compilation of detailed best-practice guidelines for physical modeling of flow and dispersion phenomena (e.g. Snyder, 1981; VDI, 2000).

Figure 3.3 shows a schematic drawing of a typical low-speed boundary-layer wind tunnel that is operated to study UBL processes (following Plate, 1999). The tunnel domain is divided into two sectors: the *development section*, in which a nature-like approach flow is established, and the actual *test section* containing the urban model at a reduced geometric scale. As for numerical simulations, the quality of the generated inflow conditions is crucial for the flow quality inside the domain of interest. By means of vortex generators at the tunnel inlet and sharp-edged roughness elements covering the test-section floor, a fully developed, statistically stationary, horizontally-homogeneous turbulent boundary-layer flow is created. Its correspondence to full-scale atmospheric conditions needs to be verified and documented. Mean flow and turbulence characteristics of the wind-tunnel approach flow are optimized to agree with standard ASL similarity assumptions. In this context, the ratio of wind-tunnel (WT) to full-scale (FS) roughness lengths, $z_{0_{WT}}/z_{0_{FS}}$, for neutral stability conditions is given by the geometrical scale ratio (Jensen's criterion). Ideally, benchmarks for the laboratory approach flow come from the field. However, since this information is not always available, the best practice is to reproduce well-established empirical relations by matching engineering references for different surface roughness (e.g. following ESDU, 1985). In order to avoid the occurrence of horizontal pressure gradients, many boundary-layer wind tunnels are equipped with height-adjustable ceilings.

Conceptual and technical approaches in physical flow and dispersion modeling have strong similarities with procedures in numerical modeling. — And indeed, physical models have to be understood as eddy-resolving *models* of a simplified reality, expressed in the reduction of the geometric and physical complexity of the problem. This, on the other hand, offers the unique chance to harmonize with computational modeling for the design of validation test cases. The theoretical background of the assumption that wind-tunnel data can be transferred to full-scale conditions is discussed in the next paragraphs.

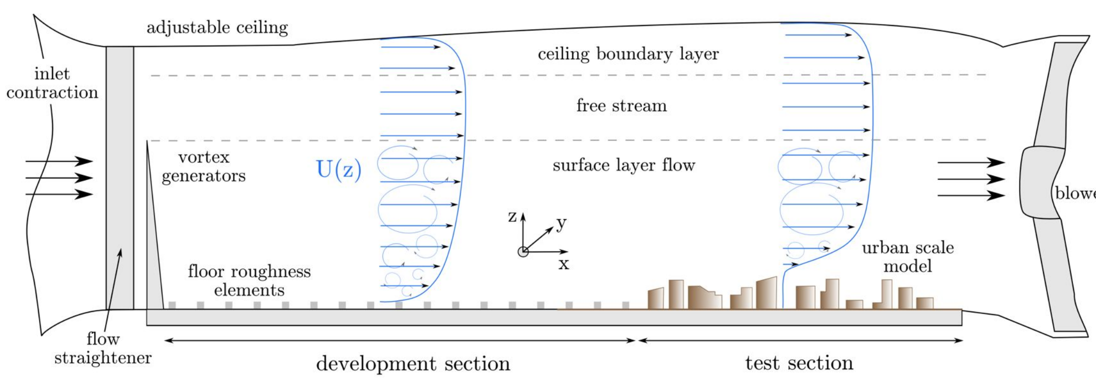

Figure 3.3: Schematic of a typical low-speed, open-return boundary-layer wind tunnel used for flow and dispersion studies in scale reduced urban models. Note that heights and distances are *not* true to scale. Modified after Plate (1999).

Similarity frameworks of physical modeling

Why does mechanically and thermally induced turbulence in boundary-layer wind tunnels correspond to full-scale conditions encountered in the natural ABL? The answer to this question is mainly based on two concepts: *Reynolds number similarity* and *Reynolds number independence*. Both will be briefly introduced in the following, and it is pointed to the reviews by Cermak (1971) and Snyder (1972) for details.

Flow similarity requirements *When are two flows with the same boundary conditions structurally similar?* — The first step toward a similarity analysis is the conversion of conservation equations that are relevant for the problem into a non-dimensional framework. This is done by introducing appropriate *reference values* for all physical quantities: L_{ref}, U_{ref}, ρ_{ref}, Θ_{ref} and so on, which are constant for the investigated problem. These are then used, for example, to nondimensionalize the ABL momentum equation (2.33), yielding

$$\frac{\partial U_i^\star}{\partial t^\star} + U_j^\star \frac{\partial U_i^\star}{\partial x_j^\star} = -\frac{1}{\rho^\star}\frac{\partial P^\star}{\partial x_i^\star} + \frac{1}{Fr^2}\Theta'^\star \delta_{3i} - \frac{2}{Ro}\epsilon_{ijk}\Omega_j^\star U_k^\star + \frac{1}{Re_{\mathrm{ref}}}\frac{\partial^2 U_i^\star}{\partial x_j^\star \partial x_j^\star}\,, \tag{3.2}$$

where the star denotes a non-dimensional variable that has been related to a reference value. The equation contains three dimensionless parameters: the densimetric *Froude number* $Fr \equiv U_{\mathrm{ref}}/(gL_{\mathrm{ref}}\Theta'_{\mathrm{ref}}/\Theta_0)^{1/2}$ describing the relative importance of inertial and buoyancy forces, the *Rossby number* $Ro \equiv U_{\mathrm{ref}}/(L_{\mathrm{ref}}\Omega_{\mathrm{ref}})$ representing the ratio of advective to Coriolis accelerations, and the *reference Reynolds number* $Re_{\mathrm{ref}} \equiv U_{\mathrm{ref}}L_{\mathrm{ref}}/\nu$. Formally, two flows of the same category are only similar if they are described by identical solutions to Eq. (3.2). This can only be achieved if the dimensionless parameters Fr, Ro, and Re plus the dimensionless boundary conditions are *identical*. If the physical modeling is conducted in a *wind* tunnel using air, ν and g are usually equal to the atmospheric values. For the modeling of neutral stratification by means of *isothermal* tunnel conditions, $Fr \to \infty$ and the buoyancy term vanishes. Since standard boundary-layer wind tunnels provide a non-rotating reference framework, deflecting effects of the Coriolis force on the flow cannot be modeled.[3] Dynamics of the Ekman layer, thus, are not adequately represented, and reliable wind-tunnel modeling typically restricts to the atmospheric surface layer. However, even for near-surface flows Coriolis effects can become important if the horizontal dimension of the wind-tunnel model is large. Depending on the magnitude of Ro, the impact of neglecting the Rossby number criterion has to be assessed. As a rule-of-thumb, Snyder (1972) recommends horizontal domain extents smaller than 5 km.

Provided that laboratory wind velocities have the same order of magnitude as encountered in atmospheric flows, fulfilling the Reynolds number criterion mainly depends on the scale $L_{\mathrm{ref}_{WT}}$ realized in the tunnel. Typical geometric scale ratios of $L_{\mathrm{ref}_{WT}}/L_{\mathrm{ref}_{FS}}$ range from 1:10^2 to 1:10^4, resulting in laboratory reference Reynolds numbers in the order of 10^6 to 10^4, several orders of magnitude lower than those of the natural ABL. Thus, Reynolds number similarity is generally *not* accomplished. The inherent characteristics of turbulence, however, provide experimentalists with a workaround.

[3] For problems on the global scale (e.g. studies of baroclinic waves) there exist special facilities, in which Coriolis effects can be simulated in rotating annuli (e.g. Harlander et al., 2011).

Reynolds number independence *When can the Reynolds-number similarity requirement be relaxed?* — The answer was first formulated by Townsend (1956), who stated that "geometrically similar flows are similar at all sufficiently high Reynolds numbers" for problems in which buoyancy and Coriolis effects are negligible. Early experiments showed that most statistical quantities in turbulent flows do not depend on the realized Reynolds number as long as it lies above a critical value Re_{crit}. Following Snyder (1972), the two exceptions are statistics of the small-scale, dissipative eddies and mean-values obtained from measurements very close to solid boundaries, where viscous effects become important. In connection with the classic Kolmogorov theory, the effect of a smaller Reynolds number is primarily reflected in a decrease of the spectral range at high frequencies, while the characteristics of the integral-scale eddies remain unchanged as long as $Re > Re_{\text{crit}}$. The gross structure of turbulence represented by the energy-containing eddies is similar over a wide range of Reynolds numbers, resulting in similar spectral shapes for eddy sizes $\ell \gg \eta$ and statistically identical integral statistics (e.g. mean values, turbulent stresses, integral length scales, etc.). The reduction of the spectral width in the wind tunnel results in the fact that the size of the dissipative eddies, transferred to full-scale conditions, is larger than of those in the natural atmosphere. The relation of the integral lengths encountered in the field and laboratory, however, is approximately proportional to the first power of geometric scale: $\ell_{0_{FS}}/\ell_{0_{WT}} \simeq L_{\text{ref}_{FS}}/L_{\text{ref}_{WT}}$. The combination with Eq. (2.17) yields

$$\frac{\eta_{FS}}{\eta_{WT}} \simeq \frac{\ell_{0_{FS}}}{\ell_{0_{WT}}} \left(\frac{L_{\text{ref}_{WT}}}{L_{\text{ref}_{FS}}}\right)^{3/4} \simeq \left(\frac{L_{\text{ref}_{FS}}}{L_{\text{ref}_{WT}}}\right)^{1/4} , \tag{3.3}$$

which shows that the Kolmogorov micro-scale in the laboratory, on the other hand, reduces only with *one-fourth power* of the scale ratio (Snyder, 1972). For a scale of 1:350, as applied in this study, the width of the laboratory eddy spectrum transferred to full-scale conditions is smaller by almost two decades compared with the field, and Eq. (3.3) yields $\eta_{FS} \simeq 4.33\,\eta_{WT}$. Thus, in full-scale conditions the laboratory micro-scale is approximately 80 times larger than the corresponding field value (e.g. yielding 8 mm instead of 0.1 mm).

Studies in urban scale-models showed that Re-independence can be easily established since flow around sharp-edged bluff bodies, for which separation points are fixed, is dominated by surface drag, and the bulk of turbulence is produced at scales comparable to the obstacle size. Plate (1999) recommends that the Reynolds number based on the mean building height, $Re_{\text{H}} = U_{\text{H}}\text{H}_{\text{m}}/\nu$, should be larger than $5 \cdot 10^3$ to $1 \cdot 10^4$. Since these values can vary based on the individual qualities of the model, it is part of the physical modeling preliminaries to determine Re_{crit} from case to case. The adjustment of the Reynolds number, however, can become tricky if other processes like stratification (Fr criterion) or scalar dispersion (matching the *Schmidt number*) are modeled (Snyder, 1972).

LES validation from wind-tunnel data

Experiments in boundary-layer wind tunnels offer great potential for an in-depth LES validation due to their flexibility concerning the conceptual design of the test scenario and the fact that inflow and boundary conditions can be controlled, documented, and systematically varied. The repeatability of laboratory experiments allows for sensitivity studies over a broad range of parameters and the assessment of the general data representativeness.

Figure 3.4 shows urban wind-tunnel models of different sophistication ranging from isolated buildings to realistic urban structures, which have been used for flow and dispersion studies at the Meteorological Institute of the University of Hamburg. Varying the level of complexity on which the numerical model is tested, can be of valuable guidance in order to disentangle error sources more readily and for the systematic development of new models. Some of the campaigns were particularly designed for the validation of eddy-resolving simulations and are compiled in an on-line database, which includes flow time series as well as detailed information about the modeled inflow conditions.[4]

If the comparison is conducted on the basis of laboratory data, modelers have to decide whether the simulation is run under full-scale or wind-tunnel conditions. Through the resulting length scale L_{ref}, the decision affects the Reynolds number of the simulation. Matching the lower wind tunnel Re may be of interest in order to conform with the experimental conditions as close as possible. The choice to simulate in wind-tunnel scale is often made for generic test cases like flow and dispersion around wall-mounted cubes or in cube arrays. In order to mimic the laboratory inflow and boundary conditions in detail, even the entire tunnel geometry can be modeled, including all walls and the development section with floor-roughness elements and vortex generators (e.g. Lee et al., 2009).

(a) **(b)**

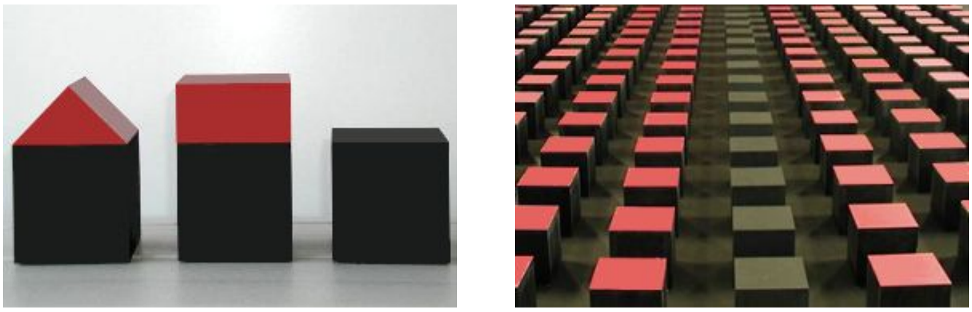

(c) **(d)**

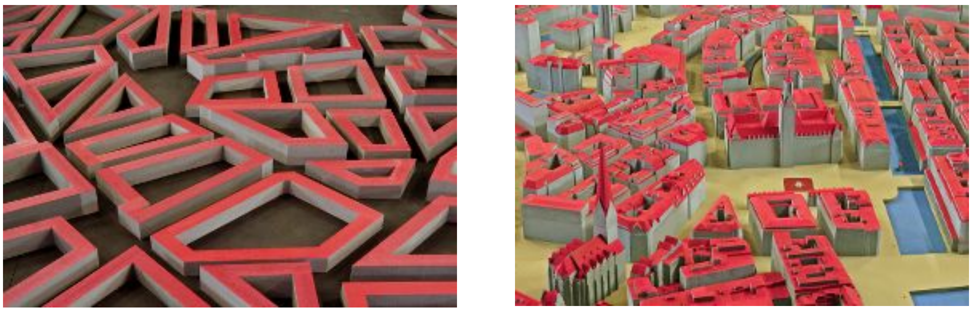

Figure 3.4: Examples of urban complexities realized in the boundary-layer wind-tunnel facility at the University of Hamburg: (a) isolated obstacles, (b) obstacle arrays as idealized urban structures (Schultz, 2008), (c) semi-idealized urban environments (Bastigkeit, 2011), (d) realistic urban sites (*here*: Hamburg city center).

[4]CEDVAL-LES hosted by the University of Hamburg; `http://www.mi.uni-hamburg.de/CEDVAL-LES-V.6332.0.html`; accessed June 10, 2012. See also Bastigkeit et al. (2010) or Bastigkeit (2011).

With regard to LES, a lower Reynolds number would enable to directly resolve a wider range of the eddy spectrum than under full-scale conditions for the same computational costs. However, like the experimenter, the modeler has to be aware of the fact that the smallest eddies are comparatively large at low Re. Among other effects, this leads to a thickening of the viscous sublayer, in which the flow is *not* Reynolds-number independent. In physical models, the relaminarization of the near-wall flow can be prevented by using aerodynamically rough surfaces on model buildings and on the tunnel floor. If the log-law is used as the surface boundary condition in LES, inaccuracies of the near-wall flow have to be anticipated when simulating in wind-tunnel scale since the lowest computational level is often located within the viscous sublayer. While this issue could be eased by switching to a rough-wall model, this is rarely done in practice for micro-meteorological applications (cf. Section 2.2.3). If the dispersion of pollutants is simulated, the numerical modeling of the (point or area) source characteristics can introduce further difficulties when carried out in wind-tunnel scale, since the exhaust flow tends to be laminar due to the smaller source radius (e.g. Saathoff et al., 1995). These and further issues are for example addressed in the best-practice guideline for micro-scale meteorological models presented by Franke et al. (2007, 2011). In order to avoid the above effects, modeling in full-scale might be preferred. Provided Reynolds number independence of the laboratory measurements, the outcome of a validation study based on integral statistics and with a focus on the energy-dominating eddy scales should be independent of scale choices.

The abstraction ultimately made in a wind-tunnel experiment is its most important trade-off. A prominent example concerns atmospheric stratification. Since the simultaneous guarantee of Reynolds-number independence and Froude-number similarity is technically very demanding, the majority of laboratory experiments is conducted under the idealization of neutral stability. Effects like radiation, evapo-transpiration, or precipitation are also out-of-scope for current wind-tunnel techniques. Hence, laboratory investigations should ideally be accompanied by field measurements and *vice versa*.

3.2.3 Field site observations

Traditionally, strong collaboration exists between field experiments and numerical approaches in boundary-layer meteorology, with a main focus on the validation of atmospheric turbulence parameterizations and their implementation in closure models. Starting at the end of the 1950s, milestone field trials have essentially shaped the understanding of ABL processes. Prominent examples are the early field experiments in Kansas (1968) and Minnesota (1973), in which the ASL was extensively probed with then revolutionary time-resolving equipment in terms of hot-wire and sonic anemometers (a review of both experiments is presented by Kaimal and Wyngaard, 1990). Similarity laws derived or verified based on these data have entered many micro-scale meteorological models and still serve as benchmarks for both numerical and laboratory results. Reviewing the classic era of micro-meteorological field experiments, Wyngaard and Peltier (1996) remark that "(...) hardly a meteorological model of any type does not contain some signature of their results." This also applies for early dispersion studies like the *"Prairie Grass"* campaign (Barad, 1958), which according to Hanna et al. (2004), "(...) has become the standard database used for evaluation of models for continuous plume releases near the ground over flat terrain."

A historical review of field studies in urban areas until the end of the last century has been presented by Roth (2000) and was more recently extended by Grimmond (2006), with a focus on progress in measuring and observing the UBL. For both ABL and UBL processes, *in-situ* techniques like ground-based sensors mounted on masts or towers still are the standard data source together with (less frequent) airborne measurements with tethered balloons or research aircraft. Starting in the 1970s, remote sensing techniques with platforms on satellites or aircraft have entered the field of atmospheric boundary-layer research and are of special importance for *micro-climatological* studies (e.g. urban heat island effects). Ground-based remote sensing has more recently proven to be a valuable complement to *in-situ* measurements of local turbulent wind and temperature structures (e.g. using sodar, lidar, scintillometers or radio acoustic sounding systems).

Field campaigns can be very costly and particularly demanding in terms of time, planning, manpower, logistics, maintenance of deployed instruments and so forth. Assuring the overall usefulness of the measured data for the intended purpose, thus, is not only of scientific interest, but also of economic importance. This task is essentially connected to the site selection and exposure of the measuring instruments. In 1954, the *World Meteorological Organization* (WMO) published a first edition of the *"Guide to Meteorological Instruments and Methods of Observation,"* in which sensing, siting, and quality assurance strategies are discussed, and best-practice recommendations are made. Over the decades, the document was subject to considerable extensions and revisions, incorporating new measurement technologies and computational data processing capacities (latest edition: WMO, 2008). Focusing on the proposed wind-data quality requirements, Wieringa (1996) examined possible data processing methods to ensure representativeness of the measurements according to the WMO standards for different user groups. More recently, Oke (2007) discussed ways to flexibly and intelligently use the WMO guideline for local, micro-climatic measurements in densely-developed urban environments, for which non-ideal siting conditions at non-standard heights over non-standard surfaces are the norm.

Within the last decade or so, a new generation of field campaigns entered the scene in micro-meteorology. These stand out as collaborative, multi-national, and inter-disciplinary initiatives between various universities, research institutions, and governmental bodies. Enhanced cooperation also fostered growing exchange between numerical modelers and experimenters. As Grimmond (2006) stated, this development has encouraged discussions about "(...) variables the models need and those that are measured; the number of sites that need to be observed to be appropriately representative for model evaluation; and the complexity of the real world versus the necessary simplification of reality in modeling."

LES validation from field data

CFD models usually provide large amounts of information about the predicted quantities in terms of spatially resolved fields. In case of LES and other unsteady methods, these fields also are time dependent. Thus, it is clear that the informative value of a model validation based on single-location, multi-height tower measurements or detached multi-point but single-height sensor data is restricted and may not allow for a conclusive appraisal of the model performance. The increasingly collaborative and multi-institutional efforts, however, also resulted in a significant rise in the number of deployed sensors and in the diversity of measurement techniques employed in recent micro-meteorological field studies. The fact that databases can be made available to a broad user community through the world wide web further resulted in an increase of detailed validation studies on the basis of field campaigns. Several of those put the focus on *urban* flow and pollutant dispersion processes in densely-built environments. Well-known examples are the DAPPLE field trial conducted in central London (Arnold et al., 2004),[5] the VALIUM project with air pollution measurements in a street canyon in Hannover, Germany (Schatzmann et al., 2006),[6] and the Joint Urban 2003 Atmospheric Dispersion Study in Oklahoma City (JU2003; e.g. Allwine and Flaherty, 2006). While DAPPLE and VALIUM aimed for observing street to neighborhood scale processes with a focus on intersections and street canyons, measurements during JU2003 extended far into the city scale and were based on an unprecedented contingent of meteorological instrumentation. All projects combined long-term site monitoring with short-term intensive operation periods and produced a large pool of reference data usable for the validation of CFD and non-CFD models.

Another validation scenario popular within the micro-meteorological community is the *Mock Urban Setting Test* (MUST), that has been intensively used for the comparison with CFD-RANS dispersion predictions (project and data overview by Biltoft, 2001; Yee and Biltoft, 2004). The test case is a representative of outdoor scale-model experiments, in which building-like obstacles are such arranged to represent an idealized urban environment (cf. Kanda, 2006b). During MUST, 120 commercial shipping containers were placed in the otherwise predominantly flat Great Basin Desert, Utah, to conduct pollutant dispersion and wind measurements within and above the artificial urban canopy (see Fig. 3.5a). Recently, a similar approach was taken in a field study conducted in Saitama, Japan: the so-called *Comprehensive Outdoor Scale Model Experiments* (COSMO) (e.g. Inagaki and Kanda, 2008, 2010). Cubes with geometric scales of 1:5 and 1:50, in reference to the typical height of residential buildings in that area, were arranged into large arrays to create a simplified city (see Fig. 3.5b). So far, measurements focused on the characterization of flow fields within and above the UCL and the extraction of organized turbulent structures. Recently, Takimoto et al. (2011) presented highly resolved spatial measurements of velocities within a cube-array street canyon by means of 2D *particle image velocimetry* (PIV) – a technique that otherwise is typically used in laboratory studies.

The similarity between field-site scale models and idealized complexities used in wind tunnels as shown in Figure 3.4b is striking. Like the laboratory cases, MUST and COSMO can be understood as mediators between physical processes occurring in highly complex genuine environments and in the flat-terrain ABL. However, the conceptual difference between indoor and outdoor scale experiments needs to be emphasized: In the laboratory, not only the urban roughness is scale-reduced but also the entire approach flow boundary layer, so that results can generally be transferred to field conditions. This, however, cannot be done with data from scale-reduced models placed in a natural ABL.

More than ten years ago, a new category of field trials was launched by the *National Center for Atmospheric Research* (NCAR), aiming at the validation of LES parameterizations: the *Horizontal Array Turbulence Studies* (HATS; cf. Horst et al., 2004). Based on

[5]Dispersion of Air Pollution and its Penetration into the Local Environment.

[6]Development and Validation of Tools for the Implementation Of European Air Quality Policy in Germany.

an approach that was first put forward by Tong et al. (1998), these campaigns are targeted on the retrieval of resolvable and subfilter-scale ASL turbulence from measurements with sonic anemometer *arrays*. Beginning with experiments over homogeneous terrain, studies were more recently extended to flow over water and snow surfaces and within vegetated canopies. Figures 3.5c,d show setups of the *Advection* Horizontal Array Turbulence Study and the *Canopy* Horizontal Array Turbulence Study (AHATS and CHATS; see Nguyen et al., 2010; Patton et al., 2011). The unique approach of HATS will be later revisited in Section 3.3.1 within the framework of *a priori* LES validation.

All of the above field campaigns provide time-dependent measurements of wind velocities, temperatures and, in many cases, also of trace gas concentrations. COSMO and HATS further offer spatially resolved data of locally confined processes, which represent a novelty in the canon of micro-meteorological observation methods. Thus, the retrieval of turbulence characteristics and fluctuation statistics in time and space is generally possible. While this is a *necessary* requirement for the usefulness of data for an in-depth LES validation, it is certainly not *sufficient*, and further criteria have to be met.

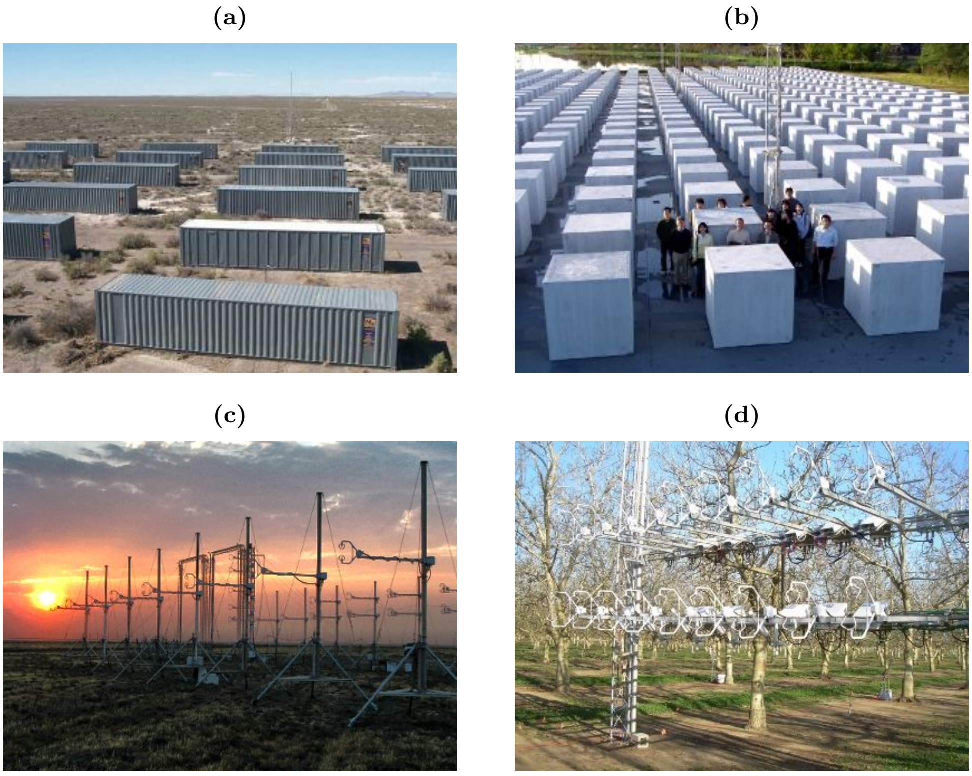

Figure 3.5: (a) MUST field trial with an array of shipping containers;[7] (b) COSMO cube-array test case at a scale of 1:5;[8] setups of the *horizontal array turbulence studies* (c) AHATS and (d) CHATS to investigate surface and canopy-layer turbulence.[9]

[7] Fig. 3.5a: Photo courtesy of U.S. Army Dugway Proving Ground West Desert Test Center, (UT) USA.
[8] Fig. 3.5b: Photo courtesy of M. Kanda, Tokyo Institute of Technology, Tokyo, Japan.
[9] Figs. 3.5c,d: Photo courtesy of NCAR's Earth Observing Laboratory, Boulder, (CO) USA.

Regarding demands on validation data, which were earlier reviewed in Section 3.1, some aspects of field measurements should be discussed. The completeness and documentation of field experiments and of resulting databases have to be assured in order to be usable in a model comparison study. Particularly for measurements in complex environments like cities, the morphometric conditions characterizing the sensor sites have to be logged in detail. Following Oke (2007), this includes proper descriptions of the urban structure, cover, fabric, and metabolism. In addition, Grimmond (2006) points out that observational programs and data sets often are only insufficiently described in publications, making the measurements basically *unusable* for further analyses by other researchers. Just as in laboratory campaigns, the processing and archiving of field data should generally be conducted in a way that is comprehensible for others.

The monitoring of ambient meteorological conditions during the trials is another crucial aspect of field experiments. Diurnal and synoptic-scale variations usually cause trends and non-stationary effects in measured time series, which can complicate the statistical analysis of signals and hamper their interpretation. Furthermore, certain weather conditions can lead to a reduction of measurement accuracy of certain instruments or even make data acquisition impossible. Since LES is naturally in need of time-dependent unsteady inflow conditions, there is the chance to include temporal trends of ambient conditions in the simulation setup. This, however, requires that the experimental boundary conditions have been measured at representative locations and were sufficiently documented. As stated by Leitl (2000), keeping record of all relevant boundary conditions often is unfeasible, which results in the fact that "(...) in a strict physical sense it is impossible to define exactly what kind of (...) situation was captured during a field experiment."

The most important drawback of micro-meteorological field measurements, however, is the usually limited statistical representativeness of derived results. This issue is connected to the averaging times that are required to reduce the inherent uncertainty (Wyngaard et al., 1984). The time slots in which approximately steady-state conditions can be anticipated tend to be short compared with the time scales of the energy-carrying, low-frequency fluctuations, which dominate statistical measures. Averaging over longer periods, on the other hand, is generally impractical due to constantly changing ambient conditions. Typical temporal means over periods of 10 min to 30 min are usually not ergodic: Repeating the experiment under the same conditions would not necessarily result in the same mean values (which can be demonstrated based on wind-tunnel measurements). Instead, observed differences in mean flow quantities can be as large as an order of magnitude or more (Schatzmann and Leitl, 2011). The interpretation of discrepancies between experiment and simulation, thus, needs to be done with much more care than when working with laboratory data, for which the statistical scatter can be more readily assessed.

The discussion showed that laboratory and field experiments have the potential to be a valuable reference for LES validation, provided that modelers and experimentalists are aware of particular downsides and uncertainties. An ideal validation database, thus, should include field data, which mirror the true complexity of the ABL, as well as laboratory data, which allow to conduct sensitivity tests and to study certain problems in isolation. Interestingly, all field studies introduced above, except the HATS campaigns, have already been complemented by comprehensive tests in boundary-layer wind tunnels.

3.3 Validation approaches for LES

Two types of validation approaches for large-eddy simulation are usually distinguished in literature: the *a priori* validation of models and parameterizations used in LES and the *a posteriori* validation of computational results from LES (e.g. Piomelli et al., 1988). Following Sagaut (2005) the terms can be defined as follows:

> **A priori validation** — the process of testing subfilter-scale models and other LES parameterizations through the comparison with reference data. The latter have to be analytically filtered in order to determine the "true" resolvable and subfilter scales. The data comparison is done off-line, i.e. without running the simulation, and can be regarded as *static*. Reference data can come from low-*Re* DNS (mostly for technical flows) or experiments in high-*Re* flows (e.g. in the ABL or other geophysical systems). *A priori* validation allows to evaluate the performance of mathematical models in isolation by disregarding their computational implementation. While this procedure offers the chance to improve the model as a self-sufficient formulation, the implications for the performance quality of the model within the simulation are ambiguous.
>
> **A posteriori validation** — the process of testing the results of an LES computation against reference solutions from DNS or experiments. This approach is dynamic and takes into account the full set of modeling, computational, and numerical uncertainties. *A posteriori* validation thus aims at testing the *implemented* models, parameterizations, boundary conditions, and numerics that determine the quality of the physical phenomena captured in the resolved fields. The assessment of the simulation quality in this way is crucial for building confidence in the capabilities of the model. It is, however, difficult to disentangle error sources and draw ultimate conclusions about necessary model improvements since the simulation results are governed by a multitude of influencing factors, which often can only be partially controlled.

The validation of the simulation results in the sense of an *a posteriori* analysis has been the center of attention during the earlier discussions in this chapter. The LES flow validation conducted in the framework of this thesis is exclusively *a posteriori*. However, while analysis strategies for an in-depth simulation validation have been lacking in LES, the *a priori* branch has been abound with creative and innovative approaches since the early stages of LES developments. Hence, a brief overview of some aspects and example studies for both validation approaches is presented in the next paragraphs.

3.3.1 A priori model validation

The test of subfilter-scale parameterizations, surface boundary conditions, and hypotheses that enter LES models is a very active research branch. New SFS or wall models for LES usually are advocated by means of thorough *a priori* comparisons with established approaches. Having a closer look at LES model formulations, which often stem from the traditional viewpoint of ensemble averaging, is increasingly considered as necessary in order to improve the simulation quality of atmospheric flows. The inherently different mindsets of ensemble-averaged and LES models were encapsulated by Kempf (2008): RANS models usually average over time on a 1D "infinite" interval and probability distributions of flow variables also comprise extremely unlikely events separated by long time scales. The SFS distributions of the same variables in an LES formulation result from an average over a finite 3D volume and are limited to features that occur close to each other in physical space. Applying statistical similarity assumptions or eddy-viscosity concepts to model *local*, *time-dependent* quantities, thus, is a questionable approach for many applications.

The core area of *a priori* studies is to test and improve SFS model formulations on the basis of processed reference data using different combinations of filter widths and filter functions. While *a priori* testing has a long tradition in engineering, many comprehensive studies also originated in the area of atmospheric boundary-layer flows within the last 15 years. Velocity and temperature data from the innovative HATS field experiments were particularly helpful to investigate peculiarities of surface-layer turbulence and its representation in LES and gave new impetus to model refinements for atmospheric application (Tong et al., 1998, 1999; Hatlee and Wyngaard, 2007). By positioning sonic anemometer arrays perpendicular to the prevailing wind direction, a direct spatial filtering in the lateral direction and an indirect spatial filtering along the streamwise direction using Taylor's frozen turbulence hypothesis is possible. Thus, a surrogate 2D filtering of turbulent ASL flow in the (x, y)-plane can be used to study the structure and fundamental dynamics of SFS fluxes. Vertical gradients of filtered variables are obtained by using two arrays at different elevations above ground (cf. instrument arrangements in Figs. 3.5c,d). In an early study, Porté-Agel et al. (2001) used HATS data to investigate the relation between SFS variables and large-scale (coherent) structures in the near-surface ABL through systematic filtering and conditional averaging techniques. As in the plane wake flow investigated by O'Neil and Meneveau (1997), direct effects of large-scale eddies were also identified in the ASL and could be related to characteristic ejection-sweep events. Focusing on the instantaneous SFS dissipation rates, the authors found that strong forward and backward scatter events between resolved and SFS fields are correlated with ejection episodes. Such dynamics could not be captured by purely stochastic backscatter models.

Kleissl et al. (2003) investigated fundamental flaws of the standard Smagorinsky model when used in atmospheric LES on the basis of HATS data. *A priori* derived model parameters for the SFS shear stress and heat flux exhibited strong dependencies on the ratio between filter width and height above ground, Δ/z, and on atmospheric stratification parameterized by the length-scale ratio, Δ/L, where L is the Monin-Obukhov length. The authors found a dependence of the Smagorinsky coefficient, C_s, on the local strain-rate magnitude, $\widetilde{\mathcal{S}}$, during stable stability conditions and for large strain rates. Since the Smagorinsky model already assumes a proportionality between the eddy viscosity of the residual motions and $\widetilde{\mathcal{S}}$ (cf. Eq. 2.30), this parameterization seems to be unusable in stable stratification. Independent of the magnitude of C_s, the tensorial misalignment of SFS fluxes and filtered strain rates could cause inaccuracies of the model predictions.

The dependence of SFS dynamics on atmospheric stability and on the proximity to the surface has been further investigated by Sullivan et al. (2003). The authors introduce the ratio between the wavelength peak in the vertical velocity spectrum and the filter cut-off, Λ_3/Δ, as an essential parameter to connect measurements of SFS variables to LES applications. Since Λ_3 decreases with decreasing height and increasing stability, the parameter comprises both effects on the performance of SFS models. In a comprehensive analysis of HATS field measurements, the authors documented that SFS contributions are always significant close to the ground (i.e. at the first grid level for typical boundary-layer

LES codes) and increase with increasing stability, i.e. in situations where Δ is comparable to or even larger than Λ_3. By double-filtering the velocity signals, the SFS fluxes were analyzed in terms of a Germano decomposition (cf. Eqs. 2.25–2.27). For large Λ_3/Δ, $\mathcal{L}_{ij}$, $\mathcal{C}_{ij}$, and $\mathcal{R}_{ij}$ were found to be of comparable magnitude. Only as $\Lambda_3/\Delta \to 0$, the SFS flux approaches the ensemble average with the SFS Reynolds stress, $\mathcal{R}_{ij}$, being the dominant term. The backscatter of energy was found to be most important at the top of the ASL, where turbulence can be well resolved and clear inertial-range behavior is established. For small Λ_3/Δ, however, the inclusion of energy backscatter might not lead to significant improvements of the SFS model quality.

Another possibility to use HATS measurements for *a priori* studies was presented by Chen and Tong (2006), who focus on the influence of subfilter-scale turbulence on resolvable-scale velocity statistics in the CBL. The authors analyze the transport equation of the one-time, one-point joint probability density functions (JPDF) of filtered velocities, which contain expressions for the conditional averages of the SFS stress and its production rate. A strong link between SFS statistics and ASL dynamics was found, which relates to the occurrence of buoyant updraft and downdraft episodes associated with convective eddies. Particularly in the presence of strong buoyant plumes, the SFS stresses turned out to be anisotropic, and their production rates are asymmetrically linked to the resolved velocities – two conditions that are not adequately captured by current SFS models. More recently, Chen et al. (2010) extended this survey to study the influence of the SFS temperature flux and its production rate on the resolvable-scale velocity-temperature JPDF. They found pronounced feedback effects for positive filtered temperature fluctuations, which are associated with the convection of near-ground eddies from regions with strong wind and temperature gradients. Such flow-history effects still cannot be realistically represented in current SFS parameterization schemes.

Surprisingly, there are only few *a priori* laboratory studies with a focus on SFS motions in the atmospheric boundary layer. The investigation of the effects of a surface-roughness transition on the spatial variability of SFS motions by Carper and Porté-Agel (2008a,b) are among the few noteworthy exceptions. The roughness transition was modeled in a boundary-layer wind tunnel, where 2D, multi-point velocity measurements were carried out by means of particle image velocimetry in (x, y) and (x, z) planes. Hence, a true spatial filtering without invoking Taylor's hypothesis could be realized. The study showed that the SFS stresses respond faster to the roughness change than the resolved strain rates. This effect cannot be captured by the eddy-viscosity approach, which assumes a proportionality between both quantities. Comprehensive tests of prevalent SFS parameterizations showed that non-linear and mixed models often were better able to capture the complex SFS dynamics within the internal boundary layer than standard eddy-viscosity approaches.

The other focal point of *a priori* tests is the representation of near-wall flow effects in LES. As discussed earlier, virtually all ABL LES codes use a condition for the wall shear stress in order to describe the complex turbulent interactions between the surface and the first computational level. Most commonly, the local, resolvable-scale, instantaneous surface shear stress is related to the filtered horizontal velocity at the first grid point through a log-law similarity assumption (or its M-O extension). This condition, however, is strictly only valid for ensemble-averaged, stationary flow over a homogeneous surface, and its adequacy for modeling instantaneous effects has to be questioned.

The wind-tunnel study by Nakayama et al. (2004) investigates the existence of an *"instantaneous wall law"* by successively filtering velocity measurements over smooth and rough surfaces. While an unconditional similarity in the instantaneous streamwise velocity profiles could not be verified, the filtered data (obtained through 1D filtering in time) tended to show a log-law behavior only for large filter time scales (i.e. as the filter operation approaches the conventional time average). Transferred into the spatial domain using Taylor's hypothesis, the results imply that Δ would need to be larger than the typical streamwise extent of near-wall elongated eddy structures and rather long grid cells are required for adequate predictions using log-law boundary conditions.

By comparing measured and modeled surface shear stresses in the flow over a rough-to-smooth transition, Chamorro and Porté-Agel (2010) could identify systematic deficiencies in standard similarity boundary conditions. Models that relax the constraints on the linearity between surface shear stress and the velocity at the first grid-point and on the locality of their correlation, however, tended to yield better *a priori* results. Further wind-tunnel studies stimulated the formulation of refined wall models for atmospheric LES (e.g. Marusic et al., 2001; Chamorro and Porté-Agel, 2009) and there is continued interest in the validation and improvement of wall models for meteorological applications.

While *a priori* studies provide crucial information needed for model refinements, some limitations of this approach have to be pointed out (cf. Sagaut, 2005). Since experimental data are in most cases available in terms of time series, a temporal filter has to be used. The accuracy of derived spatial information using Taylor's hypothesis can be sufficient for ABL flows over homogeneous surfaces, but the assumption is not easily justifiable in strongly heterogeneous flow fields like, for example, encountered in urban areas. Furthermore, the dimensionality of the applied filter has an effect on the outcome of the test. Currently available reference experiments for ABL flows usually only permit 1D and 2D filtering, and generalizations for a real 3D LES filter are more or less guesswork. Furthermore, the filter width used in an *a priori* analysis usually differs from the *effective filter width* in the simulation, since the latter varies based on the numerical method and on the proximity to domain boundaries and is often only imprecisely known (Sullivan et al., 2003). Finally, *a priori* tests cannot provide a straightforward link between the tested model and the simulation statistics. In principle, a good *a priori* validation result does not necessarily yield a satisfactory performance of the LES code as a whole and *vice versa* (Sagaut, 2005). Hence, only the *a posteriori* validation of filtered and numerically resolved flow quantities can provide a conclusive appraisal of the model quality.

3.3.2 A posteriori simulation validation

Statistical moments computed from numerically resolved LES fields are never precisely equal to those obtained from exact solutions due to the cut-off of the small scales. However, as Sagaut (2005) indicates, nearly all comparison studies with LES results are conducted without prior processing of the reference data (e.g. in terms of analytical filtering). Agreements with the experimental data still are physically meaningful if the comparison focuses on processes that are linked to scales that are contained in the resolved fields (cf.

Section 3.1.2). Besides the fact that it is usually not clear what effective filter size has to be used, filtering the reference data is also not fully satisfactory with regard to the assessment of the simulation quality, which ultimately can only be made based on the complete data representing the physical "truth" for the test scenario. Experimental and strategical requirements for an in-depth LES validation have been discussed at length in Section 3.1 and 3.2. The next paragraphs, thus, will only briefly highlight some aspects of *a posteriori* studies, in which the LES validation was at least partially conducted off the "beaten track" of a pure mean flow comparison.

Aristodemou et al. (2009) compared results from mesh-adaptive LES with wind-tunnel data of flow between idealized building blocks. While mainly concentrating on the comparison of mean flow and turbulence statistics, the authors also discussed discrepancies between numerical and experimental frequency distributions of the underling instantaneous horizontal velocity signals. Although this approach was not overly stressed in the analysis, the shape and spread of the velocity histograms provided valuable insight into the disability of the code to accurately reproduce turbulence levels in street canyon, which, in this case, was attributed to the strongly dissipative Smagorinsky model.

Recently, Lenschow et al. (2012) compared higher order moments of the vertical velocity from Doppler lidar measurements with LES results and *in situ* aircraft observations conducted in the convective boundary layer. Although the emphasis of this study was put more on the validation of the lidar measurements based on LES, the authors presented an interesting approach to gain deeper insight into the structure of turbulence based on departures from a Gaussian distribution measured with skewness and kurtosis parameters. While an overall good agreement between the different data sets was found in most cases, the higher order moments computed from LES predictions showed less dependency on stability within the surface layer, which was related to the performance of the SFS model.

The importance of comparing frequency distributions and correlation statistics has also been emphasized in the study by Lee et al. (2009), who presented a detailed comparison of LES results with field and wind-tunnel measurements of flow and contaminant concentrations in the framework of JU2003. By comparing two-point correlation statistics of the horizontal velocity components in the (y, z) inflow plane, a good structural agreement between the LES inflow turbulence and the wind-tunnel approach flow could be determined. The analysis further focused on the validation of urban contaminant dispersion from instantaneous gas cloud emissions. Since the dispersion behavior of such clouds is highly complex and non-linearly coupled to the urban flow fields, the comparison of concentration statistics at individual locations within the city was conducted based on ensembles of experimental (wind-tunnel) and numerical dispersion realizations. This approach allowed to analyze histograms of individual peak concentrations and corresponding peak times. A comparison of these histograms revealed that a good agreement of averaged quantities is not necessarily coupled to a good agreement of the underlying frequency distributions. As stated by Lee et al. (2009), the "(...) results clearly indicate the danger of selecting a single figure of merit (...) to evaluate the quality of numerical results for validation purposes."

The LES code used in the last-mentioned study is the same that is validated within the framework of this thesis. Corresponding simulation details and information about the generation of the wind-tunnel reference data are presented in the next chapter.

4 Experimental and Numerical Data Basis

ABSTRACT *Introducing the Hamburg flow validation test case, this chapter discusses features of experimental and LES data concerning their preprocessing and quality control, together with necessary harmonization steps for the comparison study. Single-point, high-resolution velocity time series from non-intrusive measurements in a boundary-layer wind tunnel using laser Doppler anemometry represent the reference values to assess the performance of the implicit LES code FAST3D-CT. This LES uses a monotone, non-linear convection scheme to model subgrid effects and is operated on a Cartesian mesh with a uniform resolution of 2.5 m within the urban roughness sub-layer. Representative mean and turbulence inflow parameters for the wind tunnel and the LES are determined from the analysis of long and short-term* in-situ *field measurements with sonic anemometers at a suburban site. Both the scale-reduced wind-tunnel model and the LES geometry include relevant morphometric and topographic details of the urban test environment. Careful scrutiny of the physical representation of turbulent scales in either model, of experimental and numerical time-series resolution qualities, and of the inherent uncertainty in statistics derived from finite-duration signals, confirms the overall comparability of both data sets.*

4.1 Introduction

The LES validation study presented in this thesis is part of a research project on the implementation and evaluation of an emergency response software tool that can be operated to predict the dispersion of airborne contaminants after their accidental or deliberate release in an urban area. The operational model CT-Analyst® had been developed by the Laboratory for Computational Physics and Fluid Dynamics of the U.S. Naval Research Laboratory (NRL) in Washington, D.C. Within the *"Hamburg Pilot Project"*,[1] CT-Analyst is adapted for operation in the city of Hamburg, Germany (Leitl et al., 2012).

[1]Funded by the German Federal Office of Civil Protection and Disaster Assistance and by the Free and Hanseatic City of Hamburg.

The prediction of hazard areas and concentration levels is based on comprehensive urban flow field calculations with NRL's LES-based CFD model FAST3D-CT, which are conducted in the run-up to the actual deployment of the emergency response tool. On the basis of these detailed LES simulations, high-resolution databases (Dispersion Nomografs$^{\text{TM}}$) of contaminant dispersion paths are generated, which can be accessed by CT-Analyst to display plume footprints within milliseconds (for details see Boris et al., 2002; Boris, 2002; Boris et al., 2011). The dispersion nomografs are derived from integrated statistics of the mean wind field and turbulent fluctuation levels within the urban roughness sublayer, which represent driving mechanisms for the dispersion process.

Figure 4.1 shows contaminant concentration levels near the surface after one hour of continuous release from a ground source in the inner city of Hamburg, as predicted by the LES model and the emergency response tool. Although the detailed information provided by FAST3D-CT has to be "boiled down" for the most part before being usable in CT-Analyst, the general characteristics of the plume footprint are preserved by the employed methodology. Clearly evident is the influence of the urban morphology on the shape of the plume edges – a feature that is owed to the ability of the urban aerodynamics code to take into account the influence of buildings, terrain, and surface forms on the air flow. The accuracy of predictions made by the operational tool, thus, inherently depends on the overall simulation quality provided by LES.

Numerical predictions from FAST3D-CT already were subject to validation tests against field observations and wind-tunnel reference data in earlier studies (e.g. Patnaik et al., 2007; Lee et al., 2009). So far, however, the assessment of the accuracy of simulated wind fields had been restricted to low-order statistical moments. The *Hamburg Pilot Project* provides an ideal framework to extend these analyses by in-depth comparisons following the LES validation hierarchy proposed in Section 3.1.2 (Fig. 3.2).

(a) **(b)**

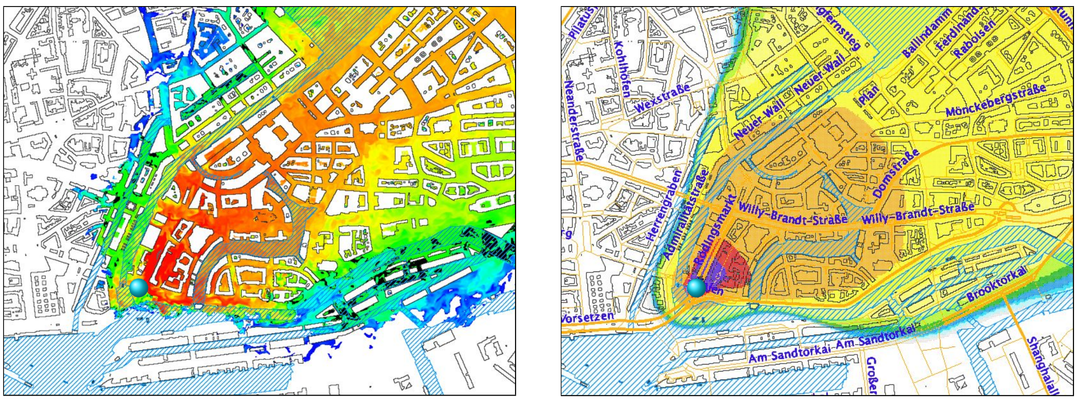

Figure 4.1: Concentration footprints at pedestrian level after one hour of continuous plume release: (a) snapshot of the instantaneous field predicted by the urban LES code FAST3D-CT, (b) screenshot of the contaminant plume predicted by the operational emergency response tool CT-Analyst. Wind is from 235° with 7 $^{\mathrm{m}}/_{\mathrm{s}}$ in 200 m height. The release site is indicated by a blue dot. Concentration levels range from blue (low) to red/purple (high).

Data for the validation study were derived from high-resolution flow simulations with FAST3D-CT conducted at NRL and comprehensive measurements in the Environmental Wind Tunnel Laboratory (EWTL) at the University of Hamburg. The computational and experimental domains are centered on the inner city of Hamburg and are shown in Figure 4.2 together with buildings and water bodies.[2] The topography of central Hamburg is predominantly flat. Figure 4.3 shows terrain elevations for the area around the inner city district. The maximum height offsets to the downtown ground-level (orange color) are approximately 20 m (northwest elevations) and 7 m (northeast elevations).

High-resolution geometry information about buildings, topography, and outlines of water bodies was provided by the Hamburg geo-information service on a commercial basis. Detailed three-dimensional building data were available at a minimum resolution of 0.5 m.

Both domains include a high percentage of water bodies. The *Elbe* river separates the industrial harbor area in the south from the Hamburg downtown district with residential and office buildings as well as major institutional complexes. Typical widths of the main river branch within the specified domains are in the order of 300 m to 500 m. To the northeast, parts of the lake *Alster* are included together with several narrow water canals traversing through the old town of the city. The bisection of the wind tunnel and LES domains by the Elbe river marks a strong change in the roughness conditions of the built-up environment. Whereas the industrial harbor area mostly features low-story storage buildings, large-area production halls, and open spaces, the inner city to the north of the river is characterized by a high-rise, high-density building structure.

The urban morphology of the downtown area corresponds to typical northern and central European cities featuring closely packed, heterogeneously shaped building geometries of similar heights as well as narrow street canyons, complex intersection structures and road systems. Based on the buildings included in the wind-tunnel domain, an average building height of $\mathrm{H_m} \simeq 34.3\,\mathrm{m}$ is obtained for the downtown district to the north of the river. Typical street canyon widths in this area are in the order of $\mathrm{W_m} \simeq 20\,\mathrm{m}$, with individual values ranging between 10 m and 50 m. The typical street-canyon aspect ratio in the inner city, thus, is given by $\mathrm{H_m/W_m} \simeq 1.72$, with single values in the order of 0.7 to > 3. Following Li et al. (2006) and Grimmond and Oke (1999), the building density implies the dominance of skimming flow regimes for most street-canyon situations, while in the presence of plazas or wide intersections chaotic wake-interference flow regimes can be anticipated. For the industrial area to the south of the river, the average building height is much lower and in the order of 21 m.

The following sections introduce relevant details of the physical and numerical modeling approaches. The selection of comparison locations, basic steps of the data preprocessing, as well as a comparative discussion of data properties and implications for the validation work are presented in conclusion.

[2] Wind-tunnel domain with a dimension of $1.4 \times 3.675\,\mathrm{km}^2$, centered at 53°32′39.60″ N 9°58′55.00″ E; FAST3D-CT domain with a dimension of $4.0 \times 4.0\,\mathrm{km}^2$, centered at 53°32′44.35″ N 9°58′51.30″ E.

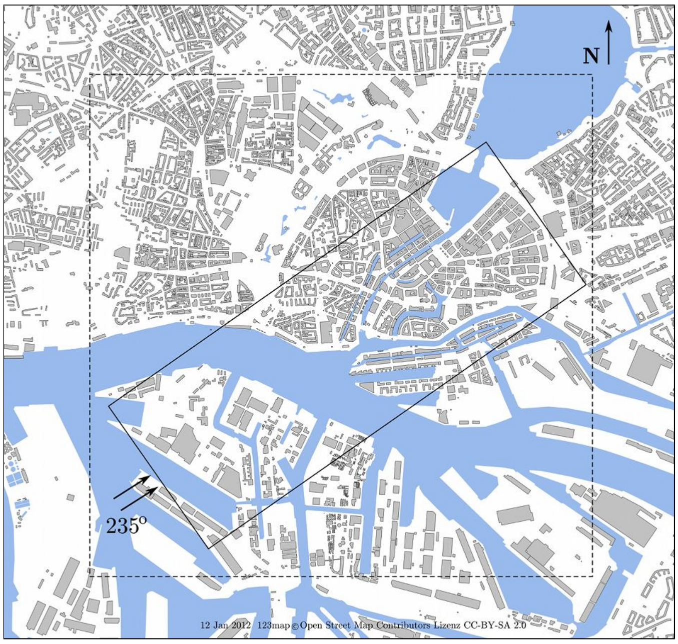

Figure 4.2: Experimental and computational domains covering the inner city of Hamburg. Solid rectangle: $1.4 \times 3.7\,\mathrm{km}^2$ wind-tunnel model area; dashed square: $4 \times 4\,\mathrm{km}^2$ simulation domain of FAST3D-CT. Map from *OpenStreetMap* (2012).

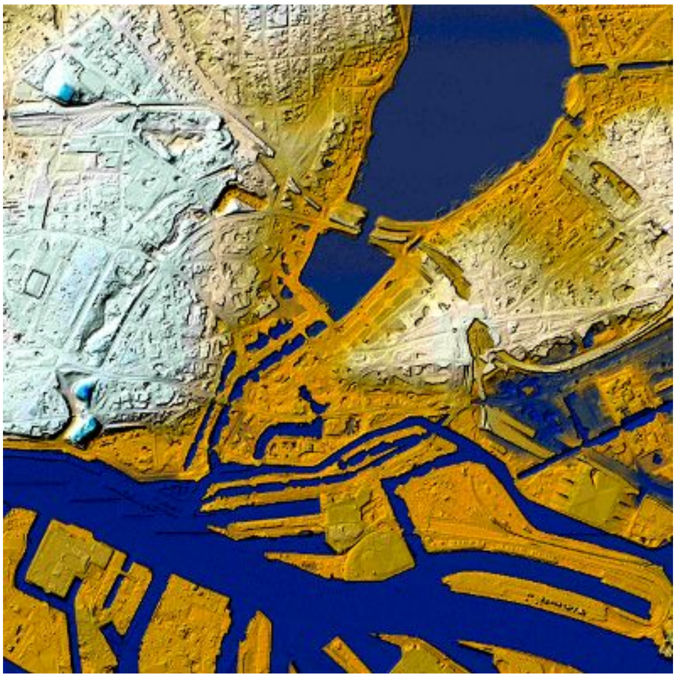

Figure 4.3: Terrain and water (dark blue) in the inner city area of Hamburg. Heights are indicated by colors from orange (ground level; low) to light blue (high).

4.2 Experimental data basis

4.2.1 Wind-tunnel model geometry

The boundary-layer wind-tunnel model area of the inner city of Hamburg as indicated in Figure 4.2 was built at a geometric scale of 1:350. The source data for buildings, terrain elements, and outlines of water bodies were available in terms of 3D-CAD data, (x, y, z) topology files, and shapefiles (geospatial vector format), respectively, and have been subject to extensive preprocessing in order to be usable for the model construction. All relevant buildings were included with a precision of up to 0.5 m under full-scale conditions (roughly 1.5 mm in model scale). The model houses were manufactured from fairly rigid polystyrene foam (*Styrodur*) and mounted on several wooden ground plates, which included reproductions of the bodies of water as well as relevant topographical elements to the northwest and northeast of the city core (see Fig. 4.3). Hilly terrain was reproduced with vertically stacked layers of thin wood plates, each having a depth of 2 mm in model scale equating to offsets of 0.7 m in the field, which yielded a step-like representation. The maximum height differences with reference to the ground plates, which represent the elevation of the city center, were 5.6 m and 17.4 m in full-scale conditions. The water level of the river branches and canals was modeled to be close to high-tide conditions, resulting in a full-scale vertical offset of 3.5 m to the ground level (1 cm model scale). The same spacing was used for the water level of the inner city lake.

The geometry data were completed by hand with some special structures of the model area. This included an approximate replication of a large concert hall (*Elbphilharmonie*) located at the river shore close to the center of the domain. The building was under construction during the project term (expected completion in 2014), but already represented a dominant roughness element in the harbor area. With a height of more than 100 m, the concert hall is going to be the tallest inhabited building in Hamburg. In addition, models of two sailing and cargo ships (*Rickmer Rickmers* and *Cap San Diego*) were included, which are permanently moored at the landing bridges of the Hamburg harbor. With lengths of 97 m and 160 m, both vessels are major flow obstacles with dimensions comparable to regular building structures in the area. Lastly, the above ground trail of a subway line proceeding on an overpass parallel to the downtown riverwalk has been added.

The most considerable abstraction of the wind-tunnel model geometry is given by the omission of all types of urban greenery between buildings – despite the fact that Hamburg is a particularly green city. This approach has been taken since research on the aerodynamically correct physical modeling of urban trees and shrubs at comparatively low wind speeds is still in its infancy and current approaches are far from being well-established. Furthermore, smaller bridges and traffic overpasses were removed since the available geometry data contained incomplete information about their depths, which could not be corrected by means of other data sources. An overview of all geometry elements incorporated in the model is presented in Appendix A.

Figures 4.4 and 4.5 show photographs of the wind-tunnel model and the corresponding real city structure with a view from the southwest above the Elbe toward the urban core. The comparison gives an impression of the level of detail provided by the scale model.

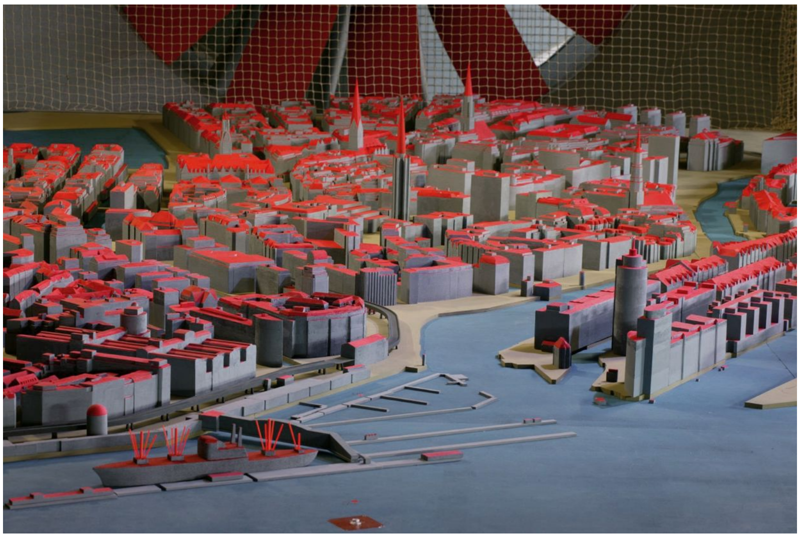

Figure 4.4: Scale model of the inner city of Hamburg mounted in the boundary-layer wind tunnel. View is from the southwesterly approach flow direction (235°).

Figure 4.5: Aerial photograph of downtown Hamburg; view from SW. Photo courtesy: Department of the Interior and Sports, Free and Hanseatic City of Hamburg.

In the harbor area to the left, the *Cap San Diego*, jetties, and the marina at the northern river shore can be seen. To the right, an anabranch of the Elbe separates the old warehouse district from the old town. Bridges connecting both districts as well as smaller non-permanent obstacles identifiable in the aerial photograph were excluded from the scale model. The fairly homogeneous height structure of the downtown area exhibits a slight increase to the northeast and is only disrupted by scattered steeples and towers.

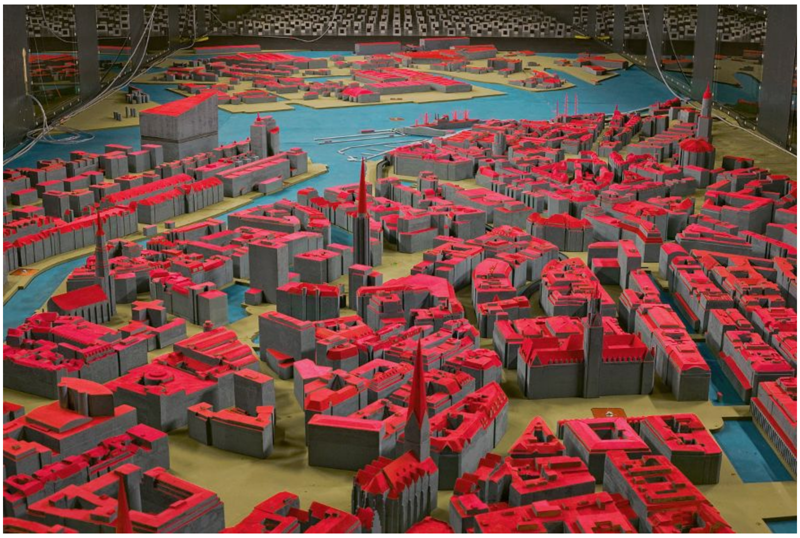

Figure 4.6: Wind-tunnel scale model of the inner with a view from 55° (NE), exactly contrary to the mean inflow direction.

Figure 4.7: Aerial photograph of downtown Hamburg; view from NE. Photo courtesy: Department of the Interior and Sports, Free and Hanseatic City of Hamburg.

A detailed overview of the inner city area is presented in Figures 4.6 and 4.7, this time with a view from the northeast. The tallest structures ($\mathcal{O}(100\,\mathrm{m})$) are the concert hall visible in the upper left corner, together with the steeples of the main churches and the city hall, which can be seen in the right center of the images. The dense packing of buildings is here and there loosened by plazas, parking areas, and canals. In the upper part of the photographs, the industrial park with mostly low-rise storehouses is recognizable.

4.2.2 Physical flow modeling

In the following, basic steps of the physical flow modeling are discussed together with principles of the flow measurement techniques and data quality assurance procedures. Further discussions on details of the modeling chain can be found in Peeck (2011).

Wind tunnel *WOTAN*

The experiments were conducted in the open-return boundary-layer wind tunnel *"WOTAN"* at the Environmental Wind Tunnel Laboratory of the University of Hamburg.[3] With a closed test section of 18 m length, 4 m width, and an adjustable ceiling height ranging between 2.75 m and 3.25 m, *WOTAN* is one of the largest facilities worldwide to model atmospheric boundary layer flows and environmental processes in complex geometries. The tunnel dimension allows for model sizes up to a geometric scale in the order of 1:100. The constructional layout of the facility only permits physical modeling in isothermal conditions, i.e. the generation of scale-reduced ABL flows under neutral stratification. At the top of the boundary layer, free-stream velocities up to 15 m/s can be realized, which corresponds to a maximum volume flow of $504,000\,\mathrm{m^3/h}$ through the test section.

Figure 4.8 presents top and side views of the wind tunnel together with their dimensioning. The design and operating mode of the tunnel correspond to a typical setup of low-speed, suction-type boundary-layer wind tunnels presented earlier in Section 3.2.2 (see Fig. 3.3). Air is sucked into the intake of the tunnel by a 130 kW 14-blade axial blower with a diameter of 3.16 m. Before entering the test section, the laboratory air has to pass through elongated and narrow honeycomb tubes, which are installed to straighten the flow. A further attenuation of velocity variations induced by the suction process is attained by a contraction of the vertical and lateral intake dimensions, resulting in an acceleration of the flow. The contraction area ratio of *WOTAN* is approximately 3.

Vortex generators (so-called *spires*) are mounted at the entrance to the boundary-layer development section. For the Hamburg campaign, an array of 7 flat vortex generators with triangular front faces was used (modified Standen spires, cf. Standen, 1972), of which each had a height of 2,350 mm and a base width of 182 mm. Close to the ground, the cross sectional area of the spires was broadened my means of low, five-sided trip plates. The subsequent 7.2 m long flow development section was covered with 25 rows of alternating floor roughness elements, arranged in staggered order to generate realistic (sub-)urban roughness conditions. Sharp-edged metal brackets of various dimensions were used as obstacles (max. height/width 100/85 mm; min. height/width 30/40 mm; for details see Peeck, 2011), of which the last rows can be seen in the uppermost part of Figure 4.6.

The Hamburg model area has a streamwise extent of 10.5 m in wind-tunnel scale and is incorporated into Figure 4.8 on the basis of *OpenStreetMap* data (note that Figure A.2 in Appendix A depicts the exact model layout based on the utilized high-resolution CAD geometry information as the more complete database). The orientation of the Cartesian coordinate system is indicated in Figure 4.8,[4] together with the location at which the reference velocity, U_{ref}, is defined (details are given later in Section 4.4.2).

[3] Further information available on `http://www.mi.uni-hamburg.de/windtunnel`; accessed July 17, 2012.
[4] The point of origin corresponds to a geographic coordinate of 53°32′50.08″ N 9°59′19.74″ E.

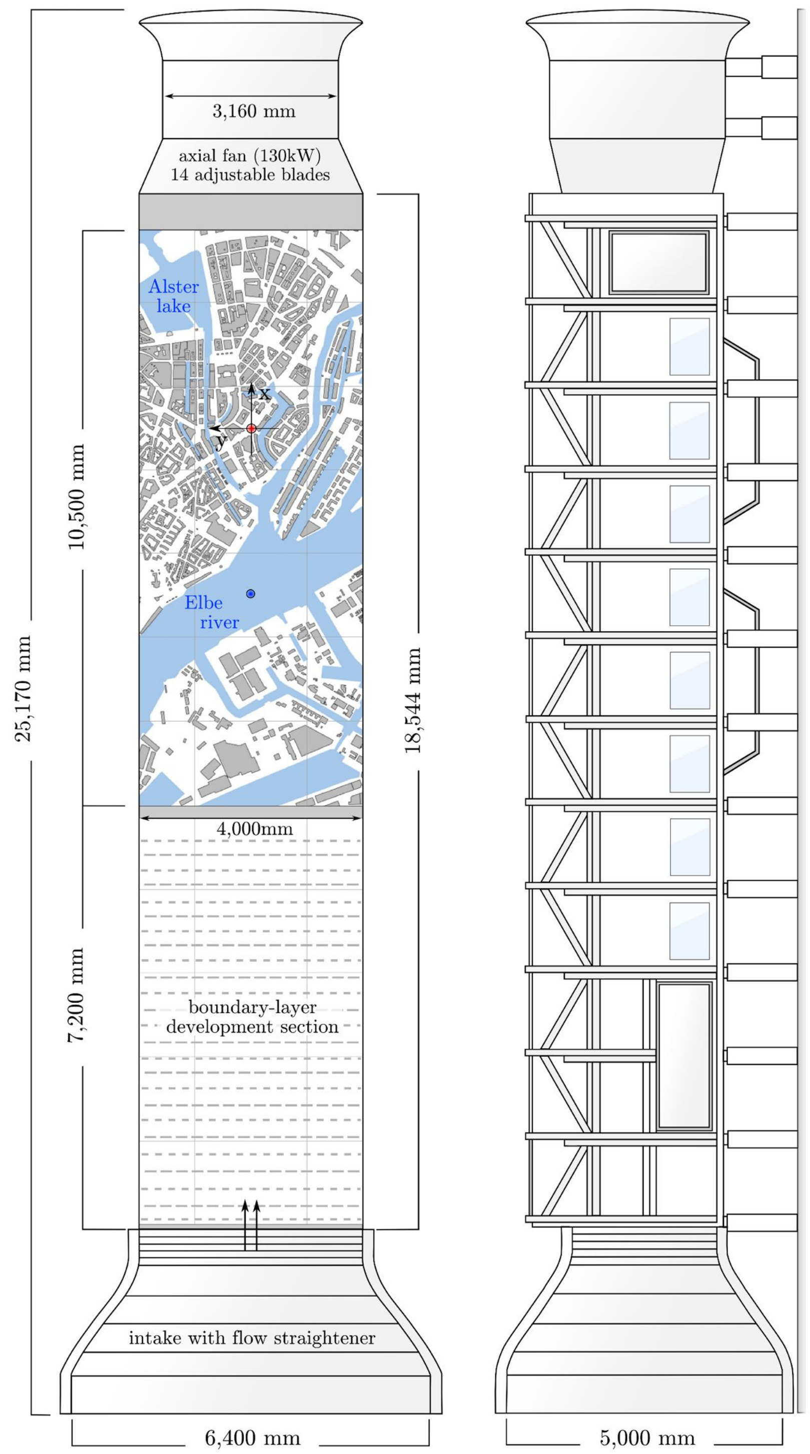

Figure 4.8: Top view (*left*) and side view (*right*) of the boundary-layer wind tunnel *WOTAN* at the University of Hamburg. Red and blue dots mark the coordinate origin and the flow reference location above the Elbe river, respectively. Background map showing the model area from *OpenStreetMap* (2012).

Flow similarity & boundary conditions

In preparation of the measurement campaign, it was verified that the design of the model and the operational mode of the tunnel are in agreement with the criteria outlined in Section 3.2.2. Since the flow is isothermal, buoyancy affects are not considered and the Froude number criterion can be omitted. Reynolds number independence has been verified through the analysis of dimensionless flow statistics obtained at different free-stream velocities U_∞ (cf. Peeck, 2011). After the critical Reynolds number is exceeded, statistical quantities expressed in relation to a reference flow velocity (e.g. U_∞ or another representative U_{ref}) are independent of the inflow velocity. For the Hamburg campaign, typical free-stream velocities in the order of $U_\infty \simeq 10\,{}^{\text{m}}\!/\!{}_{\text{s}}$ were used to ensure that dominant flow structures are Reynolds number independent. This corresponds to a typical rotational speed of 12 Hz of the axial fan. The characteristic flow Reynolds number in the test section is $Re \simeq 2.67 \cdot 10^6$ (with $\mathcal{U} \simeq U_\infty$ and $\mathcal{L} \simeq 4\,\text{m}$, as the tunnel cross section). Within the model domain, this corresponds to a value of $Re_{\text{H}} = 2.97 \cdot 10^4$, based on the average downtown building height and a typical velocity at this elevation of $U_{\text{H}} \simeq 4.55\,{}^{\text{m}}\!/\!{}_{\text{s}}$. The Reynolds number thus complies well with established criteria for the reliable physical modeling of urban flow (e.g. Plate, 1999). In order to guarantee Re-independence close to solid boundaries, model buildings and ground plates had aerodynamically rough surfaces.

Since Coriolis accelerations cannot be modeled, it has to be verified that the Rossby number is high enough to ensure that these effects are negligible in the modeled ASL. Using the typical ABL approximation of the Coriolis term (cf. Section 2.3.1), the Rossby number of the (full-scale) model domain was obtained from $Ro = U_\infty/(L_x\, f_c)$. With $L_x = 3,675\,\text{m}$ and a Coriolis parameter of $f_c \simeq 1.17 \cdot 10^{-4}\,{}^{1}\!/\!{}_{\text{s}}$ (at $\varphi = 53°$) this yields $Ro \simeq 23$. For the largest east-west extension of the domain, i.e. 3,010 m, a value of $Ro \simeq 28$ is obtained. Mid-latitude low-pressure systems, whose dynamics are characterized by the influence of the Coriolis force, typically have Rossby numbers in the range of 0.01 to 0.1. Thus, it can be argued that Coriolis effects are negligible over the entire horizontal extent of the ASL, which is also in agreement with Snyder's (1972) rule-of-thumb of $L_x < 5\,\text{km}$.

The blockage of the test section by the tunnel boundaries can affect the modeled flow, particularly in case of large model scales. Following the recommendation by VDI (2000), the ratio of the model frontal area to the tunnel cross section should be smaller than 5 %. Using an average projection height of the model equal to H_m, a blockage coefficient of $\Phi = A_{\text{model}}/A_{\text{tunnel}} \simeq 3.24\,\%$ is obtained, which meets the technical requirement.

The height limitation of the test section can generate along-wind pressure gradients due to the growth of the UBL depth. In order to avoid accelerations at the boundary-layer top, δ_∞, the height of the tunnel ceiling has been adjusted. Over the entire tunnel length, streamwise gradients of static pressure measured at δ_∞ were well below 5 % of the dynamic pressure obtained from ${}^{1}\!/\!{}_{2}\,\rho\, U_\infty^2$ as recommended by VDI (2000).

Approach flow boundary layer

The realistic representation of atmospheric turbulence conditions in the laboratory approach flow is crucial for the overall agreement of the physical model with reality. For the Hamburg campaign, value ranges of mean flow and turbulence parameters were derived from meteorological data acquired in a suburban environment about 8 km to the southeast of the downtown area.[5] *In-situ* measurements with sonic anemometers were conducted on two masts located in Hamburg-Billwerder: a 12 m meteorological mast and a 300 m radio tower, separated by a distance of 170 m. Both towers are located approximately 10 km to the east of the southernmost edge of the wind-tunnel domain (cf. Fig. 4.2). Velocity and temperature data were analyzed in terms of 1 min and 5 min averages, available over a period of three years (2007–2009) at five measurement heights (10 m, 50 m, 110 m, 175 m, and 250 m). For the derivation of turbulence statistics, spectral energy densities, and integral length scales, velocity time series with resolutions of 10 Hz to 20 Hz were analyzed. Details of the field site and the analyzed data are presented in Appendix B.

The orientation of the wind-tunnel model domain along a SW–NE axis was based on the analysis of weather-mast data for the derivation of prevalent approach flow wind directions for the city of Hamburg. Figure 4.9 shows frequency distributions of horizontal wind directions and speeds in terms of meteorological wind rose diagrams obtained at three heights above ground from the 3-year data record.[6] A clear dominance of westerly winds is apparent at all elevations, together with secondary peaks for winds from the NE and SE. Since the booms on which the anemometers are mounted, are oriented southward, measurements of northerly winds are biased by the wake flow behind the radio tower and are excluded from the analysis. The southwesterly approach flow direction (wind from 235°) for the wind-tunnel model was further motivated by the fact that the surface roughness characteristics upstream of the field site and the model inflow edge are comparable. The approach flow region to the south of the city is characterized by mixed land use with suburban and small industrial zones, which are frequently loosened by patches of cultivated areas and side branches of the Elbe river. The built environment is of low to medium height and packing density. Toward the onset of the wind-tunnel domain, however, the surface roughness increases in the industrial areas of the harbor region – a characteristic that is not seen by the field site sensors in Billwerder.

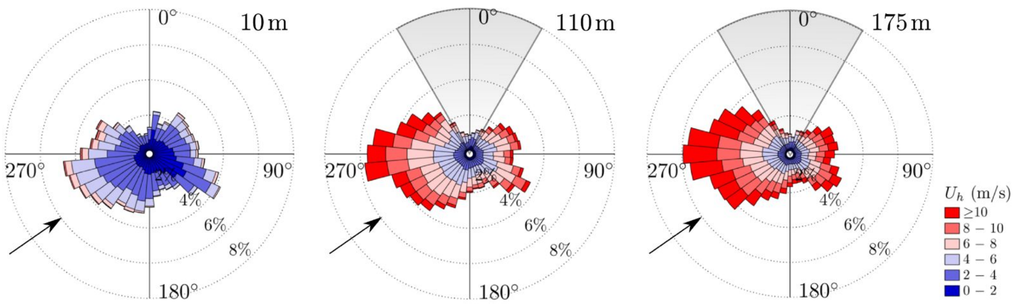

Figure 4.9: Wind rose histograms of 1 min averages of horizontal wind directions and wind speeds measured at different heights in Billwerder from 2007 to 2009. One bar represents a 10° bin. Gray cones mark the angular range influenced by the wake of the mast. Arrows indicate wind from 235°.

[5]The *"Hamburg Weather Mast"* site is operated by the Meteorological Institute of the University of Hamburg since 1967. An overview of measurements at the site is presented by Brümmer et al. (2012).

[6]The orientation of the wind rose bars indicates the direction from which the wind is blowing.

Four parameters are needed to characterize the height profile of the mean streamwise velocity in the atmospheric boundary layer: the friction velocity, u_*, the roughness length, z_0, the displacement height, d_0 (cf. log-law definition in Eq. 2.40) and the so-called *power-law parameter*, α, which is used in a further velocity profile approximation:

$$\frac{\overline{U}(z)}{U_{\mathrm{ref}}} = \left(\frac{z - d_0}{z_{\mathrm{ref}} - d_0}\right)^{\alpha} , \tag{4.1}$$

where the overbar denotes a time average. While the log-law, in general, is only used to approximate the mean velocity profile in the *surface layer*, the power-law fit is typically used to represent the velocity distribution over the entire ABL depth.

Peeck (2011) derived mean inflow parameters for the wind-tunnel model from the long-term field data available as 5 min averages, which first were filtered for an approach flow wind sector of $235° \pm 30°$ (see Table 4.1). In a next processing step, only velocity profiles corresponding to near-neutral atmospheric stability conditions, measured in terms of the stability parameter $\zeta = z/L$, were left in the data pool. Here, slight deviations from the exact state of $z/L = 0$ were permitted in order to increase the size of the remaining data samples and the statistical representativeness of derived quantities. Since different values for the acceptable bounds of a near-neutral state can be found in literature, a systematic analysis with different thresholds was conducted (i.e. $|\zeta| \leq 0.1$, $|\zeta| \leq 0.01$, and $|\zeta| \leq 10^{-3}$).[7] From these data, 1 h velocity averages were calculated at all heights and only those profiles were left in the data set for which the horizontal wind speed was $\geq 1\,\mathrm{m/s}$. The data samples were then homogenized by referencing the local velocities to the corresponding mean U_{ref_1} measured at $z_{\mathrm{ref}_1} = 175\,\mathrm{m}$. Finally, roughness lengths and profile exponents were derived through a least-squares fit of the profiles using Eq. (4.1) with $d_0 = 0$ and a modified representation of the logarithmic law according to $\overline{U}/U_{\mathrm{ref}_1} = 1/K \ln(z/z_0)$, with $K = 0.4$. Since the derivation of the roughness length from the log-law depends on the assumed depth of the surface layer, δ_{ASL}, data fits were made for different depths by systematically excluding either none, one or two of the topmost measurement points, corresponding to vertical extents of $\delta_{\mathrm{ASL}} = 250\,\mathrm{m}$, 175 m or 110 m.

Table 4.1: Roughness lengths and profile exponents derived from velocity profiles of 3-year field measurements in Billwerder for a wind direction sector of $235°\pm30°$. Results are given for different constraints on the ASL depth and the magnitude of the stability parameter, ζ, as reported by Peeck (2011).

	$\|\zeta\| \leq$ **0.1**		$\|\zeta\| \leq$ **0.01**		$\|\zeta\| \leq$ **10^{-3}**	
δ_{ASL} (m)	α	z_0 (m)	α	z_0 (m)	α	z_0 (m)
250	0.30	1.60	0.29	1.41	0.30	1.45
175	0.29	1.24	0.29	1.12	0.29	1.17
110	0.29	0.93	0.28	0.87	0.28	0.93

[7] In consultation with C. Peeck, a typo contained in the original table (cf. Peeck, 2011) has been corrected by setting the last threshold to $|\zeta| \leq 10^{-3}$ instead of $|\zeta| \leq 10^{-8}$.

The results for the mean values of z_0 and α, summarized in Table 4.1, show that the assumed surface layer depth has a great influence on the derivation of z_0, while the values of α, as expected, are only slightly affected by this variable. For a fixed δ_{ASL}, homogeneous results are obtained for different stability thresholds. The tolerated magnitude of ζ primarily affects the statistical representativeness of the results: The stricter the criterion, the smaller is the number of remaining velocity profiles. Moreover, the more values are excluded from the profiles to simulate lower ASL depths, the less representative is the obtained profile fit. Thus, on the one hand, the scatter range of z_0 and α is indicative of uncertainties that have to be expected when the ASL depth cannot definitely be derived due to a limited number of available data and slight stability variations. On the other hand, the scatter also incorporates limitations of the analysis technique that is used to derive the parameters. While an ensemble mean value of $\langle z_0 \rangle \simeq 1.19\,\mathrm{m}$ can be formally obtained from the field data, target ranges of $z_0 \simeq 1.0\,\mathrm{m}$ to $1.5\,\mathrm{m}$ and $\alpha \simeq 0.28$ to 0.30 for $z_{\mathrm{ref}_1} = 175\,\mathrm{m}$ were defined for the generation of the wind-tunnel boundary layer. The above analysis does not take into account the zero-plane displacement height, which would add a further degree of freedom to the results. Neglecting d_0 is justifiable in view of the surface roughness characteristics of the approach flow and the fact that the field data profiles revealed no curvature tendencies, which would otherwise imply that d_0 needs to be considered (cf. discussion in Stull, 1988, p. 382).

In the modeling of the wind-tunnel approach flow, it was aimed to mimic the natural atmospheric conditions as close as possible, while generating a boundary layer whose mean flow and turbulence statistics are self-consistent and in agreement with empirical benchmarks. A comparison of profile parameters of the field and laboratory boundary-layer flow is shown in Figure 4.10 together with empirical reference functions proposed in other studies. These and all subsequent results are presented in full-scale dimensions.

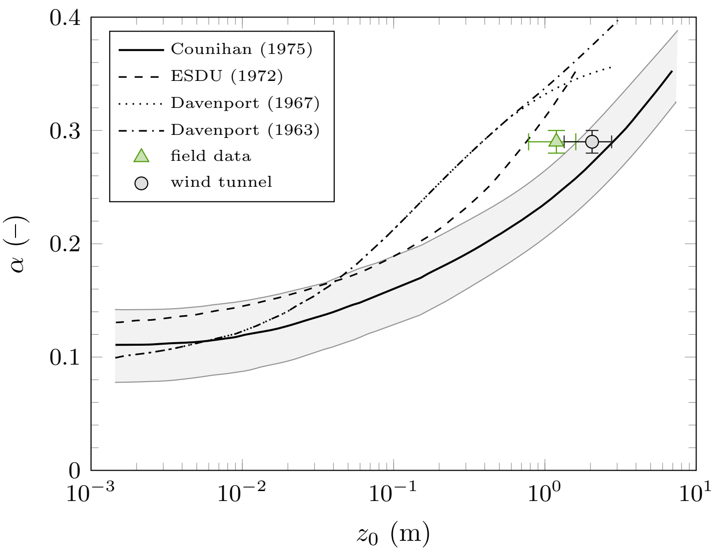

Figure 4.10: Relation between the full-scale roughness length, z_0, and the profile exponent, α, in the field and the wind tunnel in comparison to empirical functions. The gray area marks the variation range around the Counihan (1975) curve.

The wind-tunnel data were obtained from measurements at the end of the development section, 7.45 m (model scale) upstream of the coordinate origin (cf. Fig. 4.8) at three lateral positions: the tunnel centerline ($y = 0\,\mathrm{m}$) and at $y \pm 0.5\,\mathrm{m}$. A detailed outline of the measurement techniques is presented in Section 4.2.3. Statistics are only derived well above the roughness elements. Using a rule-of-thumb (Pasquill and Smith, 1983), the blending height was estimated from $z_\mathrm{r} \simeq 1.5\mathrm{H_r}$, where $\mathrm{H_r}$ is the height of the tallest roughness element, resulting in a value of 52.5 m full-scale. For heights $z \geq z_\mathrm{r}$, statistics are representative of the integrated surface characteristics in the approach flow rather than of the local roughness structure. Peeck (2011) showed that stationary and horizontally homogeneous flow conditions were established at the transition to the urban model.

The α-to-z_0 relationships (Fig. 4.10) reveal that the mean roughness length of the modeled wind-tunnel boundary layer is slightly larger (2.05 m) than the target value range determined from the field measurements, while the mean profile exponents are exactly matching. However, the scatter ranges of the field and wind-tunnel parameters, which were determined through variations of the data fit, are clearly overlapping. In general, both flows belong to comparable categories of surface roughness structure. Overall, the laboratory data are in slightly better agreement with the established functional relationship proposed by Counihan (1975), which is often consulted to verify the mutual plausibility of both parameters. As discussed above, an increased surface roughness caused by the presence of the industrial harbor area is anticipated at the inflow edge of the wind-tunnel domain, so that the tendency toward a higher z_0 in the laboratory flow is acceptable.

For the comparison of turbulence statistics, high resolution data recorded with 10 Hz (10 m mast) and 20 Hz (tower) were derived from a test case that exhibited ideal conditions for the analysis: nearly constant wind directions from SW at all heights (e.g. $232.5° \pm 11.3°$ in 50 m), near-neutral stability, and fairly strong winds over a duration of 6 h during daytime. Details of the meteorological situation and the data preprocessing steps are given in Appendix B. The wind-tunnel scatter bars represent the maximum standard deviations over all heights determined from a spatial average of the approach flow profiles.

Figure 4.11 shows comparisons of field and wind-tunnel height profiles of the mean streamwise velocity and the vertical turbulent momentum flux for a mean reference velocity of 7 m/s at 175 m in the approach flow. A good agreement between both data sets and the power-law fit with $\alpha = 0.29$ is evident over the entire boundary layer (Fig. 4.11a). The vertical flux profiles, however, differ by almost a factor of 2 near the ground (Fig. 4.11b), which may be explained by differences in the surface roughness conditions modeled in the laboratory and seen at the field site. The large scatter of the field data, however, defuses the distinctness of the disagreement. Earlier analyses of field flux profiles by Peeck (2010) reported similar ranges for $\overline{u'w'}$ from $-0.12\,\mathrm{m^2/s^2}$ to $-0.38\,\mathrm{m^2/s^2}$ for the 3-year data record. The flux profiles show a well-established constancy, which extends up to 250 m in the field, emphasizing the well-mixed state of the ABL on this day. The gray area marks a 10 % spread around the lowermost wind-tunnel value ($-0.39\,\mathrm{m^2/s^2}$). Using the *constant-flux* constraint, the wind-tunnel ASL depth is assessed to be just below 175 m.

Differences in the surface roughness are also reflected in the turbulence intensities, measured as the ratio of local rms velocities, σ_i, and corresponding mean streamwise velocities, $\overline{U}$. Height profiles of both experimental data sets are depicted in Figure 4.12.

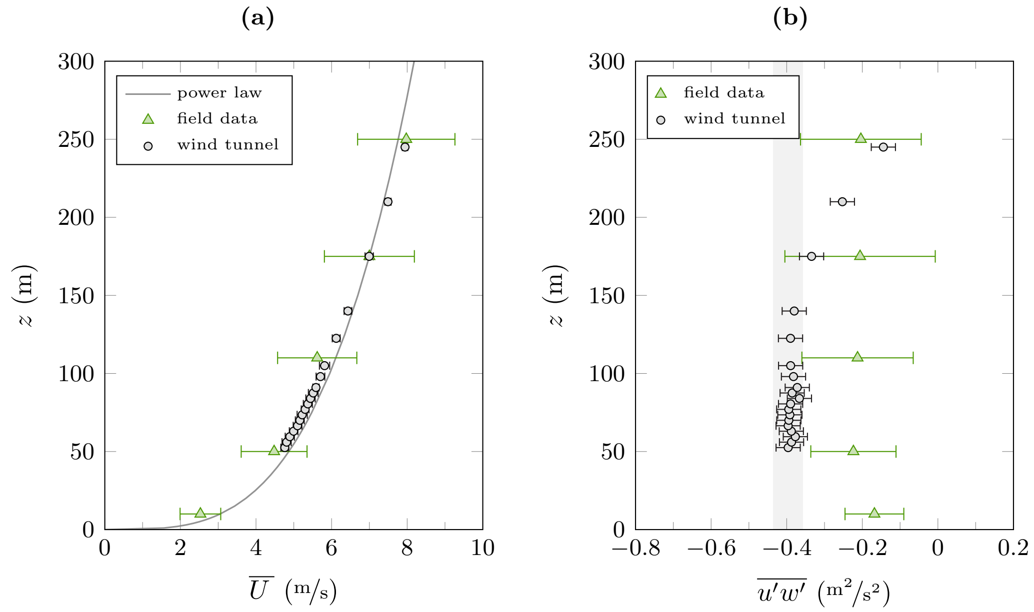

Figure 4.11: (a) Vertical profiles of the mean streamwise velocities in the field and the wind tunnel, together with a power-law fit using $\alpha = 0.29$. (b) Vertical profiles of the kinematic vertical momentum flux. The shaded area indicates a 10 % range about the lowest wind-tunnel value to assess the depth of the constant-flux layer. Results are shown for a reference velocity $U_{\mathrm{ref}_1} = 7\,\mathrm{m/s}$ at $z_{\mathrm{ref}_1} = 175\,\mathrm{m}$.

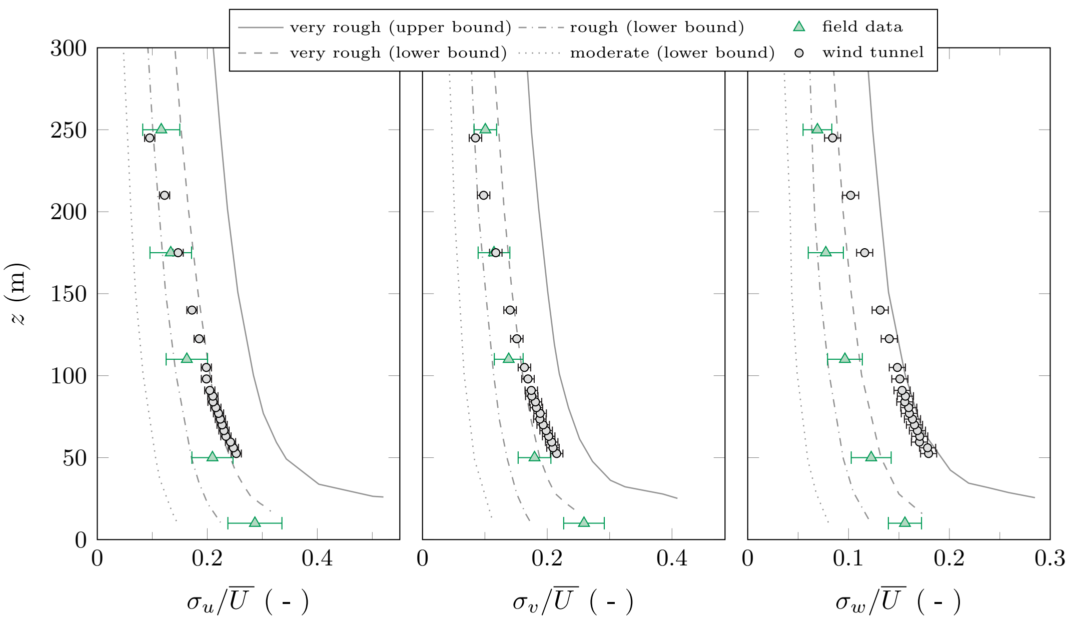

Figure 4.12: Turbulence intensities of the three wind components in the field and laboratory boundary layer in comparison to empirical boundaries for different surface roughness regimes proposed by ESDU (1985).

According to the ESDU (1985) thresholds, the field data fall well into the *"rough"* terrain category, while turbulence levels in the wind-tunnel are higher and correspond to *"very rough"* conditions. This is most obvious for the vertical velocity component, whereas the horizontal fluctuation intensities are still overlapping with the field data scatter. The smaller depth of the wind-tunnel ASL ($140\,\mathrm{m} < \delta_{\mathrm{WT}} < 175\,\mathrm{m}$) compared with the field test case is reflected in an enhanced decrease of turbulence intensities at the uppermost measurement heights. The consistency of the results is evaluated in comparison to turbulence fluctuation levels reported by Counihan (1975) for the rural ASL and by Oikawa and Meng (1995) for a suburban site. The ratios of the rms velocities, σ_k/σ_1 ($k = 2, 3$), and the turbulence levels with reference to the friction velocity, σ_i/u_*, are examined. These quantities are expected to be nearly constant over the surface layer depth. Results are listed in Table 4.2. The values and scatter ranges correspond to averages and standard deviations over the constant-flux layer, and u_* was determined from $(-\overline{u'w'})^{1/2}$ measured in 50 m (field) and 52.5 m (wind tunnel). The analysis shows that for both data sets σ_u/u_* strongly deviates from the rural Counihan value and generally corresponds better to the suburban results by Oikawa and Meng. The spanwise and vertical fluctuations show a weaker dependency on the surface roughness and are overall comparable. The rms velocity ratios also depart from the Counihan values, similarly to the trend seen in Oikawa and Meng's data. A rather strong divergence is found for the wind-tunnel's σ_w/σ_u. This feature of the laboratory flow is also identifiable in Figure 4.12 and may have resulted from the pronounced height offsets between individual floor roughness elements, which enhance vertical fluctuations. However, with regard to the fact that the spread of σ_i/u_* and σ_k/σ_1 values reported in literature is large (e.g. Panofsky, 1974), the results should not be over-interpreted. The most important conclusion from the analysis is that field and wind tunnel results are similar to each other, internally self-consistent, and in agreement with the expected behavior for flow over rough surfaces.

Figure 4.13 compares vertical profiles of the integral length scales of the U-component in x-direction (ℓ_{11_x}). Based on this quantity, characteristic sizes of the largest streamwise eddies in the surface layer can be evaluated. The results were obtained from the calculation of autocorrelation time scales, τ_{11}, by assuming frozen turbulence conditions with the local mean streamwise velocity used as the advection term (i.e. $\ell_{11_x} = \tau_{11}\,|\overline{U}\,|$). A detailed discussion on the computational methodology is given later in Section 5.4.

Table 4.2: Rms velocity ratios and turbulence intensities based on u_* for field and wind-tunnel data within the ASL in comparison to values reported by Counihan (1975) for rural terrain and by Oikawa and Meng (1995) for a suburban site.

	$\boldsymbol{\sigma_v/\sigma_u}$	$\boldsymbol{\sigma_w/\sigma_u}$	$\boldsymbol{\sigma_u/u_*}$	$\boldsymbol{\sigma_v/u_*}$	$\boldsymbol{\sigma_w/u_*}$
Counihan (1975)	0.75	0.5	2.5	1.875	1.25
Oikawa and Meng (1995)	0.96	0.65	1.93	1.82	1.22
Field data	0.87 ± 0.02	0.58 ± 0.02	2.13 ± 0.08	1.87 ± 0.09	1.24 ± 0.06
Wind tunnel	0.85 ± 0.02	0.74 ± 0.02	1.85 ± 0.03	1.58 ± 0.05	1.34 ± 0.01

Roughness boundaries determined by Counihan (1975) are used to classify the measurements. A similar increase of eddy sizes with height is obvious in both data sets. In consistency with the results presented earlier, slight differences between the roughness structure of the wind tunnel and the natural ASL can be observed. As for the turbulence intensities, the measurements from Billwerder correspond to rough terrain, while the wind-tunnel values already scratch the border to the very rough regime, which is expressed through overall smaller mean values of ℓ_{11_x}. The rather large scatter range for both data sets, however, has to be considered. At a height of 175 m, the field data scatter encompasses a range of 49 m and thereby includes almost the entire roughness classification span. Both data show a characteristic length-scale decrease at the topmost measurement heights (250 m for the Billwerder measurements and 120 m in the wind tunnel). This is a known feature of flow in the transition region following the ASL and is often attributed to an increasing intermittency (e.g. discussion by Counihan, 1975).

Another way to examine whether the wind-tunnel approach flow realistically represents dominant turbulence structures, is to compare field and laboratory energy density spectra. Figure 4.14 shows 1D auto-spectral energy densities obtained for the three velocity components at comparable measurement heights above ground (50 m and 52.5 m) in comparison to empirical relationships derived for neutrally stratified ASL flow over rural terrain on the basis of field and laboratory data (Kaimal et al., 1972; Simiu and Scanlan, 1986). The results are presented in a dimensionless frequency framework. Wind-tunnel spectral estimates at high frequencies that are affected by aliasing are indicated with a brighter shading. An in-depth description of the spectra computation is given in Appendix E.

The agreement between field and the laboratory measurements is very good for all three velocity components and is also distinct in comparison to the reference functions, where slight offsets are explainable by the roughness characteristics of the Hamburg data.

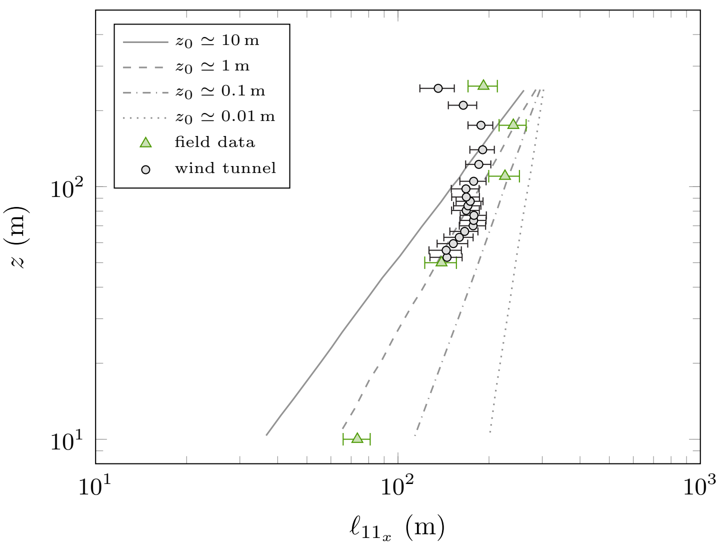

Figure 4.13: Full-scale integral length scales in longitudinal direction obtained from field and wind-tunnel measurements of the streamwise velocity. Lines indicate empirical boundaries for different roughness regimes following Counihan (1975).

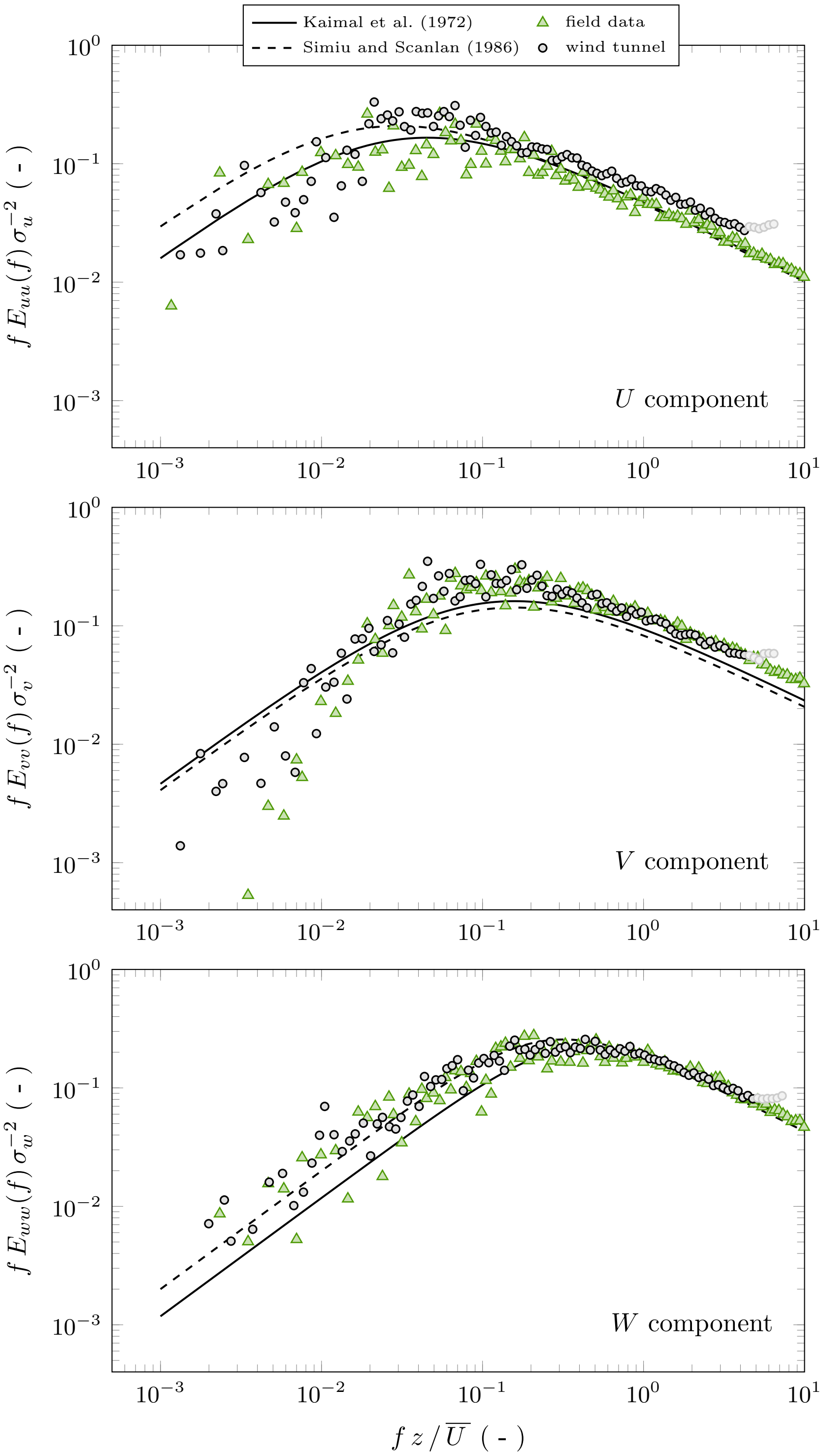

Figure 4.14: 1D auto-spectral energy densities for the three velocity components. Field data measured at $z = 50\,\mathrm{m}$, wind-tunnel data at $z = 52.5\,\mathrm{m}$ in the tunnel centerline. Empirical reference spectra from Kaimal et al. (1972) and Simiu and Scanlan (1986) are for neutral ASL flow over *rural* terrain.

For all three components, similar frequency ranges corresponding to the energy peaks can be identified, which gradually shift toward higher frequencies (i.e. smaller eddy sizes) from the streamwise component via the spanwise through to the vertical. At the low-frequency end of the spectrum, corresponding to the largest turbulence structures, slight offsets are observed for the V-spectra. Since the frequency of occurrence of these large eddies is much lower compared with vortices in the inertial subrange, the estimation of their spectral content also depends on the signal duration. The shorter measurement period in the field than in the wind tunnel (6 h as opposed to 16. 5h), thus, might be reflected in the results. A characteristic roll-off of the (scaled) energy densities with a power of $-2/3$ of the scaled frequency in the inertial subrange is evident in the wind-tunnel spectra for at least one decade. Due to the geometric scale reduction of the laboratory flow (i.e. 1:350), sampling frequencies scaled to full-scale conditions usually are lower compared with those provided by anemometer measurements in the natural atmosphere for the same advection velocities. This influences the temporal resolution of the time series and is reflected in the spectral range covered by the laboratory measurements. For the wind-tunnel time series used for the spectra comparison, a model-scale sampling frequency of approximately 450 Hz at $\overline{U} = 4.6\,\mathrm{m/s}$ resulted in a full-scale wavelength of 7 m of the smallest resolvable eddies (not taking into account spectral aliasing effects). The 20 Hz field measurements ($\overline{U} = 6.5\,\mathrm{m/s}$), in contrast, resolve the spectrum down to a wavelength of 0.65 m (not shown in Fig. 4.14 for a clearer comparison with the laboratory data). As discussed earlier in Section 3.2.2, the wind-tunnel flow, however, is generally expected to comprise turbulent structures down to sizes in the order of some millimeters (full scale), corresponding to the dissipative eddies.

Concluding the discussion, the approach flow conditions in the wind tunnel represent consistent surface layer characteristics without contradicting results for individual turbulence quantities. This is a reliable indicator for the physical quality of the modeled boundary layer and its representativeness for conditions encountered in the natural ASL for neutral stratification. The detailed comparison with field site measurements in Hamburg-Billwerder substantiated this assessment. The fact that the wind-tunnel approach flow corresponds to a slightly rougher terrain type than derived from the field data may overall yield a closer representation of the actual flow situation in the presence of the industrial harbor area, which starts approximately 4 km upstream of the domain inflow edge. This feature is not seen by the sensors at the meteorological measurement site for the same southwesterly approach flow direction. Due to the lack of further field data in the harbor area, however, this appraisal is speculative.

4.2.3 Velocity measurements

Laboratory flow measurements within the urban model of Hamburg were conducted in terms of height profiles of velocities with narrow vertical offsets between data points as well as on closely spaced horizontal measuring grids. Information on the technical measurement setup in the Hamburg flow campaign is given in Appendix A. Next, properties of the laser-based measurement technique are specified and a discussion of quality assurance strategies and the statistical representativeness of the laboratory data is presented.

Measurement techniques

Laser Doppler anemometry Measurements of *single-point*, high-resolution velocity time series were carried out with a two-component fiber-optic *laser Doppler anemometry* (LDA) system. With this technique, flow signals are optically gathered at some distance away from the hardware. An *Argon* ion-gas laser is used to create a *measuring volume* through the crossing of focused laser beams. Flow velocities are indirectly derived based on the analysis of backscattered light from seeding particles passing through this volume. Laser anemometers, thus, are *non-intrusive* flow sensing instruments that – in contrast to, e.g., hot-wire anemometers – do not physically interact with the flow at the measuring position. Because the measurement principle is purely based on properties of electromagnetic waves, the sensing process is mostly independent of ambient parameters. It is, however, required that particles are introduced to the flow. These should have adequate scattering properties, while being small enough to truly follow the fluid motion with minimal slip velocity. In this study, haze-droplets of approximately 1-2 μm diameter emitted by a commercial-grade hazer system were used. The high time resolution of the anemometer is accompanied by a high precision of the measuring location, yielding local Eulerian measurements of instantaneous turbulent velocities. Further explanations of physical and technical aspects of LDA measurements are presented in Appendix C and are, for example, discussed in great detail by Adrian (1993) or Albrecht et al. (2003).

The LDA system used in the Hamburg campaign allows for the simultaneous retrieval of two velocity components and is operated in *backscatter* and *fringe* mode. Through adjustments of the probe alignment, the streamwise and vertical velocities (U-W mode) and the streamwise and spanwise velocities (U-V mode) were measured using two laser beams of different wavelengths. Figure 4.15a shows the adjustment of an LDA probe in U-V mode. In U-W mode, the probe is tilted by 90° about the streamwise axis. The laser beams had wavelengths of 514.5 nm (green) and 488 nm (blue). The casting of the LDA probe had a diameter of 26 mm, like the instrument shown in Figure 4.15a.

(a) **(b)**

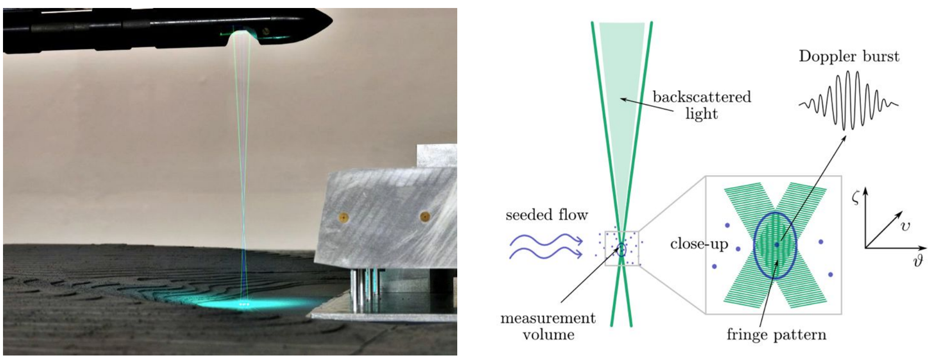

Figure 4.15: (a) 2D-laser Doppler anemometer operated in U-V mode. Probe type and focal length are the same as in the Hamburg campaign. (b) Schematic of the LDA measuring volume in a 1D setup, showing the extents along the instrument's major and minor axes (adapted from Jensen, 2004).

The ellipsoidal LDA measuring volume is defined by a principal axis, ζ, and two secondary axes, ϑ and υ. The focal length of 160 mm and an initial beam separation of 15 mm generate a volume $\delta_\vartheta \times \delta_\upsilon \times \delta_\zeta$ with dimensions of 0.08 mm × 0.08 mm × 1.6 mm. The horizontal and vertical cross sections of the volume determine the *spatial accuracy* of the measurement for the respective probe configuration. Uncertainties concerning the exact location of the measurement are dominated by the extent of the measuring volume along its principle axis. In U-V mode, ζ is aligned with the vertical axis of the tunnel coordinate system, and the secondary axes with the horizontal coordinates (see Fig. 4.15b). The full-scale horizontal resolution is hence given by 0.028 m and in the vertical direction by 0.56 m taking into account the geometric factor of 1:350. Thus, in case of U and V signals, seeding particles could have passed the volume within a vertical depth of more than half a meter full-scale. In U-W configuration, the principal axis of the LDA is oriented in crosswind (spanwise) direction. For instantaneous signals of U and W the position accuracy, thus, is mainly given by the horizontal extent of 0.56 m. Space resolution aspects of the LDA have to be particularly considered in flow regions with pronounced spatial velocity gradients. As discussed by Tropea (1995), the choice of the size of the measuring volume is an inevitable compromise between accuracy in space and accuracy in the frequency estimate of the recorded data. For smaller probe volumes, the *transit time*, T_t, of seeding particles is reduced, which results in a stronger variance of the frequency estimate. Especially in situations of low seeding quality, fewer particles might be expected to hit a smaller volume, resulting in lower sampling rates and the necessity to increase the measurement duration to obtain representative flow statistics.

Since only two components of the velocity vector were measured at a time, certain turbulence statistics cannot be deduced from the wind-tunnel measurements, like the $-\overline{v'w'}$ component of the Reynolds stress tensor or other quantities that would require simultaneous measurements of the spanwise and vertical velocities. The (average) TKE, on the other hand, can be reconstructed from a combination of U-V and U-W-mode measurements, but the differences in the spatial accuracies between the two probe alignments have to be carefully considered. Other important aspects of the general *measurability* of flow quantities with the LDA system used in the Hamburg campaign are of more technical nature. For measurements carried out in the inner city model, buildings can obstruct the laser paths and make certain measurement points inaccessible. Since in U-W-mode alignment the measuring volume and the LDA probe are at the same pitch, measurement points between buildings and close to the ground cannot be reached. It is generally possible to tilt the probe to create a vertical offset to the level of the measuring volume and reconstruct the true velocities from the knowledge of the tilting angle. This procedure, however, affects the accuracy of the measurements, with an increasing bias for larger tilting angles. For the Hamburg campaign, it was decided to omit probe tilting and confine the U-W measurements at most positions to heights above roof level.

A *burst spectrum analyzer* (BSA) was used to process the Doppler bursts. The sampling, preprocessing, and export of the detected signals were managed with a commercial data acquisition system. The software was operated in so-called *coincidence mode*, in which a sample is only taken if valid bursts were detected on both channels (i.e. for both velocity components) within a time window, whose length is optimized based on the cross section of the measuring volume and the highest expected velocity magnitudes. The measurement process was not aborted until a record duration of 170 s had been completed. The physical motivation for the specification of the signal length is discussed later.

Besides strong advantages of the LDA measurement principle over other methods, experimentalists have to be aware of some peculiarities, of which the most obvious is certainly the *discontinuous* nature of LDA time series. Since samples are only taken whenever a particle passes through the measuring volume, time intervals between consecutive signals are of random size. Spectral computations, however, require a uniform time step if techniques like the *fast Fourier transform* (FFT) are employed. As discussed by Tropea (1995), there basically are two approaches toward spectral estimation from LDA data: direct methods and signal reconstruction techniques, of which the *equidistant resampling* approach is used in this study. This crucial data preprocessing step is critically discussed in Section 4.4.2. Another characteristic of the technique is connected to the fact that the short-term particle arrival rates are correlated to the local velocity magnitudes: The LDA sampling operation is *not* independent of processes in the flow. Since a larger fluid volume is transported through the measuring volume in periods of high velocity magnitudes, a larger number of samples will be taken (Jensen, 2004). This feature also arises in homogeneously seeded flows. The *velocity/particle rate* correlation can bias flow statistics derived from the arithmetic mean of individual particle velocities toward higher magnitudes. The severity of this bias depends on the particle density in the flow and to some extent on the measurement duration. Both, the seeding conditions and systematic errors caused by the velocity/particle rate correlation have to be evaluated to document the data quality.

Free-stream velocity monitoring A *Prandtl tube* (*pitot-static tube*) was simultaneously operated together with the LDA to document the free-stream velocity, U_∞, in the tunnel during each measurement run. The free-stream velocity corresponds to the *mean* streamwise velocity component of the undisturbed flow at the top of the wind-tunnel boundary layer. The Prandtl tube was positioned near the intake in the tunnel centerline at a height of 1.74 m above the floor to assure low turbulence intensities for a faithful retrieval of the alongwind velocity component. *Bernoulli's law* is used to derive velocities from measured signals via $U_\infty = (2\rho^{-1}\, p_d)^{1/2}$, where p_d is the *dynamic pressure* determined from the difference of acquired static and stagnation pressures. Since the calculation depends on the air density, ρ, the temperature, pressure, and humidity inside the laboratory were documented several times during a measurement day. The probe is connected to a differential pressure transducer that converts the pressure signals into voltages, which, in turn, are recorded by a data acquisition system. The output of the pressure transducer was regularly calibrated against a pressure balance. This allowed for pressure measurements with an accuracy of approximately ± 0.1 Pa during the flow measurement campaign, corresponding to ± 0.41 m/s at typical ambient conditions ($p = 1013\, h$Pa and $T_a = 293$ K). In order to guarantee Reynolds number independence of the wind-tunnel flow, free-stream velocities were in the order of 10 m/s.

The monitoring of the free-stream velocity is a crucial component of the data acquisition process since this allows to reference the LDA velocities obtained within the urban model to representative approach flow conditions, which ensures that the experiments can be directly compared to the (referenced) simulation results (see Section 4.4.2).

Data quality & representativeness

Documenting the suitability and quality of experimental data is a necessary requirement for a fair and meaningful validation of a numerical model. In the next paragraphs, it is focused on an appraisal of the LDA data quality subject to the seeding conditions and the velocity/particle rate correlation, the assessment of the representativeness of the sampling duration in view of the inherent uncertainty in turbulent flows, and the inspection of the reproducibility of experimental statistics based on repeated measurements.

LDA signal quality The *accuracy* and *measurability* provided by LDA systems depends on different parts of the measurement chain (see Tropea, 1995, for an in-depth discussion). Although being an absolute measuring technique, an optimal adjustment of the laser beams and their intensity is a crucial preparatory step in the run-up to the measurements, and the entire test rig and probe alignment has to be carefully optimized. In order to ensure an unambiguous acquisition of the two velocity components, the LDA coordinate axes have to be closely aligned with the reference coordinate system of the tunnel. This was regularly checked for both the U-V and U-W configurations.

As pointed out earlier, the quality of spectral estimates from LDA measurements depends on the seeding conditions in the flow. Inhomogeneous seeding is characterized by plumes of high particle density, usually also accompanied by high advection velocities, and regions with very few or even no particles, resulting in highly intermittent short-term particle arrivals. With regard to the application of reconstruction techniques to generate equidistant time steps, bad seeding can substantially add to *resampling bias* in the new data. During each measurement run, particular attention was therefore paid to make particle densities as homogeneous as possible. The hazer system was placed outside the tunnel in front of the intake. Turbulent mixing induced by the dynamical interaction between spires and floor roughness already causes a quick dispersion of the particle clouds along the flow development section. The largest contribution toward a uniform and random particle density, however, originates from the open design of the tunnel that allows the particles to populate the entire laboratory hall and circulate through the facility.

The quality of the seeding conditions can be investigated by means of the *particle arrival time* distribution, i.e. the frequency of occurrence of short and long time lags between successive signals. For homogeneous seeding, the probability of a particle crossing the measuring volume within a certain time interval can be modeled by a *Poisson distribution* under the assumption that the location of each particle is random and unaffected by other particles in the flow (Adrian and Yao, 1987). Following McKeon et al. (2007) and Ramond and Millan (2000), the so-called *particle arrival law* is given by

$$P(\delta t) = \dot{N}\, e^{-\dot{N}\delta t} \,, \tag{4.2}$$

where $\dot{N} = N/T$ is the *mean data rate* (i.e. the mean particle arrival rate, with N being the number of detected particles and T the measurement duration), and $\delta t = t_i - t_{i-1}$ is the (non-uniform) *inter-arrival time* between consecutively sampled velocity signals. Interestingly, according to Eq. (4.2) the most likely time lag between successive signals is equal to zero. Independent of the mean data rate, seeding particles are most frequently arriving in rapid succession. By comparing theoretical and experimental functions, the level of homogeneity in the seeding can be assessed and thereby the sample quality of the measured time series. Figures 4.16 and 4.17 show the arrival law and experimental arrival time distributions obtained from LDA records in *U-V* mode at two rather different measurement points within the Hamburg model. The first is located well upstream of the downtown area above the Elbe river in a height of 45.5 m. The second test point lies deep within a narrow street canyon very close to the surface in 2.5 m height. A close-up on both locations, labeled *BL04* and *RM01*, is presented in Figure 4.27 in Section 4.4.1. The locations not only differ in the morphology of their immediate surroundings, but also in the seeding conditions that might be expected *a priori*. Close to the surface and deep within the canopy layer, fewer seeding particles can usually be found and laser light reflected from the ground or adjacent building surfaces can further cause a reduction of the *signal-to-noise* ratio of the detected Doppler bursts. Hence, valid signal rates obtained here are often substantially lower compared with points well above rooftop.

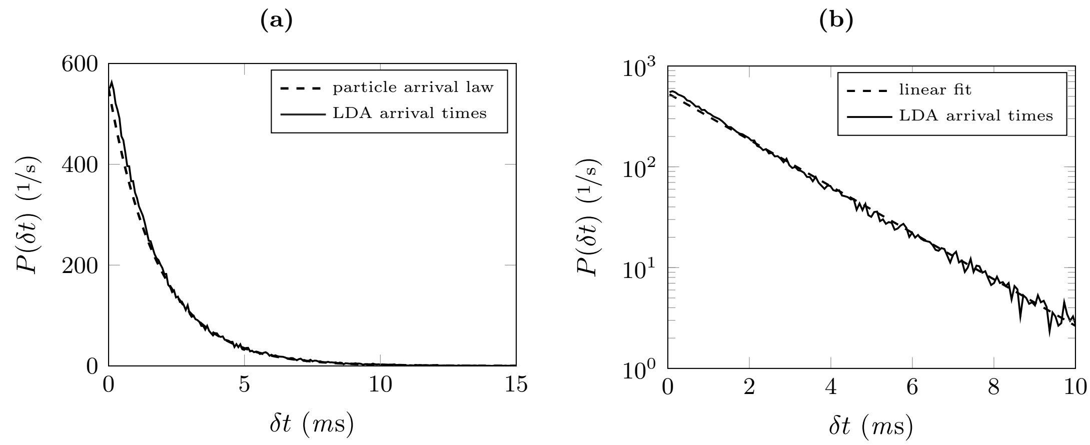

Figure 4.16: (a) Particle arrival law and (b) least squares fit of LDA inter-arrival times for a measurement taken above the Elbe river upstream of downtown Hamburg (*BL04*) in a height of $z = 45.5\,\mathrm{m}$ with a mean data rate of $\dot{N} = 551\,\mathrm{Hz}$.

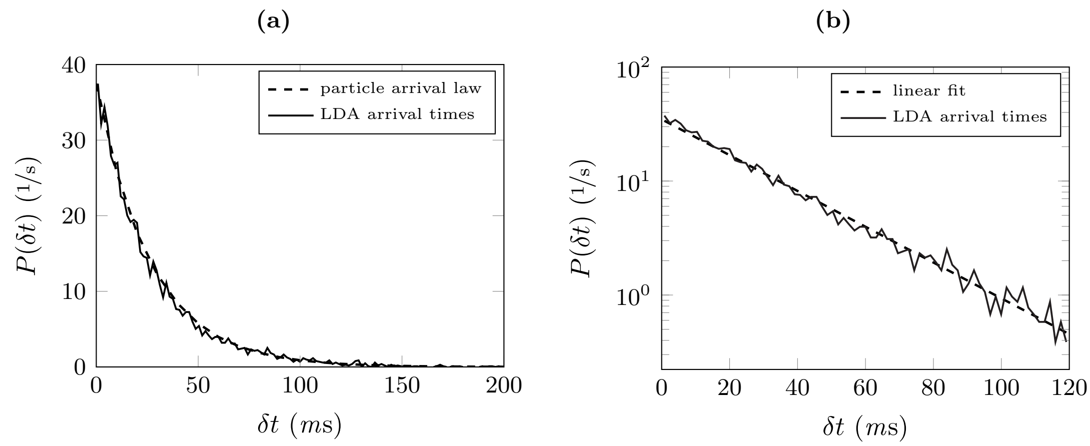

Figure 4.17: Same as Figure 4.16 but for measurements taken deep within a narrow street canyon (*RM01*) in a height of $z = 2.5\,\mathrm{m}$ with $\dot{N} = 38\,\mathrm{Hz}$.

With mean data rates of 551 Hz and 38 Hz, *BL04* and *RM01* are representative of locations with rather high and fairly low sampling frequencies within the entire data pool. As can be seen in Figures 4.16a and 4.17a, however, particle arrival rates at both locations follow the expected behavior rather well, with a clearly developed exponential decrease down to the tails. Thus, long time spans between the passage of individual particles through the measuring volume are comparatively rare events. In an inhomogeneously seeded flow, the tails would show a distinct positive offset from the theoretical curve (e.g. demonstrated in the study by Ramond and Millan, 2000). Figures 4.16b and 4.17b verify that the mean data rates determined from the intercept of a least-squares fit of the LDA data with the ordinate only marginally depart from the actual values of $\dot{N}$. The interpolated data rate for *BL04* yields 536 Hz (i.e. $\sim 3\,\%$ difference to $\dot{N}$) and 36 Hz (i.e. $\sim 5\,\%$ difference) at *RM01.* Hence, despite the deviations of temporal resolutions, the measurement quality in terms of the particle density is comparable and should allow for a reliable reconstruction of the time series through equidistant resampling approaches.

Mostly unaffected by the homogeneity of the particle seeding is the velocity/particle rate correlation, which is again examined for the two locations investigated above. Figure 4.18 shows histograms of the transit times through the measuring volume, T_t, in literature also known as *residence time.* At both positions, the distributions exhibit a significant positive *skewness*, measured as the third moment of the distribution normalized by the standard deviation. Thus, the mass of the distribution is centered at shorter transit times and the estimation of statistical moments from the LDA data can be expected to be biased. Following McKeon et al. (2007), the degree of bias inherently depends on the degree of correlation between the particle inter-arrival times and the magnitude of the measured velocities. For the selected test cases, the *sample correlation coefficients* (Pearson's R) between these quantities yield $R_{\mathrm{BL04}} = -0.12$ and $R_{\mathrm{RM01}} = -0.05$, which are fairly low but statistically significant based on an α-level of 0.05. The negative sign expresses that short inter-arrival times are statistically correlated to higher particle velocities.

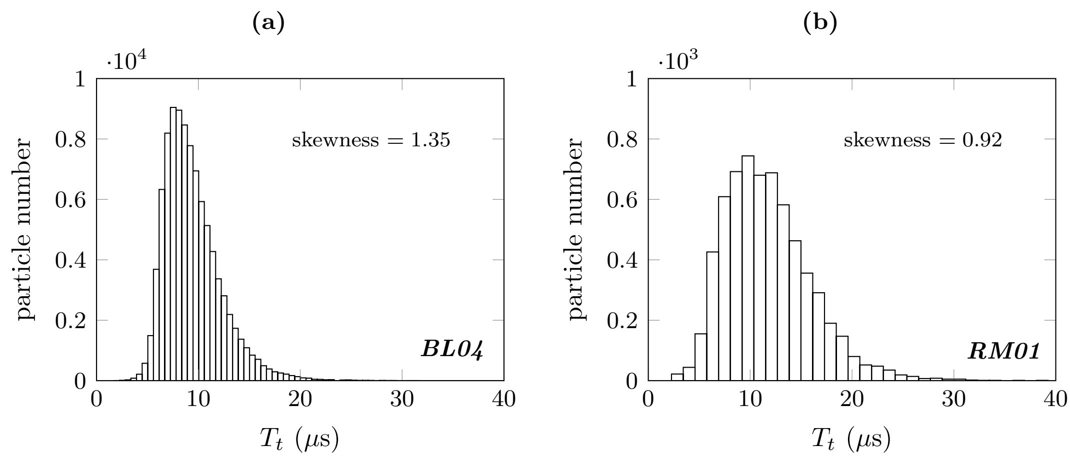

Figure 4.18: Histograms of LDA particle transit times for (a) *BL04* (45.5 m, 551 Hz) using 80 bins, and (b) *RM01* (2.5 m, 38 Hz), 32 bins. The sample skewness values correspond to the third standardized moments of the distributions.

The bias, thus, is also linked to the mean data rate, which overall determines the level of correlation between successive signals. Therefore, one approach to prevent bias of statistical estimators is based on the retrieval of statistically independent samples (cf. Jensen, 2004). Signal decorrelation can be achieved through very low particle densities or by using burst processor dead times, which ensure time lags of $\delta t \geq n\,\tau_0$ between consecutive samples, where $n \geq 2$ and τ_0 is the integral time scale of the process being measured. The data rate reduction, however, can narrow the spectral estimation potential from LDA data and also affect other time-series analysis methods. With regard to the LES validation concept advocated in this study, the decorrelation approach, thus, is unsuitable. Other bias correction techniques, however, can be applied offline as part of the data preprocessing. Such methods weight each of the recorded velocity signals by a factor that comprehends the particle arrival probability. A well-established method is the *transit time weighting* (Buchave et al., 1979), which takes the form

$$\overline{U}\,|_{\text{weighted}} = \frac{\sum_{i=1}^{N} (u_i\,T_{t_i})}{\sum_{i=1}^{N} T_{t_i}}\,, \tag{4.3}$$

for the *estimation* of unbiased temporal averages of the streamwise velocity component. Figure 4.19 shows height profiles of the unweighted and transit-time weighted velocity averages for location *BL04* and *RM01*. The velocities are referenced to the free-stream velocity U_∞ measured with the bias-free Prandtl tube. Scatter bars attached to the unweighted averages correspond to the experimentally determined statistical reproducibility of the first-order moment of U (see next paragraphs for details). A clear, non-uniform offset between the samples can be determined. The *systematic error* made by omitting bias correction of the data is in the range of 1 % to 2 % at the two inspected locations.

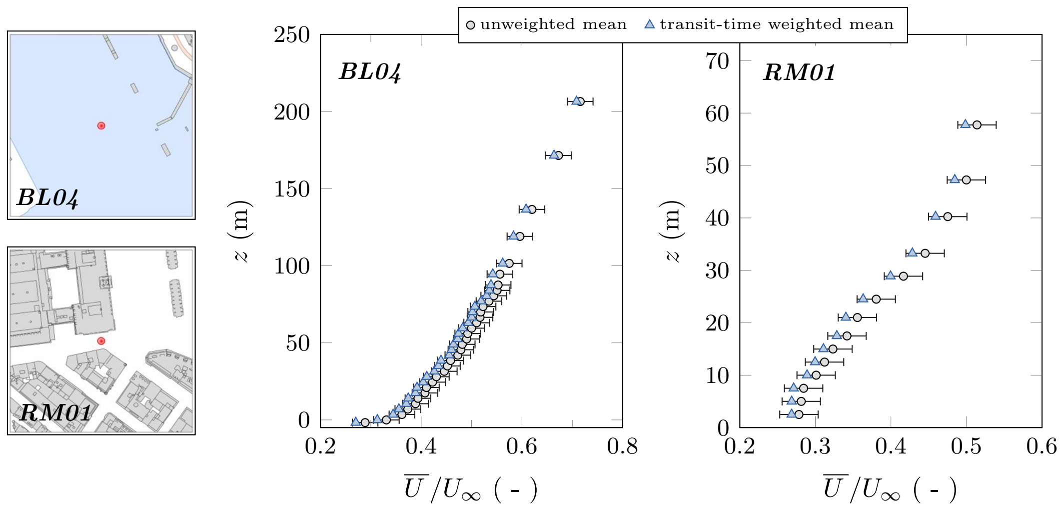

Figure 4.19: Comparison of vertical profiles of the mean streamwise velocity component computed from an unweighted and a transit-time weighted arithmetic average for measurements at position *BL04* and *RM01*.

The mean data rates obtained from an average over all heights at *BL04* and *RM01* are 513 Hz ± 89 Hz and 102 Hz ± 26 Hz, respectively. In the face of the positive correlation between the degree of bias and the magnitude of $\dot{N}$, the offsets documented in Figure 4.19 represent worst and best-case scenarios of the validation data pool. At both locations, the systematic error is smaller than the overall statistical error that is consulted to document the reproducibility of statistical quantities derived from the measurements. Thus, for the data used in this study it was decided to dispense with bias correction. This decision was further motivated by the fact that different moment estimator techniques for LDA signals exist and the choice of an appropriate method can be critical. While transit-time weighting is the recommended approach for flows with spatially homogeneous particle seeding (cf. McKeon et al., 2007), it also merely yields an *estimate* of the true temporal mean. Furthermore, the severity of the difference in velocity magnitudes is mitigated by the fact that in this study a dimensionless framework is mostly used in the comparison of velocity statistics. That is, flow quantities will be given in reference to a representative mean streamwise velocity, U_{ref}, which is also determined through LDA measurements (details are presented in Section 4.4.2). If it is assumed that the uncorrected LDA velocities tend to have higher magnitudes ($_\uparrow$) than the bias-corrected velocities ($_\downarrow$), the difference between the dimensionless quantities based on reference velocities U_{ref} measured at the same flow location, $\overline{U}^{\uparrow}/\,U^{\uparrow}_{\text{ref}}$ and $\overline{U}^{\downarrow}/\,U^{\downarrow}_{\text{ref}}$, are expected to be negligible. However, if the flow is sampled at much higher data rates than in the present case (e.g. in the order of several *k*Hz) or if absolute numbers are compared between experimental and model results, employing a suitable bias correction technique is unavoidable.

Inherent uncertainty The specification of a measurement duration that allows for the derivation of representative flow statistics is not straightforward. Since in this study all statistical analyses are based on temporal averages following Eq. (2.8), measurement times, T_{exp}, should be long enough to guarantee the *ergodicity* of the time means. In statistical terms, this involves quantifying the difference between statistics derived from finite samples and the corresponding ensemble expectation values of the population.

As opposed to field measurements, laboratory experiments have the advantage of offering stationary mean boundary conditions over arbitrarily long measurement durations. A further bonus in this regard is the scale reduction of the wind-tunnel flow: For the same reference velocities, turbulent processes happen faster in the wind tunnel than in nature (the relation between the time scales is determined by the geometric scale). In the Hamburg campaign (1:350 scale), a laboratory measurement time of 30 s, thus, equals 175 min in full-scale, provided similar reference velocities. This already is a time span over which stationarity of the meteorological conditions in the field is rarely given. Under good seeding conditions, the sample size after 30 s LDA measuring time in the tunnel can already be quite large. However, while high data rates permit a better resolution of flow structures, it is a misapprehension that flow statistics are also reliable after such short recording times. For turbulent flows in which statistics are dominated by the low-frequency variability of the larger eddies, the convergence of a sample average to the population mean depends on the frequency in which these dominant structures have passed the sensor during the measuring process. As Tropea (1995) summarizes, "(...) averaging times only have meaning when expressed in terms of integral time scales and *not* in terms of number of particles."

Figure 4.20a shows the ratio between the measurement duration and the *local* integral time scales of the streamwise velocity components in alongwind direction, τ_{11}. Every data point represents a measurement at a different (x, y, z) location within the urban model of Hamburg (for details of the sites see Section 4.4.1). For all recordings, T_{exp} was set to 170 s, which slightly exceeds a signal duration of 16.5 h in full-scale conditions. τ_{11} was chosen as a correlation measure since under typical ASL conditions the largest spatial extent of turbulent eddies is expected to be in the streamwise direction. Hence, derived autocorrelation time scales should have the longest durations. As can be seen in Figure 4.20a, the total signal length surmounts the autocorrelation times in the flow by factors in the range of 10^3 to 10^4. While these numbers do not have any implication for the actual frequency of occurrence of long-lived structures during the probing time, they indicate the *potential* of capturing these structures sufficiently often during the measurement to obtain robust statistical estimates. At lower measurement heights, the spatial extents of the canopy layer eddies are bounded by the building morphology and the autocorrelation time scales are reduced compared to the flow above the buildings. The increasing spread of $T_{\mathrm{exp}}/\tau_{11}$ at lower heights, however, has a caveat. Many of these data points correspond to measurements taken deep within the UCL, where τ_{11} is substantially reduced and may not always be the suitable measure for the most long-lived structures (e.g. τ_{22} could be more appropriate in some flow situations).

To quantify the reliability of statistics drawn from a finite-time sample of turbulent velocities, Lumley and Panofsky (1964) recommend to compute the *inherent uncertainty* as discussed earlier in Section 2.3.1. Based on Eq. (2.35), the variance of the difference between a finite-time mean and the ensemble average can be measured. Figure 4.20b shows the inherent uncertainty in terms of a standard deviation relative to the ensemble mean as a function of measuring time, T, for U-component signals measured at three heights in the wind-tunnel approach flow. Scaled to a free-stream velocity of $U_\infty = 10\,\mathrm{m/s}$, the signal duration of each record corresponds to 36 h full-scale (i.e. 370 s in model scale).

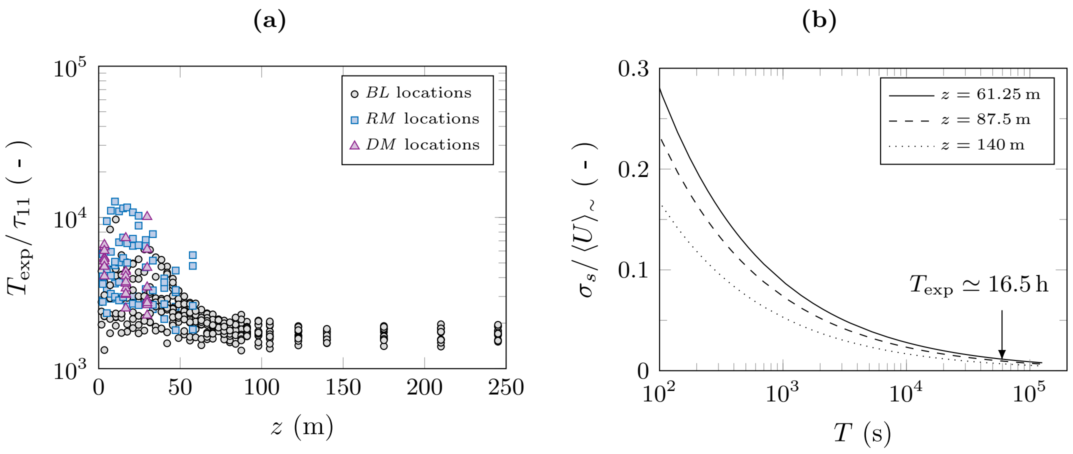

Figure 4.20: (a) Ratio between the wind-tunnel measurement duration, T_{exp}, and integral time scales at all comparison locations in the urban model. The abscissa indicates full-scale heights. (b) Inherent uncertainty of $\overline{U}$ for different full-scale measurement durations, T, relative to the approximated ensemble mean, $\langle U\rangle_\sim$, for three heights in the wind-tunnel approach flow.

Based on this particularly long measurement duration, long-term temporal means were computed as *approximations* of the true ensemble averages, i.e. $\overline{U}_{36\,\mathrm{h}} \simeq \langle U \rangle_{\sim}$, where the tilde subscript emphasizes the approximative nature of the average. As can be seen in Figure 4.20b, $\sigma_s / \langle U \rangle_{\sim}$ is high for short T (displayed in full-scale dimensions), but drops to values well below $1\,\%$ for a measurement duration of $T_{\mathrm{exp}} \simeq 16.5\,\mathrm{h}$. The minimum value of $T = 100\,\mathrm{s}$ shown on the x-axis roughly corresponds to $2\,\tau_{11}$ at all heights. In general, σ_s is high for processes with a high variability, which in this case is measured in terms of the rms velocity, σ_u, and for long autocorrelation times, and short sampling durations. Different uncertainty estimates for the three measurements, thus, arise from differences in σ_u and τ_{11}. All curves flatten drastically with T, but the decay decelerates for increasing measurement durations, since $\sigma_s \propto T^{-1/2}$. This behavior is somewhat covered by the logarithmic display of the x-axis, but has strong practical implications. A further reduction of the inherent uncertainty starting from $T_{\mathrm{exp}} \simeq 16.5\,\mathrm{h}$ by a factor of 2 (e.g. going from $1\,\%$ to $0.5\,\%$) means extending the measurement duration by a factor of 4. Even higher accuracies come at much higher prices (e.g. $0.1\sigma_s \propto (100\,T)^{-1/2}$), which are unfeasible in practical and economic terms. However, it needs to be considered that the accuracies as a function of T are not the same for every time-averaged quantity. Estimates of turbulent variances or covariances, for example, will require comparatively longer measurement times due to their higher variability (cf. Wyngaard, 1992).

For the same data, Figure 4.21a shows the actual relative difference between the finite-time averages $\overline{U}_T$ and the approximated ensemble means for increasing T (cf. also the study by Stein and Wyngaard, 2001). In Figure 4.21b, *standard errors* of the temporal means are depicted, which measure standard deviations of the error of the time average relative to the expectation value. In consistency with the results for σ_s, the relative differences clearly decrease for increasing T. Furthermore, the signal variabilities depend on the measurement height (implicitly through σ_u). Accuracy improvements of $\overline{U}_T$ as an estimate of $\langle U \rangle_{\sim}$ are harder to attain in ranges of long measurement durations, which is well reflected in the very small standard errors of the relative differences.

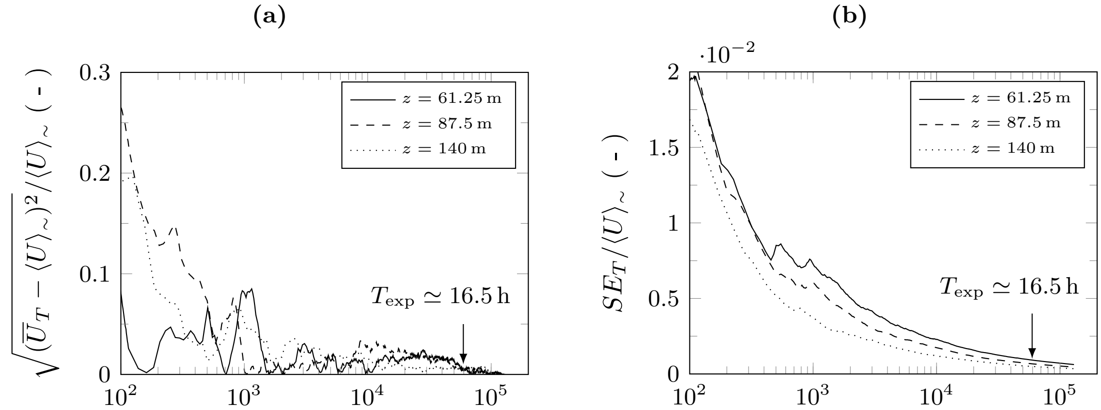

Figure 4.21: (a) Relative difference between the temporal average, $\overline{U}_T$, and the approximated ensemble average, $\langle U \rangle_{\sim}$, for increasing measurement durations. (b) Corresponding standard errors of the temporal average relative to the approximated ensemble average. Measurements taken in the tunnel approach flow.

Another strategy to specify sufficiently long probing times is based on the convergence analysis of *binning statistics* (e.g. Schultz, 2008). Here, a long time series is broken down into subsamples of gradually increasing size, possibly allowing for an overlap between the bins. Then, the convergence of the time-mean values obtained from each subsample to the long-term mean is studied as a function of ensemble size. Using this approach, Peeck (2011) determined similar qualitative and quantitative accuracy trends for the data analyzed above. However, a drawback of this method is that it implicitly assumes that the signal can be split into subsamples of uncorrelated processes. This is not the case at least for small ensemble sizes, so that the derived spread can be positively biased.

The above analysis showed that experimentalists ultimately have to make a compromise between accuracy and practical constraints by specifying an acceptable uncertainty magnitude of temporal statistics for a given problem. For this study, the threshold associated with a measurement duration of 170 s in wind-tunnel scale was linked to the reproducibility of experimental statistics. The inherent uncertainty is expected to be significantly lower than the amount of run-to-run scatter observed in the experimental time-mean values, which is the topic of the next paragraph.

Statistical reproducibility and data scatter The accuracy of statistics derived from wind-tunnel measurements does not only depend on the averaging times and the precision provided by the measuring instruments, but also on generally unavoidable statistical errors that characterize random uncertainties of the measurement process. For laboratory experiments, it is common practice to assess the overall measurement accuracy in terms of the statistical *reproducibility* of the experiment on the basis of repetitive measurements. During the Hamburg campaign, vertical profile measurements were repeated in the horizontally homogeneous approach flow (U-W mode, three repeats) and at a fixed location in the urban model (position *BL07*, cf. Fig. 4.27; U-V mode, seven repeats) under similar mean boundary conditions. For each measuring height, flow statistics were obtained from which the run-to-run scatter was determined. In order to provide a conservative assessment in view of the overall small number of repetitions, the statistical *range*, ξ, defined as the difference between the largest and smallest observed value, was computed at each height. Then, the data scatter was defined as the maximum observed range over all heights according to $\pm\,\xi_{\max}/2$ for the respective statistical measure (e.g. means, variances, and covariances). Results are summarized in Table 4.3. It has to be noted that the scatter is given in terms of *dimensionless* flow quantities, referenced to the mean streamwise velocity, U_{ref}, defined for the analyses in this study (details are provided in Section 4.4.2).

Table 4.3: Experimental reproducibility of velocity statistics in terms of the maximum dimensionless run-to-run range obtained from repetitive measurements.

mean velocities	variances	covariances
$\overline{U}/U_{\mathrm{ref}} \pm 0.0185$	$\sigma_u^2/U_{\mathrm{ref}}^2 \pm 0.0020$	$\overline{u'v'}/U_{\mathrm{ref}}^2 \pm 0.0025$
$\overline{V}/U_{\mathrm{ref}} \pm 0.0204$	$\sigma_v^2/U_{\mathrm{ref}}^2 \pm 0.0027$	
$\overline{W}/U_{\mathrm{ref}} \pm 0.0035$	$\sigma_w^2/U_{\mathrm{ref}}^2 \pm 0.0017$	$\overline{u'w'}/U_{\mathrm{ref}}^2 \pm 0.0014$

4.3 Numerical simulations with FAST3D-CT

In the following paragraphs, the LES model FAST3D-CT, developed and operated by the U.S. Naval Research Laboratory in Washington, D.C., is introduced, together with details of the Hamburg flow simulations that are relevant for the validation study. Since this CFD code uses a conceptually different LES approach than the one presented in Section 2.2.2, it is started from a brief review of the concept of the so-called *implicit LES*.

4.3.1 The implicit LES approach

"Capturing physics with numerics"

Grinstein, Margolin, and Rider (2007)

(— *Implicit large eddy simulation.*)

In order to numerically solve the LES conservation equations that are relevant for the problem of interest, the filtered equations need to be discretized on a numerical mesh with grid spacing h. This discretization process introduces *numerical errors*, of which the spatial truncation error is usually deemed most significant. As discussed by Pope (2000), the LES momentum equation satisfying the numerical solution can be written as

$$\frac{\partial \widetilde{U_i}}{\partial t} + \widetilde{U_j}\frac{\partial \widetilde{U_i}}{\partial x_j} = -\frac{1}{\rho}\frac{\partial \widetilde{p}}{\partial x_i} + \nu \frac{\partial^2 \widetilde{U_i}}{\partial x_j \partial x_j} + \frac{1}{\rho}\frac{\partial}{\partial x_j}(\tau^s_{ij} + \tau^h_{ij}) \; , \tag{4.4}$$

where the additional term τ^h_{ij} represents the *numerical stress* that depends on the respective grid spacing and arises from the discretization error. In the traditional LES approach, it is aimed to minimize τ^h_{ij} such that the LES problem is essentially decoupled from the numerical method that is used to solve it (Reynolds, 1990). This requires that the grid spacing h is small compared with the filter width, Δ, such that $\tau^h_{ij} \ll \tau^s_{ij}$.

The ratio Δ/h, thus, describes the weighting between the level up to which turbulent eddies are directly represented in the mathematical LES model and the numerical accuracy of its solution (cf. discussion by Mason, 1994). Typically, the ideal condition of a negligible numerical error cannot be met, and in most LES, Δ/h is given by 1 or $1/2$ (Pope, 2004), which is mainly due to computational cost considerations. Hence, the transition between directly resolved flow features and the parameterized SFS motions typically coincides with the computational grid scale, at which the numerical discretization errors naturally are largest (Boris et al., 1992). Depending on the numerical method and its order of accuracy, the efforts required to control numerical errors at these scales can be significant. In a thorough analysis of numerical errors in LES, Ghosal (1996) showed that the discretization errors expressed in terms of an implicit numerical stress contribution, τ^h_{ij}, are comparable to the effects of the explicitly parameterized SFS stress, τ^s_{ij}.

A new perspective on these "(...) seemingly insurmountable issues posed to LES by under-resolution" (Grinstein, 2010) was presented by Boris (1990) as a pragmatic approach now known as *implicit LES*, which challenged the traditional – and to a strong degree philosophical – dogma concerning the necessity of decoupling physics and numerics in LES. Boris argued that even if no model for the parameterization of the residual motions in

LES is used, certain numerical methods have the potential to implicitly represent SFS contributions, which mainly act to drain energy from the resolved scales at the right rate. The underlying idea is that "(...) nonlinear monotone CFD algorithms really have a built-in filter and a corresponding built-in subgrid model. These monotone integrated LES algorithms are derived from the fundamental physical laws of causality and positivity in convection and do minimal damage to the longer wavelengths while still incorporating, at least qualitatively, most of the local and global effects of the unresolved turbulence expected of a large eddy simulation" (Boris, 1990). According to this, the original (unfiltered) conservation equations are numerically solved on a grid that is too coarse to resolve the small-scale structure of turbulence, whereas the large and energy-dominant eddies can be reliably represented. The influence of the residual motions on the resolved field is given by the numerical fluxes on the grid scale. Turbulence structures smaller than few h are dissipated on the grid (Boris, 2007), and no explicit SFS model in the sense of those introduced in Section 2.2.2 is used. Hence, while solutions to the traditional LES approach using *explicit filtering* as proposed by Leonard (1974) ultimately depend on the – sometimes rather complex – interaction of two length scales, Δ and h, the implicit LES approach uses the grid spacing as a *numerical filter*, which is the only scale that determines turbulence resolution.

The implicit approach is attractive since it may not only save trouble with a view to the proper adjustment of the classic SFS parameterizations, but has direct practical effects regarding the overall computational costs of the simulation. Specifically, saving costs with the SFS model enables to employ finer grids than may be common with the traditional approach. Boris (1990) argues that increasing the grid resolution by a factor of 2 in an implicit LES "(...) will bring more improvement in the accuracy of the well resolved scales than all the work in the world on the subgrid model of a more coarsely resolved LES model with the usual filtering procedure (...)." While the increasing efficiency of the technique can be readily comprehended, it is equally easy to accuse the implicit LES approach of lacking a well-formulated theoretical and physical basis. Instead of explicit and implicit LES, sometimes the approaches are distinguished as *physical* and *numerical LES* (cf. Pope, 2004), where the latter terms could be perceived as reflective of the objections against the new approach, which particularly arose in the early years.[8] Despite initial reservations, the increasing use of the technique within the last two decades by a diverse research community demonstrated that implicit LES can be successfully applied and deliver reliable and accurate results for a wide range of flow categories, from engineering to geophysical or meteorological problems. A comprehensive review of such applications is, for example, presented in Grinstein et al. (2007). Faith in the technique was not only established through practical evidence, but furthermore has been substantiated by theoretical studies devoted to the investigation of fundamental *physical* properties of numerical algorithms that are suitable for an implicit LES (e.g. Fureby and Grinstein, 1999; Margolin and Rider, 2002). More recently, Grinstein and Fureby (2007), for example, could disclose the formal similarity between certain high-resolution numerical methods and well-known explicit SFS models of the mixed type in a direct comparison study.

[8]In general, discriminating between physical and numerical LES is misleading, since this terminology implies that traditional LES is independent of numerics, which never really is the case.

MILES & flux-corrected transport

The above discussion already alluded that not every numerical method can be used in the framework of an implicit turbulence simulation. As stated by Grinstein (2010), "(...) good and bad SGS physics can be built into the simulation model depending on the choice and particular implementation of the numerics." Boris (1990) originally presented the implicit LES approach as the so-called *monotone integrated large-eddy simulation* (MILES) – a term that gives a clearer account of the fact that particularly a certain class of non-linear, non-oscillatory, positivity-preserving (monotone) numerical methods has the potential to substitute the traditional stand-alone SFS parameterizations.

Prominent representatives of this category are *flux-corrected transport* (FCT) algorithms, which were originally developed by Boris and Book (1973) as physics-capturing, non-linear, numerical solvers for time-dependent turbulence problems and frontier flows characterized by steep gradients or physical discontinuities (e.g. compressible, supersonic flows or shocks, cf. Boris and Book, 1976; Boris, 1989; Book, 2012, for details). FCT was designed to provide accurate numerical solutions to flow problems using high-order finite-volume methods by reducing their *numerical dispersion* that can otherwise cause unphysical numerical oscillations of real flow quantities. The conceptual foundation of the initial FCT formulation was further shaped by Zalesak (1979), who discussed the problem in a multidimensional framework. In a nutshell, depending on the physical characteristics of the flow, FCT switches between high-order and low-order discretization methods in an attempt to cancel out the inherent drawbacks of both approaches – numerical dispersion and numerical diffusion. For each time step, two numerical fluxes between adjacent grid points are computed. On the one hand, a numerical flux, $\mathbf{v}_f^L$, derived from a low-order, dispersion-free but diffusive algorithm is used to prevent the generation of unphysical values, e.g., in flow regions with sharp gradients. On the other hand, a high-order flux, $\mathbf{v}_f^H$, is computed with a highly accurate scheme, which is particularly stable in smooth flow regions. The resulting effective flux, $\mathbf{v}_f$, is then obtained from a weighting of both fluxes, in which preference is given to the high-order accurate flux to the greatest possible extent. This procedure is known as *flux correction* or *flux limiting*. Following Patnaik et al. (2012), the net flux function, $\mathbf{v}_f$, can be written as

$$\mathbf{v}_f = \mathbf{v}_f^H - (1 - \Gamma)(\mathbf{v}_f^H - \mathbf{v}_f^L) , \tag{4.5}$$

where $0 \leq \Gamma \leq 1$ is the so-called *flux limiter* (note that other specifications of the flux correction are possible), and the second term on the right-hand-side represents the non-linear *correction flux* applied to the high-order scheme in terms of an intermittent, locally confined diffusion (Boris et al., 1992). In physical terms, the non-linear discretization can be interpreted as a "non-linear tensor-valued eddy-viscosity" (Grinstein and Fureby, 2012), whose main purpose is to stabilize the flow and suppress the generation of purely numerical artifacts (e.g. in terms of dispersive ripples or finite-resolution Gibbs oscillations). In the case of Eq. (4.5), the degree of smoothing at discontinuities in the flow is controlled by the value of Γ. A detailed discussion on basic principles, implementations, and applications of the FCT approach is presented in the book by Kuzmin et al. (2012).

As pointed out by Boris (1990, 2007), non-linear schemes like FCT are inherently coupled to fundamental physics principles, which make them suitable for MILES: conservation, monotonicity, causality, and locality. The *conservation* property, for example, ensures that energy drained from the resolved eddies is not lost but transferred into heat. *Monotonicity* implies that unphysical oscillations are suppressed and, in particular, that the *positivity* of certain physical quantities is preserved (e.g. by ensuring that solutions to the generalized continuity equation are non-negative everywhere in the domain). Another interesting feature arising from the monotonicity constraint is that the model also involves local, instantaneous energy backscatter effects from the unresolved to the resolved scales (cf. Fureby and Grinstein, 2002, for a detailed analysis). *Causality* and *locality* guarantee that the advection (convection) of fluid mass from one point to another is following a continuous path through all intermediate grid cells and that derivatives occurring in the conservation equations are only obtained over locally confined regions.

Non-linear algorithms like FCT were particularly designed to limit numerical errors in the smallest resolved scales (defined by the computational grid), such that the local dissipation rate captures the local flow physics. The numerical, non-linear dissipation rate in MILES using FCT was shown to scale with κ^{α}, where κ is the wavenumber connected to the eddy length scale, ℓ, and α is in the range of 3.3 to 3.8 (Boris, 2007).

FAST3D-CT and prior validation studies

The implicit LES code FAST3D-CT is a three-dimensional CFD simulation model based on the MILES formulation, using a scalable, low-dissipation, fourth-order phase-accurate FCT algorithm. In particular, FAST3D-CT was designed to deliver accurate predictions of *atmospheric* turbulence characteristics and contaminant transport (CT) within the urban roughness sublayer. A wide range of aerodynamic and thermodynamic effects in urban environments can be included in the model, e.g. atmospheric stratification, local solar heating effects on the ground and building surfaces, tree effects, and micro-physics of dispersed liquid, solid, or gaseous airborne contaminants. Savings from the MILES approach and the optimization of numerics enable to carry out highly efficient simulations regarding computational costs and computing times. The model is compatible with massively parallel computing architectures, but can also run efficiently on regular single-processor systems (Cybyk et al., 2001). The FCT scheme, LCPFCT, implemented in FAST3D-CT is described in detail by Boris et al. (1993). Important modifications for the simulation of urban flows are discussed by Patnaik et al. (2012). Adjustments of the FCT algorithm, for example, concentrated on the optimization of the low-order diffusive scheme for street canyon and intersection flow situations.

FAST3D-CT has been subject to several *a posteriori* validation studies for a variety of urban test cases of different geometric complexity. Such studies included the validation of flow and dispersion around a single wall-mounted cube (Cheatham et al., 2003) and within and above an idealized cube array environment (Patnaik et al., 2007). Detailed comparisons with a focus on concentration predictions were also conducted with the MUST outdoor scale canopy (Iselin et al., 2006) and with the JU2003 dispersion test case in Oklahoma City (Lee et al., 2009). In both studies, validation databases from comprehensive wind-tunnel measurements were used as a reference as well. Other dispersion validation tests in genuine urban environments were performed, for example, for Washington, D.C., and Los Angeles (Cybyk et al., 2001; Patnaik et al., 2007).

4.3.2 Hamburg flow simulation

The Hamburg flow simulations with FAST3D-CT were conducted on a $4 \times 4\,\mathrm{km}^2$ computational domain centered around the inner city of Hamburg, which comprised the entire wind-tunnel model area (see the indication in Fig. 4.2). The simulation was performed in full-scale (as opposed to simulating in wind-tunnel scale) on a Cartesian grid with a uniform resolution of 2.5 m within the urban RSL. The simulation ran for 7 weeks on an SGI Altix computer with 64 CPUs, using a computational time step of 0.05 s at a velocity of approximately $7\,\mathrm{m/s}$ in 200 m above ground. Equidistant real-time velocity records were extracted at the cell centers every 0.5 s over a duration of 23,250 s (i.e. approx. 6.5 h). The geometric and physical complexity of the model was adjusted to be as close as possible to the experiment. As in the laboratory, the mean inflow wind direction was from the SW (235°) and the atmospheric stratification was set to neutral. Following the specifications of the experiment, local solar heating within the UCL as well as aerodynamic effects of trees were not included. Detailed information about geometrical and numerical specifications in the LES is presented in the following paragraphs.

Geometry setup

FAST3D-CT is able to resolve complex building geometries and topographic elements and allows to specify different land use types. In order to compile the geometry database for the numerical model, the same data sets for buildings, terrain, and waterfronts were used as for the construction of the wind-tunnel scale model (cf. Section 4.2.1). All geometry information was available in the so-called *Gauss-Krüger* coordinate system (grid zone 3; GK3 using a Bessel ellipsoid) – a transverse Mercator projection that is used in few European countries, especially in Germany. FAST3D-CT, however, requires that coordinates are given in the *universal transverse Mercator* system (grid zone 32; UTM32 using the WSG84 reference ellipsoid). Besides the different geodetic datums, the GK3 central meridians have a width of 3° of longitude, while the UTM meridians are 6° apart. Thus, a coordinate transformation was necessary and could be achieved by a datum transformation, whose accuracy was determined on the basis of ground control reference points documented for both coordinate systems. For the $4 \times 4\,\mathrm{km}^2$ domain, the difference between the computed UTM32 coordinates to the control points was less than 10 cm. Next, the geometry data were rasterized on a regular mesh with a resolution of 1 m in all dimensions and stored into three 2D arrays of heights for buildings, terrain, and bodies of water (geo-referenced *digital elevation models*). The last step was to combine the three geometry tables into a single database (FASTCITY), that can be accessed by the LES code. Figures 4.22 and 4.23 show the computational domain of FAST3D-CT together with the wind-tunnel model area, including buildings, terrain, and water bodies. The color coding indicates the respective height levels.

As in the laboratory scale model, no information about urban greenery/trees or bridges and traffic overpasses was included in the numerical geometry database. Buildings are reproduced without openings to indoor areas or other passages through buildings. Both museum ships and the concert hall in the harbor area were included in the LES geometry based on the same data used for the construction of the wind-tunnel model.

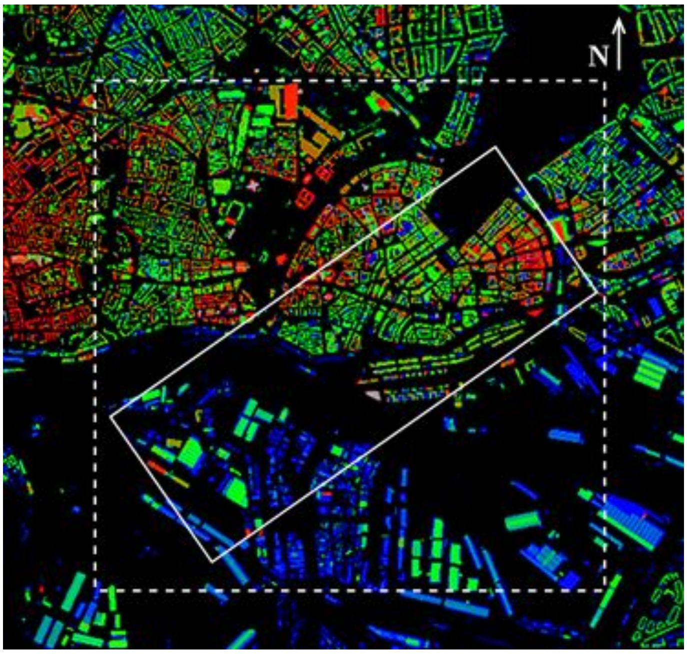

Figure 4.22: Buildings in the FAST3D-CT computational domain (dashed line). The wind-tunnel model area is indicated by a solid rectangle. Colors indicate building heights from low (light blue) to high (pink/gray). Image courtesy: NRL.

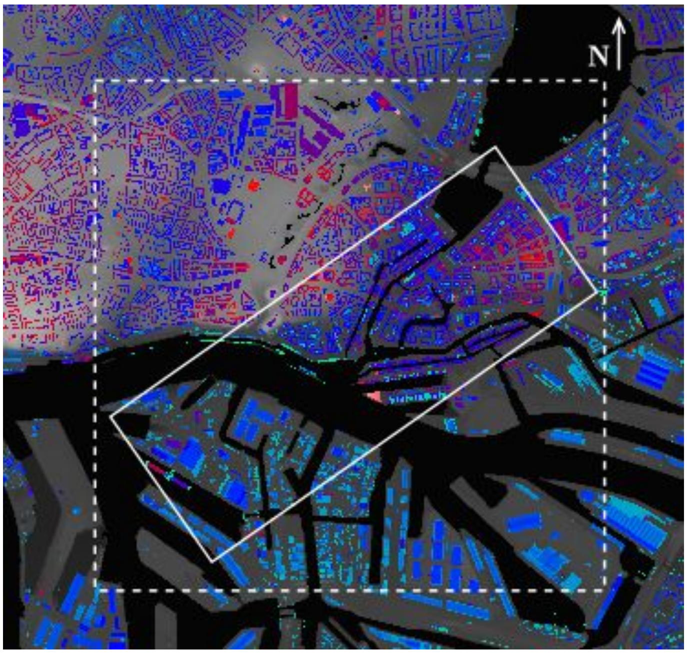

Figure 4.23: Buildings, terrain, and water in the FAST3D-CT domain. Terrain ranges from low (gray) to high (white); building heights from low (cyan) to high (pink). Water is indicated in black (zero elevation). Image courtesy: NRL.

Essentially the only difference to the wind-tunnel geometry is given by the omission of the overpass for the above-ground subway line in the numerical building database. The subway proceeds on an elevated trail, which underneath is rather permeable for the air flow (see also Figs. 4.4 or 4.5, in which the trail runs from the bottom left to the center of the images). While the architecture of the overpass and piles can be represented in detail in the wind-tunnel model, the 2.5 m resolution of the numerical grid involves the risk of creating unrealistic blockage effects and it was decided to leave this feature out.

Computational grid

The flow simulation with FAST3D-CT was conducted on a structured Cartesian grid. A uniform grid spacing in all directions of $h_i = 2.5\,\mathrm{m}$ with $i = 1, 2, 3$ was used up to a height of 101.5 m (approximately $3\,\mathrm{H_m}$; corresponding to the lowest 42 cells), covering the urban roughness sublayer and possibly parts of the adjacent inertial sublayer. From there on, the vertical grid spacing was gradually increased by using a stretching factor of 1.11 (11 %) after each node, up to the depth of the computational domain (approx. δ_{les}=1.4 km). Overall, the $4 \times 4\,\mathrm{km}^2$ domain was covered with a total of $1,600 \times 1,600 \times 80$ computational grid cells in (x, y, z) directions, resulting in overall $204.8 \cdot 10^6$ nodes.

During the grid generation process, the FASTCITY geometry database was interrogated in order to detect which of the cells contain buildings, terrain, or bodies of water and to register at what nodes suitable wall boundary conditions have to be prescribed. Using this *grid masking approach*, buildings are basically represented by blocking fully or partially occupied grid cells. While this procedure is computationally highly efficient, it leads to the generation of so-called *staircase effects*. The staggered representation is particularly pronounced for slanted surfaces (e.g. roofs), as indicated in Figure 4.24a, which shows a schematic of an (x, z) cross section through an urban domain. Similar effects, however, are also present in the horizontal (x, y) plane, e.g. for building walls proceeding at oblique angles to the orientation of the grid. In order to avoid extreme vertical gradients on the ground surface, a slightly modified masking procedure was used for the representation of rolling terrain. With the so-called *shaved-cell approach*, the true terrain elevation was approximated by gradually varying the interface of the lowermost cells. Figure 4.24b schematically depicts this method. While the course of the gridded terrain still remains inherently discontinuous, the size of the jumps between adjacent cells is significantly reduced (minimum $\delta z \simeq 5\,\mathrm{cm}$ full scale). For most parts of the city core – particularly those covered in the wind-tunnel model, terrain effects are negligible. Thus, it is assumed that the numerical representation of terrain will not be a crucial point for the validation study. The coarser reproduction of buildings in FAST3D-CT compared with the detail of the physical model, however, is potentially of importance, especially at flow locations that are strongly confined by the surrounding buildings (e.g. flow in narrow street canyons).

In the run-up to the final simulation, pretests focusing on the grid resolution were conducted. Since the results of an implicit LES inherently depend on the computational mesh and the numerical method, true grid-independence – as desirable for other CFD approaches – can never truly be achieved in MILES. However, the degree of deviation between flow statistics obtained from simulations with different mesh sizes can be used to infer information about the overall resolution requirements for the problem of interest.

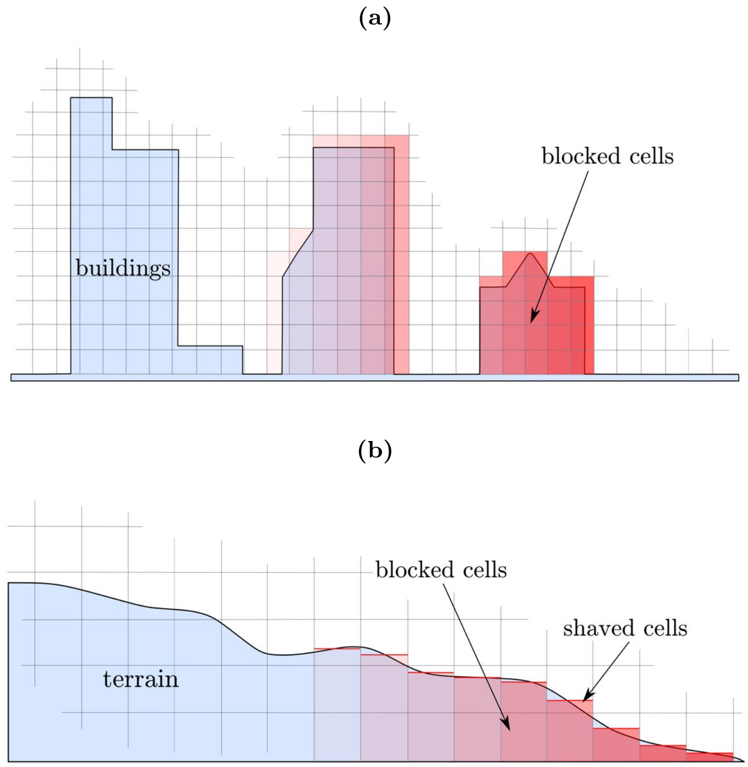

Figure 4.24: Schematic of the representation of topographical elements and buildings by the grid masking approach in FAST3D-CT: (a) blocked cells for buildings, (b) shaved cells for terrain representations.

Such a test was carried out for three grids, whose (x, y, z) mesh spacings and effective grid sizes $h_e = (h_x h_y h_z)^{1/3}$ are listed in Table 4.4. Except for *grid C*, where the resolution refinement only applies in the vertical direction, uniform cells are used. For efficiency reasons, the simulation was not conducted in the $4 \times 4\,\mathrm{km}^2$ region, but in a smaller domain based on the wind-tunnel model area. Furthermore, the pretest simulation durations, T_{les}, were significantly shorter than for the actual run in the larger domain. Figure 4.25 shows height profiles of the mean streamwise velocities for different locations in the inner city of Hamburg as derived from the FAST3D-CT simulations with the three different grids. The data were referenced to a reference velocity in a height of 45.25 m at location *BL04* (details are given in Section 4.4.2). It is emphasized that these results do not indicate how accurate the predictions are with respect to the wind-tunnel reference measurements, which will be purely based on the simulation in the larger domain and discussed in Chapter 5, but merely point out the deviations among the numerical profiles. It is evident that the variation of the vertical (1.5 m–2.5 m) and horizontal (2.0 m–2.5 m) grid resolution is not significantly reflected in the time-averaged velocities. From the slightly larger variations recognizable at locations *BL10*, *RM07* or *RM09*, no systematic trends can be determined. With regard to the relatively short simulation durations, such deviations could also reflect the inherent uncertainty associated with the time averaging.

Table 4.4: Node distance specifications for the grid resolution study with FAST3D-CT.

	$\mathbf{h_x}$ (m)	$\mathbf{h_y}$ (m)	$\mathbf{h_z}$ (m)	$(\mathbf{h_x h_y h_z})^{1/3}$ (m)	$\mathbf{T_{les}}$ (h)
grid A	2.5	2.5	2.5	2.5	2.8
grid B	2.0	2.0	2.0	2.0	1.2
grid C	2.5	2.5	1.5	2.1	1.0

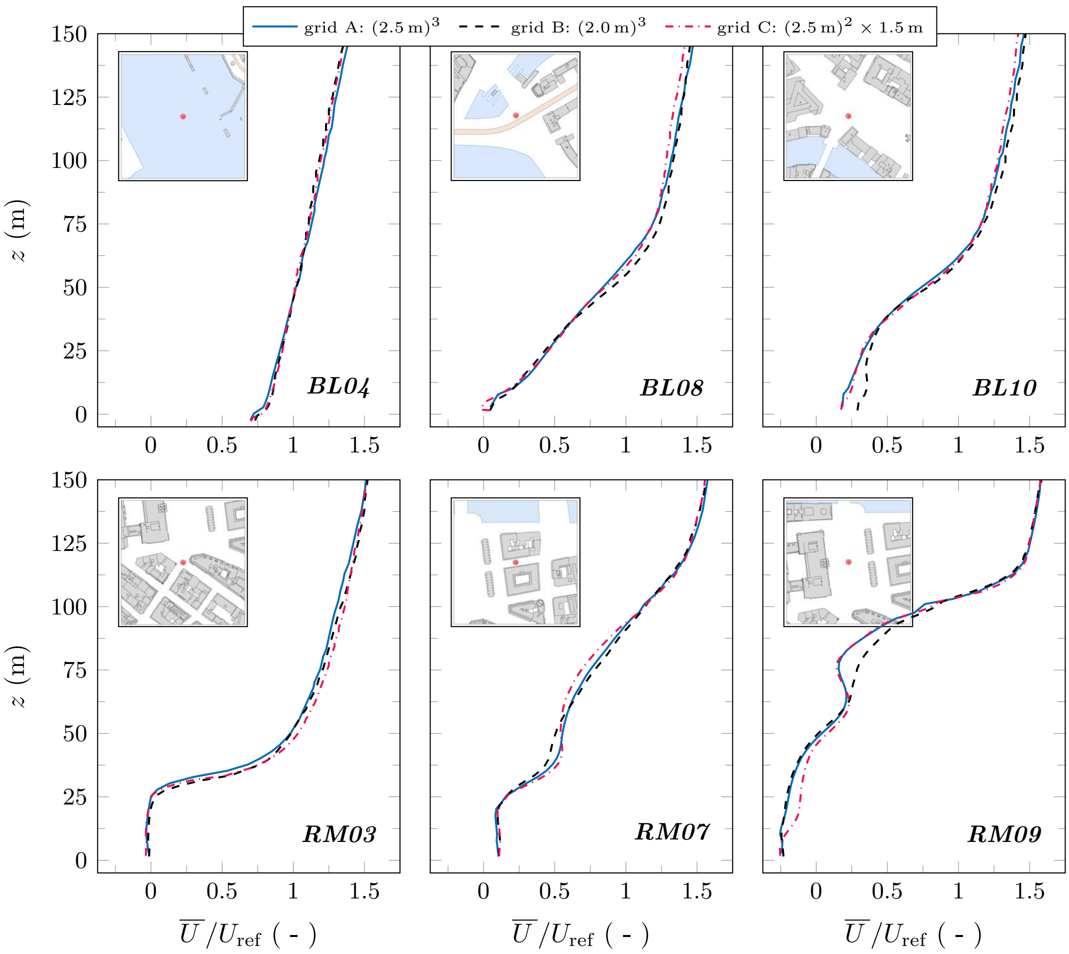

Figure 4.25: Mean streamwise velocity height profiles at different locations in the city obtained from precursor simulations with FAST3D-CT for three different grid resolutions. Images in the upper left corners show the immediate surroundings of the profile location (mean approach flow is from left to right).

Since no clear benefits from a finer resolution within the selected value range could be determined, the preference was given to the less cost-intensive 2.5 m mesh. Using this grid resolution, it is anticipated that usually $h < \ell_{EI}$: The spatial cut-off between resolved and unresolved eddies lies well beyond the production range of turbulence. However, for certain UCL flow situations in which the size of the largest eddies is bounded and significantly reduced by the geometry, this picture is likely to change, and the cut-off is expected to be shifted closer to the energy-containing eddy range.

Inflow & domain boundary conditions

As discussed earlier in Section 2.2.3, the definition of realistic turbulent inflow conditions for time-dependent CFD models is crucial for the overall accuracy of the simulation. This is particularly true for wall-bounded flows, in which memory effects are of importance. In FAST3D-CT, a *fluctuation method* is used in which artificially generated, deterministic turbulent fluctuations are superimposed on mean velocity inflow profiles. The mean velocity profiles were obtained from a power-law approximation with $\alpha = 0.29$, based on the field data information and the wind-tunnel approach flow modeling. Non-periodic wind fluctuations were derived from a realization of a deterministic function, which is constructed from a non-linear superposition of different fluctuation wavelengths and amplitudes (see Boris, 2005; Patnaik et al., 2007, for details). In order to obtain a reasonable congruence between the numerical and wind-tunnel inflow conditions, the latter were made available in terms of the approach flow measurements and the last measurement location upstream of the inner city area (profile *BL04*, cf. Fig. 4.27). This measurement position is located above the Elbe river that separates the industrial harbor from the residential downtown area. Mean and rms flow statistics from wind-tunnel measurements at two further positions (*BL08*, *BL11*) located within the downtown area were used to monitor the flow adjustments farther downstream of the inflow plane.

The selected grid spacing does not permit to directly resolve the flow close to the ground or near buildings walls. Hence, the no-slip wall boundary condition has to be replaced by an appropriate modeling approach for the wall shear stress. In FAST3D-CT, a rough-wall boundary layer model is used for this purpose, which incorporates information about the surface roughness in terms of the drag coefficient, C_D, and about the tangential velocity at the first grid point adjacent to the wall.

At the top and all lateral boundaries of the computational domain, an extra row of so-called *ghost cells* (also known as *guard cells*) is implemented to provide a buffering between the self-consistent simulation values and the analytically prescribed boundary constraints. An inflow-outflow algorithm is used over the entire boundary, which can change continuously from the analytical inflow specification described above to a simple extrapolation for the open outflow (cf. Boris, 2005). Hence, at all boundary grid points except for those associated with the inflow plane, the respective boundary conditions switch automatically during the simulation in order to adapt to the local flow situation (i.e. either representing inflow or extrapolated outflow condition).

While the lateral and outflow boundaries of the domain are relatively far away from the region of interest (i.e. the inner city area, on which the flow validation study concentrates), it can be assumed that the numerical predictions are mostly unaffected by the specified boundary constraints. The inflow and wall-boundary conditions, on the other hand, typically have a more direct effect on the simulation characteristics, which needs to be critically evaluated and discussed in the validation analysis.

4.4 Data preprocessing strategies

4.4.1 Comparison locations

The comparison of wind-tunnel measurements and LES flow predictions was conducted at 22 locations distributed across the downtown Hamburg area. With the selected comparison points it was aimed to include a variety of typical urban flow scenarios created by the unique characteristics of the surrounding building geometry. The sites include alongwind and crosswind street canyons, complex intersections, open plazas, and courtyards. Hence, the validation test sample is composed of flow situations that are challenging for CFD models due to the geometrical and physical complexity and, thus, are indicative of model strengths and limitations. At all reference locations, the quality of the wind-tunnel reference data has been verified in order to guarantee a fair comparison.

Figure 4.26 gives an overview of the horizontal locations of the comparison points. These include height profile measurements of all three velocity components along the centerline of the wind-tunnel model. On the basis of this seven (x, y) locations (referred to as *BL* positions), the downstream development of the urban boundary layer can be documented. The velocity profiles cover the entire roughness sublayer (typically 33 heights for U-V, and 22 for U-W measurements), with lowermost and topmost elevations of 1.75 m and 245 m. Further vertical profile measurements for the comparison are available in the area around the plaza in front of the city hall (*Rathausmarkt*; *RM* positions). At each of this five (x, y) locations, the horizontal wind velocities (U,V) were sampled in 14 heights ranging from 2.5 m to 57.75 m above ground. In order to investigate spatial flow patterns, densely spaced measurements on a horizontal grid were conducted at the entrance to a downtown courtyard (10 (x, y) points; *DM* positions). At each location, measurements were carried out in three heights above ground: 3.5 m, 16.63 m, and 29.75 m.

Table 4.5 lists the exact coordinates of all comparison points based on the wind-tunnel reference system and the corresponding geo-referenced Gauss-Krüger (zone 3) equivalents. A close-up view on the locations is presented in Figure 4.27 for the *BL* and *RM* profile locations and Figure 4.28 for the *DM* points.

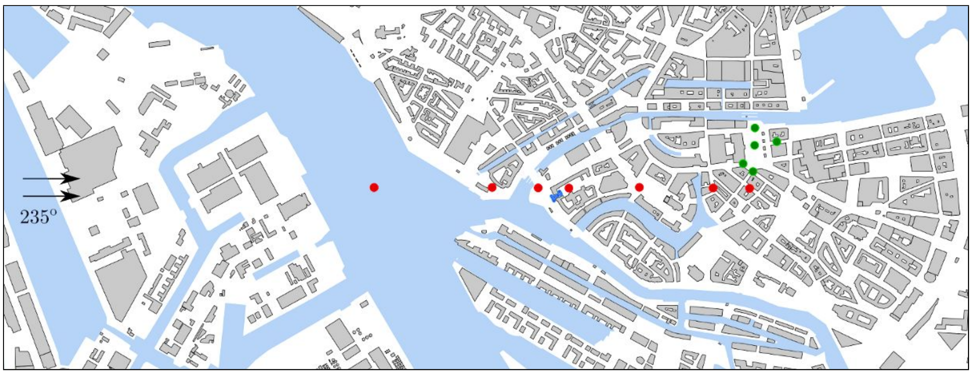

Figure 4.26: Overview of the flow comparison locations: UBL development positions (*BL*, red dots), Rathausmarkt locations (*RM*, green dots), and Rödingsmarkt courtyard measurements (*DM*, blue dots). Map from *OpenStreetMap* (2012).

As opposed to the other sites, location *BL04* above the river stands out due to its upstream distance from the inner city and the lack of any immediate building influence. Thus, this position is also consulted to compare the general approach flow conditions between the experiment and the numerical model, generated in the industrial harbor area.

For all 22 locations of the validation data pool, vertical profiles of the 3D wind vector were extracted from the FAST3D-CT simulation at 19 to 21 heights up to 126.05 m above the ground surface. The LES data locations were *not* interpolated to exactly match the measurement locations in the wind tunnel in order to avoid any approximation bias. Instead, the velocities were collected at the nearest neighboring cell centers of the computational grid. Table 4.6 lists the resulting horizontal offsets at each point, with overall minimum/maximum distances of 0.33 m and 1.46 m. For the direct comparison of results at certain elevations, height offsets between the data pairs were usually not larger than 0.25 m in regions with strong vertical gradients. Local exceptions of differences up to 1.38 m were tolerated in few cases. The offsets are clearly documented in the presentation of the validation results and critically discussed in the interpretation.

Table 4.5: Flow comparison locations together with their positions in the wind-tunnel reference system and the respective geo-referenced Gauss-Krüger (Z3) coordinates. The position IDs are used throughout the study to refer to the respective sites.

position ID	**x (mm)**	**y (mm)**	**Easting**	**Northing**	$\mathbf{U_i(x_i, t)}$	**comment**
UBL development						
BL04	-3,000	0	3564765.88	5934937.52	U,V,W	*above river*
BL07	-1,600	0	3565167.26	5935218.57	U,V,W	*train station*
BL08	-1,100	0	3565310.61	5935318.95	U,V,W	*waterfront*
BL09	-750	0	3565410.96	5935389.21	U,V,W	*open courtyard*
BL10	0	0	3565625.99	5935539.77	U,V,W	*intersection*
BL11	800	0	3565855.35	5935700.38	U,V,W	*street canyon*
BL12	1,250	0	3565984.36	5935790.71	U,V,W	*street canyon*
Rathausmarkt district						
RM01	1,128.3	288.2	3565891.61	5935848.92	U,V	*street canyon*
RM03	1,243.5	217.2	3565938.91	5935851.67	U,V	*intersection*
RM07	1,502.2	535.1	3565949.24	5935994.74	U,V	*street canyon*
RM09	1,259.1	487.7	3565889.07	5935932.37	U,V	*plaza center*
RM10	1,261.5	685.8	3565849.98	5935989.65	U,V	*plaza edge*
Rödingsmarkt courtyard						
DM01	-949.1	-88.1	3565371.56	5935323.98	U,V	*upstream entrance*
DM02	-939.6	-103.6	3565377.40	5935321.45	U,V	*upstream entrance*
DM03	-929.7	-119.6	3565383.45	5935318.85	U,V	*upstream entrance*
DM04	-920.2	-135.1	3565389.28	5935316.31	U,V	*upstream entrance*
DM10	-910.2	-99.7	3565385.04	5935328.47	U,V	*passage*
DM11	-894.1	-91.8	3565388.07	5935333.96	U,V	*passage*
DM12	-877.7	-83.8	3565391.17	5935339.55	U,V	*passage*
DM18	-868.4	-47.5	3565386.55	5935351.82	U,V	*downstream exit*
DM17	-858.8	-62.8	3565392.37	5935349.36	U,V	*downstream exit*
DM09	-847.8	-80.6	3565399.10	5935346.47	U,V	*downstream exit*

Figure 4.27: Flow comparison locations with densely spaced measurements in vertical profiles (*BL* and *RM* locations). The dimensions of the displayed areas are $210 \times 210\,\mathrm{m}^2$. The drawings are based on high-resolution 2D-CAD data. The approach flow direction is from left to right (cf. arrow in *BL04*).

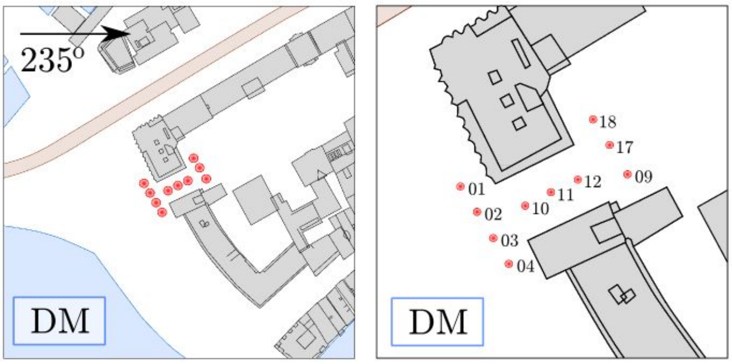

Figure 4.28: Flow comparison locations of the dense horizontal measuring array (*DM* locations): (a) immediate urban surroundings in an area of $210 \times 210\,\mathrm{m}^2$, (b) close-up view on the measurement site. The approach flow is from left to right. The drawings are based on the 2D-CAD data.

Table 4.6: Horizontal offsets between the wind-tunnel measurement locations and the FAST3D-CT data positions based on their Gauss-Krüger (Z3) coordinates. Minimum and maximum *absolute* offsets are marked in green and red, respectively.

	Position offsets (m)			
position ID	**δ Easting**	**δ Northing**	**distance**	**comment**
BL04	0.97	0.66	1.17	*above water*
BL07	-0.20	-1.01	1.03	*train station*
BL08	0.49	0.67	0.83	*waterfront*
BL09	0.80	-0.44	0.91	*open courtyard*
BL10	0.74	**0.05**	0.75	*intersection*
BL11	**0.02**	0.60	0.60	*street canyon*
BL12	-1.02	0.89	1.35	*street canyon*
RM01	-1.13	-0.92	**1.46**	*street canyon*
RM03	1.15	-0.58	1.29	*intersection*
RM07	-1.12	-0.16	1.13	*street canyon*
RM09	**-1.27**	0.09	1.27	*plaza center*
RM10	-0.34	-0.25	0.42	*plaza edge*
DM01	-0.98	-0.65	1.17	*upstream entrance*
DM02	-0.15	-0.58	0.60	*upstream entrance*
DM03	0.90	-0.78	1.19	*upstream entrance*
DM04	-0.87	-0.71	1.12	*upstream entrance*
DM10	-0.11	**-1.16**	1.17	*passage*
DM11	0.52	-0.67	0.85	*passage*
DM12	1.02	-0.08	1.02	*passage*
DM17	-0.18	-0.28	**0.33**	*downstream entrance*
DM18	-1.00	-0.22	1.03	*downstream entrance*
DM09	-1.05	-0.57	1.20	*downstream entrance*

4.4.2 Processing of velocity data

The next paragraphs give an overview of the main preprocessing steps that were taken to condition the experimental and numerical data for the comparison. In conclusion, a comparative synopsis of different data features is presented together with a discussion of expected implications for the validation study.

Removal of experimental outliers

The laser-based LDA measuring principle is prone to optical disturbances. The quality of individual signals, for example, can be affected by reflected laser light in cases where the measuring volume is located very close to the ground of building surfaces. Under the influence of scattered light, the signal-to-noise ratio of the Doppler bursts can be lowered, resulting in spurious velocity estimates. Another source for data outliers is given by dispersed dust particles that are unavoidably carried in the flow along with the actual LDA seeding particles. Dust grains passing through the measuring volume can cause detectable velocity spikes, which the processor considers valid signals. Since statistics based on arithmetic averaging are not robust to the influence of such outliers, such data have to be removed from the time series. In this context, values that lie well-beyond the expected value range are regarded as outliers. This study uses a detection criterion based on means and standard deviations of the raw time series. Only signals for which $\overline{U}_i^{\dagger} - 4\sigma_i^{\dagger} \leq U_i \leq \overline{U}_i^{\dagger} + 4\sigma_i^{\dagger}$ mutually for all $i = 1, 2$ or $i = 1, 3$ are kept (Fischer, 2011). The dagger indicates that statistics were obtained from the uncorrected data. In the Hamburg campaign, the fraction of outliers was between 0 % to 1 % for individual time series.

Orientation of the coordinate system

The coordinate system defined in FAST3D-CT uses an ordinate (y-axis) that is aligned with the geographic south-to-north axis and an abscissa (x-axis) oriented from west to east. As discussed earlier, however, the horizontal coordinates (x, y) in the wind-tunnel are defined as the streamwise (alongwind) and spanwise (crosswind) direction, respectively. In order to homogenize the two data sets, the FAST3D-CT coordinate system was rotated accordingly by a transformation of the individual velocity components, such that for the idealized case of an undisturbed approach flow $\overline{V}_{\mathrm{les}} \simeq \overline{V}_{\mathrm{wt}} \simeq 0$.

Parts of the analyses presented in Chapter 5 are concerned with the comparison of wind directions derived from the horizontal velocities, U and V. Figure 4.29 schematically depicts how angles in the horizontal plane are defined in the mutual coordinate system of FAST3D-CT and the wind tunnel, based on the polar coordinate convention (mathematically positive rotational direction). For the computation, the `atan2` function is used as an alternative to the classic arctangent, since it produces unambiguous angle results through a case differentiation based on the signs of the velocity components (i.e. it maps angles into the right quadrants). The resulting polar angles, $\beta = \mathtt{atan2}\,(V, U)$, are bounded on the interval $(-\pi, \pi]$. Since in this study the horizontal wind direction associated with the case of $V = 0$ and $U > 0$ is 235° and not 0°, the angles were transformed accordingly and bounded on $[0°, 360°)$. In the presentation of the results, horizontal wind directions, U_d, will be displayed according to the *meteorological convention* (cf. details in Section 5.2.1).

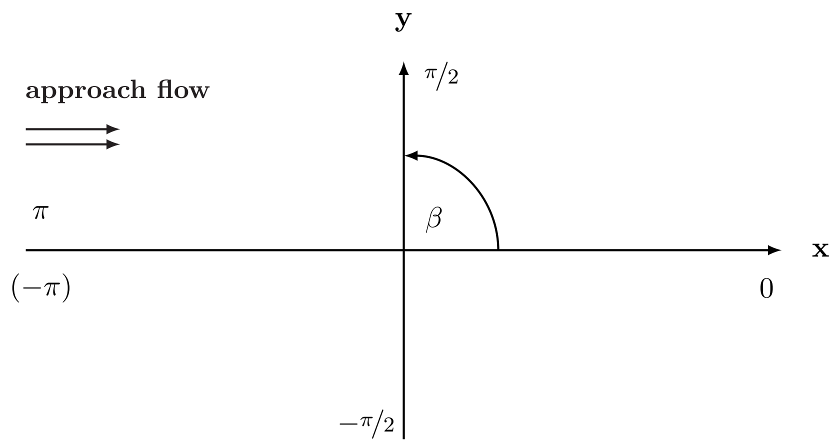

Figure 4.29: Mutual coordinate system of FAST3D-CT and the wind tunnel together with wind direction angles and their quadrants produced by the `atan2` function.

Definition of the reference elevation

All heights are specified with reference to the land surface: z values refer to the height *above ground level* (AGL). The lower boundary of $z = 0\,\mathrm{m}$, thus, has a positive vertical offset of 3.5 m to the uniform water levels of rivers, canals, and lakes within the wind-tunnel model and computational domain. Due to this convention, the few lowest comparison points at the Elbe comparison location (*BL04*) are assigned negative or close to zero values. At all other sites, elevations of the underlying terrain are negligible.

Scaling of flow quantities

Since the LES time series and each of the experimental velocity records represent single realizations of the turbulent flow field, the measured or simulated quantities need to be scaled by representative flow reference values to derive *dimensionless* quantities, which cane be directly compared. In order to scale flow variables in this study, it is sufficient to define a representative reference length scale, L_{ref}, and a reference velocity scale, U_{ref}. While L_{ref} depends on the reference system, i.e. full scale (e.g. 350 m) or model scale (1 m, correspondingly), the reference velocity is defined as the *mean* streamwise velocity observed at a common position over the duration of the measurement or the simulation.

In the wind tunnel, the monitoring of the reference velocity, U_{ref_1}, took place at a full-scale height of $z_{\mathrm{ref}_1} = 175\,\mathrm{m}$ at the end of the boundary-layer development section just upstream of the city model. This elevation was defined in agreement with one of the measurement heights of the meteorological tower in Billwerder to make a direct comparison of the approach flow characteristics possible (cf. Section 4.2.2). For each run, the reference velocity in the tunnel is indirectly derived from the measured free-stream velocity through the relation $U_{\mathrm{ref}_1} = 0.678\,U_\infty$. The constant *scaling factor* was captured by the stationary relationship of flow statistics obtained from repeated combined measurements with the Prandtl tube at the tunnel inlet and the LDA probe positioned at the reference location.

For the comparison with the LES results, the reference point was shifted further downstream to location *BL04* and moved closer to the surface. The dislocation of the reference point was motivated by two factors: First, it was desired to position the reference level inside the urban RSL to cover the determining flow physics. Secondly, the extension of the downstream distance assured that for both, the wind tunnel and the LES simulation, the flow at the reference location is consistent with the roughness characteristics of the industrial harbor area upstream of the inner city. The new, significantly lower wind-tunnel reference height of $z_{\mathrm{ref}_2} = 45.5\,\mathrm{m}$ (i.e. $1.33\,\mathrm{H_m}$) locally corresponds to a level of 49 m above the underlying water surface. Figure 4.30 schematically indicates the positions of the reference points in the wind tunnel. Considering the stationarity of the mean approach flow, the relationship between the ratios of a velocity measured at a certain height z at the new reference location (x_2, y) divided by the new (unknown) reference velocity U_{ref_2} and the same signal divided by the former reference velocity U_{ref_1} is statistically constant. The constant factor has been determined from velocity measurements at *BL04* and was later on used to convert all other scaled experimental results to the new reference location. The so-called *modulation factor*, f_{mod}, was determined through

$$f_{\mathrm{mod}} = \left(\frac{U(x_2, y, z)}{U_{ref_2}(x_2, y, z_{ref_2})} \right) \left(\frac{U(x_2, y, z)}{U_{ref_1}(x_1, y, z_{ref_1})} \right)^{-1} \tag{4.6}$$

From overall 65 velocity signals contained in the vertical profiles measured in U-V and U-W mode, an average modulation factor of 1.431 ± 0.015 was determined, where the scatter indicates the standard deviation drawn from the sample. Due to the specification of the numerical grid, the reference height of the LES data is slightly lower and lies at 45.25 m. The horizontal offsets to the wind-tunnel location are given in Table 4.6. Since the spatial deviations of the experimental and numerical reference positions are small, the effect on the later comparison is considered negligible. In later analyses (cf. Chapter 5), the quantity U_{ref} always relates to the *BL04* reference location (i.e. to U_{ref_2} at z_{ref_2}).

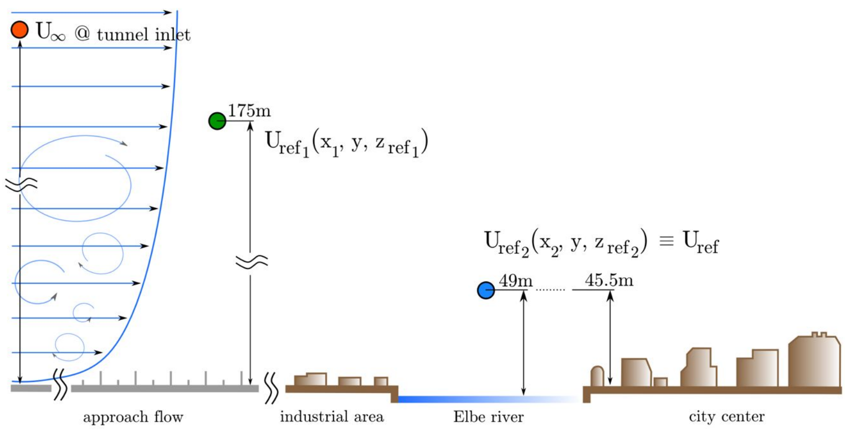

Figure 4.30: Schematic of the locations of monitoring points for the reference velocity in the wind tunnel. All points are sited in the tunnel centerline ($y = 0\,\mathrm{m}$).

Resampling of experimental data

By their nature, laser Doppler anemometers provide discontinuous flow information. The time step between detected velocity signals is not uniform since measurements are only taken whenever a particle crosses the measuring volume. As can be seen from the particle arrival law (Eq. 4.2), however, the most likely temporal separation between signals is (close to) zero. This means that even for comparatively low mean data rates the seeding particles are arriving most frequently in rapid succession, so that high-frequency velocity fluctuations are generally contained in the LDA signals (McKeon et al., 2007). For later time series analyses, the discontinuous time records are reconstructed in order to obtain equally-spaced velocity signals. The approximation quality of the reconstruction primarily depends on the quality of the measurement (cf. earlier discussion in Section 4.2.3) and the characteristics of the employed resampling approach.

A common concept to determine the new constant time step, δt_r, is to relate this quantity to the mean data rate, $\dot{N}$, according to $\delta t_r = \dot{N}^{-1}$. Thus, the temporal resolution of the reconstructed signal corresponds to the mean particle inter-arrival time. For the signal reconstruction at the new time steps, a variety of techniques exist, which involve various levels of mathematical complexity. The arguably simplest approach is using a zeroth order polynomial interpolation, better known in signal-processing as *sample-and-hold* technique (*S & H*). Following Edwards and Jensen (1983), the reconstructed value, U_r, of the velocity signal, U, using sample-and-hold is given by the expression

$$U_r(t) = \sum_i U(t_i)\,\xi(t_i) \qquad \text{with} \qquad \xi(t_i) = \begin{cases} 1 & (t_i \leq t < t_{i+n}) \\ 0 & \text{otherwise} \end{cases}, \tag{4.7}$$

where U_r is the output sample at time t and U_i represents the velocity sample at time t_i, at which the last regular measurement was taken. Hence, the latest sample value will be held constant until a new value is available within the specified constant time step δt_r.

Other more sophisticated interpolation techniques are also frequently employed for LDA data reconstructions and many scientific articles dedicated to the accuracy assessment of these techniques under different experimental and fluid-dynamical conditions exist. However, the simple *S & H* technique has certain advantages and will be used to reconstruct the data of this study. In the following, the choice of the reconstruction technique is discussed by means of a comparison with other approaches. Figure 4.31 shows a cutout of a wind-tunnel velocity time series that is reconstructed by means of four different resampling approaches: sample-and-hold, linear, cubic Hermite and cubic spline interpolations. The *S & H* reconstruction (Fig. 4.31a) shows the characteristic step-like signal shape, which is particularly pronounced for comparatively long inter-arrival times. Using a linear interpolation (Fig. 4.31b) or a piecewise cubic Hermite interpolating polynomial (Fig. 4.31c; e.g. Fritsch and Carlson, 1980) prevents the formation of such steps while preserving monotonicity. However, it is anything but certain that such better-looking reconstructions are superior to *S & H* with respect to statistics. Cubic spline interpolation (Fig. 4.31d; e.g. De Boor, 2001) also produces smooth results and offers continuity between data segments but leads to spurious overshoots, especially if the original samples are separated by large time scales. This is a known feature of spline techniques when applied to strongly fluctuating data (De Waele and Broersen, 2000).

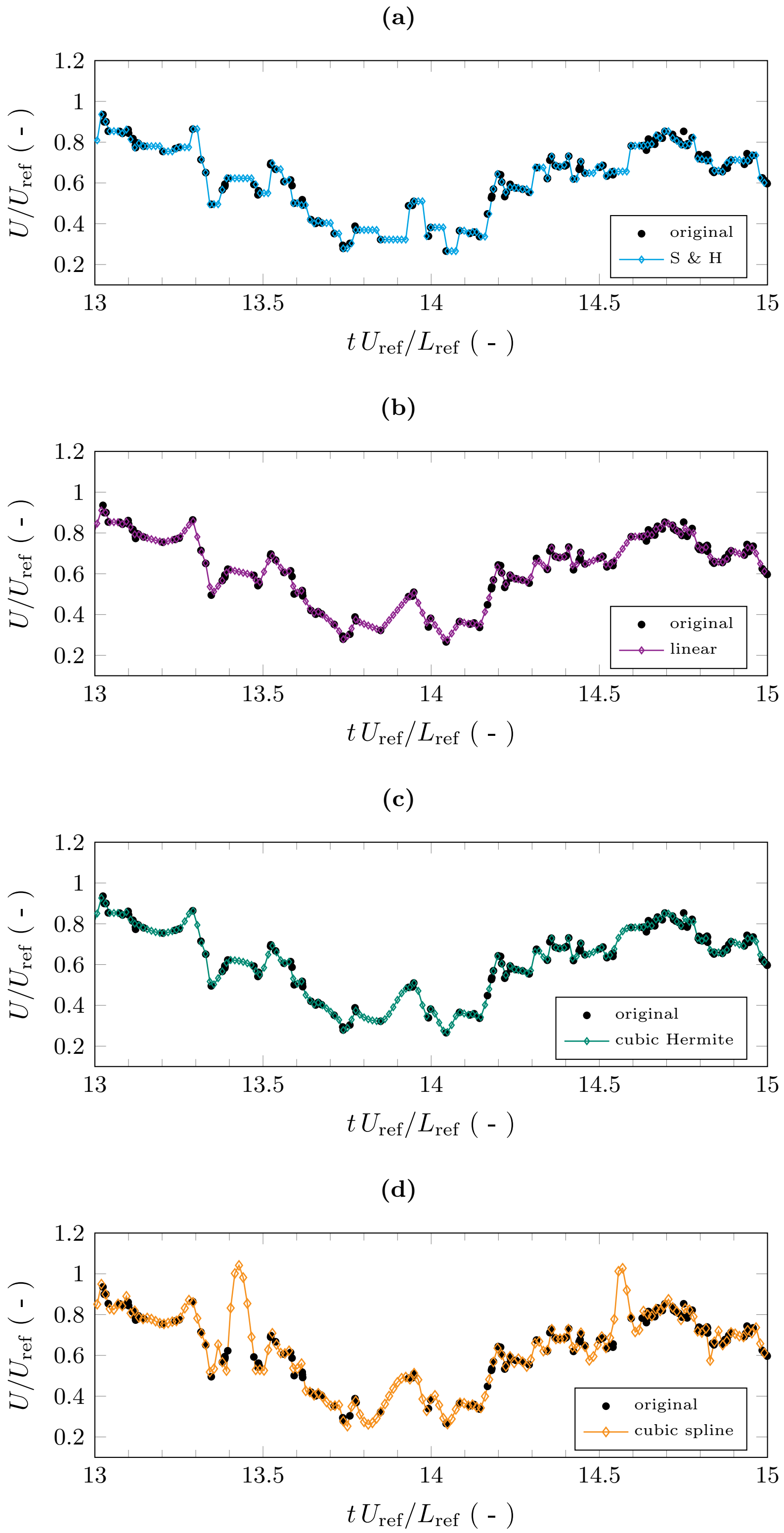

Figure 4.31: Cut-out time trace of an irregularly spaced LDA record of the streamwise velocity and its resampled versions using: (a) sample & hold, (b) linear, (c) piecewise cubic Hermite, and (d) cubic spline interpolations.

In order to quantitatively assess the reconstruction quality of the respective techniques, frequency distributions of velocity time series recorded at position *BL04* (45.5 m height) and *RM01* (2.5 m) are analyzed. Figures 4.32 and 4.33 show the normalized frequency distributions of the streamwise and spanwise velocity *fluctuations* obtained from the original LDA measurements (U-V mode) and from their equidistant data reconstructions. At both positions, all reconstruction techniques except for the cubic spline interpolation recover the original distribution very well. Although the overall signal fluctuation is higher for position *RM01*, the skewed shape of the u' distribution and the bimodal shape of the v' distribution are rather well preserved by *S & H*, linear and cubic interpolations.

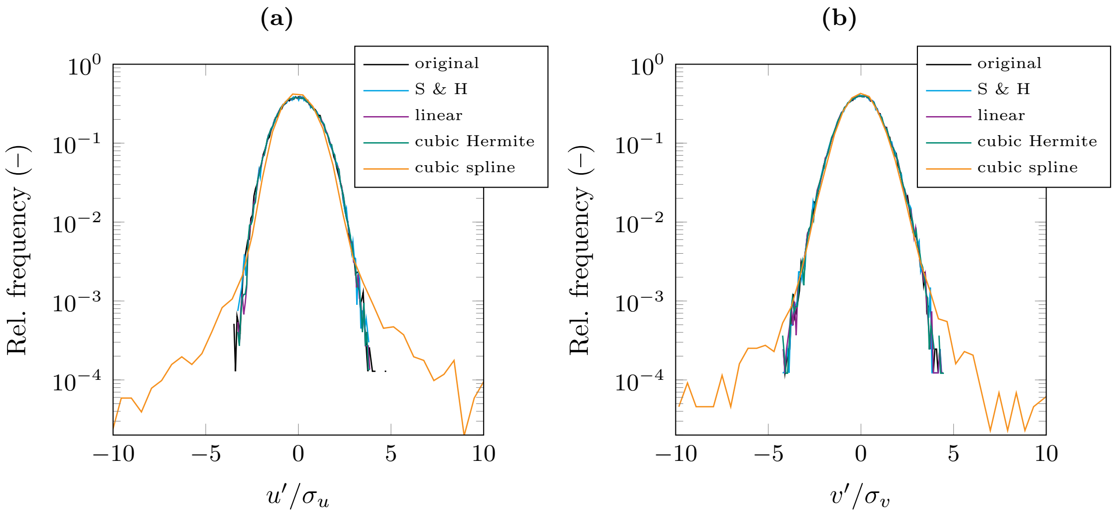

Figure 4.32: Normalized frequency distributions of (a) streamwise and (b) spanwise velocity fluctuations of the original time record and its resampled versions for a measurement taken at location *BL04* ($z = 45.5\,\mathrm{m}$; $\dot{N} = 551\,\mathrm{Hz}$).

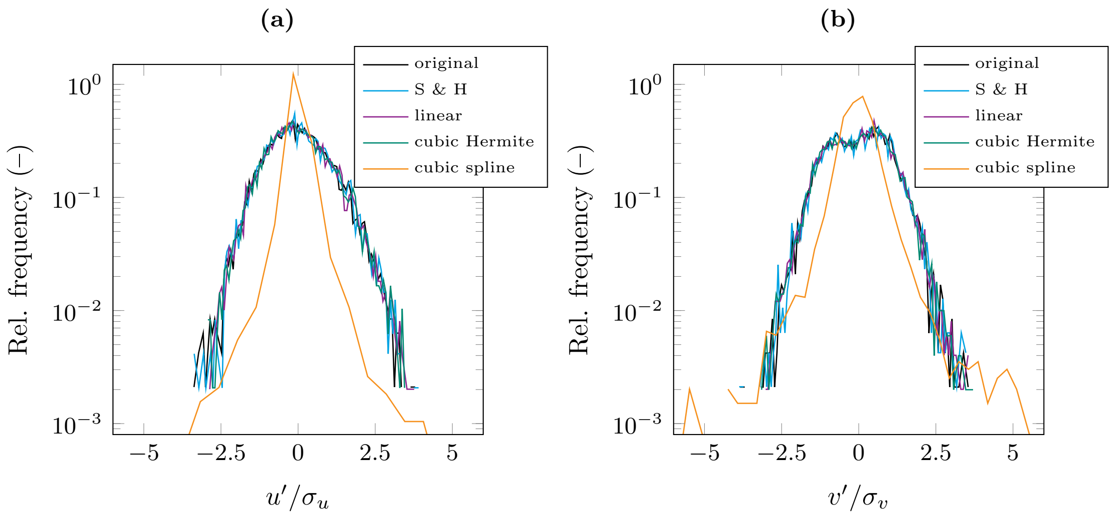

Figure 4.33: Same as Figure 4.32 but for a measurement taken at location *RM01* in a height of $z = 2.5\,\mathrm{m}$ with a sampling rate of 38 Hz.

The spurious behavior produced by the spline interpolation, which was already foreshadowed in the example shown in Figure 4.31d, clearly left its footprint in the sample distributions. Statistical moments derived from these samples are strongly biased.

Unlike higher order reconstruction techniques, the statistical bias of the *sample-and-hold* approach is rather well studied and simple rules-of-thumb exist for its assessment (e.g. Adrian and Yao, 1987; Winter et al., 1991). In general, the accuracy of *S & H* is high if the random LDA samples are on average close enough to resolve the relevant flow structures. This can be determined from the *mean data density* of the measurements. Following Winter et al. (1991), this quantity is given by the ratio of the *integral time scale* of the process, e.g. τ_{11} for the streamwise velocity component, and the *measurement time scale* derived as $\dot{N}^{-1}$. Based on experimental and model data, the authors concluded that for $\dot{N}\,\tau_{11} > 5$ low order statistics can be regarded as *unbiased*. For data densities below 2, the analysis by Winter et al. (1991) indicates that a bias in the order of 2 % to 3 % has to be anticipated for mean and rms values derived from *S & H* reconstructions in comparison to the true statistics of the irregular data sample.[9]

Figure 4.34 shows the data densities derived at all comparison locations and plotted against the measurement height. At the majority of points, the data density is high with values well above the $\dot{N}\,\tau_{11} = 5$ limit. Some locations, however, also group within the $2 < \dot{N}\,\tau_{11} < 5$ range and minor statistical bias might be anticipated here. In general, the use of *S & H* is expected to result in a good approximation of the true flow statistics. It should be noted that the derivation of the integral time scales, τ_{11}, also relied on equidistant velocity time series, which were obtained through the sample-and-hold technique.

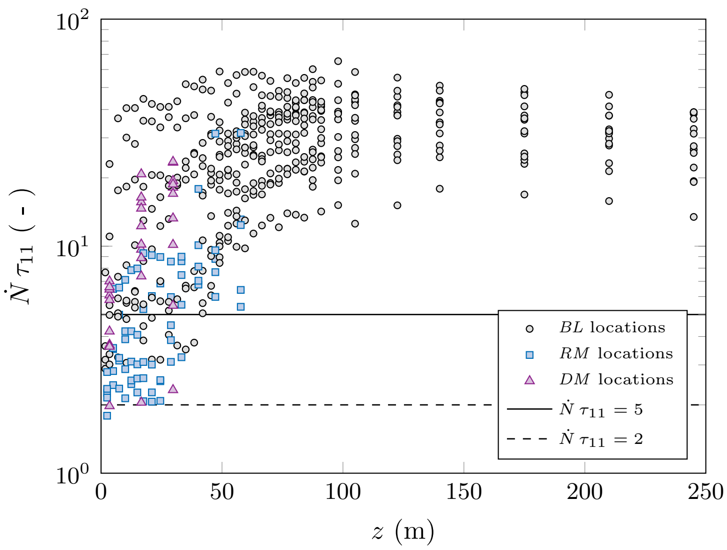

Figure 4.34: Mean experimental data densities for all comparison locations within the urban domain plotted for different measurement heights.

[9]Adrian and Yao (1987) recommend using the temporal *Taylor micro-scale* for this estimation, resulting in a more stringent criterion. However, since Reynolds number independence of the wind-tunnel data is only given for large and inertial-range eddies, it is relied on the integral time scale here.

However, the resampling does not significantly affect the general shapes of the autocorrelation functions from which the integral time scales were derived through a least-squares interpolation technique. Details are discussed in Section 5.4 and Appendix D.

Since all presented reconstruction techniques act as low-pass filters, their application has an influence on the derived turbulence spectra, especially at high frequencies. Figure 4.35 shows 1D energy density spectra of the reconstructed U component obtained at location *BL04* in comparison to established reference functions. While the spectrum of the spline-interpolated data exhibits an odd shape, the spectra corresponding to the other techniques only differ in the high frequency range. In this region, the linear and cubic interpolation spectra feature an increased energy roll-off that could be mistakenly interpreted as the onset of the dissipation range. The *S & H* estimate follows the expected $-2/3$ slope slightly longer, but shows an enhanced spectral aliasing effect at high frequencies. As discussed by Adrian and Yao (1987), *S & H* affects the spectrum in two ways: First, through additive step-noise caused by the holding mechanism, whose contribution diminishes for high data rates with $\dot{N}^{-3}$. Secondly, through a low-pass filter with a cut-off frequency of $\dot{N}/2\pi$, which designates the upper limit for an unbiased spectral estimate (cf. arrow in Fig. 4.35). At lower frequencies, i.e. for larger eddy scales, the spectra can be considered reliable estimates. In view of the fact that especially the energy-containing range and the upper decades of the inertial subrange are of importance for the validation of typical LES predictions, none of the reconstruction techniques – disregarding the spline algorithm – can be classified as superior. Consistent with the argumentation by De Waele and Broersen (2000) and Ramond and Millan (2000), sample-and-hold is selected as the method of choice in this study due to its robustness and assessable accuracy limits, which are less well-explored for the other approaches.

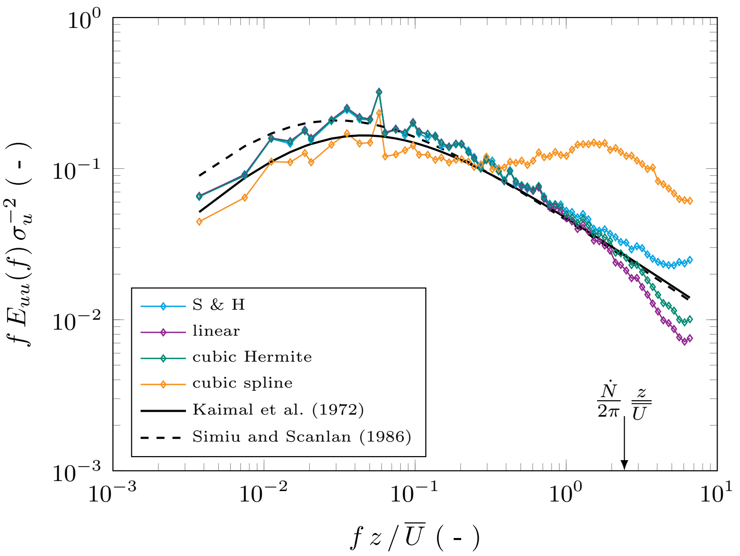

Figure 4.35: Energy density spectra of the streamwise velocity component measured at location *BL04* ($z = 45.5\,\mathrm{m}$; $\dot{N} = 551\,\mathrm{Hz}$) obtained from four different data reconstruction techniques. The arrow marks the empirical upper limit of validity of the *S & H* spectrum according to Adrian and Yao (1987).

4.4.3 Comparative summary of data properties

To conclude the chapter, this section gives a brief summary of the main flow and data characteristics of the wind-tunnel experiment and the simulations with FAST3D-CT and addresses implications for the validation study presented in Chapter 5.

Table 4.7 shows a comparative overview of important flow lengths and velocity scales, the Reynolds numbers characterizing the state of the turbulent flows, specifics of the velocity signal resolutions in space and time, and the number of available flow time series for each of the comparison locations specified earlier in Table 4.5. It has to be noted that Table 4.7 presents the experimental length and velocity scales in *model scale* in order to emphasize the geometric reduction of the flow and its implications for the state of turbulence expressed in terms of the Reynolds number.

Scales & Reynolds numbers Important length scales for the validation analysis differ by a factor of 350 between the wind tunnel and the LES reference system, which is determined by the geometric scale of the physical model. The characteristic velocity scales, however, are of similar magnitude. Thus, differences between the characteristic Reynolds numbers in both flows mostly stem from the different length scales. As discussed earlier, the turbulent flow in the wind-tunnel boundary layer is fully developed and exhibits Reynolds number independence of the dominant and inertial range flow scales. The design of the urban scale model (sharp edges, roughened surfaces) further ensures *Re*-independence of the near-wall flow within the canopy layer and prevents the formation of an overly thick viscous sublayer on walls. The reduced laboratory Reynolds number mainly has implications for the smallest eddies in the flow. These are statistically not comparable to the smallest length scales in the natural full-scale ABL. As discussed in Section 3.2.2, the Reynolds-number mismatch, in general, does not have negative implications for the comparability of wind-tunnel measurements and LES data in terms of flow statistics. Data comparisons based on time-series analyses, e.g. using spectral or joint time-frequency methods, will concentrate on the largest to integral flow length scales, which can be directly resolved by LES and reliably represented in the wind tunnel.

Signal durations The full-scale measurement durations and LES simulation times differ by a factor of 2.5, based on the 16.5 h signal duration of the wind-tunnel time series as opposed to the 6.5 h simulation results derived from FAST3D-CT. From the systematic analysis of the uncertainty of statistical estimates from finite-time wind-tunnel data (cf. Section 4.2.3), uncertainty levels for the numerical time series can be roughly estimated. In doing so, it is assumed that the LES ensemble variance and the integral time scale for the approach flow situation are of similar magnitude as the values deduced from the long-term experimental time series (cf. Figs. 4.20b and 4.21a). Since $\sigma_s \propto T^{-1/2}$, a reduction of the signal duration by a factor of 2.5 leads to an increase of σ_s for an LES time-mean by a factor of 1.58 compared to the wind-tunnel uncertainty of $< 1\,\%$, obtained for $\overline{U}$. Thus, the effect is reasonably small and not expected to severely contribute to interpretation ambiguities with regard to the comparison of flow statistics. The difference could, however, have an effect on the agreement of the turbulence power spectra in the low frequency range, i.e. for the largest, comparatively infrequent eddies (rare flow events).

Table 4.7: Comparative overview of different flow and data properties associated with the scale-reduced wind-tunnel experiment and the full-scale FAST3D-CT LES. Flow length and velocity scales are presented in the respective reference systems, i.e. in *model scale* (WT) for the experiment and *full scale* (FS) for the simulation.

	Wind-tunnel experiment		**FAST3D-CT simulation**	
	value ($\boldsymbol{WT}$)	**comment**	**value ($\boldsymbol{FS}$)**	**comment**
Flow scales				
$\mathcal{L}$ (m)	4	tunnel cross section[a]	1,400	domain height, δ_{les}
L_{ref} (m)[b]	1	flow scale	350	flow scale
z_{ref} (m)	0.13	at position *BL04*	45.25	at position *BL04*
$\mathrm{H_m}$ (m)	0.098	downtown average	34.3	downtown average
$\mathcal{U}$ (m/s)	~ 10[c]	free stream velocity	12[d]	velocity at δ_{les}
U_{ref} (m/s)	~ 4.8[e]	at z_{ref}, *BL04*	4.48	at z_{ref}, *BL04*
U_{H} (m/s)[f]	4.55	at $\sim \mathrm{H_m}$, *BL04*	4.25	at $\sim \mathrm{H_m}$, *BL04*
Reynolds numbers[g]				
Re	$2.67 \cdot 10^6$	based on $\mathcal{L}$, $\mathcal{U}$	$1.12 \cdot 10^9$	based on $\mathcal{L}$, $\mathcal{U}$
Re_{ref}	$3.20 \cdot 10^5$	based on L_{ref}, U_{ref}	$1.05 \cdot 10^8$	based on L_{ref}, U_{ref}
Re_{H}	$2.97 \cdot 10^4$	based on $\mathrm{H_m}$, U_{H}	$9.72 \cdot 10^6$	based on $\mathrm{H_m}$, U_{H}
Re_λ[h]	$2.31 \cdot 10^3$	based on Re	$4.63 \cdot 10^4$	based on Re
Signal resolutions				
T (s)	170	sampling time	23,250	simulation time
$\dot{N}$, f_s (Hz)	∼40–600	$\dot{N}$; variable	2	f_s; constant
Δ_i^3, $i = 1, 2, 3$	$0.08 \times 0.08 \times 1.6$ $0.08 \times 1.6 \times 0.08$	(mm^3); U-V mode (mm^3); U-W mode	$2.5 \times 2.5 \times 2.5$	(m^3); constant up to 101.5 m
Number of time series				
BL locations	32–34 20–31	*U-V* mode *U-W* mode	19 (21)	all points (*BL04* only)
RM locations	14	*U-V* mode	19	all points
DM locations	3	*U-V* mode	19	all points

[a] The lateral width of the test section determines the geometric boundary for the largest realizable eddy structures.

[b] The wind-tunnel value represents the characteristic (or integral) flow length scale of the dominant turbulent eddies. The LES value is specified according to this value using the geometric scale relation of 1:350.

[c] The mean value of U_∞ slightly varies from run to run (in the order of 1 %) and is recorded for every time series.

[d] Approximate value at the top of the FAST3D-CT domain, derived from a power-law extrapolation at *BL04*.

[e] Since U_{ref} is obtained from U_∞, it is subject to similar relative variations as the Prandtl-tube velocities.

[f] For both data sets, U_{H} is retrieved from the mean streamwise velocity at position *BL04* in a height that is closest to $\mathrm{H_m}$ (i.e. 35 m for the wind tunnel and 32.75 m for FAST3D-CT).

[g] Values are obtained from respective length and velocity scales and a value of $\nu = 1.5 \cdot 10^{-5}$ m²/s for air.

[h] This is an approximate value obtained from $Re_\lambda \simeq \sqrt{2\,Re}$, following Pope (2000).

Since the spectrum gives the averaged energy density per frequency increment, δf, the rate of occurrence of certain eddy structures corresponding to a particular δf has a direct effect on the representativeness of the results (cf. further discussions in Section 5.5).

Time resolution Another important distinction between both velocity data sets concerns their temporal resolution, expressed in terms of sampling frequencies. As previously reviewed, the experimental mean LDA data rates, $\dot{N}$, vary from measurement to measurement in response to the local seeding density. The sampling frequency, f_s, associated with the LES time series, on the other hand, is constant and given by 2 Hz. Even for wind-tunnel measurements with relatively high data rates (e.g. in the order of 0.6 *k*Hz), the *full-scale* sampling frequencies are lower than the LES value due to the length scale reduction by a factor of 350 (and assuming similar wind speeds). Figure 4.36 shows the ratios of LES and wind-tunnel sampling frequencies for all comparison points as a function of measurement/simulation height, z. Only those elevations are included for which $|z_{wt} - z_{les}|$ is small, and which, thus, are candidate locations for a direct comparison of time-series analysis results (e.g. spectra, frequency distributions, etc.). The ratios were obtained from the dimensionless sampling frequencies in the respective reference system, i.e. $f^{\star}_{wt} = \dot{N}\, L_{\mathrm{ref}}/U_{\mathrm{ref}}$ and $f^{\star}_{les} = f_s\, L_{\mathrm{ref}}/U_{\mathrm{ref}}$. This yields $f_r = f^{\star}_{les}/f^{\star}_{wt} \simeq f_s\, 350/\dot{N}$, where the latter approximation can be made in consideration of the small difference between the respective reference velocities obtained at z_{ref} above the Elbe river (cf. Table 4.7). The scatter plots of f_r shown in Figure 4.36 overall mirror the height and location dependence of the wind-tunnel data densities, which has been previously discussed on the basis of Figure 4.34. The sampling frequency ratios increase with decreasing comparison height and increasing downstream distance from the reference position, i.e. as the local mean LDA data rate decreases. Below the average building height of $\mathrm{H_m} = 34.3\,\mathrm{m}$, the resolution of the LES signals is significantly higher than of the experimental counterparts.

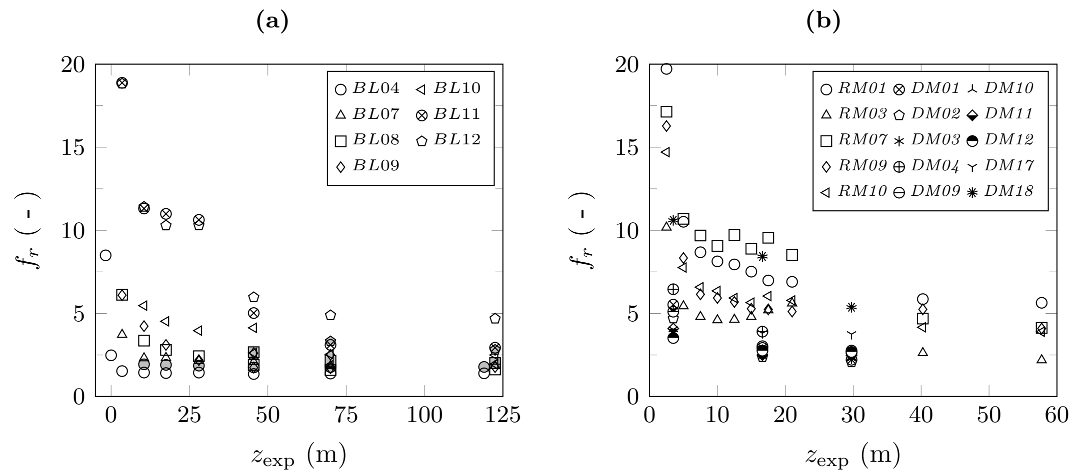

Figure 4.36: Sampling-frequency to mean data-rate ratios, f_r, for (a) the *BL* locations and (b) the *RM* and *DM* locations in all direct comparison heights. Filled symbols in (a) refer to wind-tunnel time series measured in *U*-*W* LDA mode, while empty symbols represent measurements in *U*-*V* mode. The x-axis depicts the *experimental* measurement heights.

The implications for the overall resolution potential of turbulence structures within the urban canopy layer in the experiment, however, are less severe than these numbers indicate. The smallest wavelength, λ_f, captured by the *sampled* signals is directly proportional to the local wind velocity according to $\lambda_f = U/f_{Ny}$. Here, f_{Ny} is the *Nyquist frequency* obtained from $\dot{N}/2$ and $f_s/2$, respectively, which according to the *Nyquist-Shannon sampling theorem* provides the limit for the highest frequency that the signals can contain without ambiguity (e.g. Oppenheim et al., 1999). For typical street canyon flow situations, the local velocities can be drastically reduced compared with the flow above rooftop, and spectral characteristics of the dominant (integral scale) turbulence structures should still be resolvable even with low LDA data rates. Since time-series analyses will concentrate on the energy-dominating scales, which are predicted by LES, not resolving a large part of the inertial subrange with the experimental samples will not have a negative influence on the feasibility of this validation approach. However, the quality of the spectral estimates from the experiments needs to be carefully verified on a point-by-point basis. The dependence of the structural resolution of the signals on the local flow conditions also has implications for the numerical signals. In the case of low velocity magnitudes ($< 2.5\,\mathrm{m/s}$) the numerical time series exported with 2 Hz (i.e. $f_{Ny} = 1\,\mathrm{Hz}$) tend to be *oversampled* with respect to the actually (directly) resolved length scales in the flow, which would be in the order of 2.5 m for this particular scenario.

Space resolution Both the LES and the experimental data essentially represent space-integrated velocities. In case of LES, the spatial filter is given by the grid resolution of 2.5 m, which is uniform in all directions up to a height of approximately $3\,\mathrm{H_m}$ and results in a local grid volume of $15.6\,\mathrm{m}^3$. The spatial resolution of the single-point LDA time series is given by the dimension of the measuring volume (cf. discussion in Section 4.2.3). The probing volume of $4.4 \cdot 10^{-4}\,\mathrm{m}^3$ (converted to full-scale conditions) is significantly smaller than the eddy sizes that are directly resolvable in FAST3D-CT and allows for a relatively precise designation of the experimental measurement location in space.

Geometry resolution While the setup of the urban geometry in terms of buildings, terrain, and bodies of water in the boundary-layer wind-tunnel and the LES model is based upon exactly the same database and has been harmonized to a large degree concerning the incorporated level of complexity, the detail in which obstacles are represented is slightly different. The scaled wind-tunnel model reproduces buildings with a full-scale resolution of 0.5 m, whereas the original 1 m resolution geometry tables for FAST3D-CT are incorporated into a coarser 2.5 m mesh (cf. Sections 4.2.1 and 4.3.2). Particularly for comparison points located relatively close to buildings, numerical *staircase effects* in horizontal and vertical directions are likely to locally influence the flow. In particularly unfavorable scenarios, the local street canyon width could even be virtually narrowed by about 5 m due to the computational gridding technique. In the validation study, such geometry resolution effects need to be assessed and critically evaluated point-by-point.

The other distinctive difference between the numerical model and the wind-tunnel geometry concerns the above-ground subway line, which was excluded from the FAST3D-CT building tables. As can be seen in Figure 4.27, the comparison points *BL07* and *BL08* are located in the vicinity of the trail, whose course is indicated by a brown line. Since the train station is included in both models, the influence of neglecting the subway line is likely to be unessential for comparisons at point *BL07*. For location *BL08*, however, flow effects induced by the presence of the overpass may be detectable in the experiment. As discussed earlier, the construction of the subway bridge is more or less permeable for the wind so that strong blocking effects are generally not expected.

Comparison heights The entire validation data pool contains 2×334 velocity time series from LDA measurements in U-V mode and 2×160 from measurements in U-W mode. These numbers are accompanied by a total of 3×420 velocity records of the three wind vector components extracted from the LES. As discussed in Section 4.2.3, due to technical considerations the LDA measurements in U-W mode do not offer as many vertical profile positions as in the other configuration (see also Table 4.7). For measurements in the downtown city area, the lowest measurement point in U-W mode is typically located in a height of $1.2\,\mathrm{H_m}$. Since no spatial interpolation method was used during the extraction of the FAST3D-CT velocities, horizontal offsets to the wind-tunnel comparison locations have to be accepted, which are typically in the range of few centimeters up to 1.5 m. While mean flow statistics in terms of vertical profiles of time-averaged velocities, variances or momentum fluxes (Reynolds stresses) can be directly compared between the data sets on a qualitative basis, the comparison of particular time-series information in certain heights above ground is restricted to fewer positions per profile (ensuring small vertical offsets between the respective wind-tunnel and LES data pairs). Based on the U-V reference measurements, at the *BL* locations direct comparisons are possible in 7 to 9 heights per profile, at 10 heights for the *RM* locations, and at 3 heights for the *DM* locations (tolerating a height difference of 1.12 m for one of the elevations). From the U-W measurements, which are restricted to the *BL* positions, velocity measurements at 3 to 6 heights can be directly compared based on a height offset limit of $|z_{wt} - z_{les}| = 0.25\,\mathrm{m}$. If larger offsets at particular comparison points are tolerated, for example in regions of small vertical gradients of the respective flow quantities, implications for the overall comparability and the informative value of the comparison need to be evaluated.

5 Turbulent Flow Validation of an Urban LES

ABSTRACT *The proposed LES validation concept is applied to the test scenario of flow in the inner city of Hamburg, Germany. The comparison of predictions from the implicit LES code FAST3D-CT with wind-tunnel measurements focuses on the problem-oriented application of established time-series analysis methods and flow structure characterization strategies. While the examination of low-order statistics provides a global picture of the simulation quality, the analysis reveals the necessity to study the underlying sample characteristics by means of frequency distributions of instantaneous flow quantities to truly arrive at tenable conclusions. The comparison of eddy statistics in terms of velocity correlation information and energy density spectra documents that the LES reproduces important characteristics of the energy and flux-dominating turbulence structures. Conditional averaging approaches further disclose strong similarities between ejection-sweep characteristics and the occurrence of extreme vertical momentum-flux episodes in the urban roughness sublayer. Finally, joint time-frequency analyses with the continuous wavelet transform enable to compare scale-dependent statistics of the experimental and numerical flow fields, to which the preceding diagnostics have been blind. The results of the test study not only confirm the general fitness of the tested code for its intended purpose, but also substantiate the suitability of the advocated multi-step approach for an LES validation that allows to draw wide-ranging conclusions about strengths and limitations of the simulation.*

5.1 Introduction

This chapter presents results of the LES validation study of turbulent flow in the inner city of Hamburg, Germany. Specifics of the implicit LES code FAST3D-CT, the reference experiment in the boundary-layer wind-tunnel facility, and data characteristics that are of importance for the comparison have been discussed in the previous chapter. The comparison is performed in terms of a *blind test*: Neither the experiment nor the simulation were deliberately calibrated to adjust or optimize the level of agreement between measured and predicted flow quantities. This is an important prerequisite for a fair assessment of the model performance. The only exchange of data was related to the geometry information for the setup of the wind-tunnel model and the computational domain (buildings, terrain, bodies of water) and to the task of generating comparable inflow conditions in the numerical and physical model (cf. Section 4.3.2). These steps are necessary to ensure a high degree of *comparability* between the experimental and numerical flow scenarios in terms of geometric boundary conditions and the mean and turbulent state of the approach flow boundary layer. Due to the time schedule of the *Hamburg Pilot Project*, the wind-tunnel measurements and the numerical flow simulations were conducted in quick succession. The time span separating the experimental campaign and the flow calculations with FAST3D-CT was utilized for the quality control of the reference measurements and for the specification of the comparison locations.

With regard to the verification and validation chain introduced earlier in Section 3.1.1 (cf. Fig. 3.1), the comparison of the numerical and experimental flow results presented in the next sections has to be regarded as the initial step of the procedure. At the end of this initial validation, it needs to be decided whether the determined level of agreement between simulation and experiment is *acceptable or not*. Based on the conclusions drawn from this first comparative analysis, application-specific and goal-oriented recommendations for further improvements of the numerical model – or even the experiment – have to be formulated. The validation chain can then be completed again until a satisfactory level of congruence has been obtained, which reflects both the level of description the model is expected to provide and the fitness of the model for its intended use.

The outline of this chapter and the sequence of employed analysis methods closely follows the LES validation hierarchy for near-surface atmospheric flows that has been proposed in Chapter 3 (cf. the schematic analysis sequence in Fig. 3.2). The feasibility of the different analysis methods in the present study is inherently coupled to the resolution characteristics of the available experimental reference data. Since the LDA measurements provide *single-point* time-resolved velocity signals, the comparison of spatial flow properties (e.g. based on two-point spatial correlations, length-scale energy density spectra, etc.) are not possible without invoking Taylor's frozen turbulence hypothesis and will be avoided within the urban comparison domain. Based on the available experimental and numerical data, the validation analysis continues along the lines in order to answer the specified questions:

1 **Exploratory data analysis (descriptive statistics)**

1.1 **Mean flow characteristics**

$\longrightarrow$ *Does the code capture the time-averaged flow patterns?*

Height profiles & horizontal distributions of mean flow and turbulence quantities

1.2 **Frequency distributions**

$\longrightarrow$ *Is the code able to reproduce the frequency distributions of instantaneous quantities?*

Histograms of wind speeds and directions; distribution spreads and shapes; wind direction fluctuation time scales

2 **Analysis of turbulence scales**

2.1 **Temporal autocorrelations**

⟶ *Does the code realistically reproduce integral turbulence scales?*

Shape of autocorrelation functions; integral time scales and their height and location dependency

2.2 **Frequency spectra of turbulence energy densities**

⟶ *Is the LES realistically representing the energy-containing eddies in a time-averaged framework?*

Auto-spectral energy densities & co-spectra; height development and location dependence of spectral shape characteristics

3 **Flow pattern recognition (structure identification)**

3.1 **Conditional flow sampling/averaging**

⟶ *Does the LES capture flow features induced by the UCL?*

Joint probability distributions; quadrant analysis; ejection-sweep events; anisotropy of the (numerical) Reynolds stress tensor

3.2 **Joint time-frequency analysis**

⟶ *Is the LES realistically representing the energy-containing eddies in a time-dependent framework?*

Wavelet transform methods; coefficient PDFs and intermittency; outlook on signal denoising & coherent structure extraction

The sequence of comparison methods followed here should not be regarded as the only possibility or an imperative way to proceed, but rather as indicative of the level of insight that different analysis methods provide for an LES/experiment comparison. Hence, the results will not only be interpreted with a view to determine strengths and limitations of the tested code, but also to substantiate the overall usefulness of the suggested analysis concept. This evaluation focuses on the suitability of the applied methods for an in-depth LES validation, on the potential to obtain quantitative comparison measures, as well as on the interpretability of the results and the potential to determine necessary simulation improvements. This task is closely related to the question posed in Section 1.2: *What information is necessary and/or sufficient for the performance quality appraisal?* Answering this question also involves to investigate to what extent the validation results are unambiguous, i.e. to what degree is a good or bad performance on the basis of a particular test indicative of the performance based on a different comparison method? Finally, the quality of the simulation based on the agreement with the reference experiment needs to be evaluated regarding the model's fitness for purpose. Confirming the adequateness of the simulation for its intended use inherently bears upon the question: *What level of detail is needed and how is this range connected to the purpose of the simulation and/or the expectation toward the model performance?*

Detailed discussions are provided in the following sections. Supplementary material concerning the analyses and computational details is presented in Appendices D–G.

5.2 Mean flow characteristics

In the next paragraphs, mean flow and turbulence statistics in terms of first and second order moments derived from numerical and experimental velocity time series are compared. The analysis mainly focuses on the comparison of the following statistics:

1. Height profiles of mean flow quantities, $\overline{U}$, $\overline{V}$, $\overline{U}_h$, and $\overline{U}_d$.

2. Height profiles of turbulent variances, σ_i^2 $(i = 1, 2, 3)$, and covariances, $\overline{u_1' u_k'}$ $(k = 2, 3)$.

3. Horizontal distributions of mean horizontal wind vectors, $\overline{\mathbf{U}}(x, y)$.

4. Horizontal distributions of variances, σ_i^2 $(i = 1, 2)$, and covariances, $\overline{u_1' u_2'}$.

U_h and U_d are the horizontal wind speed and the horizontal wind direction, respectively (see the next paragraphs for details). Based on the availability of reference data, points **1.** and **2.** apply to the vertically resolved measurements at the *BL* and *RM* locations, and points **3.** and **4.** to the horizontally resolved velocity measurements at the *DM* positions (see Figs. 4.27 and 4.28). The analysis puts a focus on the comparison of component-wise flow information, e.g. by evaluating the three variances instead of their integrated equivalent, the TKE (cf. Eq. 2.14). Based on the mean horizontal wind components and the derived quantities, $\overline{U}_h$ and $\overline{U}_d$, benefits from a component-wise data comparison for the appraisal of the simulation quality are illustrated.

5.2.1 Vertical mean flow characteristics

Mean flow velocities are analyzed in terms of temporal averages of the horizontal wind components and the mean magnitudes and directions of the associated horizontal wind vectors. The time-dependent horizontal wind speed, $U_h(t)$, is derived from the instantaneous streamwise and spanwise velocity components according to

$$U_h(t) = \sqrt{U^2(t) + V^2(t)}\ . \tag{5.1}$$

The corresponding horizontal wind direction, U_d, is obtained from the *arctangent* of the horizontal velocity components (cf. Section 4.4.2) and – if not stated otherwise – is calculated according to the *meteorological* wind vector convention: Wind *from* the south is associated with a direction of 180°, wind *from* the west with 270°, and so on. Furthermore, the vectors are such rotated that for $V = 0$ and $U > 0$ the derived wind direction corresponds to the specified mean inflow direction of 235° (wind *from* SW), yielding

$$U_d\,(t) = \left\{\text{atan2}(-U(t), -V(t))\ {}^{180°}/_{\pi} + 325°\right\} (\text{mod}\,360°)\ , \tag{5.2}$$

in which the modulo operation ensures that angles are bounded on the interval $[0°, 360°)$. Figure 5.1 shows a schematic of the meteorological wind direction convention in contrast to the definition of the polar angle, together with the specification of U_d (Eq. 5.2).

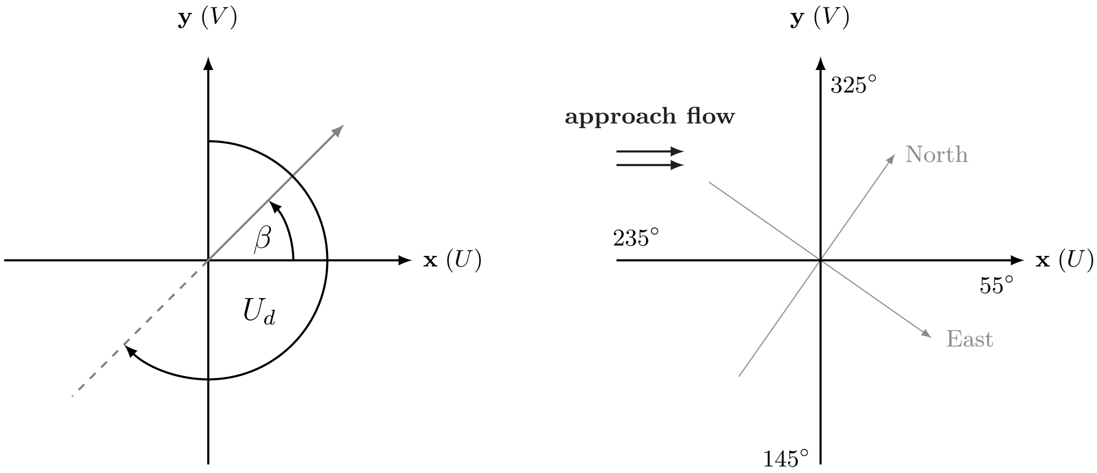

Figure 5.1: *Left*: Angle definitions for a wind vector in the (x, y) (or (U, V)) plane in polar coordinates (β) and according to the meteorological convention (U_d), illustrating the different points of origin and directions of rotation in both systems. *Right*: Rotated meteorological wind angles corresponding to the mutual coordinate system of FAST3D-CT and the wind tunnel defined for this study.

In contrast to the mathematically positive rotational direction (*anti-clockwise*) associated with polar coordinates, meteorological wind direction angles are increasing in *clockwise* direction. Another difference involves the points of origin of the two systems: While the polar angle, β, increases from the positive x-axis (i.e. from the east), the meteorological angle, U_d, increases from the y-axis (i.e. from the north). The choice of the reference system (polar or meteorological) is irrelevant for the comparison between the two data sets as long as it is consistently used. Since this study is conducted in a realistic urban environment and landmark points or buildings are addressed by their north-south/east-west orientation, preference is given to the meteorological convention.[1]

All velocity statistics are presented in a dimensionless framework using the mean streamwise reference velocity U_{ref} for scaling (cf. discussion in Section 4.4.2). In the following, height profiles of the time-mean horizontal velocity components as well as the horizontal wind speeds and directions at all 12 *BL* and *RM* locations are displayed in Figures 5.2, 5.3, 5.4, and 5.5. For a better orientation, the locations of the comparison points are depicted in the upper left corners of the plots in Figure 5.2. In all graphs, elevations below the average building height in the downtown area, $\mathrm{H_m} = 34.3\,\mathrm{m}$, are indicated by a gray shading. The temporal averages of the wind angles are based on a normalization of the instantaneous horizontal wind vectors by their respective magnitudes in order to eliminate the influence of the wind strength on the averaged wind direction.

As can be seen in the velocity-component comparison plots of $\overline{U}/U_{\mathrm{ref}}$ and $\overline{V}/U_{\mathrm{ref}}$, at most of the locations, the agreement between numerical predictions and laboratory measurements is good, as the code is able to capture the general velocity height structure.

[1] It should be noted that the `atan2` function is mathematically undefined for $U = V = 0$. Instead of returning an error value, `MATLAB` as well as other programming languages assign this case a 0° angle.

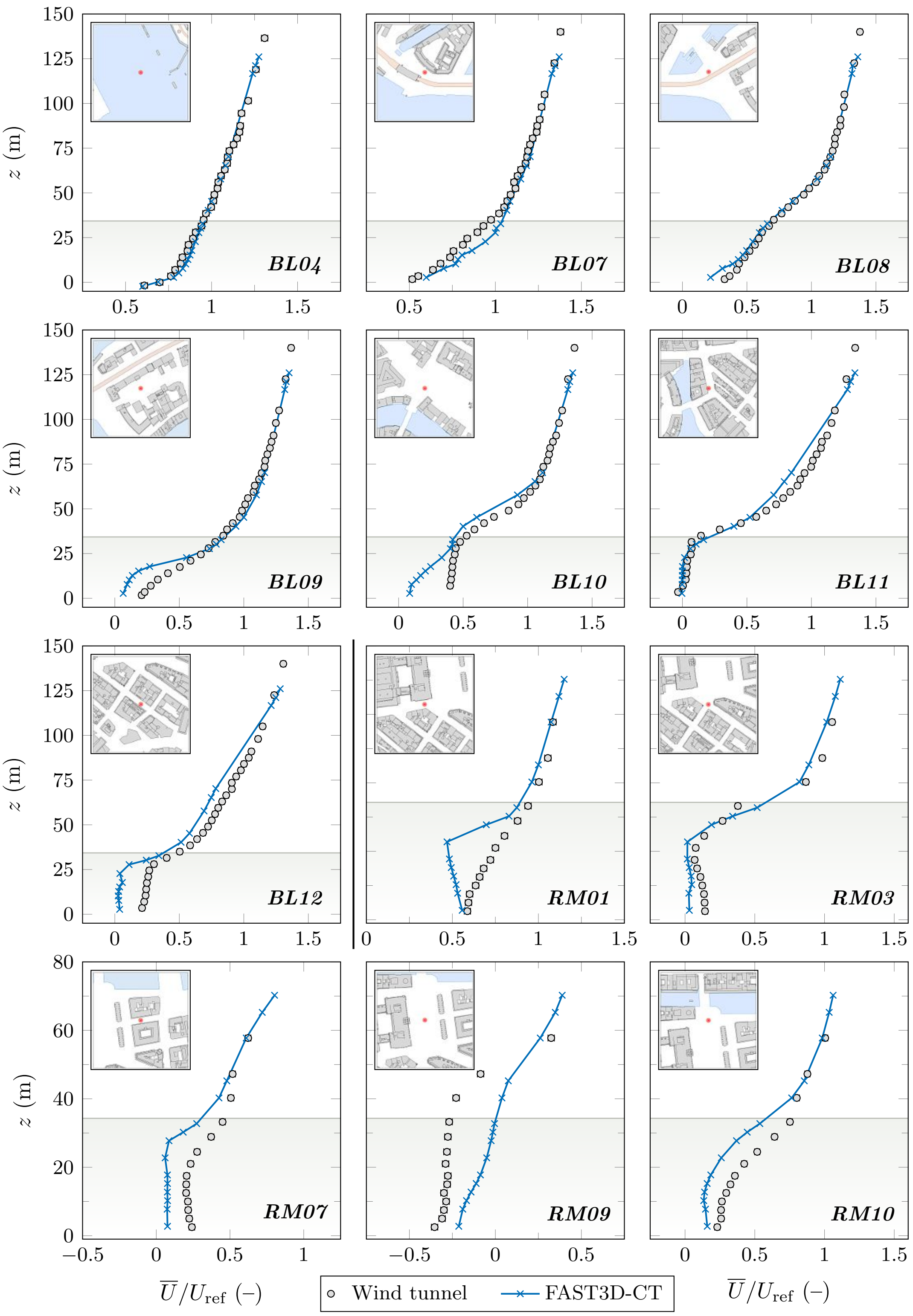

Figure 5.2: Comparison of height profiles of the mean streamwise velocity component, $\overline{U}/U_{\mathrm{ref}}$, for the *BL* and *RM* locations. The gray shading indicates heights lower than the mean building height of $\mathrm{H_m} = 34.3\,\mathrm{m}$. Note that the z-axis changes for the *RM* locations (separated by a black line in the third row).

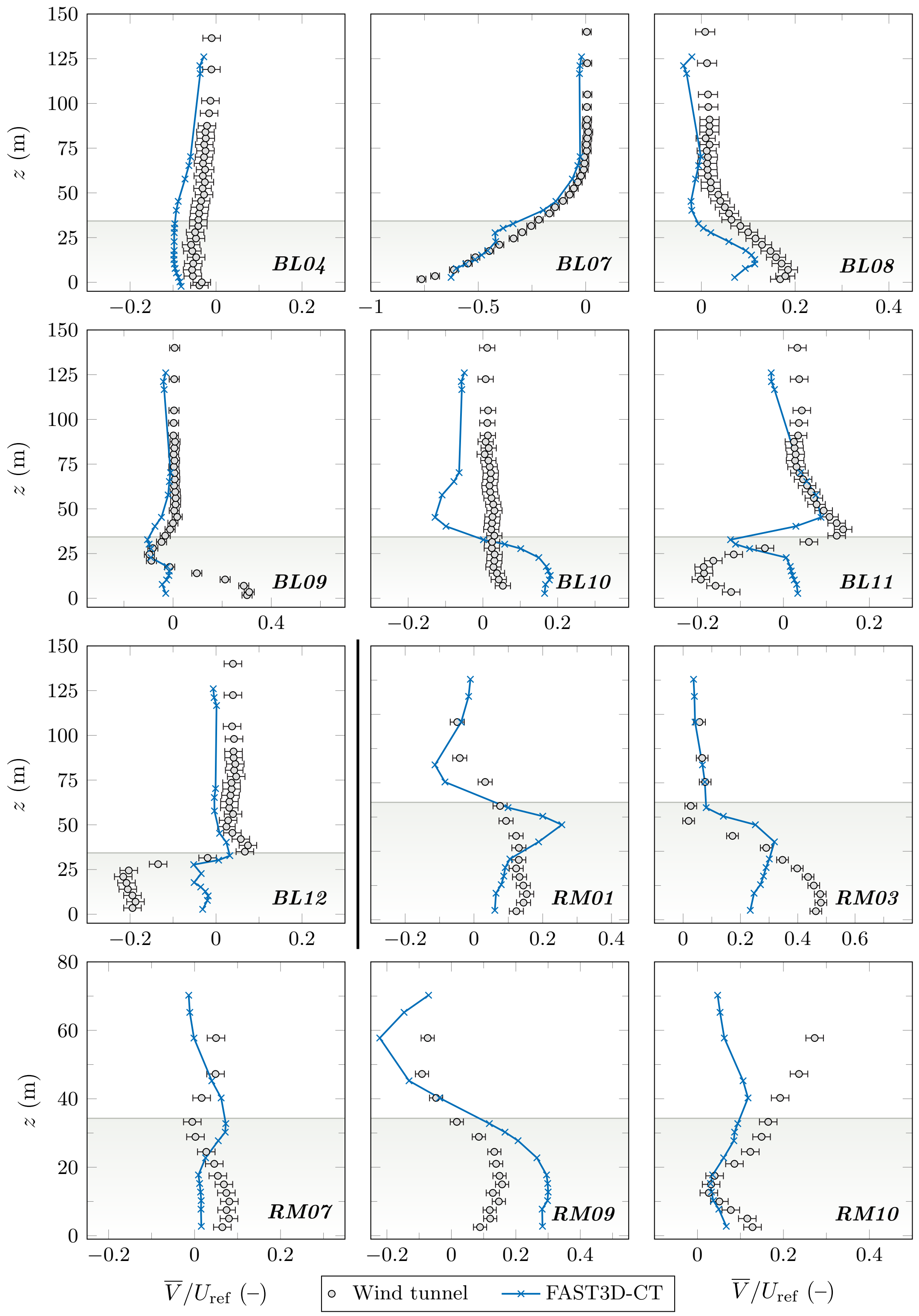

Figure 5.3: Same as in Figure 5.2, but for the mean spanwise velocity component, $\overline{V}/U_{\mathrm{ref}}$.

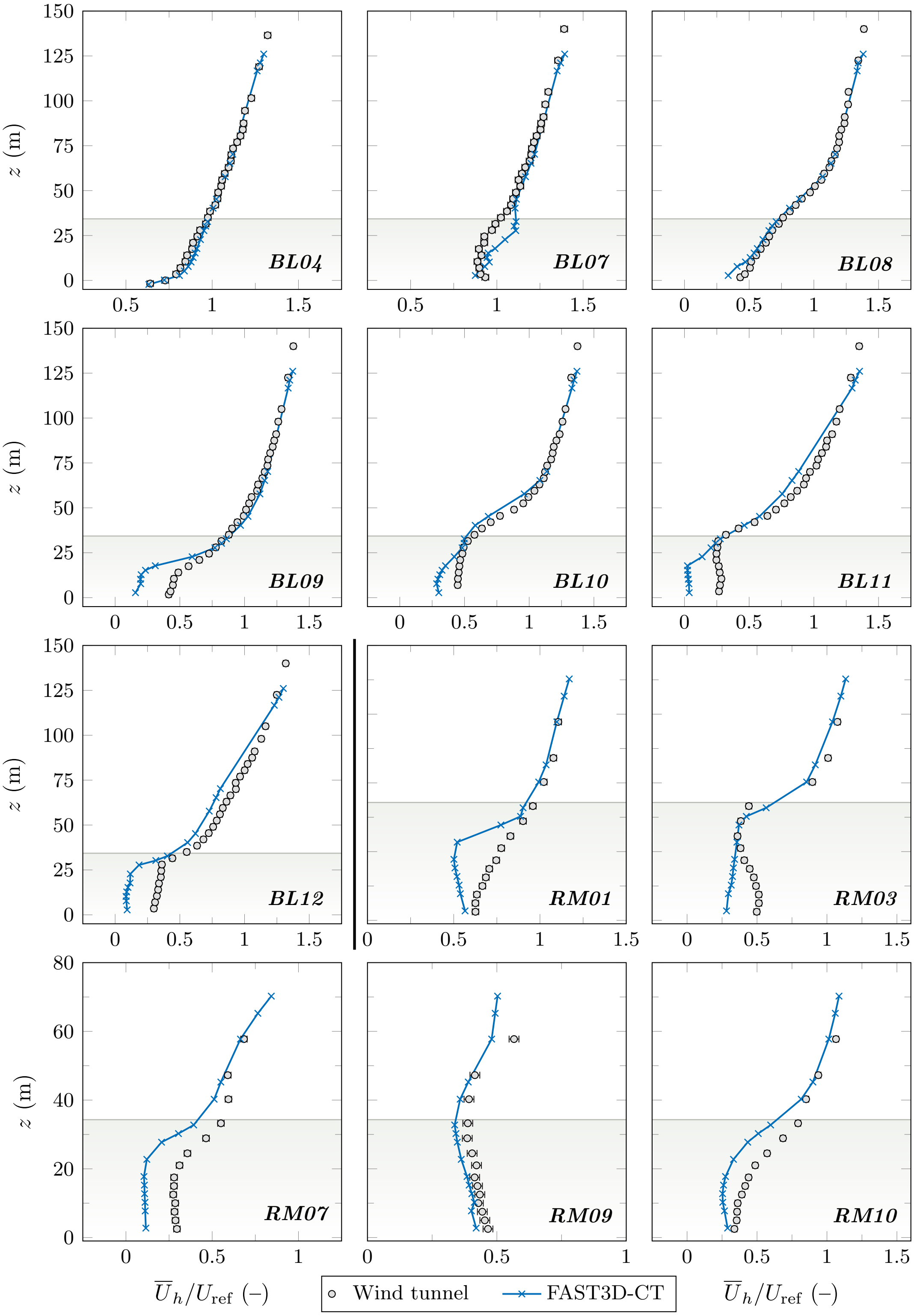

Figure 5.4: Same as in Figure 5.2, but for the mean horizontal wind speed, $\overline{U}_h/U_{\mathrm{ref}}$.

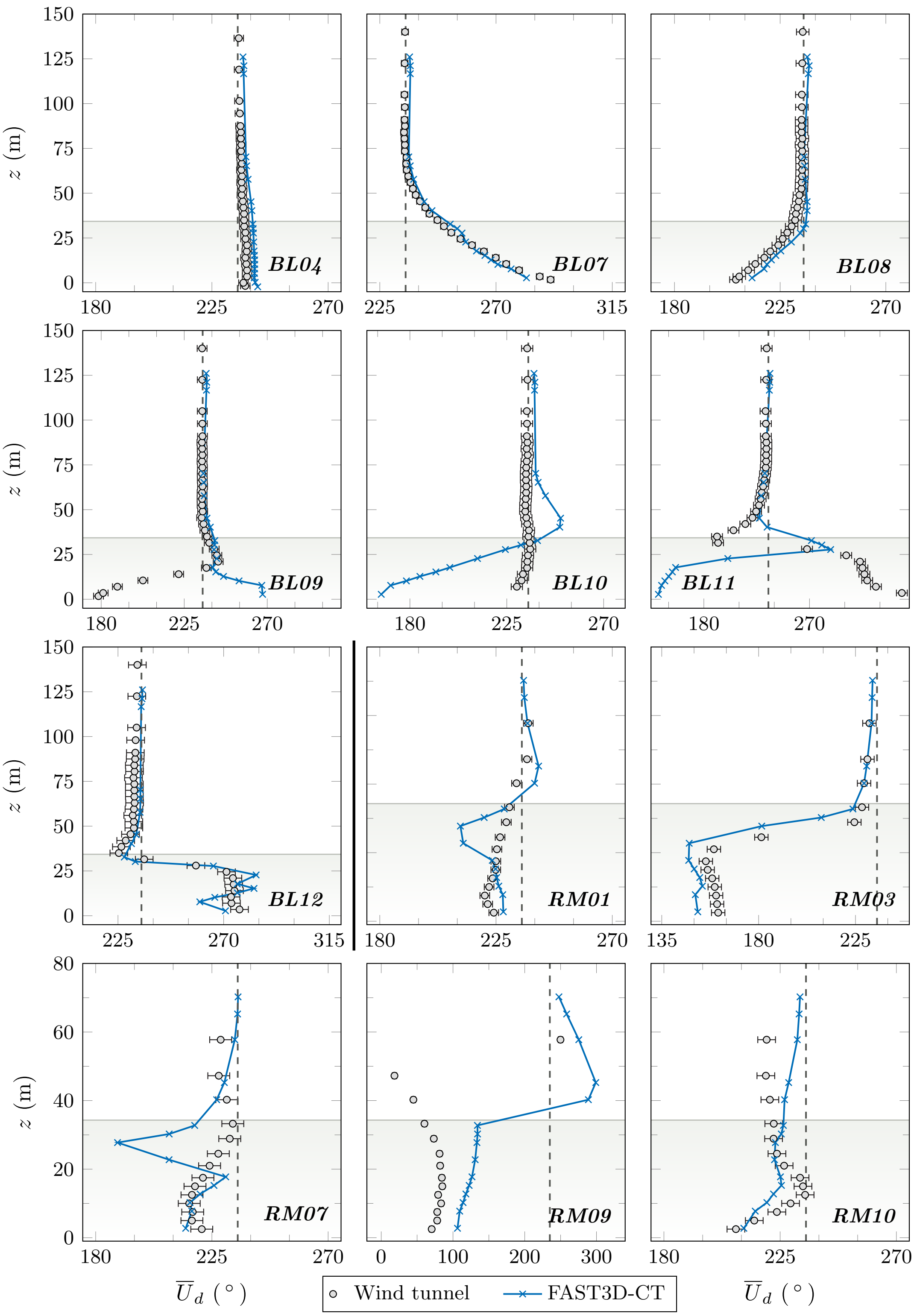

Figure 5.5: Same as in Figure 5.2, but for the mean horizontal wind direction, $\overline{U}_d$. The dashed vertical line indicates the mean approach flow direction of 235°.

At the three most upstream positions, *BL04*, *BL07*, and *BL08*, the agreement of the **streamwise velocity components** is excellent. Further downstream, the strong vertical gradients of the streamwise velocity in the vicinity of the rooftops are very well reproduced at the majority of street-canyon positions. The directional reversal of the mean streamwise flow detected at position *RM09* is also seen in the simulation, although deviations between the measured and predicted velocity magnitudes can be observed. Similar trends toward an underprediction of the magnitude of $\overline{U}/U_{\mathrm{ref}}$ are recognizable at further comparison locations for elevations below the mean building height (e.g. at positions *BL10*, *BL12*, *RM07* or *RM10*). At location *RM01*, a decrease of the streamwise velocity magnitudes with height up to approximately $0.5\,\mathrm{H_m}$ is evident in the numerical results. This trend, however, cannot be seen in the wind-tunnel data.

The temporal averages of the **spanwise velocity components**, $\overline{V}/U_{\mathrm{ref}}$, shown in Figure 5.3 exhibit some larger deviations, particularly for comparison points located in narrow street canyons. At positions *BL11* (street canyon width $W \simeq 17.5\,\mathrm{m}$) and *BL12* ($W \simeq 13.5\,\mathrm{m}$), the intensity of the pronounced lateral deflection of the flow within the canopy layer is strongly underpredicted by the LES. At *BL11* (and *BL09*), FAST3D-CT predicts a reversed sign of the spanwise velocity component in comparison to the measurements. For other locations, FAST3D-CT captures the trends in the lateral velocity very well; for example, the strong channeling effect observed at *BL07*, the complex height development at *BL08*, which appears to be mostly uninfluenced by the presence of the subway trail, or the reversal of the lateral flow deflection at the plaza site (*RM09*).

When merging both velocity components into mean **horizontal wind speeds** according to Eq. (5.1), the height profiles of $\overline{U}_h/U_{\mathrm{ref}}$ (Fig. 5.4) are mostly dominated by the relatively larger magnitudes of the streamwise velocity at the majority of locations.[2] Particularly at positions *BL10* and *RM09*, numerical over and underpredictions of individual components of the horizontal wind vector cancel each other, which results in a significantly improved level of agreement with the experiment. At the majority of comparison points, the simulation quality appraised on the basis of $\overline{U}_h/U_{\mathrm{ref}}$ is excellent. Except for comparison points at which the flow field is strongly confined by the surrounding building geometry (narrow along-wind and cross-wind street canyons), the numerical predictions are well within a factor of two of the wind-tunnel measurements. Comparing time averages of individual velocity components, however, also shows that the magnitude of the wind vector alone is generally not sufficient for the assessment of the model performance since the interpretation of the results can be ambiguous. Further information in terms of the orientation of the wind vector in the (x, y)-plane is needed.

The mean **horizontal wind directions**, $\overline{U}_d$, provide a unified picture of the directional information contained in the magnitudes and signs of the U and V components. Figure 5.5 shows that the predicted and measured flow directions in the horizontal plane are

[2] The scatter bars for the experimental values of $\overline{U}_h/U_{\mathrm{ref}}$ and $\overline{U}_d$ were derived from an *error propagation* analysis for independent variables based on the reproducibility values, ϵ_U and ϵ_V, of $\overline{U}/U_{\mathrm{ref}}$ and $\overline{V}/U_{\mathrm{ref}}$ (cf. Table 4.3), according to $\epsilon_f = ((\partial f/\partial U\,\epsilon_U)^2 + (\partial f/\partial V\,\epsilon_V)^2)^{1/2}$. At each location, the scatter bars correspond to the maximum error over all heights. The analysis is approximate because both variables are not truly uncorrelated (in general $\epsilon_{UV} \neq 0$). Since the reproducibility estimation was based on the ensemble *range* of repetitive measurements rather than on their standard deviation (cf. Section 4.2.3), it is unfeasible to *reliably* assess the general error propagation for correlated variables.

agreeing rather well at most of the comparison points. At the reference location *BL04* above the Elbe river, the slight shift toward more westerly winds compared with the mean inflow direction of 235° (indicated by a dashed line) is evident in both data sets and presumably induced by the downstream opening of the city structure by the river's anabranch (cf. Fig. 4.26). Geometry induced shifts of the flow direction below the mean building height are mostly well reproduced by FAST3D-CT. Above approximately $1.75\,\mathrm{H_m}$, the horizontal wind direction has readjusted to the mean inflow direction at nearly all comparison points except for *RM10*, at which the lateral deflection observed in the wind-tunnel model is still significant. At some UCL heights, larger deviations between the wind-tunnel measurements and the LES are evident. At the courtyard position *BL09*, for example, there is a 90° offset between the mean flow direction at the lowermost comparison points. While in the experiment the mean flow is still influenced by the southward oriented upstream entrance, the numerical model predicts very weak westerly winds. Larger deviations are also observed at the complex intersection (position *BL10*), where the experimental mean flow in the canopy layer shows only minor deviations from the approach flow direction. The LES, on the other hand, predicts flow coming from the southern street leading to one of the canals. As already indicated in the opposite signs of the numerical and experimental $\overline{V}/U_{\mathrm{ref}}$, in the narrow cross-canyon (*BL11*) the mean flow directions below $\mathrm{H_m}$ are exactly reversed. At positions exhibiting large directional deviations, FAST3D-CT generally also tends to underpredict the overall flow magnitude. However, for other complex flow situations like the recirculation regime developing on the leeward side of the city hall (*RM09*), the street-canyon position *BL12*, or the intersection flow at *RM03*, FAST3D-CT is able to reproduce the mean flow structure.

Overall, FAST3D-CT provides a realistic picture of the mean horizontal wind field at different aerodynamic situations that are representative for typical urban flow patterns. The quantitative agreement with the experimental reference measurements is found to be weaker for comparison points that are strongly confined by the urban geometry and/or for which the exact congruence of the physical and numerical building representations are crucial. Capturing the exact position and shape of the recirculation zone at *RM09*, for example, would require a high degree of agreement between the building geometries. This is also true for some of the narrow street-canyon positions, for which the ratio of canyon-width to mesh spacing, W/h_i, with values in the range of 5.5 to 7.5 in combination with "staircase effects" caused by the gridding technique are probably too small to reliably resolve the flow at the comparison points. The relatively coarser representation of buildings in FAST3D-CT may have caused some of the profile locations to virtually move closer to the building walls, which increases the influence of the prescribed wall-boundary condition on the simulation at the comparison point and could explain the underprediction of velocity magnitudes.

Mean variance profiles

Second-order velocity moments characterize the mean turbulence state of the flow and are individually compared for all components in the following Figures 5.6, 5.7, and 5.8.

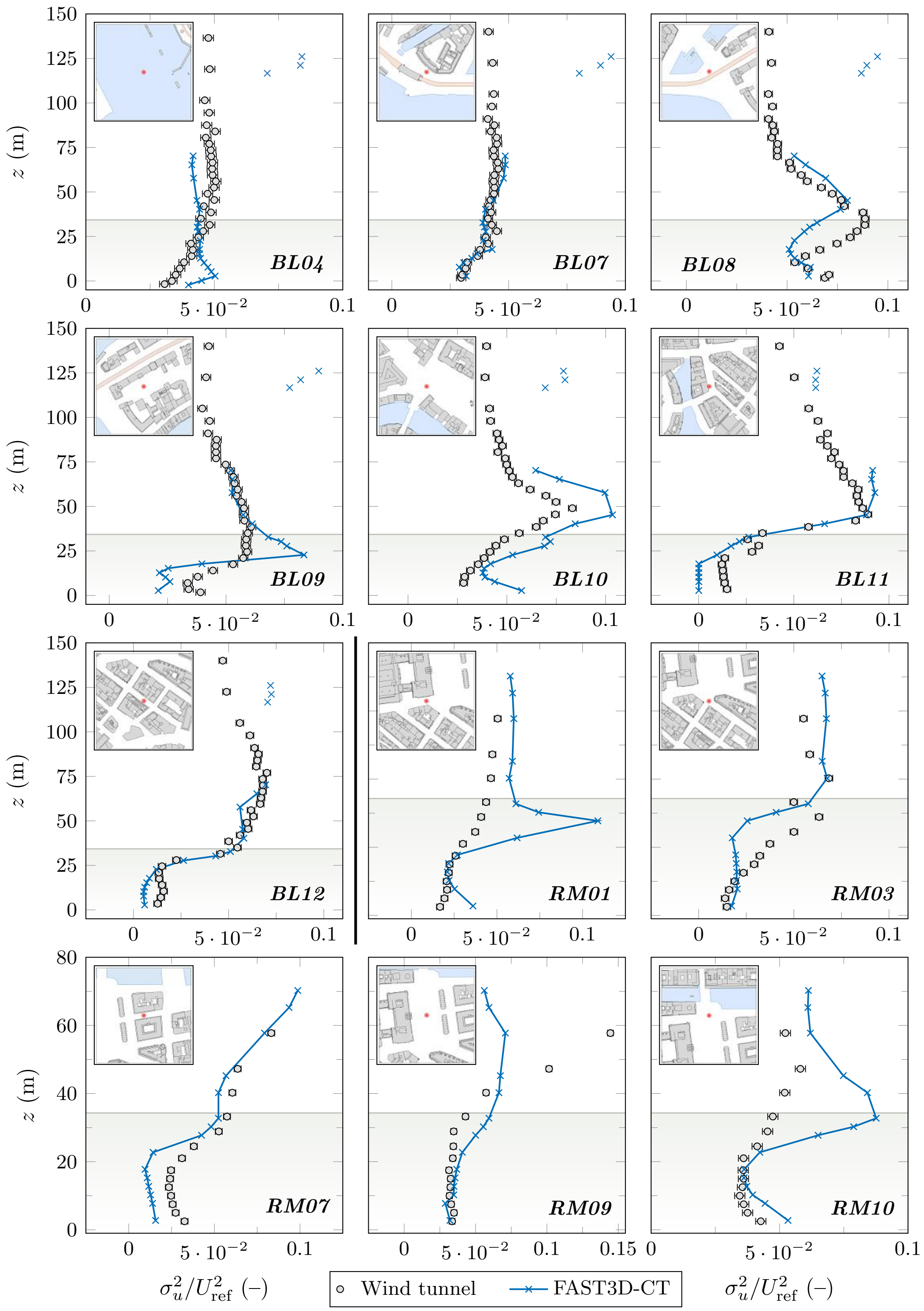

Figure 5.6: Same as in Figure 5.2, but for the variance of the streamwise component, $\sigma_u^2/U_{\mathrm{ref}}^2$.

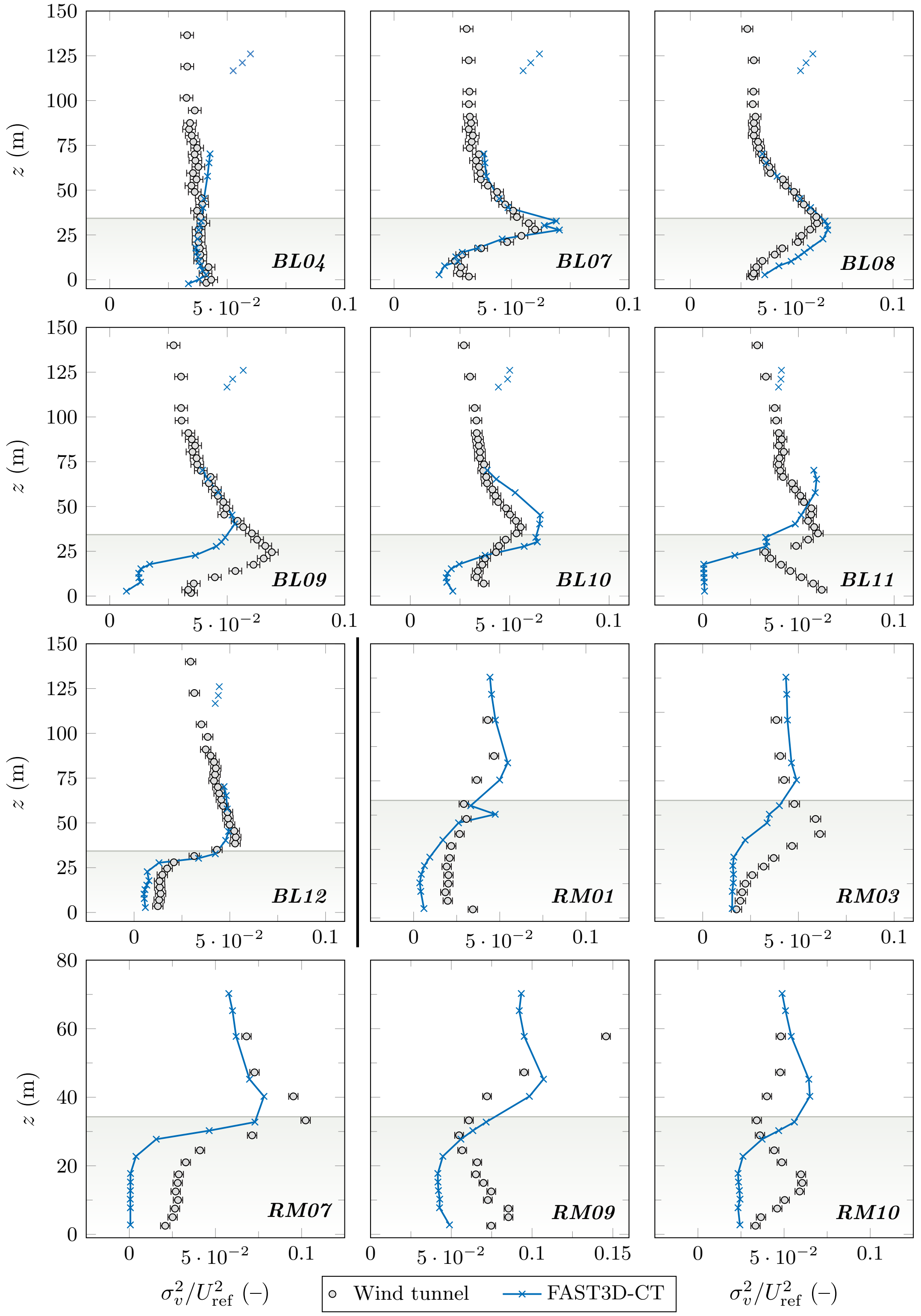

Figure 5.7: Same as in Figure 5.6, but for the variance of the spanwise component, $\sigma_v^2/U_{\mathrm{ref}}^2$.

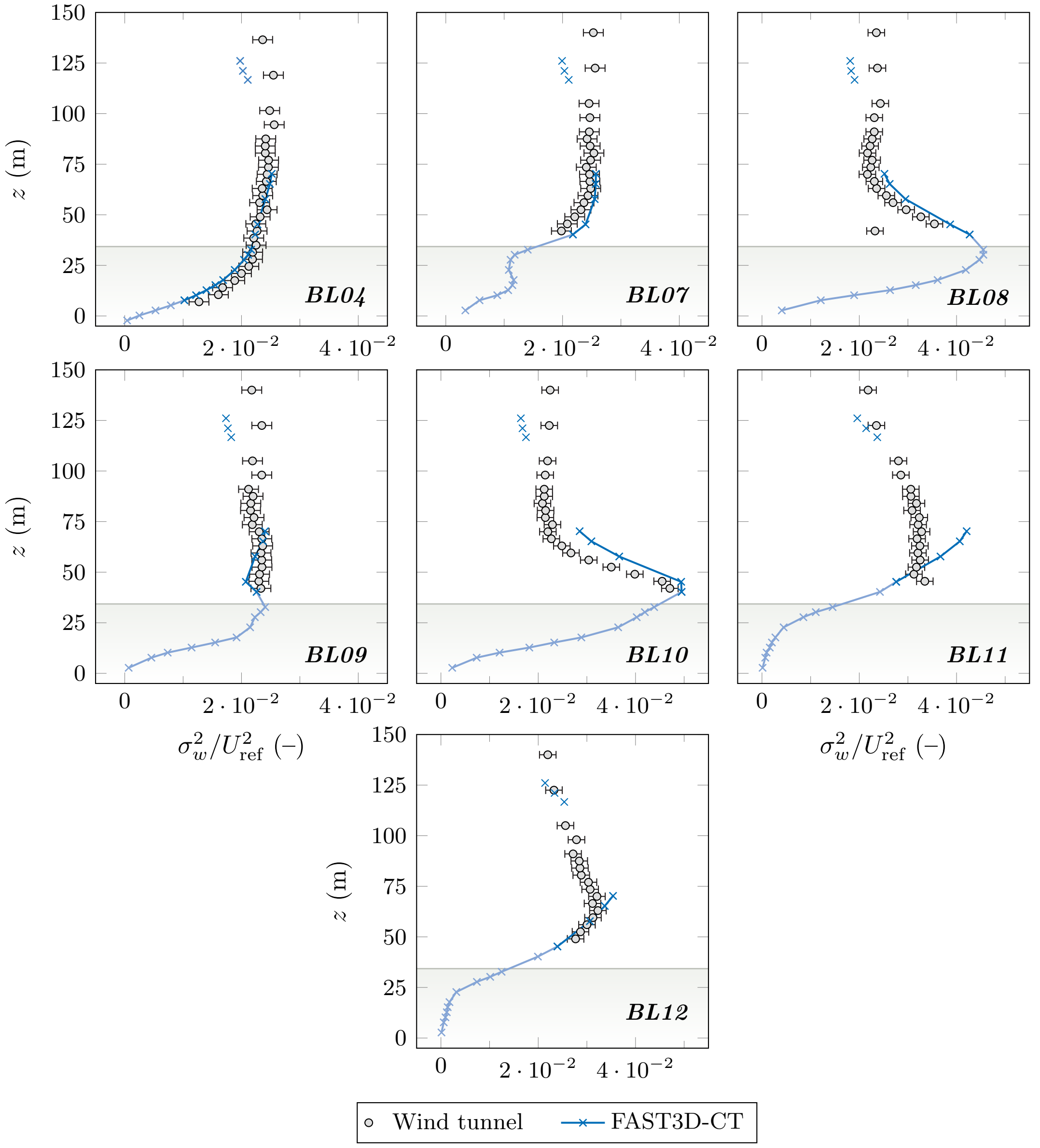

Figure 5.8: Same as in Figure 5.6, but for the variance of the vertical component, $\sigma_w^2/U_{\mathrm{ref}}^2$. Numerical data for which no experimental reference data are available for the comparison are depicted in brighter color (mostly below $\mathrm{H_m}$).

For all three variances, there is a high level of agreement with the wind-tunnel measurements at reference location *BL04*, well upstream of the inner city area. Being approximately 350 m away from the downstream shore, the turbulent variances are still rather homogeneous with height. For comparison points within the city, the qualitative agreement of the **streamwise variances** below approximately 2 $\mathrm{H_m}$ is good for the majority of positions, while at some locations the simulation shows a tendency to overestimate the characteristic variance peaks near the top of the canopy layer (e.g. *BL09*, *BL10*, *RM01* or *RM10*). In the same height range, an excellent congruence with the wind-tunnel measurements of the **spanwise variances** could be determined at *BL0*, *BL07*, *BL08*, and *BL12*. Similarly to the height profile of $\sigma_u^2/U_{\mathrm{ref}}^2$, at the lowermost simulation heights of the comparison point in the narrow cross-canyon (*BL11*), the spanwise velocity variance takes near-zero values in contrast to the experiment, which suggests a complex height structure of turbulence. Particularly at some of the *RM* locations, larger offsets of the lateral turbulence levels are found as well. At *RM10*, for example, the height developments of $\sigma_v^2/U_{\mathrm{ref}}^2$ seen in the experiment and the LES are almost exactly reversed.

The comparison of the **vertical velocity variance** (Fig. 5.8) is restricted to the *BL* locations, for which experimental measurements are mostly available only for heights above the canopy layer (cf. discussion on technical constraints of the LDA probing technique in Section 4.2.3). For elevations at which the numerical results could be validated against the experiment, the qualitative and quantitative agreement is found to be very good, except for position *BL11*.

A striking feature of the FAST3D-CT simulation results of $\sigma_u^2/U_{\mathrm{ref}}^2$ and $\sigma_v^2/U_{\mathrm{ref}}^2$ at the three highest positions of the *BL* profiles ($z = 116.68\,\mathrm{m}$, $121.12\,\mathrm{m}$, and $126.05\,\mathrm{m}$) is the clearly overpredicted magnitude. Instead of following the smooth decrease seen in the wind tunnel, the topmost numerical variances even exhibit a height increase that appears to be mostly decoupled from the flow simulation at lower heights where the agreement with the experiment is much better. For the variance of the vertical velocity component, the difference between the topmost LES and wind-tunnel values is not as drastic as for the horizontal components and is only pronounced at the river profile. As discussed in Section 4.3.2, the numerical mesh is stretched along the z-axis above a height of roughly $3\,\mathrm{H_m}$ ($101.5\,\mathrm{m}$) and the vertical cell dimensions at the extraction heights are larger than in the uniform mesh of $2.5\,\mathrm{m}$ well within the RSL (local values of h_z are $4.21\,\mathrm{m}$, $4.68\,\mathrm{m}$, and $5.19\,\mathrm{m}$ for cells in which the topmost velocity data were extracted). At these elevations, however, neither the wind-tunnel mean flow nor the turbulence statistics exhibit pronounced vertical gradients, so that it might be expected that the deviations are unlikely to have originated from the coarser resolution. Instead, most probably the artificial turbulence prescribed at the inflow plane left its footprint in the FAST3D-CT statistics. This interpretation is substantiated by the fact that the magnitudes of the variances at different locations within the urban area are remarkably similar. Furthermore, the departure from the wind-tunnel flow is significantly attenuated at comparison points further downstream in the city center. Only after the flow has passed the river, the height structure of the urban environment strongly increases (cf. Fig. 4.22), causing a further growth of the RSL and an intensification of geometry-induced turbulent mixing, which ultimately lessens the effects of leftover inflow turbulence in the self-consistent simulation results at elevations well above $3\,\mathrm{H_m}$.

Mean covariance profiles

The off-diagonal components of the Reynolds flux tensor, $\overline{u'v'}/U_{\mathrm{ref}}^2$ and $\overline{u'w'}/U_{\mathrm{ref}}^2$, are compared in the following (Figs. 5.9 and 5.10), to appraise the accuracy with which the LES is able to reproduce the vertical and lateral turbulent momentum exchange.

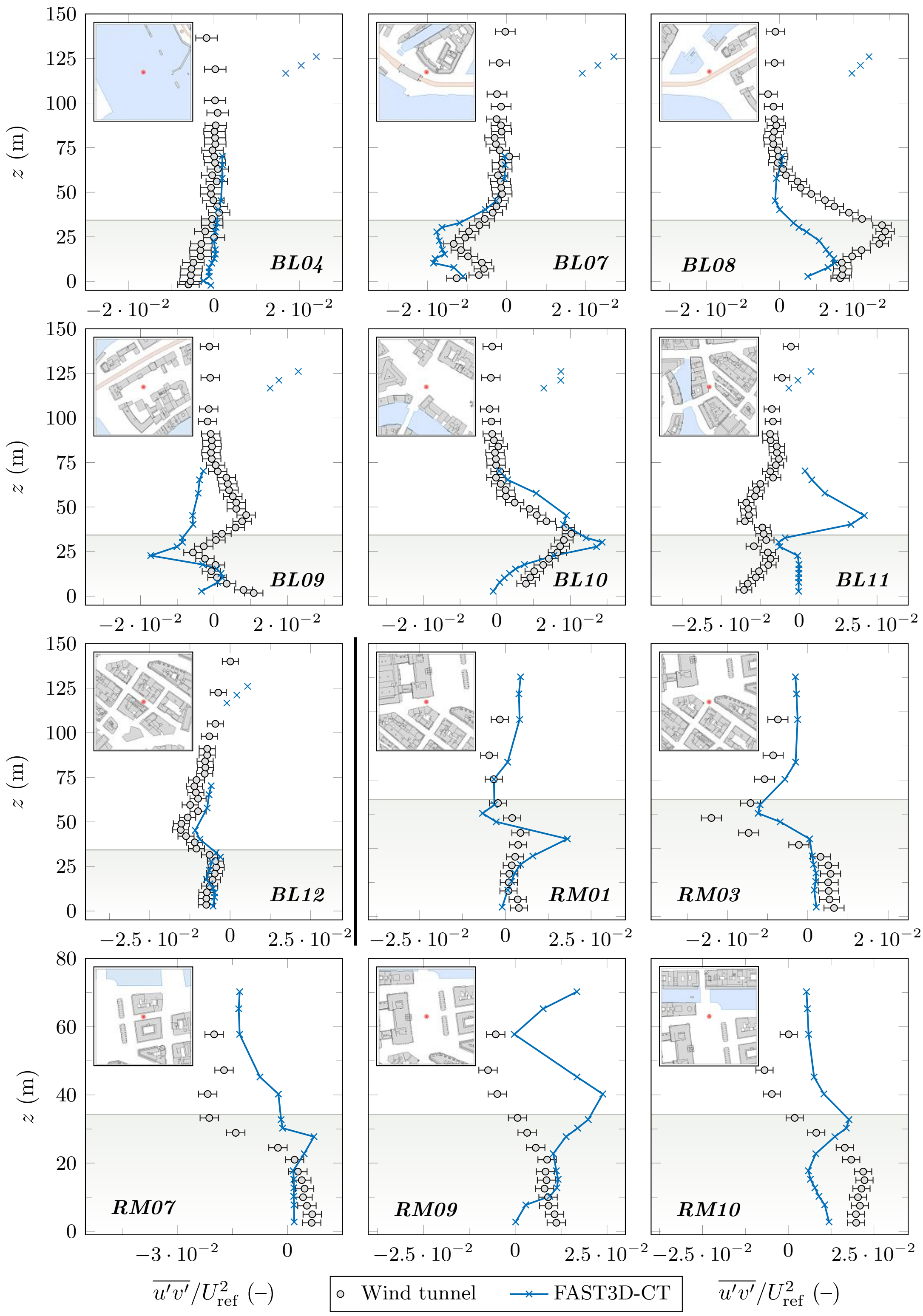

Figure 5.9: Same as in Figure 5.6, but for the covariance of the streamwise and spanwise velocity components, $\overline{u'v'}/U_{\mathrm{ref}}^2$ (lateral turbulent momentum flux).

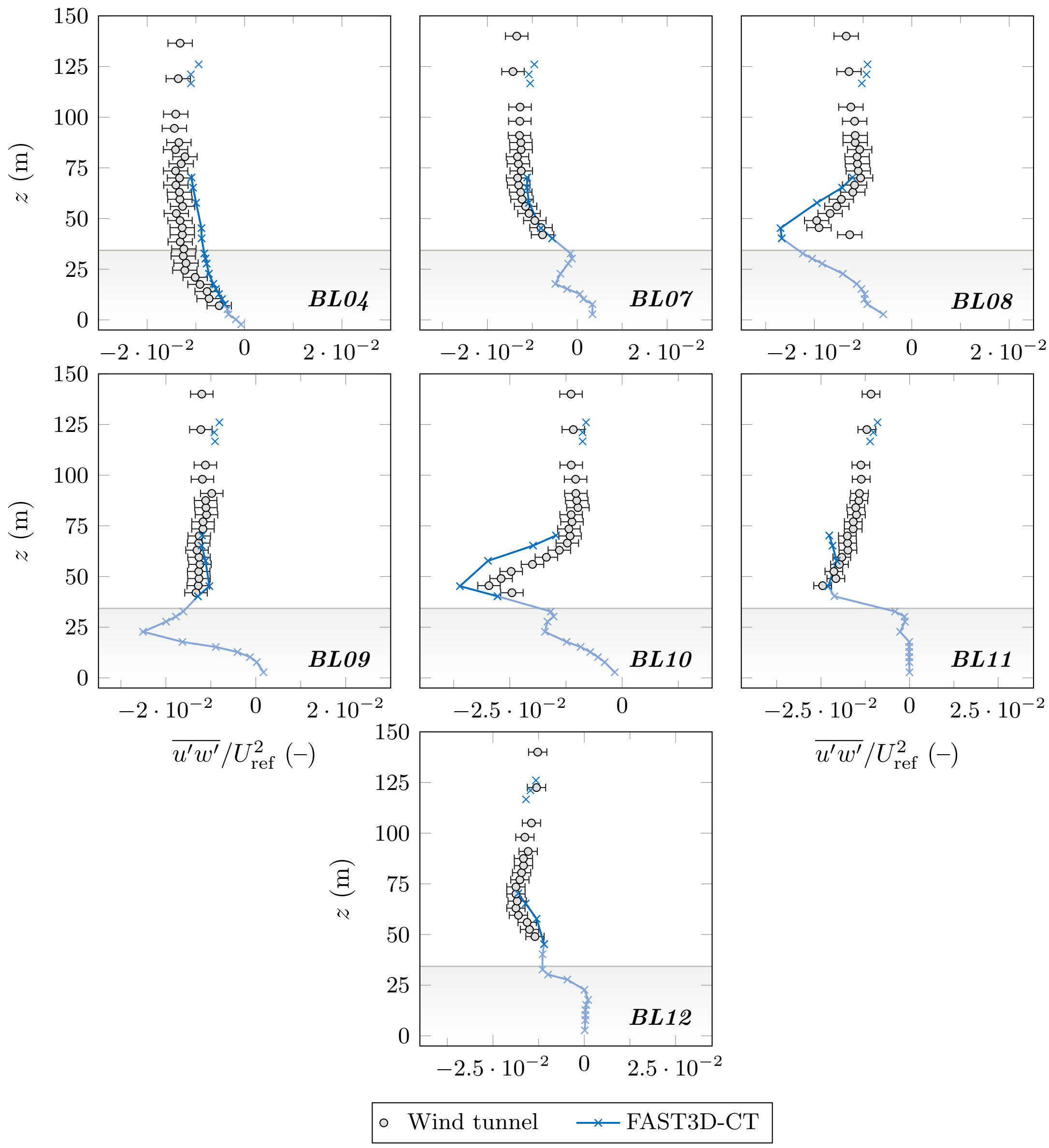

Figure 5.10: Same as in Figure 5.9, but for the covariance of the streamwise and vertical velocity components, $\overline{u'w'}/U_{\mathrm{ref}}^2$ (vertical turbulent momentum flux). Numerical data, for which no experimental reference data are available for the comparison, are depicted in brighter color (mostly below $\mathrm{H_m}$).

The **lateral momentum flux** profiles of the LES are well coinciding with the wind-tunnel statistics at the reference location *BL04* as well as for the city sites *BL07*, *BL10*, *BL12*, *RM01*, and *RM03*. The quantitative agreement is weaker at other positions, with particularly large offsets detected once more at *BL11* and at *RM09*, for which the LES classifies the mean momentum flux at some elevations into different flux quadrants than the experiment (sign reversal). At heights in which wind-tunnel data of the vertical velocity component are available, the agreement between the **vertical momentum flux** profiles is very good. For the downtown comparison points *BL08* and *BL10*, the numerical results exhibit characteristic shear-flux peaks, whose vertical positions agree well with the measurements. At both sites, maximum fluxes are observed at approximately 1.33 $\mathrm{H_m}$ (i.e. 45.5 m), in agreement with typical literature values (see Section 2.4.1). Deep within the UCL, FAST3D-CT predicts a very weak vertical momentum exchange at locations *BL11* and *BL12*. The physical validity of these results cannot be evaluated on the basis of the available experimental data, but is most likely influenced by the building resolution in the numerical model and by the proximity of the comparison points to the building boundaries. Similarly to the behavior seen in the variance profiles of the horizontal velocity components (normal fluxes), the LES strongly overestimates the magnitudes of $\overline{u'v'}/U_{\mathrm{ref}}^2$ at the three highest extraction points. In the profiles of the vertical momentum flux, this feature is not recognizable and at all locations the LES results usually fall well within the statistical scatter range of the laboratory measurements.

Like it could be concluded for the mean flow profiles, the overall agreement of the height structure of second-order statistics between LES and experiment is satisfying, but there is room for improvements. The influence of the selected grid resolution and the resulting block-like representation of the buildings in the numerical model most likely also affected the validation results of the turbulent variances and covariances.

5.2.2 Horizontal mean flow characteristics

Next, the ability of the LES to capture the mean *horizontal* flow and turbulence structure is tested based on the example of flow through a courtyard entrance (*DM* locations, see Fig. 4.28; point *DM11* is located approximately 59.5 m upstream of profile position *BL09*). The horizontal resolution of the reference measurements (distances between comparison points) is in the range of 6 m to 10 m and, thus, allows to document the spatial heterogeneity of the mean flow within this locally confined domain. The wind-tunnel data are available in terms of the horizontal velocity components, U and V, in three different heights of 0.1 $\mathrm{H_m}$ (3.5 m), 0.49 $\mathrm{H_m}$ (16.63 m), and 0.87 $\mathrm{H_m}$ (29.75 m). Just upstream of the courtyard entrance lies the waterfront, so that the approaching flow is comparatively unobstructed when hitting the windward building facades. Due to the orientation of the passage, flow channeling effects are anticipated.

In Figures 5.11, 5.12, and 5.13, the mean horizontal wind vector fields of the LES are compared to the reference measurements at all three elevations. In order to obtain reliable averages of the components of the horizontal velocity vectors, $\overline{\mathbf{U}}(x, y) = (\overline{U}_{\mathrm{vec}}, \overline{V}_{\mathrm{vec}})$, the values were derived from the averaged polar angles between the streamwise and spanwise velocity components, $\overline{\beta}$ (cf. Fig. 4.29), and the magnitude of the horizontal wind vectors by time averaging Eq. (5.1), according to

$$\overline{U}_{\mathrm{vec}} = \overline{U}_h \cos\overline{\beta} \quad \text{and} \quad \overline{V}_{\mathrm{vec}} = \overline{U}_h \sin\overline{\beta} \,, \tag{5.3}$$

so that $\overline{U}_h = (\overline{U}_{\mathrm{vec}}^2 + \overline{V}_{\mathrm{vec}}^2)^{1/2}$. For the lowest comparison height (Fig. 5.11), the agreement between experiment and simulation is very good at the majority of positions concerning the vector orientation in the (x, y)-plane as well as their local magnitudes.

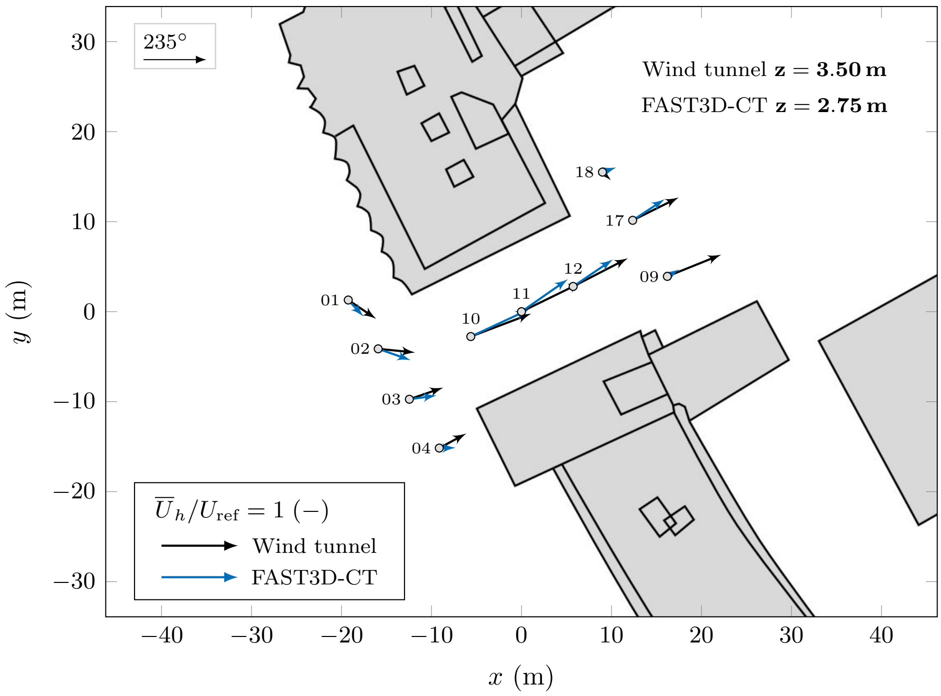

Figure 5.11: Comparison of mean horizontal wind vectors in the first height at the *DM* locations. The vertical offset between the comparison points is $|\delta z| = 0.75\,\mathrm{m}$. Reference vectors are displayed for $\overline{U}_h/U_{\mathrm{ref}} = 1\ (-)$ on the bottom left. Note that the vectors and geometries are depicted in agreement with the wind-tunnel coordinate system (i.e. the mean approach flow is from left to right).

Compared with the positions at the windward entrance, the magnitudes of the velocity vectors inside the passage nearly doubled. The largest differences are observed at the leeward exit with a pronounced magnitude offset at point *DM09* and a wind direction shift of almost 90° at *DM18*. The level of agreement in the second height (Fig. 5.12), which roughly corresponds to half of the local building height, is comparable to the lower elevation for the entrance and exit locations, while inside the alleyway (14.5 m width) the FAST3D-CT results show a slight directional offset to the measurements. In both data sets, a further enhancement of the channeling effect is recognizable, which resulted in wind magnitudes in the order of the streamwise reference velocity U_{ref}, observed at a much higher elevation of $z_{\mathrm{ref}} = 45.5\,\mathrm{m}$ (cf. lengths of reference vectors). At the topmost comparison height (Fig. 5.13), distinct directional offsets only show within the passage. However, at site *DM09*, which exhibited the largest discrepancies between simulation and observation at lower heights, the agreement has significantly improved. Particularly at the highest comparison height, the vertical offset of $|\delta z| = 0.5\,\mathrm{m}$ between numerical and experimental data pairs can already have a significant influence on the validation since the points are located in the vicinity of the rooftops (approx. H = 32 m for the upper and 30 m for the lower building). Here, strong vertical velocity gradients have to be expected. This could be an explanation for the tendency toward an overprediction of wind speeds by the LES at *DM01–04* and within the alleyway.

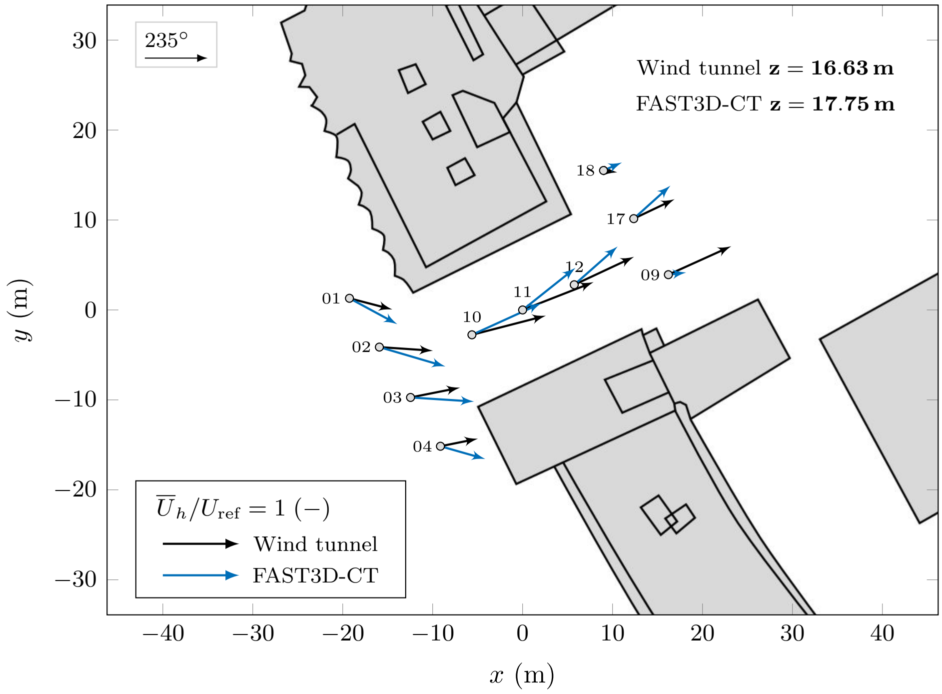

Figure 5.12: Same as in Figure 5.11, but for the second height with a vertical offset between the comparison points of $|\delta z| = 1.12\,\mathrm{m}$.

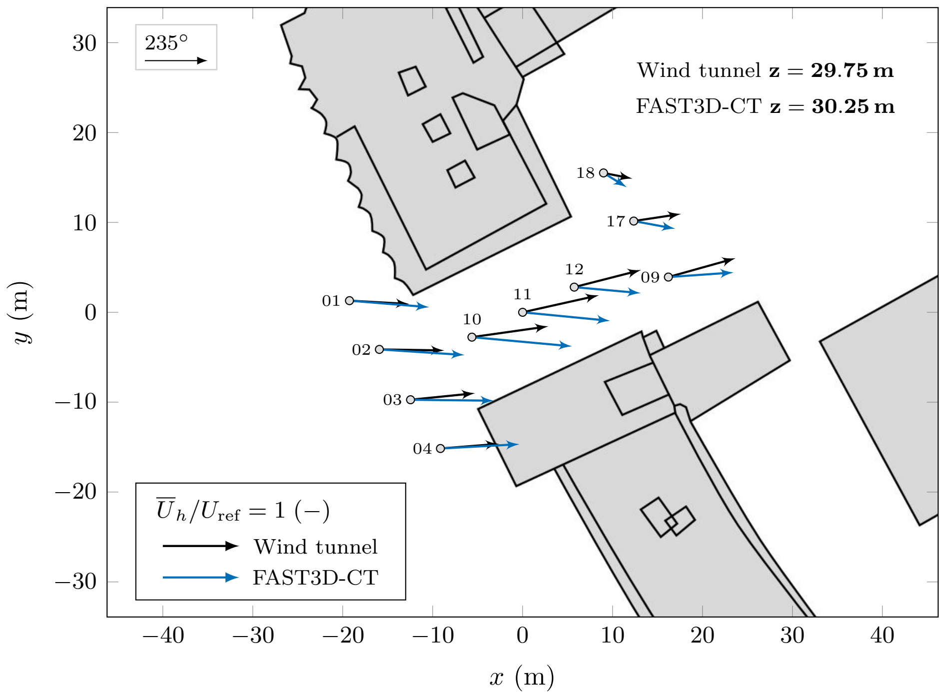

Figure 5.13: Same as in Figure 5.11, but for the third height with a vertical offset between the comparison points of $|\delta z| = 0.5\,\mathrm{m}$.

Turbulence statistics in terms of the normal fluxes, $\sigma_u^2/U_{\mathrm{ref}}^2$ and $\sigma_v^2/U_{\mathrm{ref}}^2$, and shear fluxes, $\overline{u'v'}/U_{\mathrm{ref}}^2$, are compared in Figures 5.14, 5.15, and 5.16. Locations at which the absolute difference between the LES and wind-tunnel fluxes is smaller than the statistical reproducibility of the experimental results are bordered by gray margins (values listed in Table 4.3). The agreement of the **streamwise** and **spanwise velocity variances** is notably good at locations *DM01–04*, at which FAST3D-CT accurately reproduces the height decrease of $\sigma_v^2/U_{\mathrm{ref}}^2$ and the overall spatial distribution of its streamwise counterpart. In particular, the patterns of lowest and largest absolute deviations mostly coincide with the earlier conclusions from the horizontal mean flow analysis: Significant offsets emerge at some of the alleyway positions as well as at *DM09* and *DM17*.

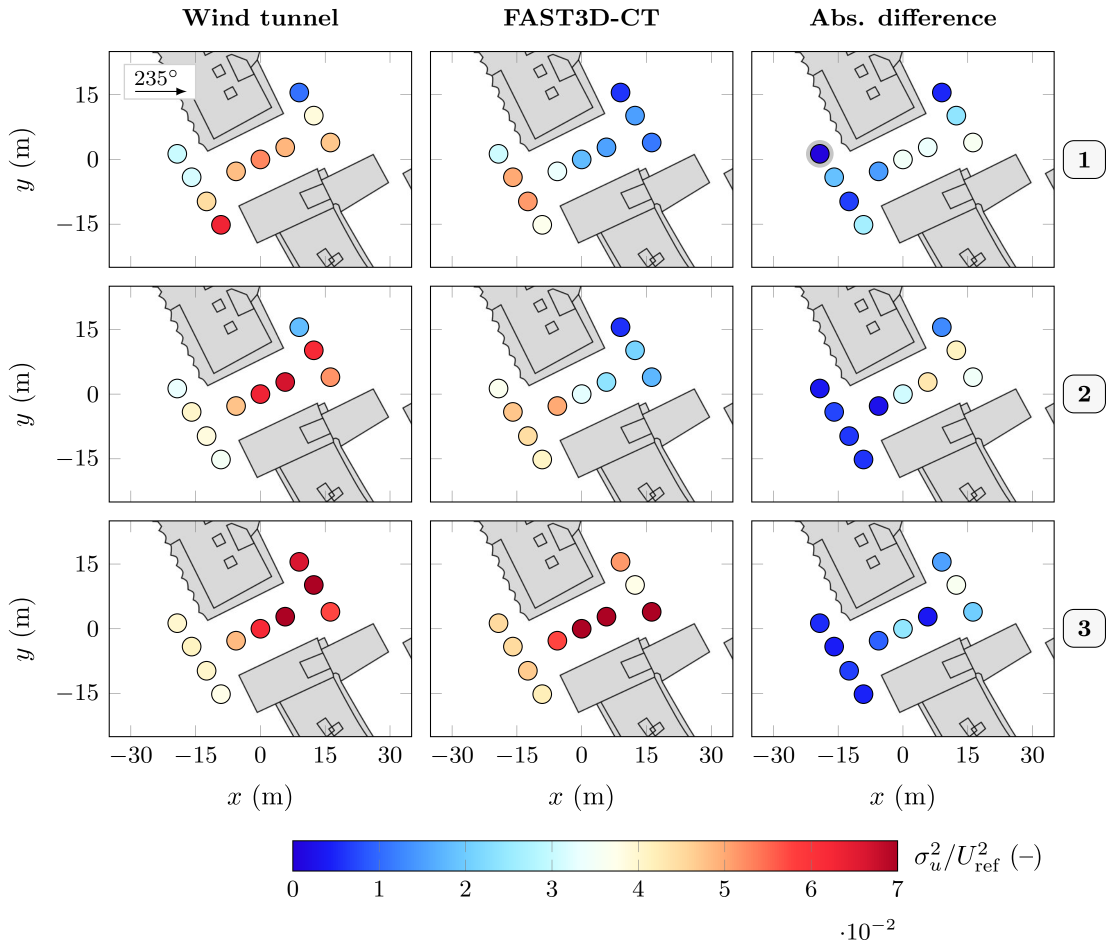

Figure 5.14: Local variances of the streamwise velocity component, $\sigma_u^2/U_{\mathrm{ref}}^2$, at the *DM* points for the wind-tunnel experiment and the numerical prediction with FAST3D-CT, together with the absolute difference between individual data pairs. The numbers on the right-hand side denote the respective height levels of the comparison (**1**: 3.5 m/2.75 m; **2**: 16.63 m/17.75 m; **3**: 29.75 m/30.25 m for the experiment/LES). Absolute differences bordered by gray margins indicate that the deviation is smaller than the statistical reproducibility of the experimental results. The mean approach flow is from left to right.

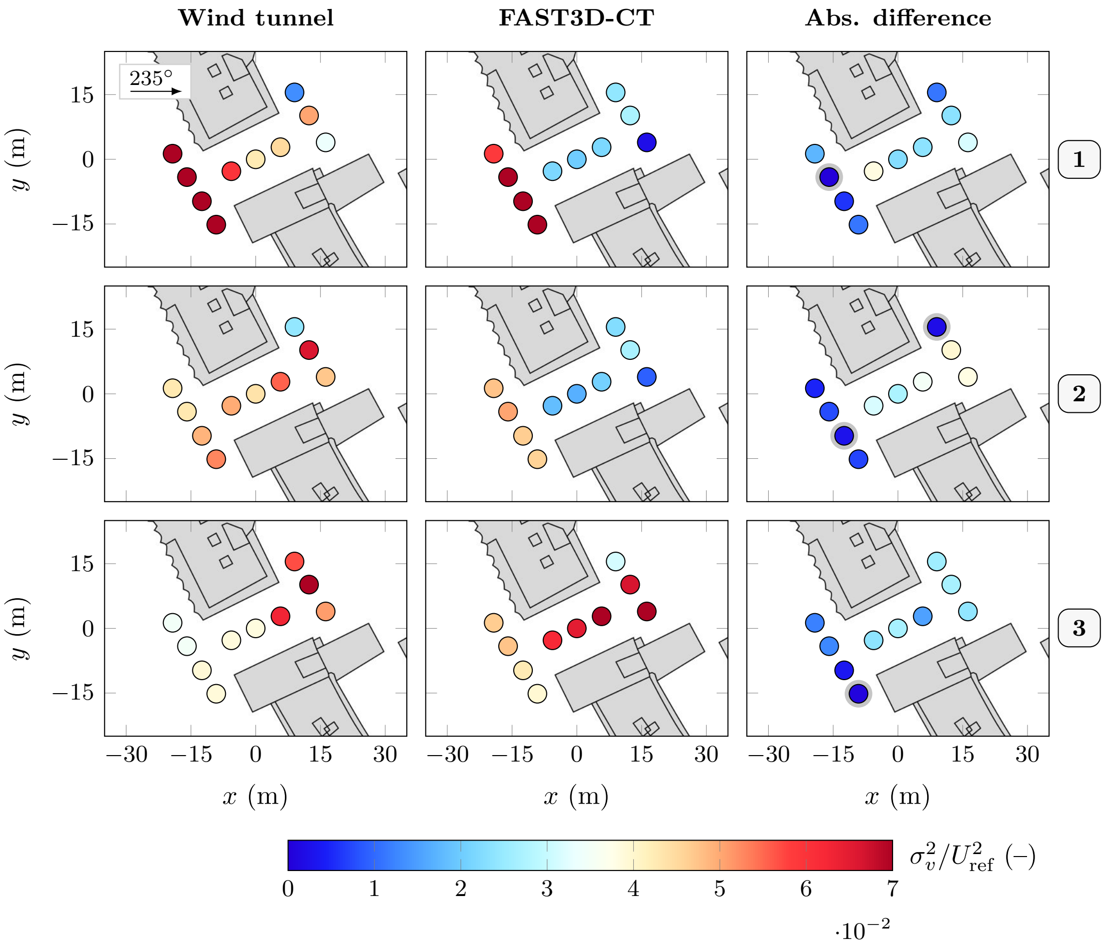

Figure 5.15: Same as in Figure 5.14, but for the local variances of the spanwise velocity component, $\sigma_v^2/U_{\text{ref}}^2$.

FAST3D-CT produces a strong increase of the spanwise variances at the highest comparison level (points *DM09–12* & *DM17*), which is not seen in the laboratory flow in this extent. This, again, could be an indicator that the LES flow at a height of $z = 30.25$ m already corresponds to the readjustment zone between the UCL and the flow conditions above rooftop (cf. also Fig. 5.13, in which the LES velocity vectors have switched toward a more westerly direction), while the laboratory flow at $z = 29.75$ m still appears to be dominated by the canopy layer geometry. The level of agreement between the **lateral turbulent momentum fluxes**, $\overline{u'v'}/U_{\text{ref}}^2$ (Fig. 5.16), is particularly high at the second comparison height. However, unlike the preceding statistics, typical locations of good or bad comparison (prediction quality patterns) cannot really be determined. The weakest congruence is detected at the lowermost level, which corresponds to the first computational level above the surface boundary, at the five locations close to the windward entrance. It should be noted that for the fluxes the interpretation of the absolute differences is not as straightforward, since the shear stress can be positive or negative depending on the dominant composition of the velocity fluctuations and their directions.

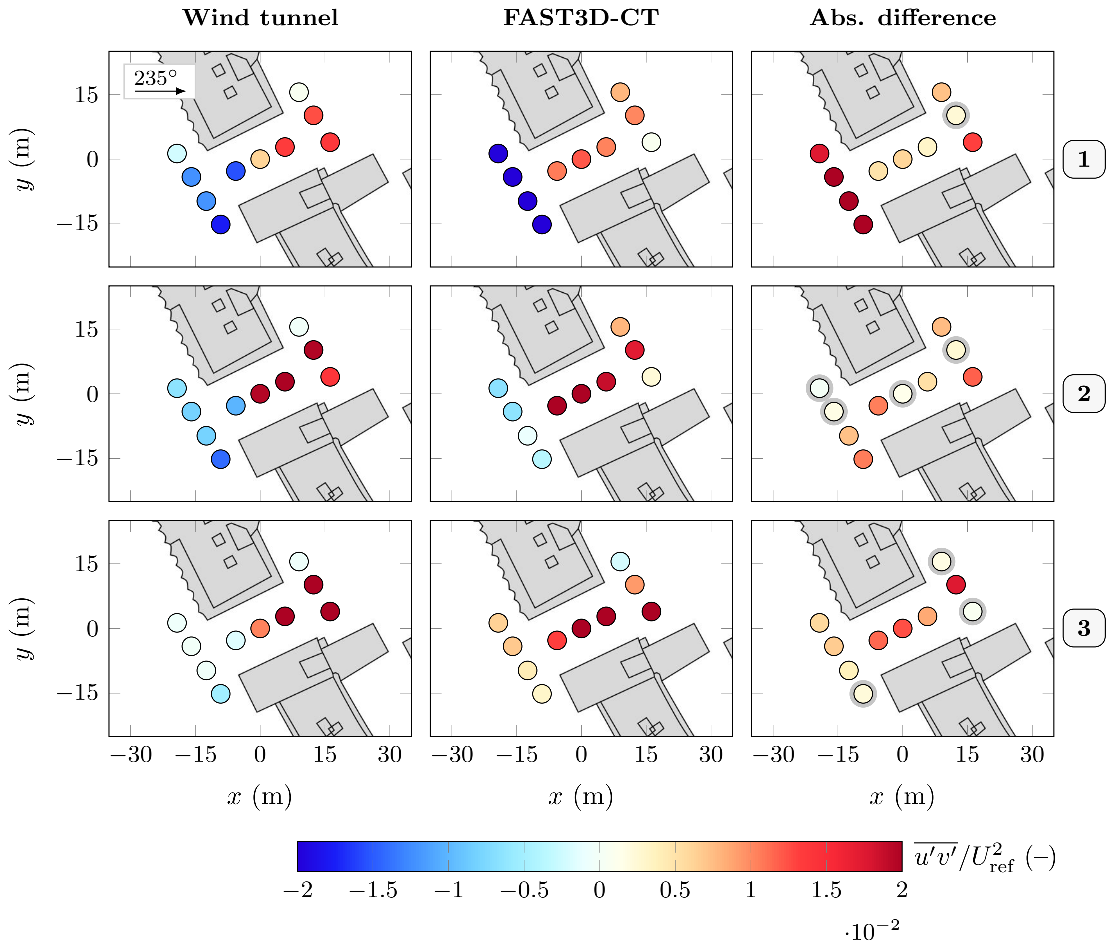

Figure 5.16: Same as in Figure 5.14, but for the lateral turbulent momentum flux, $\overline{u'v'}/U_{\mathrm{ref}}^2$. Note the change of color range for the absolute differences compared with Figures 5.14 and 5.15.

For example, while the absolute difference is small for locations *DM01–04* at the highest comparison elevation, it has to be noted that the lateral fluxes in FAST3D-CT all exhibit an opposite algebraic sign as the wind-tunnel results.

The above comparisons showed that the code is able to accurately represent complex urban flow pattern emerging in the RSL on the mean level at the majority of comparison locations. Characteristic spatial patterns of the vertical and horizontal mean flow and turbulence structure were mostly well captured. Up to this point, the LES validation is not different from the usual validation practice of RANS-based micro-scale meteorological codes, and the exploratory data analysis could be further extended to a more quantitative comparison based on scatter plots and validation metrics (e.g. Oberkampf and Barone, 2006; Britter and Schatzmann, 2007b). Figure 5.17 depicts scatter plots of wind tunnel against FAST3D-CT values for the example of horizontal velocity statistics.

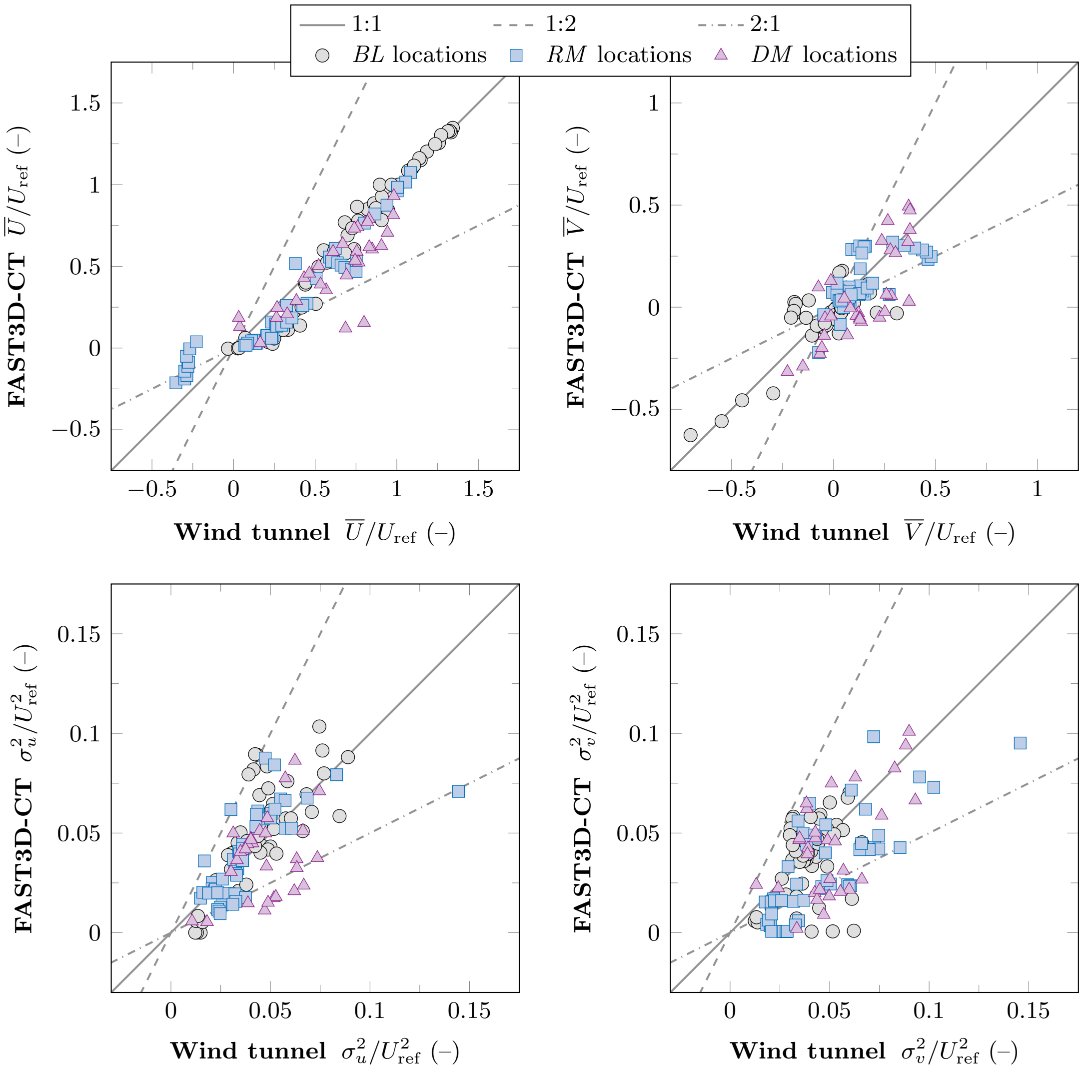

Figure 5.17: Scatter plots of wind-tunnel measurements and the FAST3D-CT simulations for the horizontal flow statistics $\overline{U}/U_{\text{ref}}$, $\overline{V}/U_{\text{ref}}$, $\sigma_u^2/U_{\text{ref}}^2$, and $\sigma_v^2/U_{\text{ref}}^2$, comprising overall 135 data pairs at all 22 comparison locations with maximum vertical offsets of $|\delta z| = 1.38\,\text{m}$ (affecting 7 *BL* points). The gray lines indicate the ideal 1-to-1 relationship and the factor-of-2 margins.

The scatter points correspond to overall 135 experimental and numerical data pairs from the *BL*, *RM*, and *DM* locations that can be directly compared due to comparatively small vertical offsets. This also means that the scatter plots only contain a fraction of the information that has been qualitatively compared in the previous graphs (Figs. 5.2, 5.3, 5.6, and 5.7). The majority of scatter points falls well within the margins of a 1:2 and 2:1 relationship between the experiment and the simulation, which was already determinable from in the previous profile comparisons. The results can be quantified based on *validation metrics* like the *factor of two of observations* (FAC2), which counts the fraction of data points for which the simulation results are within a factor of two of the experimental data ($0.5 \leq a_{\mathrm{les}}/a_{\mathrm{exp}} \leq 2.0$ and a could be any *statistical* quantity). In a next step, *acceptance thresholds* like the typical limit of FAC2 ≥ 0.5 can be used for a binary classification of the simulation quality (cf. e.g. the comprehensive review of typical performance measures and threshold values for atmospheric studies by Chang and Hanna, 2004). However, it has to be kept in mind that the calculation and interpretation of the metric values in some cases need to be optimized in order to guarantee a reliable assessment, e.g. by taking into account the statistical reproducibility of the experimental reference values, by specifying "allowed" ranges of the deviations, or by implementing case distinctions for positions at which $a_{\mathrm{exp}} \simeq 0$ (see discussion in Schatzmann et al., 2010).

Certain conclusions about the global performance quality of FAST3D-CT can be derived from the analyses in the above sections. The results confirm that it is important to evaluate the simulation based on statistics of individual velocity components instead of (or in addition to) the comparison of integrated quantities like TKE or wind speeds. At some of the comparison locations in narrow street canyons (e.g. *BL11*), the grid resolution was probably not fine enough to adequately resolve the flow. Due to the gridding technique used to represent the buildings in the LES (cf. Fig. 4.24a), some of the comparison points might have been virtually dislocated closer to the building facades than it was the case in the experiment (or in the real city). This could explain local tendencies toward an underprediction of velocity magnitudes. The level of detail with which the buildings are captured also depends on the *local* alignment of the geometries within the Cartesian numerical mesh. For more favorably located points that are also in close proximity to geometry elements, the full potential of the LES code could be realized. This is, for example, reflected in the mostly good simulation quality at *BL07* or *BL12*, for which the distances between buildings are quite small (i.e. 20.3 m and 13.5 m, respectively). Another factor influencing the validation are the horizontal offsets between the wind tunnel and LES locations (see Table 4.6), which are potentially of importance in flow regions characterized by a strong building heterogeneity in the (x, y)-plane (particularly relevant for locations *BL10*, *RM09* or *RM10*). Above a height of approximately $3\,\mathrm{H_m}$, FAST3D-CT turbulence statistics still contain signs of the artificial inflow fluctuations, which apparently "survived" at higher elevations due to the weak turbulent mixing with the self-consistent flow simulation below.

In summary, the following conclusions can be made based on the **mean flow analysis**:

- An overall good agreement of the mean flow and turbulence characteristics is determined.
- The representation of buildings through the numerical grid possibly caused discrepancies at locations that are strongly confined by the surrounding urban structure.
- The mismatch of measurement and simulation locations can potentially cause comparison ambiguities for regions with a high flow heterogeneity in the (x, y)-plane.
- Left-overs of artificially generated inflow fluctuations are still contained in the turbulent flow fields at the highest comparison points above approximately $3\,\mathrm{H_m}$.

In the following section, it will be examined which sample characteristics of the instantaneous velocity values are providing the basis for the analyzed mean quantities.

5.3 Frequency distributions

The previous analysis showed that FAST3D-CT has the potential to accurately represent mean flow patterns and turbulence statistics within and above the urban canopy layer for typical flow scenarios. However, unlike RANS simulations, LES does not only provide statistical flow information, but also predicts time-dependent characteristics of the studied scenario in terms of *instantaneous*, turbulent velocity records. A natural approach toward the performance assessment of an LES, thus, is to compare *frequency distributions* of the predicted, time-dependent quantities with those of the experiment. The comparative evaluation of frequency distribution shapes (e.g. skewness, kurtosis, unimodal or bimodal shapes, etc.) and spreads (distribution range, quantiles, etc.) can provide valuable information about the ability of the model to capture local flow features that left their signature in the frequency of occurrence of instantaneous velocities. In the next sections, frequency distributions of numerical and experimental flow quantities are evaluated. The analysis focuses on the comparison of the following quantities:

1. Meteorological wind rose diagrams of $U_h(t)$ and $U_d(t)$ at different heights.

2. Meteorological wind rose diagrams of $U_h(t)$ and $U_d(t)$ at different horizontal locations.

3. Unimodal and bimodal frequency distributions ($U(t)$, $V(t)$, $U_h(t)$, and $U_d(t)$).

4. Shape & spread analyses; outlook on statistical significance tests.

5. Fluctuation time scales of the horizontal wind vector, $\mathbf{U}(x, y, t)$.

The analysis points **1.–3.** center on a mainly qualitative comparison of central tendency, shape, and spread of the velocity distributions at different locations and elevations in the urban domain and on the discussion about the reliability of estimated statistical moments in the case of strongly skewed or multimodal distributions. Under point **4.**, the usefulness and applicability of further graphical and quantitative performance measures for the LES validation are discussed. Part **5.** is concerned with the quantification and comparison of typical fluctuation time scales of the horizontal wind vector in the simulation and the experiment, which provide a bridge between the spread of the wind direction distributions and the time-dependent information contained in the velocity signals.

5.3.1 Histograms of velocity signals

Estimating and comparing probability densities based on empirical frequency distributions of local experimental and numerical velocity records should be an essential ingredient of an in-depth LES validation since this not only allows for a more detailed assessment of the simulation quality, but is helpful in order to determine possible reasons for discrepancies observed in the flow statistics. Based on the conclusions drawn from the mean flow analysis, the following questions can be investigated:

- Accurate mean flow predictions. — *How good is the agreement between the underlying numerical and experimental velocity sample characteristics?*
- Inaccurate mean flow predictions. — *Can reasons for the mismatch on the mean-level be determined from the numerical and experimental velocity sample characteristics?*

In the following paragraphs, frequency distributions of *instantaneous* velocities and derived quantities are graphically compared in order to determine the level of agreement between FAST3D-CT and the wind-tunnel measurements. An analysis of different shape and spread parameters as well as an outlook on the application of classic statistical significance tests is provided in conclusion. For the sake of brevity, results are only displayed for some of the comparison locations. These were selected based on their representativeness for the overall performance assessment and as examples of flow patterns that typically evolve in urban environments. Because of the larger amount of available experimental data inside the canopy layer, the analysis focuses on the comparison of frequency distributions of the *horizontal* velocities. In the following analyses, the raw numerical velocity time series ($f_s = 2\,\mathrm{Hz}$) were compared to the original (i.e. *not resampled*) wind-tunnel velocity records from measurements in U-V LDA mode.

Wind rose diagrams

Figures 5.18–5.24 show meteorological *wind rose diagrams* derived from instantaneous values of horizontal wind directions and wind speeds at seven comparison locations (*BL* and *RM*), at heights in which the numerical and experimental time series can be directly compared due to relatively small vertical offsets. The displayed selection encompasses comparison points featuring high and low agreements between the experimental and numerical mean flow results. The wind rose histograms are constructed from time-dependent records of $U_h(t)$ and $U_d(t)$, derived from Eqs. (5.1) and (5.2). The wind roses display the frequency at which certain wind-speed ranges (color-coded bands) were observed from the respective wind direction bandwidths. This display offers the advantage of a paired, simultaneous analysis of both quantities. The direction in which a particular spoke of the wind rose is pointing, indicates the direction *from* which the horizontal wind is blowing with a certain percentage frequency that is specified by increasing radii of the concentric circles. In all graphs, one wind rose bar represents a 10° wind-direction band. The horizontal wind speeds, referenced by U_{ref}, are divided into six equally spaced bins. For a better orientation, vertical profiles of the mean wind direction and the horizontal velocity components shown in Section 5.1 are once more displayed for the comparison points, together with an indication of heights in which the frequency distributions are evaluated.

As can be seen in the profiles of $\overline{U}_d(z)$ at the intersection location ***BL10***, up to approximately $2\,\mathrm{H_m}$ distinct offsets between the experiment and FAST3D-CT are recognizable. These are mainly related to deviations between the mean *spanwise* velocity components. This disagreements is also reflected in the wind rose diagrams at the first and third comparison levels (Fig. 5.18), for which differences in $\overline{V}/U_{\mathrm{ref}}$ are largest. At the second comparison height, however, both the mean flow and the characteristics of the underlying velocity samples exhibit a very high level of agreement. Both wind roses feature a clear (positive) skewness toward westerly wind directions, while the mass of the distribution is centered at southwesterly winds, for which a larger fraction of strong wind speeds is observed.

At the first comparison level of the street-canyon location ***BL11*** (Fig. 5.19), the wind rose diagrams confirm the different flow *channeling* directions seen in the wind tunnel and the numerical simulation, with the latter also showing significantly reduced wind speeds.

Interestingly, the overall shapes of both distributions are otherwise rather similar, and in both data sets a slight *bimodal shape* of the wind direction distribution is evident. The upstream building is composed as a step-down notch with heights of 40 m and 23 m, respectively, so that the direct influence of the geometry representation on the LES prediction is strongly mitigated at the second comparison height ($z_{\mathrm{exp}} = 28\,\mathrm{m}$). The broadening of the flow path and the proximity to the rooftop of the downstream building (approx. 29 m) create complex flow patterns that are mirrored in the wind roses. In both data sets, the flow location is characterized by circulating winds, which exhibit two peak directions roughly corresponding to the SE–NW orientation of the street canyon. The agreement between the FAST3D-CT and the wind-tunnel frequency distributions is remarkably good. The occurrence of such multimodal distributions of flow quantities also has to be evaluated with respect to the applicability of standard measures of central location like the *mean* (as used in this comparison study) and the *median*, or of common spread measures like the *standard deviation*. If a distribution contains more than one *mode*, the results of descriptive statistics can be deceptive.[3] As illustrated by the wind rose histograms at the second comparison height, the *arithmetic averages* of the wind tunnel and FAST3D-CT wind directions with values in the range of $270° - 280°$ are more indicative of the separation region between the two peaks rather than for the true nature of the flow as reflected in the two centers of mass of the distributions.

A high level of congruence between the wind rose diagrams is also observed at the street canyon and intersection locations ***BL12*** and ***RM03*** (cf. Figs. 5.20 and 5.21). At the lowest comparison points, however, the lower magnitudes of the horizontal wind speeds in the numerical simulation are characterizing the histograms. For position *BL12*, the spreads of the FAST3D-CT wind roses at the lowest heights within the street canyon tend to be smaller than observed in the laboratory (cf. comparison height 1; Fig. 5.20). This could be a result of the LES geometry representation (i.e. virtually narrowed street canyons and stronger laterally confined flow) and/or be connected to the grid size and the potential to resolve relevant eddy structures. With $h_i = 2.5\,\mathrm{m}$, the true variability of the street-canyon flow may not be adequately captured.

Another interesting location for the histogram comparison is point ***RM07***, where wind roses are compared for three heights just above roof level (cf. Fig. 5.22; local building heights are 32 m). As the flow readjusts to the approach flow conditions above the urban canopy, a strong broadening of the wind direction histograms together with an indication of complex bimodal patterns emerge. Both the LES and the wind-tunnel data show a distribution width that spans the entire 180° SE/NW sector. With reference to the vertical profile of $\overline{U}_d(z)$ at this location, differences between the arithmetic averages at a height of $z_{\mathrm{exp}} = 33.25\,\mathrm{m}$ probably reflect the differently pronounced peaks in the bimodal wind-direction distributions. While the wind-tunnel measurements indicate a dominance of westerly over southerly winds, the LES predicts the reversed case.

The presence of a bimodal pattern in the wind-direction distributions also affects the results at location ***RM10***, where the ambivalence of the prevailing canopy layer winds is clearly mirrored in the wind rose plots of the laboratory data (cf. Fig. 5.23).

[3]Here the term *mode* denotes the most frequently occurring value (or values within a certain value range given by the bin size used to construct the histogram) within the empirical frequency distribution.

Wind roses – location *BL10*

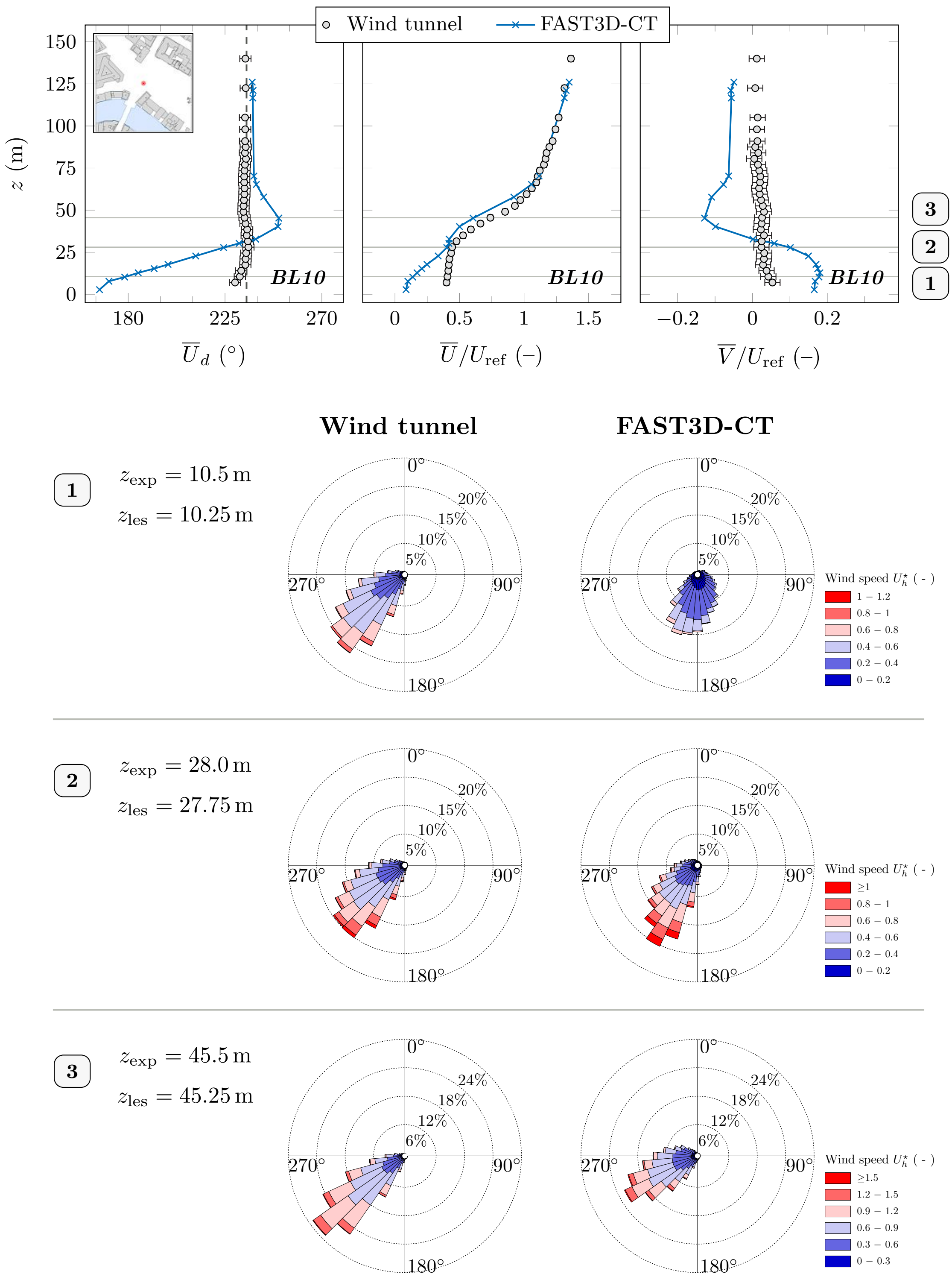

Figure 5.18: Wind rose diagrams of dimensionless horizontal wind speeds ($U_h^\star = U_h/U_{\mathrm{ref}}$) and directions in three heights at location *BL10*.

Wind roses – location *BL11*

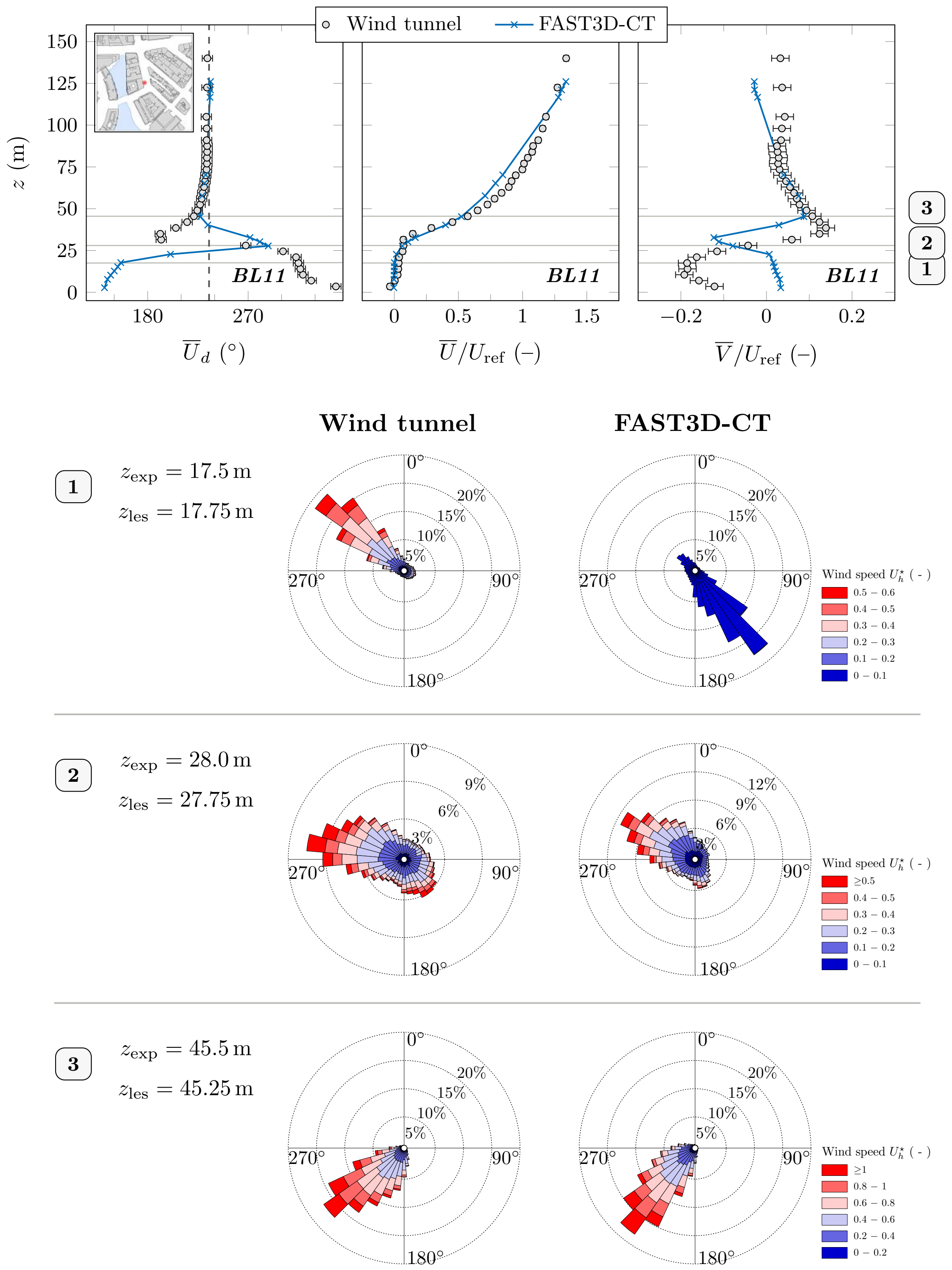

Figure 5.19: Same as in Figure 5.18, but for three comparison heights at location *BL11*.

Wind roses – location *BL12*

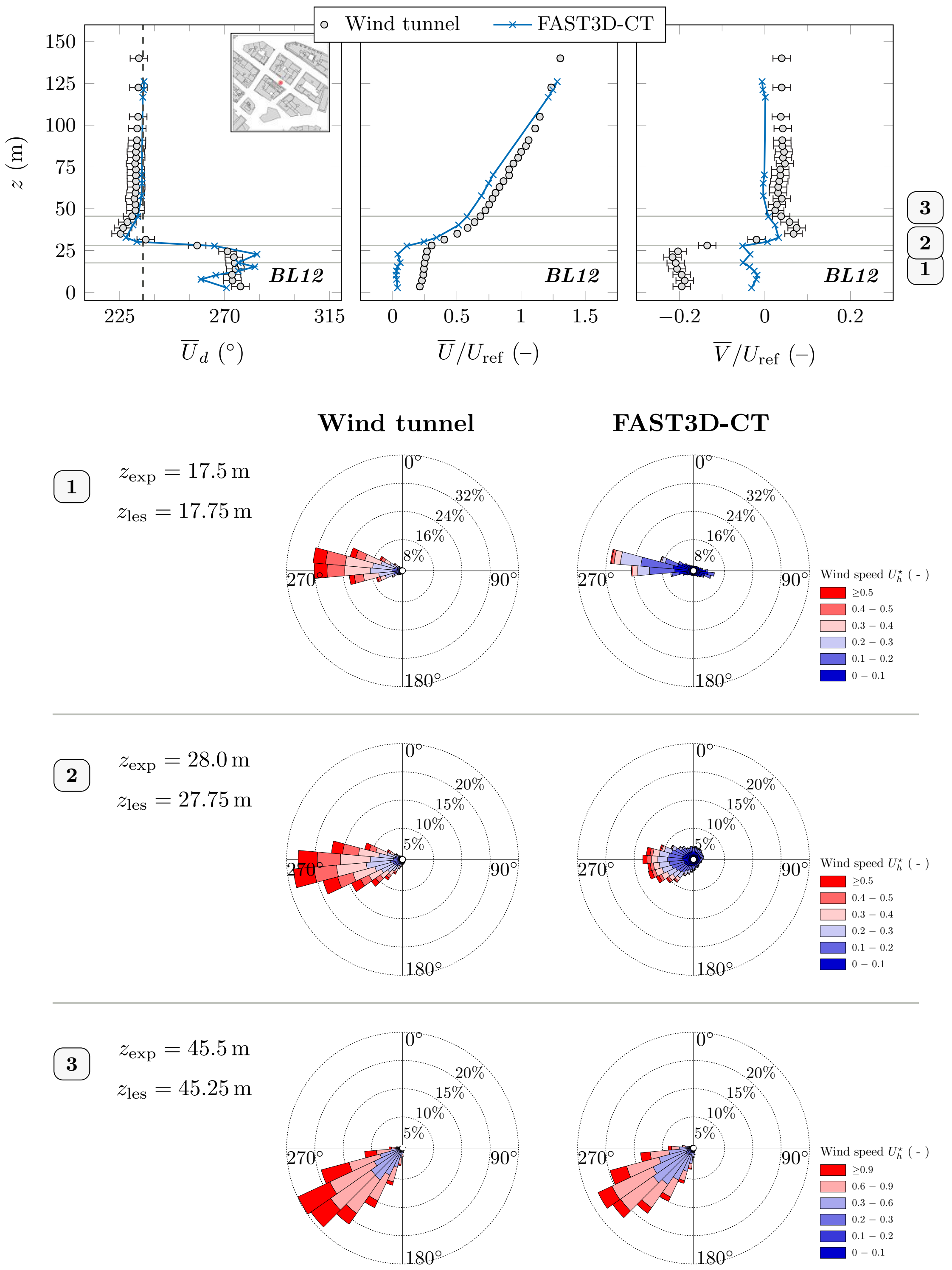

Figure 5.20: Same as in Figure 5.18, but for three comparison heights at location *BL12*.

Wind roses – location *RM03*

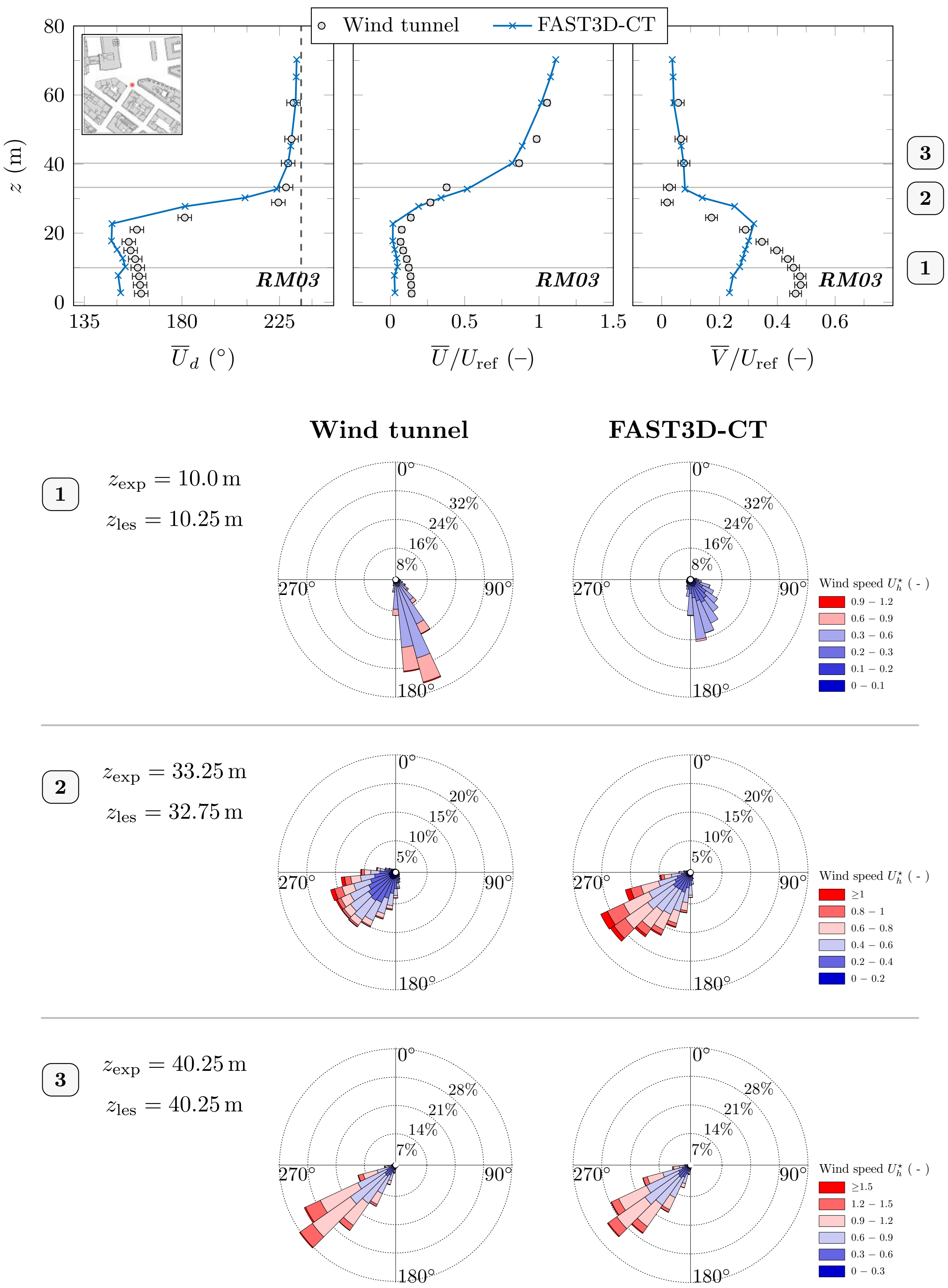

Figure 5.21: Same as in Figure 5.18, but for three comparison heights at location *RM03*.

Wind roses – location *RM07*

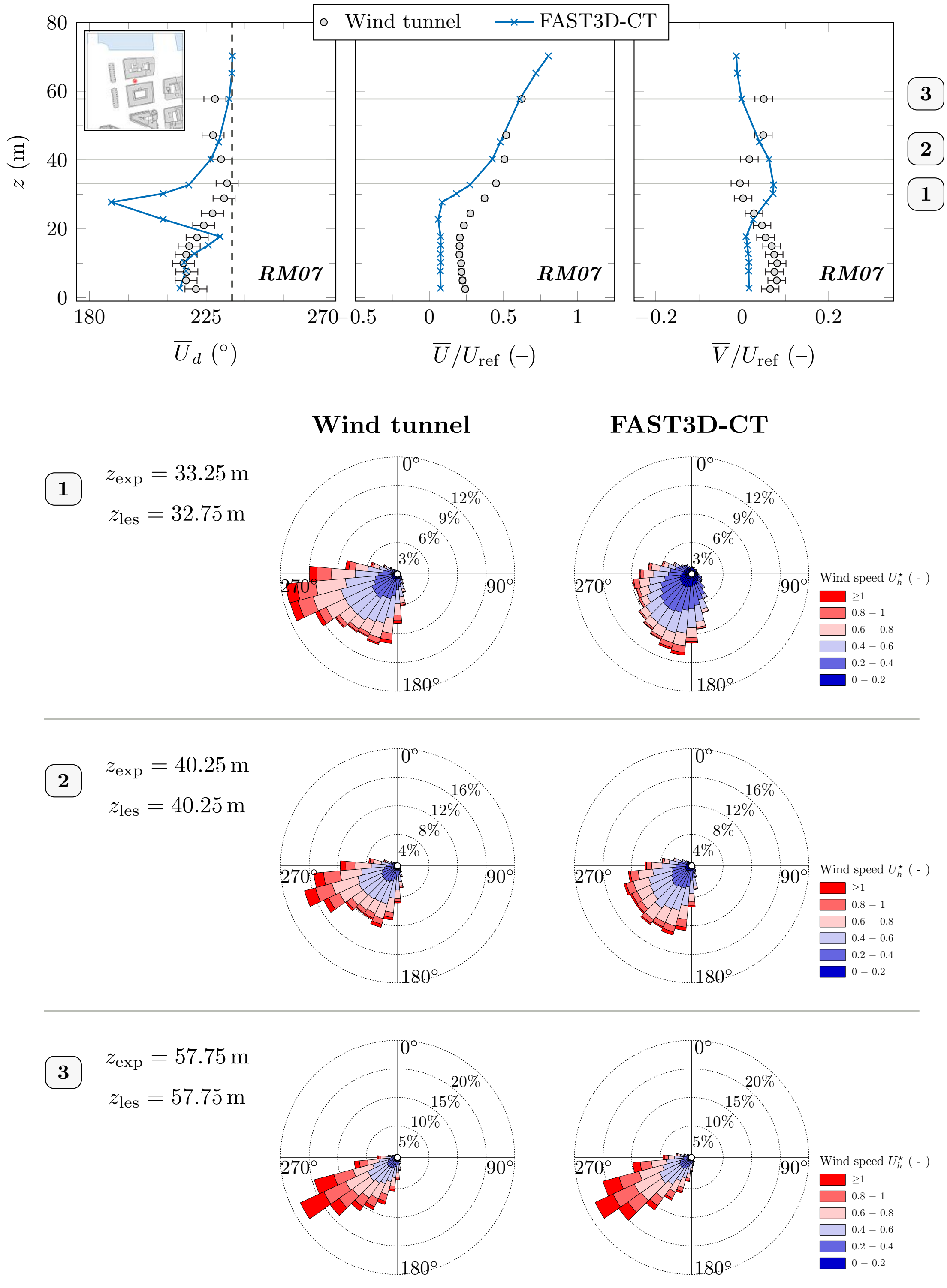

Figure 5.22: Same as in Figure 5.18, but for three comparison heights at location *RM07*.

Wind roses – location *RM10*

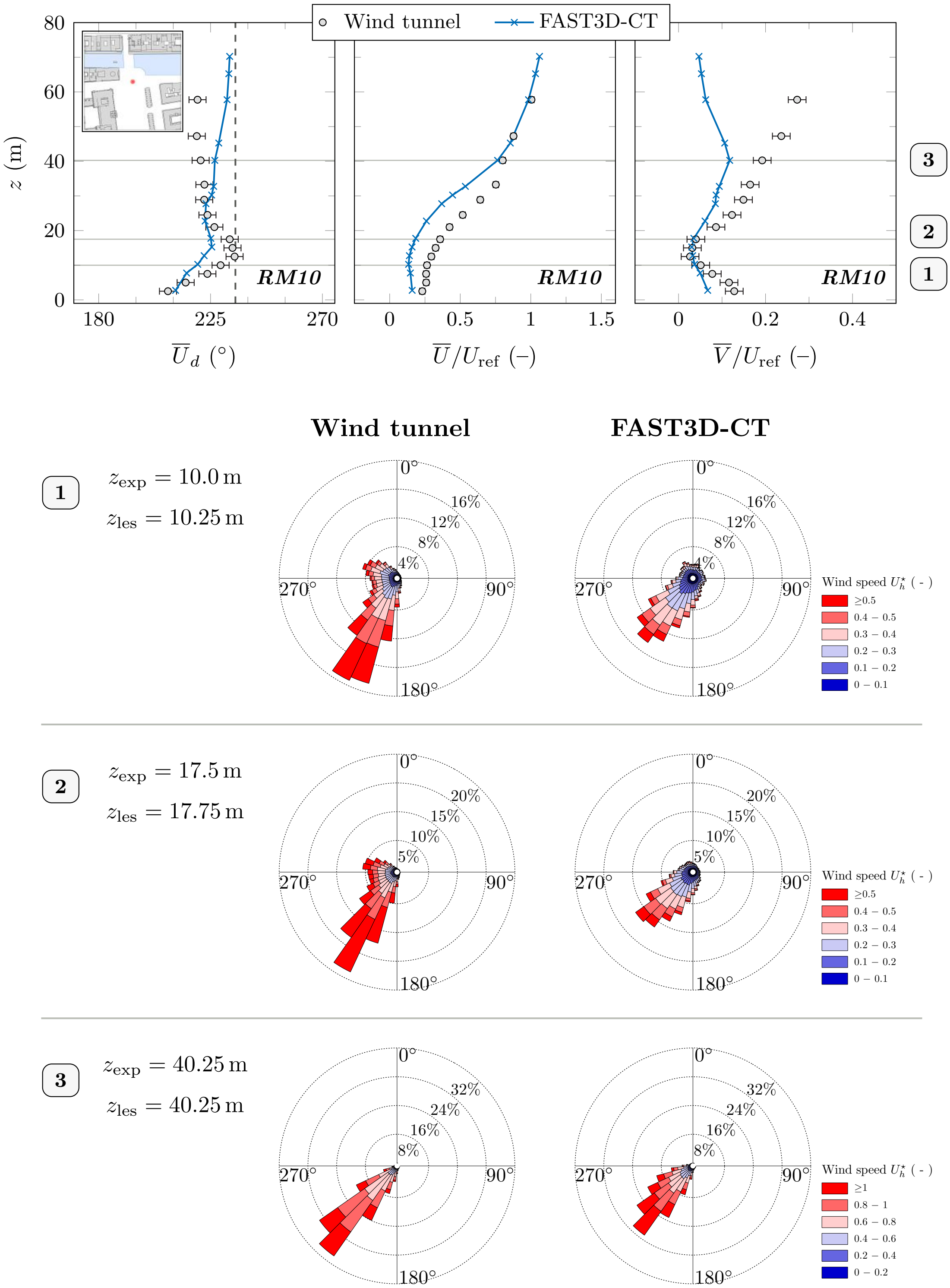

Figure 5.23: Same as in Figure 5.18, but for three comparison heights at location *RM10*.

In the wind tunnel, the flow field is influenced by winds coming from the plaza (dominant SSW wind direction peak) and – to a lesser degree – from the canal in the northeast. Rather than in a two-peak pattern, the flow complexity in the LES is captured by circulating winds in connection with a single pronounced direction peak corresponding to southwesterly winds. As discussed in the mean flow analysis, these offsets may result from slight differences in the horizontal locations of the wind tunnel and LES data pairs. Such spatial dislocations can be of importance in very heterogeneous flow situations.

For the plaza position on the leeward side of the city hall (***RM09***), wind roses are compared at six different heights above ground (see Fig. 5.24). Up to the highest comparison level of 57.75 m (approx. 1.68 H_m), the flow is considerably influenced by the laterally distorted recirculation zone evolving behind the city hall, which has an *average* local building height of approximately 40 m and a steeple with a height of 112 m. While the flow on the plaza is primarily controlled by the blockage effect of the main building, the comparison point is also influenced by the wake flow behind the tower.[4]

The lowermost comparison points within the UCL are characterized by relatively small vertical gradients of the flow field. As can be seen in the wind roses, the agreement between the observed and simulated spreads of the wind directions as well as between the wind speed distributions is very good, despite the fact that the centers of the histograms exhibit a slight offset of about 30° (cf. also the height profiles of $\overline{U}_d$). The level of congruence is reduced in the vicinity of the rooftop (comparison heights 4 & 5), where the LES predicts a faster readjustment to the ambient flow than is encountered in the wind-tunnel data. In a height of $z_{\mathrm{exp}} = z_{\mathrm{les}} = 40.25$ m, FAST3D-CT shows a bimodal wind direction distribution (dominance of northwesterly and southerly winds), caused by the flow deflection behind the city-hall tower. In the laboratory, this characteristic is first seen in the wind rose diagram associated with the highest measurement elevation of 57.75 m. As previously discussed, exactly matching the flow characteristics of this comparison scenario makes high demands on the boundary conditions in terms of the building representation in the physical and numerical model as well as on the agreement of the flow locations, which unfortunately was actually poorest for this point (1.27 m horizontal distance between experimental and numerical analysis sites; cf. Table 4.6).

In a similar way, wind rose diagrams are consulted to evaluate the LES quality based on characteristics of instantaneous velocities for the horizontally resolved flow in the courtyard entrance at all three comparison heights (***DM*** locations). Results are depicted in Figures 5.25 to 5.30. It has to be noted that the placing of the wind rose diagrams within the geometry contours is merely indicative of the actual measurement and simulation locations in order to avoid overlapping and allow for a clearer display. Hence, it is also refrained from displaying the x and y-axes as, e.g., in Figure 5.11. For the true locations of the comparison points, reference is given to Figure 4.28. For the same reasons, the percentage circles of the wind direction bars are omitted. However, since for each of the experimental and numerical data pairs the same percentage range has been used, the results remain comparable (i.e. the length of the respective wind rose bars can be directly compared between the wind tunnel and FAST3D-CT at each point).

[4]This element has an approximate dimension of $14 \times 14\,\mathrm{m}^2$ in the (x, y)-plane, so that the steeple fronts are represented by the blocking of six to seven computational cells along the horizontal axes.

Wind roses – location *RM09*

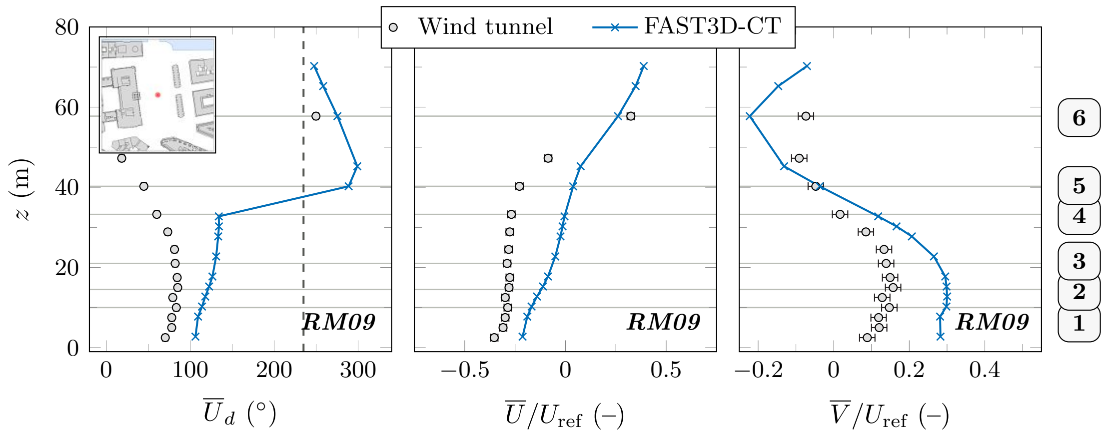

Wind tunnel | **FAST3D-CT**

1 $z_{\mathrm{exp}} = 10.0\,\mathrm{m}$ $z_{\mathrm{les}} = 10.25\,\mathrm{m}$

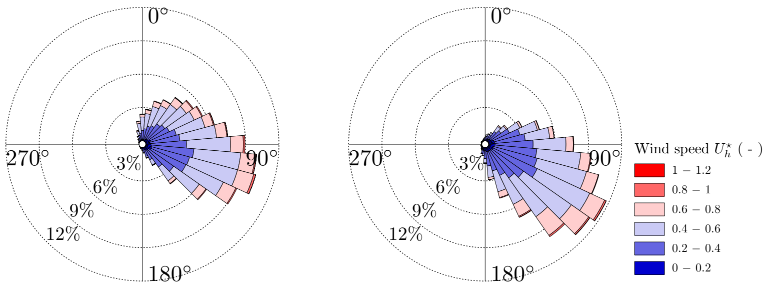

2 $z_{\mathrm{exp}} = 14.5\,\mathrm{m}$ $z_{\mathrm{les}} = 15.25\,\mathrm{m}$

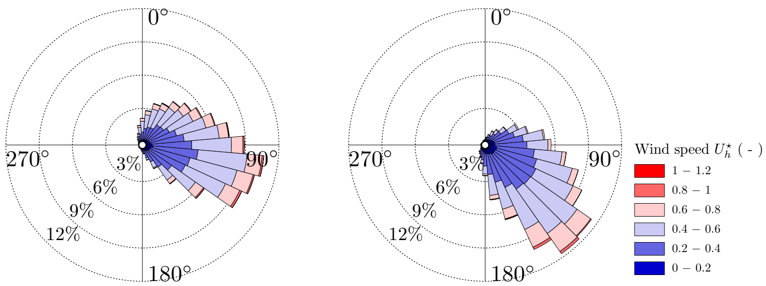

3 $z_{\mathrm{exp}} = 21.0\,\mathrm{m}$ $z_{\mathrm{les}} = 22.75\,\mathrm{m}$

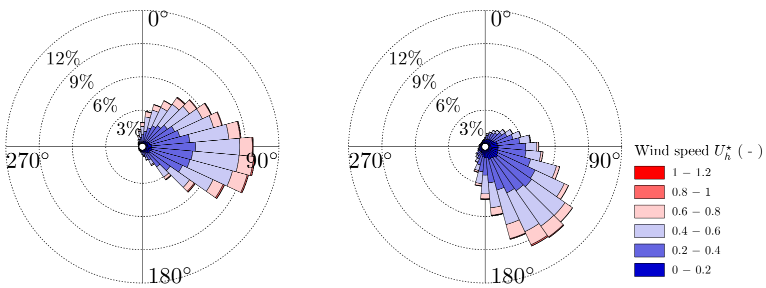

Figure continues on next page.

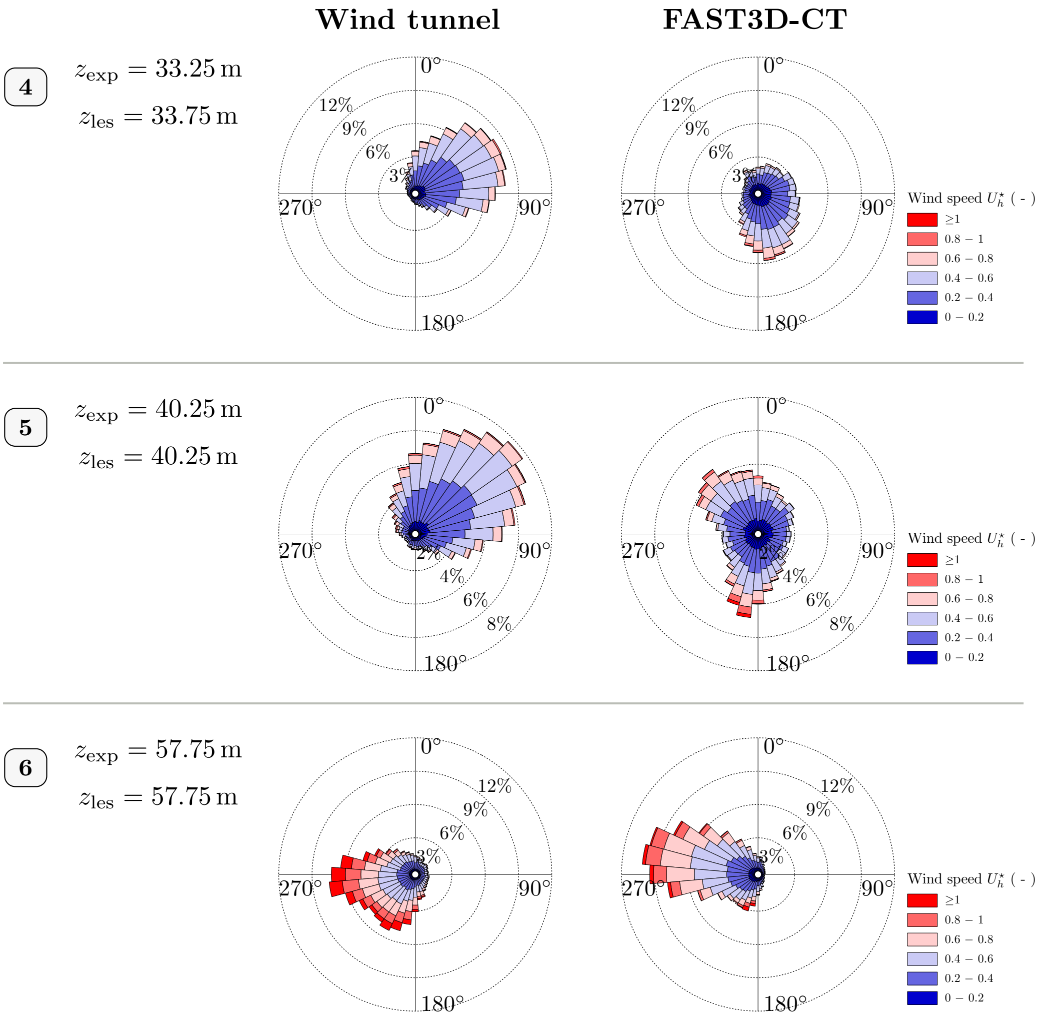

Figure 5.24: Same as in Figure 5.18, but for six comparison heights at location *RM09*.

Figures 5.25 and 5.26 show wind rose fields at the first comparison level as retrieved from both data sets. At the two lowermost comparison points on the windward side of the building complex, the laboratory and the LES histograms reflect sophisticated flow patterns, expressed in very broad experimental distributions and two-peaked LES wind roses. Despite these rather different sample characteristics, both distributions result in comparable wind direction *averages*, as documented in the comparison graphs of the mean wind vectors (see Fig. 5.11, Section 5.2.2). The informative content of these averages, hence, is questionable. At points *DM09* and *DM18*, the larger offsets observed in the mean flow are further punctuated by the wind roses, whose shapes confirm the assessment that the representation of buildings and/or the proximity of the LES data extraction points to the building walls play crucial roles for the evaluation.

Discrepancies at the passage exit are also evident at the second comparison level (Figs. 5.27 and 5.28), in which the vertical offsets between the flow locations are largest.

Wind roses – first height *DM* locations

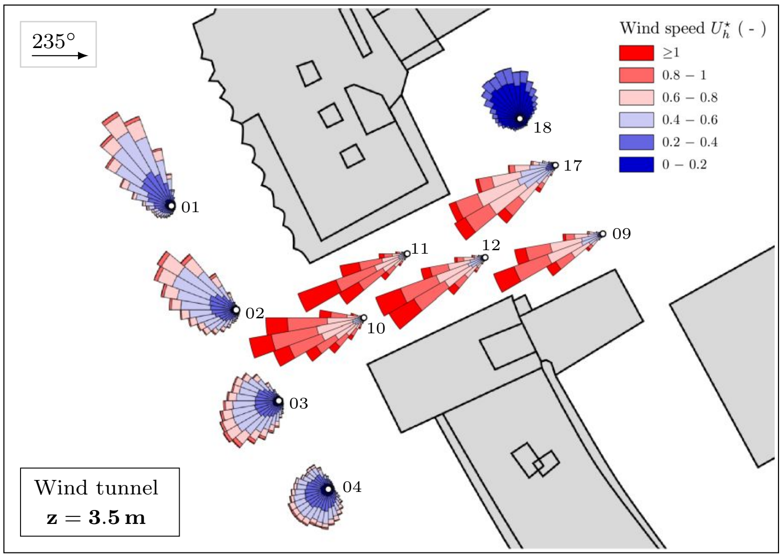

Figure 5.25: Wind rose diagrams of wind-tunnel wind speeds and directions at the *DM* locations in a height of 3.5 m. Note that the positions of the wind roses are *not* true to the exact (x, y) locations documented in Figure 4.28, but are shifted for a clearer display. The flow is approaching from the left.

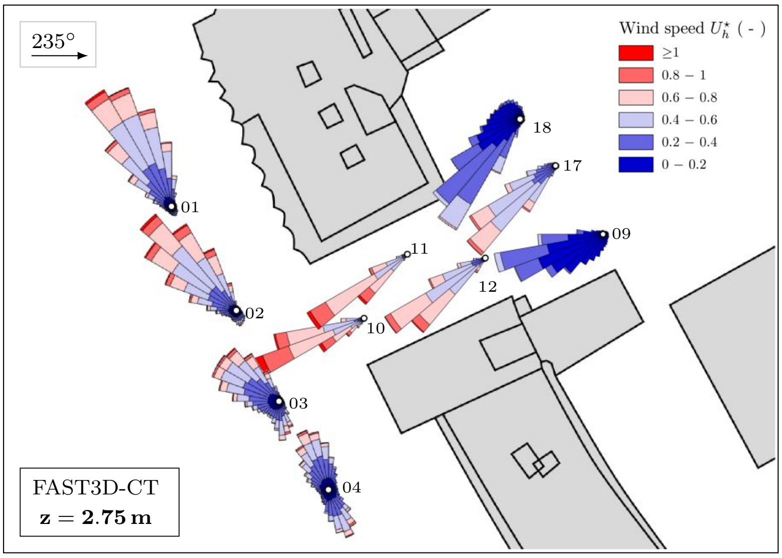

Figure 5.26: Wind rose diagrams of FAST3D-CT wind speeds and directions at the *DM* locations in a height of 2.75 m. As in Figure 5.25, the histogram locations are merely indicative of the exact comparison points.

The agreement at points *DM01–04*, however, has strongly improved, which could result from the decreased influence of the bottom boundary condition on the LES flow.

Wind roses – second height *DM* locations

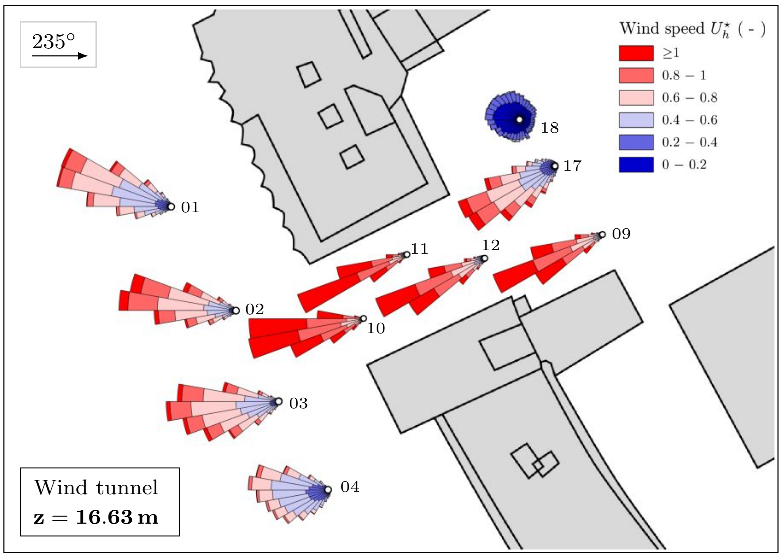

Figure 5.27: Same as in Figure 5.25, but for a height of 16.63 m.

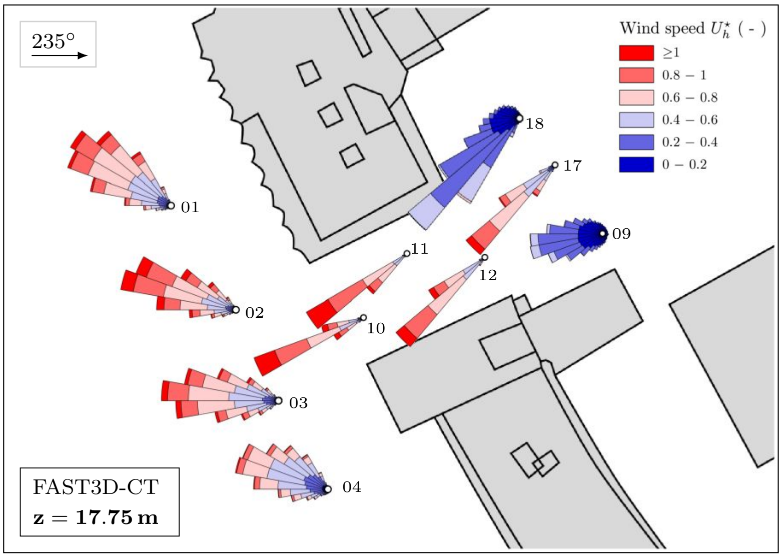

Figure 5.28: Same as in Figure 5.26, but for a height of 17.75 m.

Another notable feature of the LES flow is the very narrow width of wind direction distributions together with lower wind magnitudes within the alleyway. At position *DM11*, for example, the majority of instantaneously occurring wind directions is contained in a 20° wind angle range (i.e. covered by only two wind rose bins). While a reduction of the lateral flow variability is also discernible in the experiment, this effect is more pronounced in the LES (see also the low magnitudes of $\sigma_v^2/U_{\mathrm{ref}}^2$ displayed in Fig. 5.15).

Wind roses – third height *DM* locations

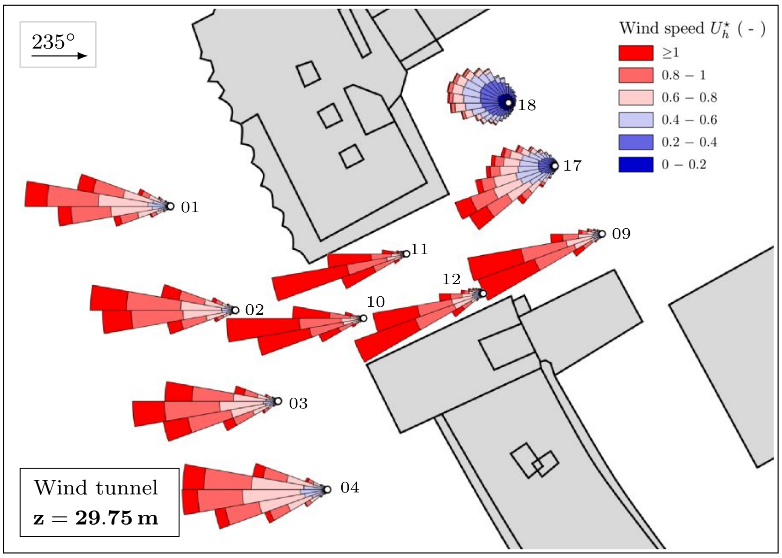

Figure 5.29: Same as in Figure 5.25, but for a height of 29.75 m.

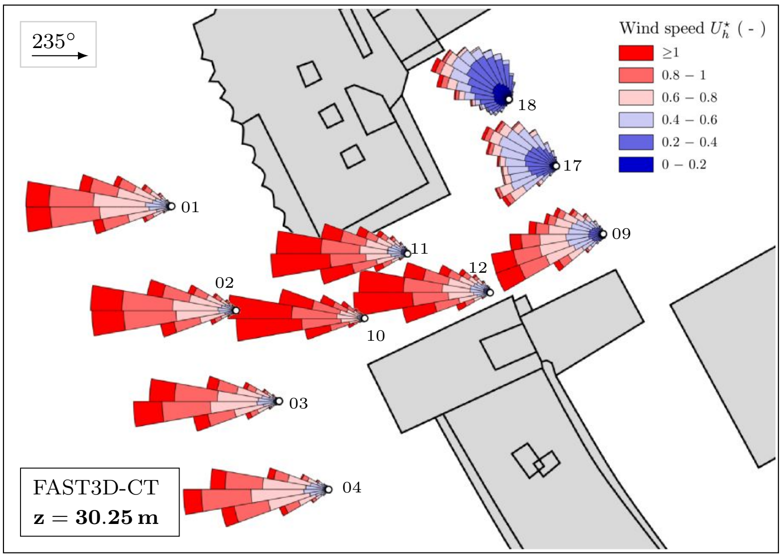

Figure 5.30: Same as in Figure 5.26, but for a height of 30.25 m.

For other street-canyon configurations (notably *BL11*, *BL12*, and *RM07*), similar tendencies toward a decrease in the lateral fluctuation intensities within the UCL are observed in the turbulence statistics and velocity distributions. As speculated earlier, such features are presumably associated with effectively smaller LES street-canyon widths as a result of the gridding technique. At the lowest comparison level, this effect is probably mitigated by the proximity to the surface and its influence on the flow structure.

Just in the vicinity of the rooftops, the level of agreement has further increased, particularly at the windward and leeward passage exits (cf. Figs. 5.29 and 5.30). However, an amplified spread of the wind direction histograms in FAST3D-CT is determined for the alleyway positions *DM09–12*. Here, the observed readjustment toward the mean approach flow direction is not evident in the wind-tunnel data. In agreement with the interpretation of the time-averaged horizontal wind vectors (Fig. 5.13), the results most likely reflect slight height offsets between numerical and experimental data pairs in combination with the existence of strong vertical flow gradients.

Distribution characteristics

The previous paragraphs showed that the analysis of frequency distributions of predicted flow quantities can provide valuable insight into the performance quality of time-dependent simulations and is helpful for a more wide-ranging interpretation of the mean flow results. As the comparison of wind-rose histograms highlighted, a high level of agreement of the time-averaged flow field is not in all cases accompanied by coinciding frequency distributions of the underlying instantaneous data samples (e.g. in case of bimodal distributions). The visual (i.e. qualitative) analysis of the shape and spread of experimental and numerical frequency distributions in the context of an LES validation can be supported by a quantitative comparison of high-order statistical moments like *skewness* and *kurtosis*. In addition, quantitative information about the distributions can be directly compared by visualization techniques like *boxplots* or *quantile-quantile graphs*, which visualize standard descriptive statistics. Furthermore, well-established statistical *significance tests* are available to quantify the level of agreement between two data sets based on their sample characteristics.

The practicality, relevance, and caveats of such approaches will be addressed in the following paragraphs. First, it is started from an in-depth comparison of component-wise frequency distributions as an extension of the preceding analysis of wind roses.

Component-wise histograms As illustrated in the previous section, wind rose plots have the advantage of a simultaneous display of horizontal wind direction distributions and the associated frequencies of occurrences of certain wind magnitudes in a certain wind sector. Drawbacks of this comparison approach, however, are connected to the fact that derived statistics like U_h and U_d can obscure the characteristics of the underlying velocity components (cf. discussion in Section 5.2.1). While being particularly illustrative for point-wise comparisons and allowing for an easy classification of flow features with reference to the building alignments, the display in polar coordinates can also hamper the appreciation of details of the distribution characteristics in some cases. Particularly for locations, at which the flow exhibits sophisticated patterns in the frequency of occurrence of certain velocity ranges, a further evaluation of component-wise histograms can be of interest. Figures 5.31–5.36 show examples of such composite analyses of individual velocity components and derived flow quantities for some of the comparison points analyzed earlier by means of wind rose diagrams. Frequency distributions of instantaneous velocities (U/U_{ref}, V/U_{ref}, and U_h/U_{ref}) were constructed using 100 bins. For the wind direction histograms (U_d/U_{ref}), 180 bins corresponding to a 2° wind angle bandwidth are used.

Figures 5.31–5.34 display velocity distributions in which **bimodal patterns** emerged in the horizontal wind direction analysis of the wind-tunnel time series and in some of the cases also in the FAST3D-CT predictions. Such sophisticated flow features reflect the inherent unsteadiness of the urban wind field and are *candidate scenarios* on the basis of which the capabilities of eddy-resolving models can be evaluated. Bimodality often reflects a random *switching* of the mean flow from one into the another regime over time scales that are long enough to produce characteristic peaks in the amplitude histograms, i.e. it is usually *not* a direct feature of the low-frequency *turbulent* variability. In built-up areas, such a switching can, for example, be associated with flow channeling into street canyons from different directions or the switching of the prevailing flow direction at a street corner from one side to the other. Unlike steady CFD models of the RANS-type, LES should be able to capture these features (cf. discussion in Hertwig et al., 2012).

At points *BL11* and *RM09*, the agreement of the bimodal wind direction patterns seen in the experiment and the LES is excellent and accompanied by a strong overlap of the *centers of mass* of the frequency distributions of U/U_{ref} and V/U_{ref}. Although the congruence of the distribution shapes of the horizontal velocities is clearly weaker at location *RM09* (Fig. 5.33) as compared to *RM07* (Fig. 5.32), the ambivalence of the prevailing wind direction is better captured by the LES in the former case. This indicates that the potential to simulate multimodal flow behavior is to a large extent coupled to the level of accuracy, with which the *location* of the individual velocity distributions is captured (e.g. measured by the mean or the median). As can be seen at *BL11*, *RM07*, and *RM09*, the occurrence of a double-peaked frequency distribution of U_d is not necessarily associated with a bimodal shape of either of the underlying velocity distributions. Instead, this pattern frequently originates from *unimodal* distributions of U/U_{ref} and V/U_{ref} that do not even feature an excessive skewness or other remarkable characteristics (see, for example, the rather Gaussian distributions of the horizontal velocity components at *BL11*; Fig. 5.31). In other cases, as illustrated on the basis of point *RM10* (Fig. 5.34), a bimodal distribution shape can also occur for U_d and one of the horizontal velocity components (here for V/U_{ref}). As was already evident in the wind rose diagram at this location, the simulation does not reproduce these features, but predicts unimodal distributions.

Figures 5.35 and 5.36 show examples of **essentially Gaussian** (*BL12*) and **strongly skewed** (*DM18*) velocity and wind direction histograms. At location *BL12*, where the time series are extracted at a height above rooftop, the agreement of the distributions is remarkably good – particularly for the lateral velocity component as well as for the horizontal wind direction. At the recirculation position *DM18*, comparatively large differences of the distribution shapes are evident for U/U_{ref} and U_h/U_{ref}, which are, however, not reflected in the associated mean values. Hence, while the distribution offsets at *BL12* would be *visually* appraised as *practically insignificant*, the opposite would be assumed for *DM18*. However, for both of the positions the *statistical significance* of the differences between the experiment and FAST3D-CT is evaluated as *high* on the basis of well-established two sample hypothesis tests. Like the informative value of summary statistics like the mean and standard deviation is deceptive when the underlying sample distribution is bimodal, the application of significance tests for model evaluation purposes has some important caveats that impede the statistical *quantification* of the simulation accuracy based on instantaneous data. These issues will be further discussed in the following paragraphs.

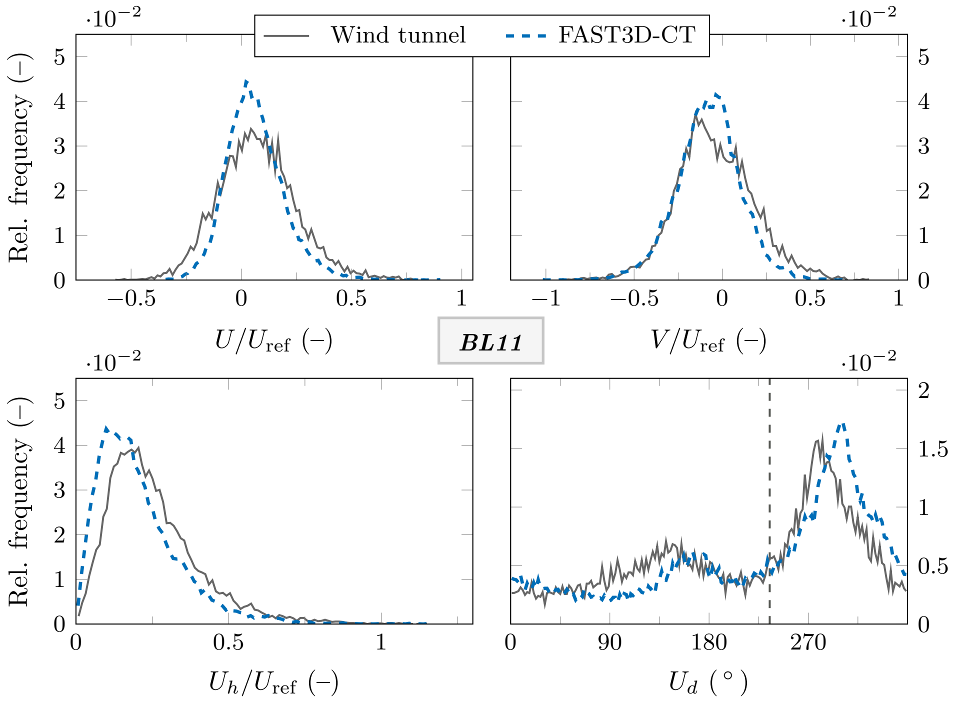

Figure 5.31: Frequency distributions of horizontal velocities, wind speeds and directions at location *BL11* in heights of 28.0 m/27.75 m (wind tunnel/FAST3D-CT).

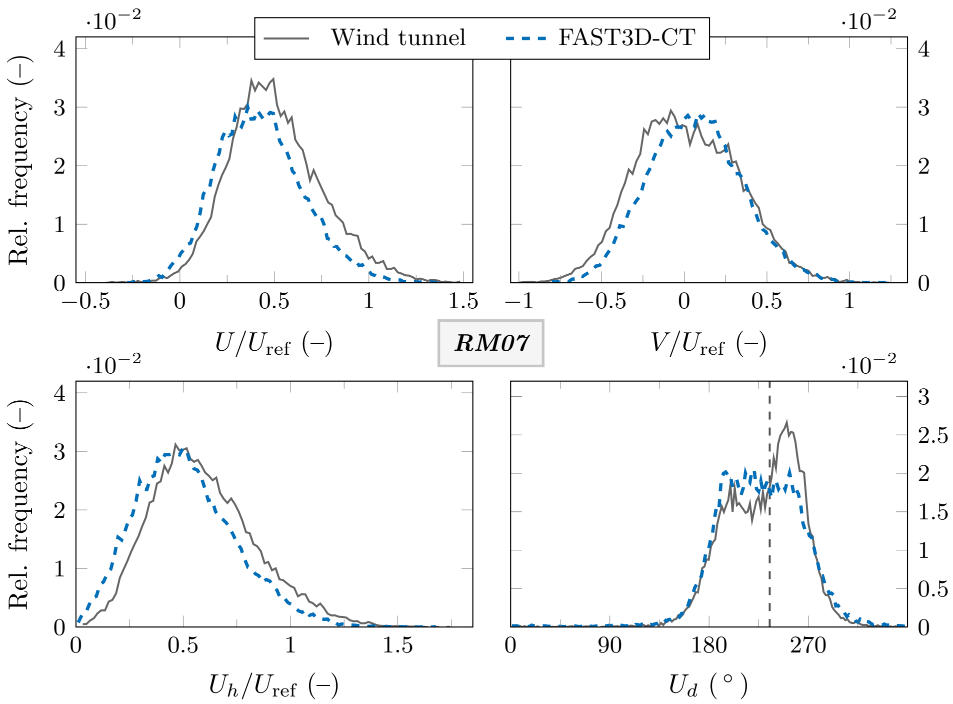

Figure 5.32: Same as in Figure 5.31, but for location *RM07* in a common height of 40.25 m in the wind tunnel and FAST3D-CT.

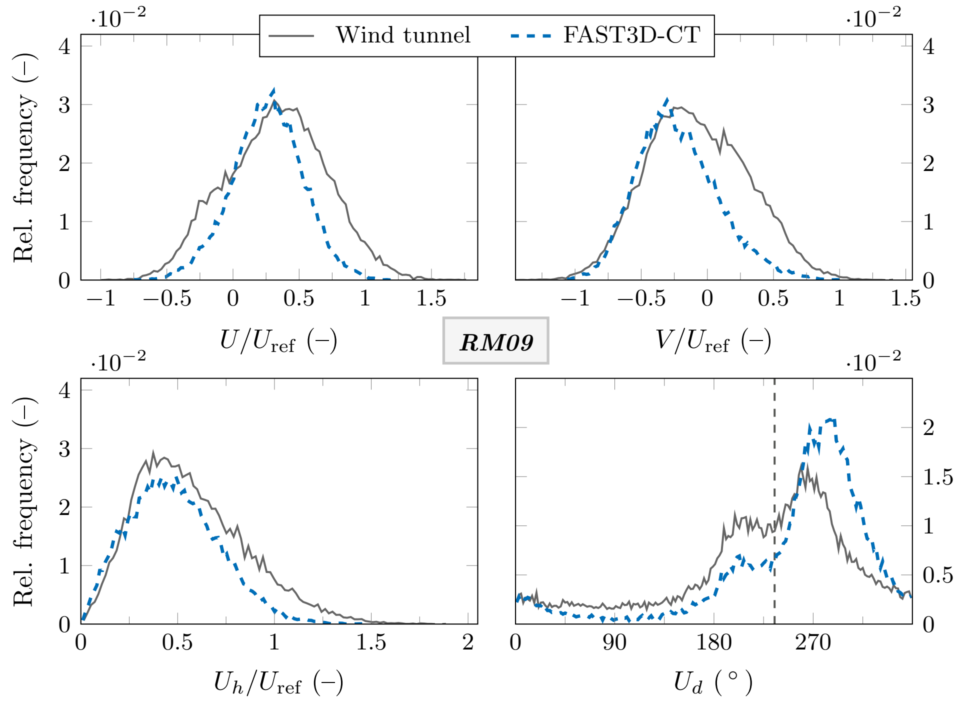

Figure 5.33: Same as in Figure 5.31, but for location *RM09* in a common height of 57.75 m in the wind tunnel and FAST3D-CT.

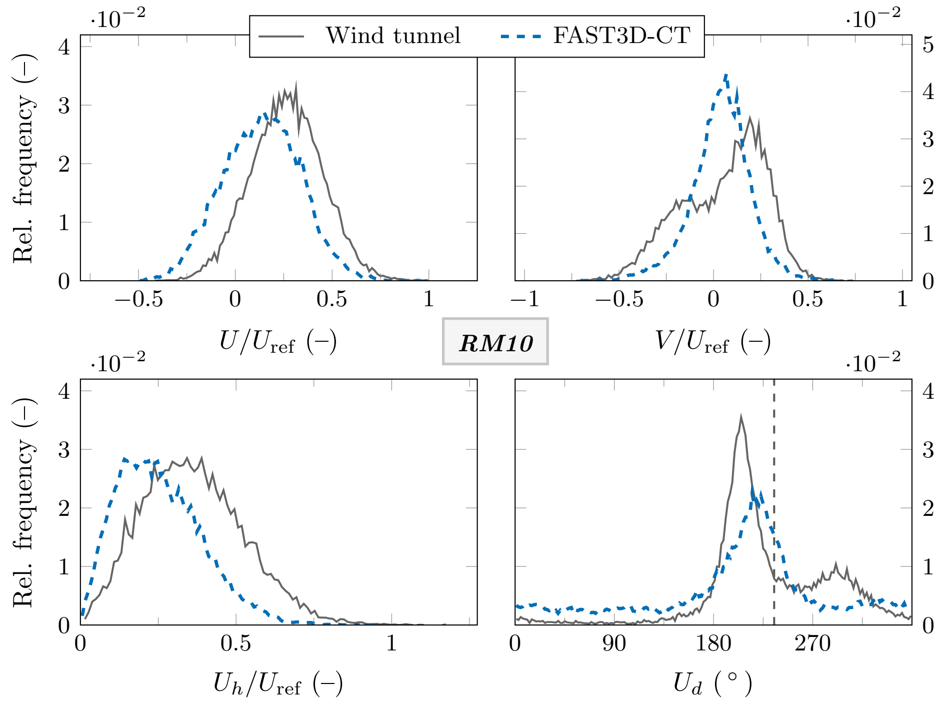

Figure 5.34: Same as in Figure 5.31, but for location *RM10* in heights of 10.0 m/10.25 m (wind tunnel/FAST3D-CT).

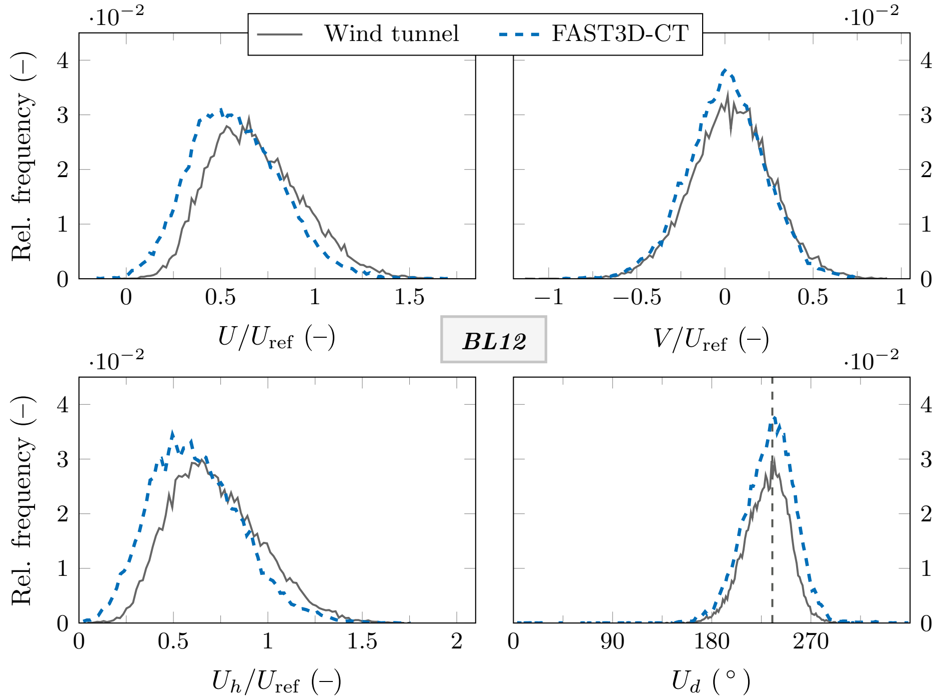

Figure 5.35: Same as in Figure 5.31, but for location *BL12* in heights of 45.5 m/45.25 m (wind tunnel/FAST3D-CT).

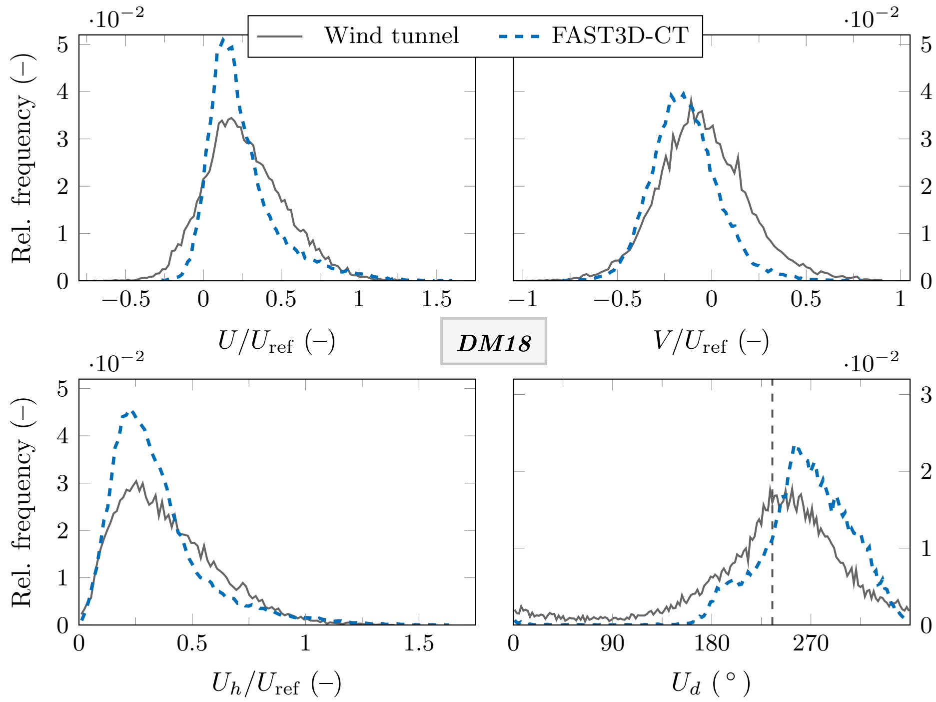

Figure 5.36: Same as in Figure 5.31, but for location *DM18* in heights of 29.75 m/30.25 m (wind tunnel/FAST3D-CT).

Shape & spread analysis A way to quantify the agreement between frequency distribution shapes of the instantaneous velocities from the reference experiment and the simulation is to compare higher order moments like the *skewness* (*here* γ_1; third moment), which quantifies the symmetry of the distributions, or the *kurtosis* (*here* β_2; fourth moment; sometimes also referred to as *flatness*), which measures the peakedness (e.g. Wilks, 2005). The shape descriptors of the distribution of the ith velocity component U_i can be defined as the third and fourth standardized moments

$$\gamma_{1_i} = \mathcal{E}\left\{\frac{(U_{i_j} - \overline{U}_i)^3}{\sigma_i^3}\right\} = \frac{1}{N\,\sigma_i^3}\sum_{j=1}^{N}\left(U_{i_j} - \overline{U}_i\right)^3 \;, \tag{5.4}$$

and

$$\beta_{2_i} = \mathcal{E}\left\{\frac{(U_{i_j} - \overline{U}_i)^4}{\sigma_i^4}\right\} = \frac{1}{N\,\sigma_i^4}\sum_{j=1}^{N}\left(U_{i_j} - \overline{U}_i\right)^4 \;, \tag{5.5}$$

where $\mathcal{E}$ is the expectation operator, and $j = 1, \ldots, N$ is the sample index. For a normally distributed (*Gaussian*) data sample $\gamma_1 = 0$ and $\beta_2 = 3$. If $\gamma_1 < 0$, the distribution is *left-skewed*: It exhibits a longer left tail, while its mass is centered to the right. For $\gamma_1 > 0$, the distribution is *right-skewed* and has a longer right tail. A *leptokurtic* distribution with $\beta_2 > 3$ exhibits a higher peak and fatter tails than a Gaussian distribution, while the *platykurtic* counterpart ($\beta_2 < 3$) is flat-topped and typically has thin tails.

Figure 5.37 displays the comparison of height profiles of skewness and kurtosis of the *streamwise* velocity component at four of the *BL* locations.[5] At all analyzed points, the agreement between the experimental and numerical shape measures is very good. This statement holds for the rather unobstructed wind field above the Elbe (*BL04*), well upstream of the downtown area, as well as for comparison points within the city. The distinct vertical variability of skewness and kurtosis found at the intersection location *BL10* is very well reproduced in the LES, which is an indication that the code is able to capture the geometry-influenced flow variability. It has to be noted, however, that the three topmost simulation values were excluded from the graphical display. In agreement with the findings from the earlier analysis of second-order statistics (see discussion in Section 5.2.1), above a height of approximately $3\,\mathrm{H_m}$ the FAST3D-CT flow field still is considerably influenced by the artificially generated turbulence at the inflow plane. This also affects the higher order moments expressed in pronounced right tails of the instantaneous velocity distributions (γ_1 in the range of $0.5 - 1.0$) and an enhanced peakedness with β_2 taking values in the order of $4.0 - 4.5$. Since these values cannot be evaluated in the same manner as the self-consistent simulation results at lower RSL levels, they are excluded at this point.

The shape parameter profiles in Figure 5.37 were derived from velocity samples for which these statistics are *meaningful*, i.e. for unimodal distributions that further do not exhibit plateaus (extremely heavy tails). Like averages or standard deviations, shape measures can lack any informative value when applied to arbitrary distributions.

[5] In analogy to the derivation of the reproducibility of the low-order moments of the wind-tunnel measurements (cf. Section 4.2.3), the scatter bars were derived from an analysis of repeated measurements yielding a maximum range of ± 0.146 for γ_1 and ± 0.203 for β_2.

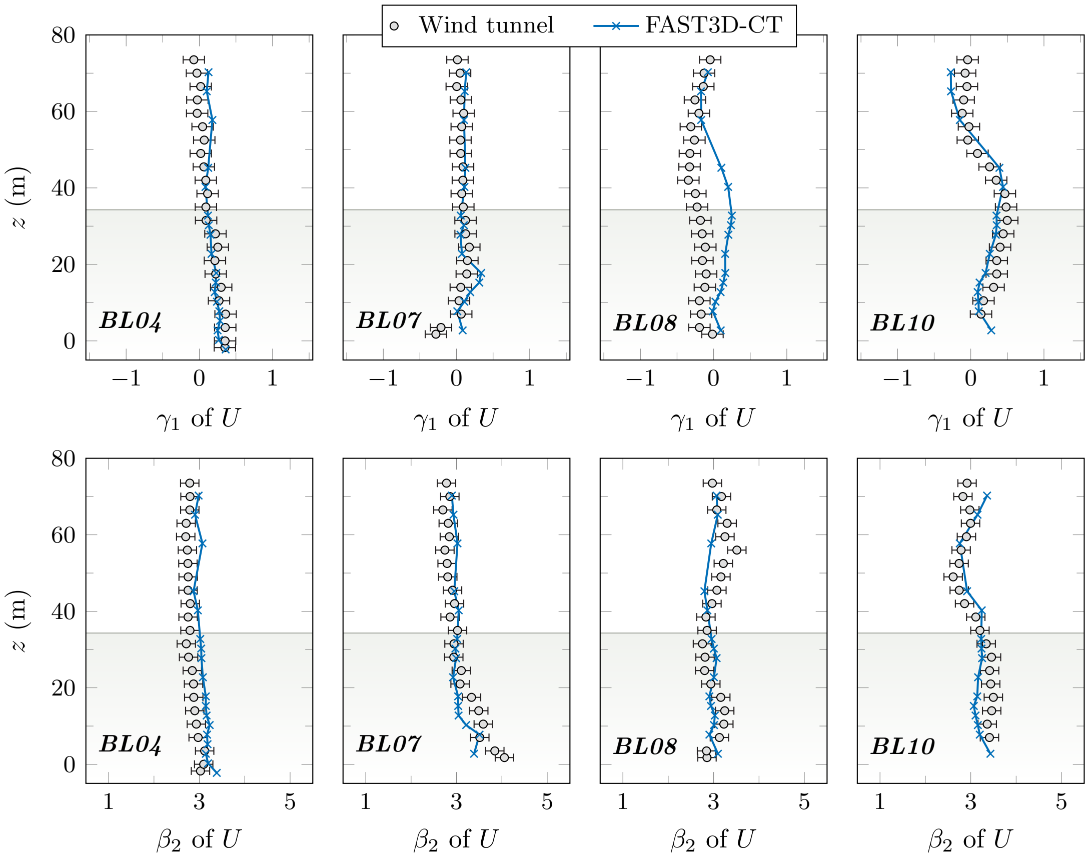

Figure 5.37: Comparison of wind-tunnel and FAST3D-CT height profiles of skewness, γ_1, and kurtosis, β_2, of the streamwise velocity component at four locations in the urban domain. Heights below $\mathrm{H_m} = 34.3\,\mathrm{m}$ are indicted by a gray shading.

The interpretation of scatter plots of observed and simulated high-order statistics as in Figure 5.38, thus, involves some caveats when shape measures are applied as black boxes. As in the scatter plot analysis of first and second-order statistics of the horizontal velocity components shown in Figure 5.17, the evaluation of γ_1 and β_2 is restricted to comparison heights for which vertical offsets between the data pairs are relatively small. Furthermore, for reasons outlined above, the comparison is restricted to heights below $3\,\mathrm{H_m}$ (only affects the *BL* positions). In both, the experiment and the LES, the majority of analyzed velocity signals exhibit more or less Gaussian shape characteristics. However, as can be seen in the scatter plots there is a tendency toward a positive skewness in the U/U_{ref} signals (i.e. a trend toward tails at high velocities), while for the spanwise components, V/U_{ref}, slightly more distributions are skewed to the left, indicating tails at low velocities. These global patterns are also seen in the LES predictions. Offsets between the shape descriptors are more pronounced for the V/U_{ref} distributions. More acute peaks, for example, are observed in some of the LES velocity distributions particularly at the *RM* locations. This trend of more *leptokurtic* numerical velocity distributions has been addressed before and is most likely associated with the flow resolution characteristics in geometrically confined situations.

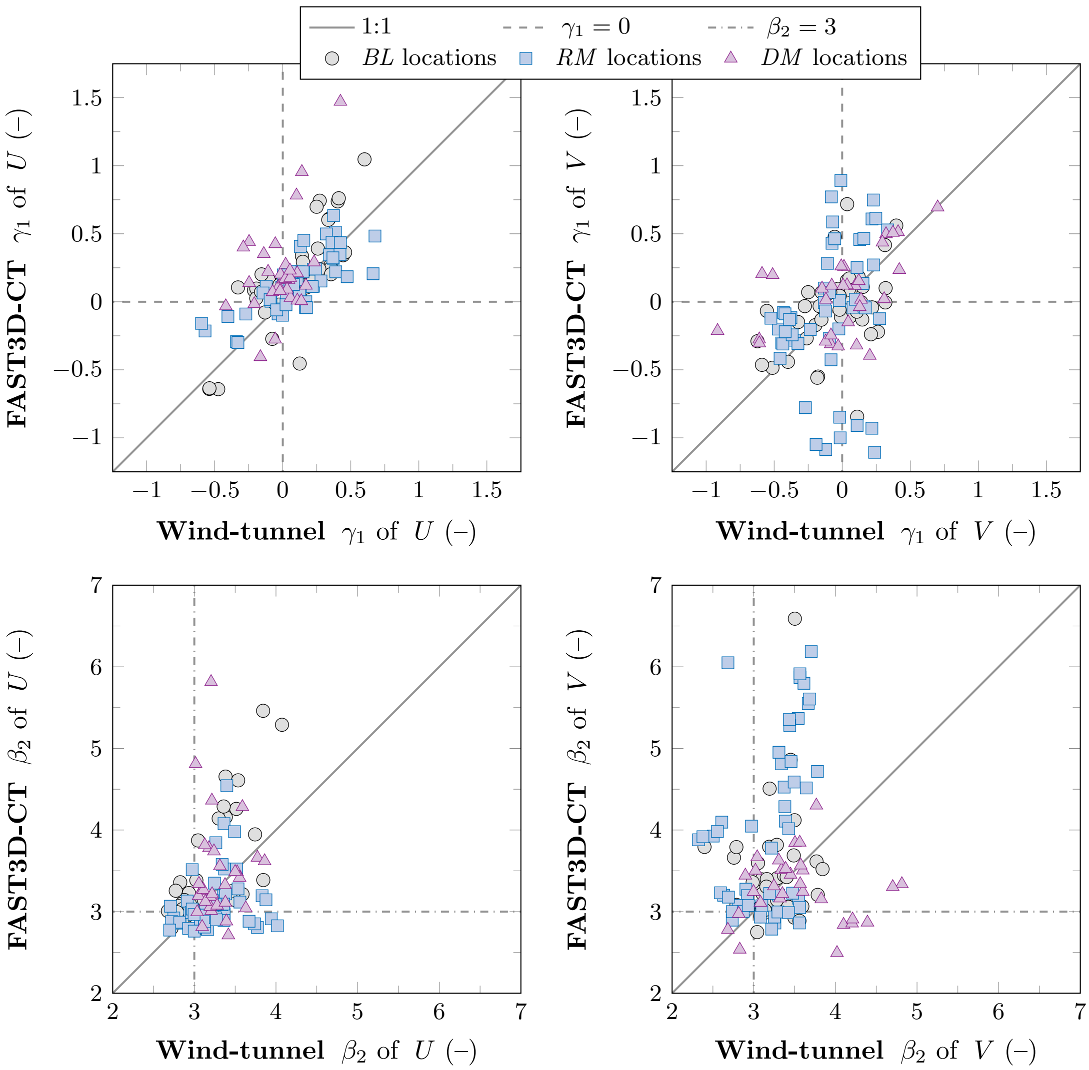

Figure 5.38: Scatter plots of wind-tunnel measurements and FAST3D-CT simulations for skewness, γ_1, and kurtosis, β_2, of the horizontal velocity components based on 128 data pairs at all 22 comparison locations, having maximum vertical offsets of $|\delta z| = 1.12\,\mathrm{m}$ (affecting 10 *DM* points). The gray lines indicate the states of $\gamma_1 = 0$ and $\beta_2 = 3$, corresponding to Gaussian distribution characteristics.

Since this analysis did not differentiate between whether or not the application of shape measures is meaningful with regard to the distribution features, drawing conclusions about the simulation accuracy can be deceptive and should, in a next step, be substantiated by point-by-point evaluations. Furthermore, it needs to be kept in mind that only a fraction of the entire data pool could be analyzed in the scatter diagrams due to the height differences between the measurement locations and the numerical cell centers.

For the *pointwise* appraisal of the simulation quality based on time series characteristics, other well-established forms of displaying data statistics could be used in a detailed LES validation. *Boxplots*, for example, are convenient for a direct visual comparison of the *five-number summaries* of experimental and numerical velocity time series (cf. the example shown in Fig. 5.39), while *quantile-quantile plots* (*Q-Q plots*) can be used to directly compare the agreement between the distributions based on the entire set of order statistics (cf. Fig. 5.40). Both approaches are *non-parametric*: No assumptions about the underlying distributions – and ultimately about the sample populations – are made (e.g. concerning normality). The boxplots shown in Figure 5.39 correspond to velocity samples for which a rather good agreement between the reference data and the simulation had been determined through a visual inspection of the histograms (*RM07* and *BL12*; cf. Figs. 5.32 and 5.35). The centerlines of the boxes mark the medians of the distributions, while the left and right boundaries represent the lower quartile ($Q^{(1)}$; i.e. the 25th percentile) and the upper quartile ($Q^{(3)}$; 75th percentile), respectively. The lengths of the *whiskers* attached to the boxes are typically based on the *interquartile range*, $IQR = Q^{(3)} - Q^{(1)}$, of the distributions. In the boxplots shown in Figure 5.39, the extents were obtained from $Q^{(1,3)} \mp 1.5\, IQR$, which corresponds to approximately ∓ 2.698 times the standard deviation of the sample for cases in which the velocities are normally distributed. The minimum and maximum velocity magnitudes of the respective samples are marked by dots. The latter, of course, have to be understood as merely indicative of the true range of the samples, since both data sets only correspond to a single, finite-time realization of the flow scenario. At both positions, the boxplots substantiate the earlier qualitative appraisal of the simulation accuracy by further providing a visual summary of locations, spreads, and shapes of the underlying sample distributions.

Q-Q plots, on the other hand, do not immediately permit a direct quantitative evaluation of derivable distribution parameters, but are helpful to compare the congruence of the entire data sets. Figure 5.40 displays Q-Q plots for the same position at *BL12* that has been analyzed before as well as for the roof-level location at *DM18*, for which stronger disagreements between the U/U_{ref} distributions were determined (Figs. 5.35 and 5.36).

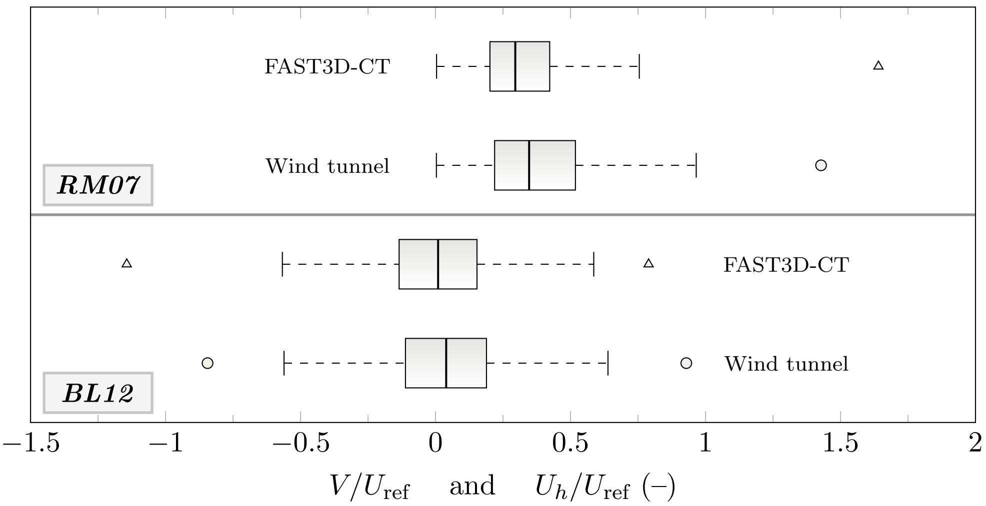

Figure 5.39: Comparison of wind-tunnel and FAST3D-CT boxplots of V/U_{ref} at location *BL12* in a height of 45.5 m/45.25 m (lower panel) and of U_h/U_{ref} at location *RM07* in a common height of 40.25 m (upper panel).

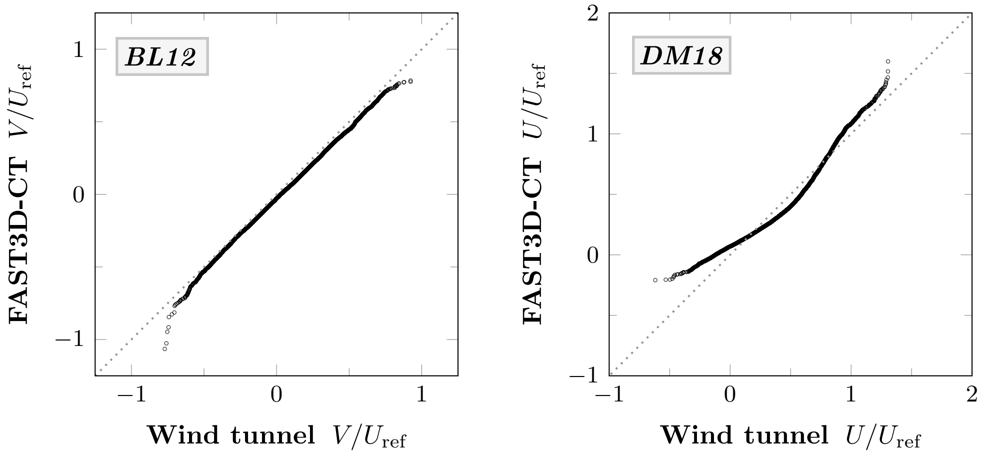

Figure 5.40: Q-Q plots constructed from wind-tunnel and FAST3D-CT data pairs of the spanwise velocity, V/U_{ref}, at location *BL12* (45.5 m/45.25 m) and of the streamwise velocity, U/U_{ref}, at location *DM18* (29.75 m/30.25 m).

At both locations, the number of instantaneous velocity signals in the wind-tunnel and the FAST3D-CT time series are not equal, and the compared quantiles were defined on the basis of the *smaller* sample size. The high level of agreement between the numerical and experimental distributions at position *BL12* is reflected in the fact that the quantiles follow a 1:1-relationship up to the far tails of the distributions. Practically no significant difference between both samples can be determined. The evaluation of the far tails of the distributions is likely to be unreliable, since the values in the tails basically represent single events in the particular realization: The general outcome of the comparison can potentially turn out different if, for example, the measurement or simulation durations were the same or if both had overall been longer/shorter. For evaluation scenarios in which special attention is directed to the tails of the frequency distributions of simulated quantities (e.g. in the analysis of concentration time series of airborne pollutants), statistical tools from the field of extreme value analysis could be revealing. At position *DM18*, the *leptokurtic* shape and stronger skewness of the numerically predicted distribution of instantaneous velocities is clearly mirrored in the curved pattern of the plot. Since Q-Q plots do not rely on integrated statistics, but simply on the sorted data of both samples, their informative value in general is high for any arbitrary distribution.

Statistical significance tests A logical next step toward a *quantification* of the agreement between experimental and numerical frequency distributions would be based on *hypothesis tests*, which provide statistical measures of the (in)significance of the observed differences between both samples and their parent populations. Several non-parametric, two-sample hypothesis tests could generally be employed (cf. e.g. Conover, 1999; Wilks, 2005). An example is the well-known *Kolmogorov-Smirnov test*, which questions the agreement of two samples by measuring the distances of their cumulative frequency distributions and using as the *null hypothesis*, $\mathcal{H}_0$, that both samples were drawn from the same (not further specified) distribution. Specific drawbacks connected to the application of classic significance tests to velocity time series are briefly illustrated on the basis of the V/U_{ref}

distributions at position *BL12* ($z_{\mathrm{exp}} = 45.5\,\mathrm{m}$), for which a high level of congruence had already been confirmed on the basis of histograms, boxplots, and Q-Q plots. Figure 5.41 shows the respective cumulative frequency distributions derived from the entire sample sizes ($\mathcal{O}(10^4)$; left plot) and based on strongly reduced sample sizes ($\mathcal{O}(10^2)$; right plot), on the basis of which the *Kolmogorov-Smirnov* test statistic is computed (see Wilks, 2005, for details). Although only marginal differences between the cumulative distributions are evident in the former case, the null hypothesis is rejected on an α-level of 0.05, and the observed differences are interpreted as *statistically significant*. In the second case, the reduced sample sizes (and the time-series lengths) are actually too small to be deemed representative of the turbulent scenario with regard to the derivation of reliable statistics (recall the discussion on the *inherent uncertainty* in Section 4.2.3). Nevertheless, $\mathcal{H}_0$ is not rejected at the same significance level, although this outcome could not have been expected based on a visual inspection of the distributions. In general, the larger the sample size the more likely it is that hypothesis tests will yield p-values significantly smaller than the prescribed α-level: The null hypothesis is rejected even if the observed differences are minuscule and their *practical significance* is trivial. This is a well-known fact and attributed to the increasing power of the test with increasing sample size: The more values can be compared, the higher is the statistical certainty that the determined differences are *real*. This also affects other tests that depend on the p-value, like the two-sample *chi-square* test, which is a common choice for binned data, or the *Wilcoxon-Mann-Whitney* test, which is a well-established method to assess the statistical significance of differences between two independent samples based on mean deviations of the ranked data.

Since the very large number of instantaneous velocity samples in the experimental and numerical time series is coupled to the necessity of reducing the *inherent uncertainty* of the derived statistics (cf. discussion in Section 4.2.3), reverting to shorter measurement times or simulation durations in order to decrease the likelihood of committing a *Type I error* by incorrectly rejecting the null hypothesis, is generally not an option.

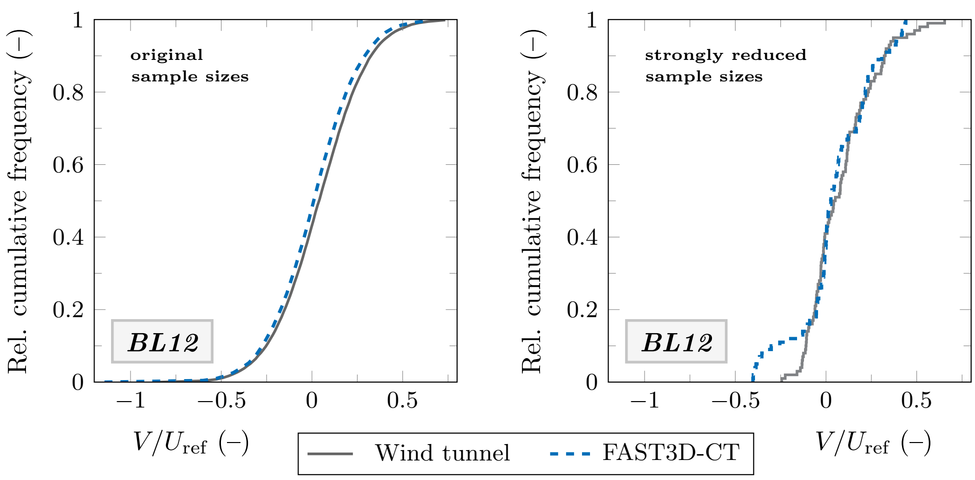

Figure 5.41: Experimental and numerical relative cumulative frequency distributions of V/U_{ref} at location *BL12* in heights of 45.5 m/45.25 m derived from the original (*left*) and from s strongly reduced sample size (*right*).

Instead, the use of hypothesis tests for the quantification of the LES accuracy could be shifted toward samples of statistical quantities, e.g. ensemble statistics resulting from repeated measurements and simulations. This approach has, for example, been applied by Patnaik et al. (2009) for the quantification of the agreement between wind tunnel and LES frequency distributions of concentration parameters obtained from ensembles of realizations using the *Wilcoxon-Mann-Whitney* test.

5.3.2 Direction fluctuation time scales

The above analysis can be expanded to the derivation of fluctuation time scales of the horizontal wind vector. Such an analysis is targeted at the quantification of typical time scales associated with a certain shift of the horizontal wind vector, which is measured by the difference between observed wind directions as a function of time lag. In that regard, "typical" is a rather elastic term since the turbulent variability of the horizontal velocity components naturally results in a broad range of instantaneous wind direction fluctuations, so that the derivation of characteristic averages strongly depends on which calculation method is deemed *representative*.

In the following paragraphs, results are presented for the example of comparison location *BL04* above the Elbe river, well-upstream of the inner city. Here, the prevailing wind direction roughly agrees with the approach flow wind direction. The wind direction fluctuations are defined – using the classic approach – as instantaneous deviations from the long-term temporal average, $u'_d(t) = U_d(t) - \overline{U}_d$. Figure 5.42 depicts examples of the relative frequency distributions of the wind angle fluctuations allocated into 125 bins for four heights at *BL04*.[6] The distributions illustrate how the value range of the wind direction fluctuations narrows with increasing distance from the ground and the distribution shapes tend to be more *leptocurtic*. Similar height-dependent variations are evident in both data sets and the agreement between the wind-tunnel measurements and the FAST3D-CT simulation with regard to the spread and shape of the fluctuation distributions is high.

The absolute differences between horizontal wind directions as a function of time lag, $|\delta U_d(t_l)|$, are compared in a next step. The evaluation is based on the observed *median* differences since the distributions of $|\delta U_d(t_l)|$ for a certain time lag tend to be strongly right-tailed. As a measure of the observed value spread, the interquartile range (IQR) of the distributions, as the difference between the 75th and 25th percentile, is reported as well. For this analysis, the resampled (equidistant) wind-tunnel data were analyzed. The time lag is defined as $t_l = n\, f^{-1}$, with $n = 0, \ldots, N/2$ and N being the number of signals in the time series. The frequency, f, either refers to the sampling frequency of the LES, f_s, or to the mean data rate of the experiment, $\dot{N}$. Hence, while the time lags are the same at all heights in FAST3D-CT since $f_s =$ const, point-to-point differences are present for the experimental data because $\dot{N}$ varies from measurement to measurement.

[6]When interpreting the displayed height information, it has to be recalled that the comparison point is located above the water surface, which has a vertical offset of −3.5 m to the ground surface in both the physical and numerical representation (cf. the definition of the reference elevation presented in Section 4.4.2). Thus, in order to relate the comparison positions to heights above the *local* underlying surface (i.e. water) it would be required to add 3.5 m to the indicated AGL values (i.e. 0.0 m above ground level equals 3.5 m above water level).

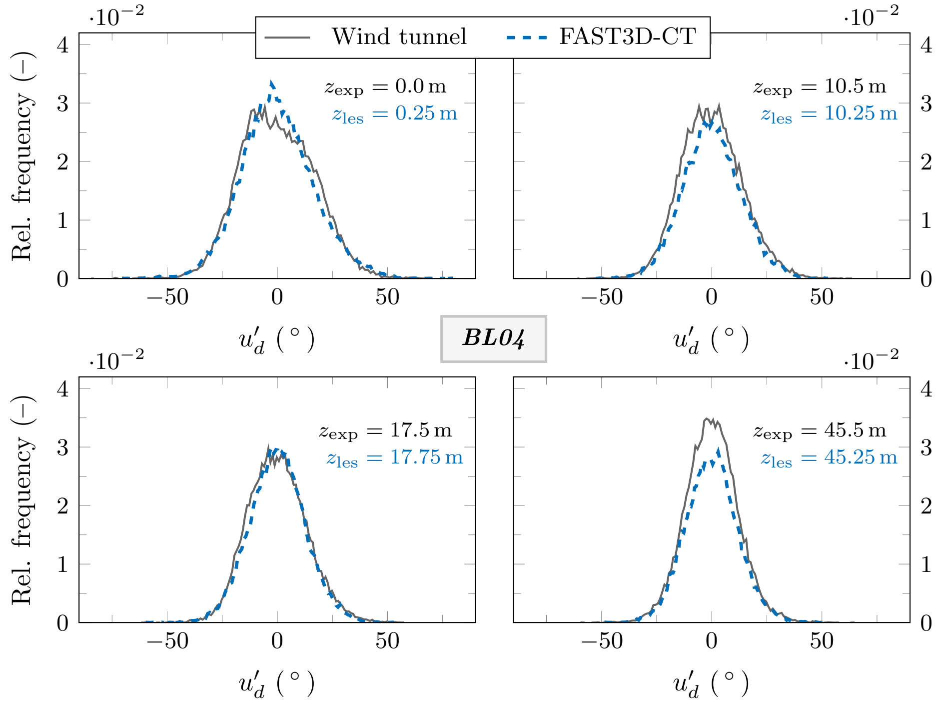

Figure 5.42: Relative frequency distributions of the absolute wind direction fluctuations, u'_d, about the *local* temporal average, $\overline{U}_d$, observed in the experiment and predicted by FAST3D-CT in four heights at location *BL04*.

Figure 5.43 shows results for six heights at position *BL04*. The time lags are displayed in full-scale dimensions and were scaled to a common reference wind speed of $U_{\mathrm{ref}} = 5\,\mathrm{m/s}$. A high level of agreement between both data sets is found for the depicted measures of central tendency and spread. The numerical model is able to reproduce the experimental statistics on a point-by-point basis, but also with respect to the overall time-development of the wind angle differences as a function of height. In all elevations, a relatively strong increase in the observed wind direction differences over roughly the first 10 s is followed by a pronounced flattening of the curves and a later leveling of the median and IQR angle differences into a plateau. The curves reveal a clear height dependence, which is readily appreciated by the decreasing magnitudes of the median wind direction differences at the maximum displayed time lag of $t_l = 60\,\mathrm{s}$. Furthermore, this decrease is accompanied by a reduction of the IQRs as a measure of the spread of the underlying distributions, which is in agreement with earlier results from the comparison of the wind direction fluctuation distributions. The magnitude of the IQRs emphasize the variability of the angle-difference samples for a specified time lag. Even for small temporal offsets, the wind direction shifts can become quite large due to the turbulent variability of the flow.

The only systematic differences noticeable in the results shown in Figure 5.43 concern the slopes of the LES curves at small time lags, which are slightly higher than their wind-tunnel counterparts, but also level off much faster. Inspecting the connection of $|\delta U_d|$ to the time lag is an insightful way to incorporate the *time-dependency* of statistical characteristics of experimental and LES flow fields in the validation study.

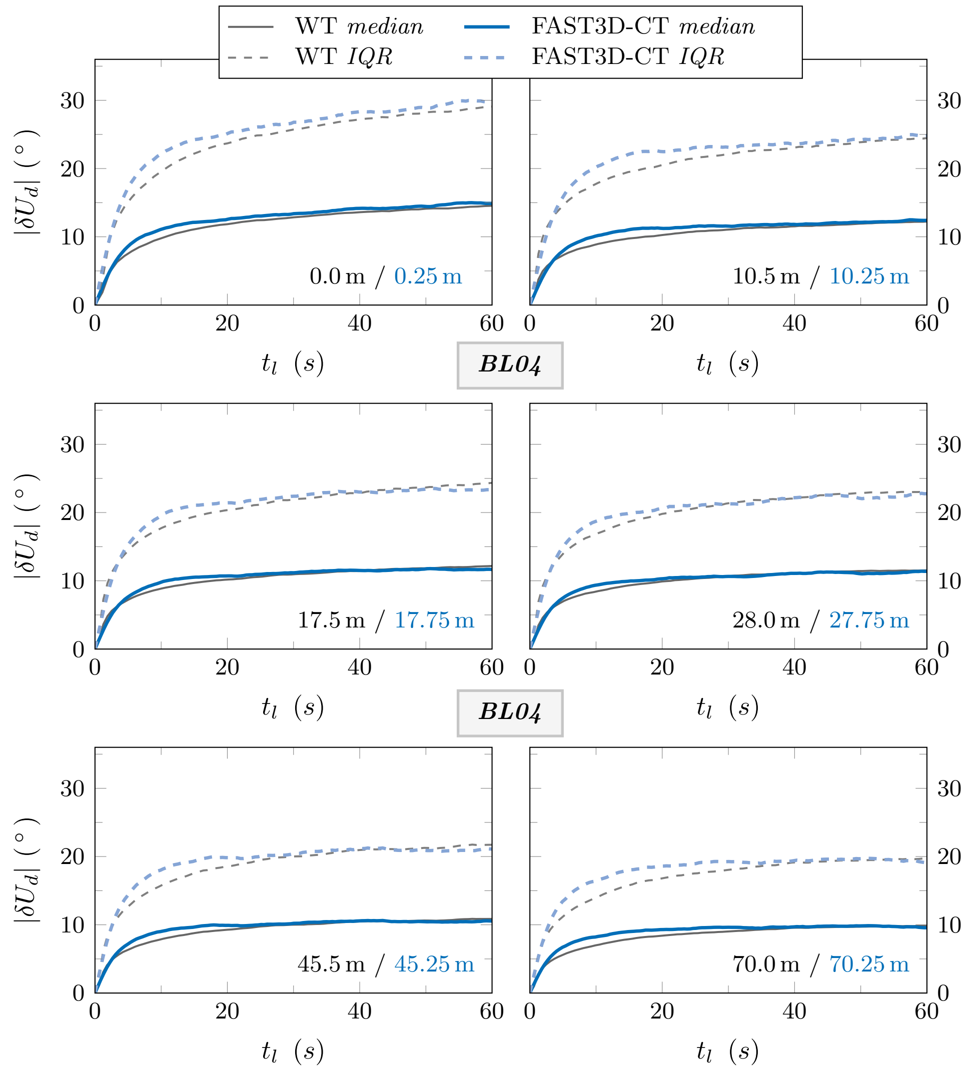

Figure 5.43: Median absolute wind direction differences together with the corresponding interquartile ranges (IQR) as a function of the associated full-scale time lags between instantaneous data samples for a reference velocity of $U_{\mathrm{ref}} = 5\,\mathrm{m/s}$. The wind tunnel and FAST3D-CT data are displayed for six heights at *BL04*.

An expansion of this analysis to locations within the inner city, however, needs to be accompanied by a high level of awareness concerning the interpretability of the results in the presence of circulating or multimodal wind direction scenarios.

The point-by-point comparison of instantaneous velocity distributions by qualitative and quantitative means further substantiated the potential of the LES code FAST3D-CT to reproduce intricate urban flow patterns that reflect the inherent unsteadiness of geometry-induced wind fields. Considering the entire experimental and numerical sample information available in the velocity time series has proven to be very useful to either substantiate that a high level of agreement between the associated mean flow statistics did not come by fluke, or to fathom potential causes for the observed discrepancies. The evaluation of high-order moments as integrated measures of the distribution characteristics can provide further insight into the simulation accuracy. By means of skewness and kurtosis parameters, information about the general state of the flow can be retrieved and used to evaluate how well these features are captured by the numerical model. The above results and discussion, however, also emphasized that these results need to be carefully verified since the informative value of summary statistics can turn out to be meaningless when applied to arbitrary distributions. The occurrence of bimodal and heavy-tailed distributions of instantaneous flow velocities or derived quantities is anything but rare in urban environments. While these features are candidate test scenarios for an in-depth validation of a time-dependent simulation, the textbook interpretation of corresponding standard statistical measures can be deceptive. Of course, this also feeds back to low-order statistics like the mean and variance that have been compared earlier in Section 5.2. Analyzing frequency distributions, thus, is not only a revealing method to determine whether the particular model was able to exploit the full potential of the LES approach, but also to guarantee a fair comparison with the experiment. Particularly if the time-dependent model is not only intended to deliver reliable mean statistics, but also give an accurate account of the value range that can be expected (e.g. to appraise the likeliness of certain extreme values), comparing frequency distributions is inevitable.

Again, emphasis needs to be laid on the fact that basically all of the above comparisons are only meaningful because both the experimental measurement durations and the numerical simulation times allow reliable statistical analyses. This, however, also entails that the *practical significance* of observed differences between the experimental and numerical velocity distributions cannot be straightforwardly assessed with classic hypothesis tests.

Main results of the **frequency distribution** comparison can be summarized as follows:

- FAST3D-CT is able to accurately reproduce experimentally observed frequency distribution characteristics at many of the comparison points and for different levels of flow complexity.
- The code has the potential to realistically resolve intricate geometry-induced flow features, e.g. reflected in the bimodality of wind direction distributions.
- As conjectured earlier in the basis of mean flow results, the grid resolution in combination with the numerical representation of buildings and offsets between the experimental and numerical flow positions are likely to be major contributors to the occurrence of discrepancies between both data sets.

With the concluding analysis of wind vector time scales, the study advanced to an important aspect of the LES validation problem – the comparison of time-related eddy statistics, which is further addressed in the next section in terms of turbulence integral time scales.

5.4 Temporal autocorrelations

In this section, one-dimensional temporal autocorrelation functions and associated integral time scales of turbulent velocities are derived from wind-tunnel measurements and simulation data of FAST3D-CT. The comparison focuses on the following aspects:

1. Discussion of derivation options for the integral time scales, τ_{ii} $(i = 1, 2, 3)$.

2. Shapes of the temporal autocorrelation functions of the three velocity components, $R_{ii}(t_l)$.

3. Vertical profiles of the integral time scales, $\tau_{ii}(z)$.

Point **1.** is examined to set the stage for the primary focus of this section – the direct comparison of empirical velocity autocorrelation functions and corresponding integral time scales together with an analysis of their height and location dependency (**2.** and **3.**). Since the time scales are directly derived from the temporal autocorrelation functions, their shape and progression with time lag are qualitatively compared in order to attempt to draw conclusions about eddy structures in the laboratory and the LES. Aspects of the computational derivation of τ_{ii} from $R_{ii}(t_l)$ are briefly discussed with a view to the specific data of this study. In all analyses, the *resampled* (equidistant time) wind-tunnel velocity data are used. Additional material for this section is presented in Appendix D.

5.4.1 Definitions & derivation strategy

The comparison of integral time scales of turbulence, τ_{ii}, in the framework of an LES validation study can provide valuable insight into the accuracy of the time-dependent turbulence simulation. Since the LES is able to directly resolve the energy-containing eddies in the flow, for which τ_{ii} can be regarded as a representative time scale, such an analysis caters directly to the eddy-resolving CFD simulation type.

Turbulence integral time scales can be retrieved from single-point velocity fluctuation time series through the calculation of one-dimensional, time-lag dependent autocorrelations. For a stationary flow, the *autocovariance* function C_{ii} of the ith fluctuating velocity component, u_i', at two different times, t_1 and t_2, only depends on the time lag defined as $t_l = t_2 - t_1$ and is given by $C_{ii}(t_l) = \mathcal{E}(u_i'(t)u_i'(t + t_l))$, where $\mathcal{E}$ is the expectation operator indicating the statistical nature of the quantity (e.g. Lumley and Panofsky, 1964; Dias et al., 2004). The one-dimensional *autocorrelation* function of the velocity component with itself results from a normalization of the autocovariance function and is given by $R_{ii}(t_l) = C_{ii}(t_l)/C_{ii}(t_l = 0)$, where $C_{ii}(t_l = 0) = \mathcal{E}(u_i'^2)$ is the variance of the velocity component. Since the investigated flow is stationary, a temporal average can be used to obtain the velocity fluctuation autocorrelation as a function of time lag through

$$R_{ii}(t_l) = \frac{1}{\sigma_i^2} \overline{\left\{U_i(t) - \overline{U}_i(t)\right\} \left\{U_i(t + t_l) - \overline{U}_i(t + t_l)\right\}} \,. \tag{5.6}$$

The function obeys *Cauchy-Schwarz's inequality*, $|R_{ii}(t_l)| \leq R_{ii}(t_l = 0) = 1$, and describes the *degree of common variation* in a variable depending on the time difference between two observations (Stull, 1988). Hence, the function measures the *memory* of the turbulent flow (Lumley and Panofsky, 1964). After taking its maximum value for $t_l = 0$, the autocorrelation function decays rapidly for increasing time lags since motions separated by sufficiently long temporal distances become statistically independent and their autocorrelation eventually drops to zero (Townsend, 1956).

The integral time scale, τ_{ii}, corresponding to the ith velocity component is defined as the time integral over the 1D temporal autocorrelation function according to

$$\tau_{ii} = \int_{t_{l_0}}^{t_{l_\infty}} R_{ii}(t_l)\, dt_l \; . \tag{5.7}$$

While the lower limit of the integral is naturally given by $t_{l_0} = 0$, the definition of the upper limit, t_{l_∞}, is not as trivial. In theory, the upper limit of the integration domain would correspond to an infinitely long time lag, assuming that $R_{ii} \to 0$ as $t_l \to \infty$. For velocity signals of finite duration, this would imply to integrate up to the maximum time lag, $t_{l_{\max}}$, which is given by $N/2\, f^{-1}$, and N is the number of samples in the time series and f the constant sampling frequency (i.e. either referring to $\dot{N}$ in the experiment or f_s in the LES). Typically, however, the duration of the signal is significantly longer than the time it takes for R_{ii} to decay to zero, and the upper integration limit is defined as the (first) zero-crossing point. Other approaches rely on the time lag after which the autocorrelation function has fallen below a certain critical value (e.g. 0.1 or $\exp(-1)$, where the latter limit corresponds to the *e-folding time* of the function). A comparative analysis concerning the influence of the selected integration domain on the derived integral scales has, for example, been presented by O'Neill et al. (2004). In some cases, computations following the above methodologies are hampered because the autocorrelation functions do not exhibit a monotone decrease in their tail region (e.g. showing plateaus or oscillations) or do not drop to zero at all. In atmospheric time series, the latter feature is often related to trends of the mean flow occurring during the measurement duration, i.e. to a violation of the stationarity assumption (cf. e.g. Dias et al., 2004). But even for statistically stationary flows, as encountered in the wind-tunnel measurements and the large-eddy simulation analyzed in this study, a strong monotone decrease of $R_{ii}(t_l)$ is often followed by the occurrence of low-magnitude fluctuations for increasing time lags. These oscillations can appear as sudden magnitude increases in the tails of R_{ii} or as fluctuations about zero. The nature and physical relevance of such oscillations in the tails are debatable (cf. e.g. Yaglom, 1987). In this study it is assumed that they reflect the increasingly random nature of the autocorrelation coefficient for larger time lags. This conjecture is supported by the fact that the structure and intensity of the fluctuations in the tails is related to the overall duration of the signal, i.e. that they also appear to be influenced by the statistical representativeness of the respective averaging times. In order to consistently derive τ_{ii} at all comparison points, for all velocity components, and for both data sets without relying on a subjective case-by-case appreciation of the shape of the R_{ii} function, this study uses an extrapolation approach for the tails similarly to the method described by Fischer (2011). While the bulk of the original R_{ii} function is preserved at small time lags, the curvature of its tail is approximated by an exponential decay through a fit of the original data. The upper integration limit, t_{l_∞}, is defined as the time lag after which the autocorrelation function has decreased to a value of 0.01 (i.e. to 1 % of its starting value). Further information and all relevant details of the computational procedures for the derivation of the temporal autocorrelations and integral time scales including the tail fitting implementation are presented in Appendix D.

Principally, it is possible to derive integral *length* scales of the dominant turbulent eddies from computed integral time scales using Taylor's frozen turbulence hypothesis (cf. the introduction to this concept in Section 2.3.1). This approach had been pursued earlier in the comparison of the wind-tunnel approach-flow boundary layer with reference measurements from the field site (focusing on the integral length scales of the streamwise eddies in x-direction, ℓ_{11_x}; Section 4.2.2; Fig. 4.13). The transformation between time and space variables, however, requires that a representative mean *advection velocity scale*, $\overline{U}_a$, exists and can be reliably determined – which is not straightforward in strongly heterogeneous flow fields of the urban canopy layer. Since most of the comparison locations are sited in the city (the only exception being *BL04*), the following validation analysis refrains from using Taylor's hypothesis and solely concentrates on temporal quantities.

5.4.2 Autocorrelations & integral time scales

Comparisons of $R_{ii}(t_l)$ and τ_{ii} are presented in full-scale dimensions, scaled to a mean reference velocity, U_{ref}, of 5 m/s observed in the mutual reference height at site *BL04*. In order to derive the full-scale time steps, the numerical and experimental time lags, t_l, were first converted into a dimensionless framework according to $t_l^{\star} = t_l \, U_{\mathrm{ref}} \, L_{\mathrm{ref}}^{-1}$, using the experimental and numerical flow reference values (cf. Table 4.7).

In the following, the location-dependent behaviors of the autocorrelation functions and integral time scales of the turbulent velocities are compared. For reasons of brevity, the presented results for the autocorrelation curves are restricted to a selection of cases. These were assorted to include flow situations and validation results that are representative of the entire comparison data pool and document the overall simulation quality.

Shapes of $\mathbf{R_{ii}(t_l)}$ as a function of height & location

Figures 5.44 and 5.45 depict autocorrelation functions of the streamwise (R_{11}), spanwise (R_{22}), and vertical (R_{33}) velocity fluctuations depending on the full-scale time lags, t_l, obtained from wind-tunnel and LES time series according to Eq. (5.6). The comparison encompasses different locations in the urban environment and focuses on two RSL heights corresponding to approximately $1.3\,\mathrm{H_m}$ and $0.5\,\mathrm{H_m}$, at which the time-series information can be directly compared due to relatively small vertical offsets between the flow locations ($|\delta z| = 0.25\,\mathrm{m}$). In contrast to the numerical data, each of the wind-tunnel time series is associated with a different mean LDA data rate, $\dot{N}$, which results in the fact that the experimental time lags defined for the *S & H* resampling slightly differ at each of the measurement locations. In general, the wind-tunnel time steps are longer than $\delta t_{\mathrm{les}} = 0.5\,\mathrm{s}$ of the simulation. The relations between the wind-tunnel and LES time intervals can be inferred from Figure 4.36 (Section 4.4.3), displaying the respective sampling-frequency to data-rate ratios. For both comparison heights, Figures 5.44 and 5.45 present the autocorrelation curves including the fitted tails (dark colors) as well as the original curves (light colors), which clearly exhibit oscillations at some locations.

Above roof level, the temporal autocorrelations of the streamwise velocity fluctuations remain significant for larger time lags compared with those of the spanwise and vertical velocity components (see Fig. 5.44). This feature is evident in the wind tunnel and the FAST3D-CT data. However, above the river (*BL04*) and at the second most upstream comparison point, *BL07*, the decrease of $R_{11}(t_l)$ with increasing time lag is clearly slower in the experiment than in the simulation, suggesting that at these positions memory effects are stronger pronounced in the laboratory flow. Further downstream in the inner-city area, the agreement between simulation and the wind-tunnel results strongly improves and consistent autocorrelation characteristics are, for example, determined above the narrow street canyon at *BL11*. In both data sets, the influence of the urban environment on the eddy structures is reflected in a faster decline of the autocorrelations compared with the river location. The accuracy with which FAST3D-CT reproduces the $R_{ii}(t_l)$ curves of the spanwise and vertical fluctuations is high as well, as e.g. seen at the intersection location *BL10*, for which the functions are overlapping.

Shifting the focus to flow locations **well below rooftop**, deep within the UCL, still a qualitatively high level of agreement between the LES velocity correlations and the reference measurements in the wind tunnel is detected (cf. examples in Fig. 5.45). Although the code does not reproduce the exact curvatures of the R_{22} and R_{33} functions at the comparison sites *RM03* and *RM09*, qualitatively the conformity of the results is high, which is reflected in the fact that in both flows the spanwise velocity fluctuations remain correlated over longer time-spans than the streamwise fluctuations. This tendency is very distinct in the experimental data measured on the plaza (*RM09*). Here, the time-dependent decay of the autocorrelation of the spanwise velocity fluctuations is significantly slower than determined in the mostly undisturbed flow above the river at *BL04* (see R_{22} in 45.5 m shown in Fig. 5.44). This characteristic might reflect the existence of long-lived eddy structures in the recirculating flow established in the wind tunnel, which is not as striking in the LES. Except for position *BL04*, where a good conformity between the experiment and FAST3D-CT is evident, the predictions of $R_{33}(t_l)$ cannot be further validated within the canopy layer due to the lack of LDA measurements.

Independent of the comparison location or height, the low-magnitude oscillations in the tails of the R_{ii} functions frequently are more pronounced in the simulation than in the experiment. Reasons for this observation could be related to differences between the experimental and numerical signal durations ($T_{\text{exp}} = 16.5\,\text{h}$; $T_{\text{les}} = 6.5\,\text{h}$) and the increasing inherent uncertainty of the autocorrelation values with increasing time lag (cf. Eq. 5.6). At this point, however, this appraisal is merely speculative and would require further systematic investigations, which were outside the scope of the present analysis.

At the three highest data extraction positions of the simulation (i.e. for $z_{\text{les}} > 3\,\text{H}_\text{m}$), a strong disconnection from the quality of the velocity autocorrelations at lower elevations is found and the largest offsets to the wind-tunnel reference are determined (not displayed for brevity). For all three velocity components, the FAST3D-CT autocorrelation functions exhibit a strong decreases with time, which is paralleled by an amplification of the tail oscillations. This observation is qualitatively in compliance with the systematic deviations detected earlier in the comparison of turbulence statistics and velocity frequency distributions (Section 5.2 and 5.3). This reinforces the assessment that the LES flow at higher elevations is still dominated by the artificially generated inflow turbulence.

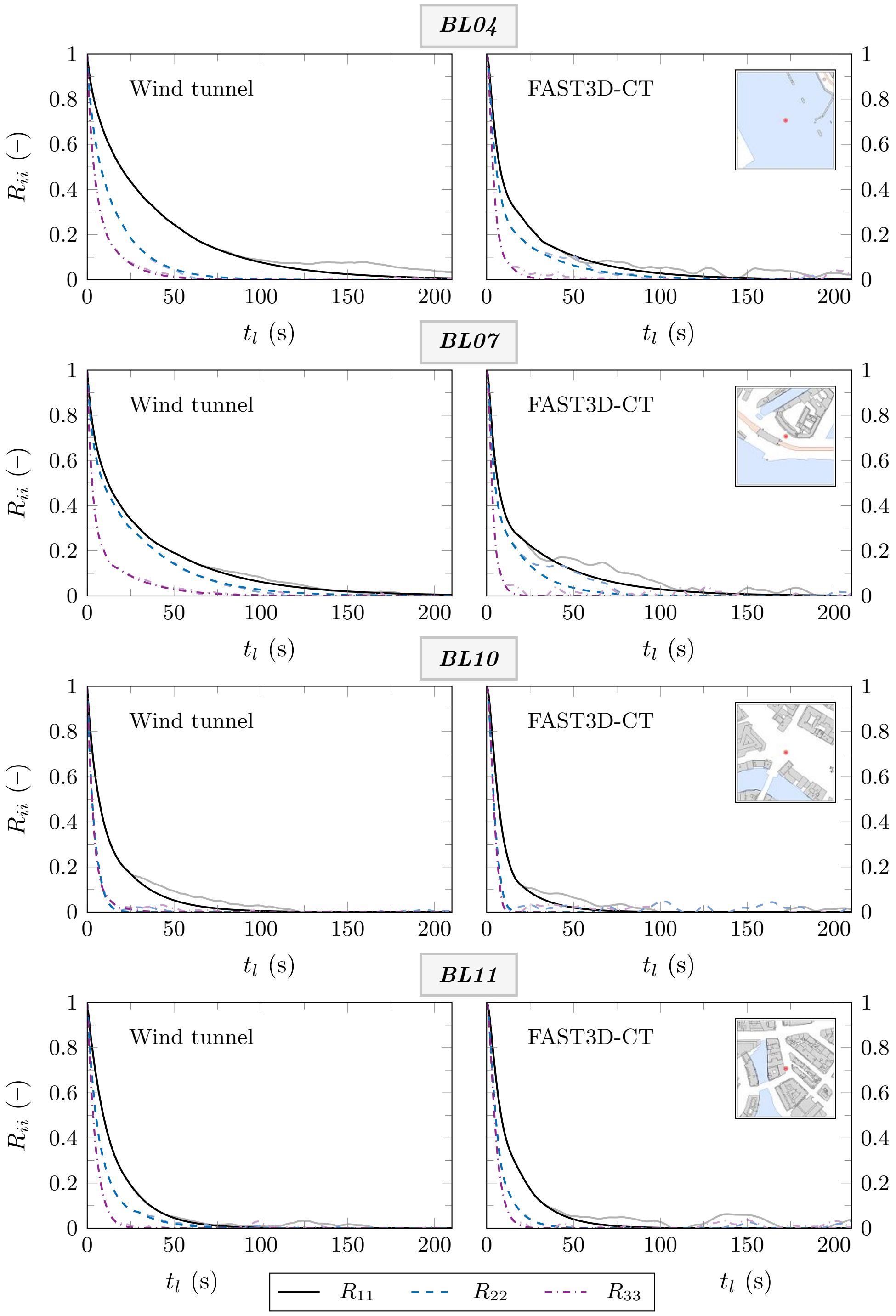

Figure 5.44: Experimental (*left*) and numerical (*right*) temporal autocorrelations as a function of time lag of the streamwise, R_{11}, spanwise, R_{22}, and vertical, R_{33}, velocitiy fluctuations at four comparison locations at a height of 45.5 m/45.25 m (wind tunnel/FAST3D-CT); i.e. at approximately 1.3 H_m. The original (unfitted) autocorrelation curves are presented in lighter colors. Full-scale times correspond to a reference velocity, U_{ref}, of 5 m/s.

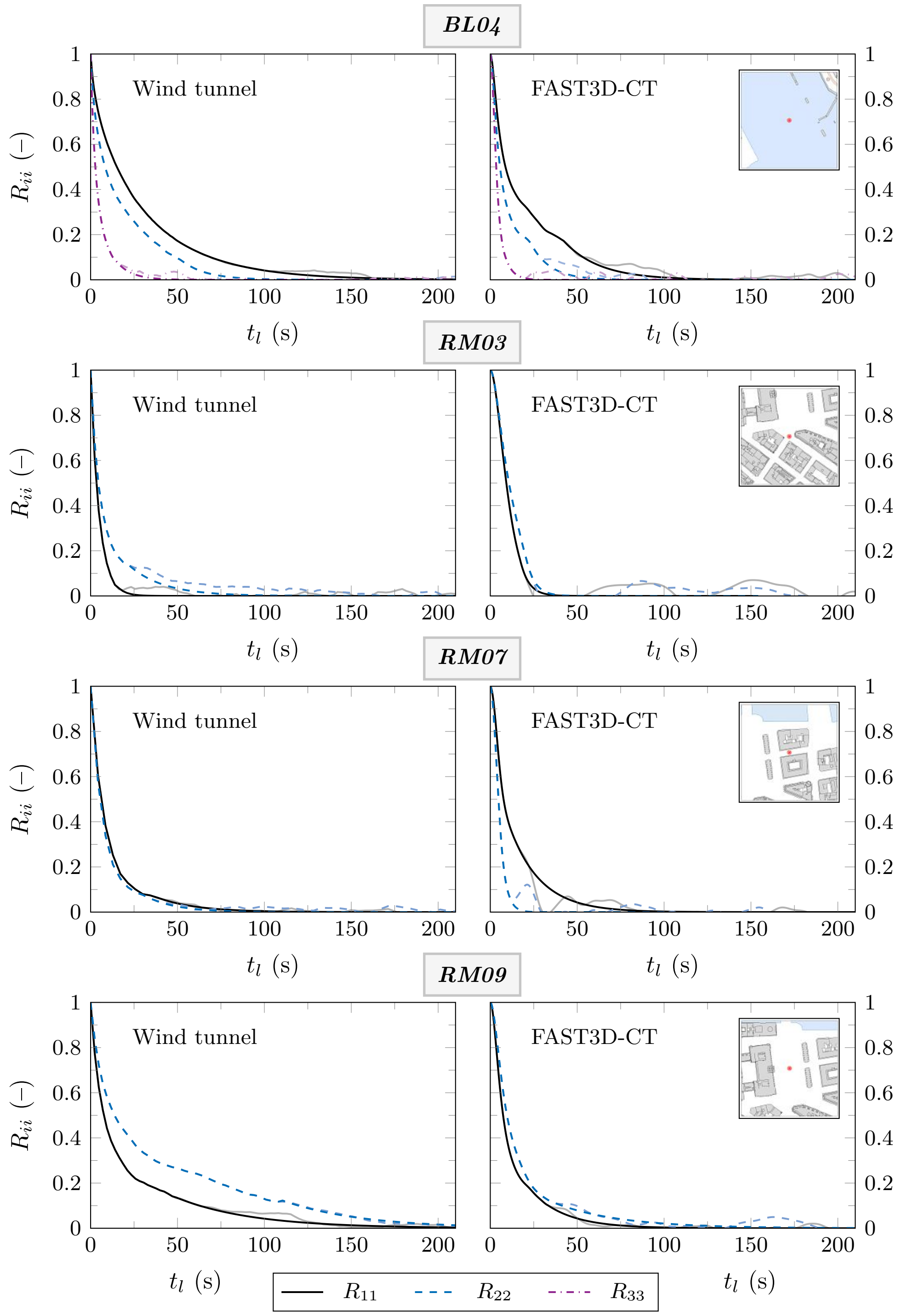

Figure 5.45: Same as in Figure 5.44, but for four comparison locations at a height of 17.5 m/17.75 m (wind tunnel/FAST3D-CT); i.e. approximately 0.5 H_m. Full-scale times correspond to a reference velocity, U_{ref}, of 5 m/s. Note that at the *RM* locations wind-tunnel measurements only exists for the horizontal velocity components and $R_{33}(t_l)$ cannot be validated.

Statements about eddy structures It is worthwhile to investigate details of the experimental and numerical autocorrelation function shapes in order to potentially derive information about the underlying turbulent eddy structures. Figure 5.46 shows close-ups on the autocorrelation curves at small time lags displayed for three example locations at different heights within the city. At all positions, the overall agreement between the LES and the wind tunnel for the analyzed velocity components is very high for both $R_{ii}(t_l)$ and τ_{ii}. A striking difference between the LES and the laboratory autocorrelations observed in Figures 5.46a–c (and in fact at all other comparison locations as well) concerns the different curvatures of the functions at short time lags (*here* below approx. 10 s). This characteristic is obvious in the linear (*left*-hand side graphs) and the semi-logarithmic display (*right*-hand side). In the latter, the experimental values of $R_{22}(t_l)$ and $R_{33}(t_l)$ virtually follow a straight line, indicating a fast exponential decay, whereas the turbulent eddy motions in FAST3D-CT seem to be slightly stronger correlated over short times (Figs. 5.46b,c). In the semi-logarithmic graphs, the symbols display the corresponding individual autocorrelation values in order to illustrate that the deviations are not just a graphical artifact caused by the unequal full-scale time steps in the experiment and the simulation. Even at locations where δt_{exp} and δt_{les} differ by less than a factor of 1.3 (e.g. in some of the *BL04* heights), the autocorrelation-function curvature in the wind tunnel is clearly higher at small time lags. While these offsets are most likely suggestive of some fundamental difference between the laboratory and the LES flow, it can merely be speculated about their origin by means of the current data basis.

A comparison of the shapes with early textbook examples discussed by Townsend (1956), however, sheds some light on the nature of the underlying eddy structures. For the example of *isotropic turbulence*, Townsend presented theoretical relationships for 1D *spatial* velocity autocorrelations as a function of spatial distance, which can generally be transferred into their temporal counterparts. Although atmospheric turbulence in general is never isotropic in the energy-containing range, the fundamental conclusions from Townsend's examples are probably conferrable. For turbulent flows, in which the eddy sizes are in some way restricted,[7] Townsend's R_{11}-function exhibits a more gentle slope at short time lags. If, on the other hand, a wide and continuous range of eddy structures is present in the flow, the initial slope near $t_l = 0$ is significantly steeper. The curvature deviations seen in Figure 5.46, hence, could be a footprint of the spatially filtered nature of the LES flow field, in which only the larger energy-dominating eddies are directly resolved – in contrast to the wind-tunnel flow, in which only the smallest eddies deviate from the natural ASL turbulence (cf. Section 3.2.2). Since all spatial scales smaller than the numerical grid ($h_i = 2.5$ m) are cut-off in FAST3D-CT, the corresponding time-scales are eliminated with them (cf. Sagaut, 2005).

Another noticeable feature encountered at various locations of the comparison domain is that some of the autocorrelation functions are composed of rapidly and slowly varying portions, which is often more pronounced for R_{11} (cf. Fig. 5.46a; *BL07* in Fig. 5.44, or *RM09* in Fig. 5.45). Reverting to the logarithmic display in Figure 5.46a, in both data sets the autocorrelation slopes are clearly steeper for lags below 10 s, which roughly corresponds to the *e-folding time* of the functions, than at the remaining time lags.

[7] Townsend (1956) refers to the special case of uniformly sized eddies.

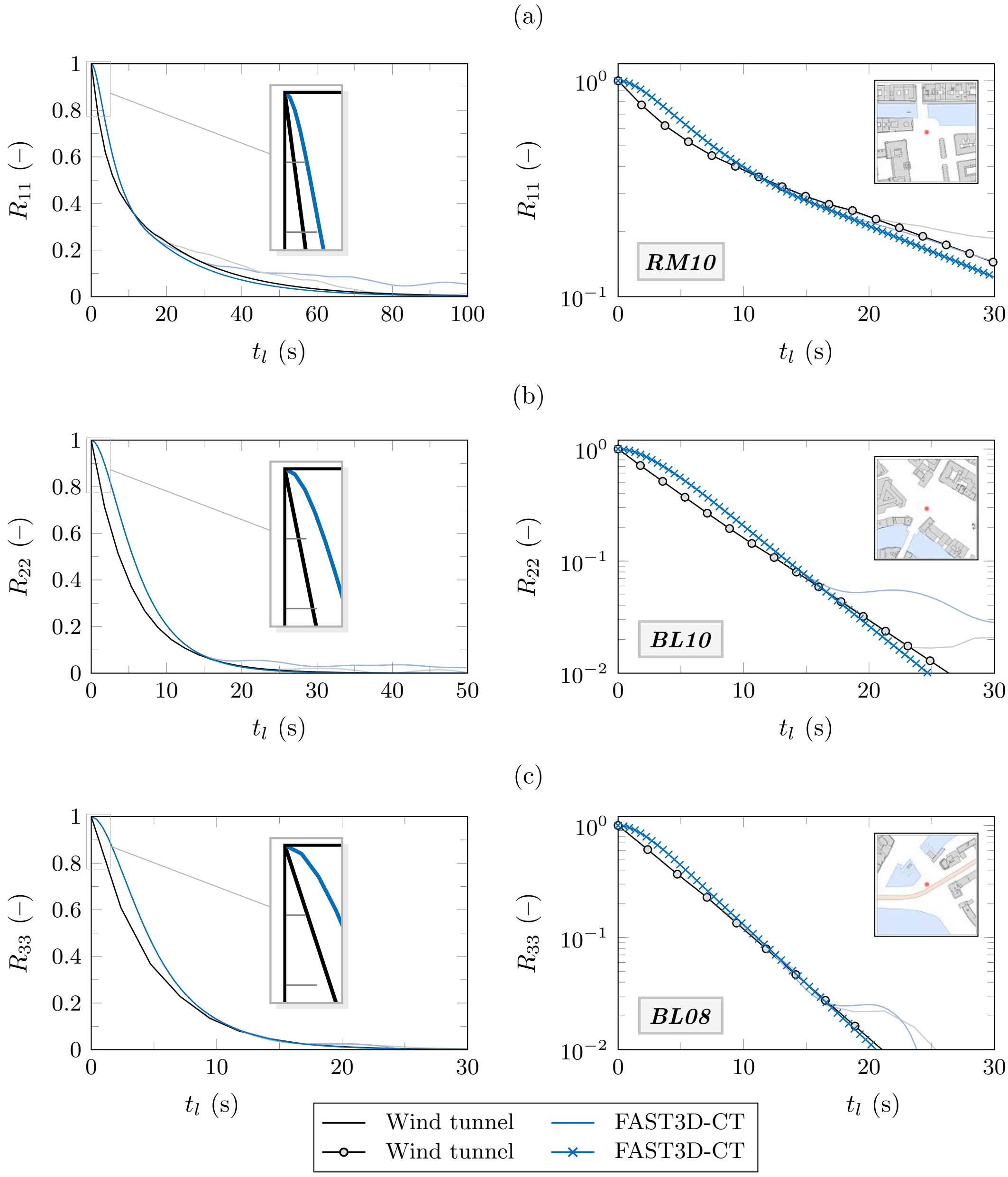

Figure 5.46: Close-up on experimental and numerical autocorrelation curves in a linear (*left*) and logarithmic (*right*) framework for (a) the streamwise velocity components, R_{11}, at location *RM10* in a common height of 40.25 m, (b) the spanwise velocity components, R_{22}, at location *BL10* in heights of 28.0 m/27.75 m (wind tunnel/FAST3D-CT), and (c) the vertical velocity components, R_{33}, at location *BL08* in heights of 45.5 m/45.25 m. The original (unfitted) autocorrelation curves are presented as well in lighter colors. Full-scale times correspond to a reference velocity of $U_{\mathrm{ref}} = 5\,\mathrm{m/s}$.

According to the discussions by Townsend (1956) or Lumley and Panofsky (1964), such shapes could be interpreted as a superposition of two autocorrelation functions. This could indicate that at certain positions the numerical and experimental flow fields are locally dominated by turbulent motions of rather different sizes and time scales (e.g. by coherent and incoherent eddy regimes). These speculations could be used as a starting point for further work that concentrates on a detailed time-dependent analysis of the corresponding local flow scenarios.

Vertical profiles of integral time scales

Figures 5.47–5.49 show height profile comparisons of the integral time scales for all three velocity components derived through Eq. (5.7), which were scaled to $U_{\mathrm{ref}} = 5\,{}^{\mathrm{m}}\!/_{\mathrm{s}}$. Results are displayed for the *BL* and *RM* locations, where it has to be recalled that measurements of the vertical velocity components are restricted only to the *BL* locations.[8]

A high level of qualitative agreement between the height dependencies of the autocorrelation time scales of the **streamwise velocity fluctuations**, τ_{11}, can be determined at most of the comparison locations shown in Figure 5.47. In the profiles of the *BL* locations, however, significantly shorter integral times are predicted by the LES at the highest elevations ($z_{\mathrm{les}} > 3\,\mathrm{H_m}$), which is in accordance with the fast decay observed in the corresponding autocorrelation functions. At both of the most upstream locations, *BL04* and *BL07*, where the direct influence of the urban environment on the eddy structures in the flow is expected to be small, the development of the numerical τ_{11} above the average building height is opposed to the characteristics seen in the laboratory. In the latter, an increase of τ_{11} reflects the scale increase of the dominant eddy structures farther away from the surface – a feature that is not reproduced by the LES. The largest deviations below roof level are observed at the street-canyon sites *BL11* and *BL12*. This could be related to the influence of the numerical boundary conditions imposed on the building walls. At other comparison points, notably the *RM* locations, *BL09*, and *BL10*, the agreement between the LES time-scale predictions and the reference experiment is remarkably high, in a qualitative and quantitative sense. This emphasizes the model's potential to specifically reproduce urban turbulence features in a realistic way.

Similar conclusions can be drawn from comparing integral time scales of the **spanwise velocity fluctuations**, τ_{22} (Fig. 5.48), for which FAST3D-CT is able to provide very accurate predictions in complex flow regimes (cf. e.g. *BL07*, *BL08*, *BL09* or *BL10*). The largest offsets are determined at position *BL11* and *RM09*, where the eddy-resolving model significantly underpredicts the comparatively large wind-tunnel time scales. At both locations, the laboratory flow is characterized by more enduring autocorrelations of the spanwise velocities compared with the streamwise fluctuations, which suggests the existence of rather long-lived motions in the lateral street canyon and on the plaza, which are not found in this extent in the LES (cf. earlier analysis of $R_{22}(t_l)$ at *RM09*, Fig. 5.45).

[8] The statistical reproducibility of the experimental result has been derived from repetition measurements, similarly to the derivation of the statistical scatter of the low-order moments outlined in Section 4.2.3. The analysis yielded full-scale maximum ranges of $\tau_{11} \pm 3.95\,\mathrm{s}$, $\tau_{22} \pm 1.85\,\mathrm{s}$, and $\tau_{33} \pm 1.17\,\mathrm{s}$, based on a mean reference velocity of $U_{\mathrm{ref}} = 5\,{}^{\mathrm{m}}\!/_{\mathrm{s}}$. The scatter incorporates effects of the natural variability of turbulent flows as well as the uncertainties of the fitting of the tails of $R_{ii}(t_l)$.

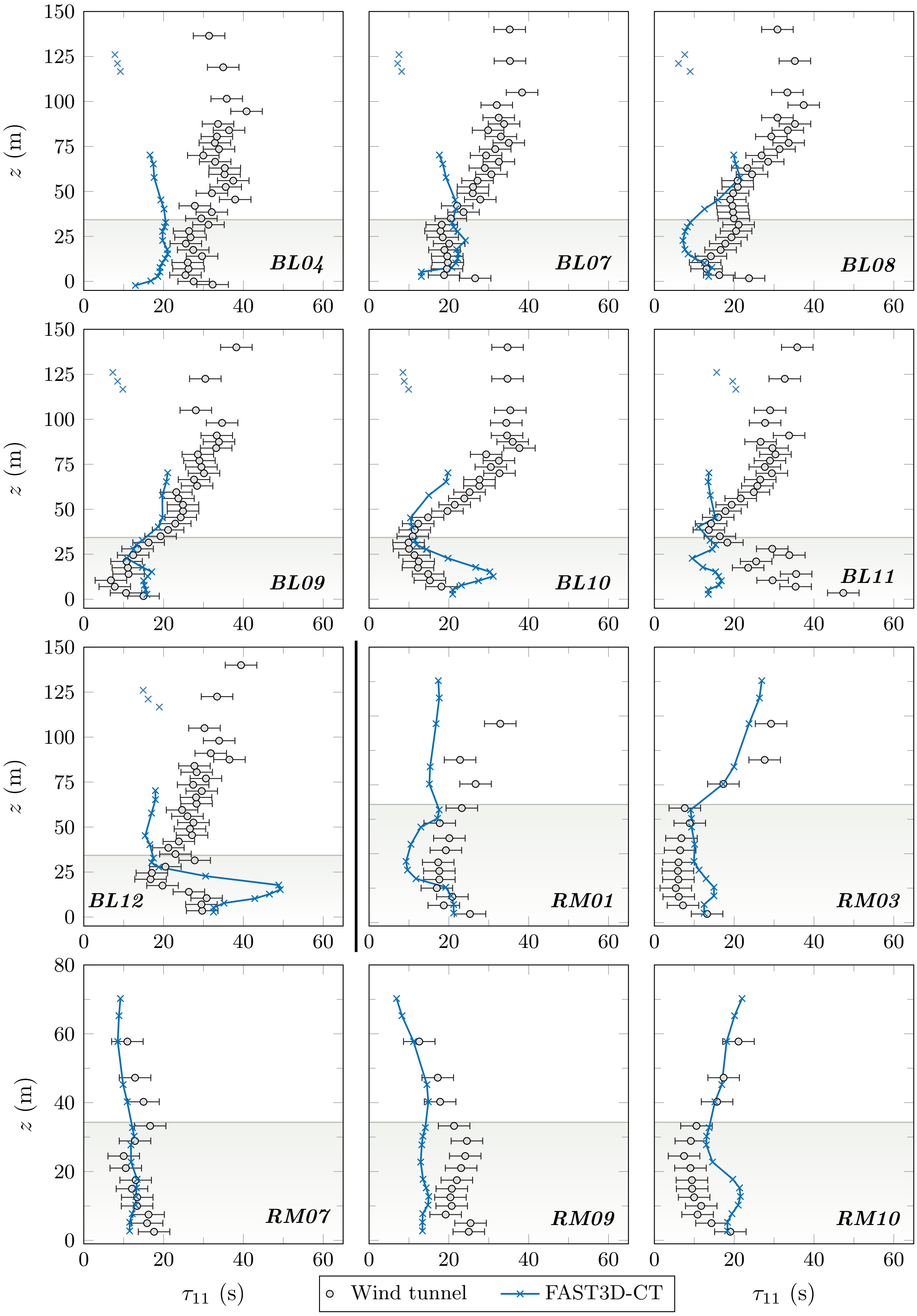

Figure 5.47: Comparison of height profiles of the autocorrelation time scales of the streamwise velocity component, τ_{11}, for the *BL* and *RM* locations ($U_{\mathrm{ref}} = 5\,\mathrm{m/s}$). The gray shading indicates heights lower than $\mathrm{H_m} = 34.3\,\mathrm{m}$. The z-axis changes for the *RM* locations (separated by a black line in the third row).

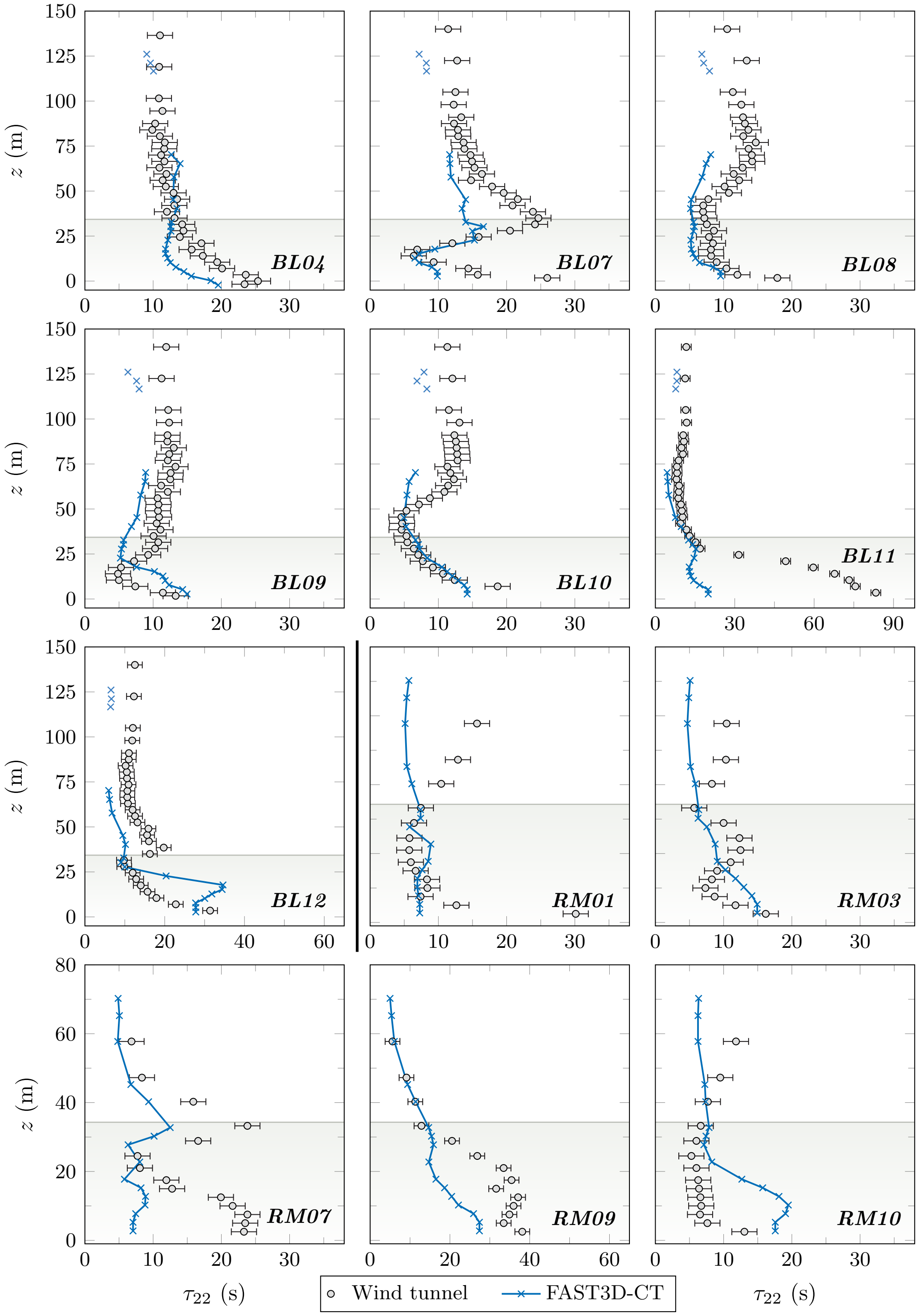

Figure 5.48: Same as in Figure 5.47, but for autocorrelation time scales of the spanwise velocity component τ_{22}.

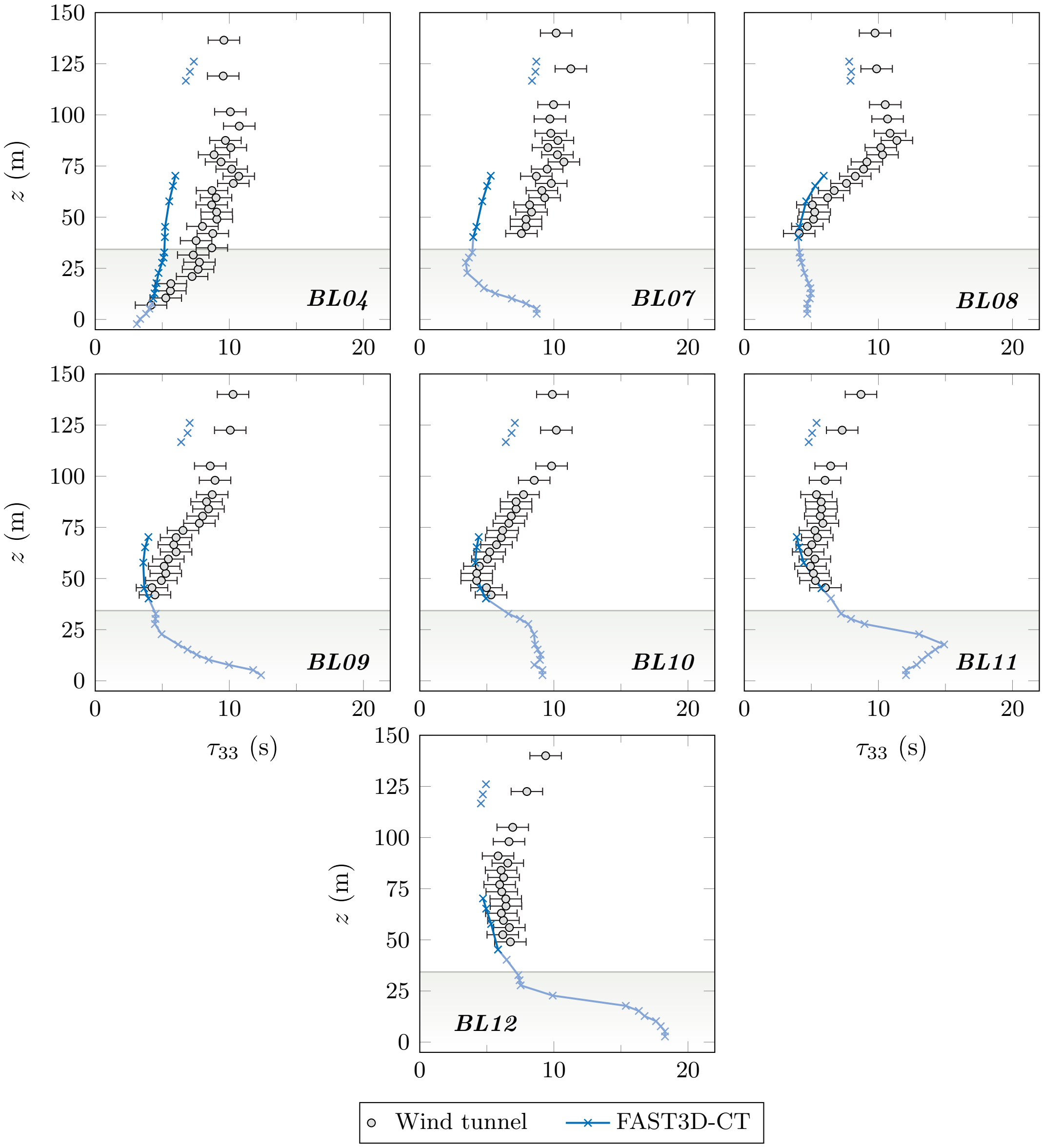

Figure 5.49: Same as in Figure 5.47, but for autocorrelation time scales of the vertical velocity component τ_{33}.

At heights in which direct comparisons can be conducted, the numerical integral time scales associated with the **vertical velocity fluctuations**, τ_{33}, are comparing very well with the experiment in the downtown area. As for τ_{11}, larger differences are noticeable at *BL04* and *BL07*. Below the average building height, FAST3D-CT predicts increased amplitudes of τ_{33} at various locations, which presumably indicates enhanced memory effects in the UCL flow fields. For τ_{22} and τ_{33}, the numerical predictions above 3 $\mathrm{H_m}$ are more consistent with the experiment than their streamwise equivalents shown earlier.

Evaluating the temporal scales in the LES flow field on the basis of single-point, time-resolved experimental data has proven to be of great value in order to build confidence in the results of the eddy-resolving simulation. The shape of the velocity autocorrelation functions can provide insight into the nature of the turbulent flow fields, while derived integral time scales can be consulted as temporal measures of the flow-dominating eddy structures, which the LES is expected to directly resolve. At many of the comparison locations, a high level of agreement between FAST3D-CT and laboratory time scales could be determined within the urban canopy layer. This result emphasizes the strength of this specific LES code to realistically predict urban aerodynamics and the characteristics of building-induced turbulence. Larger differences mostly show in situations for which the selected grid size in combination with the numerical representation of buildings is likely to hamper an adequate representation of the flow at the comparison site. This result and the apparent influence of the inflow turbulence on velocity autocorrelation characteristics at higher elevations are consistent with earlier assessments from the comparison of mean flow statistics and frequency distributions. Studying the progression of the numerical and experimental velocity autocorrelations as a function of time lag also provides information about the underlying eddy structures. Such analyses, however, need to be substantiated by further investigations, e.g. regarding the influence of the temporal filtering on the R_{ii} curvature tendencies for small time lags.

In direct comparison to the earlier validation methods, the approach followed in this section is attended by a larger degree of freedom with respect to computational aspects and directly inferable informative value. While time-dependent correlation measures certainly include a lot of relevant information about the state of the turbulent flow, accessing and interpreting these information is not trivial and ultimately involves a certain level of guesswork. This, in the end, also affects the potential to *quantify* the validation results.

Important findings from the analysis and comparison of **temporal autocorrelations & integral time scales** of turbulent velocities are recapitulated below:

- FAST3D-CT demonstrated its potential to provide a realistic picture of urban turbulence time scales, measured by velocity autocorrelations and corresponding integral times.
- Detailed investigations of $R_{ii}(t_l)$ allow to determine the influence of the scale-reduced (filtered) nature of the LES and can provide information about the structure of the flow.
- Left-overs of artificial inflow turbulence presumably caused larger deviations between the temporal characteristics above the urban roughness sublayer.

Analyzing velocity time-correlations is a first step toward the investigation of turbulence statistics that are connected to spatio-temporal flow features, and therefore, to some degree, to the structure of turbulent eddies. A logical next step is to investigate the statistical distribution of kinetic energy among different eddy scales in the flow in terms of auto-spectral energy densities, which are directly related to the Fourier transforms of the autocorrelation functions. This analysis is presented in the following section.

5.5 Energy density spectra

One-dimensional auto-spectral energy densities and co-spectra of turbulent velocity fluctuations within the urban roughness sublayer are studied in order to determine which eddy range the LES is able to resolve directly and to assess the level of accuracy of the energy distribution among these scales. The following points are discussed:

1. General shape characteristics of experimental and numerical spectra.
2. Height and/or location dependence of velocity auto-spectra of u', v', and w'.
3. Characteristics of u'-w' co-spectra.
4. Spectral scaling considerations for UCL velocity spectra.

Under **1.**, general computation and analysis procedures are introduced together with an evaluation of specific characteristics of the LES spectra compared with their wind-tunnel counterparts. Point **2.** and **3.** are concerned with the direct comparison of auto-spectral energy density distributions in a scaled frequency framework. The focus is put on the investigation of the level of agreement at structurally different flow locations within the urban domain, particularly flow above and below rooftop. Based on representative examples, dependencies of the comparison results on spectral scaling procedures for flow within the canopy layer are discussed (**4.**). In all analyses, *resampled* (equidistant time) wind-tunnel velocity data are used. Additional material is presented in Appendix E.

5.5.1 Height & location dependence

Information available from the temporal autocorrelation functions, $R_{ii}(t_l)$, of turbulent velocity fluctuations is also available in the frequency domain in terms of *auto-spectral energy densities*, $E_{ii}(f)$. Both quantities form a Fourier transform pair known as *Wiener-Khinchin relation* (e.g. Nobach et al., 2007). The advantage of the spectral representation is that the auto-spectral energy densities disclose the distribution of the signal's variance among different eddy scales in the flow, encompassed by a certain frequency increment. For a three-dimensional analysis using the entire 3D velocity vector, the spectral energy densities represent contributions to the total turbulence kinetic energy per frequency bin. Due to the resolution of the experimental data available in this study, the analysis concentrates on the comparison of 1D auto-spectral energy densities and co-spectra.

The Fourier coefficients, $\widehat{u_i}(f)$, of the discrete time series of the fluctuating velocity component, $u_i'(t)$, can be derived through a *discrete Fourier transform* (DFT) with a *fast Fourier transform* (FFT) algorithm. In this study, the *Cooley-Tukey algorithm* (Cooley and Tukey, 1965) is used, which requires the number of samples to be given as a power of two. Taking the example of the streamwise fluctuations, $u'(t)$, the *one-sided auto-spectral energy densities* are obtained from the complex-valued Fourier coefficients according to

$$E_{uu}(f_k) = \frac{2}{N f_s} \widehat{u}_k^* \widehat{u}_k = \frac{2}{N^2 \delta f_s} |\widehat{u}_k|^2 \ , \tag{5.8}$$

where the frequency index is $k = 0, \ldots, N/2$, N is the number of samples in the signal, f_s is the sampling frequency or data rate of the time series, $\delta f_s = f_k - f_{k-1}$ is the constant frequency increment, and the asterisk denotes the *complex conjugate* (Nobach et al., 2007). In the same way, energy density spectra, E_{vv} and E_{ww}, can be derived from the spanwise and vertical velocity fluctuation time series, v' and w'.

For paired signals (for example, streamwise and vertical velocity fluctuations), the so-called *cross spectrum* can be obtained from

$$E_{uw}(f_k) = \frac{2}{N^2 \delta f_s} \widehat{u}_k^* \widehat{w}_k \tag{5.9}$$

and provides information about the amplitude and phase relations between the signals. In boundary-layer research, the real and imaginary parts of the cross spectrum are often analyzed separately by using the decomposition $E_{uw}(f_k) = \mathrm{Co}_{uw}(f_k) - i\mathrm{Q}_{uw}$ (Stull, 1988). The *co-spectrum*, Co_{uw}, and the *quadrature spectrum*, Q_{uw}, are defined as

$$\mathrm{Co}_{uw}(f_k) = \mathrm{Re}\{\widehat{u}_k\}\mathrm{Re}\{\widehat{w}_k\} + \mathrm{Im}\{\widehat{u}_k\}\mathrm{Im}\{\widehat{w}_k\} \ , \tag{5.10}$$

and

$$\mathrm{Q}_{uw}(f_k) = \mathrm{Im}\{\widehat{u}_k\}\mathrm{Re}\{\widehat{w}_k\} - \mathrm{Re}\{\widehat{u}_k\}\mathrm{Im}\{\widehat{w}_k\} \ . \tag{5.11}$$

The co-spectrum represents the *coincident spectral density* (Kaiser and Fedorovich, 1998) and is of particular interest for the analysis of ASL turbulence since $\sum_k \mathrm{Co}_k = \overline{u'w'}$, yielding the vertical turbulent momentum flux.

All spectra are presented in a non-dimensional framework: Both $E_{ii}(f)$ and f are referenced to appropriate scaling quantities in order to make numerical and experimental data directly comparable. For atmospheric problems, the squared magnitude of the friction velocity, u_*, is typically used to scale the energy densities, $E_{ii}(f)$, as proposed by Kaimal et al. (1972) based on the Kansas field data (cf. Section 3.2.3). As opposed to flow over a spatially homogeneous surface, within the urban RSL the choice of a representative value of u_* can be ambiguous, as has been discussed earlier in Section 2.4.1. Instead of relying on local scaling approaches to determine u_*, this study uses the local velocity variances of the signals, σ_i^2, for scaling as, for example, suggested in the VDI (2000) guideline. Hence, dimensionless auto-spectral energy densities of the ith velocity component are given by $E_{ii}^\star(f) = f\, E_{ii}(f)\, \sigma_i^{-2}$. The frequencies are scaled by the height above ground, z, at which the measurement was taken or the data record has been extracted from the simulation, and by a representative velocity scale, which usually is defined as the *magnitude* of the *local* mean streamwise velocity, $\overline{U}(z)$. That is, $f^\star = f\, z/\overline{U}$. As will be discussed in more depth in Section 5.5.2, the choice of the characteristic velocity is important for certain UCL flow situations and potentially affects the comparison outcome.

The next paragraphs present a selection of representative validation results based on comparisons at different sites within the urban domain. Only those spectra were analyzed, for which the ratio between numerical sampling frequencies and full-scale experimental data rates was comparatively low (cf. Fig. 4.36, Section 4.4.3). Experimental u' and v' spectra were derived from measurements in U-V LDA mode. Vertical velocity spectra as well as u'-w' co-spectra were obtained from paired U-W LDA measurements.

In order to make spectral estimates amenable to a direct visual comparison, a two-step *spectral smoothing* approach has been followed, which is frequently applied in micro-meteorological data analysis (cf. Kaiser and Fedorovich, 1998). This approach uses an initial averaging over an ensemble of spectral subsamples and a subsequent averaging over exponentially increasing frequency bins (see also discussion in Kaimal and Finnigan, 1994). A detailed description of the spectral theory, specific computational steps including an in-depth discussion of the spectral smoothing approach, as well as a verification study of the written `MATLAB` code is presented in Appendix E.

Auto-spectral energy densities

The validation of FAST3D-CT on the basis of energy density spectra is based on two aspects: First, the comparison of spectral shapes, which provides information about the variance connected to certain eddy scales. Secondly, the identification and comparison of frequency ranges corresponding to the spectral peak region, which is associated with the energy-dominating eddies in the flow. From an LES, it is expected that the energy-containing turbulence is directly resolved, ideally well into the inertial subrange. In LES, the effective turbulence resolution potential is formally coupled to the filter width, the grid size and the specific properties of the employed numerical methods. But also the nature of the flow problem has an influence on the resolution qualities. The overall length scales of the energy-dominating eddies in UCL flow fields, for example, can be expected to be *smaller* than those encountered in the inertial sublayer aloft or in ASL flow over homogeneous terrain. In the case of FAST3D-CT, in which the direct simulation of turbulence only concerns structures sufficiently larger than 2.5 m, it has to be evaluated whether the grid resolution is fine enough to resolve the dominating parts of urban turbulence.

Figure 5.50 shows examples of wind-tunnel and FAST3D-CT u'-spectra taken at 0.5 $\mathrm{H_m}$ above the Elbe river (*BL04*), in order to point out some basic shape characteristics.

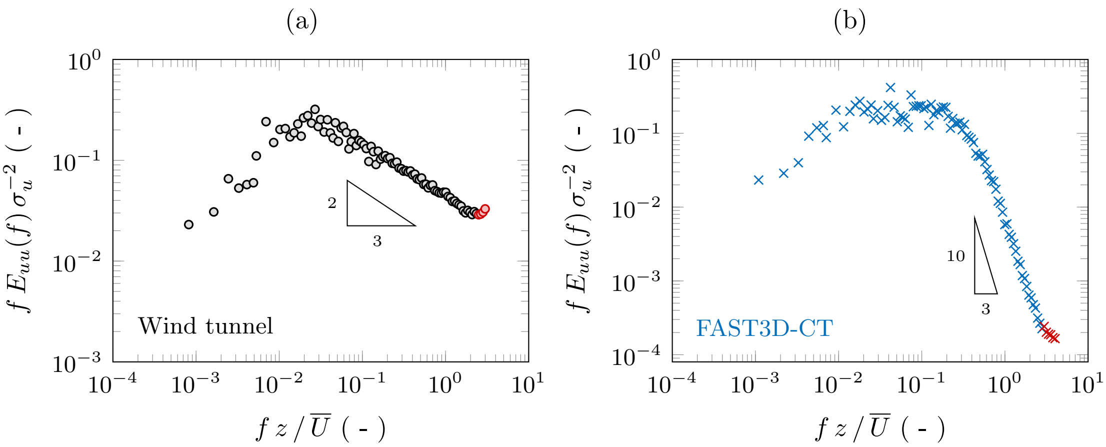

Figure 5.50: Shapes of the auto-spectral energy densities of the u'-component at *BL04* for (a) the wind tunnel in a height of 17.5 m and (b) FAST3D-CT in 17.75 m. Triangles approximate the slope of the high-frequency tails. Spectral estimates affected by aliasing are marked in red.

Both spectra occupy a similar scale range, expressed in terms of dimensionless frequency, from approximately 10^{-3} to 4. The most striking difference between the experimental and LES spectra concerns the roll-off characteristics in the high-frequency range. While the wind-tunnel spectrum shows the expected $-2/3$ power-law behavior in the inertial subrange, starting approximately at $f^{\star} \simeq 0.1$ (cf. Fig. 5.50a), a much faster energy decay is seen in the FAST3D-CT spectrum, approximately following a $-10/3$ slope (Fig. 5.50b). The Cartesian numerical grid used in FAST3D-CT effectively acts as a top-hat filter that is sharp in physical space, but oscillatory in spectral space. As discussed earlier in Section 2.2.2 (see also Fig. 2.5), this causes an attenuation of the numerical frequency spectra even at frequencies that are directly resolvable.[9] In addition, the numerical dissipation characteristics, vital for the implicit LES scheme, also influence the physical resolution in the high-frequency range near the grid cut-off and can contribute to enhanced energy loss.

In both data sets, *aliasing effects* affecting energies at the highest frequencies are evident (indicated in red color; see also Appendix E). In the following point-by-point comparison, spectral estimates exhibiting aliasing bias are *not* removed, but displayed in a brighter shading. Furthermore, the FAST3D-CT spectra are only displayed up to frequency and energy ranges that can still be compared to the wind-tunnel references: The very low energy densities of the high-frequency tails ($E^{\star}_{ii}(f) < 10^{-3}$) are cut off.

U, V, & W-spectra at $1.3\,\mathrm{H_m}$

Figure 5.51 shows comparisons of the wind-tunnel and LES energy density spectra associated with the three velocity components well above the mean building height ($z_{\mathrm{exp}} \simeq z_{\mathrm{les}} \simeq 1.3\,\mathrm{H_m}$; $|\delta z| = 0.25\,\mathrm{m}$). The displayed *BL* sites feature an increasing downstream distance from the inflow edges of the models, so that the growing influence of the urban structure on the RSL flow is detectable (see also Fig. 4.26). For all velocity components and all comparison points, the agreement between the FAST3D-CT and wind-tunnel spectra is very good in the low-frequency range, associated with the largest and rarest eddy structures, and mostly also in the spectral peak range. In direct comparison to the wind tunnel, the faster roll-off of the numerical spectra at high frequencies is very distinct. For all velocity components, the rapid decay of the LES energy densities starts immediately after the energy peak region, and no clear inertial range behavior congruent with K41 theory is identifiable. In the experimental results for location *BL04* the offset of the spectral peaks between the individual velocity components is particularly evident, with the peak energies of the horizontal components being associated with lower frequencies (longer wavelengths) than peaks in the vertical velocity spectra. At this location, the largest offsets between both data sets are found, with FAST3D-CT showing systematic shifts of energy peaks toward higher frequencies. In the streamwise velocity spectra, for example, the respective peaks are almost one frequency decade apart. At the same time, the region of highest energies is also substantially broader in the LES than in the experiment, particularly for the horizontal velocities, causing an overlap with the peak ranges of the wind-tunnel data. The offsets seen in the u'-spectra significantly decrease as the flow is increasingly influenced by the underlying city structure.

[9] The frequency cut-off corresponding to the implicit spatial filter can be determined from its temporal equivalent, which depends on the grid resolution, h_i, and a representative local flow velocity (e.g. $\overline{U}$).

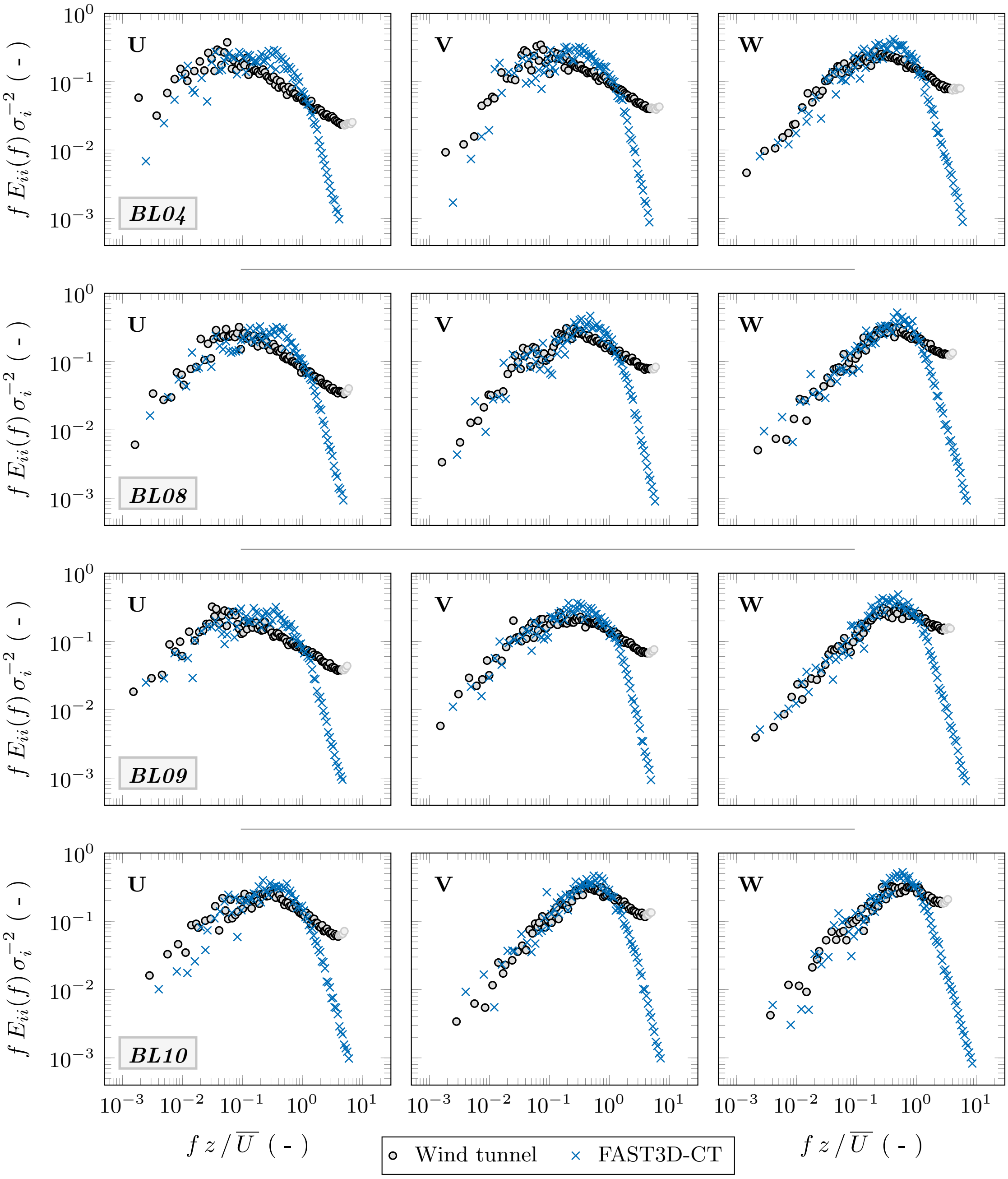

Figure 5.51: Auto-spectral energy densities of the streamwise (*left*), spanwise (*center*), and vertical (*right*) velocity fluctuations at four comparison locations in heights of 45.5 m/45.25 m (wind-tunnel/FAST3D-CT), corresponding to 1.3 $\mathrm{H_m}$.

An interesting feature of the spanwise velocity spectra at *BL08* is the double-peak pattern, which is captured very well in the simulation. This pattern could represent a structural change in the flow. While the first peak is located at a similar frequency range as observed in the experimental spectra at the upstream river location *BL04*, the second peak agrees well with the maximum-energy frequencies determined further downstream at the city locations *BL09* and *BL10*. The increasing influence of the urban roughness on the upper-level flow is reflected in the fact that the size of the energy-containing eddies, measured by the frequency location of the energy peaks, is gradually decreasing and the auto-spectra of the three velocity components tend to converge at higher frequencies (compare the differences between spectra at *BL04* and *BL10*).

U & V-spectra at 0.5 $\mathrm{H_m}$

Comparisons of auto-spectral energy densities well below rooftop in a height of 0.5 $\mathrm{H_m}$ ($|\delta z| = 0.25\,\mathrm{m}$) are presented in Figures 5.52 and 5.53 for six sites. Here, only spectra of the horizontal velocities can be directly compared since no wind-tunnel measurements of the vertical velocities are available for the UCL positions.

At the majority of positions, the experimental and numerical spectra are well overlapping in the low frequency range. At sites *BL12*, *RM01*, and *RM10*, it is obvious that the mean LDA sampling rates in the wind-tunnel were too low to resolve the inertial subrange portion of the flow. Nevertheless, at all locations the experiment provides sufficient information for a direct comparison between the energy-containing spectral ranges. In agreement with the earlier findings for flow above rooftop, the largest deviations between the peak ranges of the u'-spectra are found at *BL08*, which is situated farther upstream than the other displayed locations. Offsets also emerge in the peak magnitudes of the u' and v' energy densities at *BL08* and, less strongly pronounced, at *BL09*. Shifting to the city-center points, the auto-spectral energy densities of the horizontal velocities are mostly agreeing well. Some dubious features, however, are identifiable in the numerical spectra at the street-canyon location *BL12* (canyon width $\mathrm{W} \simeq 13.5\,\mathrm{m}$). The apparent energy oscillations at higher frequencies in the u' and v' spectra (approx. between $f_\star \simeq 1$ and 3) may reflect the obstructive influence of the building walls on the local LES flow structure. This conjecture is supported by the fact that similar oscillations were observed at the street-canyon position *BL11* (not shown), for which previous analyses indicated the relevance of the proximity to the building surface for the comparison.

U, V, & W-spectra at 3.5 $\mathrm{H_m}$

All of the previous analyses of turbulence statistics gave reason to assume that the LES flow at the outer edge of the roughness sublayer still carries signatures of the artificially generated inflow turbulence. This is further substantiated by the shape of the spectral curves at approximately 3.5 $\mathrm{H_m}$ shown in Figure 5.54 for the example of location *BL07*. The comparatively large vertical difference between the experimental and numerical flow locations ($|\delta z| = 1.38\,\mathrm{m}$) is assumed to have a negligible influence on the comparability of the results since the upper-level flow does not feature significant gradients over this distance. A considerable shift of the FAST3D-CT spectra of the horizontal velocity fluctuations toward higher frequencies (smaller eddies) can be seen in Figure 5.54, while only slight offsets to the wind-tunnel reference are evident in the w' spectrum. The energetic dominance of comparatively smaller eddies in the LES flow is in agreement with the corresponding systematically reduced integral time scales (cf. Figs. 5.47–5.49, Section 5.4.2).

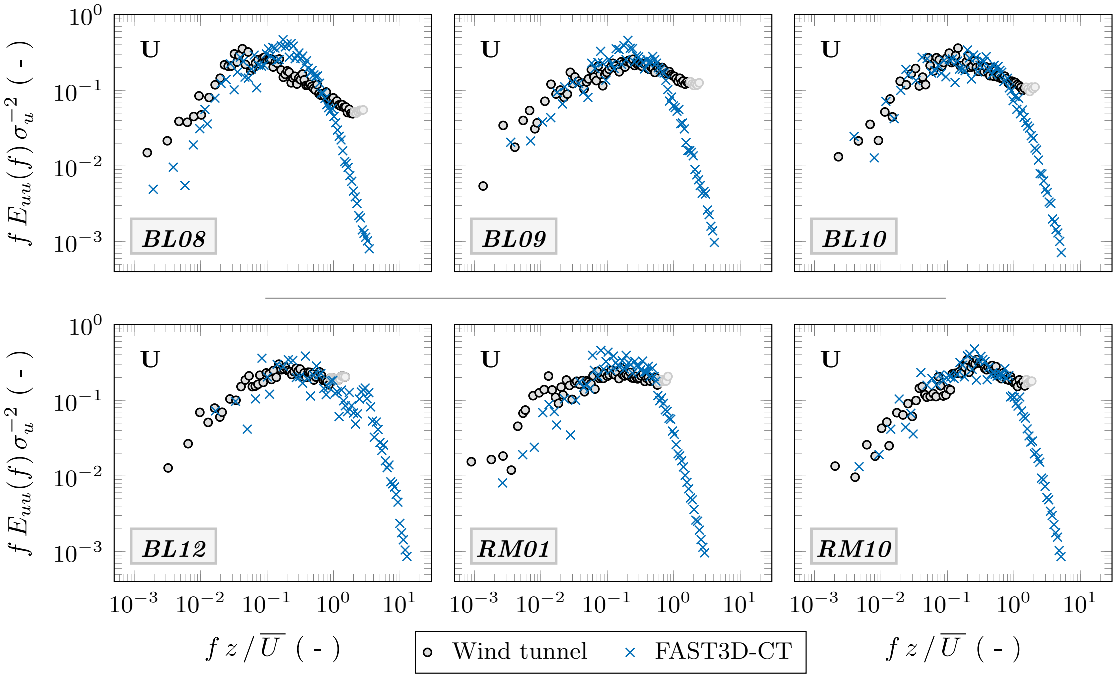

Figure 5.52: Auto-spectral energy densities of the streamwise velocity fluctuations at six comparison locations in heights of 17.5 m/17.75 m (wind-tunnel/FAST3D-CT), corresponding to 0.5 H_m.

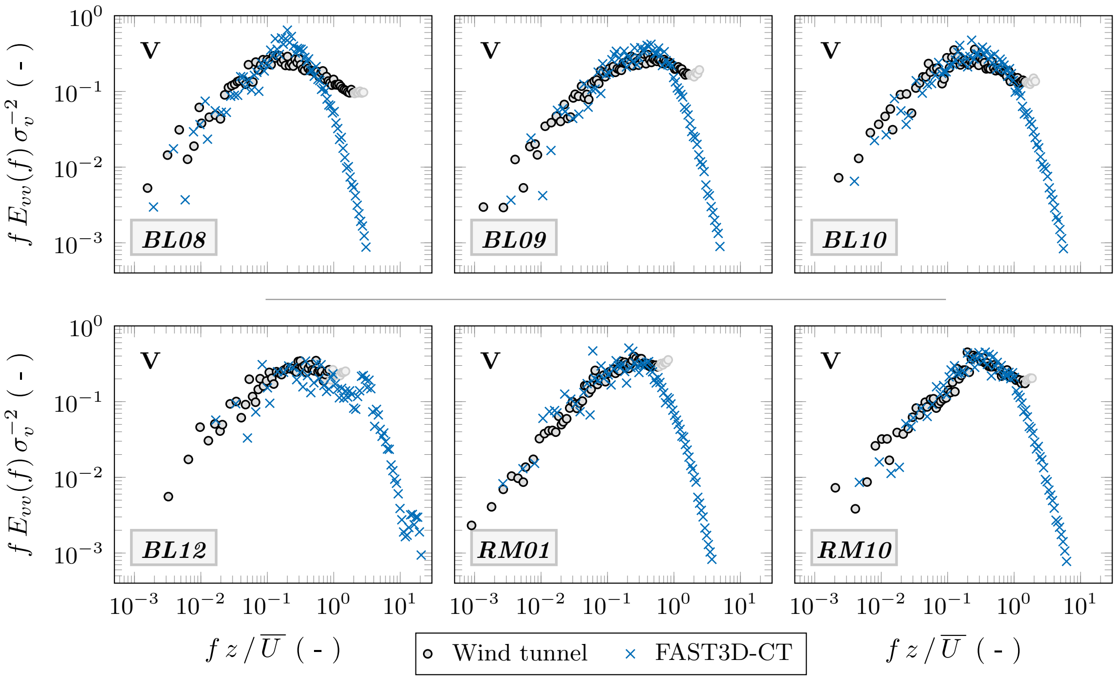

Figure 5.53: Same as in Figure 5.52 but for the spanwise velocity fluctuations.

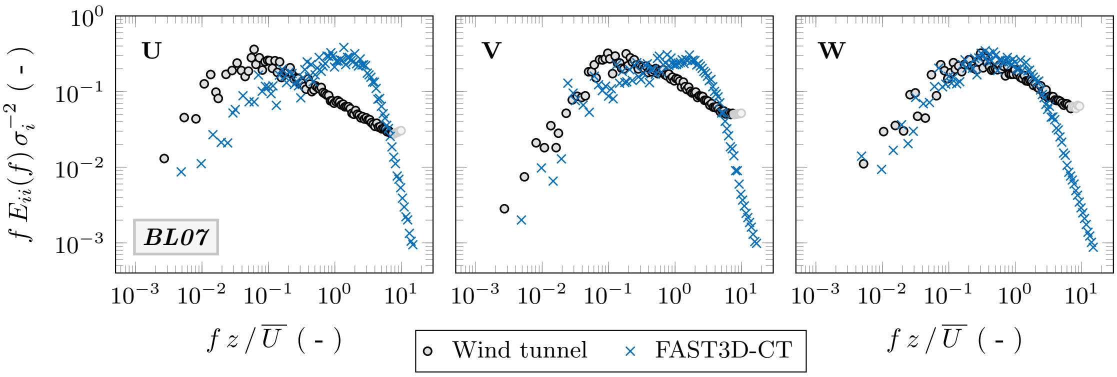

Figure 5.54: Auto-spectral energy densities of the streamwise (*left*), spanwise (*center*), and vertical (*right*) velocity fluctuations at location *BL07* in heights of 122.5 m/121.12 m (wind-tunnel/FAST3D-CT), corresponding to 3.5 $\mathrm{H_m}$.

U-W co-spectra at 1.3 $\mathrm{H_m}$

Coincident spectral densities (co-spectra, Co_{uw}) as the real part of the cross spectra, E_{uw}, were derived from simultaneous LDA measurements and numerical simulations of the streamwise and vertical velocity fluctuations following Eq. (5.10). Velocity co-spectra are of special interest since they directly relate to the kinematic vertical turbulent momentum flux, $\overline{u'w'}$. The spectral distribution of Co_{uw} among different frequencies, thus, reflects the relevance of certain eddy structures for the turbulent mixing process.

Figure 5.55 depicts comparisons between wind tunnel and FAST3D-CT curves at six of the *BL* sites in a height of 1.3 $\mathrm{H_m}$. Following the earlier argumentation, the co-spectra are not normalized by the friction velocity, u_*, but by the product of the local rms-values of both velocity components, σ_i $(i = 1, 3)$. In the results for location *BL04*, the steeper slopes of the co-spectral energies in the inertial subrange compared with their auto-spectral counterparts shown in Figure 5.51 are clearly evident. This feature is consistent with the local isotropy requirement for inertial-subrange turbulence and sustains the assumption that primarily the large, anisotropic eddy structures play dominant roles for turbulent mixing (e.g. discussions in Kaimal and Finnigan, 1994). At position *BL04*, a strong agreement between the experimental and LES spectral slopes can be observed, following the anticipated $-4/3$ power-law decay described by Wyngaard and Coté (1972) or Kaimal et al. (1972).[10] At other locations, the roll-off of the LES spectra is considerably faster, in agreement with the earlier findings for the auto-spectra. Since the co-spectra comprise information from two fluctuating velocities, the overall scatter is higher than in the one-component spectra, despite the fact that the same smoothing procedures were applied.

At the investigated positions, FAST3D-CT captures the co-spectral shapes and the flux-dominating frequency ranges very well. A slight shift of the spectral maxima toward higher frequencies (smaller eddies) from the river location *BL04* to the urban site *BL12* can be observed in both data sets, which presumably indicates the increasing influence of the urban environment on the relative size of turbulence structures above the UCL.

[10] For the unreferenced co-spectral energy densities, the slope is $-7/3$ in a double-logarithmic display.

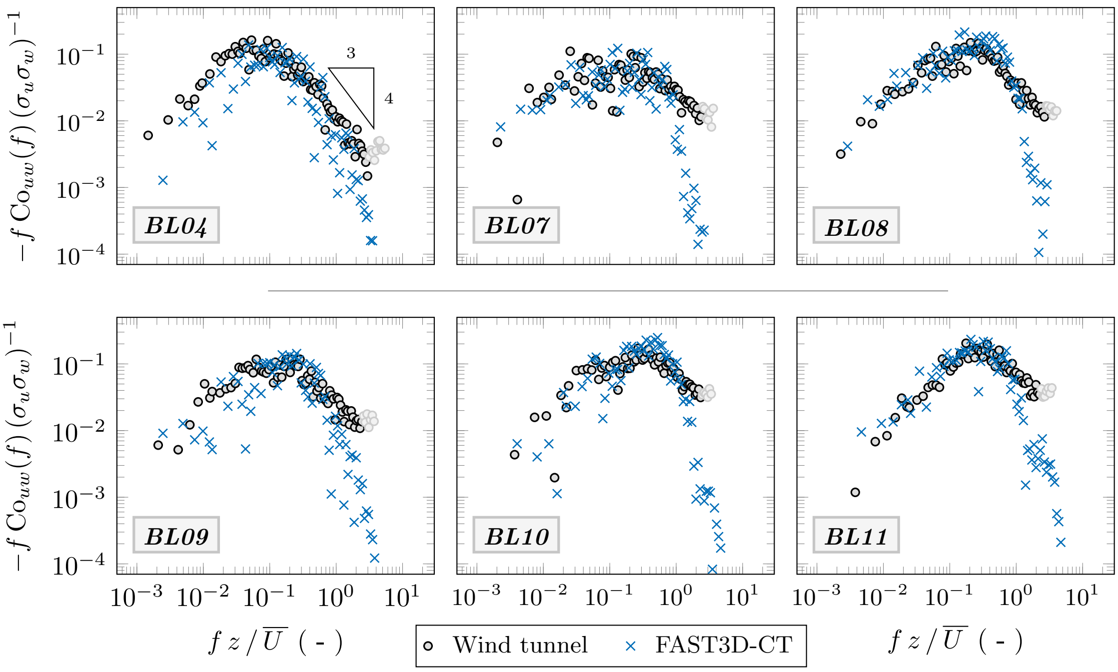

Figure 5.55: Co-spectra of streamwise and vertical velocity fluctuations at six *BL* sites in heights of 45.5 m/45.25 m (wind tunnel/FAST3D-CT; 1.3 $\mathrm{H_m}$). The triangle indicates the expected $-4/3$ slope in the inertial subrange.

5.5.2 Scaling considerations

The motivation behind spectral scaling is to bring energy density curves that correspond to the same turbulence characteristics to coincide by removing the influence of ambient parameters like the mean advection wind strength. For the validation study, scaling is crucial in order to make wind tunnel and LES data directly comparable, despite the fact that the results correspond to two different realizations of the flow scenario.

If deviations of spectral shapes of the experimental and numerical velocity fluctuations are observed, scaling should ensure that these are mirroring true differences between eddy statistics and did not result from differences in the ambient parameters. In Section 5.5.1 it had already been stated that scaling the energy densities by the squared magnitude of the friction velocity can be ambiguous in the UCL since defining an appropriate magnitude of u_* is not trivial below rooftop. Scaling with the local (height-dependent) variances, σ_i^2, overcomes this problem. In a similar way, a suitable frequency referencing can be hampered in urban areas. By scaling the frequencies, the spectra are basically shifted along the x-axis, depending on the choice of length and velocity scales. On the basis of wind-tunnel data measured in a realistic city-center model, Feddersen (2005), for example, discusses advantages of using $(z - d_0)$ as a reference length scale in order to determine differences between urban and rural turbulence features and their spectral footprint. In the present study it is found that the choice of a representative *velocity scale* can also have a considerable influence on the comparison outcome at certain flow locations.

Figure 5.56 illustrates the influence of the selected velocity scale on the agreement between v'-spectra in three heights at the plaza location *BL09*. Results are presented for three choices of velocity magnitudes: $\overline{U}$ (*left*), $\overline{V}$ (*center*), and $\overline{U}_h$ (*right*).

At the two lowest comparison levels, significant offsets between the spectral peaks using the $\overline{U}$-scaling are evident, whereas well above roof level the numerical and experimental spectra are exactly coinciding. Within the UCL, the characteristic advection velocity of the flow does not necessarily correspond to the alongwind direction of the approach flow, since the influence of the buildings usually results in very complex flow pattern, even in the mean. The analyses in Section 5.2 (mean flow) and Section 5.3 (wind roses) showed, that the plaza flow is characterized by similar mean magnitudes of the streamwise and spanwise velocities and very broad frequency distributions of instantaneous velocity samples.

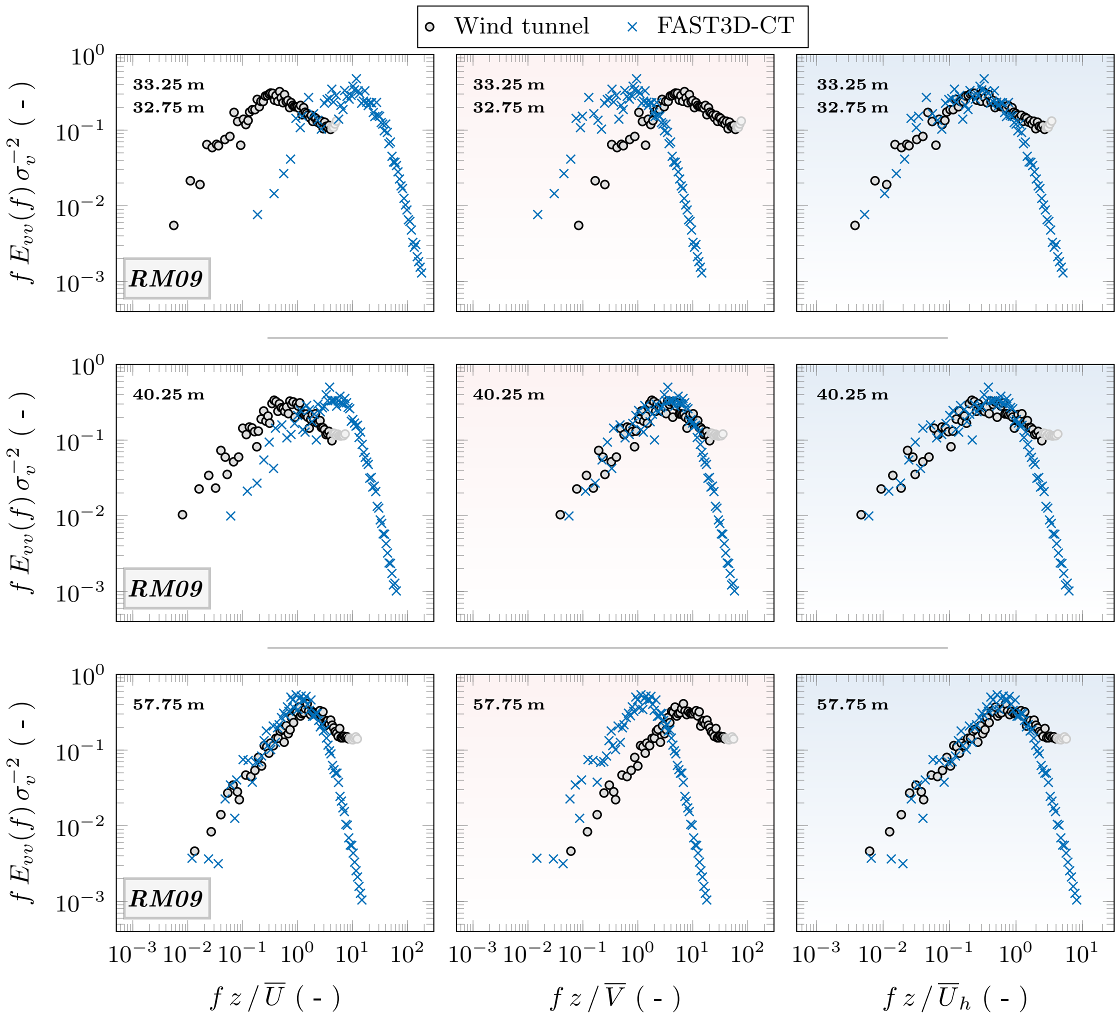

Figure 5.56: Influence of the frequency scaling on the agreement between the experimental and numerical energy-density spectra of v' in three heights at location *RM09*, with $\overline{U}$ (*left*), $\overline{V}$ (*center*), and $\overline{U}_h$ (*right*) used as characteristic velocity scales.

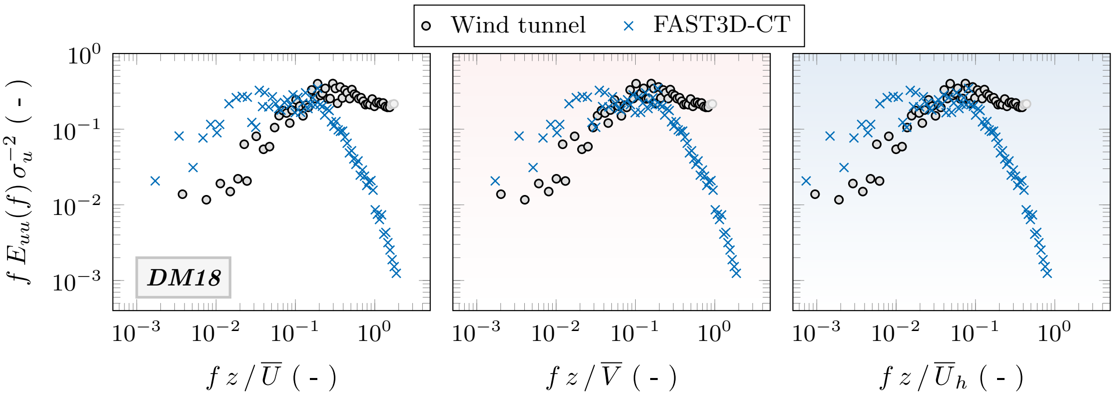

Figure 5.57: Influence of the choice of the frequency scaling on the agreement between the experimental and numerical energy-density spectra of u' in heights of 3.5 m/2.75 m (wind tunnel/FAST3D-CT) at location *DM18* with $\overline{U}$ (*left*), $\overline{V}$ (*center*), and $\overline{U}_h$ (*right*) used as characteristic velocity scales.

Complex wind rose pattern further documented the significance of the spanwise velocity on the shape of the anticipated recirculation zone on the leeward side of the city hall (cf. Fig. 5.24). Despite obvious offsets between the temporal flow statistics, the previous results have provided no indication that *significant* differences between eddy structures in the flow exist at the displayed heights (recall the comparison of integral time scales, τ_{ii}, in Section 5.4.2; e.g. Fig. 5.48). As can be seen in the center column of Figure 5.56, using the magnitude of $\overline{V}$ as the scaling velocity, however, produces ambiguous results. Combining the horizontal flow information and using the mean wind speed, $\overline{U}_h$, as the characteristic advection velocity scale, on the other hand, generates consistent results in all heights and reveals a good level of agreement between LES and experiment.

In order to confirm that using $\overline{U}_h$ as a representative velocity scale in the UCL does not, by mischance, *conceal* truly existing differences, the sensitivity analysis is conducted at another flow location that featured pronounced spectral offsets: position *DM18* at the courtyard exit (cf. Fig. 4.28). Figure 5.57 shows wind tunnel and FAST3D-CT u'-spectra at the lowest comparison height of 3.5 m and 2.75 m, respectively, which reveal that the dominant eddies in the LES and the wind-tunnel are dislocated by almost a frequency decade. The physical relevance of this shift is substantiated by the comparison of the wind roses in Figures 5.25 and 5.26, showing a circulating low wind-speed regime in the wind tunnel and a numerical flow that is still heavily influenced by the channeling in the alleyway. As expected, the choice of the reference velocity scale has no effect on the comparison result of the spectra depicted in Figure 5.57. Thus, it is anticipated that the offsets of the experimental spectra toward higher frequencies truly reflect the characteristics of the scale-reduced recirculation flow, in contrast to the numerical flow situation. Similar conclusions could also be drawn for the spectra at the upper level flow locations (cf. Fig. 5.54), where neither improvements nor aggravations of the level of agreement between the experiment and the simulation are observed as the scaling velocity is altered to $\overline{U}_h$ (not shown).

The above results underline an important strength of the tested LES code: the realistic prediction of RSL flow structures induced by urban aerodynamics. High levels of agreement between experimental and numerical auto-spectra and u'-w' co-spectra were determined for geometrically different and complex flow conditions in the downtown area (e.g. street canyons, intersections, open spaces) and for different analysis heights (*within* and *above* the UCL). As expected from a large-eddy simulation, the distribution of spectral energies among frequency ranges associated with the large and energy-containing eddies and the energy-peak regions are mostly well reproduced by the code.

On the other hand, the spectral analysis also showed that the grid resolution of 2.5 m in combination with the applied numerical scheme (and the resulting numerical dissipation characteristics) is only fine enough to directly resolve the energy-dominating turbulence scales of the urban flow field. A fast roll-off of the LES energy-density magnitudes is determined at all flow locations shortly after the spectral peak region had been reached. Energy-dominating eddies, hence, are only resolved down to the transition region into the inertial subrange and no well developed inertial range behavior is identifiable. The FCT-scheme used in FAST3D-CT to mimic the physical dissipation of turbulence energy through numerical diffusion presumably further contributed to the enhanced energy loss in the inertial subrange. Particularly in the UCL, the code is at the cusp of being a *very large-eddy simulation* (VLES; cf. earlier discussion in Section 2.2.2 and Fig. 2.5b).

Systematic deviations between the wind-tunnel auto-spectra and the simulation results were determined at flow locations that are positioned upstream of the core area of the urban domain, particularly the river location *BL04*, but also *BL07* and *BL08*, which are both located in close proximity to the water front. At these sites, the flow is still dominated by the approach flow conditions and the direct aerodynamic influence of the urban environment is only starting to control the near-surface flow field. The memory of the inflow conditions in the LES, hence, is still of importance for the general structure of the flow, while these effects are mostly "washed out" in the downtown domain. This assessment is supported by the fact that the spectral peaks of the LES are shifted toward higher frequencies, similar to the spectra obtained in a height of $3.5\,\mathrm{H_m}$, where the offsets are much more pronounced and most likely associated with artificial turbulence. As shown in the earlier analyses (e.g. regarding the integral time scales), these offsets mostly affect the streamwise and spanwise velocity components, while statistics derived from the vertical velocity are closer to the experiment. From the comparison of the auto-spectral energy densities at various height levels at location *BL04* (figures excluded from this section for brevity), a distinct height dependence of the spectral shifts could be observed. Closer to the surface, below approximately $0.5\,\mathrm{H_m}$, the LES spectra are agreeing much better with the laboratory references than at higher elevations, reflecting the influence of the industrial area at the upstream river shore and the corresponding building-induced turbulence features on the physical quality of the simulation.

Scaling the spectra based on reference quantities that are representative of the flow scenario has an immediate influence on the overall comparability of the simulation results with the experiment. Based on a pointwise sensitivity study, it could be determined that the choice of the velocity scale for the frequency scaling can be very crucial for complex flow fields of the UCL, which emphasizes that using certain concepts as a black-box can lead to ambiguities of the validation results. This assessment needs to be substantiated by further investigations of urban canopy layer velocity spectra.

The resolution potential of the velocity spectra is determined by the sampling frequency and the duration of the signals. From the graphs shown in this section, it could be determined that the LDA data rate at some of the downtown comparison points – particularly below roof level – was too low to resolve the inertial range eddies in the wind-tunnel flow. The energy-containing frequencies, which are particularly crucial for the LES validation, however, could always be experimentally resolved.

The length of the time series determines the lowest resolvable frequencies associated with the largest eddy structures in the flow. Since these eddies are much *rarer* compared with those of the energy-peak region and the inertial and dissipation ranges, the *statistical representativeness* of the low-frequency spectral estimates is directly coupled to the length of the time series. With the lengths of the experimental and numerical velocity signals not being equal (the FAST3D-CT signals are shorter by a factor of approximately 2.5; cf. Table 4.7), drawing definite conclusions about the (physical) nature of possible deviations between the numerical predictions and the reference measurements at the lowest frequencies is difficult. The same is true for the *quantification* of the agreement between the numerical and experimental spectral shapes and locations in general. One approach could be to derive height distributions of frequencies associated with the spectral energy peaks and compare those directly in a vertical profile plot, as e.g. done for $\tau_{ii}(z)$ in Section 5.4.2. In the case of broad maximum-energy regions or double-peak patterns, which were determined at some of the comparison points, the determination of characteristic frequencies of the energy-dominating eddies is, however, ambiguous.

Main conclusions from the systematic comparison of **auto-spectral energy densities** and **co-spectra** of turbulent velocities are summarized below:

- A fast roll-off of the numerical spectra occurs shortly after the spectral peak has been reached, indicating that the simulation of urban flow is at the edge to a VLES state for the current setup of grid resolution and numerical diffusion in the implicit LES code.
- At the majority of *downtown* comparison sites, FAST3D-CT captures the height and location dependence of the spectral energy distributions in frequency ranges associated with the energy-containing turbulent eddies.
- Systematic shifts of the LES energy-density peaks toward higher frequencies are observed at positions upstream of the core city area (*BL04*, *BL07*, *BL08*) and at all *BL* locations above approximately $3\,\mathrm{H_m}$, most likely reflecting the artificial LES inflow turbulence.
- The careful choice of representative spectral scaling quantities for UCL flow fields plays an important role for the comparability.

The analysis of autocorrelations in the previous and auto-spectra in this section represent classic approaches to infer information about the structure of turbulence, the characteristic scales of the dominant eddies, and the associated contributions to the variability in the flow. The validation study now has proceeded to the third and last pillar of the proposed LES validation hierarchy: the identification and recognition of eddy structures in the flow based on single-point time-resolved data. The following section deals with the application of conditional sampling methods, the inspection of joint-probability distributions of turbulent velocities, and the analysis of numerical flow anisotropy levels.

5.6 Quadrant analysis

Detailed analyses and comparisons of characteristics of numerical and experimental vertical turbulent momentum fluxes within the urban domain are presented in the next paragraphs. Among others, the following topics are investigated:

1. Joint probability distributions of the u' and w' velocity fluctuations.

2. Stress-fraction profiles, $S_i(z)$, $i = 1, \ldots, 4$, and ejection-sweep occurrence rates, T_2, T_4.

3. Dependence of stress-fractions on hole-size constraints, S_{i,H_c}.

4. Anisotropy of the numerical Reynolds stress as a function of location and height.

Step **1.** basically is an extension of the comparison of one-dimensional frequency distributions of experimental and LES velocities to the analysis of occurrence rates of certain *combinations* of u' and w'. These determine the characteristics of the covariance $\overline{u'w'}$. With **2.** and **3.** it is followed the well-established conditional averaging approach of the vertical turbulent momentum fluxes known as *quadrant analysis*. The analysis is expected to provide an insight into structural details of urban flow in the wind-tunnel and in the numerical simulation. With a so-called hole-size analysis, the occurrence of extreme events within the four stress quadrants is investigated in order to compare typical patterns in both data sets. In analysis part **4.**, finally, the *numerical* Reynolds stress tensor is analyzed by means of its level of anisotropy. This analysis aspect, however, has to be understood as an *excursus* within the framework of the validation study, since only the numerical data could be analyzed due to the lack of simultaneous measurements of the *three* velocity components in the wind-tunnel experiment.

5.6.1 Conditional flux averages

A well-known representative of conditional analysis methods from the field of flow pattern recognition is the so-called *quadrant analysis* of elements of the Reynolds stress tensor. Of particular importance in boundary-layer meteorology (and for investigations of wall-bounded turbulent flows in general) is the decomposition of the turbulent momentum flux, $\overline{u'w'}$, because of its dominant role for turbulent mixing near the surface. In the urban roughness sublayer, the "communication" between flow fields below and well above roof level by means of *ejections* of low-momentum fluid mass from the UCL or by downward *sweeps* of high-momentum fluid into the canopy layer is often investigated by means of conditional sampling methods (cf. previous review in Section 2.4.1). The occurrence of sudden burst and ejection events in turbulent boundary layers has been documented early on in the flow-visualization era of turbulence research, for example, in the influential study by Kline et al. (1967) on the structure of wall turbulence. First detailed studies of coherent motions as a specific feature of wall-bounded turbulence by means of quadrant-analysis methods were, for example, presented by Wallace et al. (1972), Willmarth and Lu (1972) or Lu and Willmarth (1973).

The principal procedure of quadrant analysis is the classification (*conditional resampling*) of the instantaneous turbulent momentum fluxes into one of four quadrants based on the respective composition of the algebraic signs of u' and w'. From the paired velocity fluctuations in each of the quadrants, a *conditional average* of the momentum flux contributions can be obtained. Following the notation used by Raupach (1981), the conditional average of the kinematic turbulent momentum flux corresponding to the ith quadrant is given by

$$\overline{(u'w')}_i^c = \lim_{T\to\infty} \frac{1}{T} \int_0^T u'(t)w'(t)\, I_i(t)\, dt \;, \tag{5.12}$$

where the superscript, c, next to the overbar denotes the *conditional* nature of the temporal average, T is the signal duration, and $I_i(t)$ is a trigger function defined as

$$I_i(t) = \begin{cases} 1, & \text{if } [u'(t), w'(t)] \text{ is in the } i\text{th quadrant,} \\ 0, & \text{otherwise .} \end{cases} \tag{5.13}$$

The frequency of occurrence of instantaneous fluxes in one of the quadrants can be counted as $T_i = N_i/N$, where N_i represents the number of velocity fluctuation pairs in the ith quadrant and N is the total number of instantaneous covariances $u'w'$ in the time series. (Note that this approach is equivalent to defining T_i as $\overline{I_i(t)}$ following Raupach, 1981, who further relates this quantity to *time fractions* in order to discuss scaling approaches)

The conditional averages derived through Eq. (5.12) are typically referenced to the time mean of the vertical momentum flux, $\overline{u'w'}$, obtained from traditional temporal averaging, which results in an expression for the relative contributions (*flux* or *stress fractions*) from individual quadrants to the total flux according to

$$S_i = \overline{(u'w')}_i^c \,/\, \overline{u'w'} \;, \tag{5.14}$$

such that $\sum_i S_i = 1$. Figure 5.58 shows a schematic of the quadrant separation of the instantaneous momentum flux, $u'w'$, based on the composition of the signs of the streamwise and vertical velocity fluctuations.[11] In the first and third quadrant, labeled Q_1 and Q_3, u' and w' both have the same sign (positive or negative) and the conditional averages, thus, result in *positive* flux values, $\overline{(u'w')}_{1,3}^c > 0$. The corresponding fluid motions are typically denoted as *outward* and *inward* (also: *wallward*) *interactions* (Wallace et al., 1972). The second quadrant, Q_2, is composed of velocity fluctuations with $u' < 0$ and $w' > 0$, which are associated with the upward *ejection* of momentum. The opposite process is the downward *sweep* of momentum with $u' > 0$ and $w' < 0$, associated with the fourth quadrant, Q_4. The conditional averages of ejection and sweep events result in negative covariance values, $\overline{(u'w')}_{2,4}^c < 0$.

If it is assumed that the conventional momentum flux average, $\overline{u'w'}$, is negative (as it is the case in boundary-layer flows), the flux fractions S_i will be negative for events in $Q_{1,3}$ and positive in $Q_{2,4}$ (cf. allocation in Fig. 5.58). That is, ejections and sweeps make positive contributions to the Reynolds stress component $-\overline{u'w'}$, while outward and inward interactions result in negative contributions (e.g. Oikawa and Meng, 1995).

[11] As addressed in Section 2.1.3, the terms "stress" and "flux" are often used interchangeably in literature in order to address the covariances of velocity fluctuations, independent of the external sign.

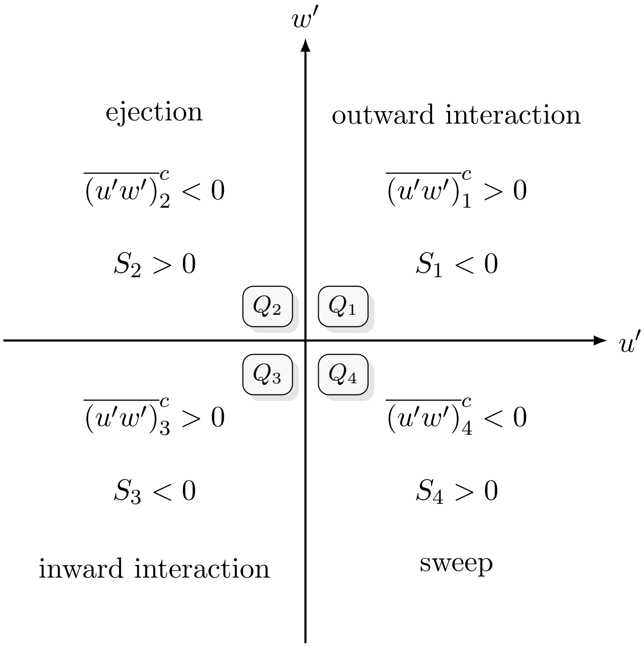

Figure 5.58: Four quadrants of the instantaneous vertical turbulent momentum flux, $u'w'$, and the corresponding stress fractions, S_i, for cases in which the conventional flux average yields $\overline{u'w'} < 0$.

The instantaneous flux magnitudes, $u'w'$, occurring within the four quadrants can exceed the value of the conventional mean turbulent momentum flux, $\overline{u'w'}$, by far. To determine the relative importance of large amplitude contributions to the flux fractions, only those fluctuation combinations are analyzed that result in covariance magnitudes larger than a certain threshold (cf. Willmarth and Lu, 1972). This approach is known in literature as *hole-size analysis* and contributes with an interesting aspect to the LES validation study since extreme events occurring in the flow can be analyzed and compared to the laboratory situation.[12] In this study, it is followed the approach by Raupach (1981) and the successive filtering of extreme events is implemented by putting another constraint on the trigger function I_i (Eq. 5.13) by only counting covariance values in the conditional average of the ith quadrant for which $|(u'w')_i| \geq H_c\,|\overline{u'w'}|$, with H_c being the hole size used to define the threshold ($H_c = 0, 1, 2, \ldots, 30$ in this study). The dependence of $S_{i,H_c} = \overline{(u'w')}_{i,H_c}^c \,/\, \overline{u'w'}$ on the hole size provides valuable information about the flow state.

The following results were obtained from the *original* (not resampled) wind-tunnel LDA data from measurements in *U-W* mode and from the FAST3D-CT velocity time series. All computations were conducted with `MATLAB`. The quadrant analysis of $u'w'$ is restricted to the *BL* flow locations (vertical velocity component only measured here) and mostly to heights above the UCL ($z \geq 1.2\,\mathrm{H_m}$) except for the river location *BL04*, where measurements are available starting from $z \simeq 0.3\,\mathrm{H_m}$. Direct comparisons of the time-series analysis results are only carried out in heights for which $|\delta z| = 0.25\,\mathrm{m}$.

[12] As outlined by Willmarth and Lu (1972), requiring the flux contributions to exceed certain threshold values implies that a hyperbolic *hole region* is cut out of the (u', w') plane in each of the quadrants.

Joint probability distributions

The flux fractions defined in Eq. (5.14) are related to the joint probability distribution, $\rho(u'/U_{\mathrm{ref}}, w'/U_{\mathrm{ref}})$, of velocity fluctuations in the $(u'/U_{\mathrm{ref}}, w'/U_{\mathrm{ref}})$ plane (cf. discussions by Raupach, 1981; Christen et al., 2007). Hence, the initial step of the comparison of quadrant characteristics in the FAST3D-CT and wind-tunnel flow focuses on the shape of the joint probability density functions (JPDFs) of u' and w'. These indicate the probability to find paired values of the streamwise and vertical velocity fluctuations within small amplitude bandwidths around the instantaneous values, i.e. $u'^{\star} + du'^{\star}$ and $w'^{\star} + dw'^{\star}$ (corresponding to the bin size for classic histogram analyses). As in the previous sections, the star superscript indicates a referenced (i.e. dimensionless) flow quantity. The integration of the JPDF over the analyzed value range yields

$$\int\int \rho(u'^{\star} w'^{\star})\, du'^{\star}\, dw'^{\star} = 1 \,. \tag{5.15}$$

Figures 5.59 and 5.60 depict results for six *BL* locations in a height of approximately $1.3\,\mathrm{H_m}$. Since the comparison points are allocated along the streamwise axis of the mutual coordinate system of the simulation and the wind tunnel, the downstream development of the probability distributions can be studied in order to determine effects of the increasing influence of the urban roughness on the flow state. The JPDFs were derived through a *bivariate kernel density estimation* (cf. e.g. Silverman, 1986, for a detailed text on density estimation in statistics). The employed algorithm uses a second-order Gaussian function as the kernel for the density estimation and is non-parametric, i.e. no assumptions about the underlying data distributions are made such that features like bimodality are resolvable. Details about the methodology implemented in the code are described by Botev et al. (2010). It is pointed to Appendix G for a reference to `MATLAB`'s File Exchange, from which the analysis code can be retrieved.

Figure 5.59 shows height contours of the joint probability densities of the streamwise and vertical velocity fluctuations obtained from the experimental (*left*) and the large-eddy simulation (*right*) for the three most upstream comparison locations. The qualitative agreement between the wind tunnel and the FAST3D-CT flow structures is convincing and reflected in similar shapes and extents of the ellipsoidal height-level contours of the probability densities. The same is true for the flow locations situated further downstream above the city core, displayed in Figure 5.60. At all points, the shapes of the height levels can be characterized as an ellipse in the $(u'/U_{\mathrm{ref}}, w'/U_{\mathrm{ref}})$ plane, for which the semi-major axes are oriented along a diagonal through the Q_2 and Q_4 quadrants. Thus, the largest instantaneous flux amplitudes are associated with the occurrence of ejection and sweep episodes in the flow, while fluxes in the outward and inward interaction quadrants generally feature a smaller value range. At the upstream positions *BL04* and *BL07*, the height contours are fairly symmetrical about the semi-major and semi-minor axes of the ellipsoidal distributions both in the experiment and the simulation, and the peaks of the distributions are centered at low amplitudes of u'/U_{ref} and w'/U_{ref}. This picture changes when moving to comparison sites above the densely built-up environment, where the flow fields above roof level in the laboratory and the LES are increasingly affected by the underlying urban roughness.

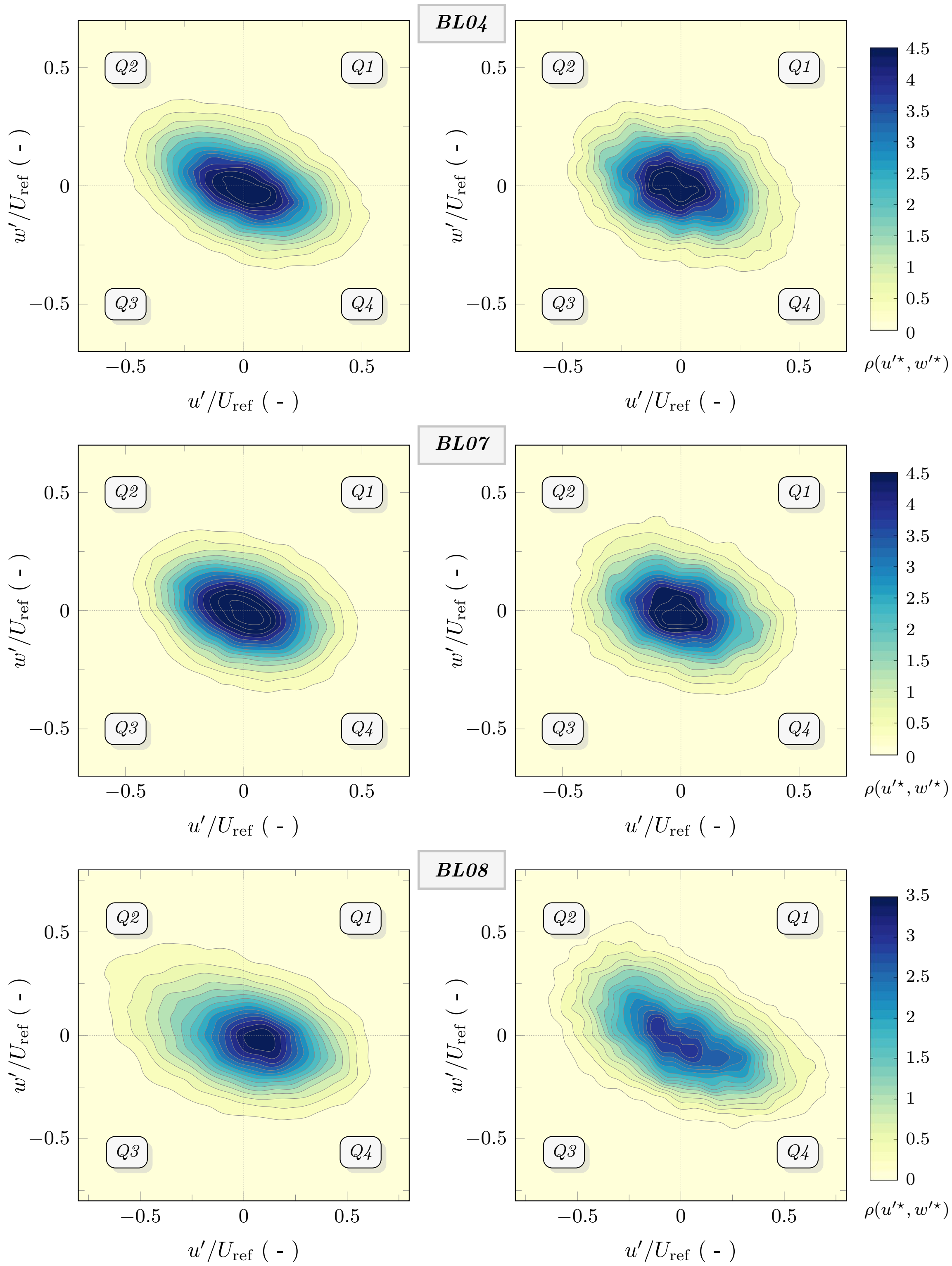

Figure 5.59: Joint probability density contours of the streamwise and vertical velocity fluctuations in the wind tunnel (*left*) and the LES (*right*) at comparison points *BL04*, *BL07*, and *BL08* in heights of 45.5 m/45.25 m (wind tunnel/FAST3D-CT; approximately 1.3 $\mathrm{H_m}$). Note that $u'^{\star} = u'/U_{\mathrm{ref}}$ and $w'^{\star} = w'/U_{\mathrm{ref}}$ in the colorbar legend.

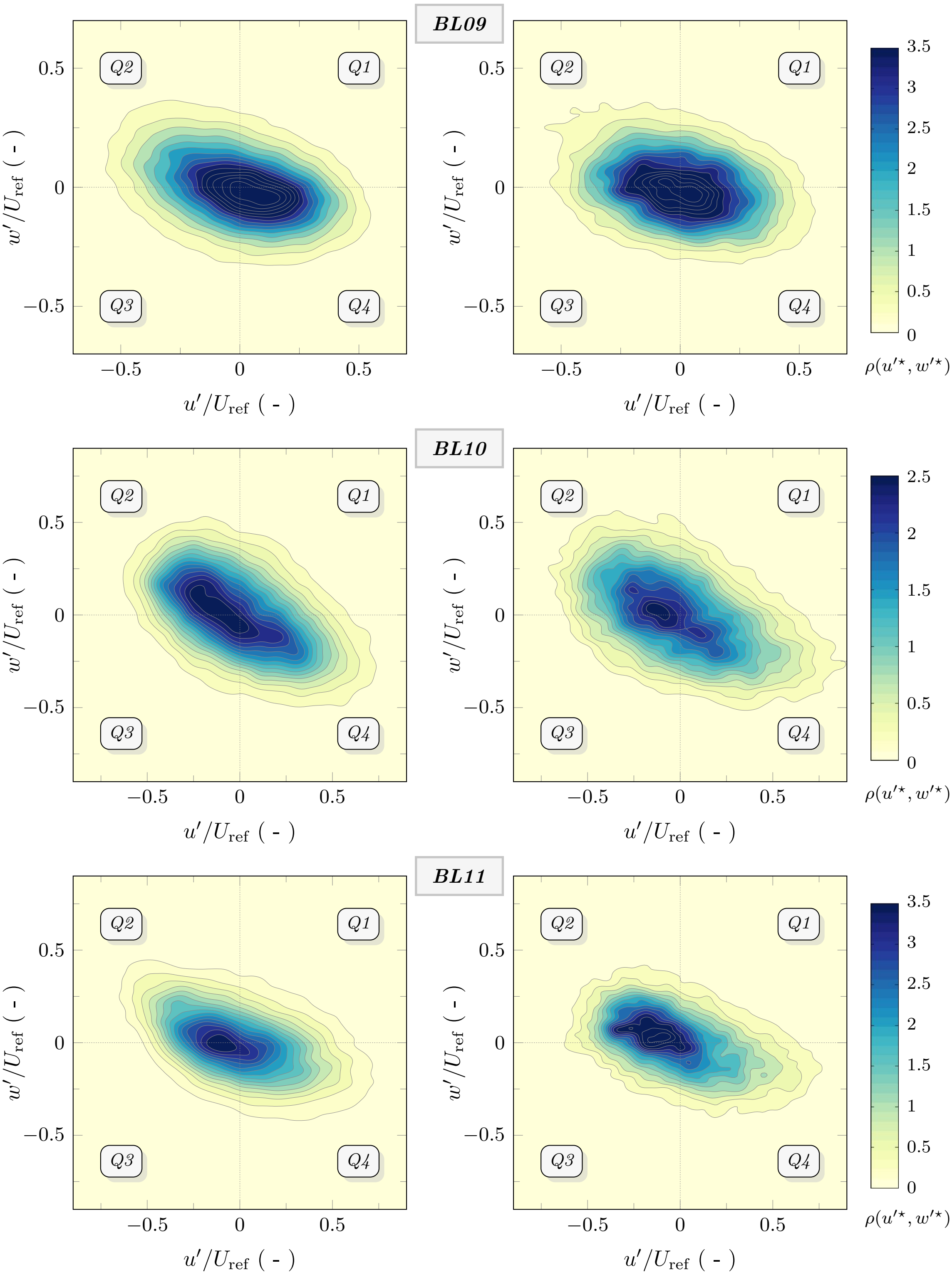

Figure 5.60: Same as in Figure 5.59, but for locations *BL09*, *BL10*, and *BL11*. *Left*: wind tunnel; *right*: FAST3D-CT.

Structural changes can be clearly determined at locations *BL08* (waterfront), *BL10* (complex intersection), and *BL11* (narrow crosswind street canyon). In all cases, the distribution peaks are dislocated away from the center of the velocity-fluctuation plane and similar tendencies toward an increase of flux contributions from the ejection and sweep quadrants are found (cf. the very good agreement of the joint probability density contours at *BL10* and *BL11*). These results agree well with the enhanced mean vertical momentum exchange, $\overline{u'w'}/U_{\mathrm{ref}}^2$, observed above the top of the urban canopy layer at the city-center sites as opposed to the comparatively low mean covariance amplitudes at the river and waterfront positions *BL04* and *BL07* (cf. Fig. 5.10; Section 5.2.1).

The inclination of the probability ellipses in the velocity-fluctuation plane are further compared in order to retrieve information about the paired occurrence probabilities of certain amplitudes of u'/U_{ref} and w'/U_{ref}. A high level of agreement between the LES predictions and the reference experiment is determined at all locations except for *BL08*, where larger occurrence rates in the sweep quadrant have been derived from the laboratory measurements. Overall, the different shapes of the probability density contours at each of the comparison locations indicate that the flow field uniquely corresponds to the respective *local* characteristics of the underlying building structure.

A common feature of the numerical results at all analyzed positions is the enhanced variability of the probability contour lines in the $(u'/U_{\mathrm{ref}}, w'/U_{\mathrm{ref}})$ plane. This characteristic is presumably caused by the eddy-scale truncation in the numerical simulation. In the wind tunnel, small-scale turbulence structures of more or less random nature are likely to add to a smoother shape of the bivariate frequency distributions, whereas in FAST3D-CT only eddy structures sufficiently larger than the grid size of 2.5 m directly contribute to the momentum flux. While those larger structures are expected to be responsible for the bulk of turbulent momentum exchange in the flow, the neglect of small-scale turbulence possibly affects the general appearance of the joint frequency distributions.[13]

Another important factor that may have contributed to the different levels of variability observed in the joint velocity probabilities is the longer full-scale duration of the wind-tunnel velocity signals, which adds to the overall *statistical representativeness* of the experimental results (cf. discussion in Section 4.2.3).

Flux-fraction profiles

Vertical profiles of S_i (cf. Eq. 5.14) at six of the *BL* locations are shown in Figures 5.61 and 5.62, together with the height-dependent difference $\delta S_{4,2} = S_4 - S_2$, quantifying the local dominance of either ejection or sweep contributions, and with the *flux exuberance* defined as $Ex = (S_1 + S_3)/(S_2 + S_4)$ (Shaw et al., 1983), which is interpreted as a measure of the relative importance of organized motions ($Q_{2,4}$) over unorganized *counter-flux* events ($Q_{1,3}$) in the local flux balance (Christen et al., 2007). Results for location *BL12* are not shown, since here reference measurements are only available from a height of 49 m upwards, so that only very few data pairs are directly comparable.

[13] It is emphasized that the *original* LDA velocity time series generally contain information about the high-frequency scales in the flow (even if the *mean* data rate is only moderately high) due to the time-dependency of the particle density and the resulting varying sampling frequencies of the signal (see also Section 4.4.2 and discussion in McKeon et al., 2007).

In the flux-fraction profiles at all comparison locations, the general dominance of ejection and sweep events over inward and outward interaction contributions to the total flux is obvious. Turbulent mixing in the urban roughness sublayer, thus, is primarily influenced by the downward motion of high-momentum fluid (sweeps) and the upward motion of low-momentum fluid (ejections), which is in agreement with findings from other studies on surface-layer turbulence and flow characteristics within and above urban canopies (e.g. Raupach, 1981; Rotach, 1993a; Oikawa and Meng, 1995; Feddersen, 2005; Christen et al., 2007). Ejection and sweep episodes are often associated with organized (coherent) eddy motions in the roughness sublayer (cf. the conceptual picture of turbulent motion in the UBL presented by Coceal et al., 2007, which has been presented in adapted form in Fig. 2.13b), and are primarily attributed to large-scale eddy structures, while velocity fluctuation combinations in the first and third quadrant are mostly attributed to small-scale, unorganized turbulence (e.g. Christen et al., 2007). This aspect is further addressed in later paragraphs dealing with the hole-size analysis.

The agreement between flux fractions obtained from the LES and the wind-tunnel measurements is overall good, regarding the ability of the simulation to capture the overall flux magnitudes in the respective quadrants. At the most upstream locations, *BL04* and *BL07* (Fig. 5.61), the largest amplitude offsets between numerical and experimental S_i profiles are determined, while the overall height-dependent characteristics of the stress fractions is well reproduced. At the downtown location *BL10*, above the complex intersection, the qualitative and quantitative agreement is remarkably good. In both the experiment and the simulation, the lowest comparison points at *BL10* are associated with a dominance of sweep motions (see also the evolution of $\delta S_{4,2}$), while ejection events are dominating at higher elevations in the RSL. At all positions except for *BL11*, the LES flux fractions derived at heights above approximately $3\,\mathrm{H_m}$ are dominated by the downward movement of momentum through sweep motions, which is in contrast to the systematic ejection-dominance observed in the wind-tunnel experiment and reported in other studies (cf. Section 2.4.1). Consistent with the conclusions from the previous analyses, the simulation values in these heights are most likely biased by artifacts of the inflow turbulence. The comparison results in these heights, thus, do not truly reflect the potential of the code to capture the fundamental turbulence characteristics of the urban flow field in a self-consistent simulation.

At lower elevations of the urban roughness sublayer, but well above $\mathrm{H_m}$), an ejection dominance is determined in the laboratory flow, except for the locations *BL10* and *BL04*, where at the latter a prevalence of sweeps is detected in heights below the mean building height, which is also captured by the LES. While several studies could document a dominance of sweep contributions within and just above the canopy layer, it is clear that the immediate urban surrounding of the measurement or simulation site has a direct influence on the specific characteristics of the flow. Especially at locations *BL08* and *BL10*, the experimental and numerical height profiles of $\delta S_{4,2}$ exhibit strong gradients in a region between approximately 1.3 to $2\,\mathrm{H_m}$, which possibly reflects strong turbulent exchange processes between the flow field that is directly influenced by the canopy-layer turbulence and the upper-level air masses. This enhancement is also mirrored in the flux exuberance profiles, $Ex(z)$, shown on the right-hand side of Figure 5.61 and 5.62.

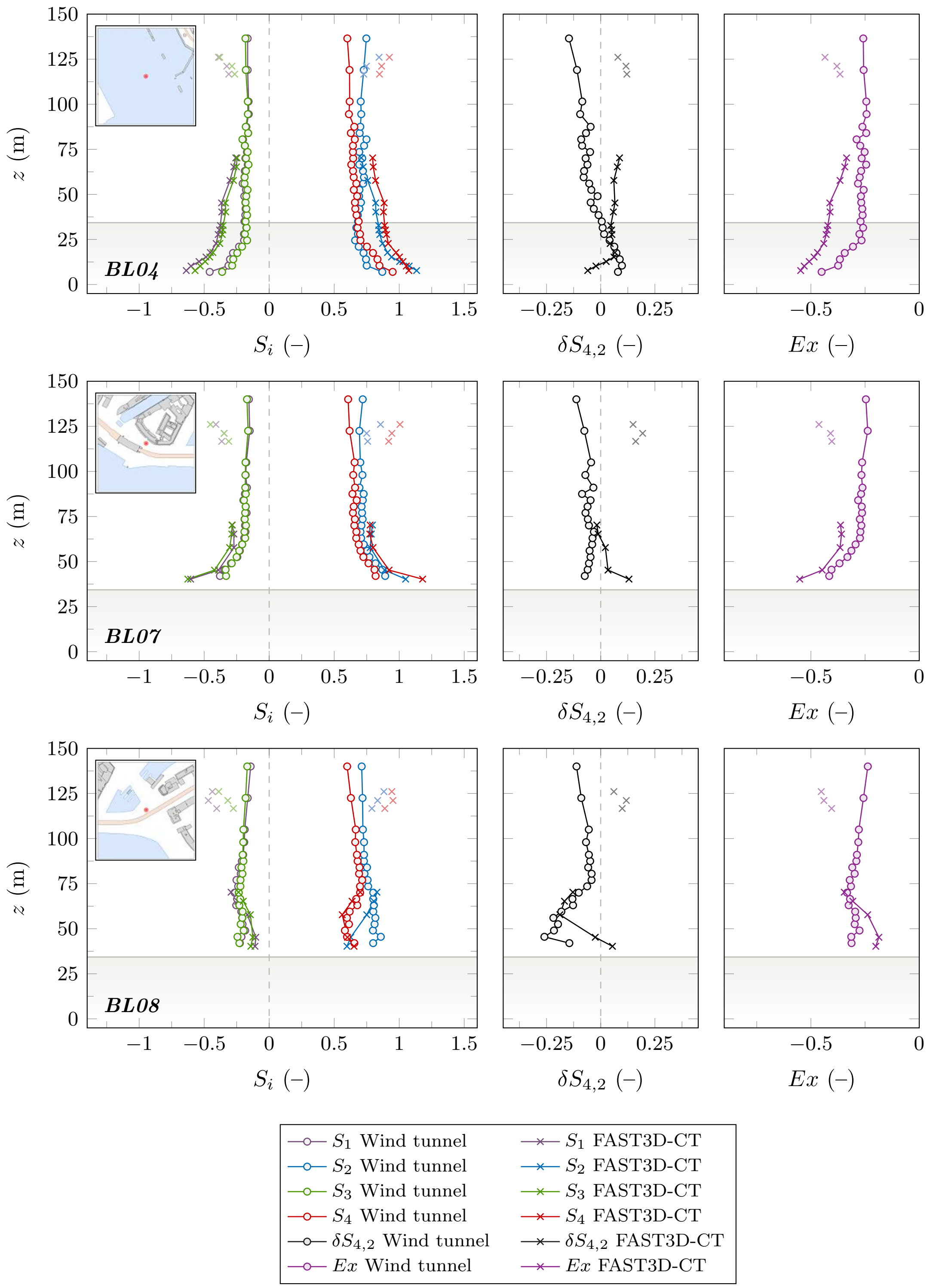

Figure 5.61: Vertical profiles of the four flux fractions $S_{1,\dots,4}$ (*left*), of the local difference between sweeps and ejections, $\delta S_{4,2}$ (*center*), and of the exuberance, Ex (*right*), at comparison points *BL04*, *BL07*, and *BL08*. The gray shading indicates heights lower than the mean building height of $\mathrm{H_m} = 34.3\,\mathrm{m}$.

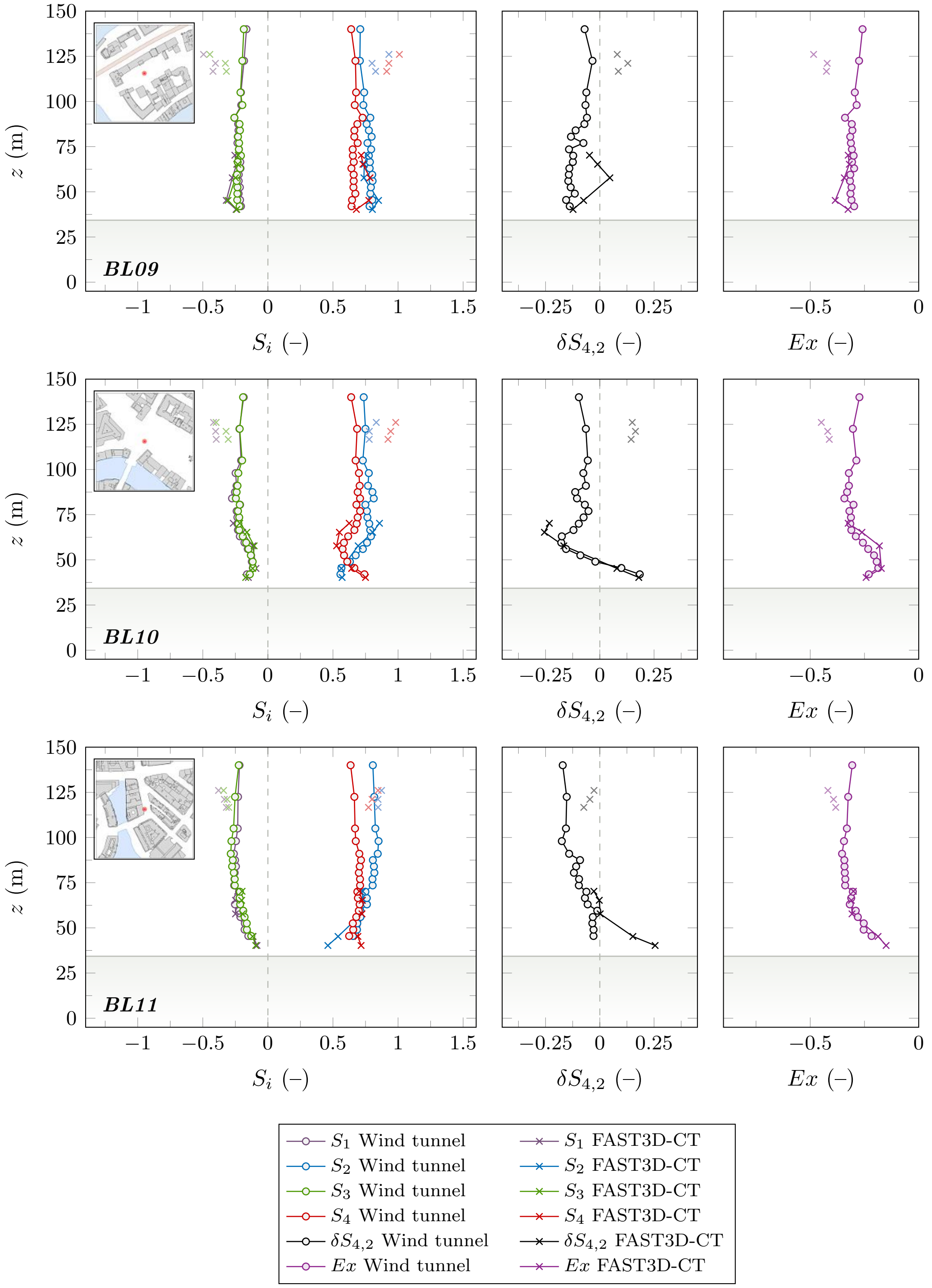

Figure 5.62: Same as in Figure 5.61, but for the comparison points *BL09*, *BL10*, and *BL11*.

The smaller the *magnitude* of the exuberance (i.e. the closer the values are to zero), the more efficient is the vertical turbulent momentum exchange through ejections and sweeps. The largest magnitudes of Ex up to values of -0.6 are determined at the lowest comparison heights at *BL04* and *BL07*. In contrast to that, at the inner-city points the momentum exchange efficiency above the UCL is overall enhanced. The smallest Ex magnitudes were observed at location *BL10* ($Ex \simeq -0.18$ and -0.17 in the wind-tunnel and FAST3D-CT, respectively, in $1.3\,\mathrm{H_m}$) and *BL11* ($Ex \simeq -0.22$ and -0.19), which were well reproduced by the simulation. The height ranges of the most efficient exchange processes approximately agree with those reported by Christen et al. (2007) based on street-canyon field measurements ($1.0 < z/\mathrm{H_m} < 1.25$). Since no experimental data are available for the analysis of flow patterns in the canopy layer, no further conclusions about the height structure of momentum exchange can be drawn at this point.

In addition to the above analyses, Figure 5.63 shows vertical profiles of the occurrence rates of ejection and sweep events, T_2 and T_4, which directly relate to the relative time fractions during which a certain flux quadrant is occupied over the duration of the measurement or the numerical simulation. An outstanding feature of the qualitative height structures of T_2 and T_4 is that the relation of the ejection/sweep occurrence rates often shows a distinctly reversed behavior compared with the relation of the ejection/sweep flux fractions, S_2 and S_4 (Figs. 5.61 and 5.62). Thus, the dominance of one flux over the other is not necessarily associated with a higher occurrence rate and *vice versa*. This characteristic is seen in the laboratory data as well as in the LES. For example, although the flux fractions associated with ejection events in the upper flow layers are significantly larger in the wind tunnel than those associated with sweep events, the occurrence rates are lower at all positions. At the intersection location *BL10*, the opposite trends of $S_{2,4}$ and $T_{2,4}$ are particularly striking and indicate that the sweep dominance observed at the lowest comparison heights is associated with comparatively rare flux contributions from this quadrant. This behavior is often attributed to the fact that the dominance of either ejections or sweeps at a certain height is primarily caused by infrequently occurring momentum-exchange events of relatively strong amplitudes, while more frequently occurring motions are overall associated with smaller instantaneous fluxes (cf. Raupach, 1981, for further discussions). This is also confirmed by recalling the structures seen in the JPDFs (Figs. 5.59 and 5.60). At location *BL10* (45.5 m/45.25 m height), for example, combinations of $u'^{\star}$ and $w'^{\star}$ that exhibit *large* amplitudes are most frequently occurring in the sweep quadrant, while the peak of the joint probability distribution is shifted toward *low* fluctuation velocities in the ejection quadrant.

The fact that the LES reproduces this feature is a valuable indicator for the accuracy with which time-dependent characteristics of the dominant, large-scale eddy structures are captured. Possible causes for the quantitative offsets observed at some of the comparison locations could be the slight deviations between the experimental and numerical flow locations in the (x, y)-plane and/or be related to the overall grid resolution that determines the potential of the code to resolve the energy-carrying eddies. As discussed in connection with the analysis of energy-density spectra in Section 5.5, particularly at the *downtown* flow locations, the turbulence-dominating eddy structures are associated with relatively higher frequencies (smaller length scales) as observed over more homogeneous surfaces.

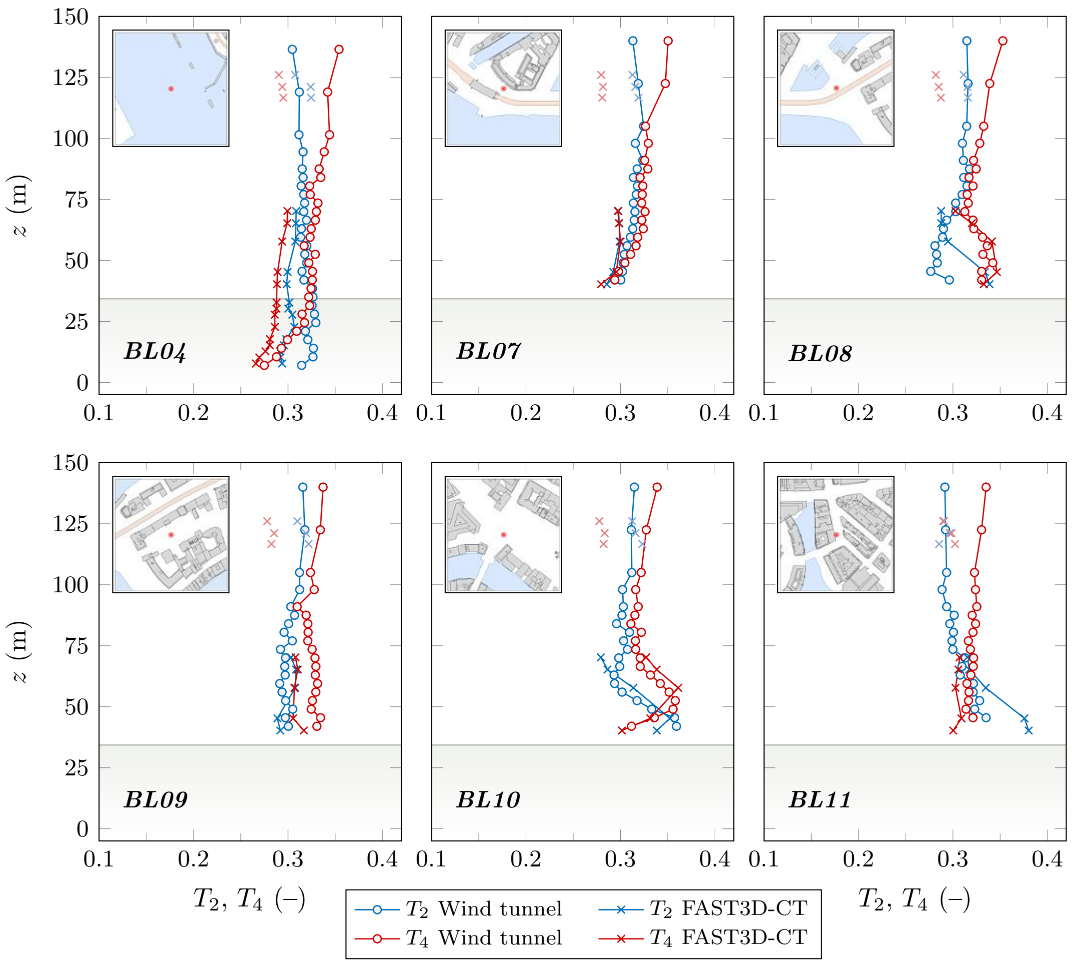

Figure 5.63: Relative occurrence rates of ejection and sweep events, T_2 and T_4, in the wind-tunnel experiment and FAST3D-CT in different heights at the *BL* comparison locations. The gray shading indicates heights lower than the mean building height of $\mathrm{H_m} = 34.3\,\mathrm{m}$.

The same development is also apparent in the u'-w' co-spectra in $1.3\,\mathrm{H_m}$ (Fig. 5.55). The relative resolution capability based on a fixed mesh size of $h_i = 2.5\,\mathrm{m}$, hence, may be decreased, causing the potential to reliably represent the momentum exchange accomplished by the large eddies to be reduced.

Extreme events

So far, the results suggested that the momentum exchange between the urban canopy layer and the adjacent parts of the roughness sublayer is influenced by the occurrence of strong and intermittent episodes of downward penetrations of air masses into the UCL and the upward bursts of low-momentum fluid into the upper-level flow field. Such "organized" events are characterized by high amplitudes of the $u'w'$ covariances (i.e. high correlations between the velocity fluctuations), while "unorganized" events tend to occur more frequently and are associated with smaller covariances. As can be determined from the joint probability distributions of the streamwise and vertical velocity fluctuations (Figs. 5.59 and 5.60), the most frequent combinations are in fact associated with comparatively low magnitudes of $u'^{\star}$ and $w'^{\star}$. The occurrence patterns of strong ejection and sweep events, on the other hand, are often related to the propagation of large-scale coherent eddy structures (e.g. as hairpin or horseshoe vortices; cf. the review paper by Adrian, 2007) at the top of the canopy layer (e.g. numerical studies by Kanda et al., 2004; Coceal et al., 2007).

Through the introduction of a hole size, H_c, as a further constraint on the conditional averaging process, the low-amplitude contributions can be successively filtered out from the quadrants. Thus, the remaining influence of strong but comparatively rare contributions to the overall momentum transport in the laboratory and the LES can be studied. Results of this analysis are shown in Figures 5.64 to 5.69 for two heights, $1.3\,\mathrm{H_m}$ and $2\,\mathrm{H_m}$, at the *BL* locations. Depicted are the flux-fraction magnitudes, $|S_{i,H_c}|$, as a function of the hole size, H_c, which takes a maximum value of 30. In the case of $H_c = 0$, the flux fractions correspond to the values previously depicted in the S_i profiles in heights of 45.5 m/45.25 m and 70.0 m/70.25 m (wind tunnel/FAST3D-CT), respectively (cf. Figs. 5.61 and 5.62).

At all positions it is observed that the dominance of contributions from ejection and sweep quadrants (Q_2 and Q_4) over the interaction quadrants (Q_1 and Q_3) is preserved as the hole size increases. These differences, however, are more drastic at the downtown locations (see e.g. Figs. 5.68 or 5.69). The overall agreement of the hole-size dependent flux fractions computed from wind tunnel and the LES velocity time series with regard to their qualitative evolution is good at most locations. As determined in the comparison of the S_i profiles for $H_c = 0$, shown in the preceding section, *quantitative* offsets are evident at many of the direct comparison heights, which are of course also reflected in the hole-size analysis. Distinct differences can be observed at the river location *BL04* (Fig. 5.64), where the LES predicts a persistent prevalence of downward sweeps, which in both heights only cease to contribute after the analysis range of $H_c = 30$ is exceeded. Even though large-amplitude sweep events can also be determined in the wind-tunnel flow, their contributions are overall smaller and of similar amplitude as in the ejection quadrant. Furthermore, the laboratory flux fractions as a function of H_c are fairly indistinguishable in both heights, which presumably mirrors the rather homogeneous height structure of the momentum exchange above the undisturbed river surface (see also Fig. 5.61). At location *BL08*, significant differences between the experiment and the simulation are evident in the ejection quadrant at the first comparison height ($1.3\,\mathrm{H_m}$; Fig. 5.66). Here, the S_2 contributions in the wind tunnel remain significant up to large hole sizes, whereas only very few ejection events having amplitudes larger than $10\,|\overline{u'w'}|$ are detected in the FAST3D-CT time series, and the decreasing trend is found to be symmetrical to the development in the sweep quadrant (Q_4). For the second analysis height (70.0 m/70.25 m) at the same location, however, a very good qualitative and quantitative agreement of the flux-fraction evolution in all four quadrants is determined. Further remarkably good congruences between the momentum-exchange characteristics in terms of extreme events are found at the inner-city locations *BL10* and *BL11* (Figs. 5.68 and 5.69). At both sites and for both analysis heights, the behavior of $|S_{i,H_c}|$ seen in the experiment and the simulation is quantitatively very similar.

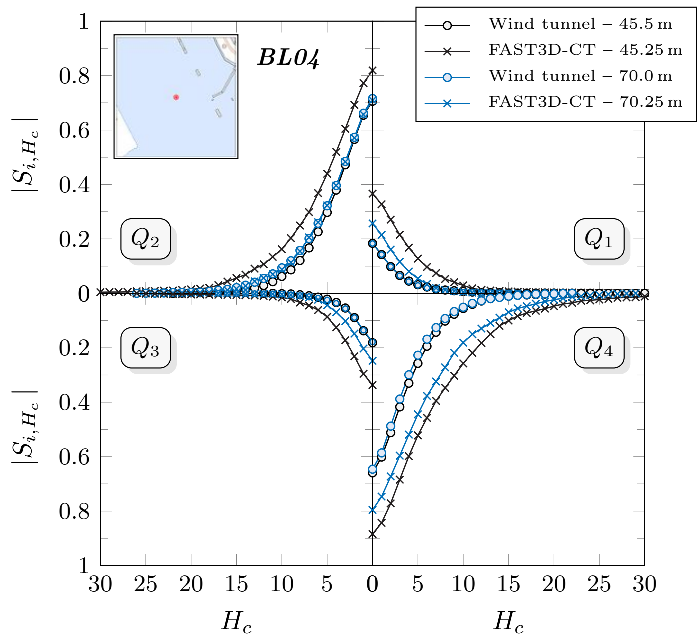

Figure 5.64: The four flux fractions, S_{i,H_c}, as a function of the hole size, H_c, at location *BL04* for comparison heights of 45.5 m/45.25 m and 70.0 m/70.25 m (wind tunnel/FAST3D-CT), being equal to 1.3 $\mathrm{H_m}$ and 2 $\mathrm{H_m}$, respectively.

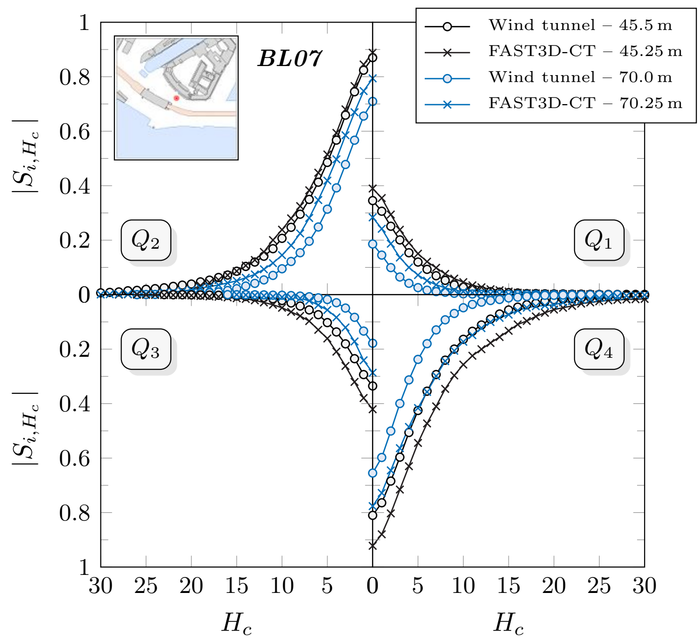

Figure 5.65: Same as in Figure 5.64, but for comparison location *BL07*.

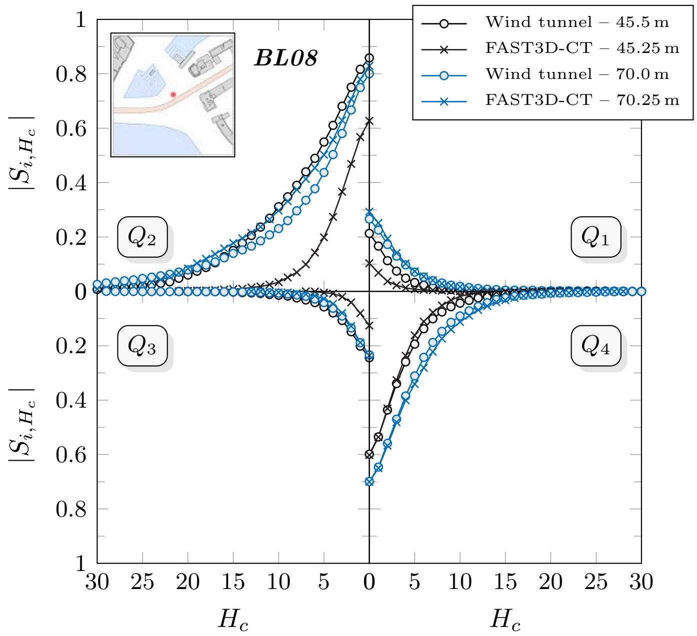

Figure 5.66: Same as in Figure 5.64, but for comparison location *BL08*.

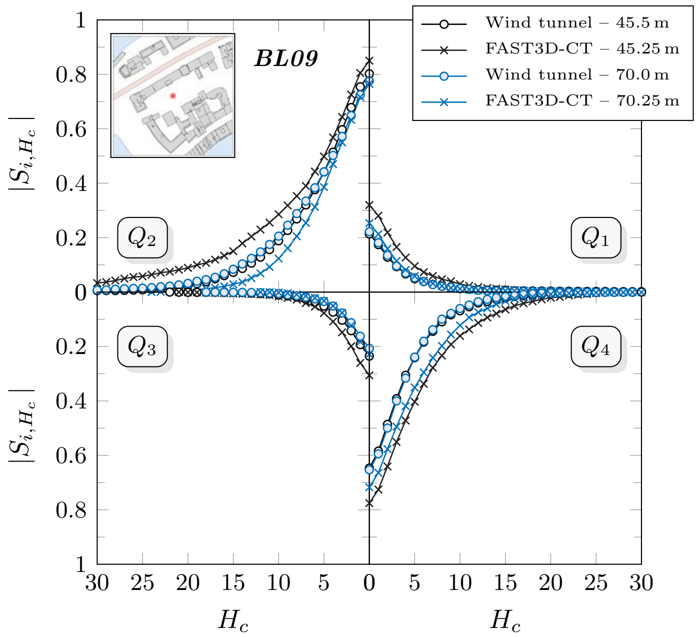

Figure 5.67: Same as in Figure 5.64, but for comparison location *BL09*.

At comparison location *BL10*, for example, the sweep-dominance characteristics at the lower height closer to roof level ($1.3\,\mathrm{H_m}$) and the prevalence of ejection motions further up at approximately $2\,\mathrm{H_m}$, associated with significant turbulent flux contributions at large H_c, are agreeing extremely well.

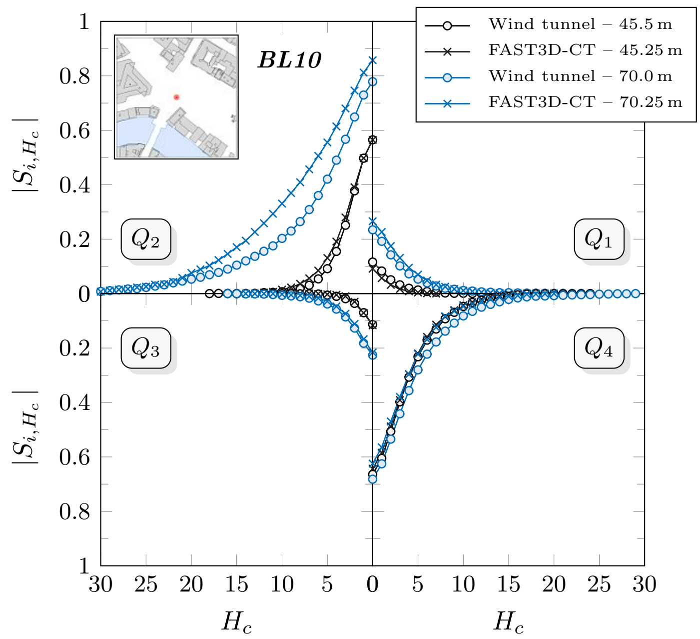

Figure 5.68: Same as in Figure 5.64, but for comparison location *BL10*.

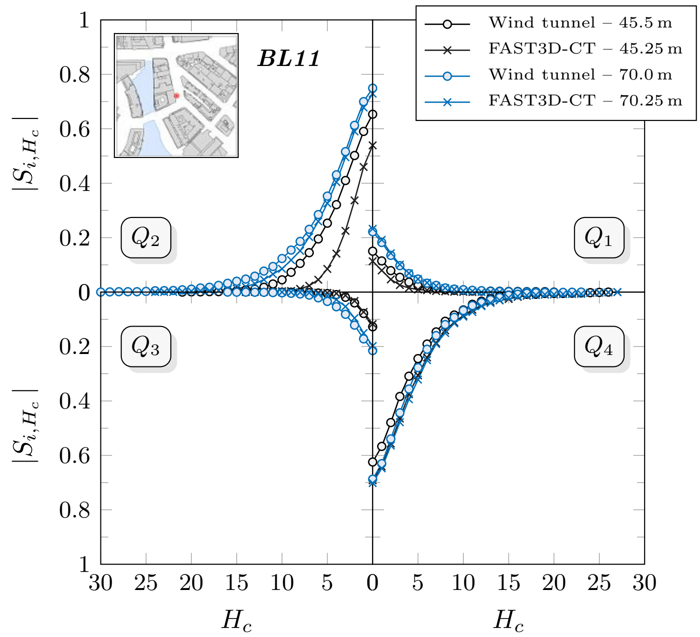

Figure 5.69: Same as in Figure 5.64, but for comparison location *BL11*.

The flux analysis showed that the LES provides a realistic picture of the urban flow structure. While at some locations *quantitative* differences to the experiment emerged, *qualitatively* the LES results are in very good agreement with the reference data and with expectations based on other studies on urban turbulence up to heights of at least $2\,\mathrm{H_m}$.

5.6.2 Anisotropy of the LES Reynolds stress tensor

Another promising approach to derive quantifiable information about the structure and the state of the turbulent flow is based on analyses of the (an)isotropy levels of turbulent stresses. Isotropy is referred to as a state of the flow in which statistical quantities derived at a certain point in space show no directional dependency. Being mathematically more precise, an isotropic velocity field is invariant under translations, rotations, and reflections of the coordinate system (Pope, 2000). In particular, this is mirrored in equal magnitudes of the turbulent variances of the three velocity components: $\overline{u_1'u_1'} = \overline{u_2'u_2'} = \overline{u_3'u_3'} = {}^2\!/_3\,k$, with k being the turbulence kinetic energy (cf. Eq. 2.14).

The level of anisotropy in a turbulent flow can be studied by means of the *deviatoric* parts of the Reynolds stress tensor, i.e. of its off-diagonal components that determine the turbulent momentum exchange. Following the notation presented in Pope (2000), the off-diagonal anisotropic fluxes, a_{ij}, are given by the difference between the total flux and the isotropic components

$$a_{ij} = \overline{u_i'u_j'} \; - \; \frac{2}{3} k \, \delta_{ij} \; , \tag{5.16}$$

where δ_{ij} is the *Kronecker delta*. Normalizing the anisotropy tensor with the TKE yields

$$b_{ij} = \frac{a_{ij}}{2k} = \frac{\overline{u_i'u_j'}}{\overline{u_k'u_k'}} \; - \; \frac{1}{3}\delta_{ij} \; . \tag{5.17}$$

The normalized anisotropy tensor has zero trace, and it can be shown that only two independent *invariants* exist (cf. details in Pope, 2000, p. 393 et seq.). By means of these invariants, the state of anisotropy of the Reynolds stress tensor can be studied. This kind of analysis was first proposed by Lumley (1978). The two invariants of the anisotropy tensor, here denoted as ξ and υ, can be defined as

$$6\upsilon^2 = b_{ij}b_{ji} \qquad \text{and} \qquad 6\xi^3 = b_{ij}b_{jk}b_{ki} \; . \tag{5.18}$$

Furthermore, the sum of the three eigenvalues of the matrix b_{ij} is zero, i.e. only two of the three eigenvalues, λ_i ($i = 1, 2, 3$), are independent so that $\lambda_3 = -(\lambda_1 + \lambda_2)$. The two invariants are related to the two independent eigenvalues, e.g. λ_1 and λ_2, by expressing b_{ij} in terms of its principal axes, which results in the following equations:

$$\upsilon^2 = \frac{1}{3}(\lambda_1^2 + \lambda_1\lambda_2 + \lambda_2^2) \qquad \text{and} \qquad \xi^3 = -\frac{1}{2}\lambda_1\lambda_2(\lambda_1 + \lambda_2) \; . \tag{5.19}$$

In every turbulent flow, the eigenvalues of the anisotropy tensor, b_{ij}, can be computed in order to construct the invariant pairs (ξ, υ) according to Eq. (5.19). The results can be visualized in the (ξ, υ)-plane in order to determine information about the characteristic *shape* of the Reynolds stress tensor. It is common practice to depict special *limiting states* of the Reynold stress tensor, for example, in terms of the so-called *Lumley triangle* (see Table 11.1 in Pope, 2000, for details). Such a representation is shown on the left-hand side of Figure 5.70, together with an indication of the limiting regimes. These are given by the isotropic state, $3C$ (lower vertex), for which all three eigenvalues are zero, by the two-component axisymmetric state, $2C$, for which two eigenvalues are identical and the third vanishes, and by the one-component state, $1C$, with only one remaining non-zero eigenvalue. The vertices are connected by two straight and one curvilinear line, which represent further regimes. In particular, turbulence with two identical eigenvalues and one smaller eigenvalue of the anisotropy tensor is mapped on the line from $3C$ to $2C$ ($\xi < 0$) and the shape of the stress tensor can be classified as *"pancake"*-like. The line from $3C$ to $1C$ marks the other axisymmetric case ($\xi > 0$), in which one large eigenvalue and two smaller identical eigenvalues were obtained. The corresponding turbulence shapes are *"cigar"*-like. In the case of one vanishing eigenvalue and two eigenvalues of different amplitudes, a state of two-dimensional turbulence is reached (curve from $1C$ to $2C$) and the tensor shape is characterized by an ellipse (see definitions and discussions in Pope, 2000; Sullivan et al., 2003; Klipp, 2010a).

In general, there are different ways how to define the invariants of the system. More recently, for example, Banerjee et al. (2007) have presented an approach based on *barycentric* coordinates. In contrast to the classic Lumley triangle, this approach works on a linear domain using barycentric maps that can be constructed from an arbitrary basis. In this method, the anisotropy tensor (Eq. 5.16) is represented by a linear combination of three basis matrices, which represent the three limiting states of turbulence anisotropy. The corresponding coefficients are determined from the eigenvalues of b_{ij} according to

$$C_{1C} = \lambda_1 - \lambda_2 \ , \quad C_{2C} = 2(\lambda_2 - \lambda_3) \ , \ \text{ and } \quad C_{3C} = 3\lambda_3 + 1 \ . \tag{5.20}$$

The coefficients are normalized so that $C_{1C} + C_{2C} + C_{3C} = 1$ and are bounded on $[0, 1]$.

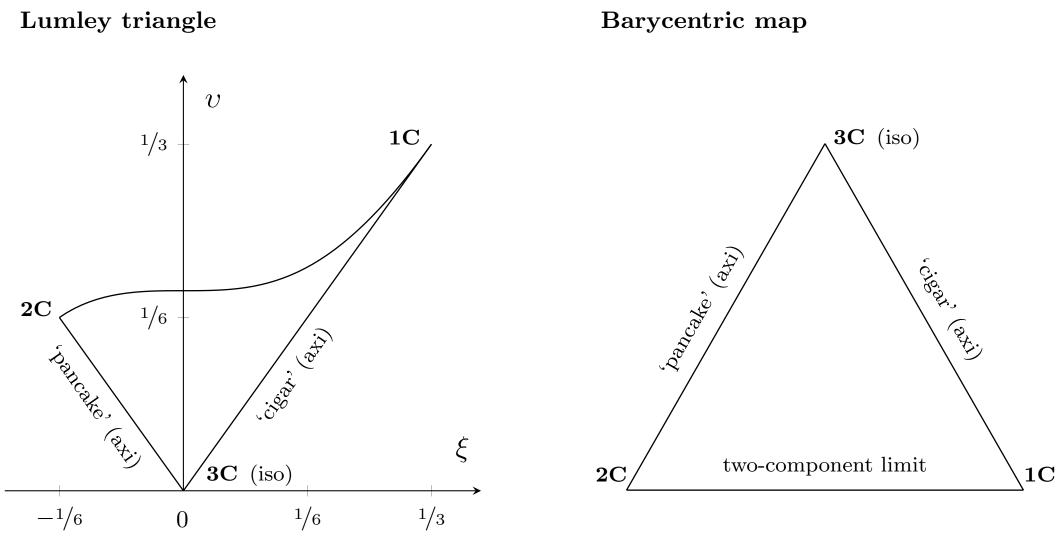

Figure 5.70: Boundaries of the anisotropy-invariant maps and the corresponding Reynolds-stress shapes: (*left*) the Lumley triangle in the (ξ, υ) plane (Pope, 2000); (*right*) the barycentric map according to Banerjee et al. (2007). The abbreviations *"iso"* and *"axi"* refer to *isotropic* and *axisymmetric*, respectively.

The vertices of the barycentric map as shown on the right-hand side of Figure 5.70 represent the limiting states of the anisotropy tensor and can generally be constructed from arbitrary basis points. However, the use of an *equilateral* triangle is preferable in order to guarantee a reliable visual interpretation of the data (Banerjee et al., 2007). Specific coordinates of points within the barycentric map can be constructed from $x_b = \mathbf{C} \cdot \mathbf{x}$ and $y_b = \mathbf{C} \cdot \mathbf{y}$, where $\mathbf{C}$ is a vector that comprises the coefficients in Eq. (5.20), and $\mathbf{x}$ and $\mathbf{y}$ refer to the map coordinates.[14]

In the same way as in Lumley's representation, all *realizable* Reynolds stresses fall within the triangle, but their coordinates now depend linearly on the eigenvalues (compare the expressions in Eq. 5.20 in contrast to those in Eq. 5.19). In the barycentric map shown in Figure 5.70, every vertex is associated with the case that one of the coefficients, C_{1C}, C_{2C} or C_{3C}, yields exactly 1 (one of the limiting states is reached), while at the opposite lines the respective coefficient is exactly 0, which indicates the reduction of that contribution. An advantage of this representation, as outlined by Banerjee et al. (2007), is the fact that points within the map (representing the results for a certain flow location, say) are given by the *barycentric* coordinates (C_{1C}, C_{2C}, C_{3C}), which is of help in order to categorize the respective flow state more distinctly than in the Lumley triangle, in which the transitions between flow states are not as straightforwardly determinable.

In the following, the Reynolds stress anisotropy states of the LES flow field in the urban test environment are examined. At this point, the analysis is restricted to the numerical predictions because information about the three-dimensional local velocity fluctuations is needed, which were not measured in the wind-tunnel campaign.[15] This analysis part, thus, has to be understood as an *excursus* from the previous validation approach, since the results based on the FAST3D-CT predictions cannot be evaluated against the experimental reference, and their accuracy cannot be determined. Nevertheless, studying the anisotropy levels can contribute to a fundamental understanding of structures in urban flow fields and might already be illuminative with regard to the sensitivity of the LES flow states to the respective location in the urban domain. Furthermore, the analysis can be understood as a feasibility test concerning the general applicability of more advanced stress analysis methods within the framework of an LES validation based on *suitable* reference data (e.g. measurements with 3D LDAs or 3D sonic anemometers).

Figures 5.71 to 5.73 show results of the analysis of LES Reynolds fluxes at all *BL* and *RM* locations and for all data extraction heights. The color coding of the height levels has been defined so that flow locations below the average building height of 34.3 m are indicated in blue, while points above the UCL are marked in reddish colors. The analysis is conducted with both invariant maps in order to compare the informative value of either representation.

At all comparison points, it can be clearly determined that the numerical Reynolds stresses are anisotropic everywhere, ranging from the lowest computational points well below roof level to the largest data extraction heights at the outer edges of the RSL.

[14] In the present analysis, the coordinates were defined as $\mathbf{x} = (0, 1, 0.5)$ and $\mathbf{y} = (0, 0, \sqrt{0.75})$.

[15] Recall that the LDA system used to acquire the data for this study was run in 2D mode for the simultaneous retrieval of *two* velocity components at a time (i.e. *U*-*V* and *U*-*W* mode). Hence, the full 3×3 Reynolds stress matrix cannot be derived from the experiment.

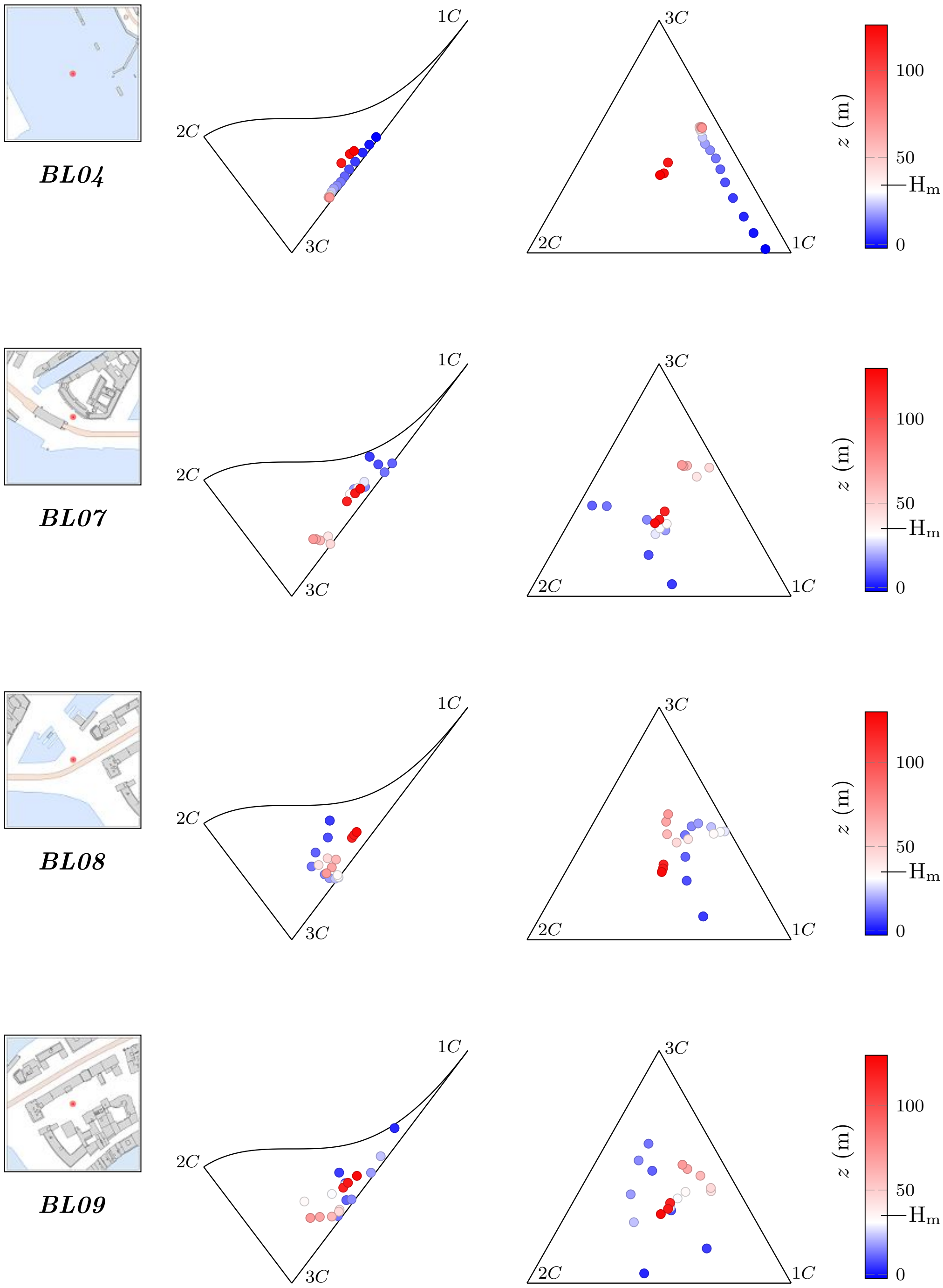

Figure 5.71: Lumley triangles (*left*) and barycentric maps (*right*) of the LES Reynolds stress tensor as a function of height at various urban locations.

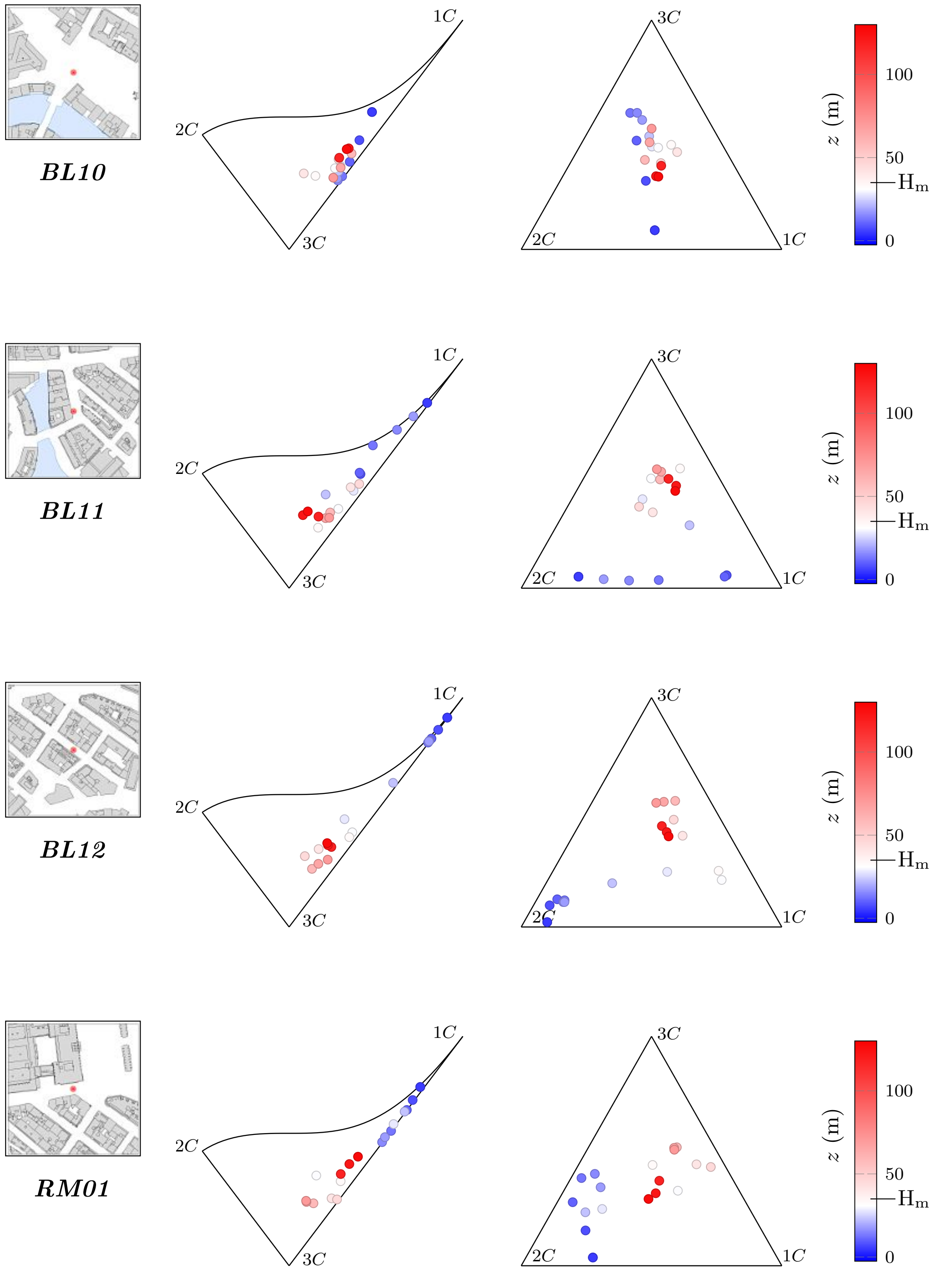

Figure 5.72: Same as in Figure 5.71, but for further locations.

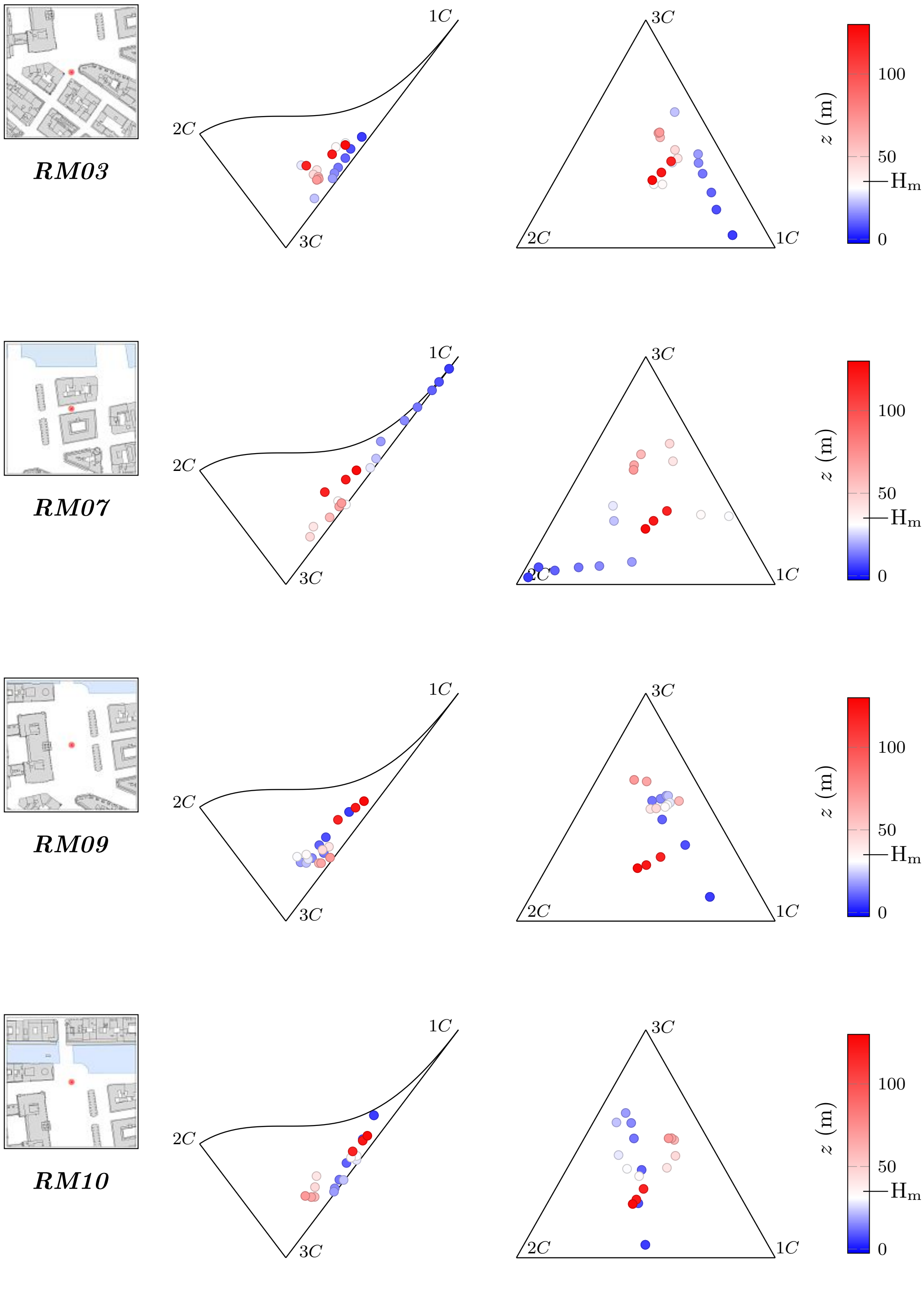

Figure 5.73: Same as Figures 5.71 and 5.72, but for further locations.

However, quite different height-dependent tensor states are encountered at individual sites, reflecting the inherently geometry-related turbulence characteristics. Particularly below the mean building height, deep within the UCL, the existence of a variety of Reynolds stress shapes is evident, which is connected to the pronounced heterogeneity of the urban flow field and its dependence on the immediate building surroundings. In that, the river location *BL04* is a great exception, as it is sufficiently far away from the urban structures at the upstream and downstream shores, so that the turbulence regime is comparable to ASL flow over homogeneous (rough) surfaces (cf. discussions in the earlier sections). This circumstance is clearly reflected in the shape and height development of the anisotropy tensor, which is close to axisymmetric ($\xi > 0$; one large, two smaller eigenvalues), indicating the dominance of "cigar" shapes (prolate spheroids). This finding is in agreement with the analysis of DNS channel-flow data by Kim et al. (1987) (also presented and discussed by Pope, 2000), revealing essentially the same stress structure within the *logarithmic layer* as seen at *BL04*.[16] More recently, Sullivan et al. (2003) used the Lumley triangle representation to study the structure of the SFS stresses in the atmospheric surface layer under different stability conditions based on HATS data (cf. Section 3.3.1), and also documented a preference of axisymmetry in the logarithmic layer.

Moving on to the first city positions at the waterfront (*BL07*, *BL08*), the axisymmetry is broken up and the Reynolds stress anisotropy levels show a pronounced height variability. From the analysis of the city positions, certain conjectures about the response of the Reynolds stress tensor to the local geometry conditions can be made. At locations that are strongly confined by buildings (e.g. narrow street canyons), the shape of the Reynolds tensor is essentially two-dimensional (cf. *BL11* and *RM07*, with the UCL points grouping along the line from $2C$ to $1C$) or it is characterized by a state of two-component axisymmetry in the "pancake" regime with $\xi < 0$ (oblate spheroids; cf. *BL12* and *RM01*). For this interpretation, the depiction in the barycentric map is clearly beneficial since in the classic Lumley triangle, the regime transitions cannot be as easily perceived (although it is emphasized that both invariant maps contain the same information with regard to the magnitudes of the three eigenvalues). At positions located farther away from the surrounding buildings (e.g. *BL09*, *BL10*, *RM09*, and *RM10*), the shape of the anisotropy tensor and its height dependence cannot be characterized as distinctly. In fact, these positions stand out due to sophisticated transitions between "pancake" and "cigar" shapes, which presumably reflect interactions between a variety of eddy structures. Interestingly, the closest conformity with the stress structure at the river location is determined at the intersection *RM03*, where a state close to axisymmetric ($\xi > 0$) is found at heights below rooftop (Fig. 5.73). The three highest data extraction points of the simulation (marked in dark red in Figs. 5.71–5.73) are characterized by similar magnitudes of the invariant coordinates and are far from isotropic. Picking up the earlier assumptions that the flow is still to a large degree influenced by the inflow conditions, the results shown in the anisotropy maps presumably mirror the stress composition of the artificial turbulence functions defined at the inflow plane.

[16] Banerjee et al. (2007) later analyzed the same DNS data set by means of barycentric coordinates and determined deviations to the original structural interpretation based on the Lumley-triangle map. These, however, mainly affect the flow regions close to the wall and not so much the logarithmic layer.

The strong variability of the tensor shapes for flow in urban environments was also documented by Klipp (2010), who investigated turbulence data from street-canyon measurements during the Joint Urban 2003 field campaign in Oklahoma City (cf. Section 3.2.2). Similar to the results presented above, Klipp found stronger levels of anisotropy at points below roof level, while the stresses in the vicinity of the canopy top were more disorganized and overall closer to the isotropic state (although this regime, as in the present study, was never truly reached). Due to the varying meteorological boundary conditions during the field campaign, the results of Klipp (2010) are, however, characterized by a high degree of scatter in individual analysis heights.

The in-depth comparison of FAST3D-CT and wind-tunnel results based on structural analyses of the vertical turbulent momentum flux gave insight into eddy-structure characteristics of both flows and added to the overall understanding of the capabilities of the LES code. Quadrant analysis can be applied to spatially unresolved velocity data (like the single-point wind-tunnel measurements of this study), but the results can still contribute to the understanding of the *spatial structure* of the flow, which is an important aspect for the validation of an eddy-resolving model. The above analysis showed that FAST3D-CT produces vertical momentum exchange characteristics that are qualitatively in good agreement with the reference measurements concerning the dominance of a prevailing upward and downward transport of air masses through turbulent motions.

By adding a simply formulated additional constraint to the conditional sampling process, the analysis of contributions from particularly large-amplitude events allowed to explore the value space of the simulation in contrast to the experiment. Naturally, conjectures about spatial flow characteristics from single-point data always involve a certain level of speculation, but even if the results are just regarded as *indicative of* local flow characteristics, the informative value for a simulation evaluation study is high. Further extensions of the conditional averaging approach could for example focus on similar decompositions of the spanwise momentum flux, $\overline{u'v'}$, which is of particular importance below roof level and provides insight into the lateral momentum transport in the canopy layer. In general, an extension of the experimental validation database to further velocity measurements in *U-W* LDA mode *below* roof level is very desirable in order to fully appreciate the performance quality of the code.

Analyzing the shapes of the anisotropic Reynolds stress tensor, b_{ij}, offers a great opportunity for an in-depth comparison between experiment and LES. As for quadrant analyses, the great advantage of the method is that single-point data can be used to infer information about the *spatial* turbulence structure, reflected in the preferred shapes of the Reynolds tensor at certain locations in the flow field. Although such a direct comparison could not be made with the current experimental validation database, the pure analysis of the FAST3D-CT stresses already revealed that a tremendous amount of information about the structure of the flow can be retrieved. Similarly to other more advanced analysis methods, the interpretation of the results on the basis of invariant maps requires a high level of awareness of the strengths and limitations of the analysis approach in general. In the above analyses it was also discussed that the choice of the anisotropy map, for example, does have a clear influence on the interpretability of the results and, hence, on the overall informative value retrievable from the comparison.

A special focus of this section was put on the analysis of the largest eddy scales, which contribute with high-amplitude velocity covariances to the turbulent momentum exchange and determine the level of anisotropy in the flow. Compared with the turbulence structures at the other end of the eddy spectrum, the energy-carrying and flux-transporting large-scale vortices are comparatively rare and the statistical significance of analyses of these structures is strongly coupled to the measurement or simulation duration. Although it can be expected that differences between the inherent uncertainty of low-order statistical moments obtained from the longer wind-tunnel and shorter FAST3D-CT time series in this study are negligible (cf. Section 4.4.3), it is generally not possible to draw such conclusions for more sensitive parameters (e.g. for S_{i,H_c}, which measures the relevance of extreme flux contributions associated with the large, infrequently occurring eddies). As concluded earlier in the comparison of energy density spectra, integral time scales, and temporal autocorrelations, the shorter duration of the LES velocity signals compared with the experimental time series causes a reduction of the representativeness of statistics that are directly related to the large eddy structures.

Main conclusions from the comparative study of **quadrant-analysis results** and the analysis of **anisotropy levels** of the numerical Reynolds stresses are compiled below:

- Joint probability distributions, vertical momentum flux fractions, and ejection/sweep characteristics determined from FAST3D-CT are in good agreement with those of the reference experiment.
- Quantitative differences determined between the conditional flux averages presumably originate from grid resolution aspects, locally enhanced geometry influences due to the gridding and/or horizontal offsets between the locations of the numerical and experimental data pairs.
- The hole-size analysis underlined the capability of FAST3D-CT to capture the intricate combination of infrequent occurrence rates and extreme flux-contributions associated with the passage of large-scale turbulent structures above the UCL.
- The upper RSL flow field of the numerical simulation exhibits a dominance of downward turbulent momentum transport (sweep motions) and is characterized by an anisotropic state of turbulence far away from axisymmetry, which presumably depicts the superposition of artificial eddy structures from the inlet plane.

In the following final section of this chapter, it is turned toward a joint time-frequency analysis framework to retrieve time-dependent information about eddy structures in the urban flow field and compare scale-dependent characteristics of the experiment and the numerical simulation.

5.7 Wavelet transform analysis

In the following paragraphs, the application of the continuous wavelet transform to experimental and numerical velocity-fluctuation time series is introduced and results from a systematic comparison of time-frequency information derived from laboratory and LES flow data are presented. The basic outline of this section is as follows:

1. Selection of a suitable analyzing wavelet for experimental & LES flow data.

2. Qualitative comparison of local wavelet energy-density spectra.

3. Quantitative comparison of scale-dependent wavelet-coefficient frequency distributions.

4. Outlook on coherent structure extraction potential using orthonormal wavelets.

After a general introduction to definitions and terminologies of the continuous wavelet transform in preparation of the comparative analyses, implications following from the choice of the wavelet function (**1.**) are discussed. Then, the wind tunnel and LES wavelet coefficients are analyzed qualitatively (**2.**) and quantitatively (**3.**) by comparing scale-dependent coefficient frequency distributions and their statistical properties in terms of high-order moments. Finally, the section closes with point **4.** presenting a brief outlook on comparison strategies based on *discrete* wavelet transforms. For all analyses, the *resampled* (equidistant) wind-tunnel time series are used. Additional material for this section is presented in Appendix F.

5.7.1 Continuous wavelet transform

Wavelet transforms belong to the class of so-called *joint time-frequency analysis* methods, which permit the temporal localization of frequencies contained in a time-dependent signal. With regard to the application to turbulent flows, this means that the occurrence of eddy structures associated with certain frequencies (or spatial scales) can be studied in a time-dependent framework. Hence, the wavelet transform basically adds the time dimension to classic analyses based on Fourier transforms by using two-parametric wave functions of limited temporal support instead of non-local sinusoids. While the time information of the signal is completely delocalized in Fourier space, in wavelet space the locality of frequency events is preserved (Farge, 1992), which enables to identify their occurrence in the time domain. This quality of the technique adds a further dimension to standard validation approaches for time-dependent, eddy-resolving numerical simulations by offering the potential to study and compare time-frequency information of turbulent flows.

The introduction of mathematical foundations of the *continuous wavelet transform* (CWT) dates back to the early and mid 1980s and originated from the investigation of geophysical phenomena (cf., e.g., pioneering works by Morlet, 1981; Grossmann and Morlet, 1984; Grossmann et al., 1985). Since then, wavelet transform methods evolved to prominent analysis tools in signal processing and, among other scientific areas, became increasingly popular in research on the structure of turbulent flows (see early reviews by Meneveau, 1991; Farge, 1992) as well as on their time-dependent numerical simulation (e.g. Schneider and Vasilyev, 2010).

The following paragraphs briefly present important mathematical definitions together with an introduction to typical wavelet-analysis terminologies. The theoretical aspects mainly follow the explanations by Farge (1992), Kaiser (1994), Addison (2002), Nobach et al. (2007), and Farge et al. (2012), and it is pointed to these references for detailed explications. A further valuable resource about wavelet theory is presented by Heil and Walnut (2006) in terms of a compilation of landmark papers.

Definitions & wavelet nomenclature

Admissibility Wavelets are oscillating, square-integrable, localized functions whose location and shape are manipulated during the transform process to unfold the time-frequency content of the analyzed signal (Addison, 2002). Various waveforms of different shape characteristics can be used for the CWT, given that they comply with a simple mathematical constraint known as *admissibility condition.* According to this constraint, the square-integrable wavelet function, $\psi(t)$, being real or complex, must fulfill

$$C_\psi = \int_0^\infty \frac{1}{|f|} \, |\hat{\psi}(f)|^2 \, df < \infty \; , \tag{5.21}$$

where C_ψ is the *admissibility constant*, whose value depends on the particular waveform, and $\hat{\psi}(f)$ is the Fourier transform of the wavelet. Eq. (5.21) implies

$$\int_{-\infty}^{\infty} \psi(t) \, dt = 0 \qquad \text{so that} \qquad \hat{\psi}(f=0) = 0 \; , \tag{5.22}$$

signifying that $\psi(t)$ has to have zero mean, so that its Fourier transform has no component at zero frequency (Farge, 1992). For some applications it may be of importance that higher order moments of the wavelet are vanishing, too, in order to guarantee sufficient localization in physical and spectral space. This aspect is discussed in one of the next sections. When using *complex* wavelet functions, $\hat{\psi}$ is required to be real and vanishing for negative frequencies (Addison, 2002). Following Nobach et al. (2007), $\psi(t)$ should further be centered around zero and feature a rapid amplitude decay for increasing t.

Wavelet analysis The function $\psi(t)$ is usually denoted as *mother wavelet* in order to stress the fact that the actual analysis is performed through a sequence of scaling and shifting processes, generating *daughter wavelets* with which the signal is convoluted. The analyzing function depends on two real-valued parameters:

$$\psi_{s,n}(t) = \frac{1}{\sqrt{s}} \, \psi\left(\frac{t-n}{s}\right) \; . \tag{5.23}$$

Through the *translation* parameter, n, the center of the wavelet is dislocated along the time axis, which allows to analyze different parts of the signal. With the *dilation* parameter, $s > 0$, also denoted as the *scale* of the wavelet, the mother function can be stretched ($s > 1$) or compressed ($0 < s < 1$). The $s^{-1/2}$ factor ensures normalization of the wavelet, such that all dilated versions have the same finite energy (Kaiser, 1994).

Farge (1992) compares the family of scaled and translated wavelets to a *"mathematical microscope,"* for which the mother wavelet determines the optical properties, while the scale and translation define resolution and position of the field of view. With a stretched version of the wavelet (large s), the field of view is wider and the low frequency content of the signal can be resolved, while with a squeezed wavelet (small s) it is zoomed in on the high-frequency components. From these considerations it can be deduced that the wavelet transform offers a *variable* time-frequency resolution: At large scales, the wavelet is less well localized in time than at small scales, while the frequency resolution is better than for the contracted wavelets. This is in compliance with the *uncertainty principle* in signal processing, stating that a signal can never be equally well localized in time *and* frequency. The variable resolution properties of the wavelet transform, however, are particularly favorable since high-frequency components in a signal occur over shorter durations than their low-frequency counterparts (Hubbard, 1998). It is pointed to Appendix F for details.

Analogous to the classic Fourier-transform process, the *continuous wavelet transform* of a time-dependent signal with zero mean and finite energy content, e.g. velocity fluctuations $u'(t)$, is given by a convolution with a new basis that, in this case, is composed of members of the wavelet family, $\psi_{s,n}(t)$, yielding

$$W_n(s) = \frac{1}{\sqrt{s}} \int_{-\infty}^{\infty} u'(t)\, \psi^* \left(\frac{t-n}{s} \right) dt \ , \tag{5.24}$$

where the asterisk denotes the complex conjugate. The *wavelet coefficients*, $W_n(s)$, contain time-frequency information about $u'(t)$. With the amplitudes of the coefficients, the level of agreement between features of the analyzed signal and the local, scale-dependent *shape* of the wavelet is measured. Like the Fourier transform, the CWT is *reversible* and the original signal can be reconstructed from the wavelet coefficients without loss of information. The transform further complies with the *Parseval relation*, ensuring that the energy content of the signal is preserved in wavelet space (cf. details in Nobach et al., 2007).

Choice of the analyzing function

Figure 5.74 depicts two frequently used wavelets in their temporal and spectral representation: the real-valued *Mexican-hat wavelet* (Fig. 5.74a) and the complex *Morlet wavelet* (Fig. 5.74b). Three scaled versions of each wavelet are presented, corresponding to different magnitudes of the dilation parameter ($s = 0.5$, 1.0, 2.0) at a fixed translation ($n = 0$).

The Mexican-hat wavelet, also known as *Marr wavelet*, is defined as the second derivative of the Gaussian function:

$$\psi_2(t) = N_{\psi_2}\ (1 - t^2) \exp\left(-\frac{t^2}{2} \right) \ , \tag{5.25}$$

where $N_{\psi_2} = 2\,\pi^{-1/4} 3^{-1/2}$ is a *normalization factor* that is introduced to let the wavelet have unit energy. Its Fourier transform as a function of *angular frequency*, $\omega = 2\pi f$, is

$$\hat{\psi}_2(\omega) = N_{\psi_2}\ \omega^2\ \exp\left(-\frac{\omega^2}{2} \right) \ . \tag{5.26}$$

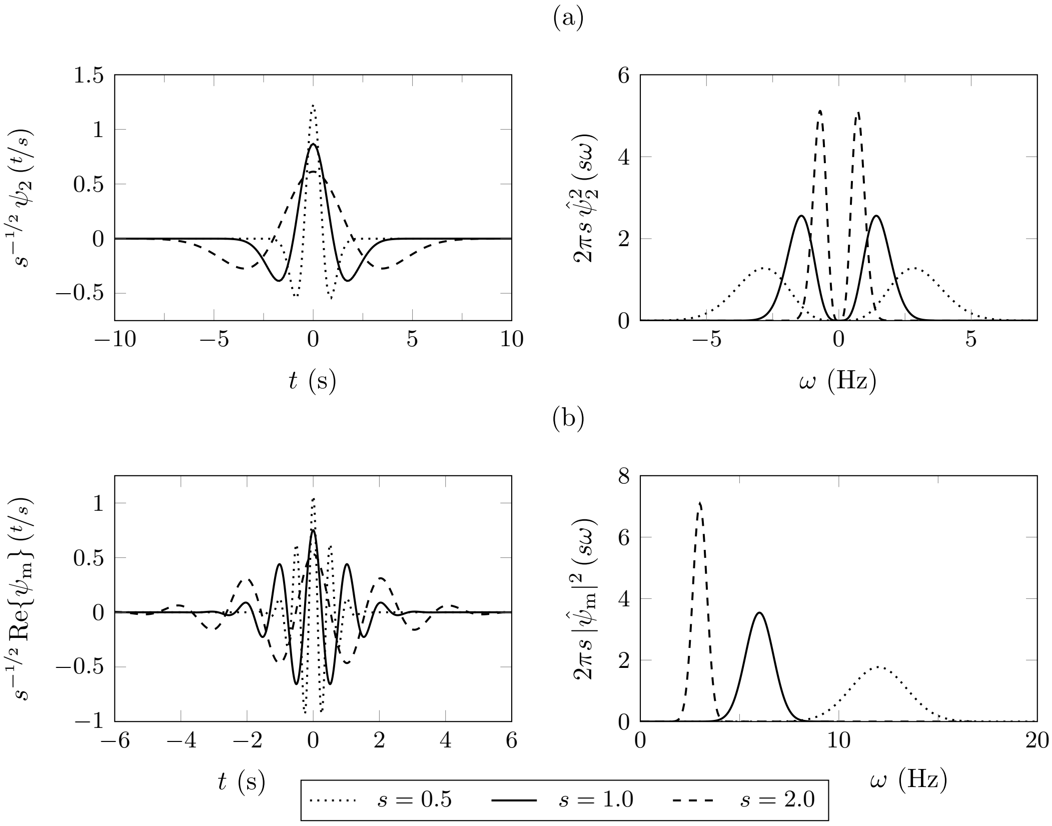

Figure 5.74: Influence of the scale parameter on the wavelet shape in the time (*left*) and frequency domain (*right*) by means of the wavelet's energy spectrum: (a) Mexican-hat wavelet; (b) Morlet wavelet, for which only its real part is depicted as a function of time. The scale is successively increased, $s = 0.5$, 1.0, and 2.0, while the translation is constant ($n = 0$).

For many analyses, however, the use of complex wavelets is advisable because they allow for the retrieval of *modulus* and *phase* information. The Morlet wavelet is defined as

$$\psi_\mathrm{m}(t) = N_{\psi_\mathrm{m}}\ \exp\left(i\omega_0 t\right)\ \exp\left(-\frac{t^2}{2}\right) \tag{5.27}$$

and is one of the most widely applied complex wavelets. In Eq. (5.27), ω_0 is the *central frequency* of the mother wavelet and $N_{\psi_\mathrm{m}} = \pi^{-1/4}$ is a normalization factor. The Fourier transform of the Morlet wavelet is given by

$$\hat{\psi}_\mathrm{m}(\omega) = N_{\psi_\mathrm{m}}\ \mathcal{H}(\omega)\ \exp\left(-\frac{(\omega-\omega_0)^2}{2}\right)\ , \tag{5.28}$$

in which $\mathcal{H}$ is the *Heaviside* function, ensuring that $\hat{\psi}_\mathrm{m}$ is zero at negative frequencies (Torrence and Compo, 1998). Strictly speaking, the Morlet wavelet does *not* satisfy the admissibility condition in Eq. (5.21) since its integral over the time domain does *not* vanish (cf. Eq. 5.22). However, for large enough central frequencies (preferably $\omega_0 > 5$;

Farge et al., 2012), the deviations of the wavelet's mean from zero are smaller than typical magnitudes of computer round-off errors and the Morlet function is *practically admissible* for a CWT (cf. Farge, 1992, for further discussions).

The influence of the scale parameter, s, on the extent of the wavelet functions is well recognizable in Figure 5.74, together with the impact of the scale-normalization factor, $s^{-1/2}$ (Eq. 5.23) on the amplitudes of the compressed and dilated wavelet versions in the time domain. In a similar way, the normalization of the Fourier transform of the wavelets, $\hat{\psi}$, by multiplication with $\sqrt{2\pi s}$ ensures comparability between wavelets at different scales in the frequency domain.[17] As discussed above, the features of the analyzing function define the resolution properties of the CWT, and it is generally recommended to begin a wavelet-based analysis by determining a "suitable" wavelet function based on the characteristics of the signal. Both depicted wavelets are characterized by an exponential amplitude decay in the time and frequency domain. The number of oscillations and the respective temporal and spectral bandwidths, however, are different. The Mexican-hat wavelet, $\psi_2(t)$, exhibits a single dominant peak in physical space and is better localized in time than the Morlet wavelet, $\psi_{\mathrm{m}}(t)$, which has a stronger periodicity that is coupled to the selected value of ω_0 (Nobach et al., 2007). In the frequency domain, this picture is reversed with the Morlet wavelet offering a better resolution.

Studies applying both wavelets to *atmospheric* measurements over various surface forms ranging from homogeneous terrain to plant and urban canopies can be found in literature (see, e.g., Gao and Li, 1993; Collineau and Brunet, 1993a,b; Krusche and de Oliveira, 2004; Feigenwinter and Vogt, 2005; Thomas and Foken, 2005; Barthlott et al., 2007). The detection and analysis of coherent ejection-sweep events, for example, can be approached by applying the Mexican-hat wavelet to turbulent *temperature* time series. The sudden enhancement of turbulent mixing is typically reflected in so-called *ramp structures*, i.e. in abrupt changes of temperature fluctuations followed by periods of slow variations, similar to a sawtooth-function pattern. Such structures cause distinct undulation patterns in the Mexican-hat wavelet coefficients (Collineau and Brunet, 1993b), which can be tracked down in time due to the comparatively good temporal localization of the wavelet.

For the characterization of large-scale organized motions based on turbulent *velocity* data, however, it is typically not clear what patterns can be anticipated, since the turbulent velocity field, in contrast to scalars, is characterized by a high level of variability in both magnitude and direction. In their discussion about particular pitfalls of CWT analyses of *turbulence*, Farge et al. (2012) address the fact that the use of real-valued wavelets like the Mexican-hat function harbors the risk that patterns in the wavelet coefficient graphs are interpreted as resulting from the passage of coherent flow structures, while in fact they are merely reflecting correlations among the wavelets themselves.

In the present validation study, it is relied on the use of the complex Morlet wavelet because the resulting coefficients comprise information about the magnitude and phase of the signals, making interpretations of the transform graphs less prone to misinterpretations. Furthermore, the function is better suited to analyze the LES velocity data, as will be discussed next.

[17] Strictly, the normalization factor of the Fourier representation of the wavelet, $\hat{\psi}$, is given by $\sqrt{2\pi s/\delta t}$, where δt is a time increment that was set to 1 s in the above example (Fig. 5.74).

Wavelet and Fourier energy spectra Since the scale parameter is inversely proportional to frequency, the scale dependency of the wavelet coefficients can be transferred into a frequency dependency according to $s = f_\psi / f$, where f_ψ is the *characteristic frequency* of the respective wavelet function (Addison, 2002). As stated above, the energy of the analyzed signal is conserved in wavelet space, making it is possible to define a *local* energy density spectrum based on the magnitudes of the wavelet coefficients and the characterizing parameters of the analyzing wavelet, C_ψ and f_ψ, according to

$$T^\psi(f, n) = \frac{1}{f_\psi C_\psi} \left| W\left(\frac{f_\psi}{f}, n\right) \right|^2 . \tag{5.29}$$

By further integrating the time-dependent wavelet energies over the duration of the signal, the *global* wavelet energy spectrum can be obtained:

$$E^\psi(f) = \int_{-\infty}^{\infty} T^\psi(f, n)\, dn . \tag{5.30}$$

As discussed in detail by Farge et al. (2012), Eq. (5.30) approximates the Fourier energy density spectrum to a degree that is coupled to the number of vanishing moments of the mother wavelet. The higher the number of vanishing moments of the analyzing wavelet the better is the wavelet approximation of a power-law behavior in Fourier space. Hence, in order to reliably represent particularly steep spectral slopes within the global wavelet spectrum, the mother wavelet should exhibit a high number of vanishing moments. In the following, this dependency is illustrated based on the validation data.

Figure 5.75 shows auto-spectral energy densities of streamwise velocity fluctuations from wind-tunnel measurements and simulations with FAST3D-CT at the river location *BL04* in heights of 45.5 m and 45.25 m, respectively. The spectra were derived through the continuous wavelet transform and the classic Fourier transform of the signals. The latter procedure has already been discussed at length in Section 5.5 and Appendix E. Like in the Fourier analysis, the CWT is applied in a discretized manner to the finite-time, finite-resolution velocity signals. For efficiency reasons, the wavelet transform computation is conducted in Fourier space making use of the *convolution theorem*. The computational procedure follows the approach recommended by Torrence and Compo (1998) and is described in Appendix F in detail. The CWT computations were conducted with the Mexican-hat wavelet and the Morlet wavelet (setting ω_0 to 6) in order to illustrate the advantages of the latter for the particular use in the LES validation study.

The CWT spectra are obtained from Eq. (5.29) and a discretized version of Eq. (5.30).[18] Using the same scaling procedure as for the Fourier energy densities, the global wavelet spectra of the streamwise velocity fluctuations were referenced by the variance of the signals and the frequencies according to $E_{uu}^{\psi\star} = f\, E_{uu}^{\psi}\, \sigma_u^{-2}$.

[18]The admissibility constants were obtained from Eq. (5.21), which yields an analytical solution for the Mexican-hat wavelet of $C_{\psi_2} = {}^4\!/_3\sqrt{\pi} \simeq 2.363$. The equivalent for the Morlet wavelet has been obtained from a numerical integration using a high-order *adaptive quadrature* algorithm that is optimized for oscillatory signals (`MATLAB`'s built-in function `quadgk`), yielding a value of $C_{\psi_\mathrm{m}} \simeq 0.531$ for $\omega_0 = 6$. As characteristic frequencies, f_ψ, the barycentric wavelet frequencies are used, i.e. $f_{\psi_2} = \sqrt{5/2}/2\pi \simeq 0.2516$ Hz and $f_{\psi_\mathrm{m}} \simeq 0.968$ Hz (cf. Torrence and Compo, 1998; Addison, 2002).

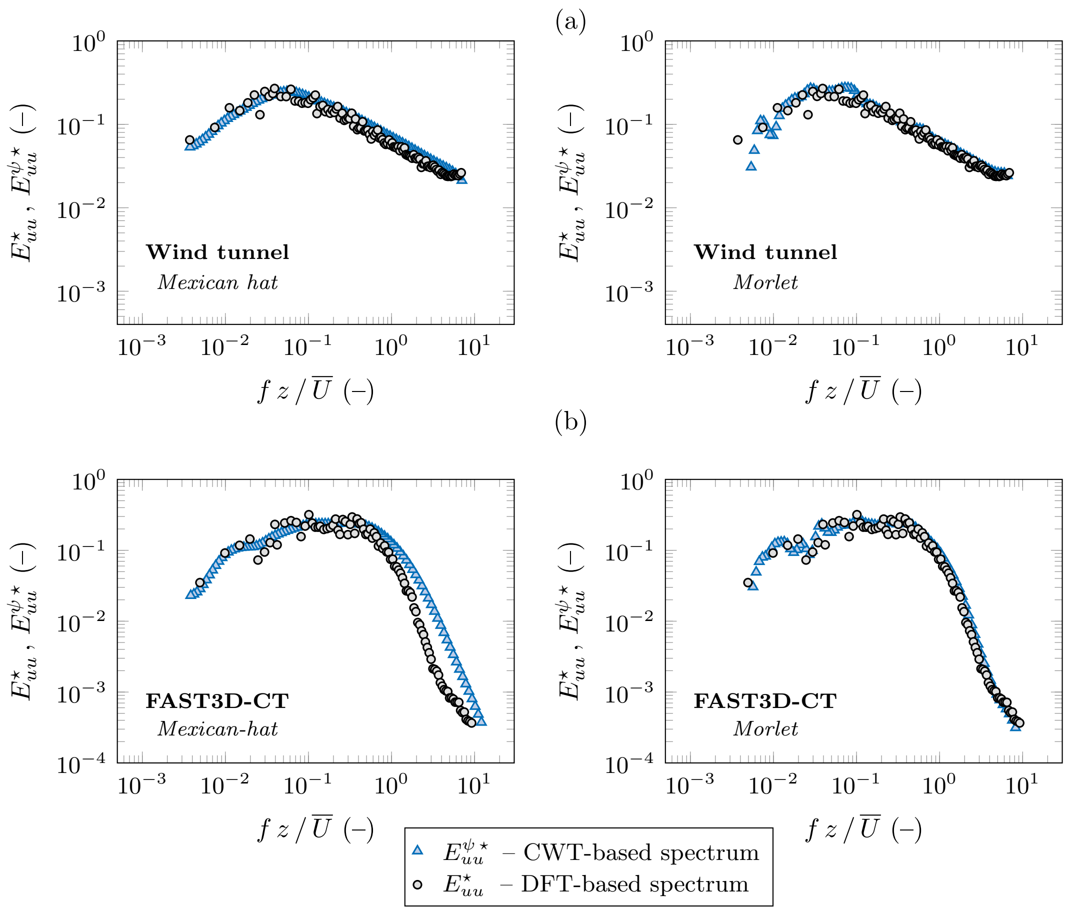

Figure 5.75: Scaled auto-spectral energy densities of the streamwise velocity fluctuations at location *BL04* derived from continuous wavelet transforms using the Mexican-hat wavelet (*left*) and the Morlet wavelet (*right*) in comparison to the classic discrete Fourier transform (DFT) spectra: (a) wind-tunnel spectra in a height of 45.5 m; (b) FAST3D-CT spectra in a height of 45.25 m.

Figures 5.75a and 5.75b show spectra derived from experimental and LES data, respectively. While the $-2/3$ slope of the wind-tunnel inertial subrange is well captured with both analyzing wavelets, clear offsets emerge between the Mexican-hat wavelet-based spectrum and the classic Fourier spectrum in the analysis of the LES data. Apparently, the much steeper slope of the LES spectrum (approximately $-10/3$, cf. Fig. 5.50b in Section 5.5), which is a result of the spatial cut-off of eddies smaller than the numerical grid, cannot be adequately resolved with this wavelet, which only has two vanishing moments. When using the Morlet wavelet, for which due to the high number of vanishing moments for $\omega_0 = 6$ spectral slopes up to -7 can be reproduced (Farge et al., 2012), the agreement with the Fourier-based spectrum of the FAST3D-CT velocity fluctuations is high. Since the fast spectral energy decay is a characteristic of all LES codes due to the presence of the filter, it is important to use mother wavelets with a *high* number of vanishing moments.

Local wavelet energy spectra

The information available in the wavelet coefficients (Eq. 5.24) can be visually exploited by means of contour plots of $W_n(s)$ or of derived quantities like the local wavelet energies (Eq. 5.29) in the time-scale (or time-frequency) plane. In the following, a qualitative comparison of such time-dependent frequency spectra is presented, for which all computations were conducted using the Morlet wavelet.

Figures 5.76 and 5.77 depict the squared *modulus* of the complex-valued wavelet coefficients, referenced by the (global) variance of the streamwise velocity, $|W_n(f)|^2 \, \sigma_u^{-2}$, as a function of full-scale time in hours (abscissa) and scaled frequencies (ordinate), which were obtained from measurements and simulations of the streamwise velocity fluctuations in heights of 45.5 m/45.25 m (wind tunnel/FAST3D-CT; approx. 1.3 $\mathrm{H_m}$) at the river location *BL04* and the downtown position *BL10*. The displayed scaled frequencies range from $f^\star = 5 \cdot 10^{-3}$ to 1 and, thus, encompass the energy-containing ranges and parts of the inertial subranges of the global spectra. The respective Fourier spectra were presented in Figure 5.51. For the displayed frequency range, the local wavelet spectra are neither affected by aliasing at the highest frequencies (smallest wavelets) nor by so-called *end effects* which arise from mathematical artifacts in the analysis of signal portions at the start and end boundaries (representing strong discontinuities) with large wavelets. The displayed time span roughly corresponds to the entire simulation duration of the LES by truncating the wind-tunnel wavelet coefficients accordingly. It needs to be emphasized that the temporal development of frequency-dependent wavelet energies cannot be directly compared between the wind tunnel and the LES time trace, since both data sets represent a *single realization* of the turbulent flow. It is, however, possible to compare general structural features detected in the signals.

Contrasting the two rather different comparison locations provides qualitative insights into the structural changes of turbulence structures as the flow field is increasingly affected by the underlying high-density urban canopy. At the river location *BL04*, in both the wind tunnel and in the LES the local wavelet spectra show the largest amplitudes at low frequencies, reflecting the dominance of large-scale eddies for the global energy in the unobstructed flow field well-upstream of the city center (Fig. 5.76). The largest difference between the data sets concerns the occurrence of significant spectral peaks at higher frequencies, which is more pronounced in the LES. Recalling the earlier analysis results based on classic Fourier spectra in Section 5.5 (e.g. Fig. 5.51), the numerical velocity spectra upstream of the city core and particularly at higher elevations above the surface exhibited a shift of the energy density peaks toward higher frequencies, presumably reflecting memory of the inflow conditions. This picture drastically changes at the downtown location *BL10*. The highest spectral amplitudes are now mostly dislocated to higher frequencies and are associated with shorter time spans than at the river location.[19]

[19]For the derivation of occurrence times, the variable time-frequency resolution properties of the wavelet transform need to be recalled. In particular, the low-frequency portions of the signal are better resolved in frequency than in time, which is reflected by an elongation of the associated energy amplitudes as a function of time and frequency along the time axis. Those parts of the signal associated with high frequencies, on the other hand, are better resolved in time than in frequency, and the wavelet energy peaks are elongated along the frequency axis. Both features are clearly evident in Figures 5.76 and 5.77 and caution must be paid in the derivation of occurrence time scales of low-frequency events.

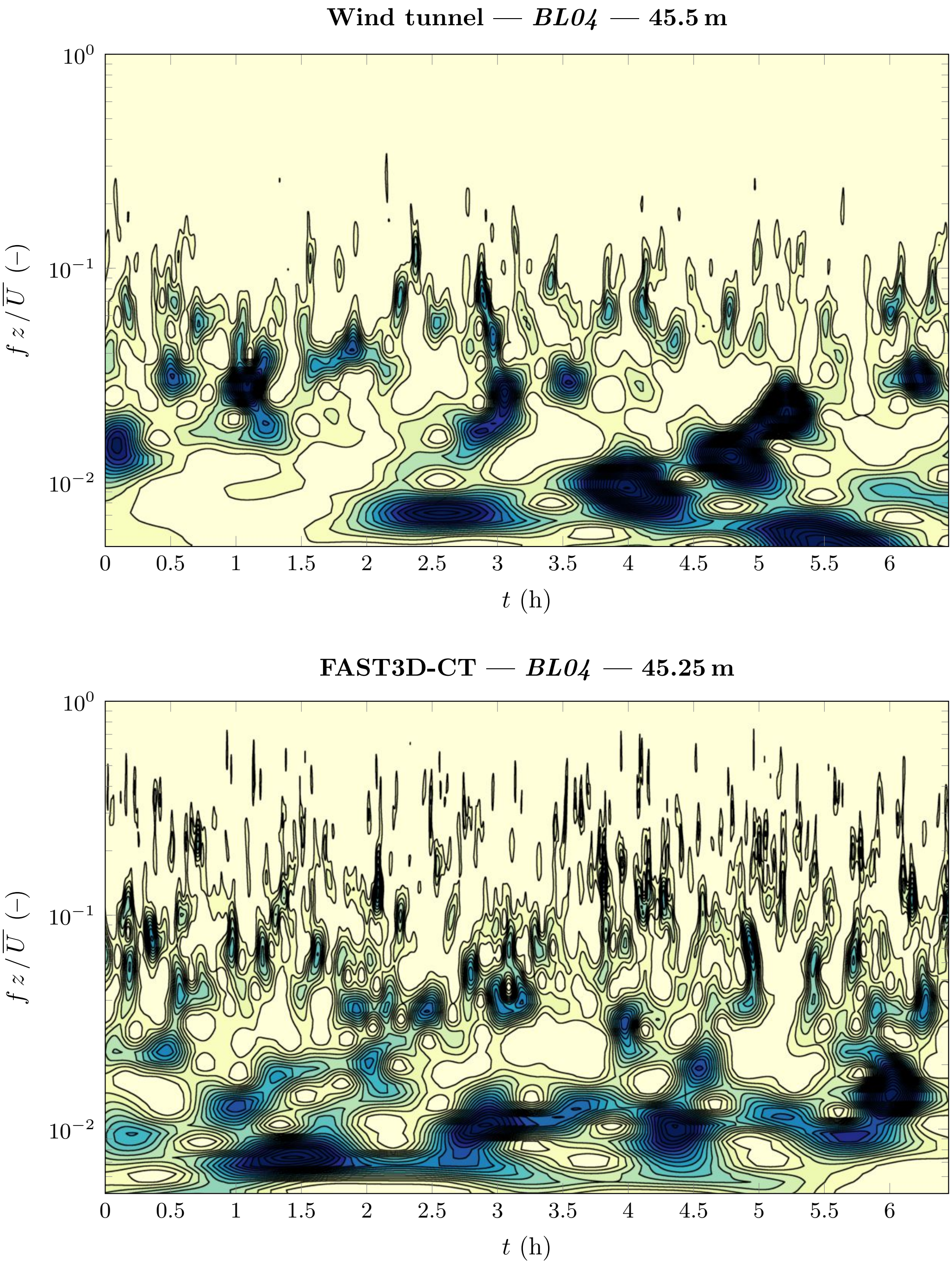

Figure 5.76: Contour graphs of the scaled local wavelet energies, $|W_n(f)|^2\,\sigma_u^{-2}$, determined from the streamwise velocity fluctuations at location *BL04* from wind-tunnel measurements (upper panel; 45.5 m height) and FAST3D-CT data (lower panel; 45.25 m height). The color range from light to dark reflects increasing magnitudes of the local wavelet energy densities.

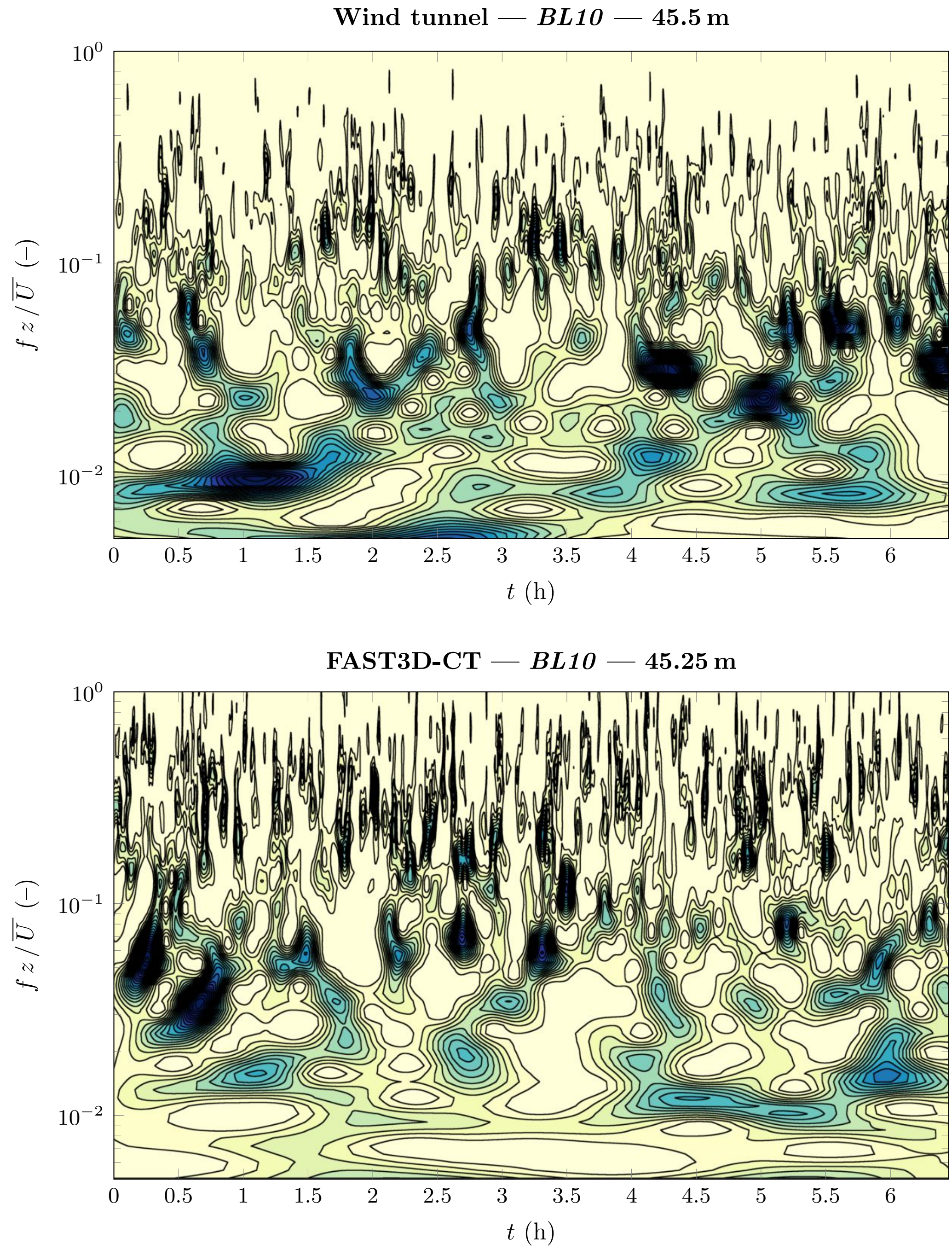

Figure 5.77: Same as in Figure 5.76, but for the streamwise velocity fluctuations at location *BL10*. The color range from light to dark reflects increasing magnitudes of the local energy densities.

This feature is seen in both the laboratory and the LES flow and illustrates the influence of the increased surface roughness on the spatial scales of the dominant flow structures. The quadrant analysis presented in the preceding Section 5.6 showed that the location above the intersection is characterized by strong and intermittent vertical momentum exchange, dominated by sweep events. The patterns seen in Figure 5.77 might be reflective of such events, which could be further investigated by comparing the CWT results for the streamwise velocity fluctuations with those of the vertical velocity component.

However, as addressed in the previous paragraphs, it is not a trivial task to directly derive information about flow structures from a graphical analysis of the local wavelet energies (or the wavelet coefficients) since target structures for turbulent *velocity* data basically do not exist. The graphs in Figures 5.76 and 5.77 show that the velocity wavelet spectra are characterized by certain noise levels and the non-periodical (random) occurrence of large energy amplitudes, which *could* be associated with the passage of organized (coherent) eddy structures. Deriving further (statistical) information about coherent structures for a *quantitative* comparison of the LES results with those of the reference experiment, however, would require to know exactly what to look for and to be able to reliably distinguish relevant from irrelevant structures.

In order to avoid such ambiguities at this point, more quantitative analysis approaches based on time/scale-dependent information contained in the wavelet transform coefficients are pursued, allowing for an unbiased comparison of the FAST3D-CT data with the wind-tunnel measurements. This approach is presented in the next section.

5.7.2 Frequency distributions of wavelet coefficients

In order to study the time-dependent structure of the turbulent flow corresponding to a certain dilation (or frequency), the wavelet coefficients are analyzed in terms of frequency distributions that can be directly compared between the experiment and the LES. For this purpose, the wavelet transform according to Eq. (5.24) is conducted for scales corresponding to frequency ranges at which the numerical simulation can be compared to the experiment, i.e. in the energy-containing range (cf. Section 5.5). Instead of analyzing the entire two-dimensional field, only wavelet coefficients corresponding to certain frequencies (or scales) are extracted, resulting in a frequency-dependent time series of wavelet coefficients. When using complex wave functions like the Morlet wavelet, the resulting wavelet coefficients are also complex and comprehend information on the modulus and phase of the signal. In order to take into account all available information stored inside the coefficients for the construction of the frequency distributions, a composite time-dependent coefficient vector consisting of real and imaginary parts of $W_n(s)$ is analyzed.

Figures 5.78 and 5.79 show frequency distributions of experimental and LES wavelet coefficients corresponding to three scaled frequencies: $f^\star = f\,z/\overline{U} = 0.25$, 0.75, and 1.0. The coefficients were obtained from a CWT of streamwise velocity fluctuations, measured and simulated in heights of 17.5 m/17.75 m (wind tunnel/FAST3D-CT; approx. $0.5\,\mathrm{H_m}$) at six sites that reflect different urban complexities. The time-dependent coefficients were normalized by the scale-dependent standard deviation of the coefficients over the entire signal duration, σ_W.

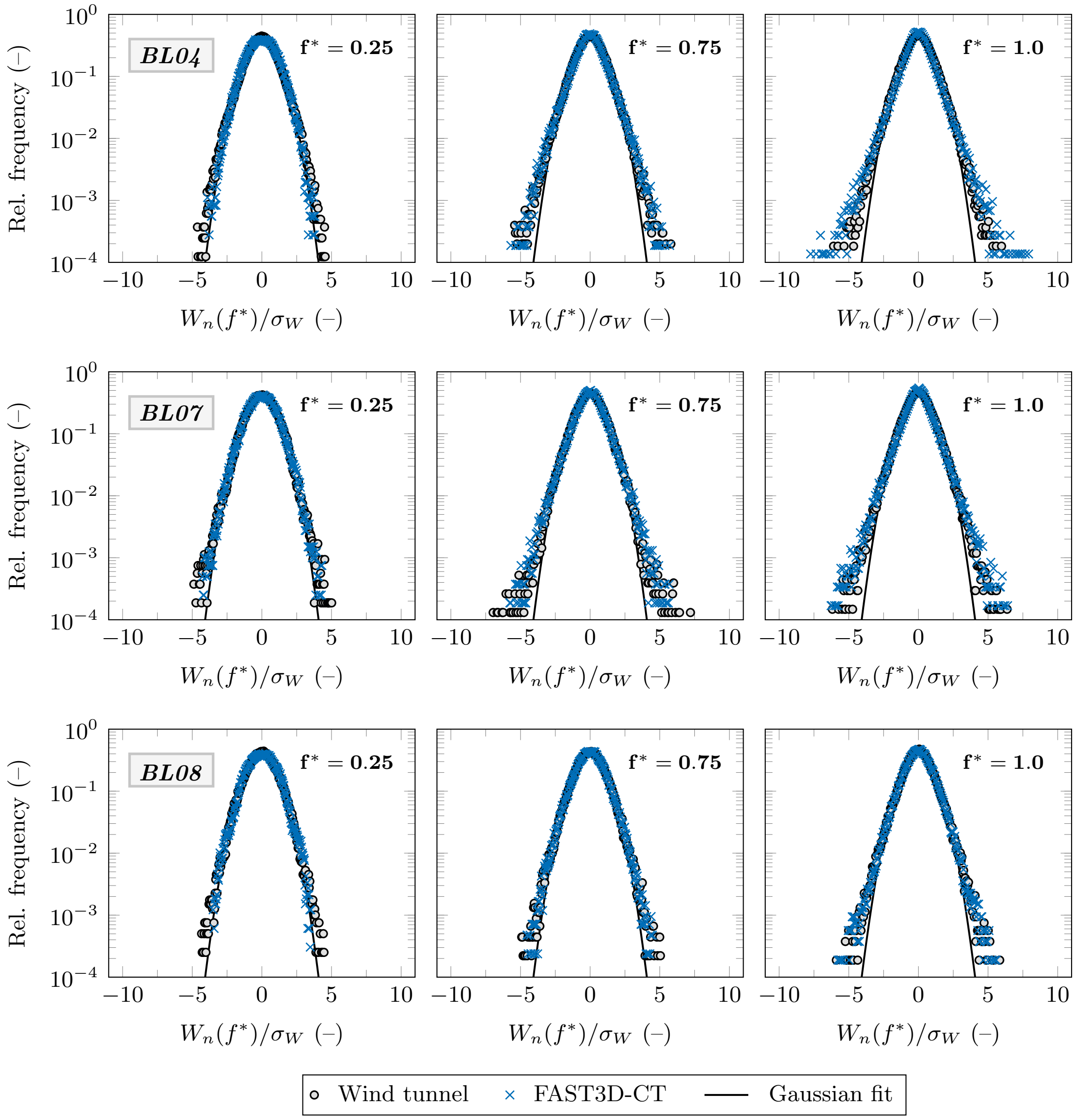

Figure 5.78: Comparison of frequency distributions of the composites of real and imaginary parts of the Morlet wavelet coefficients derived from streamwise velocity fluctuations at locations *BL04*, *BL07*, and *BL08* in heights of 17.5 m/17.75 m (wind tunnel/FAST3D-CT; approx. 0.5 H_m). The distributions correspond to scaled frequencies of $f^\star = f\,z/\overline{U} = 0.25$ (*left*), 0.75 (*center*), and 1.0 (*right*). The black lines show the corresponding Gaussian distributions.

The distributions are approximated with 200 bins. A semi-logarithmic display was selected to study the tails in detail, since they contain information about rare, intermittent events in the flow that left a distinct footprint in the amplitudes of the wavelet coefficients. For a quantification of the level of agreement between the experimental and numerical distribution shapes, kurtosis values β_2 are derived and listed in Table 5.1.

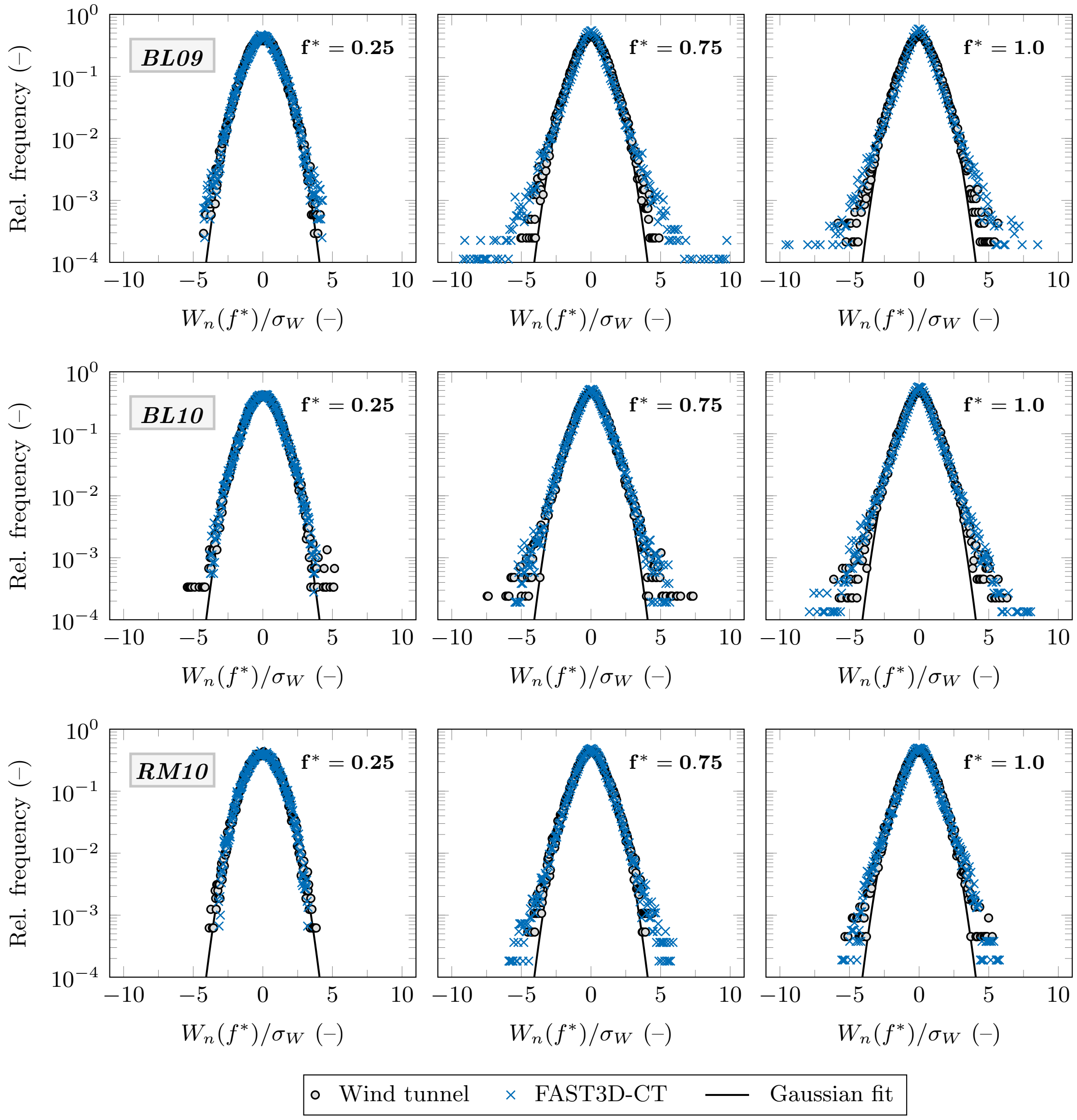

Figure 5.79: Same as in Figure 5.78, but for the comparison points *BL09*, *BL10*, and *RM10*.

A common feature is that the coefficients most often exhibit small negative or positive amplitudes. The behavior in the tails, however, is different at every analyzed location, carrying signatures of the local flow structure, but also showing a clear dependency on the frequency at which the coefficients are analyzed. The smallest deviations from a normal distribution are found for the lowest frequency. For $f^\star = 0.75$ and higher, the distributions feature heavy tails, reflecting an enhanced and *intermittent* activity in the flow associated with *rare* events (cf. Farge et al., 2012). The selected frequencies are located close to the energy peak ranges determined in the global energy spectrum and at the transition region between the turbulence production range and the inertial subrange.

Table 5.1: Comparison of experimental and LES kurtosis values, β_2, of the composite of real and imaginary parts of the Morlet wavelet coefficients corresponding to three scaled frequencies, $f^\star = 0.25$, 0.75, and 1.0. The coefficients are retrieved from the CWT of streamwise velocity fluctuations at six comparison locations in heights of 17.5 m/17.75 m (wind tunnel/FAST3D-CT; approx. 0.5 $\mathrm{H_m}$).

		$\boldsymbol{\beta_2}$ $(\mathbf{f^\star = 0.25})$	$\boldsymbol{\beta_2}$ $(\mathbf{f^\star = 0.75})$	$\boldsymbol{\beta_2}$ $(\mathbf{f^\star = 1.0})$
BL04	Wind tunnel	3.55	4.07	4.21
	FAST3D-CT	2.99	4.39	5.95
BL07	Wind tunnel	3.49	4.16	4.28
	FAST3D-CT	3.29	4.48	5.30
BL08	Wind tunnel	3.34	3.62	4.13
	FAST3D-CT	3.04	3.58	4.18
BL09	Wind tunnel	3.19	3.70	3.99
	FAST3D-CT	3.50	7.44	8.83
BL10	Wind tunnel	3.41	4.58	4.85
	FAST3D-CT	3.33	4.68	6.30
RM10	Wind tunnel	2.98	3.64	3.90
	FAST3D-CT	2.87	4.61	4.66

Because of the larger spread of the wavelet coefficients along the time axis at low frequencies (cf. Figs. 5.76 and 5.77), the analysis of frequency distributions is not particularly revealing since the coefficient time series virtually consist of low-frequency undulations which create spurious distribution patterns and, thus, are not suitable to draw conclusions about time-dependent phenomena.

The largest spreads of the coefficient distribution tails are found at $f^\star = 0.75$ and 1.0, which are located to the right of the spectral energy-density peaks at all comparison sites. It was, however, ensured that the fast roll-off of the LES spectra had not yet started at these frequencies, so that the information in the wavelet coefficients still corresponds to the numerically *resolved* scales of the flow. Deviations from a normal distribution are also recognizable in the respective kurtosis values, β_2 (cf. Table 5.1), which partially show significant offsets from the Gaussian reference value of $\beta_2 = 3$. In particular, the coefficient distributions tend to be *leptokurtic*, exhibiting higher peaks and heavier tails than the normal distributions. This feature is seen in the wind-tunnel data and the FAST3D-CT flow simulations and similar frequency-dependent distribution characteristics can be determined at different comparison locations.

While the LES predictions are qualitatively in good agreement with the wind-tunnel experiment, quantitative deviations are apparent in the kurtosis values, next to the general tendency toward more leptokurtic coefficient distributions derived from the LES data. This feature is also reflected in the pronounced tails of the numerical frequency distributions. For example, particularly large offsets to the experiment can be determined at location

BL09 (Fig. 5.79), where the FAST3D-CT coefficient tails for $f^\star = 0.75$ and 1.0 are spread out up to magnitudes of ten times the standard deviation, signifying the occurrence of short-time, large-amplitude events at this locations. At the intersection position *BL10*, comparable spreads are found, but this time they are also present in the experimental data. Both the wind-tunnel and the LES wavelet coefficient distributions exhibit extended *exponential* tails for the two highest extraction frequencies, recognizable by a linear decay in the semi-logarithmic representation. A similar tail behavior is also detected at other comparison locations, notably at the river location *BL04* ($f^\star = 1.0$; Fig. 5.78), again revealing a high level of agreement between the LES distribution patterns and the wind tunnel. It may be speculated that differences observed between the experimental and numerical frequency distributions, particularly for the highest comparison frequency, are connected to the proximity of this scale to the spectral region in which the LES velocity fluctuations exhibit the very steep energy drop. While this is not mirrored in the Fourier-based LES spectra or the *global* wavelet spectra in this frequency range, the increased level of intermittency in the time-dependent analysis framework could be an indication for the increased influence of the grid-filter.

The quantification of the level of agreement between the wavelet-coefficient frequency distributions by means of significance testing is hampered for the same reasons as discussed in Section 5.3: Since the wavelet coefficients are available at each time step of the signal, the distributions correspond to very large sample sizes so that the statistical significance of deviations detected between the experimental and numerical wavelet coefficients may not be indicative of the actual *practical* significance.

Denoising & coherent structure extraction

In meteorological applications with a focus on atmospheric turbulence as well as in other areas of fluid dynamics research, wavelet analysis methods are usually associated with the characterization, extraction, and analysis of *coherent* flow structures and connotations like flow pattern recognition. As discussed above, this task is not trivial because typically one does not know *a priori* what structures to look for.

Apart from continuous wavelet techniques, the *discrete wavelet transform* (DWT) based on the use of *orthonormal* wavelets can be applied to disentangle contributions from large-scale organized eddies in the flow from small-scale disorganized structures that are superimposed on coherent events (*wavelet thresholding* or *signal denoising*; e.g. Farge et al., 1999; Mallat, 2009; Farge et al., 2012). Unlike the CWT, the discrete wavelet transform does not contain redundancy in the derived wavelet coefficients because the scaled wavelet versions used in the analysis are orthogonal to each other (for details see Daubeschies, 1988, 1992). Typically, a *dyadic* grid arrangement is used in the DWT to couple the translation parameter to the scale of the wavelet, such that $s = 2^m$ and the size of the translation increment is $\delta n = 2^m$, with $m = 0, \ldots, M$ and $M = \log_2(N)$, where N is the number of points in the time series given as a power of 2 (Addison, 2002). Hence, the number of scales used in a DWT analysis only depends on the sample size.

As can be seen in the local wavelet energy spectra shown earlier in Figures 5.76 and 5.77, there is a certain degree of "communication" between the wavelet coefficients at different scales, reflected in elongated shapes of the coefficient contours along the frequency axis.

Such cross-talk does not occur among the DWT coefficients. Furthermore, other caveats associated with the CWT, like spurious wavelet correlation artifacts addressed earlier, are not encountered in the discrete analysis version. For the application to validation purposes, the DWT might prove useful in order to further study contributions from the largest scales in the flow in detail by eliminating the small-scale noise from the experimental signals and, if applicable, also from the LES data, in order to reconstruct the velocity time series from wavelet coefficients that only correspond to a subset of scales.

For other analyses, however, the redundancy contained in the continuous wavelet coefficients can be essential. A great advantage of the CWT of time-dependent signals like velocities time series is that information about time-frequency characteristics is available in a continuous value space due to the continuous nature of the analysis parameters. This property enables to study the wavelet-coefficient frequency distributions of the wind-tunnel velocities and the numerical simulation at arbitrarily selected frequencies (scales), which can directly correspond to the particular focus of the analysis and the inherent properties of the analyzed data. While the DWT coefficients can be analyzed in a similar way, the scales at which this analysis can be performed are fixed and determined by the signal duration (i.e. by the sample size N).

With the above analysis it has been attempted to sketch out a possible direction for the use of advanced signal processing methods for a detailed validation of LES results. The comparative CWT analyses presented in this section in terms of results obtained at different flow locations within the urban canopy layer revealed that the time-dependent characteristics in the wind tunnel and the eddy-resolving simulation are qualitatively comparable concerning structures encountered in the CWT coefficients.

The visual evaluation of the time-frequency content of velocity signals already provided insight into structural differences and similarities between the experimental data and the LES predictions and completed the prior spectral analyses based on the classic Fourier transform. While the time traces of the local wavelet energies are not directly comparable for a certain instant of time, a *qualitative* impression about the level of agreement can be gained. In order to add a more quantitative component to the analysis, frequency-dependent wavelet-coefficient distributions have been compared at several locations and for different extraction frequencies. The analysis showed that this method is sensitive enough to capture variations in the flow, in this case generated by changes of the built-up surroundings from one comparison point to the other, and allows to quantitatively compare the simulation with the experiment by means of high-order moments.

These findings could be used as a the starting point for further approaches to quantify the agreement between scale-dependent statistics of the flows, to which the diagnostics used in the preceding parts of this chapter have been blind. This could include the comparison of height profiles of scale-dependent wavelet-coefficient kurtosis values. On this basis, the agreement between experimental and numerical analysis pairs could be assessed by means of scatter plots.

The analysis strategies presented in this section explored the potential of wavelet methods in the validation of time-dependent eddy-resolving codes, by exemplifying the information level that can be exploited based on the Hamburg validation test case. Apart from discrete wavelet transform approaches, additional CWT-based investigations can be promising, too. An interesting point for further analyses, for example, would be to study cross-wavelet spectra of the streamwise and vertical velocity fluctuations as an extension of the Reynolds-stress quadrant analysis presented in Section 5.6. However, as with other statistical methods, the user has to be aware not only of particular strengths of the technique, but also of limitations and caveats, which, in the case of the CWT, have been discussed with respect to the choice of the mother wavelet.

Final conclusions from the comparative application of the **continuous wavelet transform** to turbulent velocity fluctuations are as follows:

- Due to the fast roll-off of the LES spectra at high frequencies it is advisable to use a wavelet function with a large number of vanishing moments in the analysis (e.g. the Morlet wavelet).
- Qualitative comparisons of the local wavelet energy spectra as a function of time and frequency indicated structural similarities between the wind tunnel and the FAST3D-CT flow.
- The comparative evaluation of wavelet-coefficient frequency distributions substantiated the qualitative analyses and revealed a similar dependency of the experimental and numerical distribution shapes on the flow location and the extraction frequencies.
- By analyzing the wavelet coefficient kurtosis, the level of agreement was quantified, and a tendency toward an increased flow intermittency in the LES at the highest comparison frequency ($f^{\star} = 1.0$) could be determined.

With the above CWT results Chapter 5 closes. In the following final chapter of the thesis, a synopsis of major validation results is presented together with a discussion of implications regarding the fitness for purpose of the LES-code FAST3D-CT for its intended use and possible strategies for the improvement of the simulation accuracy. Building on the evaluative discussions in Section 5.2 to 5.7, further conclusions about the applied analysis strategies are reviewed with a view to their level of insight for an LES validation. In addition, an outlook on further analysis approaches and on the general potential for a quantification of the validation results is presented. Finally, recommendations for joint activities concerning the formulation of best-practice guidelines for the validation of micrometeorological LES codes applied to predict near-surface atmospheric flow fields are given.

6 Synopsis and Outlook

"On the whole we should not overlook that since a model is never true,
but only more or less adequate (...),
deficiencies are bound to show given sufficient data."

Rasch (1980)

(— *Probabilistic models for some intelligence and attainment tests.*)

The study presented in this thesis has been motivated by the lack of proportion between the increasing use of eddy-resolving numerical methods like large-eddy simulation in micro-meteorology and environmental fluid dynamics applications as opposed to the level of scrutiny that is commonly applied to the quality of the predictions obtained.

Time-dependent three-dimensional simulations of turbulent flow originated from meteorological applications more than 40 years ago. However, it was only with the rapidly rising computational capacities in recent years that the technique has become increasingly applicable and affordable for a broad community. This development is paralleled by the availability of commercial and open-source CFD codes, which further augmented the status of LES as an important tool for the investigation of atmospheric turbulence phenomena. Today, hardly any meteorological research area focusing on meso-scale or micro-scale processes is unaffected by the eddy-resolving approach. One of the key areas of application is research on flow and dispersion processes in the near-surface atmospheric boundary layer over various surface forms ranging from homogeneous land types over hilly or mountainous terrain to plant or urban canopies (cf. Chapter 2). Besides fundamental studies, LES is increasingly applied to "real-life problems" of practical concern, for example to answer urban micro-climatological and environmental questions. Hence, quality and accuracy assessments of the predicted scenarios are becoming more and more crucial.

Based on the example of highly complex urban boundary-layer flow, this thesis showed that only through a rigorous validation of LES predictions on the basis of *qualified* reference experiments and through the application of *model-specific* tests, the suitability of time-dependent, turbulence-resolving codes for their intended use can be documented, and the bounds of uncertainty in the results can be quantified.

6.1 Lessons learned from the validation of FAST3D-CT

The essential statement advocated in this thesis is that the *time-dependent nature* of large-eddy simulation has to be taken into account if validation of the numerical results is expected to provide a *true* assessment of the capabilities and limitations of the code. The results of the validation test scenario presented in Chapter 5 document that this goal can be reached if the usual validation approach based on the comparison of low-order turbulence statistics is extended by the analysis of *time-dependent* turbulence features.

Chapter 3 introduced a novel LES validation concept based on a sequence of well-established time-series analysis methods. The proposed validation hierarchy (cf. Fig. 3.2) represents a holistic approach toward flow characterization and distinguishes three comparison levels:

1. Exploratory data analysis (*here: descriptive statistics, frequency distributions*)
2. Analysis of turbulence scales (*here: temporal autocorrelations, energy density spectra*)
3. Flow structure identification (*here: quadrant analyses, continuous wavelet transforms*) .

This analysis sequence has been applied to validate turbulent flow predictions by the urban aerodynamics code FAST3D-CT, which was developed and operated by the U.S. Naval Research Laboratory in Washington, D.C., and is based on an *implicit* LES approach (Section 4.3). Qualified reference data have been generated through measurements in the specialized boundary-layer wind-tunnel facility of the University of Hamburg.

A particularly challenging test scenario was selected for this study: turbulent flow in the densely built-up urban center of Hamburg, Germany (Section 4.1).

Specific analysis methods used in the validation process are shown in parentheses in the above list and were selected with regard to the availability of the experimental reference data as *single-point*, *time-resolved* velocity signals.

In the next sections, main conclusions drawn from the in-depth validation of FAST3D-CT are presented, and the discussion on the model's fitness for purpose is extended. It is started with a recapitulation of steps taken to document the quality of the experimental reference data and their suitability for the validation of eddy-resolving simulations. Then, the emphasis is put on a synopsis of strengths and limitations of the validated LES code regarding the realistic representation of turbulent flow structures in a complex urban environment, based on the results introduced in Chapter 5. Furthermore, the general applicability of the proposed validation sequence is evaluated.

Possibilities to improve the performance of the numerical model are discussed from a *practical* and *academic* point of view, together with prospects of using multi-point experimental reference data for the characterization of spatial flow structures as an extension of the approach presented. The conclusion of this chapter provides general recommendations, addressing the necessity to *harmonize* quality assurance procedures for eddy-resolving models applied to micro-meteorological or environmental fluid mechanics problems in the near-surface atmospheric boundary layer.

6.1.1 LES validation results

Quality of the reference experiment

Prior to any comparison between measurements and simulation, it was verified and documented that the laboratory experiment and the generated reference data are fulfilling specific quality demands. This concerns the representativeness of the wind-tunnel model for the physical problem of interest (*similarity requirements*), the qualification of the measured velocity data for advanced signal processing (*signal quality and resolution properties*), and the statistical robustness of derived quantities (*experimental reproducibility*).

Verifying the suitability of the reference experiment is a necessary step of the model validation process that ensures a meaningful and equitable comparison with the simulation. Since the proposed LES validation scheme puts a strong emphasis on the analysis of time series and the comparison of structural flow characteristics, the adequacy of the wind-tunnel velocity signals for advanced processing has been a major focus of the quality assurance efforts. The corresponding analysis procedures applied to the wind-tunnel data are documented in detail in Section 4.2 and 4.4. In particular, the following points were ensured:

- Geometric and dynamic similarity requirements are met by the experiment.
- Inflow conditions comply with field observations (suburban tower measurements) and general surface layer characteristics.
- Signal quality provided by the utilized laser Doppler anemometer (LDA) setups is high and systematic technical bias effects are small.
- Signal duration is long enough to minimize the inherent uncertainty and to allow for a statistically representative analysis of large eddies in the flow.
- Sampling frequencies are high enough to capture turbulence structures that are directly resolved in LES.
- The statistical reproducibility of experimental results, as derived from measurement repetitions, is high.
- Bias resulting from resampling of LDA signals (for spectral analyses) is minimized.

For the study, 22 vertical profile locations distributed all across the inner city area were selected based on their representativeness for typical flow scenarios in the urban roughness sublayer. With a total of 2×334 experimental time series from LDA measurements in U-V mode (horizontal wind components) and 2×160 from measurements in U-W mode (streamwise and vertical velocity components), the Hamburg validation scenario draws upon an extensive and diverse reference data pool.

Suitability of the validation concept

The validation study has been performed as a *blind test*. Apart from information on the wind-tunnel inflow conditions, no experimental results were communicated to the numerical side prior to the final simulation run. For the setup of both the wind-tunnel model and the computational domain, the same information on buildings and terrain was used, and other important physical constraints were harmonized (cf. Section 4.3.2).

1. Exploratory data analysis Starting with the analysis of *mean flow and turbulence statistics* (Section 5.2), the detailed comparison of numerical results with wind-tunnel measurements has shown that FAST3D-CT is able to realistically capture typical urban *mean* flow patterns at structurally diverse locations within the built-up environment.

Judging from the comparison of first and second order statistical moments, characteristic urban flow scenarios like recirculating regimes, channeling effects or strong lateral flow deflections at street-level are mostly found to be in good qualitative and quantitative agreement with the experiment. At some sites and in certain analysis heights, however, systematic deviations between LES and wind-tunnel velocity statistics have been determined. A detailed evaluation of these discrepancies is presented at the end of this section.

From the mean flow analysis alone, no conclusions about the particular structure of the underlying data samples can be drawn, which in this case consist of *instantaneous* turbulent velocities. Instead, all information available in the time-dependent signals is condensed into single-number parameters. Gaining insights into the *value range* and *occurrence probabilities* of predicted quantities in connection with the general time dependency of the investigated scenario, however, are key reasons to prefer LES-based methods over significantly less expensive steady-state RANS alternatives.

A simple, yet rarely pursued way to extend the otherwise inherently static exploratory analysis is to focus on *frequency distributions* of time-resolved velocities or of derived quantities, as presented in Section 5.3. Comparisons of velocity and wind direction histograms show that FAST3D-CT has the potential to reproduce sophisticated geometry-induced flow patterns, which are, for example, expressed in the occurrence of *bimodal* or strongly skewed distributions. In these situations, the informative value of measures like mean and standard deviation (location and spread of the distributions) can be strongly deceptive. The same is true for higher-order shape measures like skewness and kurtosis, which are otherwise most helpful in adding a quantitative component to the distribution comparison.

2. Analysis of turbulence scales LES is expected to directly resolve energy and flux-dominating turbulent eddies. Comparing statistical measures associated with these scales of motion, hence, provides valuable information about the adequacy of the computation.

Due to the restriction of the reference data to *single-point* measurements, dominant turbulence *time scales* and *temporal autocorrelations* have been analyzed in this study (as opposed to turbulence *length scales* and *spatial correlations*; Section 5.4). Comparing the shapes of numerical and experimental temporal autocorrelation functions has furthered confidence in the model's ability to deliver a realistic picture of energy-dominating turbulence in the urban roughness sublayer. Furthermore, it can be examined how the space-filtered nature of LES leaves footprints in the autocorrelation curves (stronger level of correlation over short time lags due to the reductions of the range of eddy scales).

The general height development of derived integral time scales associated with the three velocity components is well reproduced in the computation at most of the comparison locations, particularly inside the UCL. Given the complexity of the flow situation and the general sensitivity of integral measures based on correlations, the encountered level of agreement with the experiment allows for wide-ranging conclusions about the general adequacy of the specific numerical approach for urban flow computations.

Investigating the distributions of *spectral energy densities* among different scales in the flow is a natural extension of the correlation approach (cf. Section 5.5).

From the comparative analysis of velocity spectra in this study, a fast roll-off of the LES spectra has been determined shortly after the spectral peak, in the transition region between the production range and inertial subrange. Hence, with a uniform grid resolution of 2.5 m in the lower levels of the urban roughness sublayer and the specific dissipation scheme implemented in FAST3D-CT, the computations is already at the edge of being a *very large-eddy simulation*. However, particularly at locations within the downtown area below and above rooftop, the spectral shapes in the energy-dominating frequency range exhibit a very high level of agreement with the experimental counterparts. This concerns both the peak locations and the energy distributions among the largest eddies in the flow (low frequencies), showing that the LES provides a mostly accurate picture of the directly resolved scales in comparison to the experiment.

The analysis also highlighted the particular importance of an adequate spectral scaling approach for urban flow fields in order to ensure the general comparability of results.

3. Flow structure identification The indirect retrieval of *structural* flow information from velocity time series has been conducted in the framework of a *quadrant analysis* of the vertical turbulent momentum flux at various urban sites (Section 5.6). Qualitatively, the relationships between the dominance of contributions from a particular quadrant to the average flux and the occurrence characteristics of the underlying flow events exhibit a close resemblance between experiment and LES. This congruence is also reflected in the joint frequency distributions of instantaneous pairs of streamwise and vertical velocities.

By introducing a hole-size constraint to the conditional re-sampling process, the occurrence of flux contributions linked to infrequent, large-amplitude events in the flow has been compared. This analysis shows that FAST3D-CT reproduces the hole-size dependent evolution of momentum flux fractions in a realistic way, concerning the relative dominance of downward sweeps of high-momentum fluid into the UCL and upward ejections of low-momentum fluid into the RSL, up to heights of approximately $3\,\mathrm{H_m}$.

To further deepen the analysis of time-dependent flow structures in the wind tunnel and the simulation, the classic spectral time-series analysis has been expanded into a *joint time-frequency* framework. Here, scale-dependent analyses of the urban flow field based on the *continuous wavelet transform* reveal a high level of agreement between experimental and numerical local wavelet energy spectra.

In order to quantify the comparison, frequency distributions of wavelet coefficients have been evaluated, which were obtained at energetically dominant frequencies. In both data sets, similar characteristics for the occurrence of rare but energetically significant turbulence episodes are determined. Depending on the extraction frequency and the comparison location, the shapes of the wavelet coefficient PDFs feature heavy tails, which is an indication for an increased level of intermittency in the flow. By comparing the corresponding kurtosis values, a strong qualitative agreement between the laboratory flow field and the LES predictions has been found.

Discussion Despite the strong performance of FAST3D-CT described in the previous paragraphs, the analysis has also revealed some systematic deviations from the experimental reference. These concerned the tendency toward an underprediction of velocity magnitudes at some comparison points located within the urban canopy layer and in close proximity to vertical boundaries (building facades). On the other hand, systematic deviations have been observed at the outer edge of the urban roughness sublayer (above approx. $3\,\mathrm{H_m}$). These discrepancies could be explained by the following aspects:

> **Inflow conditions** — At the outer edge of the urban roughness sublayer, well above the UCL, the numerical results consistently feature deviations from the experiment. These differences are expressed in strongly enhanced turbulent variances and covariances, in a high kurtosis of the frequency distributions of instantaneous velocities, in significantly reduced integral time scales, and in offsets between spectral energy peaks by more than one decade toward higher frequencies. In all analyses it has been determined that these effects are stronger pronounced for the horizontal velocities. Those features are most likely linked to the artificial turbulence generated at the inflow plane, which "survived" in the upper flow levels and still significantly affects the computation. This conjecture is supported by the fact that the offsets are attenuated as the flow is advected over the inner city area, where enhanced turbulent mixing with the lower-level flow results in more realistic predictions.
>
> **Grid resolution** — The grid size of 2.5 m used in the simulation, in combination with the computational representation of buildings by a rather simple grid masking approach strongly affect the resolution potential of LES within the urban canopy. Near boundaries such as building facades, the introduction of stair case geometry patterns by the cell blocking ultimately has an effect on the flow. Since entire cells are blocked, the positions of building boundaries do not exactly correspond to the better resolved representation in the wind-tunnel model: Depending on the alignment of the buildings within the numerical grid, the comparison points at some of the sites are located closer to buildings than in the wind tunnel, which can result in underpredictions of velocity magnitudes, particularly in narrow street canyons.
>
> **Dissipation representation** — The physical resolution potential of the simulation is also affected by the numerical dissipation characteristics used in the implicit LES scheme. Although a grid-resolution of 2.5 m should allow to resolve at least one frequency decade of inertial subrange turbulence, the FCT-scheme in its current configuration seemed to contribute to an enhanced energy loss (identifiable in the turbulence spectra). Especially within the urban canopy, the setup of FAST3D-CT in this study only allowed to resolve the energy-dominating turbulence scales, which is characteristic for a *very large-eddy simulation* (VLES).

The general comparability of the data has also been affected by spatial offsets between comparison locations in the experiment and the LES (see discussion in Section 4.4.3). Seemingly marginal differences of 0.25 m can have a significant influence on the results in regions of strong gradients (e.g. near roof level). The same is true for spatial offsets in the (x, y) plane in strongly heterogeneous flow situations (e.g. intersections).

Another aspect concerning the comparability of statistical results is related to the temporal durations covered by the experimental and numerical time series. As discussed in Chapter 4, the inherent uncertainty of turbulence statistics can only be reduced in signals of sufficiently long duration. While it was assessed that the difference between the experimental and numerical time-series lengths ($T_{\mathrm{exp}} \simeq 16.5\,\mathrm{h}$ vs. $T_{\mathrm{les}} \simeq 6.5\,\mathrm{h}$) leaves the comparability of *global statistics* mostly unaffected, this may not be the case for the more sensitive *eddy statistics*. The representativeness of integral time scales or low-frequency spectral energy densities, for example, can be heavily affected by the occurrence rates of large eddies in the flow: The longer the time series, the more energy-dominating structures have likely passed the sensors, and the more robust are statistics associated with this eddy class. This fact has to be kept in mind when interpreting and comparing such measures.

The Hamburg validation test case showed that the in-depth LES validation scheme proposed in this thesis allows for more wide-ranging conclusions on the quality of the predictions compared with the sole analysis of low-order statistics. Only by including analysis methods that are targeted at the resolved eddy structures in LES and at the time-dependent nature of the simulation, trust in the adequacy of the turbulence simulation can be furthered and deviations to the reference experiment can be holistically investigated.

6.1.2 Fitness for purpose & simulation improvements

The results of the validation study overall documented that FAST3D-CT provides *realistic* and *reliable* predictions of complex flow characteristics in the urban environment. The strongest potential of the simulation in its current setup lies in the representation of sophisticated geometry-induced turbulence characteristics within the UCL.

An important application of FAST3D-CT is the provision of urban wind data for the use in an emergency response tool operated by first responders in the case of accidental or deliberate contaminant releases in cities (CT-Analyst; cf. Section 4.1 and Boris, 2002). The LES data are utilized to derive typical velocity fluctuation characteristics that directly affect dispersion patterns. For this purpose, the predictions are condensed into nomografs, containing *integrated* information about flow paths (Boris et al., 2011). The LES data are typically incorporated up to elevations of $2\,\mathrm{H_m}$, so that the spurious predictions of upper-level flow characteristics determined in the present study are not directly affecting the database for the operational model. Regarding the accuracy levels of predicted flow fields in the UCL and in the lower roughness sublayer, it can be stated that FAST3D-CT, in the current simulation setup, is fit for its purpose.

Shifting from a practical toward a more scientific point of view, there surely is potential for model improvements. Re-running the Hamburg case with a more detailed representation of building elements would certainly lead to a better understanding of some of the discrepancies determined in the present study, and it is expected that quality improvements will particularly emerge at comparison points located in narrow streets. The same is true for refinements of the grid resolution in conjunction with the FCT-scheme, and for improvements of the numerical inflow conditions. The latter task, however, is not trivial since the artificial generation of realistic inflow turbulence requires comprehensive knowledge about its time-space structure for the respective problem of interest.

6.1.3 Experimental & methodical extensions

Three-dimensional multi-point data

The depth of the validation process is inherently coupled to the amount and type of information that is accessible from suitable, at best *model-specific*, reference experiments. For the test case presented in this thesis, 2D high-resolution *single-point* velocity time series were available in space-filling vertical profiles and horizontal measuring arrays. This allowed for the general categorization and comparison of mean flow and turbulence statistics at various urban sites, together with the derivation of high-order statistics and the application of advanced time-series analysis methods.

A significant extension of the existing database could, for example, be made by using 3D LDA probes that facilitate the simultaneous retrieval of all three velocity components and would enable to include further analysis approaches. In an ideal situation, an LES validation database from laboratory experiments would consist of such single-point 3D measurements, offering a high temporal resolution, in combination with multi-point measurements that typically feature a comparatively low time resolution.

Space-resolved measurements offer great potential to further ease the LES validation issue (see also discussion by Adrian et al., 2000). In the wind tunnel, measuring techniques like *particle image velocimetry* (PIV) can currently be applied to acquire highly-resolved information about the spatial structure of turbulence at moderate temporal resolutions. An example of a 2D (planar) PIV measurement is shown in Figure 6.1 in terms of four consecutive snapshots of the flow on the leeward side of a wall-mounted cube, measured in the boundary-layer wind-tunnel facility at the University of Hamburg. The PIV image contains overall 21,360 points at which measurements of the streamwise and vertical velocity components are available (details given in Hertwig, 2009). This resolution would allow to directly compare statistical spatial patterns, space correlations or integral length scales in LES with the reference experiment.

In the analysis of single-point time series there is a always a certain level of speculation involved when drawing conclusions about actual spatial structures in the flow. Spatially resolved data, on the other hand, enable to study the space characteristics of the flow in detail. Furthermore, PIV data can be analyzed by means of well-established structure identification methods like the *proper orthogonal decomposition* (POD), which has been proposed for the application to turbulent flows by Lumley (1967) (cf. reviews by Berkooz et al., 1993; Holmes et al., 1996). As discussed by Hertwig et al. (2011), POD and stochastic estimation methods could be used to build further bridges between experiment and LES.

Quantification of comparison results

The ultimate step of a validation effort is to incorporate all information gathered during the comparison and condense the results into a *one-dimensional* space, allowing to draw a binary conclusion about the adequacy of the simulation. In validation studies aimed at RANS-based simulations, the quantification of the performance quality and the decision about the quality of the model are often coupled to statistical measures known as *validation metrics*, which are based on the quantitative evaluation of differences between experimental and numerical statistics (cf. Section 3.1). Defining threshold values or acceptance margins for these metrics is one way to easily assess the performance of a model and/or to quantitatively compare the adequacy of different models.

In general, such measures can also be applied in an LES validation as an extension of the exploratory data analysis focusing on low-order statistics (cf. Section 5.2). However, it is emphasized that the definition of suitable accuracy thresholds for a *yes-or-no* decision on the simulation quality is not trivial and for velocity statistics mostly relies on case-by-case definitions. For even more sensitive statistical measures like, for example, high-order moments, integral time scales, or peak frequencies of spectral energy distributions, threshold-based assessments can be even more ambiguous and have to be formulated in close connection to the purpose of the simulation and with regard to general levels of uncertainty connected to the computation of eddy statistics.

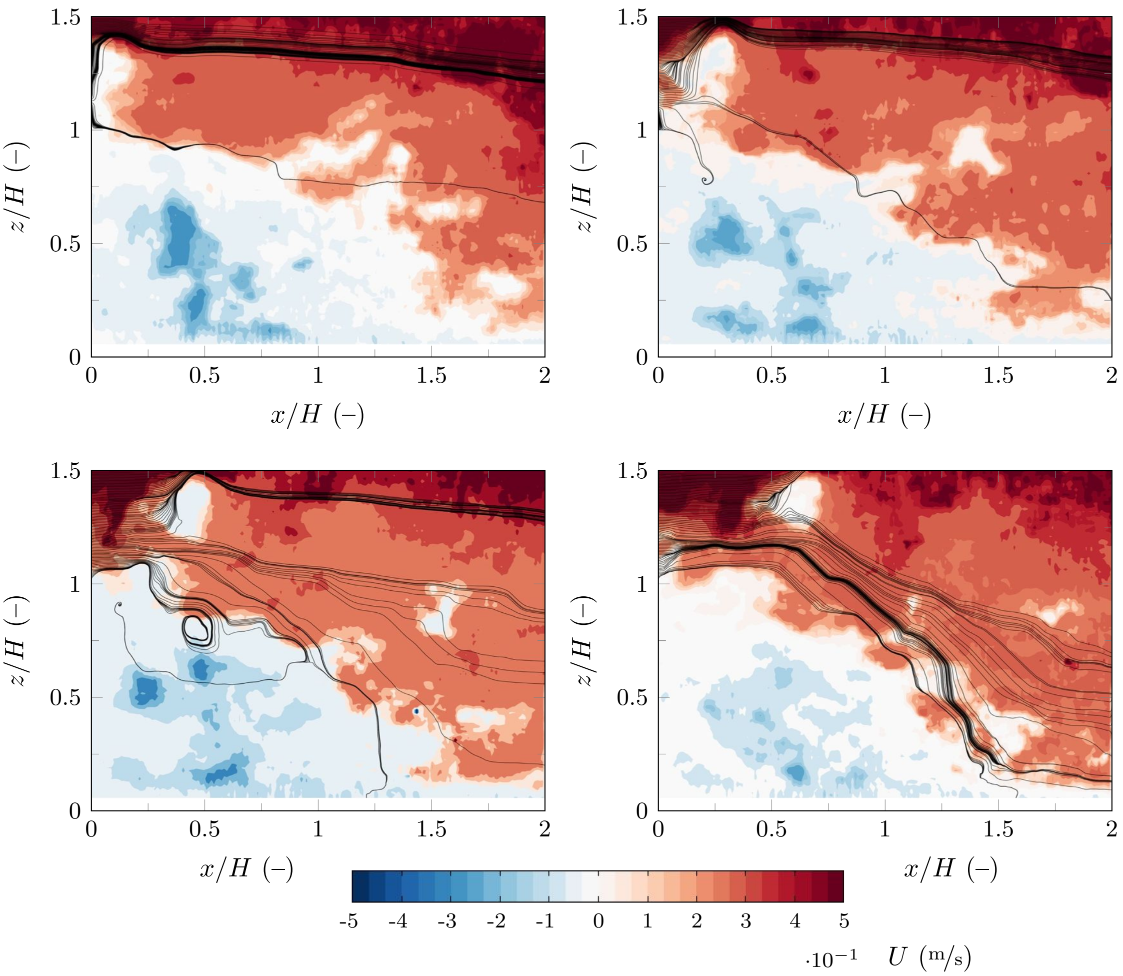

Figure 6.1: Contours of instantaneous streamwise velocities together with streamlines on the leeward side of a wall-mounted cube derived from boundary-layer wind-tunnel measurements with 2D particle image velocimetry in the (x, z) plane. Spatial coordinates are given in reference to the side length of the cube, H.

6.2 General conclusions & recommendations

The example of the Hamburg-city flow validation test case illustrated the potential of advanced turbulence analysis methods for a detailed assessment of the performance of eddy-resolving time-dependent simulations. With well-established signal analysis approaches and by means of suitable and quality-controlled reference data, a high level of detail can be incorporated in the validation of LES, which by far exceeds the informative value available from the comparison of low-order flow statistics. Only through a holistic validation approach can the potential of the simulation to realistically reproduce the temporal (and spatial) characteristics of the turbulent flow be evaluated.

The approach pursued in this thesis puts a strong emphasis on the comparison of eddy statistics and structural turbulence information and, thus, allows to draw wide-ranging conclusions about the quality of the predictions and to build more tenable confidence in the capabilities of the model. The analysis showed that it is important to be aware of specific properties of numerical and experimental data in order to ensure their overall comparability. Sufficiently long simulation and measurement durations, for example, are needed to obtain statistically representative quantities.

The study has demonstrated that measurements in specialized boundary-layer wind tunnels are an ideal complement to campaigns in the field. While only the latter can capture the true physical complexity of natural atmospheric boundary layers, the former offer the potential to systematically study physical processes in isolation. With constant mean inflow boundary conditions, wind-tunnel experiments are in general repeatable, which allows to document the statistical reproducibility of measured quantities as a crucial prerequisite for an equitable comparison with the simulation. Furthermore, the model-character of laboratory studies offers the possibility to harmonize experiments with numerical simulations for the validation process, as shown in this study.

Hence, there are essentially two ingredients for a successful model validation:

- the *availability of qualified reference measurements* and the
- *application of model-specific analysis strategies.*

However, in the specific case of micro-meteorological LES, neither have standards been established with regard to the kind of measurements that can be labeled *"qualified,"* nor is there a general consensus about which analysis methods exactly are *"model-specific"* and are offering sufficient insight into simulation quality.

As discussed by Adrian et al. (2000), turbulence measurements for the quality control of LES predictions (and LES model formulations) should ideally be designed to meet the characteristics of the simulation as closely as possible (e.g. with respect to temporal and spatial resolution properties). Considering micro-meteorological applications, joint activities involving field and laboratory measurements have the greatest potential for this task: While extensive databases, covering a multitude of measurement locations and flow scenarios, can be generated in boundary-layer wind tunnels, the complexity of the near-surface atmosphere under variable meteorological conditions can only be captured in data from field campaigns.

The hierarchy of LES-specific analysis strategies introduced in this thesis represents a viable approach to the validation issue. However, LES validation will remain a challenge – and therefore, unfortunately, also a side-topic – as long as there are no community-wide activities to streamline efforts in this regard. The micro-meteorological community has shown before that multi-national, multi-institutional activities for the harmonization of validation approaches for flow in urban environments are feasible (cf. Section 3.1.2).

COST732 (Schatzmann and Britter, 2011) is a great example on how collaboration and exchange between experimentalists and numerical modelers can result in broadly accepted quality standards and best-practice protocols for numerical models, which were in this case based on steady RANS approaches. It is strongly encouraged that similar activities are also pursued for LES validation, involving developer and user communities on the numerical side as well as experimentalists in the field and in wind-tunnel laboratories. Activities in this regard need to focus on the joint formulation of validation procedures, stressing the role of advanced turbulence analysis methods and flow pattern recognition techniques, as well as on the compilation of data standards (concerning type and quality requirements) for reference experiments with regard to micro-meteorological and environmental fluid mechanics applications in the near-surface atmosphere.

"What would our heroes say to all this,
Reynolds who never saw hot-wire measurements of his turbulent stresses,
Prandtl who never saw computer solutions of his turbulence models?
Would they be amazed by the spectacular progress we have made?
Perhaps they would be amused to find that with all our hot wires and computers
we have still not achieved an engineering understanding of turbulence,
and that it is still as important and fascinating and difficult a phenomenon
as when the first steps in studying it were taken by Reynolds and Prandtl."

Bradshaw (1972)

(— *The understanding and prediction of turbulent flow.*)

Appendix A

Wind-tunnel model & measurement setup

Figure A.1 shows a schematic drawing of the general flow measurement setup that was used during the Hamburg wind-tunnel campaign. Apart from the probing instruments, all technical devices were positioned outside the tunnel. The LDA probe was moved with an automated 3D traversing system. The traverse controller and the signal acquisition system of the Prandtl tube (pitot-static tube) were controlled by custom-made software (using `LabView`). Both were connected to the commercial data acquisition system of the LDA measurement unit,[1] allowing for an automated traversing toward the specified location and a simultaneous initialization and abortion of the LDA and pressure measurements. The Prandtl-tube signal was recorded by a pressure transducer,[2] delivering voltage signals to an analog-to-digital converter,[3] which was connected to the measurement computer. All programs run on a usual PC with a `Microsoft Windows` operating system.

2D-CAD sketches of the Hamburg wind-tunnel model are presented in Figure A.2. The drawing on the left-hand side includes buildings, jetties, and the above-ground trail of a subway line. Contour lines of the topographic elements and the bodies of water in the physical model are shown in the drawing on the right-hand side.

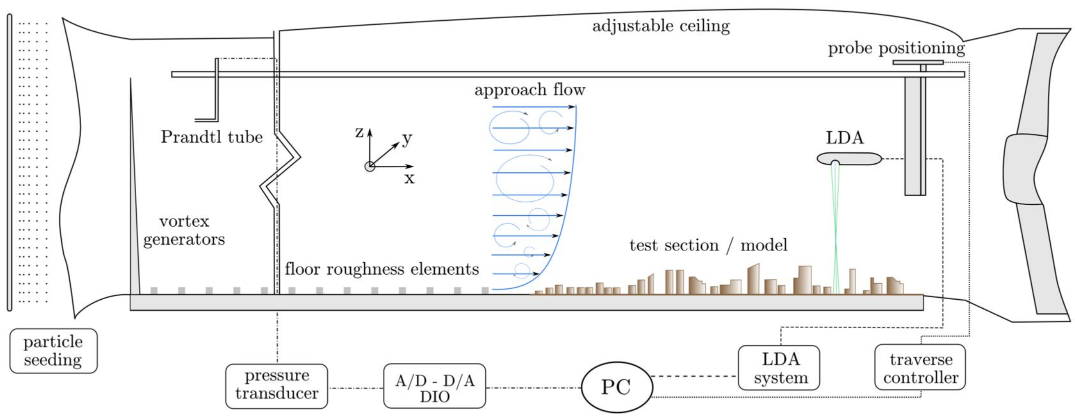

Figure A.1: Schematic of the wind-tunnel setup for flow measurements in the Hamburg campaign with the LDA probe aligned in U-V mode. The flow is approaching from the left. Note that distances and heights are *not* true to scale.

[1]`Dantec Dynamics BSA flow software v4.50`.
[2]`MKS Baratron type 170M-26B`.
[3]`IOtech DAQBook 2000`.

Buildings were represented with a precision of approximately 1.5 mm model scale. Terrain was only included at two positions in the model: close to the lateral boundary in positive y-direction and, again, close to the domain outlet boundary. The vertical depth of each hill layer was 2 mm in model scale. In order to avoid effects of the lateral tunnel boundaries, flow measurements were primarily conducted within the centerpiece of the model, bordered by the outer ground plates.

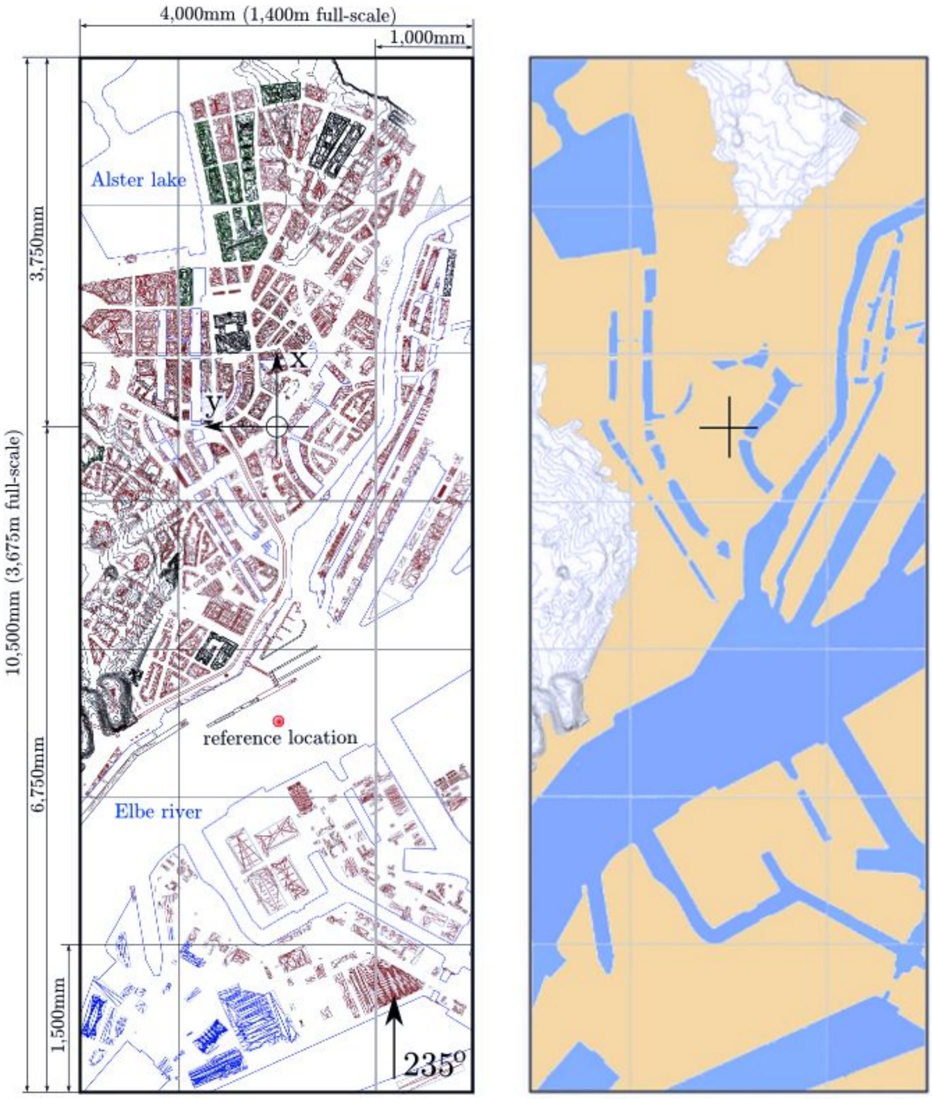

Figure A.2: 2D-CAD sketches of the Hamburg wind-tunnel model including buildings (left) as well as topography and water bodies (right). Lines within the model area mark the borders of the ground plates on which buildings and terrain elements were mounted. The coordinate origin as well as the position of the flow reference location are specified. The approach flow is from bottom to top (arrow).

Appendix B

Field data & measurement site

Benchmark values for the physical modeling of realistic approach flow conditions were derived from meteorological field measurements in the suburban environment of Hamburg-Billwerder. The measurement site has been operated by the Meteorological Institute of the University of Hamburg since 1967 (for a recent review see Brümmer et al., 2012).[1] Since 2000, turbulence measurements are made by means of 3D ultrasonic anemometers (`METEK USA-1` model type) mounted on two masts. Both are located approximately 8 km to the southeast of the city center and about 10 km off to the east of the inflow area of the wind-tunnel domain.[2] Figure B.1a shows the 300 m radio tower on which sonic anemometers are mounted on platforms in heights of 50 m, 110 m, 175 m, and 250 m.[3] Near-surface measurements are made in 10 m height on the second mast, which is separated from the tower by a distance of 170 m to the northeast (Fig. B.1b). Figure B.1c shows the immediate surroundings of the field site with a view toward the southwest from the 280 m tower platform. For a wind direction sector of $235° \pm 30°$, the surface characteristics are suburban in combination with smaller industrial parks and patches of arable land.

(a) **(b)** **(c)**

Figure B.1: Meteorological measurement site in Hamburg-Billwerder: (a) 300 m radio transmission tower, (b) 12 m meteorological mast, (c) view toward the southwest from the 280 m platform of the radio tower.[4]

[1] Further details also available on `http://wettermast-hamburg.zmaw.de`; accessed July 27, 2012.
[2] Radio mast located at 53°31′9.0″ N 10°06′10.3″ E; meteorological mast at 53°31′11.7″ N 10°06′18.5″ E.
[3] Since mid 2010, a further sonic anemometer is installed on the 280 m platform.
[4] Figs. B.1a–c: Photo courtesy of I. Lange, Meteorological Institute, University of Hamburg.

Raw data processing

In order to derive a representative roughness length, z_0, and profile exponent, α, for the southwesterly approach flow sector, a 3-year data record was analyzed covering 2007 to 2009 (cf. Peeck, 2011). This period was selected because the instruments were operated continuously and only few discontinuities (e.g. due to hardware or software malfunctions) had impacts on the data series.

A peculiarity of the tower data, however, is the fact that the measurements are biased for approach flow wind directions ranging from the NW to the NE. Since the booms, on which the instruments are mounted, are oriented southward, the measurements are directly affected by the wake flow developing behind the 2 m-diameter mast. With a boom extent of 4 m, the instruments were located approximately 6 m away from the tower and measurements are expected to be unreliable for a wind direction sector of $0° \pm 30°$.

The measured data are routinely archived in processed form by the Meteorological Institute and are available in terms of 1 min and 5 min statistical values of the three wind components and temperature (averages and standard deviations over the respective time periods). The processed data also contained information about derived velocity and temperature quantities like the vertical momentum and heat flux, the inverse of the Monin-Obukhov length, and wind gust statistics. Starting from January 2010, raw velocity and temperature signals with temporal resolutions of 10 Hz (meteorological mast) and 20 Hz (radio tower) have been routinely archived as well, and were analyzed in the present study for the derivation of turbulence statistics. A brief overview of the main data preprocessing steps, needed to obtain the required parameters and field statistics, is given below.

Long-term data — 2007–2009 Profile and roughness parameters for the selected approach flow direction of the Hamburg wind-tunnel model (wind from 235°) were computed from the 3-year data based on 5 min averages. The main steps of the derivation of z_0 and α were already outlined in detail in Section 4.2.2. Therefore, just a brief summary of the preparatory steps is given here:

1. Filter data for an approach flow sector of $235° \pm 30°$.
2. Remove profiles that contain error values (marked by 99999 placeholders).
3. Filter data for neutral stratification using different ζ thresholds.
4. Obtain 1 h averaged velocity profiles.
5. Keep only those profiles with mean horizontal wind speeds being ≥ 1 m/s.

High-resolution data — 19 March 2010 Turbulence statistics, integral length scales, and auto-spectral energy densities were determined from high resolution sonic data. The data recordings that were available until spring 2010 featured one almost ideal test case for the analysis. On March 19, 2010, fairly strong winds (average wind speeds > 3 m/s) were recorded between 10:00 and 16:00 CET with nearly constant directions from the southwest (on average between 220° and 240°). The atmospheric stability can be classified as near-neutral, based on a time and height-averaged stability parameter of $\zeta \simeq 0.05$.

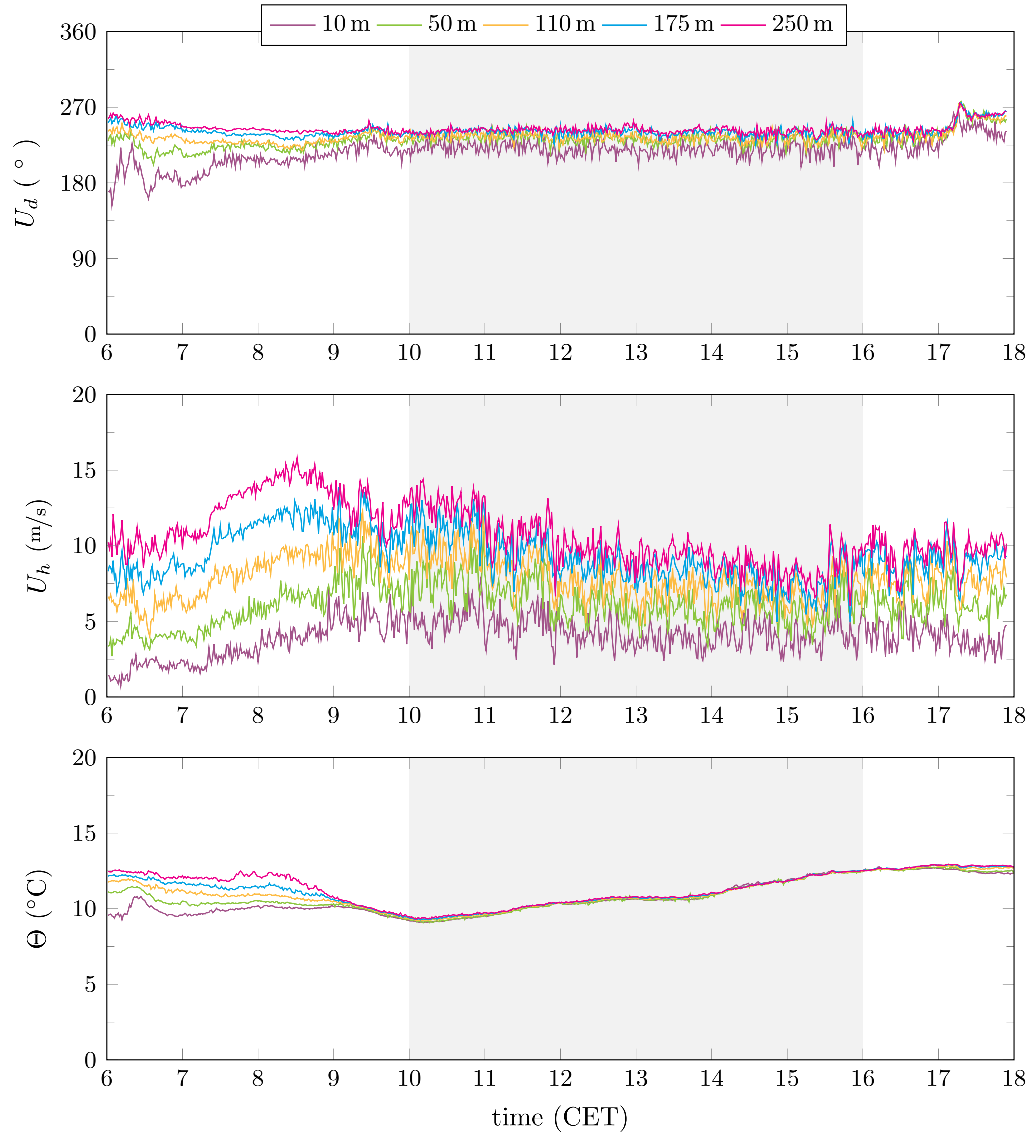

Figure B.2: Time series of horizontal wind direction U_d, wind speed U_h, and potential temperature Θ measured on March 19, 2010, from 6:00 to 18:00 CET. Shown are 1 min time averages. The gray area indicates the time period over which turbulence statistics have been determined for this study.

Figure B.2 shows time series of 1 min averages of the horizontal wind direction, U_d, wind speed, U_h, and potential temperature, Θ, for this day. The gray area marks the 6 h analysis time span. The very well-mixed state of the boundary layer for this period of time is also clearly reflected in potential temperatures that are almost constant with height.

The sonic anemometers were carefully aligned according to the meteorological wind coordinate convention, i.e. the horizontal wind components represent the *meridional* wind from the south to the north (V_{met}) and the *zonal* wind from west to east (U_{met}), respectively. In the laboratory, however, U and V correspond to the streamwise (*alongwind*) and spanwise (*crosswind*) velocity components. In order to make turbulence statistics comparable, the raw field data were first rotated into the mean horizontal wind direction, $\phi = \overline{U_d}$, obtained over consecutive data blocks of 5 min duration, so that the time average of the new lateral velocity becomes $\overline{V}_{\text{met}_1} \simeq \overline{V} \simeq 0$ (see Kaimal and Finnigan, 1994). Formally, the coordinate transformation was conducted according to

$$\begin{aligned} U_{\text{met}_1} &= U_{\text{met}} \cos\phi + V_{\text{met}} \sin\phi \quad \text{and} \\ V_{\text{met}_1} &= V_{\text{met}} \cos\phi - U_{\text{met}} \sin\phi \; . \end{aligned} \tag{B.1}$$

Systematic errors of the horizontal wind-direction values due to slight deviations from an exact north-south alignment of the sonic anemometers are expected to be in the order of 2° to 3° (I. Lange 2012, *pers. comm.*, August 1, 2012).

Profiles of the mean streamwise velocity, the vertical turbulent momentum flux, and the turbulence intensities of the three velocity components (cf. Figs. 4.11a,b and 4.12) were obtained by breaking down the 6 h data record into 72 consecutive subsamples of 5 min duration. This period represents a typical time span over which statistical estimates from meteorological field data are archived. For each of the bins, the respective statistics were computed from the raw velocity signals. The results presented in Section 4.2.2 correspond to time averages and standard deviations obtained from 72 individual values. Since the meteorological boundary conditions were nearly constant over the analyzed period of time, the data scatter represents the inherent uncertainty associated with the turbulent variability of the atmosphere.

The alongwind integral length scales, ℓ_{11}, were retrieved from velocity subsamples of a longer 30 min duration. A sufficiently long data record is necessary to obtain representative results from the calculation of the temporal autocorrelations and to subsequently derive the integral time scales, τ_{11}. On the other hand, the durations were short enough to ensure that trends in the velocities were negligible and would not affect the derivation of fluctuating quantities and resulting statistics (cf. Fig. B.2). Integral times were determined from the integration of the normalized empirical autocorrelation functions from $t_l = 0$ (zero time-lag) to t_{l_∞}, representing the time lag for which the autocorrelation dropped down to 1 % of its initial value (i.e. from 1.0 to 0.01). Length scales were determined by multiplying the integral times with the local advection velocity defined as the mean streamwise velocity over the respective 30 min time span (Taylor hypothesis, cf. Taylor, 1938). The computational procedure follows the same scheme as the processing of the wind-tunnel measurements and LES data described in Section 5.4 and explained in detail in Appendix D. At each height, 12 values of ℓ_{11} were determined, of which averages and standard errors (scatter bars) are depicted in Figure 4.13.

For the calculation of 1D auto-spectral energy densities, the entire 6 h data record in 50 m height has been used. In order to reduce the variability of the spectral estimates, however, the series was broken down into chunks of approximately 110 min (yielding a power-of-2 number of samples to be used in the FFT) and an average spectrum was obtained from the ensemble mean over the subspectra. As in the analysis of the integral length scales, a detrending algorithm was *not* applied to the subsamples. Smoothing procedures and further aspects of the spectra computation are discussed in detail in Appendix E.

Appendix C

LDA measurement principle

The measurement principle of a *laser Doppler anemometry* (LDA) system is based on the scattering of light from small tracer particles (solid or liquid), which are introduced into the flow. These seeding particles usually have diameters in the order of few microns so as to guarantee that they can follow the motion of the fluid with no slip. At the same time, the particles should be good scatterers in the visible range of the electromagnetic spectrum (*Mie scattering* regime). Due to the particles' motion, the frequency of the scattered light differs from the frequency of the incident laser light. The tracer thus acts like a moving transmitter, whose traversing through the measuring volume causes a *Doppler frequency shift* of the scattered light (cf. Albrecht et al., 2003). Continuous-wave lasers are required as light sources since they provide monochrome, coherent light, a Gaussian intensity distribution in the cross-section of the laser beam, and a low expansion of the beam's width. The scattered photons are collected by a receiver and focused on a photo detector. The receiving optics are often integrated in the same housing as the transmitting optics. This is the so-called *backscatter mode.* Fundamental physical aspects incorporated in the LDA system that was used during the wind-tunnel flow measurements are described in detail by Jensen (2004) and are summarized below.

The standard working point for most LDA systems is the *fringe mode*, i.e. the laser beam is split up into two rays. After being emitted from the probe, the beams intersect at a common point at a well-known crossing angle, γ. The interference of the beams in the intersection volume causes modulations of the laser light intensity. Parallel planes of high intensity, known as fringes, bordered by dark planes, are the characteristic interference patterns. For a given optical system, the fringe distance, δ_f, is constant throughout the measuring volume and uniquely corresponds to the wavelength of the emitted laser light, λ, and the crossing angle of the beams through the relation

$$\delta_f = \frac{\lambda}{2\,\sin\left(\gamma/2\right)}\;. \tag{C.1}$$

The fringes are orientated in such a way that they propagate perpendicular to the direction of motion in which the signal is measured, e.g. the x-axis. Whenever a seeding particle moves through the interference patterns, the intensity of the scattered light fluctuates at a frequency f_D, as the areas of constructive and destructive interference are being traversed. This frequency is directly connected to the instantaneous velocity, U, of the particle and the fringe distance. The velocity is then given by the simple relation

$$U = \delta_f\, f_D = \frac{\lambda\, f_D}{2\,\sin\left(\gamma/2\right)}\;. \tag{C.2}$$

While this procedure yields explicit information about the magnitude of the velocity, it does not yet contain *directional sensitivity*: The receiving and analyzing instruments cannot distinguish between positive and negative frequencies which would arise in the case of $U < 0$. Furthermore, zero velocity values cannot be measured (Jensen, 2004).

In the LDA system used in the Hamburg measurement campaign, the ambiguity of flow direction is overcome by the superposition of a constant frequency shift, f_0, on one of the two laser beams. The frequency shift is created by a constantly vibrating piezo crystal – the *Bragg cell*. Typically, the Bragg cell is used for both the beam splitting and the overlap of the frequency shift onto the diffracted beams. The frequency of the scattered light yields

$$f_D \simeq f_0 + \frac{2\,\sin\left(\gamma/2\right)}{\lambda}\,U\ . \tag{C.3}$$

Figuratively speaking, the frequency shift dislocates the interference pattern at a constant velocity. In the case of zero velocity of a particle, its frequency, f_D, is exactly equal to f_0. For positive velocities, $f_D > f_0$ applies. Negative velocities will cause $f_D < f_0$. Whereas the detection of positive velocities is only limited by the measurement technique, negative velocities are only measurable as long as their magnitude is above a certain threshold value that is defined by the frequency shift f_0. The direction of motion can be measured unambiguously as long as

$$U > -\frac{\lambda\, f_0}{2\,\sin\left(\gamma/2\right)}\ . \tag{C.4}$$

Figure C.1 schematically depicts the experimental setup for 1D LDA measurements of a single velocity component in backscatter and fringe mode. In order to simultaneously measure two velocity components – as in this study – two laser beams of different wavelengths are used. The intersection of the *four* (split-up) beams defines the measuring volume. The measurement of all three velocity components becomes possible by combining a 1D LDA system with a 2D system.

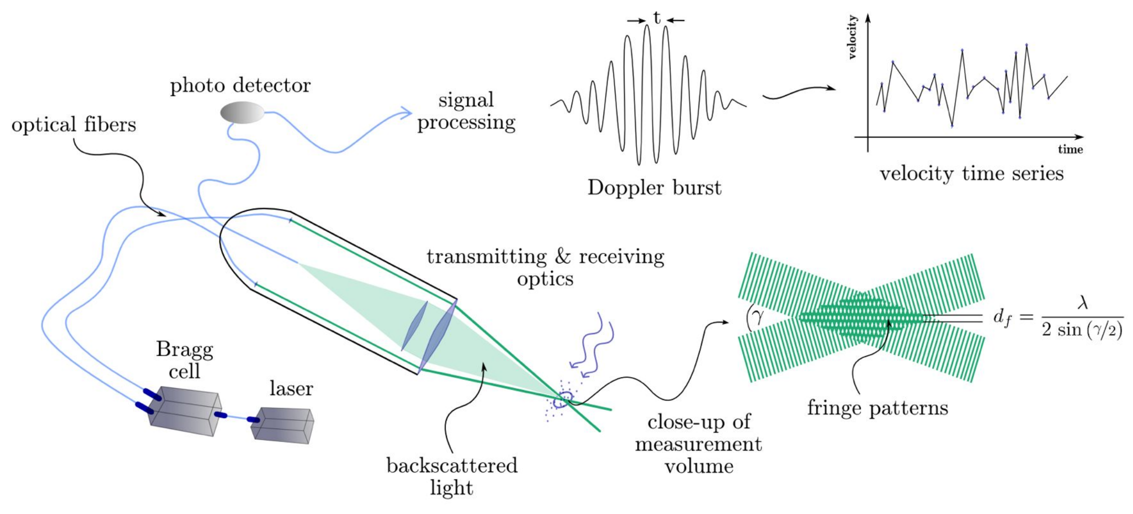

Figure C.1: Schematic of the measurement principle of a 1D LDA system operated in backscatter and fringe mode. Adapted from Jensen (2004).

Appendix D

Temporal autocorrelations – Curve fitting

This section briefly describes the computational steps of the temporal autocorrelation and integral time scale derivations, of which results are presented in Section 5.4. All calculations are conducted with `MATLAB`. The emphasis of the following paragraphs is on the curve-fitting procedure, which is implemented to consistently determine the autocorrelation time scales, τ_{ii}, from the area under the lag-dependent autocorrelation function curve, $R_{ii}(t_l)$, for all velocity components, at all direct comparison locations, and for both the experimental and the numerical time series.

The autocorrelation time scale, τ_{ii}, of the ith component of the fluctuating velocity vector is defined as the integral time scale of the empirical autocorrelation function according to Eq. (5.7) given in Section 5.4, which is reproduced here

$$\tau_{ii} = \int_{t_{l_0}}^{t_{l_\infty}} R_{ii}(t_l)\, dt_l \; . \tag{D.1}$$

In this study, the upper limit of the integral, t_{l_∞}, is defined as the time at which the magnitude of R_{ii} has dropped down to a value of 0.01 or below (i.e. reaching 1 % of the starting value, 1). After an initially strong monotone decrease, $R_{ii}(t_l)$ shows a tendency toward low-magnitude oscillations, which are caused by the random nature of turbulent fluctuations, and whose strength is coupled to the duration of the analyzed signals (cf. discussion in Section 5.4.1). Such random fluctuations of the autocorrelation curves at moderate to large time lags are evident in the experimental data as well as in the numerical simulation results. Figure D.1a shows example curves of $R_{ii}(t_l)$, with $i = 1, 2, 3$, derived from experimental velocity signals in a height of 14 m at location *BL04*. In all curves, oscillations of varying degrees are evident, which prevent a montone decrease of the functions (cf., for example, $R_{11}(t_l)$ showing a strongly elongated tail). These oscillations can be better examined when reverting to a semi-logarithmic display as illustrated in Figure D.1b. In order to determine a consistent estimate of the upper integration limit used in Eq. (D.1), smoothing the tails is inevitable.

Programming sequence The `MATLAB` code for the derivation of R_{ii} as a function of time lag, t_l, and for the subsequent calculation of τ_{ii}, as the integral parameter of the temporal autocorrelation function, completes the following process structure:

1. Load LES or *S & H*-reconstructed wind-tunnel velocity time series.
2. Derive velocity fluctuations $u'_i(t)$ from instantaneous signals $U_i(t)$.
3. Obtain normalized autocorrelation function $R_{ii}(t_l)$ using the built-in `xcorr` function and reference the results to the signal's variance.

4. Downsize the autocorrelation vector to the number of unique lags (i.e. $N/2$).
5. Use curve fitting to smooth the tails of $R_{ii}(t_l)$.
6. Derive autocorrelation time scales, τ_{ii}, by integrating R_{ii} from $t_l = 0$ to t_{l_∞}, where the latter is defined as the point at which $R_{ii}(t_{l_\infty}) \leq 0.01$.

Step **5.** is completed using a first-order polynomial fit of the logarithmized $R_{ii}(t_l)$ data in the region of moderately large time lags. As can be seen in Figure D.1b, at comparatively small time lags the auto-correlation function approximately follows a straight line when displayed on a semi-logarithmic graph. This approximate linearity will be used as a basis for the fitting, resulting in an exponential decrease of the fitted tails when converted back into a linear framework.[1] The procedure is optimized so that the largest part of the original correlation data at small to moderate time lags will be preserved and only the early *tail region* is extrapolated through the fit. The extent up to which the original values are kept is adjusted by the parameter `cut` which can be modulated depending on the shape of the correlation curves. For both, the wind-tunnel and the numerical data, `cut` was typically chosen so that the original curves are retained up to values between once to twice the *e-folding* time of R_{ii} (i.e. up to time lags for which $0.37 \leq R_{ii}(t_l) \leq 0.14$). The `MATLAB` calculation sequence for the curve fitting is as follows:

- Determine the starting point for the curve fitting from the input parameter `cut`, which typically is in the range of -1 to -2.
- Find the time lag, $t_{l_{\mathrm{cut}}}$, for which $R_{ii}(t_{l_{\mathrm{cut}}}) \leq \exp(\mathtt{cut})$.
- Use the built-in `polyfit` function for a linear fit of the logarithm of R_{ii} in the early tail region (starting from $t_{l_{\mathrm{cut}}}$) to derive the fitted curve according to $R_{ii_{\mathrm{fit}}}(t'_l) = p_1\, t'_l + p_2$, where $p_{1,2}$ are the fit parameters.
- Determine the first intersection point, $t_{l_{\mathrm{int}}}$, between $\ln(R_{ii}(t_l))$ and $R_{ii_{\mathrm{fit}}}(t'_l)$.
- Extrapolate the fitted tail curve from the intersection point to the maximum time lag.
- Concatenate the original autocorrelation function, $R_{ii}(t_l)$, and the tail fit, $\exp(R_{ii_{\mathrm{fit}}}(t'_l))$, at the intersection point, so that for $t_l < t_{l_{\mathrm{int}}}$ the original data are used and for $t_l \geq t_{l_{\mathrm{int}}}$ the extrapolated curves.

Figure D.1c shows the fit functions adjusted to the early tails of the autocorrelation curves in a semi-logarithmic display. As can be seen in the graphs, the largest deviations between the fits and the original curves occur at time lags for which the magnitudes of R_{ii} have already decreased to fairly low values. Hence, it can be anticipated that the contributions from the tail regions to the integral in Eq. (D.1) play a minor role compared with the correlation values at $t_l < t_{l_{\mathrm{int}}}$. This is important in cases where the original autocorrelation function drops below a value of 0.01 earlier than the concatenated function, which could occur in situations where the slopes of $R_{ii}(t_l)$ are extremely steep.

[1] As can be seen in Figure D.1b, not all autocorrelation curves follow distinct straight lines at small time lags. On the basis of the autocorrelation curve of the streamwise velocity fluctuation, R_{11}, for example, it can be seen that the decrease during the first 10 s is stronger than during the adjacent piece up to approximately 80 s. In order to avoid bias, only the straight part of the curve at moderate time lags is fitted. Furthermore, the original data will be preserved at small time lags.

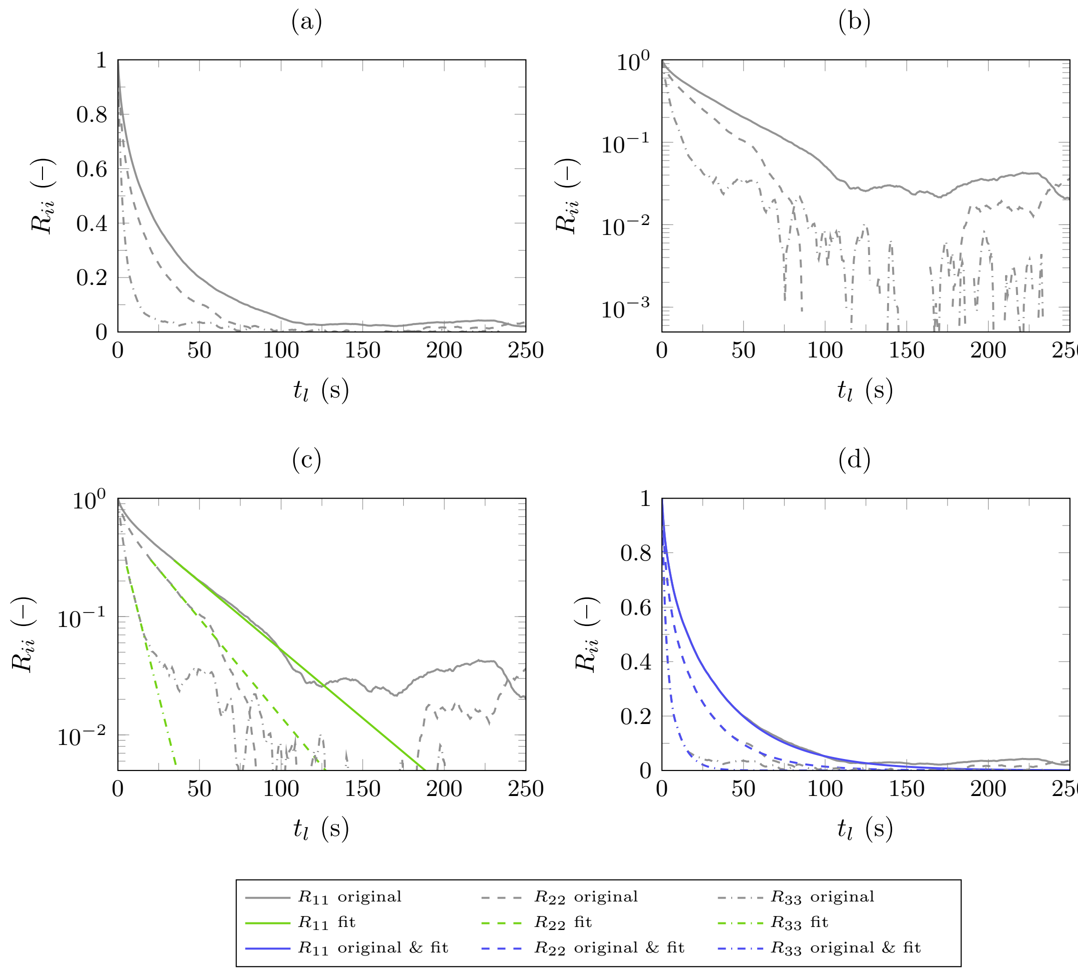

Figure D.1: Exemplification of the fitting procedure applied to the autocorrelation function tails. (a) Original autocorrelation curves of the three velocity components as functions of time lag using a linear display, (b) original curves using semi-logarithmic axes, (c) original curves together with the respective fit functions of their tails, (d) concatenated autocorrelation function using the original and fitted curves. The autocorrelation functions are derived from experimental velocity time series at a height of 14 m at location *BL04*.

Figure D.1d finally depicts the concatenated original and fitted autocorrelation values. As required, deviations to the original curves only affect the tails.

The general calculation and curve fitting procedure was also used for the numerical and experimental data in order to make the derived time scales directly comparable. For quality assurance, the experimental integral time scales of the streamwise velocity fluctuations, τ_{11}, were compared to results derived by an independent analysis software written in `C` by Fischer (2011), which uses a similar linear extrapolation procedure. This comparison revealed a very high level of quantitative agreement.

Appendix E

Calculation of velocity spectra

In the following paragraphs, details of the one-dimensional turbulence energy density spectra calculations are briefly presented. All computations are conducted in `MATLAB`. Apart from relevant theoretical background of the discrete Fourier transform, the particular computing strategies pursued in this study are introduced, and a verification of the developed code on the basis of artificial signals of known spectral content is presented in conclusion.

Relevant equations Following the *Wiener-Khinchin theorem*, the auto-spectral energy density of a square-integrable signal of finite energy (e.g. turbulent velocities) can be related to the Fourier transform of its autocorrelation function. For signals sampled at discrete time intervals, the *discrete Fourier transform* (DFT) provides a discrete representation of the signal's spectral content (Pope, 2000). Following Nobach et al. (2007), a finite time series composed of N samples of a variable $\Phi_n = \Phi(t_n = n\,\delta t_s)$ obtained at discrete time intervals δt_s over a sampling duration of $T = N\delta t_s$ can be decomposed into a *finite* sum of Fourier coefficients $\widehat{\Phi}_k$ according to

$$\widehat{\Phi}_k = \widehat{\Phi}(f_k = k\,\delta f_s) = \sum_{n=0}^{N-1} \Phi_n \exp\left(-\frac{2\pi i n k}{N}\right) , \tag{E.1}$$

with $n, k = 0, 1, \ldots, N-1$ and discrete, equally spaced frequencies

$$f_k = k\,\delta f_s = \frac{k}{N\delta t_s} = \frac{k f_s}{N} = \frac{k}{T} . \tag{E.2}$$

Here, f_s denotes the sampling frequency of the time series, which is given by $f_s = N/T$, and $\delta f_s = 1/T = f_k - f_{k-1}$ is a constant frequency increment. The energy of the signal is conserved by the Fourier transform (*Parseval's theorem*) so that

$$\sum_{n=0}^{N-1} |\Phi_n|^2 = \frac{1}{N} \sum_{k=0}^{N-1} |\widehat{\Phi}_k|^2 . \tag{E.3}$$

The transform is completely reversible and the *inverse DFT* is given by

$$\Phi_n = \Phi(t_n = n\,\delta t_s) = \frac{1}{N} \sum_{k=0}^{N-1} \widehat{\Phi}_k \exp\left(\frac{2\pi i n k}{N}\right) . \tag{E.4}$$

The *auto-spectral energy density* of the discrete signal can be estimated from its Fourier coefficients obtained from Eq. (E.1) according to

$$S_{\Phi\Phi}(f_k) = \frac{1}{N f_s} \widehat{\Phi}_k^* \widehat{\Phi}_k = \frac{1}{N f_s} |\widehat{\Phi}_k|^2 , \tag{E.5}$$

where the asterisk denotes the *complex conjugate* of the complex Fourier coefficients. It should be noted that the above expression gives spectral energies for frequencies on the interval $[0, f_s]$. This is called a *two-sided spectrum*, since for f_k greater than the *Nyquist frequency*, $f_{Ny} = f_s/2$, the energy densities $S_{\Phi\Phi}(f_k)$ are equal to those at the corresponding folded lower frequencies (Oppenheim et al., 1999; Stull, 1988; Nobach et al., 2007). Hence, usually the second half of the spectrum is folded back onto the first half to obtain unambiguous *one-sided auto-spectral energy densities* according to

$$E_{\Phi\Phi}(f_k) = \frac{2}{N f_s}\widehat{\Phi}_k^*\widehat{\Phi}_k = \frac{2}{N^2 \delta f_s}|\widehat{\Phi}_k|^2 \ , \tag{E.6}$$

where the frequency index k now runs from 0 to $N/2$, such that the maximum resolvable frequency is given by the Nyquist frequency $f_{N/2} = f_{Ny} = f_s/2$. Eq. (E.6) represents the spectral variance (or energy) of the signal per frequency bandwidth, δf_s. The multiplication with 2 ensures that no energy is lost due to the truncation of the two-sided Fourier series. Two values of $E_{\Phi\Phi}(f_k)$, however, are unique and should not be doubled. These are associated with the DC component, f_0, and the Nyquist frequency.

Alternatively, the autospectral energy densities can also be computed in wavenumber space, for wavenumbers $\kappa_k = 2\pi/\lambda_k = 2\pi f_k/c$ following

$$E_{\Phi\Phi}(\kappa_k) = \frac{2}{N^2 \delta\kappa_s}|\widehat{\Phi}_k|^2 = \frac{c}{\pi N^2 \delta f_s}|\widehat{\Phi}_k|^2 = \frac{c}{2\pi}E_{\Phi\Phi}(f_k) \ , \tag{E.7}$$

with $k = 0, 1, \ldots, N/2$, the wavenumber increment $\delta\kappa_s = 2\pi\,\delta f_s/c$, wavelength λ_k, and phase speed c. In particular, this means that the frequency and wavenumber spectra are related through $\kappa_k E_{\Phi\Phi}(\kappa_k) = f_k E_{\Phi\Phi}(f_k)$. For turbulent velocity signals, a mean local advection velocity $\overline{U}_a$ can be used to represent the phase speed assuming *frozen turbulence* conditions (Taylor's hypothesis; cf. Taylor, 1938).

For a set of paired, discrete signals Φ_n and Ψ_n, their auto-spectral energy densities can be combined to retrieve information about their amplitude and phase relations as a function of frequency. The so-called *cross spectrum* of the signals is given by

$$E_{\Phi\Psi}(f_k) = \frac{2}{N^2 \delta f_s}\widehat{\Phi}_k^*\widehat{\Psi}_k \ , \tag{E.8}$$

where the Fourier coefficients are obtained from Eq. (E.1) for each of the signals. In the atmospheric sciences, it is common practice to decompose the cross spectrum $E_{\Phi\Psi}(f_k)$ into its real and imaginary part according to $E_{\Phi\Psi}(f_k) = \mathrm{Co}_{\Phi\Psi}(f_k) - i\mathrm{Q}_{\Phi\Psi}$ (Stull, 1988), where the *co-spectrum*, $\mathrm{Co}_{\Phi\Psi}$, and the *quadrature spectrum*, $\mathrm{Q}_{\Phi\Psi}$, are defined as

$$\mathrm{Co}_{\Phi\Psi}(f_k) = \mathrm{Re}\{\widehat{\Phi}_k\}\mathrm{Re}\{\widehat{\Psi}_k\} + \mathrm{Im}\{\widehat{\Phi}_k\}\mathrm{Im}\{\widehat{\Psi}_k\} \tag{E.9}$$

and

$$\mathrm{Q}_{\Phi\Psi}(f_k) = \mathrm{Im}\{\widehat{\Phi}_k\}\mathrm{Re}\{\widehat{\Psi}_k\} - \mathrm{Re}\{\widehat{\Phi}_k\}\mathrm{Im}\{\widehat{\Psi}_k\} \ . \tag{E.10}$$

The co-spectrum (sometimes also referred to as *coincident spectral density*; Kaiser and Fedorovich, 1998) is of particular interest for the analysis of turbulence, since it is directly related to the *covariance* between the variables Φ and Ψ through $\sum_k \mathrm{Co}_k = \overline{\Phi\Psi}$ (for example yielding the vertical turbulent momentum flux $\overline{u'w'}$). Furthermore, a normalized amplitude spectrum, the so-called *spectral coherence*, $\mathrm{Coh}_{\Phi\Psi}$, can be constructed via

$$\mathrm{Coh}^2_{\Phi\Psi}(f_k) = \frac{\mathrm{Q}^2_{\Phi\Psi}(f_k) \, + \, \mathrm{Co}^2_{\Phi\Psi}(f_k)}{E_{\Phi\Phi}(f_k)\, E_{\Psi\Psi}(f_k)} \,, \tag{E.11}$$

which yields a real number bounded on the interval $[0, 1]$ that can be interpreted as a frequency-dependent correlation coefficient between both signals (Stull, 1988).

In order to obtain the DFT from Eq. (E.1), a recursive algorithm known as *fast Fourier transform* (FFT) is usually employed when dealing with large data sets in order to save computational time. For this study, `MATLAB`'s built-in function `fft` was used to compute the Fourier coefficients of the velocity signals. This FFT function is based on the so-called *Cooley-Tukey algorithm* (Cooley and Tukey, 1965), which requires that the number of samples in the time series is given as a power of two, i.e. $N = 2^m$ with $m \in \mathbb{N}_0$.

In boundary-layer meteorology, energy density spectra are usually obtained from single-point time series and displayed in frequency space, omitting the use of Taylor's hypothesis for a wavenumber space conversion. A variety of approaches for the graphical representation of turbulence spectra can be used (see detailed overview in Stull, 1988). In order to determine spectral peak frequencies more readily while not cutting off information in the high frequency range, the quantity $f_k\, E_{\Phi\Phi}$ can be plotted against a *logarithmic* frequency axis. An interesting quality of this representation is that the area under the spectral curve for any arbitrary frequency bandwidth δf_k is directly proportional to the variance of the signal associated with this frequency range. More commonly, however, a *double-logarithmic* display is employed to investigate the existence of a power-law behavior in the inertial subrange (apparent as a straight line in a log-log graph). Due to the multiplication of the energy densities with the frequency vector, the characteristic $f_k^{-5/3}$ slope within the inertial subrange is modified into a $f_k^{-2/3}$ slope.

Spectral smoothing The energy density spectra obtained from velocity time series usually exhibit strong variability, particularly in the high frequency range. When using a double-logarithmic representation, the layout of the raw spectra tends to be especially "noisy" and can severely hamper further analyses like the derivation of frequency ranges associated with the integral scale eddies (spectral peaks), the investigation of the power-law behavior in the inertial subrange, or the direct comparison of two spectra in a single plot (e.g. experimental and numerical velocity spectra, as in this study). Hence, smoothing methods are routinely applied to post-process the raw spectra. This study follows Kaiser and Fedorovich (1998) who used a two-step smoothing procedure that is frequently applied in micro-meteorological turbulence studies. In a first step, the original time series is divided into subsamples of equal length that are still long enough to cover the low-frequency variability for a reliable estimate of the spectral energy of the largest and integral scale eddies in the flow. From each of these subsamples, energy spectra are computed and the first smoothed version of the spectrum is obtained from an ensemble average over all subspectra. The number of subsamples needs to be specified in the `MATLAB` code (parameter `nsub`) and should be a power of 2 to permit using the FFT. Besides the smoothing effect, subspectra averaging has a further impact on the averaged spectrum: Since the lowest resolvable frequency directly depends on the length of the time series, the division into subsamples inevitably results in a loss of low-frequency spectral content. The value of `nsub`, thus, should be carefully adjusted to the specific flow problem and attuned to the sample characteristics of the original signal. Since the number of subsamples should not be too large, spectral averaging alone is usually not sufficient to improve the spectral layout. In a second smoothing step, the mean spectrum is averaged over exponentially increasing frequency increments (i.e. over equal intervals with respect to the logarithm of frequency, see Kaimal and Finnigan, 1994). Since the energy densities in the low-frequency range are associated with comparatively rare events, the frequency averaging is implemented so that these are not smoothed. The degree of smoothing can be adjusted in the code by specifying the starting value of the frequency bin size (parameter `incr`). A decreasing value of `incr` will lead to a corresponding delay in the beginnings of the averaging process in terms of frequencies and in extension of the unaltered low-frequency range.

Figure E.1 illustrates the smoothing steps on the basis of an 1D energy density spectrum of the streamwise velocity determined from wind-tunnel LDA measurements. In this example, the raw spectrum was computed from a time series with $N = 2^{16}$ samples ($T \simeq 16.5\,\mathrm{h}$ full scale). The spectral averaging was conducted over an ensemble of `nsub` $= 8$ subspectra, so that $N_{\mathrm{sub}} = 2^{13}$ and $T_{\mathrm{sub}} \simeq 2\,\mathrm{h}$. The parameter `incr` was set to 0.05 and determined the starting value for the frequency averaging. As can be seen in the graphs, about one decade of low-frequency content is lost due to the subsample division but a large fraction of the energy densities prior to the spectral peak is still resolved. Finally, the additional frequency averaging allows to identify power-law behavior in the inertial subrange, while in the low-frequency range the original values of the first smoothing step are kept. A detailed verification of the smoothing procedure will be presented in one of the next sections.

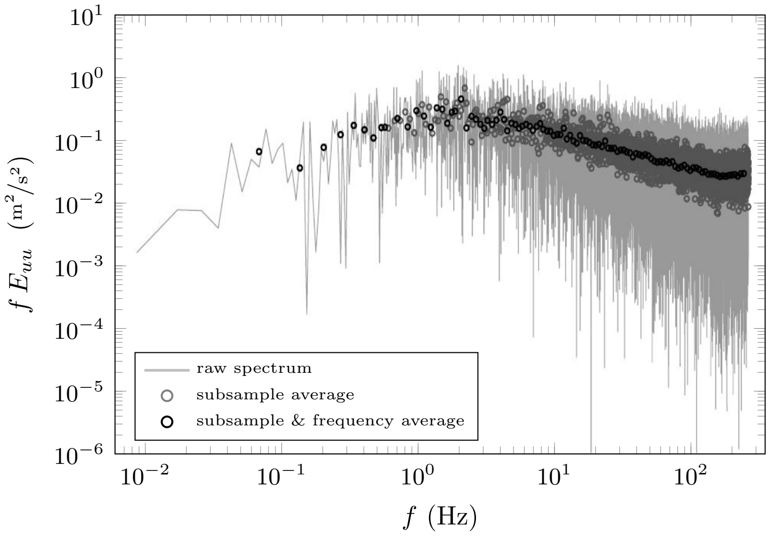

Figure E.1: 1D energy density spectrum of the streamwise velocity in its raw appearance and after applying subsample and frequency averaging.

Aliasing & end effects Two features of the DFT of finite-time, finite-resolution signals have to be taken into account during the analysis (cf. Stull, 1988; Nobach et al., 2007). One is the so-called *aliasing effect* connected to the finite values of δf_s and $f_{\max}$. If the process being sampled contains frequencies higher than the sampling frequency of the signal, the corresponding energy is folded back into the neighboring lower frequencies. Aliasing can falsify the spectral shape at the high-frequency end just below the Nyquist frequency by causing a deceiving increase of the energy densities. This effect is also recognizable in the spectra shown in Figure E.1 and remains unaffected by the smoothing method. In general, it is not possible to remove frequencies resulting in aliasing from the sampled time series in a *digital* post-processing step. During the sampling process, however, *analog* anti-aliasing procedures can be employed as low-pass filters to remove frequencies larger than f_{Ny}. In the case of this study, analog filtering is not conducted and the velocity spectra have to be inspected for aliasing at the highest resolved frequencies on a case-by-case basis. Since the raw LDA time series have been *reconstructed* for an equidistant time-step using a sample-and-hold algorithm, aliasing effects are expected to be slightly enhanced due to the additive step-noise (cf. Adrian and Yao, 1987).

The second effect is related to the finite duration of the signals. Since the Fourier transform uses ever-oscillating sinusoids as basis functions, a periodicity of the sampled signal is implicitly assumed (Stull, 1988). In atmospheric turbulence, however, such infinite oscillations never occur, and the beginning and end of measured signals are marked by sudden amplitude jumps. These sharp edges can cause the so-called *leakage* of spectral energy into non-physical frequency components. Such *end effects* can be reduced by applying window functions that smooth the edges by tapering the signal to zero. For long signal durations compared with the lowest physically relevant frequencies, end effects are negligible and, therefore, data were not conditioned in this study.

Spectral scaling In order to determine universal behavior and to make spectra of different data sets comparable, energy densities and associated frequencies are usually scaled in boundary-layer meteorology. When dealing with velocity signals, U_i, the spectral energy is derived from the (mean-free) fluctuating components, u_i'. This yields fE_{ii}, which has the same physical unit as the variance of the signal. Hence, the spectral energy can be scaled by the respective *local* values of σ_i^2 of the ith velocity component. Another common scaling approach in micro-meteorology is the use of the friction velocity, u_*^2, for all velocity components. Since a representative value for u_* is not well-defined for flow in the *urban canopy layer*, this study uses the first scaling method. In boundary-layer meteorology, frequencies are typically scaled by the measurement height, z, and the local mean advection velocity in terms of the averaged streamwise component, $\overline{U}$, yielding

$$f_k^\star = \frac{f_k\, z}{\overline{U}} \; . \tag{E.12}$$

The scaled auto-spectral energy densities and co-spectra, on the other hand, are given by

$$E_{uu}^\star(f_k) = \frac{f_k\, E_{uu}(f_k)}{\sigma_u^2} \;; \quad E_{vv}^\star(f_k) = \frac{f_k\, E_{vv}(f_k)}{\sigma_v^2} \;; \quad E_{ww}^\star(f_k) = \frac{f_k\, E_{ww}(f_k)}{\sigma_w^2} \;, \tag{E.13}$$

and

$$\mathrm{Co}^{\star}_{uw}(f_k) = \frac{f_k\,\mathrm{Co}_{uw}(f_k)}{\sigma_u\,\sigma_w}\,. \tag{E.14}$$

Programming sequence The `MATLAB` code developed for the calculation of one-dimensional *auto-spectral energy densities*, E_{uu}, E_{vv}, and E_{ww}, from LDA velocity time series completes the following process structure:

1. Load *S & H* reconstructed LDA velocity time series.
2. Derive velocity fluctuations, $u_i'(t)$, from instantaneous velocity signals, $U_i(t)$.
3. Downsize the samples in the time series to the next power of 2.
4. Obtain Fourier coefficients, $\hat{u}_i$, by using the built-in `fft` function.
5. Use Eq. (E.6) to derive one-sided spectral energy densities.
6. Divide energy densities associated with the DC and Nyquist frequency by 2.
7. Smooth spectra over the specified number of subsamples (`nsub`).
8. Smooth spectra over increasing frequency bins (`incr`).
9. Scale derived quantities according to Eqs. (E.12) and (E.13).
10. Compute reference spectra following Kaimal et al. (1972) and Simiu and Scanlan (1986).

In order to compute *co-spectra* between the streamwise and vertical velocity fluctuations, Co_{uw}, paired LDA velocity time series from measurements in *U*-*W* mode were analyzed with a separate code. The program structure is as follows:

1. Complete step 1. to 6. of the auto-spectral energy density analysis for both signals.
2. Obtain the co-spectrum according to Eq. (E.9).
3. Smooth spectra over the specified number of subsamples (`nsub`).
4. Smooth spectra over increasing frequency bins (`incr`).
5. Scale co-spectra according to Eqs. (E.12) and (E.14).

The analysis of the velocity data predicted by the LES code FAST3D-CT was conducted in the same way as for the wind-tunnel data described above. Since the duration of the numerical signals was shorter by a factor of 2.5, the number of subsamples specified for the spectral averaging was at least lower by a factor of 2 compared with the respective experimental reference measurements.

Reference spectra

Different empirical power-law functions were proposed in literature for the approximation of turbulence spectra in the atmospheric surface layer. Two well-established formulations were presented by Kaimal et al. (1972) and Simiu and Scanlan (1986), based on the comprehensive analysis of field and laboratory data. While the Kaimal et al. spectra are better known to the micro-meteorological community, the Simiu & Scanlan functions originated from a wind engineering background. It is important to note that both formulations were derived for the case of neutrally stratified, stationary flow over horizontally homogeneous (rural) terrain. Hence, in this study comparisons with the empirical reference spectra are restricted to the wind-tunnel approach flow and the field data measured in Billwerder. The original equations for the scaled 1D auto-spectral energy densities with respect to the friction velocity, u_*^2, are:

Kaimal et al. (1972) – original:

$$\frac{f\,E_{uu}}{u_*^2} = \frac{105 f^\star}{(1+33f^\star)^{5/3}}\ ; \quad \frac{f\,E_{vv}}{u_*^2} = \frac{17 f^\star}{(1+9.5f^\star)^{5/3}}\ ; \quad \frac{f\,E_{ww}}{u_*^2} = \frac{2 f^\star}{\left(1+5.3f^{\star 5/3}\right)}\ . \tag{E.15}$$

Simiu and Scanlan (1986) – original:

$$\frac{f\,E_{uu}}{u_*^2} = \frac{200 f^\star}{(1+50f^\star)^{5/3}}\ ; \quad \frac{f\,E_{vv}}{u_*^2} = \frac{15 f^\star}{(1+9.5f^\star)^{5/3}}\ ; \quad \frac{f\,E_{ww}}{u_*^2} = \frac{3.36 f^\star}{\left(1+10f^{\star 5/3}\right)}\ . \tag{E.16}$$

Here, $f^\star$ denotes the scaled frequency vector derived from Eq. (E.12). The dependency of the curves on the measurement height, z, and the local mean advection velocity of the signal, thus, is included in these functions. The difference between both reference spectra is subtle and mostly concerns the low-frequency range. In this thesis, the reference spectra were transformed into an the alternative scaling form using the *local* velocity variance, σ_i^2, of the ith velocity component for the normalization of the energy densities (e.g. VDI, 2000). The original functions were converted by using empirical relationships between the friction velocity and the root-mean-square velocities reported in the survey by Counihan (1975) for similar boundary conditions: $\sigma_u/u_* \simeq 2.5$, $\sigma_v/u_* \simeq 1.875$, and $\sigma_w/u_* \simeq 1.25$. The modified reference functions, thus, are:

Kaimal et al. (1972) – modified:

$$\frac{f\,E_{uu}}{\sigma_u^2} = \frac{16.8 f^\star}{(1+33f^\star)^{5/3}}\ ; \quad \frac{f\,E_{vv}}{\sigma_v^2} = \frac{4.8 f^\star}{(1+9.5f^\star)^{5/3}}\ ; \quad \frac{f\,E_{ww}}{\sigma_w^2} = \frac{1.3 f^\star}{\left(1+5.3f^{\star 5/3}\right)}\ . \tag{E.17}$$

Simiu and Scanlan (1986) – modified:

$$\frac{f\,E_{uu}}{\sigma_u^2} = \frac{32 f^\star}{(1+50f^\star)^{5/3}}\ ; \quad \frac{f\,E_{vv}}{\sigma_v^2} = \frac{4.3 f^\star}{(1+9.5f^\star)^{5/3}}\ ; \quad \frac{f\,E_{ww}}{\sigma_w^2} = \frac{2.2 f^\star}{\left(1+10f^{\star 5/3}\right)}\ . \tag{E.18}$$

Code verification

In the following, the adequate functionality and reliability of the `MATLAB` code written for the spectral analysis is verified on the basis of generic test signals of known frequency content and spectral behavior. It is differentiated between the general performance of the code in terms of the spectral analysis and the smoothing algorithms that are employed to improve the appearance of the spectral curves in a log-log display.

Test of spectral analysis method The reliability of the code is tested on the basis of three artificial signals for which the results of a spectral analysis are *a priori* known. These signals are:

1. A periodic function composed of three sinusoids with different periods:

$$\Phi_1(t) = \sin(2\pi f_1 t) + \sin(2\pi f_2 t) + \sin(2\pi f_3 t) \ , \tag{E.19}$$

   with $f_1 = 16^{-1}$, $f_2 = 32^{-1}$, and $f_3 = 128^{-1}$.

2. A single realization of a Gaussian white noise process:

$$\Phi_2(t) = \varepsilon_g(t) \ , \tag{E.20}$$

   with a mean value of 0 and a variance of 1.

3. A single realization of a first order autoregressive process, $AR(1)$:

$$\Phi_3(t) = \varphi_1 \, \Phi_3(t-1) + \varepsilon_w(t) + c \ , \tag{E.21}$$

   with $\varphi_1 = 0.95$, ε_w being additive white noise of zero mean, and $c = 0$.

For each signal was $N = 2^{10}$ and $\delta t_s = 1\,\mathrm{s}$. The white noise processes were derived from the built-in `MATLAB` functions `randn` (Gaussian white noise) and `rand`, which generate *pseudo-random* numbers. For each of the signals, a certain spectral behavior is anticipated. The sine-wave function should result in a spectrum with three discrete peaks of equal amplitude corresponding to the input frequencies f_1, f_2, and f_3. For the Gaussian white noise process, the spectral variance should be more or less equally distributed among all frequencies. For the $AR(1)$ process, the spectral variance is known analytically and given by the function

$$E_{\Phi_3\Phi_3}(f) = \frac{\sigma^2_{\varepsilon_w}}{1 + \varphi_1 - 2\varphi_1 \cos(2\pi f)} \ , \tag{E.22}$$

where $\sigma^2_{\varepsilon_w}$ is the variance of the additive white noise.
Figure E.2 shows signals and spectral results obtained with the `MATLAB` code.

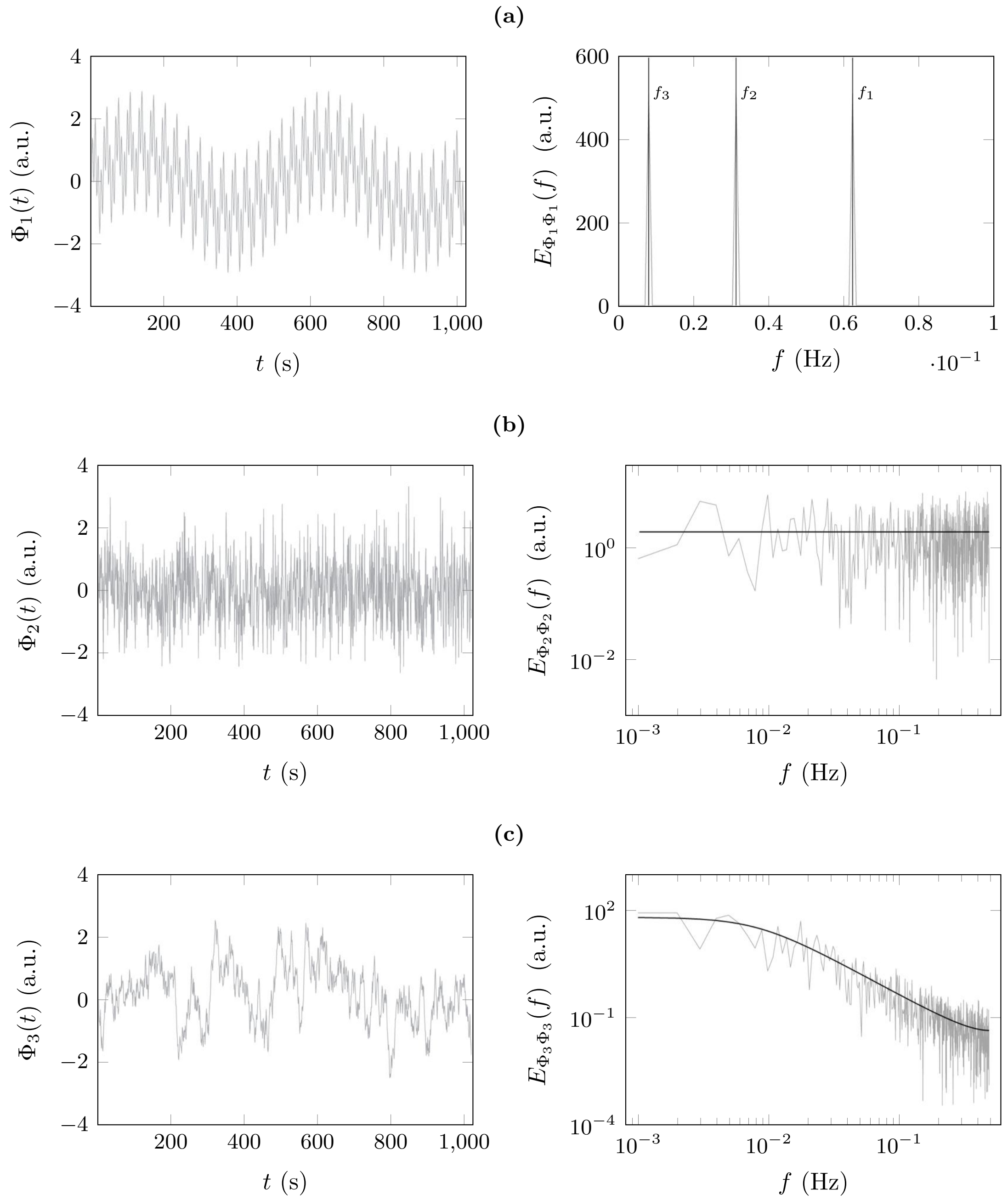

Figure E.2: Test signals, $\Phi_i(t)$, (*left*) and their auto-spectral energy densities, $E_{\Phi_i\Phi_i}(f)$, (*right*) obtained from the `MATLAB` analysis code for (a) overlapping sinusoidal waves with three different frequencies, (b) a realization of a Gaussian white noise, (c) a realization of a first-order autoregressive process. The thick black lines indicate the expected spectral behavior.

For all test functions, the energy density spectra show the expected shape. In the spectrum of the sine-wave signal (Fig. E.2a), a slight spectral leakage around the peak frequencies is recognizable as a broadening of the curves. As discussed above, this feature is caused by end effects and the use of exact harmonics in the Fourier transform. Both the Gaussian white noise and the $AR(1)$ process show the anticipated behavior in frequency space, with random contributions for each frequency increment characterizing $E_{\Phi_2\Phi_2}$ and a power-law behavior at high frequencies for $E_{\Phi_3\Phi_3}$. The seemingly enhanced amplitude variability of the spectra at high frequencies is an optical byproduct of the log-log representation. Hence, if a double-logarithmic display is desired, spectral smoothing should be employed.

Test of smoothing methods Next, the performance of the two smoothing methods – spectral ensemble averaging and frequency averaging – is tested to evaluate the potential and reliability of both approaches. The test signal is a realization of an $AR(1)$ process (cf. Eq. E.21) with $N = 2^{15}$ samples (comparable to a typical wind-tunnel velocity sample size) separated by $\delta t_s = 1\,\mathrm{s}$. The auto-regressive process has been chosen as the test case, since, similarly to turbulence spectra, it exhibits a characteristic energy roll-off at high frequencies, and its spectral shape can be analytically derived and used as a basis for the comparison. Figure E.3 depicts smoothed energy-density spectra using a double-logarithmic representation after applying spectral averaging over different ensemble sizes.

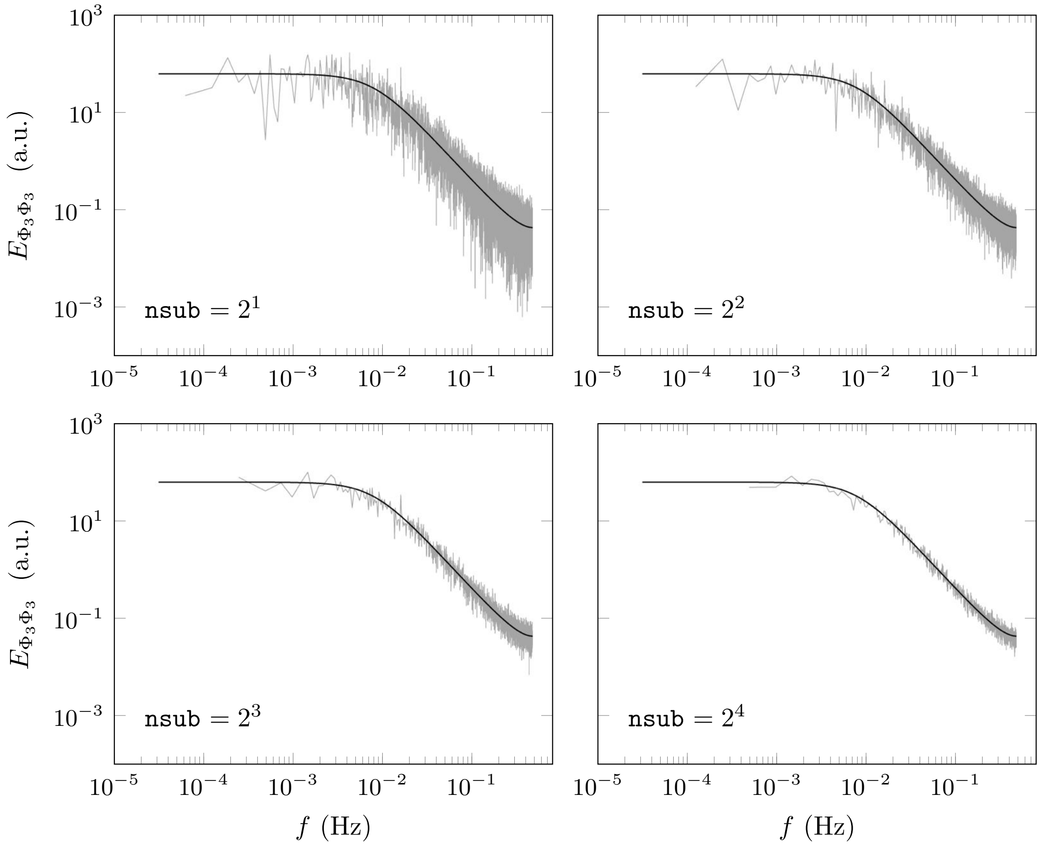

Figure E.3: Ensemble-averaged energy-density spectrum of an $AR(1)$ process for an increasing ensemble size specified by the subsample number, `nsub`. The thick black lines represent the analytic reference spectrum of the process.

By increasing the value of `nsub`, the original signal is decomposed into a larger number of shorter subsamples and the smoothing caused by the spectral ensemble averaging becomes more effective. Evidently, the increasing degree of smoothing does not affect the very good agreement of the numerically determined spectra with the analytical reference curves. As discussed above, a crucial drawback of a large number of subsamples, however, is the successive loss of low-frequency information in the resulting mean spectra.

Next, the frequency-averaging procedure was tested on the ensemble-averaged spectrum with `nsub=2` for increasing sizes of the starting bandwidth, `incr`. Figure E.4 displays the results. As `incr` grows, the degree of smoothing increases and successively affects a wider range of the spectrum ("moving" to lower frequencies). As demanded from the code, energy densities at the lowest frequencies remain unchanged at all smoothing levels. The very good congruence with the analytic target function endures up to the final collapse of both curves in the high-frequency range for the largest averaging increment.

The above tests verify the validity of the `MATLAB` script. Since its development, the code has been used by the author and other researchers to analyze different data sets (LDA, sonic anemometers, hot-wires, numerical predictions) and was successfully compared to an independently developed `C` algorithm (Fischer, 2011), which further confirmed its stability.

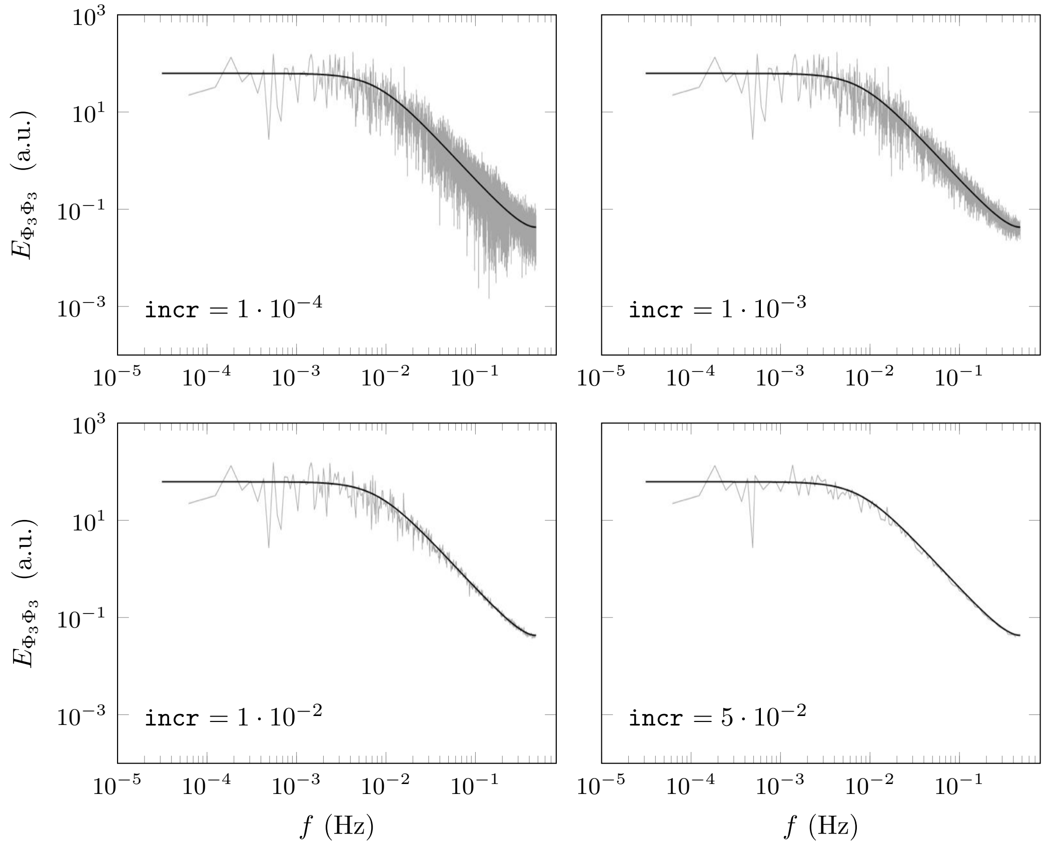

Figure E.4: Frequency smoothing of an ensemble-averaged $AR(1)$ energy-density spectrum with `nsub` $= 2$ (cf. Fig. E.3) for an increasing averaging bandwidth, `incr`. The thick black lines represent the analytic reference spectrum of the process.

Appendix F

Wavelet transforms – Additions to theory & computation

Information about resolution aspects of the wavelet transform as well as a detailed descriptions of computational procedures used in the validation study are presented in the following paragraphs as additions to the discussions in Section 5.7. In conclusion, the `MATLAB` code written for the velocity data analysis is verified against artificial test signals of known spectral content and temporal behavior.

Time-frequency resolution aspects

Compliant with Heisenberg's *uncertainty principle*,[1] it is impossible to simultaneously localize a signal in time *and* frequency (Fourier) space. The better localized a signal is in physical space, the wider is its Fourier transform spread out in spectral space as a function of frequency (Hubbard, 1998). The uncertainty principle, thus, naturally puts a limit to the amount of information that can be derived from a signal – or, more precisely, to the *certainty* or localization of the retrieved information. This concept can be directly transferred to the continuous wavelet transform in order to illustrate the resolution potential of the method in the time-frequency plane. The spread of the squared magnitude of the wavelet function $|\psi_{s,n}(t)|^2$ can be measured by its standard deviation, σ_t, in the time domain and by σ_f in the frequency domain as the standard deviation of the energy densities, $|\hat{\psi}_{s,n}(f)|^2$ (Addison, 2002). From the uncertainty principle it follows that

$$\sigma_t \, \sigma_f \geq \frac{1}{4\pi} \, . \tag{F.1}$$

Increasing the resolution in the time or frequency domain by lowering σ_t or σ_f, thus, will cause the other variance measure to increase. The resolution properties can be visualized in terms of so-called *Heisenberg boxes* in the joint time-frequency domain for which the surface areas are bounded through Eq. (F.1), i.e. by the heights and lengths of the boxes, σ_f and σ_t, respectively. Figure F.1 depicts idealized Heisenberg boxes for the classic Fourier transform (Fig. F.1a) and the continuous wavelet transform (Fig. F.1b) using dyadic increments for the wavelet's scale. The classic Fourier analysis of a signal represents an extreme case of the interplay between σ_t and σ_f, yielding high resolution in frequency space at the cost of temporal localization (distinct spectral peaks versus not localized sinusoidal functions in physical space).

A main advantage of the wavelet transform in comparison to other representatives of joint time-frequency analysis methods, notably the *short-time Fourier transform*, is the variable resolution in time and frequency that is coupled to the scale of the wavelet.

[1]Better known as *Gabor limit* or *Fourier's uncertainty principle* in the context of signal processing.

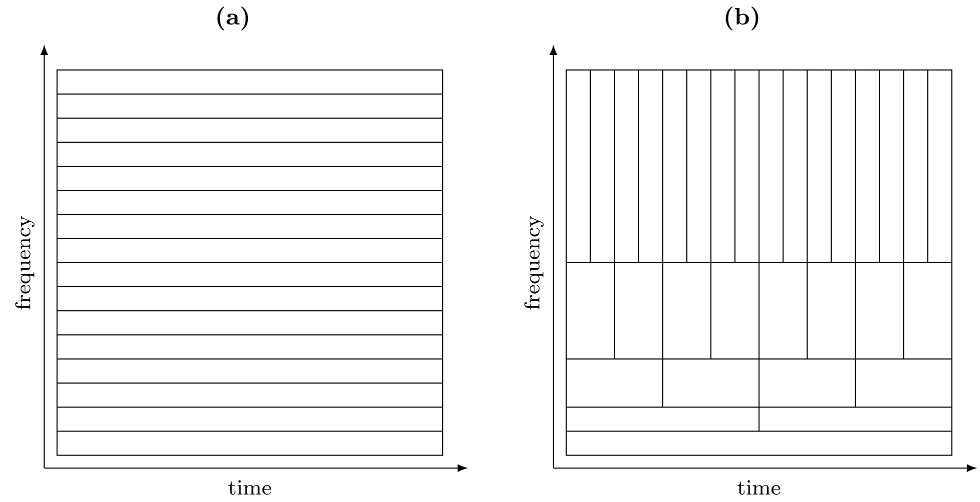

Figure F.1: Idealized Heisenberg frames in the time-frequency plane for (a) a classic harmonic analysis with the Fourier transform and (b) for the continuous wavelet transform with dyadic scale increments. Adapted from Hubbard (1998).

As can be seen in Figure F.1b, at low frequencies (strongly elongated wavelets), the time resolution is poor and the spectral information is basically spread among all coefficients at that scale (horizontally elongated Heisenberg boxes). As the wavelet is compressed, high-frequency portions of the signal become visible. However, since the temporal spread, σ_t, of the wavelet is decreasing, its frequency spread measured by σ_f is increasing, causing a poorer resolution of the high frequency portions of the signal for the benefit of a more accurate temporal localization (vertically elongated Heisenberg boxes).

Discrete computation in spectral space

For the analyses presented in Section 5.7, a *discretized* version of the continuous wavelet transform is applied to the discretely sampled experimental and numerical data. For efficiency reasons, the discrete CWT computation can be shifted into spectral space using an effective FFT algorithm and exploiting the *convolution theorem*. The procedure follows the recommendations and detailed instructions given by Torrence and Compo (1998). Essential steps are presented in the following paragraphs (further details can be found, for example, in Meyers et al., 1993; Kaiser, 1994; Addison, 2002)

In order to conduct the CWT in spectral space, the wavelet as a function of scale and translation, $\psi_{n,s}(t)$, has to be transferred into spectral space. The Fourier transform of the wavelet is given by

$$\hat{\psi}_{s,n}(f) = \int\limits_{-\infty}^{\infty} \frac{1}{\sqrt{s}}\, \psi\left(\frac{t-n}{s}\right) \exp(-2\pi i f t)\; dt \;, \tag{F.2}$$

which can be simplified (Addison, 2002) to

$$\hat{\psi}_{s,n}(f) = \sqrt{s}\,\hat{\psi}(sf)\,\exp(-2\pi i f n)\;, \tag{F.3}$$

where the Fourier transform of the wavelet, $\hat{\psi}$, is usually given by an analytical expression (cf. Eqs. 5.26 or 5.28, for the analytical Fourier representations of the Mexican-hat and Morlet wavelet functions, respectively). The CWT (Eq. 5.24) can be alternatively performed through a convolution of the spectral representations of the analyzed signal, $\Phi(t)$, and the wavelet, $\psi(t)$, in terms of their Fourier transforms, $\widehat{\Phi}(f)$ and $\hat{\psi}(f)$, according to

$$W_n(s) = \frac{1}{\sqrt{s}} \int_{-\infty}^{\infty} \widehat{\Phi}(f)\,\hat{\psi}^*(sf)\,\exp(2\pi i f n)\,df\;, \tag{F.4}$$

where the asterisk denotes the complex conjugate. For the analysis of a discrete signal $\Phi_n = \Phi(t_n = n\,\delta t_s)$ obtained at time intervals δt_s over a sampling duration of $T = N\delta t_s$, where N is the number of samples and $n = 0, \ldots, N-1$, Eq. (F.4) is employed in a discretized form. Following Torrence and Compo (1998), the *discrete-time* continuous wavelet transform is given by

$$W_n(s) = \sqrt{\frac{2\pi s}{\delta t_s}} \sum_{k=0}^{N-1} \widehat{\Phi}_k\,\hat{\psi}^*(s\omega_k)\,\exp(i\omega_k n \delta t_s)\;, \tag{F.5}$$

where the frequency index k runs from 0 to $N-1$ and $\omega = 2\pi f$ is the angular frequency. The term preceding the the sum is a normalization factor connected to the spectral representation of the wavelet. It is used to ensure that the wavelet functions have unit energy at each scale. Based on recommendations by Torrence and Compo (1998), the angular frequency vector ω_k is defined in the following way

$$\omega_k = \begin{cases} 2\pi k/(N\delta t_s) & \text{for } k \le N/2 \\ -2\pi(N-k)/(N\delta t_s) & \text{for } k > N/2\;. \end{cases} \tag{F.6}$$

From a computational point of view, Eq. (F.5) can be implemented by simultaneously obtaining the inverse Fourier transform of the product of $\widehat{\Phi}_k$ and $\hat{\psi}^*(s\omega_k)$ for all defined scales at all translations n. This procedure is applied in this study by using an FFT algorithm (Cooley and Tukey, 1965), which requires that the number of samples in the signal, N, is given by a power of 2. Furthermore, a scale vector has to be defined on the basis of which the frequency content of the signal can be evaluated. Again, it is followed Torrence and Compo (1998) and the series of scales, s_j, is obtained as a fractional power of 2 according to $s_j = s_0\,2^{j\,\delta j}$, where s_0 is the starting value corresponding to the smallest scale, δj is the spacing between scales and $j = 0, \ldots, J$, where J is the total number of scales given by

$$J = \frac{1}{\delta j}\,\log_2\left(\frac{N\,\delta t_s}{s_0}\right)\;. \tag{F.7}$$

For the results presented in Section 5.7.1, s_0 was set to $1\delta t_s$ and δj to $1/8$.

Code verification

In the following, the performance of the CWT analysis code written in MATLAB for the validation study is evaluated by applying the transform algorithm to four artificial signals of known frequency content and known time dependency. These signals are:

1. A periodic function, $\Phi_1(t)$, composed of a sinusoidal wave with a period of 128 s that is first superimposed for one cycle by a sinusoid with a period of 32 s, followed by a second sinusoid with a period of 16 s, overlapping for half a cycle.
2. A chirp signal given by a sinusoidal function whose frequency is continuously increasing from a starting value of $f_0 = 0$ to the end point at which $f_1 = 64^{-1}$ according to

$$\Phi_2(t) = \sin(2\pi f_{\mathrm{chirp}} t) \; , \tag{F.8}$$

   with $f_{\mathrm{chirp}} = (f_1 - f_0)/N$, and N is the sample size.
3. A signal, $\Phi_3(t)$, that consists only of a single peak at one instant in time (*Dirac spike*).
4. A single realization of a Gaussian white noise process:

$$\Phi_4(t) = \varepsilon_g(t) \; , \tag{F.9}$$

   with a mean value of 0 and a variance of 1.

For each signal was $N = 2^{10}$ and $\delta t_s = 1\,\mathrm{s}$. The Gaussian white noise has been derived from the built-in MATLAB function `randn`, which generates *pseudo-random* numbers.

The Morlet wavelet with $\omega_0 = 6$ is used in this analysis (cf. Eqs. 5.27 and 5.28). For this wavelet, the scale is related to the period of the signal according to $T_\Phi = 1.03s$, i.e. the scale amplitude of the wavelet almost exactly corresponds to the time-scale of the signal.

Figures F.2 to F.5 show time series of the analyzed signals together with the moduli of the complex Morlet wavelet coefficients, $|W_n(s)|$, which are displayed in the time-scale plane using a log_2 y-axis. The black lines give the so-called *cone of influence*. Outside the cone, the wavelet coefficients are biased by discontinuities at the starting and end points of the signal (Torrence and Compo, 1998).

For all academic test cases, the wavelet coefficients in terms of their moduli are capturing the essential information of the signals at the right scales and at the right times. The onsets and endings of the wave superpositions in signal Φ_1 are accurately reproduced (Fig. F.2), keeping in mind the general resolution potential of the transform and recalling that for the Morlet wavelet the scale s is approximately equal to the Fourier period of the signal (see above note). The coefficient graphs of the chirp signal (Fig. F.3) exactly reflect the behavior seen in the time series above the contour plot: the time-dependent increase of the signal's frequency, marked by increasing amplitudes of the wavelet coefficients at decreasing scales. In the wavelet coefficients of the Dirac-spike signal, Φ_3, the time-frequency resolution characteristics of the wavelet are reflected quite distinctly (Fig. F.4). At small scales (high frequencies), the signal is well localized in time. From the coefficient graphs, the position of the spike can be accurately determined. However, as the scale increases, this information is blurred along the time axis.

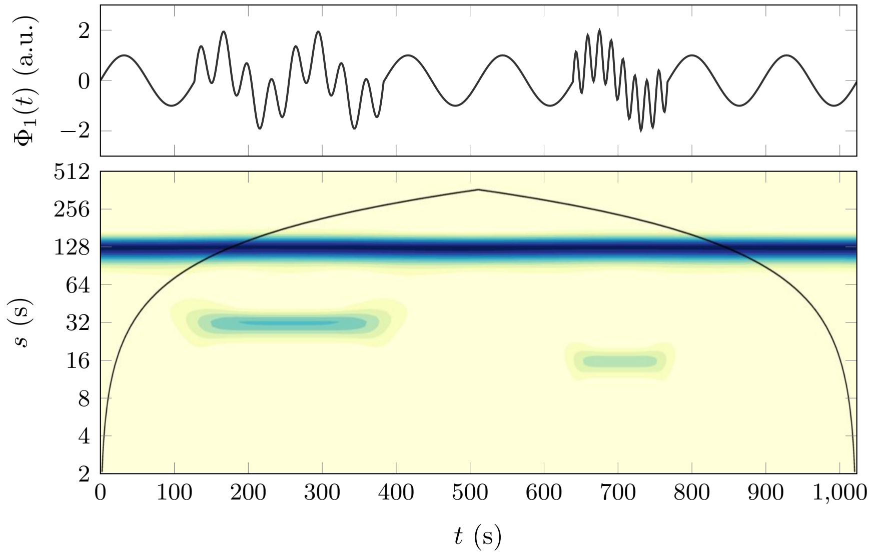

Figure F.2: Wavelet analysis of a sinusoidal signal, $\Phi_1(t)$, shown in the upper panel. The contours display the modulus of the complex wavelet coefficients, $|W_n(s)|$, derived from a CWT using the Morlet wavelet. The black line marks the cone of influence, outside of which the wavelet coefficients are affected by end effects. The darker the shading of the contour plot, the higher are the amplitudes of the moduli, signifying strong correlations with the wavelet at the respective scale.

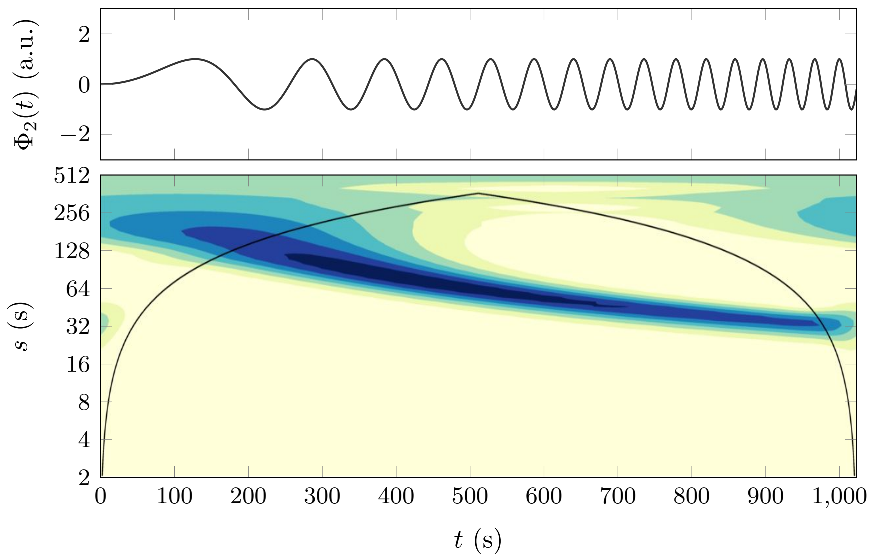

Figure F.3: Same as in Figure F.2, but for a chirp signal.

The analysis of the Gaussian white noise signal, Φ_4, reveals a similar behavior (Fig. F.5). As expected from a random process, there is activity at all scales (all frequencies) together with the characteristic "elongation" of the coefficients along the time and scale axes.

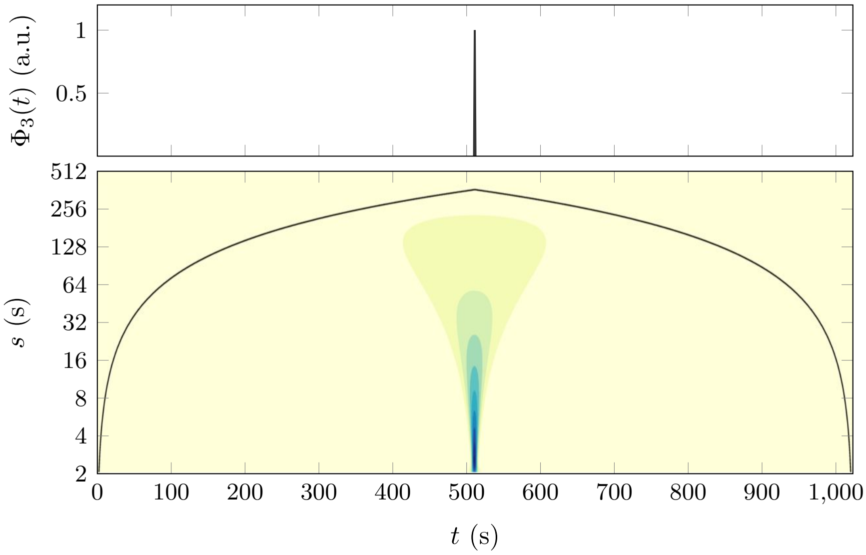

Figure F.4: Same as in Figure F.2, but for a Dirac-spike signal.

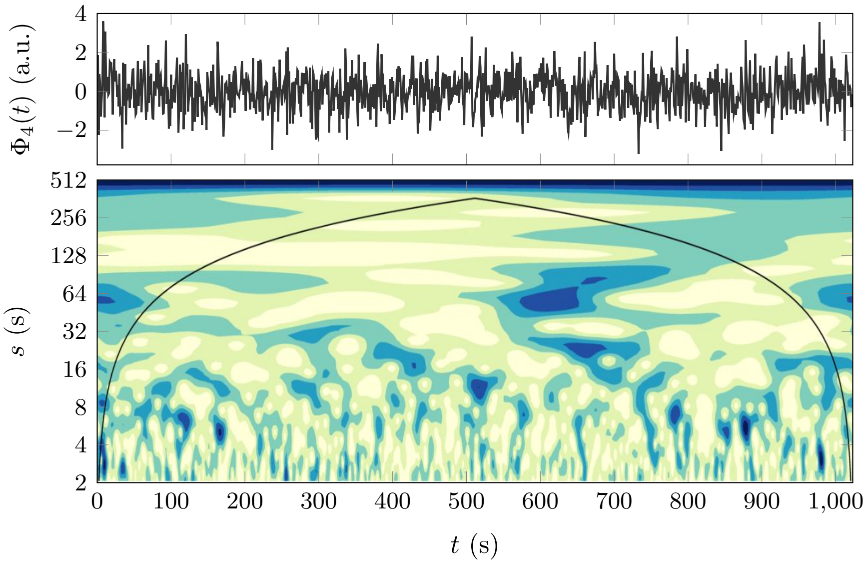

Figure F.5: Same as in Figure F.2, but for a Gaussian white noise signal.

During its development stage, the code has been applied to a variety of further academic test signals, and comparisons between Fourier and the global wavelet spectra were made, documenting the reliability of the code concerning the reproduction of energy density levels. Since this aspect has been discussed at length in Section 5.7.1 based on the comparative analysis of DFT and CWT energy density spectra of turbulent velocities, no further comparisons are made at this point.

Appendix G

Further programs & resources

All computational analyses presented in this thesis were conducted in MATLAB. An exception concerns the preprocessing of the raw wind-tunnel velocities as exported from the LDA signal-acquisition system. Handling of the raw data was conducted with a software package written in C by Fischer (2011), which had been specifically conceptualized for the processing and consistent quality control of 2D-LDA wind-tunnel measurements at EWTL. An important aspect of the preprocessing concerns the removal of spurious velocity signals recognized as outliers (cf. Section 4.4.2). Furthermore, the program carries out the sample-and-hold resampling and, in addition, exports the equidistant velocity signals. Those as well as the original, non-equidistant velocity time series were used in all further calculations in the validation study.

For the analysis and visualization of frequency distributions of horizontal wind speeds and directions in polar coordinates by means of wind roses (Section 5.3), the function `wind_rose.m` from MATLAB's File Exchange was applied in a customized form.[1] Adjustments for the use in this thesis concerned the adaptation of the bar display in agreement with the meteorological wind direction convention (i.e. the wind-rose bars point in the direction *from* which the wind is approaching) and minor layout changes.

The calculations of joint probability densities by means of a bivariate kernel density estimation (Section 5.6) were conducted with an unaltered version of the function `kde2d.m` from MATLAB's File Exchange.[2] Detailed descriptions of the theoretical foundations of the analysis approach are presented by Botev et al. (2010).

This thesis is written in LaTeX using the MiKTeX implementation for Microsoft Windows and the MacTeX implementation for Mac OS X. Results were for the most part visualized by means of the LaTeX package PGFPlots and – in a minority of cases – directly with MATLAB. Schematics and sketches were created with the LaTeX package TikZ and the vector graphics editor Inkscape.

[1] http://www.mathworks.com/matlabcentral/fileexchange/17748-windrose; accessed August 3, 2012.
[2] http://www.mathworks.com/matlabcentral/fileexchange/17204; accessed September 18, 2012.

Bibliography

Addison, P. S.: 2002, *The illustrated wavelet transform handbook: Introductory theory and applications in science, engineering, medicine and finance*, Institute of Physics Publishing, London.

Adrian, R. J.: 2007, Hairpin vortex organization in wall turbulence, *Physics of Fluids* **19**, 041301.

Adrian, R. J. (ed.): 1993, *Selected Papers on Laser Doppler Velocimetry*, S.P.I.E. Milestone Series, S.P.I.E. Optical Engineering Press, Bellingham (WA).

Adrian, R. J., Meneveau, C., Moser, R. D. and Riley, J.: 2000, Final report on 'Turbulence Measurements for LES' workshop, *Technical report*, Department of Theoretical and Applied Mechanics, University of Illinois at Urbana-Champaign, Urbana (IL), USA.

Adrian, R. J. and Yao, C. S.: 1987, Power spectra of fluid velocities measured by laser Doppler velocimetry, *Experiments in Fluids* **5**, 17–28.

Albrecht, H.-E., Borys, M., Damaschke, N. and Tropea, C.: 2003, *Laser Doppler and Phase Doppler Measurement Techniques*, 1st edn, Springer, Berlin, Heidelberg.

Allwine, K. J. and Flaherty, J. E.: 2006, Joint Urban 2003: Study Overview and Instrument Locations, *Report PNNL-15967*, Pacific Northwest National Laboratory, Richland (WA), USA.

Anderson, W. and Meneveau, C.: 2011, Dynamic roughness model for large-eddy simulation of turbulent flow over multiscale, fractal-like rough surfaces, *Journal of Fluid Mechanics* **679**, 288–314.

Andrén, A.: 1995, The structure of stably stratified atmospheric boundary layers: A large-eddy simulation study, *Quarterly Journal of the Royal Meteorological Society* **121**, 961–985.

Andrén, A., Brown, A. R., Mason, P. J., Graf, J., Schumann, U., Moeng, C.-H. and Nieuwstadt, F. T. M.: 1994, Large-eddy simulation of a neutrally stratified boundary layer: A comparison of four computer codes, *Quarterly Journal of the Royal Meteorological Society* **120**, 1457–1484.

Anselmet, F., Gagne, Y., Hopfinger, E. and Antonia, R.: 1984, High-order velocity structure functions in turbulent shear flows, *Journal of Fluid Mechanics* **140**, 63–89.

Aristodemou, E., Bentham, T., Pain, C., Colvile, R., Robins, A. and ApSimon, H.: 2009, A comparison of mesh-adaptive LES with wind tunnel data for flow past buildings: Mean flows and velocity fluctuations, *Atmospheric Environment* **43**, 6238–6253.

Arnold, S., ApSimon, H., Barlow, J., Belcher, S. et al.: 2004, Introduction to the DAPPLE Air Pollution Project, *Science of the Total Environment* **332**, 139–153.

Arya, S. P.: 2001, *Introduction to Micrometeorology*, International Geophysics Series No. 42, 2nd edn, Academic Press, San Diego.

ASME: 2006, Guide for verification and validation in computational solid mechanics, *ASME V&V 10-2006*, The American Society of Mechanical Engineers, New York (NY), USA.

Austin, J., Brimblecombe, P. and Sturges, W. (eds): 2002, *Air Pollution Science for the 21st Century*, Developments in Environmental Sciences, Elsevier, Amsterdam.

Banerjee, S., Krahl, R., Durst, F. and Zenger, C.: 2007, Presentation of anisotropy properties of turbulence, invariant versus eigenvalue approaches, *Journal of Turbulence* **8**, N32.

Barad, M. L.: 1958, Project Prairie Grass. A field program in diffusion, *Geophysical Research Paper No. 59, Vols I and II, AFCRF-TR-58-235*, Air Force Cambridge Research Center, Bedford (MA), USA.

Bardina, J., Ferziger, J. H. and Reynolds, W. C.: 1980, Improved subgrid models for large eddy simulation, *AIAA Paper 1980-1357*.

Barthlott, C., Drobinski, P., Fesquet, C., Dubos, T. and Pietras, C.: 2007, Long-term study of coherent structures in the atmospheric surface layer, *Boundary-Layer Meteorology* **125**, 1–24.

Bastigkeit, I.: 2011, *Erzeugung von Validierungsdaten für wirbelauflösende mikroskalige Strömungs- und Ausbreitungsmodelle*, PhD thesis, University of Hamburg. In German.

Bastigkeit, I., Fischer, R., Leitl, B. and Schatzmann, M.: 2010, Fundamental quality requirements for the generation of LES specific validation data sets from systematic wind tunnel model experiments, *Proceedings of The Fifth International Symposium on Computational Wind Engineering (CWE2010)*, Chapel Hill (NC), USA.

Beare, R. J., Macvean, M. K., Holtslag, A. A. M., Cuxart, J., Esau, I., Golaz, J.-C., Jimenez, M. A., Khairoutdinov, M., Kosovic, B., Lund, D. L. T. S., Lundquist, J. K., McCabe, A., Moene, A. F., Noh, Y., Raasch, S. and Sullivan, P.: 2006, An intercomparison of large-eddy simulations of the stable boundary layer, *Boundary-Layer Meteorology* **118**, 247–272.

Behrens, J.: 2006, *Adaptive Atmospheric Modeling: Key Techniques in Grid Generation, Data Structures, and Numerical Operations with Applications*, Vol. 54 of *Lecture Notes in Computational Science and Engineering*, Springer, Berlin, Heidelberg.

Berkooz, G., Holmes, P. J. and Lumley, J. L.: 1993, The proper orthogonal decomposition in the analysis of turbulent flows, *Annual Review of Fluid Mechanics* **25**, 539–575.

Biltoft, C. A.: 2001, Customer Report for MOck Urban Setting Test (MUST), *DPG Document No. WDTC-FR-01-121*, West Desert Test Center, U.S. Army Dugway Proving Ground, Dugway (UT), USA.

Bonnet, J. P., Coiffet, F., Delville, J., Druault, P., Lamballais, E., Largeau, J. F., Lardeau, S. and Perret, L.: 2003, The generation of realistic 3D unsteady inlet conditions for LES, *AIAA Paper 2003-0065*.

Book, D. L.: 2012, The conception, gestation, birth, and infancy of FCT, *in* D. Kuzmin, R. Löhner and S. Turek (eds), *Flux-Corrected Transport: Principles, Algorithms, and Applications*, second edn, Scientific Computing, Springer, pp. 1–21.

Boris, J. P.: 1989, New directions in computational fluid dynamics, *Annual Review of Fluid Mechanics* **21**, 345–385.

Boris, J. P.: 1990, On large eddy simulation using subgrid turbulence models, *in* J. L. Lumley (ed.), *Whither Turbulence? Turbulence at the Crossroads*, Vol. 357 of *Lecture Notes in Physics*, Springer, pp. 344–353.

Boris, J. P.: 2002, The threat of chemical and biological terrorism: Preparing a response, *Computing in Science and Engineering* **4**, 22–32.

Boris, J. P.: 2005, Dust in the wind: Challenges for urban aerodynamics, *AIAA Paper 2005-5393*.

Boris, J. P.: 2007, More for LES: A brief historical perspective of MILES, *in* F. F. Grinstein, L. G. Margolin and W. J. Rider (eds), *Implicit Large Eddy Simulation: Computing Turbulent Fluid Dynamics*, Cambridge University Press, pp. 9–38.

Boris, J. P. and Book, D. L.: 1973, Flux-corrected transport I: SHASTA – A fluid transport algorithm that works, *Journal of Computational Physics* **11**, 38–69.

Boris, J. P. and Book, D. L.: 1976, Solution of the continuity equation by the method of flux-corrected transport, *in* B. Alder, S. Fernbach, M. Rotenberg and J. Killeen (eds), *Methods in Computational Physics*, Vol. 16, Academic Press, pp. 85–129.

Boris, J. P., Grinstein, F. F., Oran, E. S. and Kolbe, R. L.: 1992, New insights into large eddy simulation, *Fluid Dynamics Research* **10**, 199–228.

Boris, J. P., Landsberg, A. M., Oran, E. S. and Gardner, J. H.: 1993, LCPFCT – Flux-corrected transport algorithm for solving generalized continuity equations, *Report NRL/MR/6410-93-7192*, U.S. Naval Research Laboratory, Washington (DC), USA.

Boris, J. P., Obenschain, K., Patnaik, G. and Young, T. R.: 2002, CT-Analyst: Fast and accurate CBR emergency assessment, *Proceedings of the First Joint Conference on Battle and Management for Nuclear, Chemical, Biological, and Radiological Defense*, Williamsburg (VA), USA.

Boris, J., Patnaik, G. and Obenschain, K.: 2011, The how and why of Nomografs for CT-Analyst, *Report NRL/MR/6440-11-9326*, Naval Research Laboratory, Washington (DC), USA.

Botev, Z. I., Grotowski, J. F. and Kroese, D. P.: 2010, Kernel density estimation via diffusion, *Annals of Statistics* **38**, 2916–2957.

Bou-Zeid, E., Meneveau, C. and Parlange, M.: 2005, A scale-dependent Lagrangian dynamic model for large eddy simulation of complex turbulent flows, *Physics of Fluids* **17**, 025105.

Boussinesq, J.: 1877, Essai sur la théorie des eaux courantes, *Mémoires présentés par divers savants à l'Académie des Sciences, Paris, France,* **23**, 1–680. In French.

Bradshaw, P.: 1972, The understanding and prediction of turbulent flow, *Aeronautical Journal* **76**, 403–418.

Branford, S., Coceal, O., Thomas, T. G. and Belcher, S. E.: 2011, Dispersion of a point-source release of a passive scalar through an urban-like array for different wind directions, *Boundary-Layer Meteorology* **139**, 367–394.

Breuer, M.: 2002, *Direkte numerische Simulation und Large-Eddy Simulation turbulenter Strömungen auf Hochleistungsrechnern*, Habilitation, Technische Fakultät der Universität Erlangen-Nürnberg, Shaker Verlag, Aachen. In German.

Britter, R. E. and Hanna, S. R.: 2003, Flow and dispersion in urban areas, *Annual Review of Fluid Mechanics* **35**, 469–496.

Britter, R. and Schatzmann, M. (eds): 2007a, *Background and justification document to support the model evaluation guidance and protocol*, COST Action 732, University of Hamburg, Germany.

Britter, R. and Schatzmann, M. (eds): 2007b, *Model evaluation guidance and protocol document*, COST Action 732, University of Hamburg, Germany.

Brown, A. R., Derbyshire, S. H. and Mason, P. J.: 1994, Large-eddy simulation of stable atmospheric boundary layers with a revised stochastic subgrid model, *Quarterly Journal of the Royal Meteorological Society* **120**, 1485–1512.

Brown, G. L. and Roshko, A.: 1974, On density effects and large structure in turbulent mixing layers, *Journal of Fluid Mechanics* **64**, 775–816.

Brümmer, B., Lange, I. and Konow, H.: 2012, Atmospheric boundary layer measurements at the 280m high Hamburg weather mast 1995–2011: mean annual and diurnal cycles, *Meteorologische Zeitschrift* **21**, 319–335.

Buchave, P., George Jr., W. K. and Lumley, J. L.: 1979, The measurement of turbulence with the laser-Doppler anemometer, *Annual Review of Fluid Mechanics* **11**, 443–503.

Businger, J. A., Wyngaard, J. C., Izumi, Y. and Bradley, E. F.: 1971, Flux-profile relationships in the atmospheric surface layer, *Journal of the Atmospheric Sciences* **28**, 181–189.

Carper, M. A. and Porté-Agel, F.: 2008a, Subfilter-scale fluxes over a surface roughness transition. Part I: Measured fluxes and energy transfer, *Boundary-Layer Meteorology* **126**, 157–179.

Carper, M. A. and Porté-Agel, F.: 2008b, Subfilter-scale fluxes over a surface roughness transition. Part II: A priori study of large-eddy simulation models, *Boundary-Layer Meteorology* **127**, 73–95.

Cermak, J. E.: 1971, Laboratory simulation of the atmopsheric boundary layer, *AIAA Journal* **9**, 1746–1754.

Cermak, J. E.: 1976, Aerodynamics of buildings, *Annual Review of Fluid Mechanics* **8**, 75–106.

Cermak, J. E.: 1984, Physical modelling of flow and dispersion over complex terrain, *Boundary-Layer Meteorology* **30**, 261–292.

Chamorro, L. P. and Porté-Agel, F.: 2009, Velocity and surface shear stress distributions behind a rough-to-smooth surface transition: A simple new model, *Boundary-Layer Meteorology* **130**, 29–41.

Chamorro, L. P. and Porté-Agel, F.: 2010, Wind-tunnel study of surface boundary conditions for large-eddy simulation of turbulent flow past a rough-to-smooth surface transition, *Journal of Turbulence* **11**, N1.

Champagne, F. H.: 1978, The fine-scale structure of the turbulent velocity field, *Journal of Fluid Mechanics* **86**, 67–108.

Chang, J. C. and Hanna, S. R.: 2004, Air quality model performance evaluation, *Meteorology and Atmospheric Physics* **87**, 167–196.

Cheatham, S. A., Boris, J. P. and Cybyk, B. Z.: 2003, Simulation of flow and dispersion around a surface-mounted cube, *Report NRL/MR/6410-03-8705*, U.S. Naval Research Laboratory, Washington (DC), USA.

Chen, Q., Liu, S. and Tong, C.: 2010, Investigation of the subgrid-scale fluxes and their production rates in a convective atmospheric surface layer using measurement data, *Journal of Fluid Mechanics* **660**, 282–315.

Chen, Q. and Tong, C.: 2006, Investigation of the subgrid-scale stress and its production rate in a convective atmospheric boundary layer using measurement data, *Journal of Fluid Mechanics* **547**, 65–104.

Cheng, H. and Castro, I. P.: 2002a, Near wall flow over urban-like roughness, *Boundary-Layer Meteorology* **104**, 229–259.

Cheng, H. and Castro, I. P.: 2002b, Near-wall flow development after a step change in surface roughness, *Boundary-Layer Meteorology* **105**, 411–432.

Cheng, W. C. and Liu, C.-H.: 2011, Large-eddy simulation of turbulent transports in urban street canyons in different thermal stabilities, *Journal of Wind Engineering and Industrial Aerodynamics* **99**, 434–442.

Chlond, A. and Wolkau, A.: 2000, Large-eddy simulation of a nocturnal stratocumulus-topped marine atmospheric boundary layer: An uncertainty analysis, *Boundary-Layer Meteorology* **95**, 31–55.

Chow, F. K. and Moin, P.: 2003, A further study of numerical errors in large-eddy simulations, *Journal of Computational Physics* **184**, 366–380.

Chow, F. K. and Street, R. L.: 2009, Evaluation of turbulence closure models for large-eddy simulation over complex terrain: Flow over Askervein hill, *Journal of Applied Meteorology and Climatology* **48**, 1050–1065.

Chow, F. K., Street, R. L., Xue, M. and Ferziger, J. H.: 2005, Explicit filtering and reconstruction turbulence modeling for large-eddy simulation of neutral boundary layer flow, *Journal of the Atmospheric Sciences* **62**, 2058–2077.

Chow, F. K., Weigel, A. P., Street, R. L., Rotach, M. W. and Xue, M.: 2006, High-resolution large-eddy simulations of flow in a steep alpine valley. Part I: Methodology, verification, and sensitivity experiments, *Journal of Applied Meteorology and Climatology* **45**, 63–86.

Christen, A., van Gorsel, E. and Vogt, R.: 2007, Coherent structures in urban roughness sublayer turbulence, *International Journal of Climatology* **27**, 1955–1968.

Coceal, O., Dobre, A. and Thomas, T. G.: 2007, Unsteady dynamics and organized structures from DNS over an idealized building canopy, *International Journal of Climatology* **27**, 1943–1953.

Coirier, W. J.: 2005, Evaluation of CFD codes, US perspective, *in* M. Schatzmann and R. Britter (eds), *COST732 – Quality Assurance of Microscale Meteorological Models*, University of Hamburg, Germany.

Coleman, G. N., Ferziger, J. H. and Spalart, P. R.: 1990, A numerical study of the stratified turbulent Ekman layer, *Journal of Fluid Mechanics* **213**, 313–348.

Collineau, S. and Brunet, Y.: 1993a, Detection of turbulent coherent motions in a forest canopy, Part I: Wavelet analysis, *Boundary-Layer Meteorology* **65**, 357–379.

Collineau, S. and Brunet, Y.: 1993b, Detection of turbulent coherent motions in a forest canopy, Part II: Time-scales and conditional averages, *Boundary-Layer Meteorology* **66**, 49–73.

Conover, W. J.: 1999, *Practical Nonparametric Statistics*, John Wiley & Sons, New York.

Cooley, J. W. and Tukey, J. W.: 1965, An algorithm for the machine calculation of complex Fourier series, *Mathematics of Computation* **19**, 297–301.

Counihan, J.: 1975, Adiabatic atmospheric boundary layers: A review and analysis of data from the period 1880 - 1972, *Atmospheric Environment* **9**, 871–905.

Cybyk, B. Z., Boris, J. P., Young, T. R., Emery, M. H. and Cheatham, S. A.: 2001, Simulation of fluid dynamics around complex urban geometries, *AIAA Paper 2001-0803*.

Daubeschies, I.: 1988, Orthonormal bases of compactly supported wavelets, *Communications on Pure and Applied Mathematics* **41**(7), 909–996.

Daubeschies, I.: 1992, *Ten lectures on wavelets*, CBMS-NSF Regional Conference Series in Applied Mathematics, SIAM.

Davenport, A. G.: 1963, The relationship of wind structure to wind loading, *Proceedings of the N.P.L. Symposium on Wind Effects on Buildings and Structure*, H.M.S.O. London, UK.

Davenport, A. G.: 1967, The dependence of wind loads on meteorological parameters, *Proceedings of the Conference on Wind Loads on Buildings*, University of Toronto Press, University of Toronto, Canada.

De Boor, C.: 2001, *A Practical Guide to Splines*, Applied Mathematical Series, revised edn, Springer, Berlin, Heidelberg.

De Waele, S. and Broersen, P. M. T.: 2000, Error measures for resampled irregular data, *IEEE Transactions on Instrumentation and Measurement* **49**, 216–222.

Deardorff, J. W.: 1970a, A numerical study of three-dimensional turbulent channel flow at large Reynolds numbers, *Journal of Fluid Mechanics* **41**, 453–480.

Deardorff, J. W.: 1970b, A three-dimensional numerical investigation of the idealized planetary boundary layer, *Geophysical Fluid Dynamics* **1**, 377–410.

Deardorff, J. W.: 1970c, Convective velocity and temperature scales for the unstable planetary boundary layer and for Rayleigh convection, *Journal of the Atmospheric Sciences* **27**, 1211–1213.

Deardorff, J. W.: 1974a, Three-dimensional numerical study of the height and mean structure of a heated planetary boundary layer, *Boundary-Layer Meteorology* **7**, 81–106.

Deardorff, J. W.: 1974b, Three-dimenional numerical study of turbulence in an entraining mixed layer, *Boundary-Layer Meteorology* **7**, 199–226.

Deardorff, J. W.: 1980, Stratocumulus-capped mixed layers derived from a three-dimensional model, *Boundary-Layer Meteorology* **18**, 495–527.

Dias, N. L., Chamecki, M., Kan, A. and Okawa, C. M. P.: 2004, A study of spectra, structure and correlation functions and their implications for the stationarity of surface-layer turbulence, *Boundary-Layer Meteorology* **110**, 165–189.

Domaradzki, J. A. and Rogallo, R. S.: 1990, Local energy transfer and nonlocal interactions in homogeneous, isotropic turbulence, *Physics of Fluids A* **2**, 413–426.

Domaradzki, J. A. and Saiki, E. M.: 1997, Backscatter models for large-eddy simulations, *Theoretical and Computational Fluid Dynamics* **9**, 75–83.

Dyer, A. J. and Hicks, B. B.: 1970, Flux-gradient relationships in the constant flux layer, *Quarterly Journal of the Royal Meteorological Society* **96**, 715–721.

Edwards, R. V. and Jensen, A. S.: 1983, Particle-sampling statistics in laser anemometers: sample-and-hold systems and saturable systems, *Journal of Fluid Mechanics* **133**, 397–411.

ERCOFTAC: 2000, *Quality and Trust in Industrial CFD: Best Practice Guidelines*, ERCOFTAC Special Interest Group, M. Casey and T. Wintergerste (eds). Version 1.0.

ESDU: 1972, Characteristics of wind speed in the lower layers of the atmosphere near the ground: strong winds (neutral atmosphere), *ESDU 72026*, Engineering Sciences Data Unit, London, UK.

ESDU: 1985, Characteristics of atmospheric turbulence near the ground. Part II: single point data for strong winds (neutral atmosphere), *ESDU 85020*, Engineering Sciences Data Unit, London, UK.

Farge, M.: 1992, Wavelet transforms and their application to turbulence, *Annual Review of Fluid Mechanics* **24**, 395–457.

Farge, M., Schneider, K. and Kevlahan, N.: 1999, Non-Gaussianity and coherent vortex simulation for two-dimensional turbulence using an adaptive orthogonal wavelet basis, *Physics of Fluids* **11**, 2187–2201.

Farge, M., Schneider, K., Pannekoucke, O. and Nguyen van yen, R.: 2012, Multiscale representations, *in* H. J. S. Fernando (ed.), *Handbook of Environmental Fluid Dynamics*, Vol. II: Systems, Pollution, Modeling, and Measurements, CRC Press.

Feddersen, B.: 2005, *Wind tunnel modelling of turbulence and dispersion above tall and highly dense urban roughness*, PhD thesis, Swiss Federal Institute of Technology. Diss. ETH No. 15934.

Fedorovich, E., Nieuwstadt, F. T. M. and Kaiser, R.: 2001a, Numerical and laboratory study of a horizontally evolving convective boundary layer. Part I: Transition regimes and development of the mixed layer, *Journal of the Atmospheric Sciences* **58**, 70–86.

Fedorovich, E., Nieuwstadt, F. T. M. and Kaiser, R.: 2001b, Numerical and laboratory study of a horizontally evolving convective boundary layer. Part II: Effects of elevated wind shear and surface roughness, *Journal of the Atmospheric Sciences* **58**, 546–560.

Feigenwinter, C. and Vogt, R.: 2005, Detection and analysis of coherent structures in urban turbulence, *Theoretical and Applied Climatology* **81**, 219–230.

Feigenwinter, C., Vogt, R. and Parlow, E.: 1999, Vertical structure of selected turbulence characteristics above an urban canopy, *Theoretical and Applied Climatology* **62**, 51–63.

Finnigan, J. J.: 2000, Turbulence in plant canopies, *Annual Review of Fluid Mechanics* **32**, 519–571.

Finnigan, J. J.: 2004, Advection and modeling, *in* X. Lee, W. Massman and B. Law (eds), *Handbook of Micrometeorology*, Vol. 29 of *Atmospheric and Oceanographic Sciences Library*, Kluwer Academic Publishers, pp. 209–244.

Fischer, R.: 2011, *Entwicklung eines problemorientierten Software-Pakets zur automatisierten Aufbereitung, Analyse und Dokumentation von im Windkanal produzierten Daten zur LES-Validierung*, PhD thesis, University of Hamburg. In German.

Franke, J., Hellsten, A., Schlünzen, H. and Carissimo, B. (eds): 2007, *Best practice guideline for the CFD simulation of flows in the urban environment*, COST Action 732, University of Hamburg, Germany.

Franke, J., Hellsten, A., Schlünzen, K. H. and Carissimo, B.: 2011, The COST 732 Best Practice Guideline for CFD simulation of flows in the urban environment: a summary, *International Journal of Environment and Pollution* **44**, 419–427.

Frenzen, P. and Vogel, C. A.: 1995, On the magnitude and apparent range of variation of the von Karman constant in the atmospheric surface layer, *Boundary-Layer Meteorology* **72**, 371–392.

Frisch, U.: 1995, *Turbulence: The Legacy of A. N. Kolmogorov*, Cambridge University Press, Cambridge.

Frisch, U., Sulem, P.-L. and Nelkin, M.: 1978, A simple dynamical model of intermittent fully developed turbulence, *Journal of Fluid Mechanics* **87**, 719–736.

Fritsch, F. N. and Carlson, R. E.: 1980, Monotone piecewise cubic interpolation, *SIAM Journal of Numerical Analysis* **17**, 238–246.

Fröhlich, J.: 2006, *Large Eddy Simulation turbulenter Strömungen*, B. G. Teubner Verlag, Leipzig.

Fureby, C. and Grinstein, F. F.: 1999, Monotonically integrated large eddy simulation of free shear flows, *AIAA Journal* **37**, 544–556.

Fureby, C. and Grinstein, F. F.: 2002, Large eddy simulation of high-Reynolds-number free and wall-bounded flows, *Journal of Computational Physics* **181**, 68–97.

Gao, W. and Li, B. L.: 1993, Wavelet analysis of coherent structures at the atmosphere-forest interface, *Journal of Applied Meteorology* **32**, 1717–1725.

Garratt, J. R.: 1994, *The Atmospheric Boundary Layer*, Cambridge University Press, Cambridge.

Germano, M.: 1986, A proposal for a redefinition of the turbulent stresses in the filtered Navier-Stokes equations, *Physics of Fluids* **29**, 2323–2324.

Germano, M., Piomelli, U., Moin, P. and Cabot, W. H.: 1991, A dynamic subgrid-scale eddy viscosity model, *Physics of Fluids A* **3**, 1760–1765.

Ghosal, S.: 1996, An analysis of numerical errors in large-eddy simulations of turbulence, *Journal of Computational Physics* **125**, 187–206.

Gopalakrishnan, S. G. and Avissar, R.: 2000, An LES study of the impacts of land surface heterogeneity on dispersion in the convective boundary layer, *Journal of the Atmospheric Sciences* **57**, 352–371.

Gopalakrishnan, S. G., Roy, S. B. and Avissar, R.: 2000, An evaluation of the scale at which topographical features affect the convective boundary layer using large eddy simulations, *Journal of the Atmospheric Sciences* **57**, 334–351.

Gousseau, P., Blocken, B., Stathopoulos, T. and van Heist, G. J. F.: 2011, CFD simulation of near-field pollutant dispersion on a high-resolution grid: A case study by LES and RANS for a building group in downtown Montreal, *Atmospheric Environment* **45**, 428–438.

Grant, H. L., Stewart, R. W. and Moilliet, A.: 1962, Turbulence spectra from a tidal channel, *Journal of Fluid Mechanics* **12**, 241–268.

Grimmond, C. S. B.: 2006, Progress in measuring and observing the urban atmosphere, *Theoretical and Applied Climatology* **84**, 3–22.

Grimmond, C. S. B. and Oke, T. R.: 1999, Aerodynamic properties of urban areas derived from analysis of surface form, *Journal of Applied Meteorology* **38**, 1262–1292.

Grimmond, C. S. B., Roth, M., Oke, T. R., Au, Y. et al.: 2010, Climate and more sustainable cities: Climate information for improved planning and management of cities (producers/capabilities perspective), *Procedia Environmental Sciences* **1**, 247–274.

Grinstein, F. F.: 2010, Verification and validation of CFD based turbulent flow experiments, *Encyclopedia of Aerospace Engineering*, John Wiley & Sons, pp. 515–523.

Grinstein, F. F. and Fureby, C.: 2007, On flux-limiting-based implicit large eddy simulation, *Journal of Fluids Engineering* **129**, 1483–1492.

Grinstein, F. F. and Fureby, C.: 2012, On monotonically integrated large eddy simulation of turbulent flows based on FCT algorithms, *in* D. Kuzmin, R. Löhner and S. Turek (eds), *Flux-Corrected Transport: Principles, Algorithms, and Applications*, second edn, Scientific Computing, Springer, pp. 67–90.

Grinstein, F. F., Margolin, L. G. and Rider, W. J. (eds): 2007, *Implicit Large Eddy Simulation: Computing Turbulent Fluid Dynamics*, Cambridge University Press, Cambridge.

Grossmann, A. and Morlet, J.: 1984, Decomposition of Hardy functions into square integrable wavelets of constant shape, *SIAM Journal on Mathematical Analysis* **15**, 723–736.

Grossmann, A., Morlet, J. and Paul, T.: 1985, Transforms associated to square integrable group representations I: General results, *Journal on Mathematical Analysis* **26**, 2473–2479.

Grötzbach, G.: 1981, Numerical simulation of turbulent temperature fluctuations in liquid metals, *International Journal of Heat and Mass Transfer* **24**, 475–490.

Gu, Z. L., Jiao, J. Y. and Su, J. W.: 2011, Large-eddy simulation of the wind field and plume dispersion within different obstacle arrays using a dynamic mixing length subgrid-scale model, *Boundary-Layer Meteorology* **139**, 439–455.

Hanna, S. R., Hansen, O. R. and Dharmavaram, S.: 2004, FLACS CFD air quality model performance evaluation with Kit Fox, MUST, Prairie Grass, and EMU observations, *Atmospheric Environment* **38**, 4675–4687.

Harlander, U., von Larcher, T., Wang, Y. and Egbers, C.: 2011, PIV- and LDV-measurements of baroclinic wave interactions in a thermally driven rotating annulus, *Experiments in Fluids* **51**, 37–49.

Hatlee, S. C. and Wyngaard, J. C.: 2007, Improved subfilter-scale models from the HATS field data, *Journal of the Atmospheric Sciences* **64**, 1694–1705.

Heil, C. and Walnut, D. F.: 2006, *Fundamental Papers in Wavelet Theory*, first edn, Princeton University Press.

Heisenberg, W.: 1948, Zur statistischen Theorie der Turbulenz, *Zeitschrift für Physik* **124**, 628–657. In German.

Hertel, C. and Fröhlich, J.: 2011, Error reduction in LES via adaptive moving grids, *in* M. V. Salvetti, B. Geurts, J. Meyers and P. Sagaut (eds), *Quality and Reliability of Large-Eddy Simulations II*, Vol. 16 of *ERCOFTAC Series*, Springer, pp. 309–318.

Hertwig, D.: 2009, Detection of coherent structures in atmospheric boundary layer flows: A comparative wind tunnel study using POD, LSE, and wavelets, Diplomarbeit, University of Hamburg.

Hertwig, D., Efthimiou, G. C., Bartzis, J. G. and Leitl, B.: 2012, CFD-RANS model validation of turbulent flow in a semi-idealized urban canopy, *Journal of Wind Engineering and Industrial Aerodynamics* **111**, 61–72.

Hertwig, D., Leitl, B. and Schatzmann, M.: 2011, Organized turbulent structures – Link between experimental data and LES, *Journal of Wind Engineering and Industrial Aerodynamics* **99**, 296–307.

Hess, G. D. and Clarke, R. H.: 1973, Time spectra and cross-spectra of kinetic energy in the planetary boundary layer, *Quarterly Journal of the Royal Meteorological Society* **99**, 130–153.

Högström, U.: 1996, Review of some basic characteristics of the atmospheric surface layer, *Boundary-Layer Meteorology* **42**, 55–78.

Högström, U., Bergström, H. and Alexandersson, H.: 1982, Turbulence characteristics in a near neutrally stratified urban atmosphere, *Boundary-Layer Meteorology* **23**, 449–472.

Holmes, P. J., Lumley, J. L. and Berkooz, G.: 1996, *Turbulence, Coherent Structures, Dynamical Systems and Symmetry*, Cambridge University Press, Cambridge.

Hopke, P. K.: 2009, Contemporary threats and air pollution, *Atmospheric Environment* **43**, 87–93.

Horst, T. W., Kleissl, J., Lenschow, D. H., Meneveau, C., Moeng, C.-H., Parlange, M. B., Sullivan, P. P. and Weil, J. C.: 2004, HATS: Field observations to obtain spatially filtered turbulence fields from crosswind arrays of sonic anemometers in the atmospheric surface layer, *Journal of the Atmospheric Sciences* **61**, 1566–1581.

Huang, J., Cassiani, M. and Albertson, J. D.: 2009, The effects of vegetation density on coherent turbulent structures within the canopy sublayer: A large-eddy simulation study, *Boundary-Layer Meteorology* **133**, 253–275.

Hubbard, B. B.: 1998, *The World According to Wavelets: The Story of a Mathematical Technique in the Making*, 2nd edn, AK Peters, Natick (MA).

Hussain, M. and Lee, B.: 1980, A wind tunnel study of the mean pressure forces acting on large groups of low-rise buildings, *Journal of Wind Engineering and Industrial Aerodynamics* **6**, 207–225.

Hutton, A. G. and Casey, M. V.: 2001, Quality and trust in industrial CFD – A European initiative, *AIAA Paper 2001-0656*.

Inagaki, A., Castillo, M. C. L., Yamashita, Y., Kanda, M. and Takimoto, H.: 2012, Large-eddy simulation of coherent flow structures within a cubical canopy, *Boundary-Layer Meteorology* **142**, 207–222.

Inagaki, A. and Kanda, M.: 2008, Turbulent flow similarity over an array of cubes in near-neutrally stratified atmospheric flow, *Journal of Fluid Mechanics* **615**, 101–120.

Inagaki, A. and Kanda, M.: 2010, Organized structure of active turbulence over an array of cubes within the logarithmic layer of atmospheric flow, *Boundary-Layer Meteorology* **135**, 209–228.

Iselin, J. P., Patnaik, G., Leitl, B., Harms, F. and Young, T. R.: 2006, FAST3D-CT validation results using MUST field and wind tunnel data, *Proceedings of the 86th AMS Annual Meeting / 6th Symposium on the Urban Environment*, Atlanta (GA), USA.

Jensen, K. D.: 2004, Flow measurements, *Journal of the Brazilian Society of Mechanical Sciences and Engineering* **26**, 400–419.

Jiménez, J.: 2003, Computing high-Reynolds-number turbulence: Will simulations ever replace experiments?, *Journal of Turbulence* **4**, N22.

Kaimal, J. C. and Wyngaard, J. C.: 1990, The Kansas and Minnesota experiments, *Boundary-Layer Meteorology* **50**, 31–47.

Kaimal, J. C., Wyngaard, J. C., Izumi, Y. and Coté, O. R.: 1972, Spectral characteristics of surface-layer turbulence, *Quarterly Journal of the Royal Meteorological Society* **98**, 563–589.

Kaimal, J. and Finnigan, J. J.: 1994, *Atmospheric Boundary Layer Flows: Their Structure and Measurement*, Oxford University Press, Oxford.

Kaiser, G.: 1994, *A Friendly Guide to Wavelets*, first edn, Birkhäuser Boston.

Kaiser, R. and Fedorovich, E.: 1998, Turbulence spectra and dissipation rates in a wind tunnel model of the atmospheric convective boundary layer, *Journal of the Atmospheric Sciences* **55**, 580–594.

Kanda, M.: 2006a, Large-eddy simulations on the effect of surface geometry of building arrays on turbulent organized structures, *Boundary-Layer Meteorology* **118**, 151–168.

Kanda, M.: 2006b, Progress in the scale modeling of urban climate: Review, *Theoretical and Applied Climatology* **84**, 23–33.

Kanda, M., Moriwaki, R. and Kasamatsu, F.: 2004, Large-eddy simulation of turbulent organized structures within and above explicitly resolved cube arrays, *Boundary-Layer Meteorology* **112**, 343–368.

Kaneda, Y. and Ishihara, T.: 2006, High-resolution direct numerical simulation of turbulence, *Journal of Turbulence* **7**, N20.

Kastner-Klein, P. and Rotach, M. W.: 2004, Mean flow and turbulence characteristics in an urban roughness sublayer, *Boundary-Layer Meteorology* **111**, 55–84.

Kempf, A., Klein, M. and Janicka, J.: 2005, Efficient generation of initial- and inflow-conditions for transient turbulent flows in arbitrary geometries, *Flow, Turbulence and Combustion* **74**, 67–84.

Kempf, A. M.: 2008, LES validation from experiments, *Flow, Turbulence and Combustion* **80**, 351–373.

Kim, J.-J. and Baik, J.-J.: 2001, A numerical study of the effects of ambient wind direction on flow and dispersion in urban street canyons using the RNG k–ε turbulence model, *Atmospheric Environment* **38**, 3039–3048.

Kim, J., Moin, P. and Moser, R.: 1987, Turbulence statistics in fully developed channel flow at low reynolds number, *Journal of Fluid Mechanics* **177**, 122–166.

Klein, M., Sadiki, A. and Janicka, J.: 2003, A digital filter based generation of inflow data for spatially developing direct numerical or large eddy simulation, *Journal of Computational Physics* **186**, 652–665.

Kleissl, J., Meneveau, C. and Parlange, M. B.: 2003, On the magnitude and variability of subgrid-scale eddy-diffusion coefficients in the atmopsheric surface layer, *Journal of the Atmospheric Sciences* **60**, 2372–2388.

Kline, S. J., Reynolds, W. C., Schraub, F. A. and Runstadler, P. W.: 1967, The structure of turbulent boundary layers, *Journal of Fluid Mechanics* **30**, 741–773.

Klipp, C.: 2010, Turbulence anisotropy in an urban canyon and intersection, *Proceedings of the 90th Annual AMS Meeting / 16th Conference on Air Pollution Meteorology*, Atlanta (GA), USA. `https://ams.confex.com/ams/90annual/techprogram/paper_160716.htm`.

Klipp, C.: 2010a, Surface layer anisotropic turbulence, *Proceedings of the 5th International Symposium on Computational Wind Engineering*, Chapel Hill, North Carolina.

Kolmogorov, A. N.: 1941, The local structure of turbulence in incompressible viscous fluid for very large Reynolds numbers, *Dokl. Akad. Nauk S.S.S.R.* **30**, 299–303. In Russian.

Kolmogorov, A. N.: 1962, A refinement of previous hypotheses concerning the local structure of turbulence in a viscous incompressible fluid at high Reynolds number, *Journal of Fluid Mechanics* **13**, 82–85.

Kolmogorov, A. N.: 1991, The local structure of turbulence in incompressible viscous fluid for very large Reynolds numbers, *Proceedings of the Royal Society of London. Series A, Mathematical and Physical Sciences* **434**, 9–13. English translation of the 1946 Russian original paper.

Kosović, B. and Curry, J. A.: 2000, A large-eddy simulation study of a quasi-steady, stably stratified atmospheric boundary layer, *Journal of the Atmospheric Sciences* **57**, 1052–1068.

Kraichnan, R. H.: 1959, The structure of isotropic turbulence at very high Reynolds numbers, *Journal of Fluid Mechanics* **5**, 497–543.

Kraichnan, R. H.: 1974, On Kolmogorov's inertial range theories, *Journal of Fluid Mechanics* **62**, 305–330.

Krusche, N. and de Oliveira, A. P.: 2004, Characterization of coherent structures in the atmospheric surface layer, *Boundary-Layer Meteorology* **110**, 191–211.

Kuzmin, D., Löhner, R. and Turek, S. (eds): 2012, *Flux-Corrected Transport: Principles, Algorithms, and Applications*, Scientific Computing, 2nd edn, Springer.

Lee, M.-Y., Harms, F., Young, T., Leitl, B. and Patnaik, G.: 2009, Model- and application-specific validation data for LES-based transport and diffusion models, *Proceedings of the 89th Annual AMS Meeting / 8th Symposium on the Urban Environment*, Phoenix (AZ), USA. `https://ams.confex.com/ams/pdfpapers/149943.pdf`.

Leitl, B.: 2000, Validation data for microscale dispersion modelling, *EUROTRAC Newsletter* **22**, 28–32.

Leitl, B., Hertwig, D., Harms, F., Peeck, C., Schatzmann, M., Patnaik, G., Boris, J., Obenschain, K., Fischer, S. and Rechenbach, P.: 2012, Emergency response tool for accidental releases, *Short Course on Urban and Technical Meteorology (Lecture Notes)*, Universidad National de Colombia, Bogotá.

Lenschow, D. H., Lothon, M., Mayor, S. D., Sullivan, P. P. and Canut, G.: 2012, A comparison of higher-order vertical velocity moments in the convective boundary layer from lidar with in situ measurements and large-eddy simulation, *Boundary-Layer Meteorology* **143**, 107–123.

Leonard, A.: 1974, Energy cascade in large-eddy simulation of turbulent fluid flows, *Advances in Geophysics* **18A**, 237–248.

Lesieur, M. and Métais, O.: 1996, New trends in large-eddy simulation of turbulence, *Annual Review of Fluid Mechanics* **28**, 45–82.

Letzel, M. O., Krane, M. and Raasch, S.: 2008, High resolution urban large-eddy simulation studies from street canyon to neighbourhood scale, *Atmospheric Environment* **42**, 8770–8784.

Letzel, M. O. and Raasch, S.: 2003, Large eddy simulation of thermally induced oscillations in the convective boundary layer, *Journal of the Atmospheric Sciences* **60**, 2328–2341.

Li, X.-X., Britter, R. E., Norford, L. K., Koh, T.-Y. and Entekhabi, D.: 2012, Flow and pollutant transport in urban street canyons of different aspect ratios with ground heating: Large-eddy simulation, *Boundary-Layer Meteorology* **142**, 289–304.

Li, X.-X., Liu, C.-H., Leung, D. Y. C. and Lam, K. M.: 2006, Recent progress in CFD modelling of wind field and pollutant transport in street canyons, *Atmospheric Environment* **40**, 5640–5658.

Liepmann, H. W.: 1979, The rise and fall of ideas in turbulence, *American Scientist* **67**, 221–228.

Lilly, D. K.: 1967, The representation of small-scale turbulence in numerical simulation experiments, *in* H. H. Goldstine (ed.), *Proceedings of the IBM Scientific Computing Symposium on Environmental Sciences*, Yorktown Height, New York, pp. 195–210.

Liu, C.-H., Barth, M. C. and Leung, D. Y. C.: 2004, Large-eddy simulation of flow and pollutant transport in street canyons of different building-height-to-street-width ratios, *Journal of Applied Meteorology* **43**, 1410–1424.

Liu, Y. S., Cui, G. X., Wang, Z. S. and Zhang, Z. S.: 2011, Large eddy simulation of wind field and pollutant dispersion in downtown Macao, *Atmospheric Environment* **45**, 2849–2859.

Löbig, S., Dörnbrack, A., Fröhlich, J., Hertel, C., Kühnlein, C. and Lang, J.: 2009, Towards large eddy simulation on moving grids, *Proceedings in Applied Mathematics and Mechanics* **9**, 445–446.

Lorenz, E. N.: 1963, Deterministic nonperiodic flow, *Journal of Atmospheric Sciences* **20**, 130–141.

Louka, P., Belcher, S. E. and Harrington, R. G.: 2000, Coupling between airflow in streets and the well-developed boundary layer aloft, *Atmospheric Environment* **34**, 2613–2621.

Lu, S. S. and Willmarth, W. W.: 1973, Measurements of the structure of the Reynolds stress in a turbulent boundary layer, *Journal of Fluid Mechanics* **60**, 481–511.

Lumley, J. L.: 1965, Interpretation of time spectra measured in high-intensity shear flows, *Physics of Fluids* **8**, 1056–1062.

Lumley, J. L.: 1967, The structure of inhomogeneous turbulent flows, *in* A. M. Yaglom and V. I. Tatarski (eds), *Atmospheric Turbulence and Radio Wave Propagation*, pp. 166–178.

Lumley, J. L.: 1978, The computational modelling of turbulent flows, *Advances in Applied Mechanics* **18**, 123–176.

Lumley, J. L.: 1983, Atmospheric modelling, *Proceedings of the 8th Australasian Fluid Mechanics Conference*, University of Newcastle, New South Wales, Australia.

Lumley, J. L. and Panofsky, H. A.: 1964, *The Structure of Atmospheric Turbulence*, Interscience Publishers, New York.

Lumley, J. L. and Yaglom, A. M.: 2001, A century of turbulence, *Flow, Turbulence and Combustion* **66**, 241–286.

Lund, T. S., Wu, X. and Squires, K. D.: 1998, Generation of turbulent inflow data for spatially-developing boundary layer simulations, *Journal of Computational Physics* **140**, 233–258.

Mallat, S.: 2009, *A Wavelet Tour of Signal Processing: The Sparse Way*, third edn, Academic Press.

Margolin, L. G. and Rider, W. J.: 2002, A rationale for implicit turbulence modeling, *International Journal of Numerical Methods in Fluids* **39**, 821–841.

Marusic, I., Kunkel, G. J. and Porté-Agel, F.: 2001, Experimental study of wall boundary conditions for large-eddy simulation, *Journal of Fluid Mechanics* **446**, 309–320.

Maruyama, Y., Tamura, T., Okuda, Y. and Ohashi, M.: 2012, LES of turbulent boundary layer for inflow generation using stereo PIV measurement data, *Journal of Wind Engineering and Industrial Aerodynamics* **104-106**, 379–388.

Mason, P. J.: 1989, Large-eddy simulation of the convective atmospheric boundary layer, *Journal of the Atmospheric Sciences* **46**, 1492–1516.

Mason, P. J.: 1994, Large-eddy simulation – A critical review of the technique, *Quarterly Journal of the Royal Meteorological Society* **120**, 1–26.

Mason, P. J. and Derbyshire, S. H.: 1990, Large-eddy simulation of the stably-stratified atmospheric boundary layer, *Boundary-Layer Meteorology* **53**, 117–162.

Mason, P. J. and Thomas, D. J.: 1992, Stochastic backscatter in large-eddy simulations of boundary layers, *Journal of Fluid Mechanics* **242**, 51–78.

Mason, P. J. and Thomson, D. J.: 1987, Large-eddy simulation of the neutral-static-stability planetary boundary layer, *Quarterly Journal of the Royal Meteorological Society* **113**, 413–443.

McKeon, B. J., Comte-Bellot, G., Foss, J. F., Westerweel, J. et al.: 2007, Particle-based techniques, *in* C. Tropea, A. L. Yarin and J. F. Foss (eds), *Springer Handbook of Experimental Fluid Mechanics, Part B: Measurement of Primary Quantities*, Springer, chapter 5, pp. 287–361.

Meeder, J. P. and Nieuwstadt, F. T. M.: 2000, Large-eddy simulation of the turbulent dispersion of a reactive plume from a point source into a neutral atmospheric boundary layer, *Atmospheric Environment* **34**, 3563–3573.

Meneveau, C.: 1991, Analysis of turbulence in the orthonormal wavelet representation, *Journal of Fluid Mechanics* **232**, 469–520.

Meneveau, C. and Katz, J.: 2000, Scale-invariance and turbulence models for large-eddy simulation, *Annual Review of Fluid Mechanics* **32**, 1–32.

Meneveau, C., Lund, T. S. and Cabot, C. H.: 1996, A Lagrangian dynamic subgrid-scale model of turbulence, *Journal of Fluid Mechanics* **319**, 353–385.

Mestayer, P.: 1982, Local isotropy and anisotropy in a high-Reynolds-number turbulent boundary layer, *Journal of Fluid Mechanics* **125**, 475–503.

Meyers, S. D., Kelley, B. G. and O'Brien, J. J.: 1993, An introduction to wavelet analysis in oceanography and meteorology: With application to the dispersion of Yanai waves, *Monthly Weather Review* **121**, 2858–2866.

Michioka, T. and Chow, F. K.: 2008, High-resolution large-eddy simulation of scalar transport in atmospheric boundary layer flow over complex terrain, *Journal of Applied Meteorology and Climatology* **47**, 3150–3169.

Michioka, T., Sato, A., Takimoto, H. and Kanda, M.: 2011, Large-eddy simulation for the mechanism of pollutant removal from a two-dimensional street canyon, *Boundary-Layer Meteorology* **138**, 195–213.

Mittal, R.: 2005, Computational modeling in biohydrodynamics: trends, challenges, and recent advances, *IEEE Journal of Oceanic Engineering* **29**, 595–604.

Mittal, R. and Iaccarino, G.: 2005, Immersed boundary methods, *Annual Review of Fluid Mechanics* **37**, 239–261.

Moeng, C.-H.: 1984, A large-eddy-simulation model for the study of planetary boundary-layer turbulence, *Journal of the Atmospheric Sciences* **41**, 2052–2062.

Moeng, C.-H., Cotton, W. R., Bretherton, C., Chlond, A., Khairoutdinov, M., Krueger, S., Lewellen, W. S., MacVean, M. K., Pasquier, J. R. M., Rand, H. A., Siebesma, A. P., Stevens, B. and Sykes, R. I.: 1996, Simulation of the stratocumulus-topped planetary boundary layer: Intercomparison among different numerical codes, *Bulletin of the American Meteorological Society* **77**, 261–278.

Moeng, C.-H., Dudhia, J., Klemp, J. and Sullivan, P.: 2007, Examining two-way grid nesting for large eddy simulation of the PBL using the WRF model, *Monthly Weather Review* **135**, 2295–2311.

Moffatt, H. K.: 2002, G. K. Batchelor and the homogenization of turbulence, *Annual Review of Fluid Mechanics* **34**, 19–35.

Moin, P. and Mahesh, K.: 1998, Direct numerical simulation: A tool in turbulence research, *Annual Review of Fluid Mechanics* **30**, 539–578.

Moore, G.: 1965, Cramming more components into integrated circuits, *Electronics* **38**(8).

Morlet, J.: 1981, Sampling theory and wave propagation, *Proceedings of the 51st Annual International Meeting of the Society of Exploration Geophysicists*, Los Angeles (CA), USA.

Nakayama, A., Noda, H. and Maeda, K.: 2004, Similarity of instantaneous and filtered velocity fields in the near wall region of zero-pressure gradient boundary layer, *Fluid Dynamics Research* **35**, 299–321.

Nguyen, K., Oncley, S., Horst, T., Sullivan, P. and Tong, C.: 2010, Investigation of subgrid-scale turbulence in the atmospheric surface layer using AHATS field data, *Proceedings of the 63rd Annual Meeting of the APS Division of Fluid Mechanics*, Vol. 55, Long Beach, (CA) USA. `http://meetings.aps.org/link/BAPS.2010.DFD.EC.2`.

Nieuwstadt, F. T. M., Mason, P. J., Moeng, C.-H. and Schumann, U.: 1993, Large-eddy simulation of the convective boundary layer: A comparison of four computer codes, *in* F. Durst, B. E. Launder, R. Friedrich and F. W. Schmidt (eds), *Turbulent Shear Flows 8*, Springer, pp. 343–367.

Nobach, H., Tropea, C., Cordier, L., Bonnet, J. P., Delville, J., Lewalle, J., Farge, M., Schneider, K. and Adrian, R. J.: 2007, Review of some fundamentals of data processing, *in* C. Tropea, A. L. Yarin and J. F. Foss (eds), *Springer Handbook of Experimental Fluid Mechanics, Part D: Analysis and Post-Processing of Data*, Springer.

Oberkampf, W. L. and Barone, M. F.: 2006, Measures of agreement between computation and experiment: Validation metrics, *Journal of Computational Physics* **217**, 5–36.

Oberkampf, W. L. and Roy, C. J.: 2010, *Verification and Validation in Scientific Computing*, Cambridge University Press, Cambridge.

Oberkampf, W. L. and Trucano, T. G.: 2002, Verification and validation in computational fluid dynamics, *Progress in Aerospace Sciences* **38**, 209–272.

Obukhov, A. M.: 1946, Turbulence in an atmosphere with a non-uniform temperature, *Tr. Inst. Teor. Geofiz. Akad. Nauk. S.S.S.R.* **1**, 95–115. In Russian.

Obukhov, A. M.: 1962, Some specific features of atmospheric turbulence, *Journal of Geophysical Research* **67**, 3011–3014.

Obukhov, A. M.: 1971, Turbulence in an atmosphere with a non-uniform temperature, *Boundary-Layer Meteorology* **2**, 7–29. English translation of the 1946 Russian original paper.

Oikawa, S. and Meng, Y.: 1995, Turbulence characteristics and organized motion in a suburban roughness sublayer, *Boundary-Layer Meteorology* **74**, 289–312.

Oke, T. R.: 1976, The distinction between canopy and boundary-layer urban heat islands, *Atmosphere* **4**, 268–277.

Oke, T. R.: 1987, *Boundary Layer Climates*, 2nd edn, Routledge, London.

Oke, T. R.: 1988, The urban energy balance, *Progress in Physical Geography* **12**, 471–508.

Oke, T. R.: 2007, Siting and exposure of meteorological instruments at urban sites, *in* C. Borrego and A.-L. Norman (eds), *Air Pollution Modeling and its Application XVII*, Springer, chapter 66, pp. 615–631.

O'Neil, J. and Meneveau, C.: 1997, Subgrid-scale stresses and their modelling in a turbulent plane wake, *Journal of Fluid Mechanics* **349**, 253–293.

O'Neill, P. L., Nicolaides, D., Honnery, D. and Soria, J.: 2004, Autocorrelation functions and the determination of integral length with reference to experimental and numerical data, *Proceedings of the 15th Australasian Fluid Mechanics Conference*, The University of Sydney, Sydney, Australia.

Onsager, L.: 1945, The distribution of energy in turbulence, *Proceedings of the American Physical Society*, Vol. 68 of *Physical Review*, Columbia University, New York.

Oort, A. H. and Taylor, A.: 1969, On the kinetic energy spectrum near the ground, *Monthly Weather Review* **97**, 623–636.

OpenStreetMap: 2012, 12 Jan 2012 – 123map © Open Street Map Contributors Lizenz CC-BY-SA 2.0.

Oppenheim, A. V., Schafer, R. W. and Ruck, J. R.: 1999, *Discrete-Time Signal Processing*, 2nd edn, Prentice Hall, New Jersey.

Orszag, S. A.: 1970, Analytical theories of turbulence, *Journal of Fluid Mechanics* **41**, 363–386.

Orszag, S. A. and Patterson, G. S.: 1972, Numerical simulation of three-dimensional homogeneous isotropic turbulence, *Physical Review Letters* **28**, 76–79.

Panofsky, H. A.: 1974, The atmospheric boundary layer below 150 meters, *Annual Review of Fluid Mechanics* **6**, 147–177.

Panskus, H.: 2000, *Konzept zur Evaluation hindernisauflösender mikroskaliger Modelle und seine Anwendung auf das Modell MITRAS*, PhD thesis, University of Hamburg. In German.

Park, S.-B., Baik, J.-J., Raasch, S. and Letzel, M. O.: 2012, A large-eddy simulation study of thermal effects on turbulent flow and dispersion in and above a street canyon, *Journal of Applied Meteorology and Climatology* **51**, 829–841.

Pasquill, F. and Smith, F. B.: 1983, *Atmospheric Diffusion: Study of the dispersion of windborne material from industrial and other sources*, 3rd edn, John Wiley & Sons, New Jersey.

Patnaik, G., Boris, J. P., Grinstein, F. F., Iselin, J. P. and Hertwig, D.: 2012, Large scale urban simulations with FCT, *in* D. Kuzmin, R. Löhner and S. Turek (eds), *Flux-Corrected Transport: Principles, Algorithms, and Applications*, second edn, Scientific Computing, Springer, pp. 91–117.

Patnaik, G., Boris, J. P., Lee, M.-Y., Young Jr., T., Leitl, B., Harms, F. and Schatzmann, M.: 2009, Validation of an LES urban aerodynamics model with model and application specific wind tunnel data, *The Seventh Asia-Pacific Conference on Wind Engineering*, Taipei, Taiwan.

Patnaik, G., Grinstein, F. F., Boris, J. P., Young, T. R. and Parmhed, O.: 2007, Large-scale urban simulations, *in* F. F. Grinstein, L. G. Margolin and W. J. Rider (eds), *Implicit Large Eddy Simulation: Computing Turbulent Fluid Dynamics*, Cambridge University Press.

Patton, E. G., Horst, T. W., Sullivan, P. P., Lenschow, D. H. et al.: 2011, The canopy horizontal array turbulence study, *Bulletin of the American Meteorological Society* **92**, 593–611.

Peeck, C.: 2010, Vergleichende Bewertung verschiedener Auswertemethoden zur Bestimmung von Parametern der Windgrenzschicht am Hamburger Wettermast, *Student report*, University of Hamburg. In German.

Peeck, C.: 2011, Einfluss urbaner Rauigkeitsstrukturen auf das bodennahe Windfeld der Stadt Hamburg, Diplomarbeit, University of Hamburg. In German.

Perret, L., Delville, J., Manceau, R. and Bonnet, J. P.: 2006, Generation of turbulent inflow conditions for large eddy simulation from stereoscopic PIV measurements, *International Journal of Heat and Fluid Flow* **27**, 576–584.

Piomelli, U.: 1999, Large-eddy simulation: achievements and challenges, *Progress in Aerospace Sciences* **35**, 335–362.

Piomelli, U.: 2008, Wall-layer models for large-eddy simulation, *Progress in Aerospace Sciences* **44**, 437–446.

Piomelli, U.: 2010, Large-eddy simulation of turbulent flows: Introduction, *in* U. Piomelli, C. Benocci and J. van Beeck (eds), *Large eddy simulation and related techniques*, VKI-LS 2010-04, von Kármán Institute for Fluid Dynamics, Sint-Genesius-Rode, Belgium.

Piomelli, U., Cabot, W. H., Moin, P. and Lee, S.: 1991, Subgrid-scale backscatter in turbulent and transitional flows, *Physics of Fluids A* **3**, 1766–1771.

Piomelli, U., Moin, P. and Ferziger, J. H.: 1988, Model consistency in large eddy simulation of turbulent channel flows, *Physics of Fluids* **31**, 1884–1891.

Plate, E. J.: 1971, Aerodynamic characteristics of atmospheric boundary layers, *AEC Crit. Rev. Ser. TID-15465*, Technical Information Center, U.S. Department of Energy.

Plate, E. J.: 1999, Methods of investigating urban wind fields – physical models, *Atmospheric Environment* **33**, 3981–3989.

Pope, S. B.: 2000, *Turbulent Flows*, Cambridge University Press, Cambridge.

Pope, S. B.: 2004, Ten questions concerning the large-eddy simulation of turbulent flows, *New Journal of Physics* **6**, 1–24.

Porté-Agel, F., Meneveau, C. and Parlange, M. B.: 2000, A scale-dependent dynamic model for large-eddy simulation - Application to a neutral atmospheric boundary layer, *Journal of Fluid Mechanics* **415**, 261–284.

Porté-Agel, F., Parlange, M. B., Meneveau, C. and Eichinger, W. E.: 2001, A priori field study of the subgrid-scale heat fluxes and dissipation in the atmospheric surface layer, *Journal of the Atmospheric Sciences* **58**, 2673–2698.

Porté-Agel, F., Parlange, M. B., Meneveau, C., Eichinger, W. E. and Pahlow, M.: 2000a, Subgrid-scale dissipation in the atmospheric surface layer: Effects of stability and filter dimension, *Journal of Hydrometeorology* **1**, 75–87.

Powell, D. C. and Elderkin, C. E.: 1974, An investigation of the application of Taylor's hypothesis to atmospheric boundary layer turbulence, *Journal of the Atmospheric Sciences* **31**, 990–1002.

Pullen, J., Boris, J. P., Young, T., Patnaik, G. and Iselin, J.: 2005, A comparison of contaminant plume statistics from a Gaussian puff and urban CFD model for two large cities, *Atmospheric Environment* **39**, 1049–1068.

Ramamurthy, P., Pardyjak, E. R. and Klewicki, J. C.: 2007, Observations of the effects of atmospheric stability on turbulence statistics deep within an urban street canyon, *Journal of Applied Meteorology and Climatology* **46**, 2074–2085.

Ramond, A. and Millan, P.: 2000, Measurements and treatment of LDA signals, comparison with hot-wire signals, *Experiments in Fluids* **28**, 58–63.

Rasch, G.: 1980, *Probabilistic models for some intelligence and attainment tests*, expanded edn, University of Chicago Press.

Raupach, M. R.: 1981, Conditional statistics of Reynolds stress in rough-wall and smooth-wall turbulent boundary layers, *Journal of Fluid Mechanics* **108**, 363–382.

Raupach, M. R., Antonia, R. A. and Rajagopalan, S.: 1991, Rough-wall turbulent boundary layers, *Applied Mechanics Reviews* **44**, 1–25.

Raupach, M. R. and Thom, A. S.: 1981, Turbulence in and above plant canopies, *Annual Review of Fluid Mechanics* **13**, 97–129.

Reynolds, O.: 1895, On the dynamical theory of incompressible viscous fluids and the determination of the criterion, *Philosophical Transactions of the Royal Society of London, Series A* **186**, 123–164.

Reynolds, W.: 1990, The potential and limitations of direct and large eddy simulations, *in* J. Lumley (ed.), *Whither Turbulence? Turbulence at the Crossroads*, Vol. 357 of *Lecture Notes in Physics*, Springer, pp. 313–343.

Richardson, L. F.: 1922, *Weather Prediction by Numerical Process*, Cambridge University Press, Cambridge.

Roache, P. J.: 1998, *Verification and Validation in Computational Science and Engineering*, Hermosa Publishers, New Mexico.

Robinson, S. K.: 1991, Coherent motions in the turbulent boundary layer, *Annual Review of Fluid Mechanics* **23**, 601–639.

Rodi, W.: 1997, Comparison of LES and RANS calculations of the flow around bluff bodies, *Journal of Wind Engineering and Industrial Aerodynamics* **69-71**, 55–75.

Rogallo, R. S. and Moin, P.: 1984, Numerical simulation of turbulent flows, *Annual Review of Fluid Mechanics* **16**, 99–137.

Rotach, M. W.: 1993a, Turbulence close to a rough urban surface - Part I: Reynolds stresses, *Boundary-Layer Meteorology* **65**, 1–28.

Rotach, M. W.: 1993b, Turbulence close to a rough urban surface - Part II: Variances and gradients, *Boundary-Layer Meteorology* **66**, 75–92.

Rotach, M. W.: 1995, Profiles of turbulence statistics in and above an urban street canyon, *Atmospheric Environment* **29**, 1473–1486.

Roth, M.: 2000, Review of atmospheric turbulence over cities, *Quarterly Journal of the Royal Meteorological Society* **126**, 941–990.

Saathoff, P. J., Stathopoulos, T. and Dobrescu, M.: 1995, Effects of model scale in estimating pollutant dispersion near buildings, *Journal of Wind Engineering and Industrial Aerodynamics* **54/55**, 549–559.

Saddoughi, S. G. and Veeravalli, S. V.: 1994, Local isotropy in turbulent boundary layers at high Reynolds number, *Journal of Fluid Mechanics* **268**, 333–372.

Sagaut, P.: 2005, *Large Eddy Simulation for Incompressible Flows: An Introduction*, 3rd edn, Springer, Berlin, Heidelberg.

Salim, S. M., Buccolieri, R., Chan, A. and Di Sabatino, S.: 2011, Numerical simulation of atmospheric pollutant dispersion in an urban street canyon: Comparison between RANS and LES, *Journal of Wind Engineering and Industrial Aerodynamics* **99**, 103–113.

Schatzmann, M., Bächlin, W., Emeis, S., Kühlwein, J., Leitl, B., Müller, W. J., Schäfer, K. and Schlünzen, H.: 2006, Development and validation of tools for the implementation of European air quality policy in Germany (Project VALIUM), *Atmospheric Chemistry and Physics* **6**, 3077–3083.

Schatzmann, M. and Britter, R.: 2011, Quality assurance and improvement of micro-scale meteorological models, *International Journal of Environment and Pollution* **44**, 139–146.

Schatzmann, M. and Leitl, B.: 2002, Validation and application of obstacle-resolving urban dispersion models, *Atmospheric Environment* **36**, 4811–4821.

Schatzmann, M. and Leitl, B.: 2011, Issues with validation of urban flow and dispersion CFD models, *Journal of Wind Engineering and Industrial Aerodynamics* **99**, 169–186.

Schatzmann, M., Olesen, H. and Franke, J. (eds): 2010, *COST 732 model evaluation case studies: Approaches and results*, COST Action 732, University of Hamburg, Germany. ISBN 3-00-018312-4.

Schlatter, P. and Örlü, R.: 2010, Assessment of direct numerical simulation data of turbulent boundary layers, *Journal of Fluid Mechanics* **659**, 116–126.

Schlegel, F., Stiller, J., Bienert, A., Maas, H.-G., Queck, R. and Bernhofer, C.: 2012, Large-eddy simulation of inhomogeneous canopy flows using high resolution terrestrial laser scanning data, *Journal of Fluid Mechanics* **142**, 223–243.

Schlünzen, K. H.: 1997, On the validation of high-resolution atmospheric mesoscale models, *Journal of Wind Engineering and Industrial Aerodynamics* **67/68**, 479–492.

Schmidt, H. and Schumann, U.: 1989, Coherent structure of the convective boundary-layer derived from large-eddy simulations, *Journal of Fluid Mechanics* **200**, 511–562.

Schneider, K. and Vasilyev, O. V.: 2010, Wavelet methods for computational fluid dynamics, *Annual Review of Fluid Mechanics* **42**, 473–503.

Schultz, A. M.: 2008, *Systematische Windkanaluntersuchungen zur Evaluierung von Parametrisierungsansätzen für die städtische Rauigkeitsschicht*, PhD thesis, University of Hamburg. In German.

Schumann, U.: 1975, Subgrid scale model for finite difference simulations of turbulent flows in plane channels and annuli, *Journal of Computational Physics* **18**, 376–404.

Schumann, U.: 1995, Stochastic backscatter of turbulence energy and scalar variance by random subgrid-scale fluxes, *Proceedings: Mathematical and Physical Sciences* **451**, 293–318.

Shaw, R. H. and Schumann, I.: 1992, Large-eddy simulation of turbulent flow above and within a forest, *Boundary-Layer Meteorology* **61**, 47–64.

Shaw, R. H., Tavangar, J. and Ward, D. P.: 1983, Structure of Reynolds stress in a canopy, *Journal of Climate and Applied Meteorology* **22**, 1922–1931.

Sherwin, S. J. and Blackburn, H. M.: 2005, Three-dimensional instabilities and transition of steady and pulsatile axisymmetric stenotic flows, *Journal of Fluid Mechanics* **533**, 297–327.

Silverman, B. W.: 1986, *Density Estimation for Statistics and Data Analysis*, Chapman & Hall, London.

Simiu, E. and Scanlan, R. H.: 1986, *Wind Effects on Structures*, 2nd edn, John Wiley & Sons, New Jersey.

Smagorinsky, J.: 1963, General circulation experiments with the primitive equations: I. The basic experiment, *Monthly Weather Review* **91**, 99–164.

Smedman-Högström, A.-S. and Högström, U.: 1975, Spectral gap in surface-layer measurements, *Journal of the Atmospheric Sciences* **32**, 340–350.

Snyder, W. H.: 1972, Similarity criteria for the application of fluid models to the study of air pollution meteorology, *Boundary-Layer Meteorology* **3**, 113–134.

Snyder, W. H.: 1981, Guideline for fluid modeling of atmospheric diffusion, *Report EPA-600/8-81-009*, U.S. Environmental Protection Agency, Research Triangle Park (NC), USA.

Sorbjan, Z.: 1986, On similarity in the atmospheric boundary layer, *Boundary-Layer Meteorology* **34**, 377–397.

Spalart, P. R.: 2009, Detached-eddy simulation, *Annual Review of Fluid Mechanics* **41**, 181–202.

Sreenivasan, K. R. and Antonia, R. A.: 1997, The phenomenology of small-scale turbulence, *Annual Review of Fluid Mechanics* **29**, 435–472.

Sreenivsan, K. R.: 1995, On the universality of the Kolmogorov constant, *Physics of Fluids* **7**, 2778–2784.

Standen, N. M.: 1972, A spire array for generating thick turbulent shear layers for natural wind simulation in wind tunnels, *Report LTR-LA-94*, National Aeronautical Establishment, Canada.

Stein, A. F. and Wyngaard, J. C.: 2001, Fluid modeling and the evaluation of inherent uncertainty, *Journal of Applied Meteorology* **40**, 1769–1774.

Stull, R. B.: 1988, *An Introduction to Boundary Layer Meteorology*, Kluwer Academic Publishers, Dordrecht.

Stull, R. B.: 2000, *Meteorology for Scientist and Engineers*, 2nd edn, Brooks/Cole Thomson Learning, Pacific Grove (CA).

Sullivan, P., Moeng, C.-H., Stevens, B., Lenschow, D. H. and Mayor, S. D.: 1998, Structure of the entrainment zone capping the convective atmospheric boundary layer, *Journal of the Atmospheric Sciences* **55**, 3042–3064.

Sullivan, P. P., Horst, T. W., Lenschow, D. H., Moeng, C.-H. and Weil, J. C.: 2003, Structure of subfilter-scale fluxes in the atmospheric surface layer with application to large-eddy simulation modelling, *Journal of Fluid Mechanics* **482**, 101–139.

Sullivan, P. P., McWilliams, J. C. and Moeng, C.-H.: 1996, A grid nesting method for large-eddy simulation of planetary boundary-layer flows, *Boundary-Layer Meteorology* **80**, 167–202.

Sullivan, P. P. and Patton, E. G.: 2011, The effect of mesh resolution on convective boundary layer statistics and structures generated by large-eddy simulation, *Journal of the Atmospheric Sciences* **68**, 2395–2415.

Takimoto, H., Sato, A., Barlow, J., Moriwaki, R., Inagaki, A., Onomura, S. and Kanda, M.: 2011, Particle image velocimetry measurements of turbulent flow within outdoor and indoor urban scale models and flushing motions in urban canopy layers, *Boundary-Layer Meteorology* **140**, 295–314.

Tamura, T.: 2008, Towards practical use of LES in wind engineering, *Journal of Wind Engineering and Industrial Aerodynamics* **96**, 1451–1471.

Taylor, G. I.: 1935, Statistical theory of turbulence. Parts I-III, *Proceedings of the Royal Society of London. Series A, Mathematical and Physical Sciences* **151**, 421–464.

Taylor, G. I.: 1938, The spectrum of turbulence. Part I., *Proceedings of the Royal Society of London. Series A, Mathematical and Physical Sciences* **164**, 476–490.

Taylor, G. I.: 1970, Some early ideas about turbulence, *Journal of Fluid Mechanics* **41**, 3–11.

Tennekes, H. and Lumley, J. L.: 1972, *A First Course in Turbulence*, MIT Press, Cambridge (MA).

Thomas, C. and Foken, T.: 2005, Detection of long-term coherent exchange over spruce forest using wavelet analysis, *Theoretical and Applied Climatology* **80**, 91–104.

Tominaga, Y. and Stathopoulos, T.: 2011, CFD modeling of pollution dispersion in a street canyon: Comparison between LES and RANS, *Journal of Wind Engineering and Industrial Aerodynamics* **99**, 340–348.

Tominaga, Y. and Stathopoulos, T.: 2012, CFD modeling of pollution dispersion in building array: Evaluation of turbulent scalar flux modeling in RANS model using LES results, *Journal of Wind Engineering and Industrial Aerodynamics* **104-106**, 484–491.

Tong, C., Wyngaard, J. C. and Brasseur, J. G.: 1999, Experimental study of the subgrid-scale stresses in the atmosperic surface layer, *Journal of the Atmospheric Sciences* **56**, 2277–2292.

Tong, C., Wyngaard, J. C., Khanna, S. and Brasseur, J. G.: 1998, Resolvable- and subgrid-scale measurements in the atmospheric surface layer: Technique and issues, *Journal of the Atmospheric Sciences* **55**, 3114–3126.

Torrence, C. and Compo, G. P.: 1998, A practical guide to wavelet analysis, *Bulletin of the American Meteorological Society* **79**, 61–78.

Townsend, A. A.: 1956, *The Structure of Turbulent Shear Flow*, Cambridge University Press, Cambridge.

Tropea, C.: 1995, Laser Doppler anemometry: recent developments and future challenges, *Measurement Science and Technology* **6**, 605–619.

Tullio, M. D. D., Cristallo, A., Balaras, E. and Verzicco, R.: 2009, Direct numerical simulation of the pulsatile flow through an aortic bileaflet mechanical heart valve, *Journal of Fluid Mechanics* **622**, 259–290.

Uehara, K., Murakami, S., Oikawa, S. and Wakamatsu, S.: 2000, Wind tunnel experiments on how thermal stratification affects flow in and above urban street canyons, *Atmospheric Environment* **34**, 1553–1562.

Van der Hoven, I.: 1957, Power spectrum of horizontal wind speed in the frequency range from 0.0007 to 900 cycles per hour, *Journal of Meteorology* **14**, 160–164.

VDI: 2000, Environmental meteorology – Physical modelling of flow and dispersion processes in the atmospheric boundary layer – Application of wind tunnels, *Guideline VDI-3783-12*, Verein Deutscher Ingenieure (The Association of German Engineers), Beuth Verlag, Berlin.

VDI: 2005, Environmental meteorology – Prognostic microscale wind field models – Evaluation for flow around buildings and obstacles, *Guideline VDI-3783-9*, Verein Deutscher Ingenieure (The Association of German Engineers), Beuth Verlag, Berlin.

Voller, V. R. and Porté-Agel, F.: 2002, Moore's law and numerical modeling, *Journal of Computational Physics* **179**, 698–703.

von Weizsäcker, C. F.: 1948, Das Spektrum der Turbulenz bei grossen Reynoldsschen Zahlen, *Zeitschrift für Physik* **124**, 614–627. In German.

Walko, R. L., Cotton, W. R. and Pielke, R. A.: 1992, Large-eddy simulations of the effects of hilly terrain on the convective boundary layer, *Boundary-Layer Meteorology* **58**, 133–150.

Wallace, J. M., Eckelmann, H. and Brodkey, R.: 1972, The wall region in turbulent shear flow, *Journal of Fluid Mechanics* **53**, 39–48.

Werner, H. and Wengle, H.: 1993, Large-eddy simulation of turbulent flow over and around a cube in a plane channel, *in* F. Durst, R. Friedrich, B. Launder, F. Schmidt, U. Schumann and J. Whitelaw (eds), *Selected Papers from the 8th Symposium on Turbulent Shear Flows*, Springer, pp. 155–168.

Wieringa, J.: 1996, Does representative wind information exist?, *Journal of Wind Engineering and Industrial Aerodynamics* **65**, 1–12.

Wilks, D. S.: 2005, *Statistical Methods in the Atmospheric Sciences*, 2nd edn, Academic Press, Waltham (MA).

Willmarth, W. W. and Lu, S. S.: 1972, Structure of the Reynolds stress near the wall, *Journal of Fluid Mechanics* **55**, 65–92.

Winter, A. R., Graham, L. J. W. and Bremhorst, K.: 1991, Effects of time scales on velocity bias in LDA measurements using sample and hold processing, *Experiments in Fluids* **11**, 147–152.

WMO: 2008, Guide to meteorological instruments and methods of observation, *Guideline WMO-No. 8 (7th edition)*, World Meteorological Organization, Geneva, Switzerland.

Wyngaard, J. C.: 1992, Atmospheric turbulence, *Annual Review of Fluid Mechanics* **24**, 205–233.

Wyngaard, J. C.: 2004, Toward numerical modeling in the terra incognita, *Journal of the Atmospheric Sciences* **61**, 1816–1826.

Wyngaard, J. C.: 2010, *Turbulence in the Atmosphere*, Cambridge University Press, Cambridge.

Wyngaard, J. C., Bach, W. D., Burk, S., Cotton, W. R., Ferziger, J. H., Hanna, S. R., Moin, P., Ohmstede, W. and Weil, J. C.: 1984, Large-eddy simulation: Guidelines for its application to planetary boundary layer research, *Report under Contract No. 0804*, The U.S. Army Research Office, Research Park Triangle (NC), USA.

Wyngaard, J. C. and Clifford, S. F.: 1977, Taylor's hypothesis and high-frequency turbulence spectra, *Journal of the Atmospheric Sciences* **34**, 922–929.

Wyngaard, J. C. and Coté, O. R.: 1972, Cospectral similarity in the atmospheric surface layer, *Quarterly Journal of the Royal Meteorological Society* **98**, 590–603.

Wyngaard, J. C. and Peltier, L. J.: 1996, Experimental micrometeorology in an era of turbulence simulation, *Boundary-Layer Meteorology* **78**, 71–86.

Wyngaard, J. C. and Tennekes, H.: 1970, Measurements of the small-scale structure of turbulence at moderate Reynolds numbers, *Physics of Fluids* **13**, 1962–1969.

Xie, Z.-T. and Castro, I. P.: 2006, LES and RANS for turbulent flow over arrays of wall-mounted obstacles, *Flow, Turbulence and Combustion* **76**, 291–312.

Xie, Z.-T. and Castro, I. P.: 2008, Efficient generation of inflow conditions for large eddy simulation of street-scale flow, *Flow, Turbulence and Combustion* **81**, 449–470.

Xie, Z.-T. and Castro, I. P.: 2009, Large-eddy simulation for flow and dispersion in urban streets, *Atmospheric Environment* **43**, 2174–2185.

Xie, Z.-T., Hayden, P., Voke, P. R. and Robins, A. G.: 2004, Large-eddy simulation of dispersion: comparison between elevated and ground-level sources, *Journal of Turbulence* **5**, N31.

Yaglom, A. M.: 1987, *Correlation Theory of Stationary and Related Random Functions I: Basic Results*, Springer.

Yee, E. and Biltoft, C. A.: 2004, Concentration fluctuation measurements in a plume dispersing through a regular array of obstacles, *Boundary-Layer Meteorology* **111**, 363–415.

Zabusky, N. J.: 1981, Computational synergetics and mathematical innovation, *Journal of Computational Physics* **43**, 195–249.

Zabusky, N. J.: 1984, Computational synergetics, *Physics Today* **37**, 36–46.

Zalesak, S. T.: 1979, Fully multidimensional flux-corrected transport algorithms for fluids, *Journal of Computational Physics* **31**, 335–362.

Zhou, Y.: 1993, Interacting scales and energy transfer in isotropic turbulence, *Physics of Fluids A* **5**, 2511–2524.

List of Figures

List of Tables